SYNTHESIS OF NOVEL HYDROGELS WITH UNIQUE MECHANICAL PROPERTIES

EDITED BY: Yi Cao, Kerstin G. Blank and Fei Sun
PUBLISHED IN: Frontiers in Chemistry

frontiers Research Topics

frontiers

ISSN 1664-8714
ISBN 978-2-88966-259-3
DOI 10.3389/978-2-88966-259-3

About Frontiers

Frontiers is more than just an open-access publisher of scholarly articles: it is a pioneering approach to the world of academia, radically improving the way scholarly research is managed. The grand vision of Frontiers is a world where all people have an equal opportunity to seek, share and generate knowledge. Frontiers provides immediate and permanent online open access to all its publications, but this alone is not enough to realize our grand goals.

Frontiers Journal Series

The Frontiers Journal Series is a multi-tier and interdisciplinary set of open-access, online journals, promising a paradigm shift from the current review, selection and dissemination processes in academic publishing. All Frontiers journals are driven by researchers for researchers; therefore, they constitute a service to the scholarly community. At the same time, the Frontiers Journal Series operates on a revolutionary invention, the tiered publishing system, initially addressing specific communities of scholars, and gradually climbing up to broader public understanding, thus serving the interests of the lay society, too.

Dedication to Quality

Each Frontiers article is a landmark of the highest quality, thanks to genuinely collaborative interactions between authors and review editors, who include some of the world's best academicians. Research must be certified by peers before entering a stream of knowledge that may eventually reach the public - and shape society; therefore, Frontiers only applies the most rigorous and unbiased reviews.
Frontiers revolutionizes research publishing by freely delivering the most outstanding research, evaluated with no bias from both the academic and social point of view. By applying the most advanced information technologies, Frontiers is catapulting scholarly publishing into a new generation.

What are Frontiers Research Topics?

Frontiers Research Topics are very popular trademarks of the Frontiers Journals Series: they are collections of at least ten articles, all centered on a particular subject. With their unique mix of varied contributions from Original Research to Review Articles, Frontiers Research Topics unify the most influential researchers, the latest key findings and historical advances in a hot research area! Find out more on how to host your own Frontiers Research Topic or contribute to one as an author by contacting the Frontiers Editorial Office: researchtopics@frontiersin.org

SYNTHESIS OF NOVEL HYDROGELS WITH UNIQUE MECHANICAL PROPERTIES

Topic Editors:
Yi Cao, Nanjing University, China
Kerstin G. Blank, Max Planck Institute of Colloids and Interfaces, Germany
Fei Sun, Hong Kong University of Science and Technology, Hong Kong

Citation: Cao, Y., Blank, K. G., Sun, F., eds. (2020). Synthesis of Novel Hydrogels with Unique Mechanical Properties. Lausanne: Frontiers Media SA.
doi: 10.3389/978-2-88966-259-3

Table of Contents

frontiers in Chemistry

EDITORIAL
published: 20 October 2020
doi: 10.3389/fchem.2020.595392

Editorial: Synthesis of Novel Hydrogels With Unique Mechanical Properties

Ying Li[1], *Kerstin G. Blank*[2], *Fei Sun*[3] *and Yi Cao*[4,5,6,7]*

[1] *Institute of Advanced Materials and Flexible Electronics (IAMFE), School of Chemistry and Materials Science, Nanjing University of Information Science and Technology, Nanjing, China,* [2] *Mechano(bio)chemistry, Max Planck Institute of Colloids and Interfaces, Potsdam, Germany,* [3] *Department of Chemical and Biological Engineering, The Hong Kong University of Science and Technology, Kowloon, China,* [4] *National Laboratory of Solid State Microstructures, Department of Physics, Nanjing University, Nanjing, China,* [5] *Institute for Brain Sciences, Nanjing University, Nanjing, China,* [6] *Chemistry and Biomedicine Innovation Center, Nanjing University, Nanjing, China,* [7] *Shenzhen Research Institute of Nanjing University, Shenzhen, China*

Keywords: hydrogel, mechanical property, network topology, crosslinking, biomaterials

Editorial on the Research Topic

Synthesis of Novel Hydrogels With Unique Mechanical Properties

Hydrogels are wet polymeric or supramolecular networks showing properties of both solid and liquid. They are promising materials for a broad range of applications, including cell culturing (Caliari and Burdick, 2016), tissue engineering (Vedadghavami et al., 2017), wound dressing (Ghobril and Grinstaff, 2015), controlled drug release (Li and Mooney, 2016), flexible electronics (Yang and Suo, 2018), and soft robotics (Liu et al., 2020), just to name a few. In many of these applications, the mechanical properties of hydrogels play an important role and have gathered increasing attention. However, despite considerable progress and increasing numbers of papers published in recent years, it remains challenging to formulate hydrogels with controlled mechanical properties to meet diverse applications.

To provide a forum to discuss the latest researches in this field, we created a Research Topic on "Synthesis of Novel Hydrogels with Unique Mechanical Properties." In this Research Topic, we have published 13 papers, including 12 research articles, and one review. These papers highlight several emerging trends in this direction.

First, biomacromolecules are widely used as the building blocks to modulate the mechanical properties of hydrogels (Li et al., 2020). For example, Xiang et al. showed that photo-hardening and photo-weakening hydrogels can be engineered using a visible light-cleavable fluorescent protein, PhoCl, designed by the Campbell group (Zhang et al., 2017). The mechanical properties of the hydrogels are altered based on photo-induced bond rupture and the subsequent unfolding of the proteins. Lu et al. reported that hydrogels with high mechanical strength can be prepared by incorporating albumin in the hydrogel network. They introduced a heat-processing approach to partially unfold and aggregate albumin, which added abundant physical crosslinks to the chemically crosslinked hydrogels. The hybrid crosslinking mechanism is responsible for the high compressive and tensile strength of the resulting hydrogels. Another interesting example is the work by Cui et al. It is shown that hybrid hydrogels made of DNA and synthetic polymers can serve as recyclable gene carriers for cell-free protein synthesis. To achieve optimal production yield, the hydrogels should be neither too soft nor too hard. Soft hydrogels are easily damaged by the shaking forces during protein production. On the other hand, hard hydrogels exhibited dense network structures, which slowed down the diffusion of the reactants and lowered the efficiency of protein production.

Edited by:
Pellegrino Musto, National Research Council (CNR), Italy

Reviewed by:
Hyunwoo Yuk, Massachusetts Institute of Technology, United States

***Correspondence:**
Yi Cao
caoyi@nju.edu.cn

Specialty section:
This article was submitted to Polymer Chemistry, a section of the journal Frontiers in Chemistry

Received: *16 August 2020*
Accepted: *10 September 2020*
Published: *20 October 2020*

Citation:
Li Y, Blank KG, Sun F and Cao Y (2020) Editorial: Synthesis of Novel Hydrogels With Unique Mechanical Properties. Front. Chem. 8:595392. doi: 10.3389/fchem.2020.595392

Second, crosslinking chemistry is emphasized for hydrogel preparation. To incorporate new building blocks, such as proteins, novel hydrogel-crosslinking methods have been developed. Camp et al. reported an optimized ruthenium-catalyzed photo-crosslinking strategy to trigger the formation of dityrosine in artificial proteins in a controllable fashion, yielding hydrogels of predictable mechanical strength. Using the same catalyst, Farajollahi et al. showed that the ruthenium-mediated photoreaction led to unexpected disulfide metathesis in minicollagen. The obtained hydrogels were crosslinked by redox sensitive disulfide bonds and their mechanical properties were modulable and reconfigurable. In parallel to the photo-chemistry approach, enzyme mediated crosslinking is also biocompatible and controllable, making the resulting hydrogels suitable for biomedical applications. Shen et al. reported a novel dual enzyme strategy to fabricate hydrogels of tunable strength. They employed a dual enzyme system, HRP@GOx, with distinct catalytic activities for orthogonal reactions. In a fast reaction, tyrosine-modified chondroitin sulfate was crosslinked to form the first network. In a slow polymerization of various monomers, a second network was formed. Temporally decoupling the two-reaction kinetics allowed the hydrogel to be easily fabricated using 3D printing while further polymerization allowed for tuning the mechanical properties. This new technique is expected to find broad biomedical applications.

Third, it is increasingly realized that hydrogel network topology, other than the specific crosslinking chemistry, is important for the mechanical properties of hydrogels. Grad et al. showed that the same crosslink can lead to distinct viscoelastic behaviors, depending on the structure and organization of the polymer to be crosslinked. A self-assembled semi-flexible fibrous network displayed a relaxation time almost two orders of magnitude slower than a flexible random-coil network of four-armed polyethylene glycol. It is proposed that the distinct stress-relaxation behaviors of the two systems are determined by their different network topologies. In the random-coil network, crosslink dissociation causes immediate relaxation while in the fibrous network multiple bonds need to dissociate to allow network relaxation. This shows that it is possible to decouple the microscopic and macroscopic dynamics of hydrogels using different network topology.

Fourth, computational studies can provide tremendous insights. Using molecular dynamics simulations, Zidek et al. investigated hydrogels made of linear chain connected micelles. It was shown that the micelles transform into fibrils upon deformation and that such evolution largely depends on strain rates. Their model also suggested a set of conditions in which the micelle-to-fibril transition is favorable, which may inspire future experimental studies. Moreover, simulations using mesoscopic models can bridge the conformational change of polymer chains at the microscopic level to the deformation of hydrogel at the macroscopic level. To this end, Lei et al. constructed coarse-grained bead-spring models for hydrogels made of a single network of polyacrylamide. They studied the strain and fracture behavior using dissipative particle dynamics. It is shown that the simulations adequately replicate the hyperelasticity and the viscoelasticity of the hydrogels observed experimentally. It was further possible to predict the fracture stretch, based on the fracture stretch of C-C bonds. It is interesting to see whether this model can be used to also predict the mechanical behavior of more complex network structures.

Last but not least, the connection of diverse mechanical properties with specific applications has been exemplified in numerous systems. Malik et al. optimized chitosan/xanthan gum hybrid hydrogels for antiviral drug delivery. Kong et al. reported the synthesis of alginate fibroid hydrogels crosslinked by dynamic ionic interactions. These hydrogels were suitable for the removal of heavy metal ions in water. Zhang et al. demonstrated that metal ion crosslinked organohydrogels can be fabricated in water-cryoprotectant binary solvent. The hydrogels exhibited high toughness and function properly at extreme temperatures as low as -20°C and -45°C. They are promising for applications in harsh temperature conditions. The mechanical properties of hydrogels are obviously important for tissue engineering. Bao et al. summarized the recent development of hydrogels made of natural polymers for cartilage repair and regeneration. Clearly, the mechanical properties of the hydrogels played a pivotal role in this direction.

In summary, this Research Topic highlights the importance of mechanical properties for the development of specific hydrogel applications and provides experimental methods and theoretical frameworks to design hydrogels with controllable and predictable mechanical properties.

AUTHOR CONTRIBUTIONS

All authors listed have made a substantial, direct and intellectual contribution to the work, and approved it for publication.

FUNDING

YC thanked the National Natural Science Foundation of China (11674153) and the Basic Research Project of Science and Technology Plan of Shenzhen (JCYJ20170818110643669) for financial support.

ACKNOWLEDGMENTS

We thank all the authors, reviewers and editors who contributed to this Research Topic.

REFERENCES

Caliari, S. R., and Burdick, J. A. (2016). A practical guide to hydrogels for cell culture. *Nat. Methods* 13, 405–414. doi: 10.1038/nmeth.3839

Ghobril, C., and Grinstaff, M. W. (2015). The chemistry and engineering of polymeric hydrogel adhesives for wound closure: a tutorial. *Chem. Soc. Rev.* 44, 1820–1835. doi: 10.1039/C4CS00332B

Li, J., and Mooney, D. J. (2016). Designing hydrogels for controlled drug delivery. *Nat. Rev. Mater.* 1:16071. doi: 10.1038/natrevmats.2016.71

Li, Y., Xue, B., and Cao, Y. (2020). 100th Anniversary of Macromolecular Science Viewpoint: Synthetic Protein Hydrogels. *ACS Macro Lett.* 9, 512–524. doi: 10.1021/acsmacrolett.0c00109

Liu, X., Liu, J., Lin, S., and Zhao, X. (2020). Hydrogel machines. *Mater. Today* 36, 102–124. doi: 10.1016/j.mattod.2019.12.026

Vedadghavami, A., Minooei, F., Mohammadi, M. H., Khetani, S., Rezaei Kolahchi, A., Mashayekhan, S., et al. (2017). Manufacturing of hydrogel biomaterials with controlled mechanical properties for tissue engineering applications. *Acta Biomater.* 62, 42–63. doi: 10.1016/j.actbio.2017.07.028

Yang, C., and Suo, Z. (2018). Hydrogel ionotronics. *Nat. Rev. Mater.* 3, 125–142. doi: 10.1038/s41578-018-0018-7

Zhang, W., Lohman, A. W., Zhuravlova, Y., Lu, X., Wiens, M. D., Hoi, H., et al. (2017). Optogenetic control with a photocleavable protein, PhoCl. *Nat. Methods* 14, 391–394. doi: 10.1038/nmeth.4222

Conflict of Interest: The authors declare that the research was conducted in the absence of any commercial or financial relationships that could be construed as a potential conflict of interest.

frontiers in Chemistry

ORIGINAL RESEARCH
published: 10 January 2020
doi: 10.3389/fchem.2019.00905

Ion-Induced Synthesis of Alginate Fibroid Hydrogel for Heavy Metal Ions Removal

Chuncai Kong[1], *Xueqi Zhao*[1], *Yingju Li*[1], *Sen Yang*[1], *Yong Mei Chen*[2]* *and Zhimao Yang*[1]*

[1] School of Science, MOE Key Laboratory for Non-Equilibrium Synthesis and Modulation of Condensed Matter, Xi'an Jiaotong University, Xi'an, China, [2] College of Bioresources Chemical and Materials Engineering, Shaanxi University of Science & Technology, Key Laboratory of Leather Cleaner Production, China National Light Industry, Xi'an, China

Design and synthesis of environmentally friendly adsorbents with high adsorption capacities are urgently needed to control pollution of water resources. In this work, a calcium ion-induced approach was used to synthesize sodium alginate fibroid hydrogel (AFH). The as-prepared AFH has certain mechanical strength, and the mechanical strength is enhanced especially after the adsorption of heavy metal ions, which is very convenient for the recovery. AFH exhibited excellent adsorption performances for Cu^{2+}, Cd^{2+}, and Pb^{2+} ions and displayed very high saturated adsorption capacities (Qe) of 315.92 $mg{\cdot}g^{-1}$ (Cu^{2+}), 232.35 $mg{\cdot}g^{-1}$ (Cd^{2+}), and 465.22 $mg{\cdot}g^{-1}$ (Pb^{2+}) with optimized pH values (3.0–4.0) and temperature (303 K). The study of isotherms and kinetics indicated that adsorption processes of heavy metal ions fitted well with the pseudo-second-order kinetics model and the Langmuir model. Pb^{2+} was found to have the strongest competitiveness among the three heavy metal ions. Thus, AFH has great application prospects in the field of heavy metal ions removing from wastewater.

Keywords: fibroid hydrogel, sodium alginate, heavy metal ions removal, adsorption kinetics, adsorption isotherms

OPEN ACCESS

Edited by:
Yi Cao,
Nanjing University, China

Reviewed by:
Kai Tao,
Tel Aviv University, Israel
Xiaoying Lin,
University of Maryland, College Park, United States

***Correspondence:**
Yong Mei Chen
chenyongmei@sust.edu.cn
Zhimao Yang
zmyang@mail.xjtu.edu.cn

Specialty section:
This article was submitted to Polymer Chemistry, a section of the journal Frontiers in Chemistry

Received: *01 December 2019*
Accepted: *16 December 2019*
Published: *10 January 2020*

Citation:
Kong C, Zhao X, Li Y, Yang S, Chen YM and Yang Z (2020) Ion-Induced Synthesis of Alginate Fibroid Hydrogel for Heavy Metal Ions Removal. Front. Chem. 7:905. doi: 10.3389/fchem.2019.00905

INTRODUCTION

With rapid global development, water contamination caused by industrialization and a growing population has been an urgent problem that must be solved. Toxic heavy metal ions in wastes derived from the emission load of industry are the most harmful contaminants to human beings (Chen et al., 2009). Heavy metal elements are generally highly toxic, refractory, and tend to accumulate over time, causing great harm to human health. For instance, trace amounts of cadmium (Cd^{2+}) in the human body eventually accumulate and causes various diseases related to the lungs, bone, kidneys, liver, immune system, and reproductive organs (McDowell, 2003). Because of its importance in enzyme synthesis, bone and tissue development Copper (Cu) is an indispensable trace element in the human body. However, divalent copper (Cu^{2+}) ion is carcinogenic and toxic, resulting in a variety of complications and liver cirrhosis once it accumulates in the viscera (Bilal et al., 2013). Lead (Pb^{2+}) is non-biodegradable and tends to accumulate in living tissues, leading to various kinds of disorders and diseases (Chen et al., 2010). Thus, it is urgent to solve the problem of heavy metal ions contamination of water.

To date, four common methods (including physical, chemical, physiochemical, and biological) have been developed to remove heavy metal ions from wastewater (Wang et al., 2003; Kurniawan et al., 2006; Wang and Chen, 2009; Fu and Wang, 2011; Chukwuemeka-Okorie et al., 2018).

Physical methods include evaporation and dilution. Chemical methods mainly contain chemical precipitation method and electrolysis method. Biological methods are those in which microorganisms are used for degradation. Physicochemical methods are processes like adsorption, ion reduction, and ion exchange. Adsorption has the advantages of low cost, easy to obtain, availability, and environmentally friendly, thus, it has been widely applied in industrial effluent treatments. Hence, many kinds of adsorbents have been designed and synthesized (including silica, magnetic particles, grapheme, and hydrogel) to meet the demands for water treatment (Liu et al., 2013; Wang et al., 2015; Hayati et al., 2017; Zhao et al., 2017; Alizadehgiashi et al., 2018; Qi et al., 2019).

Hydrogel is one of the excellent adsorbents that has three-dimensional (3D) hydrophilic polymer networks and is capable of absorbing ions and retaining water within their networks. Removal of heavy metal ions using hydrogel involves the adsorption through interactions with functional groups dangling on polymer chains such as carboxyl, hydroxyl and amino groups (Kaşgöz et al., 2003; Zhou et al., 2018). Luo reported a tough polyampholyte/graphene oxide hydrogel adsorbent for the removal of Pb^{2+} (216.1 $mg{\cdot}g^{-1}$) and Cd^{2+} (153.8 $mg{\cdot}g^{-1}$) ions (Zhou et al., 2016). Wang reported a freeze-thaw method to synthesize PVA/CMC hydrogels with a high degree of crosslinking, and the hydrogels showed excellent adsorption capacities for heavy metal ions including Ag^{+} (8.4 $mg{\cdot}g^{-1}$), Cu^{2+} (5.5 $mg{\cdot}g^{-1}$), Ni^{2+} (6.0 $mg{\cdot}g^{-1}$), and Zn^{2+} (5.3 $mg{\cdot}g^{-1}$) (Wang and Wang, 2016). Though lots of efforts have been made to prepare various hydrogel-based composites for the removing of heavy metal ions, facile design, and synthesis of environment friendly hydrogels with high adsorption capacities are still urgently needed.

For this purpose, we developed a calcium ion (Ca^{2+})-induced crosslinking approach to fabricate sodium alginate fibroid hydrogel (AFH). AFH was used for the removal of Cd^{2+}, Cu^{2+}, and Pb^{2+} ions and the effects of temperature, adsorption time, pH values, and interfering ions on the adsorption capacity and removal ratio were systematically investigated. The optimized conditions of AFH for adsorption behaviors were analyzed via adsorption kinetics and adsorption isotherms. AFH was capable of efficiently removing heavy metal ions and had very high saturated adsorption capacities (Q_e) for Cu^{2+} (315.92 $mg{\cdot}g^{-1}$), Cd^{2+} (232.35 $mg{\cdot}g^{-1}$), and Pb^{2+} (465.22 $mg{\cdot}g^{-1}$) ions. The easily prepared AFH with high adsorption performances for various heavy metal ions has great potential in the controlling pollution of water resources.

MATERIALS AND METHODS

Materials

Sodium hydroxide (NaOH), calcium sulfate ($CaSO_4$), lead nitrate [$Pb(NO_3)_2$], cupric nitrate [$Cu(NO_3)_2{\bullet}3H_2O$], calcium nitrate [$Cd(NO_3)_2{\bullet}4H_2O$], Sodium alginate (SA), and hydrochloric acid (HCl) were obtained from Aladdin Reagent. All these chemicals were used without further purification.

Methods

Preparation of Alginate Fibroid Hydrogel

In a typical synthesis of AFH, 5.0 g of SA was added to 95.0 mL of deionized water at room temperature and stirred for 5 h to produce a polymer solution. A 10 mL injection syringe (Φ16 mm) was then used to inject the as-prepared dispersion of SA into a super-saturated solution of $CaSO_4$. After 30 min of crosslinking, the product was rinsed three times with deionized water to form the desired hydrogel. The prepared hydrogels were dried at 40°C for 24 h before the adsorption of heavy metal ions.

Preparation of Heavy Metal Ions Stock Solutions

Stock solutions of each heavy metal ions of 1,000 $mg{\bullet}L^{-1}$ were prepared. Exact amounts of 2.744 g of $Cd(NO_3)_2{\bullet}4H_2O$, 3.802 g of $Cu(NO_3)_2{\bullet}3H_2O$, and 1.599 g of $Pb(NO_3)_2$ were each dissolved in 1,000 mL of Milli-Q water, respectively. Solutions with certain required concentrations could be obtained by diluting the as-prepared stock solution.

Characterizations

Morphologies of the as-prepared materials were investigated using a field-emission scanning electron microscope JSM-7000F (FE-SEM, JEOL, Japan). Thermal gravimetric analysis (TGA) of the production was carried out on an SDT-Q600 (TA instruments, USA) under Ar atmosphere from 25°C to 800°C with a heating rate of $10^{\circ}C{\bullet}min^{-1}$. ICP-OES was carried out on Optima 8000 (PerkinElmer, USA). A tensile tester (SHIMADZU AGS-X) with a 500 N load cell was used for the tensile test. The cylindrical hydrogel samples with or without heavy metal ions adsorbed were selected for all tests. The upper clamp was pulled by the load cell at a constant velocity of 50 mm/min.

Adsorption of Heavy Metal Ions

Adsorption of metal ions by AFH were carried out as follows: A certain quantity of as-prepared dried hydrogels was added into the heavy metal aqueous solution with a certain concentration. After a specified time of adsorption reaction, aliquots of the solutions were collected to test the adsorbed heavy metal ions concentration using ICP-OES.

The equilibrium adsorption capacity (Q_e, $mg{\cdot}g^{-1}$) is defined as the amount of heavy metal adsorbed per gram of dried gel at equilibrium. Q_e can be obtained by Equation (1) (Zhang et al., 2018):

$$Q_e = \frac{(C_0 - C_e)\,V}{M} \tag{1}$$

where C_0 and C_e ($mg{\cdot}L^{-1}$) are the initial and equilibrium concentrations, respectively, for each metal ion in solution; V (L) is the solution volume and M (g) is the mass of the dried hydrogel.

The removal ratio (R) for each metal ion in solution at a specific time can be calculated by Equation (2)

$$R = \frac{(C_0 - C_t)}{C_0} \times 100\% \tag{2}$$

where C_t($mg{\cdot}L^{-1}$) is the concentration of each metal ion at a specific time.

Adsorption Kinetics

The main rate-limiting factor can be determined through adsorption kinetics. Equations (3) and (4) represent the first-order kinetics and second-order kinetics, respectively (Li et al., 2016).

$$\lg(Q_e - Q_t) = \lg Q_e - \frac{K_1 t}{2.303} \quad (3)$$

$$\frac{t}{Q_t} = \frac{1}{K_2 Q_e^2} + \frac{t}{Q_e} \quad (4)$$

where Q_e (mg·g^{-1}) and Q_t (mg·g^{-1}) are the equilibrium adsorption capacities and the adsorption capacities at specific time t (h), respectively. t (h) is the reaction time, K_1 (h^{-1}) is the first-order kinetics rate constant, and K_2 (g·(mg·min)$^{-1}$) is the second-order kinetics rate constant.

Adsorption Isotherms

The adsorption behaviors of AFH can by described by the Langmuir and Freundlich isotherm models (Zhang et al., 2017). The Langmuir isotherm model can be represented by Equations (5) and (6):

$$Q_e = \frac{Q_m K_L C_e}{1 + K_L C_e} \quad (5)$$

$$\frac{C_e}{Q_e} = \frac{C_e}{Q_m} + \frac{1}{K_L Q_m} \quad (6)$$

where, C_e (mg·L^{-1}) is the equilibrium concentration for each metal ion, Q_e (mg·g^{-1}) is the equilibrium adsorption capacity, Q_m (mg·g^{-1}) is the theoretical saturation adsorption capacity and K_L is the Langmuir isotherm model constant.

In the Langmuir isotherm adsorption process, the separation factor (R_L) can be used to evaluate the pros and cons of an adsorption system (linear, irreversible, favorable and unfavorable) (Meena et al., 2005). R_L was calculated according to Equation (7):

$$R_L = \frac{1}{1 + K_L C_0} \quad (7)$$

Freundlich isotherm model can be written by Equations (8) and (9):

$$Q_e = K_F C_e^{\frac{1}{n}} \quad (8)$$

$$\log Q_e = \log K_F + \frac{1}{n} \log C_e \quad (9)$$

where C_e (mg·L^{-1}) is the equilibrium concentration for each metal ion, Q_e (mg·g^{-1}) is the equilibrium adsorption capacity, K_F is the Freundlich isotherm constant and n is the Freundlich isotherm constant and the adsorption process is favorable when the value of n is between 1 and 10.

Competitive Adsorption

The adsorption competitiveness of different metal ions can be written as Equations (10) and (11) (Yan et al., 2011):

$$K_d = \frac{\frac{Q_i}{C_i}}{\frac{Q_1}{C_1} + \frac{Q_2}{C_2} + \cdots \frac{Q_j}{C_j}} \quad (10)$$

$$\alpha = \frac{K_d(T)}{K_d(I)} \quad (11)$$

where K_d is the partition coefficient of a certain metal ion, i = 1, 2.. j, and j = 1, 2,…, Q_i (mg·g^{-1}) and C_i (mg·g^{-1}) are the equilibrium adsorption capacity and initial concentration of a certain metal ion. α is the selectivity coefficient of a certain metal ion. $K_d(T)$ is the partition coefficient of ions with stronger competitiveness, and $K_d(I)$ is the partition coefficient of ions with weaker competitiveness. In the adsorption system, the sum of the partition coefficient values is 1, and the larger the value, the stronger the competitiveness of the ions.

RESULTS AND DISCUSSION

Natural sodium alginate (SA) was used as a macromolecule and Ca^{2+} served as crosslinker for fabricating AFH (Xie et al., 2012; Basu et al., 2017; Wang et al., 2019). **Figure 1** shows a schematic illustration for the preparation of AFH and its adsorption process for heavy metal ions. With optimized concentrations of SA (52.7 mg·ml^{-1}) and $CaSO_4$ (2.5 mg·ml^{-1}) and continuous injection of SA solution into the $CaSO_4$ solution, fibrous-shaped hydrogels with a diameter of 1 mm were obtained after crosslinking for 30 min. The as-prepared hydrogel contains a lot of adsorption sites that can interact with heavy metal ions (Mahou et al., 2015).

As shown in **Figure 2a**, the freshly prepared AFH are colorless and transparent, and the color turns blue after the adsorption of Cu^{2+} ions. However, AFH with Cd^{2+} and Pb^{2+} are light colored. SEM images in **Figure 2b** display that the AFH contain lots of voids, and these voids could result in more adsorption channels for heavy metal ions including Cu^{2+}, Cd^{2+}, and Pb^{2+}. Both the heavy metal ion-adsorbed and non-adsorbed AFH have certain toughness and strength, and this is very convenient for recovery after adsorption of heavy metal ions. It is worth noting that AFH exhibits enhanced mechanical strength after the adsorption of heavy metal ions (**Figure 2c**). Thermal gravimetric analysis (TGA) can be used to analyze the weight loss of dried hydrogel material with temperature. As shown in **Figure 2d**, there are three stages during the thermal decomposition of blank AFH. The first stage (room temperature to about 190°C) can be attributed to dehydration, and the weight loss is about 12 wt.% (Shamshina et al., 2014). The second stage (∼200 to 280°C) is due to the breakdown of alginate polymer chains and has a weight loss of about 30.1 wt.%. The third stage (654–700°C) is due to the evaporation of CO_2 and formation of carbonized materials, and the weight loss is about 12.5 wt.% (Narayanan and Han, 2017; Dipankar et al., 2018). Due to the combination of adsorbed heavy metal ions and functional groups in the hydrogel, AFH with

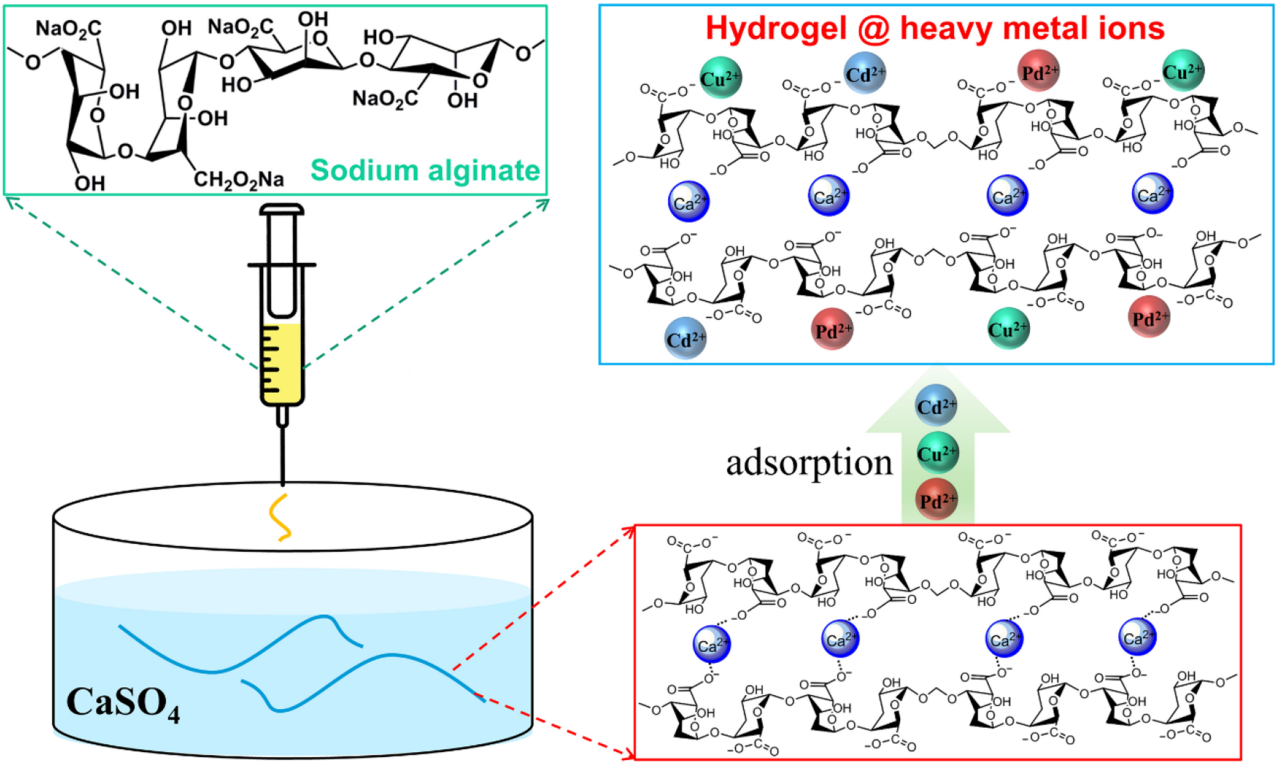

FIGURE 1 | Schematic illustration of the AFH preparation process and their adsorption for heavy metal ions. SA solution is injected into a super-saturated solution of $CaSO_4$, AFH is formed after crosslinking for 30 min. The adsorbent, AFH, is then added into an aqueous solution of heavy metal ions to remove toxic ions.

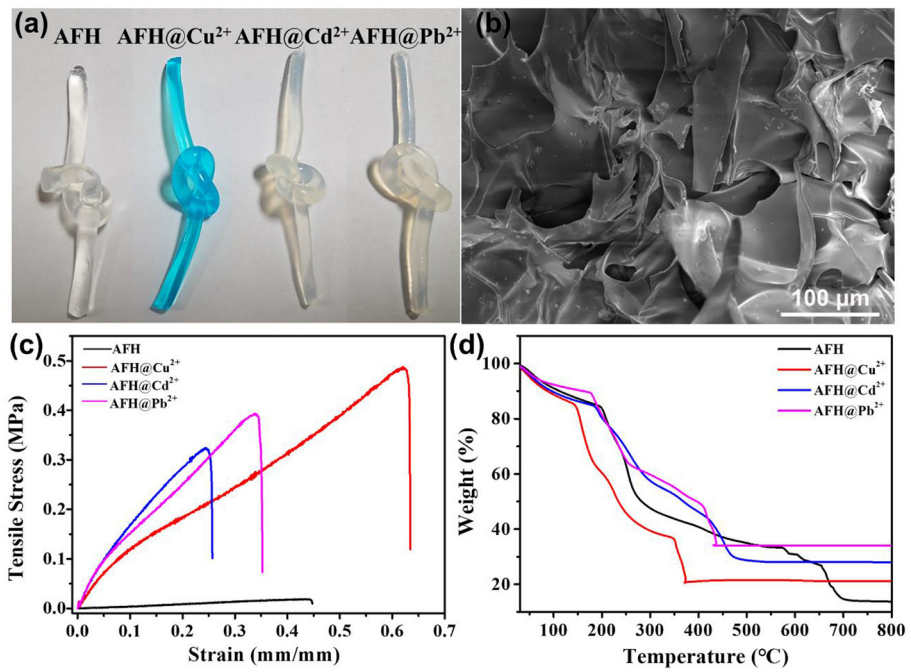

FIGURE 2 | (a) Optical images of AFH without and with heavy metal ions adsorbed, **(b)** SEM image of AFH, **(c)** strain–stress curves of AFH with Cu^{2+}/Cd^{2+}/Pb^{2+} ion adsorbed, **(d)** TGA curve of without and with heavy metal ions adsorbed.

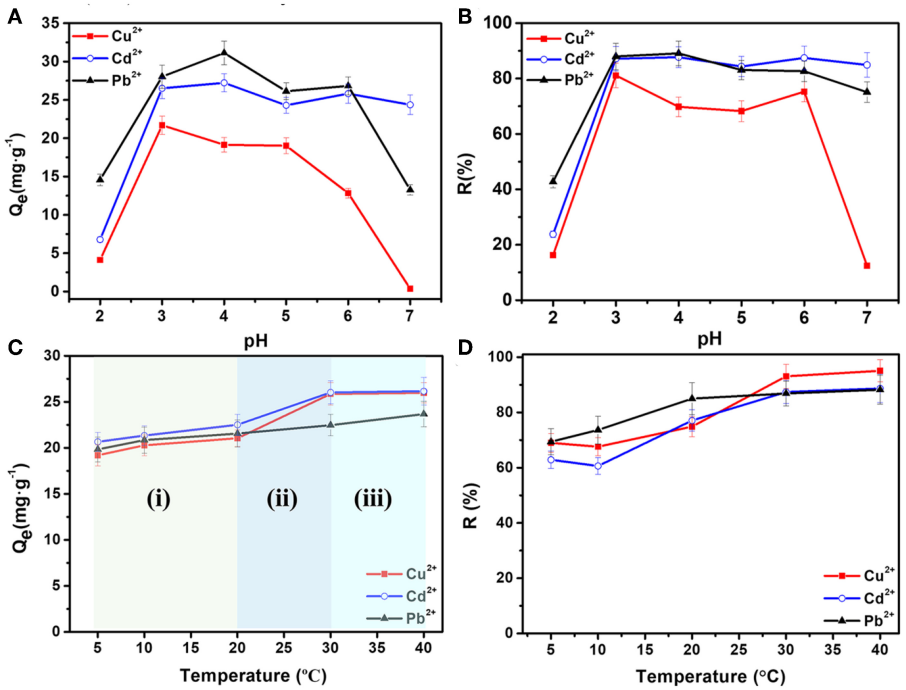

FIGURE 3 | Effects of pH values on **(A)** equilibrium adsorption capacities and **(B)** removal ratios; effect of temperature on **(C)** equilibrium adsorption capacities and **(D)** removal ratios of Cd^{2+}, Cu^{2+}, and Pb^{2+} ions.

heavy metal ions adsorbed show less weight loss compared with blank AFH, and they also have lower stable temperature.

To study the adsorption performances, previously dried hydrogel samples were used to remove heavy metal ions. **Figures 3A,B** illustrate the effect of pH values on the adsorption capacity and removal ratios of Cd^{2+}, Cu^{2+}, and Pb^{2+} ions by AFH. C_0 is 40 mg·L^{-1}, V_0 is 20 mL, M is 30 mg, t is 24 h, and T is 30°C. The Q_e values first increased and then decreased with an increase in pH values from 2.0 to 7.0. At lower pH, the concentration of hydrogen ions in SA chains is higher, and thus hydrogen ions compete more strongly for the electrons pair than the heavy metal ions. As a result, the removal of Cd^{2+}, Cu^{2+}, and Pb^{2+} ions is not effective. As the pH increases, protonation of the carboxyl group decreases gradually, more and more carboxyl groups can chelate with heavy metal ions resulting in enhanced adsorption (Wu and Li, 2013; Li et al., 2016; Wahab et al., 2019). However, the increasing concentration of OH^- as pH increases to 7.0 can causes some of the heavy metal ions to precipitate. Thus, removal of Cu^{2+} and Pb^{2+} ions is not satisfactory at pH of 7.0 (Panchan et al., 2018). The optimal pH values are 4.0 for Cd^{2+} and Pb^{2+} ions, and 3.0 for Cu^{2+} ions, respectively. Also, the corresponding removal ratios (R%) for each heavy metal ion is more than 80%.

Figures 3C,D illustrate the effect of temperature on the removing of Cd^{2+}, Cu^{2+}, and Pb^{2+} ions, in which C_0 was 40 mg·L^{-1}, V_0 was 20 mL, M was 30 mg, t was 24 h, and pH was 4.0. The equilibrium adsorption capacities (Q_e) can be analyzed in three stages. In the first stage (i) from 5 to 20°C, Q_e increases slightly with temperature. In the second stage (ii) from 20 to 30°C, the adsorption capacity has a significant augment. Whereas, in the third stage (iii) from 30 to 40°C, the adsorption capacities and removal ratios have only slight changes. In general, the adsorption capacities and removal ratios of heavy metal ions become a little larger at higher temperature. There are two possible reasons for this. One is that the higher degree of crosslinking at higher temperature can result in an increasing number of pores in AFH, which further increases the number of adsorption active sites. Another one can be attributed to the decrease in boundary layer thickness of the adsorbent, causing a lower mass transfer resistance of adsorbate (Kalagasidis Krušić et al., 2012).

Many kinds of metal ions always coexist in the sewage. To better understand effects of other ions on the removal of heavy metal ions, Na^+ and Ca^{2+} ions were selected as interfering ions for adsorption experiments, and the effects of the concentration ratios of interfering ions to heavy metal ions (1:1, 2:1, and 3:1) were also studied. As shown in **Figure 4**, the order of influence for the three heavy metal ions in this study is Cd^{2+} > Cu^{2+} > Pb^{2+}. Na^+ ions had only a slight effect on the adsorption capacities and removal ratios even when the concentration of Na^+ was high. Among the three heavy metal ions, the adsorption for Pb^{2+} is almost unaffected by the presence of Na^+ and Ca^{2+} ions, indicating its good anti-interfering absorbability of Pb^{2+}. However, the removal ratio of Cd^{2+} decreased from 82.91 to 54.30% with an increasing concentration of Ca^{2+} ions. This is because Ca^{2+}, as interfering ions in solution, may combine with

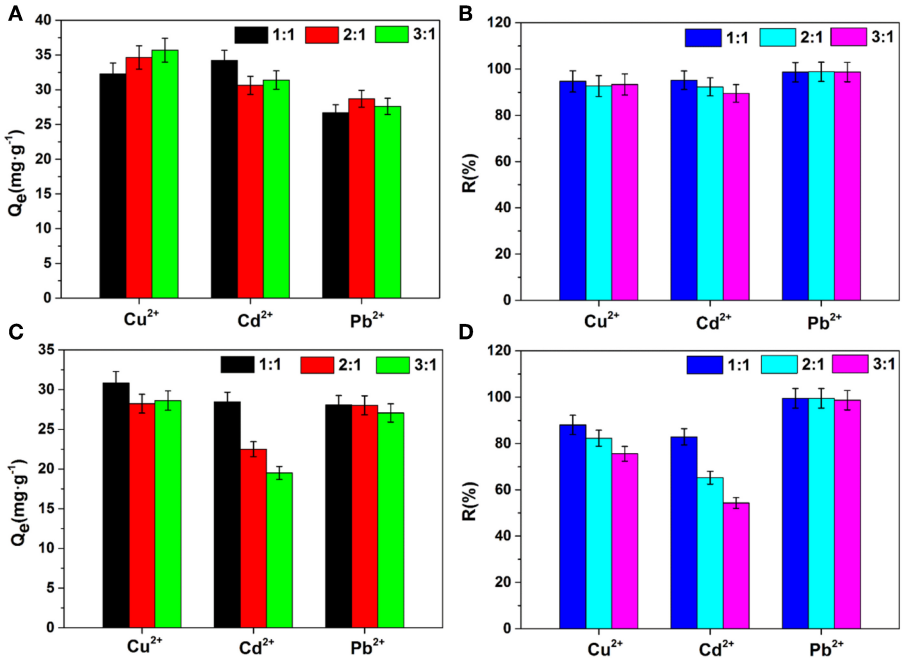

FIGURE 4 | Effects of interfering ions on adsorption capacities and removal ratios **(A,B)** Na^{+} ion, **(C,D)** Ca^{2+} ion. Concentration ratios of interfering ions to heavy metal ions are 1:1, 2:1, and 3:1.

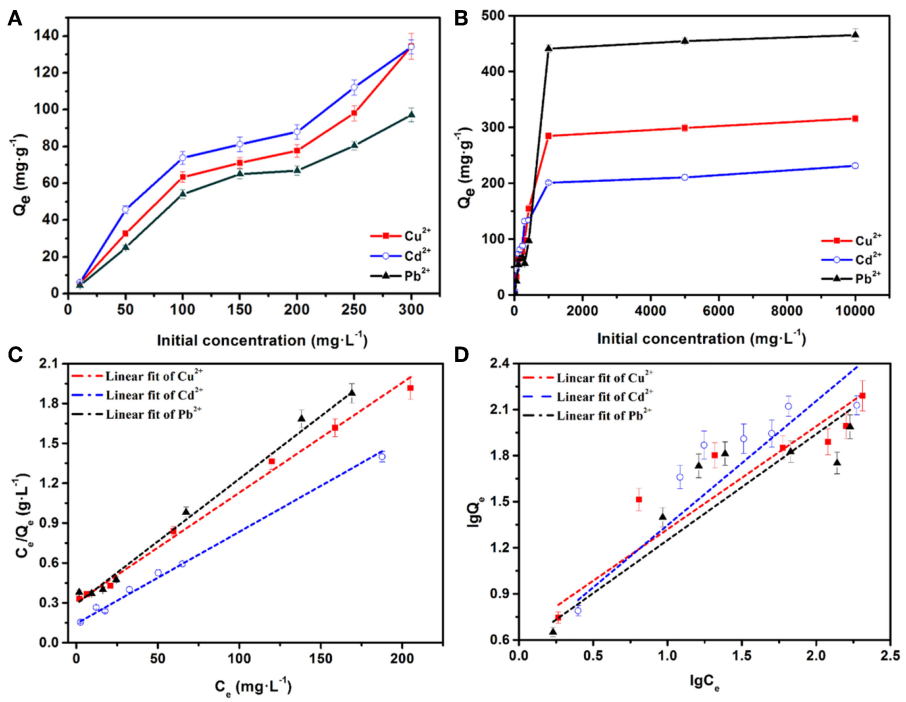

FIGURE 5 | (A,B) Effects of initial concentrations on the adsorption capacities of Cd^{2+}, Cu^{2+}, and Pb^{2+} ions, the equilibrium isotherm analysis using the **(C)** Langmuir and **(D)** Freundlich models.

adsorption sites inside AFH, and thus, Ca^{2+} has a competitive relationship with the adsorption of heavy metal ions. The ability of sodium alginate to bind with divalent cations is in the order of $Pb^{2+} > Cu^{2+} > Cd^{2+}$, so Cd^{2+} is affected the most (Zhou et al., 2018). In addition, when interfering ions with high ionic strength coexist with heavy metal ions, the large concentration difference reduces the porosity and effective adsorption sites of hydrogel, and thus affect adsorption of heavy metal ions (Yang and Jiang, 2014).

Figures 5A,B illustrate the effects of different initial concentrations of heavy metal ions on the adsorption by AFH. The experimental conditions were 24 h of adsorption at 303 K with 30 mg of AFH. The initial heavy metal ion concentrations were found to have a significant effect on the adsorption capacities. At relatively low ion concentrations (0–300 $mg{\cdot}L^{-1}$), the adsorption capacities increased very quickly with the increasing of initial ion concentrations. They then reach an equilibrium adsorption capacity when the concentrations are very high (1,000–10,000 $mg{\cdot}L^{-1}$). There are two explanations for this phenomenon. First, the quality of the hydrogel is constant throughout the adsorption process. When the ions concentration increases, the chance of collision between heavy metal ions and the hydrogel increases, and this results in an increase in equilibrium adsorption capacity. Second, the number of active adsorbed sites on AFH is definite, and it meets the adsorption requirement when the ion concentration is low. In contrast, the active sites gradually saturate as an increasing amount of heavy metal ions react with them, and this means that the adsorption can reach saturation (Zhang et al., 2018).

To better understand the adsorption isotherms, Langmuir and Freundlich models were applied to simulate experimental results. **Figures 5C,D** show the fitting curves for the adsorption of Cu^{2+}, Cd^{2+}, and Pb^{2+} ions using Langmuir and Freundlich models, respectively. As displayed in **Table 1**, the correlation coefficients (R^2) calculated using Langmuir model are 0.993 (Cd^{2+}), 0.974 (Cu^{2+}), and 0.974 (Pb^{2+}), which are higher than the R^2 values obtained using the Freundlich model. Therefore, the adsorptions of Cd^{2+}, Cu^{2+}, and Pb^{2+} fit the Langmuir isotherm model better than the Freundlich isotherm model. In addition, the adsorption of each of these heavy metal ions is a monolayer

TABLE 1 | Langmuir and Freundlich isotherm parameters of the heavy metal ions adsorption.

Metal ions	Langmuir isotherm				Freundlich isotherm		
	R^2	K_L ($L{\cdot}mg^{-1}$)	Q_m($mg{\cdot}g^{-1}$)	R_L	R^2	K_F ($mg^{1-1/n}{\cdot}L^{1/n}{\cdot}g^{-1}$)	n
Cu^{2+}	0.993	0.016	315.92	0.059–0.862	0.877	5.76	1.862
Cd^{2+}	0.974	0.030	232.32	0.032–0.769	0.773	6.30	1.920
Pb^{2+}	0.974	0.031	465.22	0.031–0.763	0.893	4.35	1.565

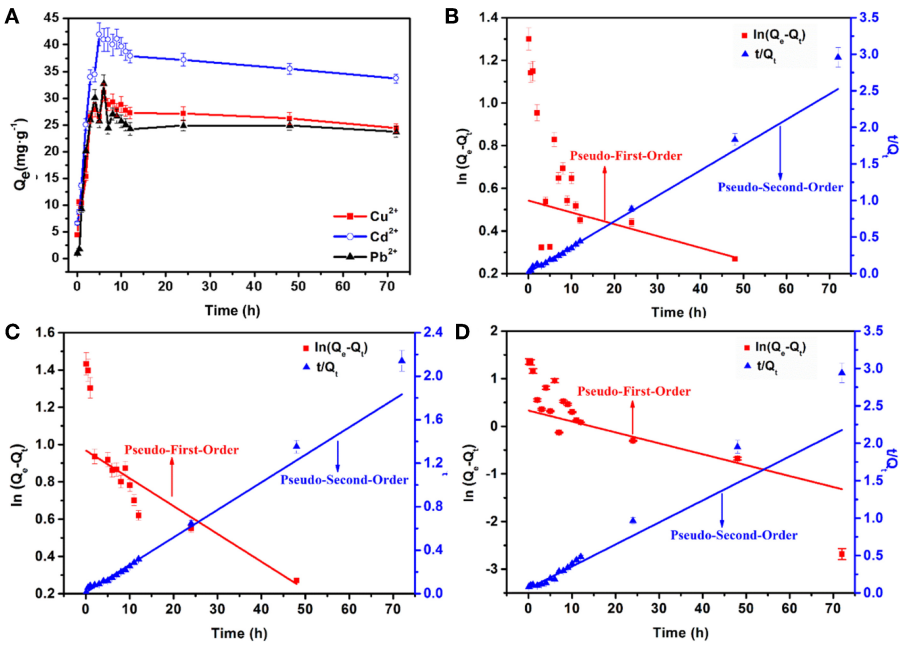

FIGURE 6 | (A) Effects of adsorption time on the capacities of AFH for Cu^{2+}, Cd^{2+}, and Pb^{2+} ions, the plots of pseudo-first-order and pseudo-second-order kinetics models for **(B)** Cu^{2+}, **(C)** Cd^{2+} and **(D)** Pb^{2+}.

adsorption process. The separation factors (R_L) for Cu^{2+}, Cd^{2+}, and Pb^{2+} ions are 0.059–0.862, 0.032–0.769, and 0.031–0.763, respectively. All of the separation factors were between 0 and 1, indicating that the adsorption processes are very favorable (Yan et al., 2011). The saturated adsorption capacities calculated using the Langmuir isotherm model are 232.35 $mg{\cdot}g^{-1}$ (Cd^{2+}), 315.92 $mg{\cdot}g^{-1}$ (Cu^{2+}), and 465.22 $mg{\cdot}g^{-1}$ (Pb^{2+}), and these are quite close to the experimental results (**Figure 5B**). As shown in **Table S1**, the saturated adsorption capacities of the as-prepared AFH were very competitive compared with other adsorbents.

Adsorption kinetic is also one significant aspect of an adsorption system that must be studied including the mass transport and chemical reaction processes. **Figure 6A** illustrates the effects of reaction time on the adsorption capacities of Cd^{2+}, Cu^{2+}, and Pb^{2+} within 72 h at 303 K with an initial concentration of 70 mg L^{-1}. Three stages are observed during the adsorption process. In the first adsorption stage (0–5 h), Q_e increases rapidly, Q_e then gradually decreases in the second stage (5–12 h), and in the third stage (12–72 h) reaches an equilibrium. The Q_e values for Cd^{2+}, Cu^{2+}, and Pb^{2+} ions at 12 h are 37.8, 27.2, and 24.2 $mg{\cdot}g^{-1}$, respectively, and the corresponding R values are 91.8, 87.4, and 81.1%, respectively (as shown in **Figure S1**). The pseudo-first-order and pseudo-second-order kinetics models were applied to explore the kinetics processes of heavy metal ions adsorption. The plots are shown in **Figures 6B–D**, and the calculated corresponding parameters are displayed in **Table S2**. From the fitting data using the pseudo-second-order kinetics equation, R^2 is higher than that obtained by the pseudo-first-order model. Also, the theoretical equilibrium adsorption capacities ($Q_{e,2}$) is quite close to the experimental results ($Q_{e,exp}$). As mentioned, the results suggest that the main rate-limiting factor is chemisorption in the adsorption process (Yan et al., 2011; Li et al., 2016). The rate constants reflect the speed at which the heavy metal ions to reach adsorption equilibrium. As K_2 increased, the time required to reach equilibrium is shorter. Therefore, the adsorption rate order of AFH for these three heavy metal ions is: $Cu^{2+} > Cd^{2+} > Pb^{2+}$.

Many kinds of heavy metal ions always coexist in the waste water, and so it is essential to study the adsorption competitiveness among different metal ions. The experimental conditions were 24 h of adsorption at 303 K with an initial heavy metal ion solution concentration of 40 $mg{\cdot}L^{-1}$, and 30 mg of AFH. The partition coefficient (K_d) and selectivity coefficient (α) were used to characterize the competitiveness of a certain heavy metal ion. **Table S3** shows that Pb^{2+} has the strongest competitiveness when the three ions coexisted. The adsorption capacity between heavy metal ions and AFH is mainly related to the electronegativity and hydration radius of heavy metal ions. The electronegativities of Cu^{2+}, Cd^{2+}, and Pb^{2+} are 1.90, 1.69, and 2.33, respectively. The stronger electronegativity of a heavy metal ion induces the enhanced adsorption ability. Furthermore, the ion with the smaller hydration radii has stronger competitiveness, and Pb^{2+} ions has the smallest hydration radii among the three heavy metal ions (Cu^{2+}: 4.19 Å, Cd^{2+}: 4.26 Å, and Pb^{2+}: 4.01 Å; Volkov et al., 1997).

CONCLUSION

In summary, sodium alginate fibroid hydrogels are prepared through a Ca^{2+} ion-induced crosslinking method, and their application in the adsorption of heavy metals is investigated. AFH has a network structure and shows excellent potential in the treatment of wastewater including Cu^{2+}, Cd^{2+}, and Pb^{2+}. And the enhanced mechanical strength after the adsorption of heavy metal ions will be very convenient for its recovery. The adsorption capacities are pH-sensitive, especially for Cu^{2+} and Pb^{2+}. With an increase in temperature, the adsorption capacities and removal ratios are enhanced. The coexistence of Na^{+} barely affects the adsorption of heavy metal ions, but the coexistence of Ca^{2+} leads to the reduced removal of Cd^{2+}. The adsorption process fits the Langmuir isotherm model and pseudo-second-order kinetic, and the main rate-limiting factor is chemisorption. Pb^{2+} has the strongest competitiveness when the three ions coexist. It is noteworthy that the saturated adsorption capacities of AFH for Cu^{2+}, Cd^{2+}, and Pb^{2+} are as high as 315.92, 232.35, and 465.22 $mg{\cdot}g^{-1}$, respectively. These values are comparable to that of reported absorbents, suggesting AFH is an effective adsorbent and has great potential applications in the treatment of heavy metal ions contaminated wastewater.

DATA AVAILABILITY STATEMENT

The datasets generated for this study are available on request to the corresponding author.

AUTHOR CONTRIBUTIONS

YC and ZY conceived this study. CK, XZ, and YL made the experiments and analyzed the data. CK made the draft of the manuscript with support of SY, YC, and ZY. All authors have made direct contribution to the work and approved this paper for publication.

FUNDING

This work was supported by National Natural Science Foundation of China (11674263, U1866203), China Postdoctoral Science Foundation (2019M663690), the Fundamental Research Funds for the Central Universities and the World-Class Universities (Disciplines), and the Characteristic Development Guidance Funds for the Central Universities. International Science & Technology Cooperation Program was supported by Ministry of Science and Technology of China and Shaanxi Province (S2020-YF-GHZD-0029). Xi'an Weiyang District Science and Technology Fund (201916).

SUPPLEMENTARY MATERIAL

The Supplementary Material for this article can be found online at: https://www.frontiersin.org/articles/10.3389/fchem.2019.00905/full#supplementary-material

REFERENCES

Alizadehgiashi, M., Khuu, N., Khabibullin, A., Henry, A., Tebbe, M., Suzuki, T., et al. (2018). Nanocolloidal hydrogel for heavy metal scavenging. *ACS Nano* 12, 8160–8168. doi: 10.1021/acsnano.8b03202

Basu, A., Hong, J., and Ferraz, N. (2017). Hemocompatibility of Ca2+-Crosslinked nanocellulose hydrogels: toward efficient management of hemostasis. *Macromol. Biosci.* 17:1700236. doi: 10.1002/mabi.201700236

Bilal, M., Shah, J. A., Ashfaq, T., Gardazi, S. M. H., Tahir, A. A., Pervez, A., et al. (2013). Waste biomass adsorbents for copper removal from industrial wastewater—a review. *J. Hazard. Mater.* 263, 322–333. doi: 10.1016/j.jhazmat.2013.07.071

Chen, H., Zhao, J., Dai, G., Wu, J., and Yan, H. (2010). Adsorption characteristics of Pb(II) from aqueous solution onto a natural biosorbent, fallen *Cinnamomum camphora* leaves. *Desalination* 262, 174–182. doi: 10.1016/j.desal.2010.06.006

Chen, S., Zou, Y., Yan, Z., Shen, W., Shi, S., Zhang, X., et al. (2009). Carboxymethylated-bacterial cellulose for copper and lead ion removal. *J. Hazard. Mater.* 161, 1355–1359. doi: 10.1016/j.jhazmat.2008.04.098

Chukwuemeka-Okorie, H. O., Ekemezie, P. N., Akpomie, K. G., and Olikagu, C. S. (2018). Calcined corncob-kaolinite combo as new sorbent for sequestration of toxic metal ions from polluted aqua media and desorption. *Front. Chem.* 6:273. doi: 10.3389/fchem.2018.00273

Dipankar, D., Shengmin, Z., and Insup, N. (2018). Synthesis and characterizations of alginate- α -tricalcium phosphate microparticle hybrid film with flexibility and high mechanical property as a biomaterial. *Biomed. Mater.* 13:025008. doi: 10.1088/1748-605X/aa8fa1

Fu, F., and Wang, Q. (2011). Removal of heavy metal ions from wastewaters: a review. *J. Environ. Manage.* 92, 407–418. doi: 10.1016/j.jenvman.2010.11.011

Hayati, B., Maleki, A., Najafi, F., Daraei, H., Gharibi, F., and McKay, G. (2017). Adsorption of Pb2+, Ni2+, Cu2+, Co2+ metal ions from aqueous solution by PPI/SiO2 as new high performance adsorbent: Preparation, characterization, isotherm, kinetic, thermodynamic studies. *J. Mol. Liq.* 237, 428–436. doi: 10.1016/j.molliq.2017.04.117

Kalagasidis Krušić, M., Milosavljević, N., Debeljković, A., Üzüm, Ö. B., and Karadag, E. (2012). Removal of Pb2+ ions from water by Poly(Acrylamide-co-Sodium Methacrylate) hydrogels. *Water Air Soil Poll.* 223, 4355–4368. doi: 10.1007/s11270-012-1200-y

Kaşgöz, H., Özgümüş, S., and Orbay, M. (2003). Modified polyacrylamide hydrogels and their application in removal of heavy metal ions. *Polymer.* 44, 1785–1793. doi: 10.1016/S0032-3861(03)00033-8

Kurniawan, T. A., Chan, G. Y. S., Lo, W.-H., and Babel, S. (2006). Physico–chemical treatment techniques for wastewater laden with heavy metals. *Chem. Eng. J.* 118, 83–98. doi: 10.1016/j.cej.2006.01.015

Li, J., Tong, J., Li, X., Yang, Z., Zhang, Y., and Diao, G. (2016). Facile microfluidic synthesis of copolymer hydrogel beads for the removal of heavy metal ions. *J. Mater. Sci.* 51, 10375–10385. doi: 10.1007/s10853-016-0258-0

Liu, T., Yang, X., Wang, Z.-L., and Yan, X. (2013). Enhanced chitosan beads-supported Fe0-nanoparticles for removal of heavy metals from electroplating wastewater in permeable reactive barriers. *Water Res.* 47, 6691–6700. doi: 10.1016/j.watres.2013.09.006

Mahou, R., Borcard, F., Crivelli, V., Montanari, E., Passemard, S., Noverraz, F., et al. (2015). Tuning the properties of hydrogel microspheres by adding chemical cross-linking functionality to sodium alginate. *Chem. Mater.* 27, 4380–4389. doi: 10.1021/acs.chemmater.5b01098

McDowell, L. R. (2003). "Chapter 15 - aluminum, arsenic, cadmium, lead, and mercury," in *Minerals in Animal and Human Nutrition, 2nd Edn.* eds L. R. McDowell (Amsterdam: Elsevier), 473–495. doi: 10.1016/B978-0-444-51367-0.50018-0

Meena, A. K., Mishra, G. K., Rai, P. K., Rajagopal, C., and Nagar, P. N. (2005). Removal of heavy metal ions from aqueous solutions using carbon aerogel as an adsorbent. *J. Hazard. Mater.* 122, 161–170. doi: 10.1016/j.jhazmat.2005.03.024

Narayanan, K. B., and Han, S. S. (2017). Dual-crosslinked poly(vinyl alcohol)/sodium alginate/silver nanocomposite beads – a promising antimicrobial material. *Food Chem.* 234, 103–110. doi: 10.1016/j.foodchem.2017.04.173

Panchan, N., Niamnuy, C., Dittanet, P., and Devahastin, S. (2018). Optimization of synthesis condition for carboxymethyl cellulose-based hydrogel from rice straw by microwave-assisted method and its application in heavy metal ions removal. *J. Chem. Technol. Biotechnol.* 93, 413–425. doi: 10.1002/jctb.5370

Qi, P., Luo, R., Pichler, T., Zeng, J., Wang, Y., Fan, Y., et al. (2019). Development of a magnetic core-shell Fe3O4@TA@UiO-66 microsphere for removal of arsenic(III) and antimony(III) from aqueous solution. *J. Hazard. Mater.* 378:120721. doi: 10.1016/j.jhazmat.2019.05.114

Shamshina, J. L., Gurau, G., Block, L. E., Hansen, L. K., Dingee, C., Walters, A., et al. (2014). Chitin–calcium alginate composite fibers for wound care dressings spun from ionic liquid solution. *J. Mater. Chem. B* 2, 3924–3936. doi: 10.1039/C4TB00329B

Volkov, A. G., Paula, S., and Deamer, D. W. (1997). Two mechanisms of permeation of small neutral molecules and hydrated ions across phospholipid bilayers. *Bioelectrochem. Bioenerg.* 42, 153–160. doi: 10.1016/S0302-4598(96)05097-0

Wahab, N., Saeed, M., Ibrahim, M., Munir, A., Saleem, M., Zahra, M., et al. (2019). Synthesis, characterization, and applications of Silk/Bentonite clay composite for heavy metal removal from aqueous solution. *Fron. Chem.* 7:654. doi: 10.3389/fchem.2019.00654

Wang, J., and Chen, C. (2009). Biosorbents for heavy metals removal and their future. *Biotechnol. Adv.* 27, 195–226. doi: 10.1016/j.biotechadv.2008.11.002

Wang, L.-Y., and Wang, M.-J. (2016). Removal of heavy metal ions by poly(vinyl alcohol) and carboxymethyl cellulose composite hydrogels prepared by a freeze–thaw method. *Acs Sustain. Chem. Eng.* 4, 2830–2837. doi: 10.1021/acssuschemeng.6b00336

Wang, Q., Ju, J., Tan, Y., Hao, L., Ma, Y., Wu, Y., et al. (2019). Controlled synthesis of sodium alginate electrospun nanofiber membranes for multi-occasion adsorption and separation of methylene blue. *Carbohydr. Polym.* 205, 125–134. doi: 10.1016/j.carbpol.2018.10.023

Wang, X., Pei, Y., Lu, M., Lu, X., and Du, X. (2015). Highly efficient adsorption of heavy metals from wastewaters by graphene oxide-ordered mesoporous silica materials. *J. Mater. Sci.* 50, 2113–2121. doi: 10.1007/s10853-014-8773-3

Wang, Y.-H., Lin, S.-H., and Juang, R.-S. (2003). Removal of heavy metal ions from aqueous solutions using various low-cost adsorbents. *J. Hazard. Mater.* 102, 291–302. doi: 10.1016/S0304-3894(03)00218-8

Wu, N., and Li, Z. (2013). Synthesis and characterization of poly(HEA/MALA) hydrogel and its application in removal of heavy metal ions from water. *Chem. Eng. J.* 215–216, 894–902. doi: 10.1016/j.cej.2012.11.084

Xie, L., Jiang, M., Dong, X., Bai, X., Tong, J., and Zhou, J. (2012). Controlled mechanical and swelling properties of poly(vinyl alcohol)/sodium alginate blend hydrogels prepared by freeze–thaw followed by Ca2+ crosslinking. *J. Appl. Polym. Sci.* 124, 823–831. doi: 10.1002/app.35083

Yan, H., Dai, J., Yang, Z., Yang, H., and Cheng, R. (2011). Enhanced and selective adsorption of copper(II) ions on surface carboxymethylated chitosan hydrogel beads. *Chem. Eng. J.* 174, 586–594. doi: 10.1016/j.cej.2011.09.064

Yang, G.-X., and Jiang, H. (2014). Amino modification of biochar for enhanced adsorption of copper ions from synthetic wastewater. *Water Res.* 48, 396–405. doi: 10.1016/j.watres.2013.09.050

Zhang, M., Song, L., Jiang, H., Li, S., Shao, Y., Yang, J., et al. (2017). Biomass based hydrogel as an adsorbent for the fast removal of heavy metal ions from aqueous solutions. *J. Mater. Chem. A* 5, 3434–3446. doi: 10.1039/C6TA10513K

Zhang, W., Deng, Q., He, Q., Song, J., Zhang, S., Wang, H., et al. (2018). A facile synthesis of core-shell/bead-like poly (vinyl alcohol)/alginate@PAM with good

adsorption capacity, high adaptability and stability towards Cu(II) removal. *Chem. Eng. J.* 351, 462–472. doi: 10.1016/j.cej.2018.06.129

Zhao, Z., Zhang, X., Zhou, H., Liu, G., Kong, M., and Wang, G. (2017). Microwave-assisted synthesis of magnetic Fe3O4-mesoporous magnesium silicate core-shell composites for the removal of heavy metal ions. *Microporous Mesoporous Mater.* 242, 50–58. doi: 10.1016/j.micromeso.2017.01.006

Zhou, G., Luo, J., Liu, C., Chu, L., and Crittenden, J. (2018). Efficient heavy metal removal from industrial melting effluent using fixed-bed process based on porous hydrogel adsorbents. *Water Res.* 131, 246–254. doi: 10.1016/j.watres.2017.12.067

Zhou, G., Luo, J., Liu, C., Chu, L., Ma, J., Tang, Y., et al. (2016). A highly efficient polyampholyte hydrogel sorbent based fixed-bed process for heavy metal removal in actual industrial effluent. *Water Res.* 89, 151–160. doi: 10.1016/j.watres.2015.11.053

Conflict of Interest: The authors declare that the research was conducted in the absence of any commercial or financial relationships that could be construed as a potential conflict of interest.

frontiers in Chemistry

ORIGINAL RESEARCH
published: 23 January 2020
doi: 10.3389/fchem.2019.00950

Disulfide Crosslinked Hydrogels Made From the Hydra Stinging Cell Protein, Minicollagen-1

Sanaz Farajollahi[1,2], Patrick B. Dennis[1], Marquise G. Crosby[1], Joseph M. Slocik[1,2], Anthony T. Pelton[1,2], Cheri M. Hampton[1,2], Lawrence F. Drummy[1], Steven J. Yang[3], Meredith N. Silberstein[3], Maneesh K. Gupta[1] and Rajesh R. Naik[4]**

[1] Materials and Manufacturing Directorate, Air Force Research Laboratory, Wright-Patterson Air Force Base, Dayton, OH, United States, [2] UES Inc., Dayton, OH, United States, [3] Sibley School of Mechanical and Aerospace Engineering, Cornell University, Ithaca, NY, United States, [4] 711th Human Performance Wing, Air Force Research Laboratory, Wright-Patterson Air Force Base, Dayton, OH, United States

Minicollagens from cnidarian nematocysts are attractive potential building blocks for the creation of strong, lightweight and tough polymeric materials with the potential for dynamic and reconfigurable crosslinking to modulate functionality. In this study, the *Hydra magnipapillata* minicollagen-1 isoform was recombinantly expressed in bacteria, and a high throughput purification protocol was developed to generate milligram levels of pure protein without column chromatography. The resulting minicollagen-1 preparation demonstrated spectral properties similar to those observed with collagen and polyproline sequences as well as the ability to self-assemble into oriented fibers and bundles. Photo-crosslinking with $Ru(II)(bpy)_3^{2+}$ was used to create robust hydrogels that were analyzed by mechanical testing. Interestingly, the minicollagen-1 hydrogels could be dissolved with reducing agents, indicating that ruthenium-mediated photo-crosslinking was able to induce disulfide metathesis to create the hydrogels. Together, this work is an important first step in creating minicollagen-based materials whose properties can be manipulated through static and reconfigurable post-translational modifications.

Keywords: minicollagen-1, hydrogel, cysteine rich domain, disulfide crosslinking, photo-crosslinking, polyproline

OPEN ACCESS

Edited by:
Fei Sun,
Hong Kong University of Science and Technology, Hong Kong

Reviewed by:
Songzi Kou,
Shenzhen Peking University Hong Kong University of Science and Technology Medical Center, China
Artur J. M. Valente,
University of Coimbra, Portugal

***Correspondence:**
Patrick B. Dennis
patrick.dennis.6@us.af.mil
Rajesh R. Naik
rajesh.naik@us.af.mil

Specialty section:
This article was submitted to Polymer Chemistry, a section of the journal Frontiers in Chemistry

Received: *12 November 2019*
Accepted: *31 December 2019*
Published: *23 January 2020*

Citation:
Farajollahi S, Dennis PB, Crosby MG, Slocik JM, Pelton AT, Hampton CM, Drummy LF, Yang SJ, Silberstein MN, Gupta MK and Naik RR (2020) Disulfide Crosslinked Hydrogels Made From the Hydra Stinging Cell Protein, Minicollagen-1. Front. Chem. 7:950. doi: 10.3389/fchem.2019.00950

INTRODUCTION

Marine organisms have proven to be a rich resource for the discovery of biomaterials with unique properties that hold promise for the creation of new advanced materials, such as strong, lightweight polymers, adhesives and biophotonic structures (Crookes et al., 2004; Degtyar et al., 2014; Petrone et al., 2015). The phylum *Cnidaria* includes sea anemones, corals as well as jellyfish, and members of this phylum possess specialized stinging cells, termed nematocysts, used for prey capture, defense and locomotion (Ozbek et al., 2009). Upon stimulation, the nematocyst undergoes explosive release of a stylet within 700 ns, generating an acceleration of 5,400,000 x g (Nuchter et al., 2006). The rapid deployment of the piercing structure is enabled due to the high osmotic pressure (150 bars) stored in the nematocyst capsule (Weber, 1989), which is generated by the accumulation of polyglutamic acid and ions within the capsule (Weber, 1990). In addition to the stylet, a tubule is everted from the nematocyst for the delivery of venom (Ozbek et al., 2009). The nematocyst capsule is composed of outer and inner walls, where the function of the outer wall is proposed to direct organization and assembly of the inner wall (Engel et al., 2002). It has been

demonstrated by specific proteolytic digestion of the outer wall that the inner wall is sufficient for the containment of the high nematocyst osmotic pressure (Kurz et al., 1991). High resolution microscopy showed that the inner wall is made up of oriented fibrils that display a striated pattern reminiscent of banding patterns observed with collagen fibers (Holstein et al., 1994). Screening of a *Hydra magnipapillata* capsule wall cDNA library indicated the presence of small molecular weight structural proteins, termed minicollagens, consisting of a central domain made up of collagen-like Gly-X-Y repeats, where the X and Y positions are high in proline (Kurz et al., 1991). Flanking the central collagen-like domain are two proline-rich domains that are in turn flanked by cysteine-rich domains (CRDs) at the amino and carboxy termini of the protein (Kurz et al., 1991). Like long collagens, minicollagens form a complex made up of three polypeptide chains where the polyproline regions and terminal CRDs are thought to splay out from a rigid, trihelical rod-like collagen center (Engel et al., 2001). In *H. magnipapillata*, 21 minicollagen isoforms were identified through proteomic analysis, and members of the minicollagen family were found as components of the inner capsule wall as well as the venom delivering tubule (Kurz et al., 1991; Engel et al., 2001; Adamczyk et al., 2008; Balasubramanian et al., 2012). The key domains involved in assembly of nematocyst structures are thought to be the CRDs, which have been identified in other nematocyst proteins in addition to the minicollagens (Kurz et al., 1991; Engel et al., 2002; Balasubramanian et al., 2012). The CRDs are proposed to perform two functions in the creation of nematocyst structures. First, they function as multimerization domains that control organization and self-assembly of higher order protein complexes (Meier et al., 2007; Tursch et al., 2016). Second, they contain stored intrachain disulfide bonds that are mobilized at the right time to create interchain crosslinks that stabilize the protein complexes (Meier et al., 2007; Beckmann et al., 2015). Thus, it is proposed that compaction and hardening of minicollagen oriented fibrils occurs through disulfide bond isomerization of the cysteines contained in the terminal cysteine rich domains (Engel et al., 2001). In this model, minicollagens represent a "brick-and-mortar" approach to the creation of strong, bio-based materials, where individual multimeric units can be patterned and enzymatically or chemically crosslinked into tough, resilient final materials.

Such a material could be leveraged as a protein-based hydrogel, a class of material that has found extensive use in tissue engineering due to inherent biocompatibility (Zhang and Khademhosseini, 2017). Collagen-based hydrogels (particularly Type I) are popular substrates for cell culturing and tissue engineering due to the abundance of collagen in natural extracellular matrices (Antoine et al., 2014, 2015). In recent years, to enhance hydrogel tunability and mechanical strength, collagen has been functionalized or additional crosslinkers have been added which compromise the biocompatibility of the resulting hydrogels (Antoine et al., 2015; Li et al., 2018). One simple method to create tunable protein-based hydrogels has been established via controlling the level of disulfide crosslinking in keratin-based gels where intramolecular disulfide bonds from cysteine side chains were reduced and later oxidized to forms intermolecular disulfide bonds to construct keratin-based hydrogels (Cao et al., 2019). Minicollagen-1 as a potential material for protein-based hydrogels may possess both the biocompatibility of collagen and tunability of keratin by disulfide crosslinking of its cysteine rich domains.

In this study, the *H. magnipapillata* minicollagen isoform, minicollagen-1, is expressed and purified from an *E. coli* expression system. Secondary structure analysis is carried out to determine how the recombinant minicollagen isoform compares to collagen and polyproline sequences in response to environmental perturbations. Electron microscopy is also employed to study how self-assembly of the minicollagen from the prokaryotic expression system compares to minicollagen preparations synthesized in mammalian cell culture systems. Finally, taking advantage of the relatively high levels of minicollagen afforded by bacterial expression, hydrogels are created and studied for their mechanical properties.

MATERIALS AND METHODS

All reagents were obtained from Sigma-Aldrich and were used as received, unless otherwise mentioned. All solutions were made using water with resistivity recorded at 18.2 MΩ·cm obtained from a Barnstead GenPure system. Corning pH meter 430 was used to adjust the pH of stirred solutions by dropwise addition of either acid or base as required.

Expression, Purification, and Staining of Recombinant recMinicollagen-1 in *Escherichia coli*

A codon optimized minicollagen-1 isoform coding sequence was synthesized (GenScript, Piscataway, NJ) and cloned into a pST44 expression vector (Tan et al., 2005) under ampicillin selection. The resulting pST44-minicollagen-1 or pST44-EFP-minicollagen-1 construct was then transformed into *E. coli* BL21 DE3 cells. Four liters of autoclaved LB media was inoculated and cells were grown at 37°C using with continuous air sparging of the media. Once cell cultures reached an optical density (OD_{600nm}) of 0.6–0.8, expression of the minicollagen-1 was induced with 0.4 mM isopropyl β-D-1-thiogalactopyranoside (IPTG obtained from GOLDBio) for 18 h at 25°C. Bacterial cultures were then centrifuged and then re-suspended with lysis buffer (50 mM Tris pH 8, 100 mM NaCl, 100 μg/mL lysozyme) followed by sonication. Lysed cells were then heat treated at 80°C, for 30 min followed by cooling in an ice bath for another 30 min. Denatured contaminant proteins were removed by centrifugation and the supernatant was adjusted to a pH of 3.5 using 1M HCl followed by centrifugation. The supernatant was then adjusted to pH of 8.5 with 1M NaOH, followed by lyophilization to dryness. The resulting protein powder was dissolved in 25 ml of deionized water and treated with equal

Abbreviations: CRD, cysteine rich domain; IMAC, immobilized metal affinity chromatography; SDS-PAGE, sodium dodecyl sulfate polyacrylamide gel electrophoresis; DTT, dithiothreitol; EF-P, elongation factor P; CRB, chelating reducing buffer.

volume of saturated ammonium sulfate with continuous stirring. The precipitate was removed by centrifugation and re-suspended in 10 mL of deionized water. Ten milliliters of absolute ethanol was then added and the sample cooled at −20°C for 1 h before centrifugation. The supernatant was mixed with 10 mL of saturated ammonium sulfate and shaken vigorously followed by centrifugation in a swinging bucket rotor. The top organic phase containing the expressed minicollagen-1 was then removed and evaporated to dryness. The powder was re-suspended in 10 mL deionized water followed by dialysis in deionized water 24 h. The minicollagen-1 sample was then lyophilized to dryness, weighed and the purified protein powder stored at −80°C until use.

Minicollagen-1 samples were run on 12% polyacrylamide gel and fixed in 20% glacial acetic acid and 15% methanol for 30 min. The gels were then stained in solution of 20% glacial acetic acid, 15% methanol and 0.1% Coomassie R-250 for 24 h at room temperature.

Circular Dichroism Spectra of Recombinant Minicollagen-1

Circular dichroism spectra were collected on a Jasco J-815 CD spectrometer from 300 to 180 nm at a scan rate of 20 nm/min and averaged over 3 repetitive scans using a quartz cuvette with a 1 cm pathlength. Minicollagen-1 was prepared at a concentration of 1.4 μM in water and treated with select agents. CD spectra were collected and subtracted from the corresponding reference spectrum of water, or the treatment agent only. Temperature studies were performed using a peltier controlled cuvette holder. CD spectra were collected for minicollagen-1 during heating at 25°C, 50°C, 70°C, and 90°C.

Transmission Electron Microscopy of Recombinant Minicollagen-1

To prepare samples for TEM, 4 μl of either undiluted (1 mg/ml) or diluted (0.1 mg/ml) minicollagen-1 was applied to a 400 mesh copper grid supporting a thin carbon film. The sample was allowed to adhere for 1 min before staining with Uranyl-less stain for 3 min, washing, then blotting to dryness with Whatman #1 filter paper. Samples were imaged on a Ceta camera on a Thermo Fisher Scientific Talos TEM operating at 200 kV and using a 40 μm objective aperture.

Ellman's Reagent Assay

Quantification of free sulfhydryl on bacterially expressed minicollagen-1 protein was obtained by using cysteine hydrochloride monohydrate as a standard for the Ellman's reagent assay (ThermoScientific). The reaction buffer contains 0.1 M sodium phosphate buffer solution (pH 8.0), and 1 mM ethylenediaminetetraacetic acid (EDTA). The reagent solution were prepared by dissolving 4 mg of Ellman's reagent in 1 ml of reaction buffer. Various concentrations of standard was prepared by dissolving cysteine-HCl in reaction buffer. Minicollagen-1 protein then dissolved in reaction buffer to final concentration of 1 mg/ml. For the assay, 15 μl of each sample was mixed with 150 μl of Ellman's reagent solution and incubated at room temperature for 15 min. Then the absorbance at 412 nm was obtained using the plate reader (SpectraMax M3, Molecular Device).

Photo-Crosslinking of Recombinant Minicollagen-1 Hydrogels

Solutions of minicollagen-1 in water were photo-chemically crosslinked to form hydrogels using tris(2,2-bipyridyl) dichloro ruthenium (II) hexahydrate ($Ru(II)(bpy)_3^{2+}$) as the catalyst and ammonium persulphate (Bio Rad) as the electron acceptor. Hydrogel cylinders for mechanical testing were prepared from a 17 wt% minicollagen-1 solution containing 37 mM ammonium persulfate and 2.2 mM $Ru(II)(bpy)_3^{2+}$. The mixture was transferred into cylinders cut out of a small transfer pipette bulb (1.5 ml) and photo-crosslinked under white lamp light within 5 min. Post crosslinking, the hydrogels were transferred into 20 mM EDTA and 10 mM EGTA for removal of the photo-crosslinker catalyst. The crosslinked cylinders are 2.5 mm in diameter and 3–4 mm in height. To evaluate effect of reducing agent on the hydrogels, 10 wt% of rhodamine labeled minicollagen hydrogel was made at the bottom of an Eppendorf tube cap (dome shaped hydrogel) using the above photo-crosslinking protocol. Hydrogels were then submerged in solutions of DTT (10 mM), CRB (10 mM EDTA, 1 mM EGTA, 1% β-mercaptoethanol), βME (1% β-mercaptoethanol) and 10 mM EDTA/1 mM EGTA for 3 h to analyze the effect of the reducing reagents.

Determination of Equilibrium Swelling Degree

The swelling capacity of minicollagen-1 hydrogels was determined by incubating them in deionized water at room temperature for 2 days and then drying the hydrogels at room temperature until no change in dimensions of hydrogel was observed. The swelling degree was calculated using the following equation:

$$Swelling\ degree = \frac{Vs - Vd}{Vd} \times 100$$

Where Vs and Vd are, respectively, volume of hydrogel in swollen and dried state.

Mechanical Testing

Compressive modulus of 17 wt% minicollagen-1 hydrogel was performed using CellScale Microsquisher (Microtester G2). In this setup, a tungsten microbeam of 0.5588 mm in diameter is fixed on one end to a vertical actuator and on the other end to a 4 × 4 mm^2 compression platen, which was tracked by a camera to record the displacement. As the beam moved to compress the hydrogel, deflection was measured in real time by the relative position of the beam at the camera and at the motor. Force was calculated by the Microsquisher software using the following equation:

$$Force = \frac{Deflection \times 3 \times Beam\ Modulus \times Beam\ Area\ Moment\ of\ Intertia}{Beam\ Length^3}$$

Where

$$Beam\ Area\ Moment\ of\ Intertia = \frac{\pi \times radius^4}{4}$$

Each gel was sequentially compressed to final strains of 5, 10, and 15% within 50 s, held for 1 s followed by recovery within 50 s. The compressive elastic modulus was calculated as the slope of the linear portion of the stress versus strain curve and reported for each final strain as an average of measurements obtained from three different gels.

RESULTS

Previous studies have identified the minicollagens as a major component of the nematocyst capsule inner wall (Kurz et al., 1991; Holstein et al., 1994). Up to now, there have been no studies of minicollagen mechanical properties from hydrogels made of the isolated protein. In order to determine how a crosslinked minicollagen network may function to form an elastic material capable of withstanding extreme pressures, we have synthesized the coding region for minicollagen-1 from *H. magnipapillata* and subcloned it into a bacterial expression vector for large scale production in *E. coli*. The *H. magnipapillata* minicollagen-1 has been well-studied and represents the canonical form of the minicollagen family with a central collagen-like set of 14 Gly-X-Y repeats immediately flanked at both ends with polyproline regions and cysteine rich domains at both the amino and carboxyl termini (**Figure 1A**). Thus, proline is the most abundant amino acid in minicollagen primary structures. In minicollagen-1, prolines occupy the Y position of 86% of the three amino acid repeats and at both the X and Y positions in 36% of the repeats (**Supplementary Figure 1**). Both hexa-histidine tagged and untagged versions of minicollagen-1 were created for bacterial expression in *E. coli*, where the hexa-histidine tagged form of minicollagen-1 was initially used for screening of bacterial expression. Western blotting of His-minicollagen-1 isolated using IMAC yielded a dominant polypeptide with a 25–30 kDa apparent molecular weight that cross reacted with an anti-hexa-histidine antibody (**Figure 1B**). When expression was carried out at a larger scale, the net yields of recombinant minicollagen-1 were poor. This was likely due to the consecutive proline stretches before and after the collagen-like domain that are known to cause translational stalling in other proteins (Doerfel et al., 2013; Ude et al., 2013). To mitigate this, a bicistronic construct was created where the *E. coli* translation elongation factor EF-P was expressed with the His-tagged minicollagen-1 (**Supplementary Figure 2**). EF-P was previously reported to increase expression of proteins that contain stretches of more than two consecutive prolines by limiting ribosomal stalling that occurs when a third consecutive proline is being translated (Doerfel et al., 2013; Ude et al., 2013). One observation that assisted in the identification of purified, recombinant minicollagen-1 by SDS-PAGE was that it stained metachromatically with Coomassie R-250, a phenomenon observed with mammalian collagens and other proteins with high proline content (Hattori et al., 1996). Metachromatic staining results in purple rather than the blue staining observed with most other orthochromatically stained proteins and gives strong support to the conclusion that the purified material is minicollagen-1 (**Supplementary Figure 2A**). *E. coli* was transformed with minicollagen-1 constructs either without or with co-expressed EF-P and eight colonies of each were analyzed for minicollagen-1 expression by Coomassie R-250 metachromatic staining (**Supplementary Figures 2B,C**). The results indicated that co-expression with EF-P did result in increased expression of minicollagen-1 by ∼3 fold (**Supplementary Figures 2B,C**). Therefore, all future large scale expressions of recombinant minicollagen-1 were carried out with co-expressed EF-P.

Although the hexa-histidine tag would allow for column purification of the recombinant minicollagen-1, a purification protocol was developed where the tag would not be needed so that non-tagged versions of recombinant minicollagen-1 could also be purified in large amounts without column chromatography (Materials and Methods). The final step in the optimized minicollagen purification protocol is lyophilization which produces an off white, cotton-like protein sample that demonstrates good solubility in water, easily dissolving at concentrations up to 10 wt% (**Figure 1C**). As was observed with the initial Western blotting of the recombinant minicollagen-1, SDS-PAGE analysis of the purified His-tagged and non-tagged variants, followed by Coomassie R-250 staining indicated an abnormally high apparent molecular weight for the monomeric form of the protein (between 30 and 35 kDa) that stained metachromatically (**Figure 1D**). This apparent molecular weight is likely due to the particular characteristics of the minicollagen-1 protein in terms of its ability to bind SDS, as mass spectrometry analysis indicated a peak with good agreement to the predicted mass of the monomeric protein (**Supplementary Figure 3**). The lack of additional orthochromatically stained proteins on the gel, even at high levels of protein loading, indicated that the recombinant minicollagen-1 preparations were largely free of contaminating proteins. The net yield of purified, recombinant minicollagen-1 was estimated at ∼18 mg per liter of culture. One additional characteristic that makes analysis of recombinant minicollagen-1 expression difficult using SDS-PAGE is its tendency to diffuse out of the gel during fixing and staining. This greatly reduces the ability to see low levels of protein using SDS-PAGE, however the presence of a hexa-histidine tag decreases the diffusion of recombinant minicollagen-1 out of the gel compared to the non-tagged version of the protein (**Figure 1D**). Together the data indicate that *E. coli* is able to heterologously express Hydra minicollagen-1 in milligram quantities. Furthermore, we have developed an easily scalable columnless purification protocol that yields recombinant minicollagen-1 with near homogenous protein purity.

The cnidarian minicollagens are unique in that they contain both G-X-Y collagen-like repeats as well as flanking polyproline stretches. Many studies have looked into secondary structure characterization of both of these proline-rich sequences individually (Tiffany and Krimm, 1972; Gutierrez-Cruz et al., 2001; Whittington et al., 2005; Lopes et al., 2014). Thus, secondary structure of the purified, recombinant minicollagen-1 was compared to the secondary structure of a high molecular weight collagen. For this, circular dichroism (CD) spectroscopy was performed on the recombinant minicollagen-1 and purified type I bovine dermal collagen. The CD spectrum for type I bovine collagen demonstrated a strong negative

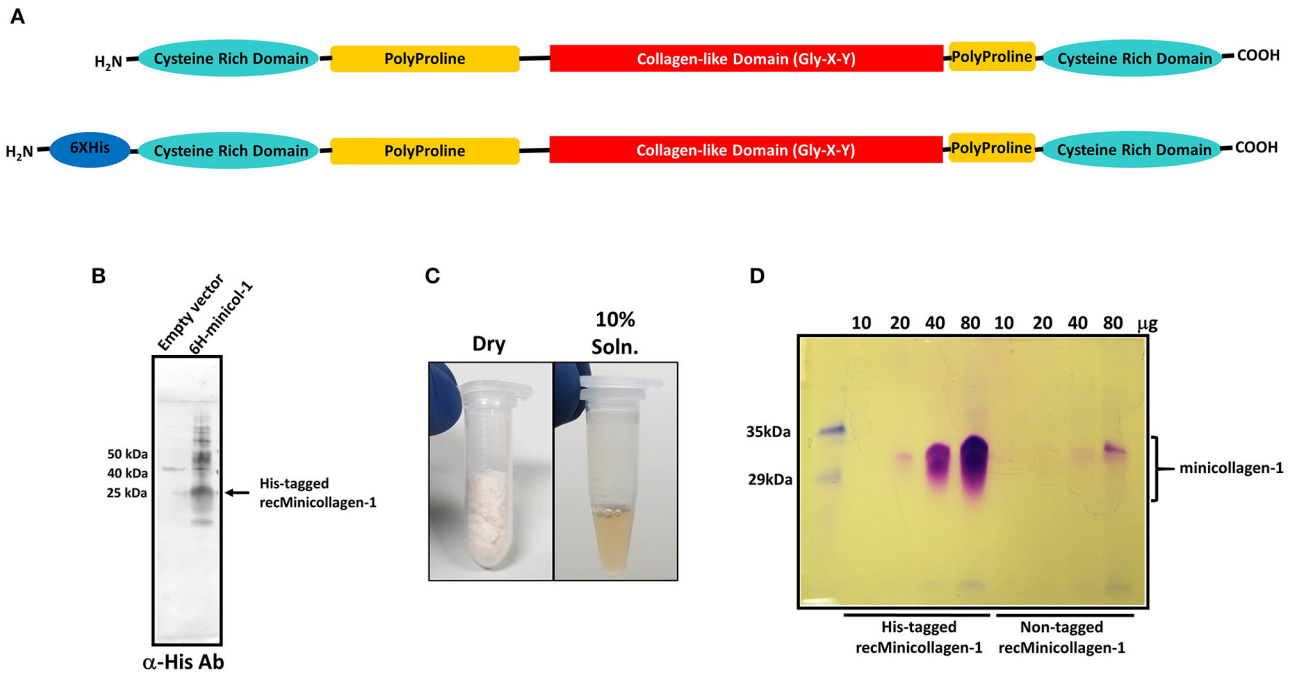

FIGURE 1 | (A) Schematic of the minicollagen-1 domain structure with the individual domains labeled. **(B)** Western blot analysis of extracts from bacteria transformed with empty vector or a vector containing the hexa-histidine tagged minicollagen-1. The blot was probed with an anti-hexa-histidine antibody and the position of the tagged recombinant minicollagen-1 is indicated. **(C)** Purified, lyophilized recombinant minicollagen-1 (30 mg) is shown (left panel) with a 10 wt% solution of recombinant minicollagen-1 in water (right panel). **(D)** SDS-PAGE of the hexa-histidine-tagged and non-tagged recombinant minicollagen-1 expressed and purified from bacteria after staining with Coomassie R-250. The amount of protein loaded in each lane is indicated at the top.

ellipticity at 198 nm and a pronounced positive ellipticity at 222 nm (**Figure 2A**). These absorbances are hallmarks of the extended polyproline II helix found in the trihelical quaternary structure of the long collagens and are in good agreement with numerous other collagen CD spectra published previously (Tiffany and Krimm, 1972; Lopes et al., 2014). CD spectroscopy of the recombinant minicollagen-1 demonstrated a clear negative ellipticity at 207 nm, with a small hump often observed below 200 nm, and a minor positive ellipticity seen at 222 nm similar to type I bovine collagen (**Figure 2B**). The presence of the hexa-histidine tag had little effect on the recombinant minicollagen-1 spectrum, with the spectra for the two recombinant minicollagen-1 forms being nearly identical (**Supplementary Figure 4**). The CD spectra for both forms of the recombinant minicollagen-1 are similar to those observed for polyproline sequences which adopt an extended polyproline II secondary structure (Tiffany and Krimm, 1972; Gutierrez-Cruz et al., 2001; Whittington et al., 2005; Lopes et al., 2014). However, it does not appear that the recombinant minicollageni is adopting a trihelical quaternary structure (see Discussion).

TEM analysis of the nematocyst inner capsule wall indicates an ordered array of striated structures that are reminiscent of ordering observed with the long collagens (Starborg et al., 2013). Additionally, minicollagen-1 expressed in a human cell line forms rod like structures that self-organize into oriented bundles (Engel et al., 2001). Therefore, the ability of the recombinant minicollagen-1 to self-assemble into ordered structures was analyzed by TEM. A dilute solution (0.1 mg/ml) of the non-tagged recombinant minicollagen-1 was dropped cast onto a TEM grid and analyzed after staining (**Supplementary Figure 5**). The resulting micrographs showed a predominance of small lightly stained globular structures throughout the visual field with no indication of higher ordered structuring. When the non-tagged recombinant minicollagen-1 sample was concentrated 10 fold (1 mg/ml) and the TEM analysis repeated, significant self-assembly was observed (**Figure 3**). Bundles of fibrils could be seen with various levels of organization. In some fields, small fibril bundles were observed with chains of globules (**Figure 3A**). In other fields, fibrils were seen coming together to form small (**Figure 3B**) or large (**Figure 3C**) bundles where the fibrils appear both globular and defined in certain areas of the bundle. Some oriented structures were observed to be very compact, demonstrating a striated appearance that indicates a tighter packing of the fibrils (**Figure 3D**). When a high concentration of the hexa-histidine tagged version of minicollagen-1 was analyzed by TEM, self-assembly appeared to occur, but the resulting structures were less oriented demonstrating a more chaotic organization (**Supplementary Figure 6**). This lack of oriented self-assembly may explain why the hexa-histidine tagged form of recombinant minicollagen-1 fixes well in the gel after SDS-PAGE compared to the non-tagged version of the protein. Together, the data suggest that recombinant minicollagen-1 self assembles into highly oriented fiber bundles in response to increasing

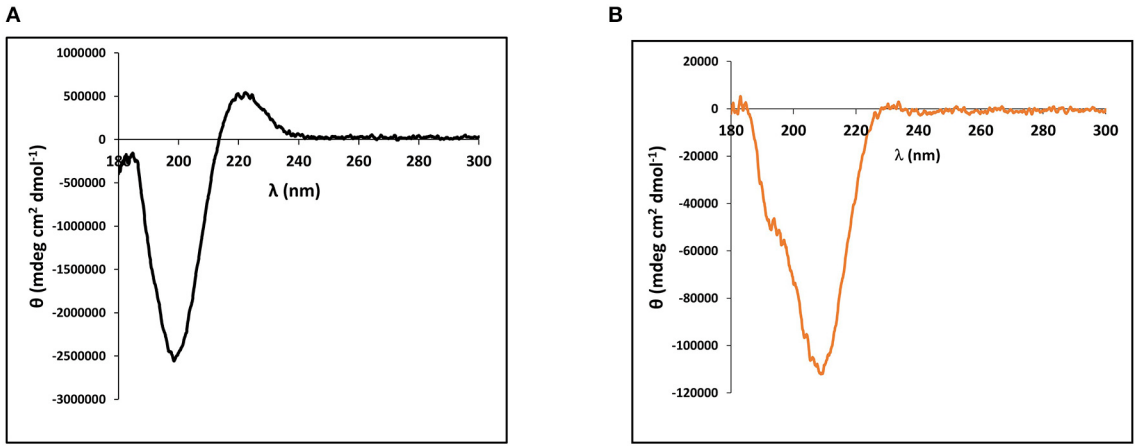

FIGURE 2 | Circular dichroism (CD) spectroscopy performed on **(A)** 90 nM type I bovine dermal collagen and **(B)** Solution of 1.4 μM of purified, bacterially expressed, non-tagged recombinant minicollagen-1.

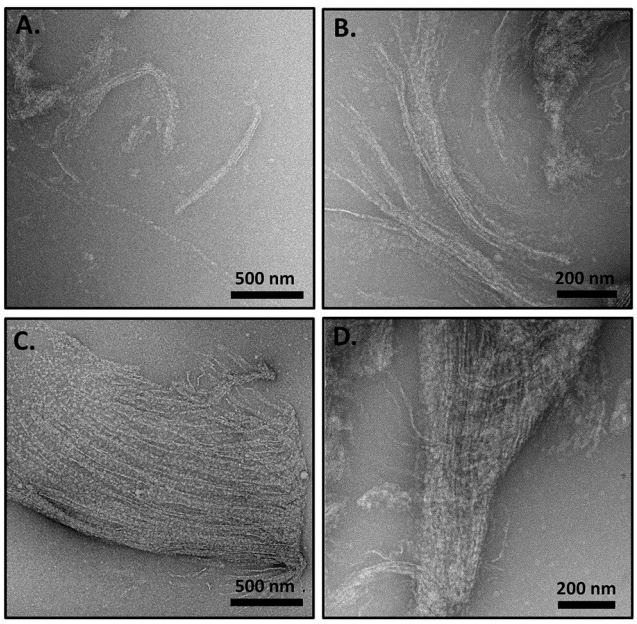

FIGURE 3 | (A–D) TEM analysis of concentrated (1 mg/ml), non-tagged recombinant minicollagen-1 purified from bacteria. The scale bar distance is indicated on the figure.

protein concentration and that this ordering is disrupted with hexa-histidine modification of the amino terminus.

The existence of the G-X-Y collagen-like repeats and the stretches of polyproline present in the minicollagen-1 primary structure raised the question of how similar the properties of recombinant minicollagen-1 were to those of polyproline sequences and the high molecular weight collagens. The sensitivity of the long collagens to temperature is well documented (Tiffany and Krimm, 1972; Lopes et al., 2014), therefore the thermal stability of the recombinant minicollagen-1 secondary structure was measured by CD spectroscopy while exposed to increasing temperatures ranging from 25 to 90°C (**Figure 4**). The secondary structure of recombinant minicollagen-1 demonstrated remarkable thermal stability as evidenced by minor changes in the negative elipticity at 207 nm as well as the minor hump below 200 nm. These ellipticities decreased somewhat as the temperature increased from 25°C to 90°C. Heating the recombinant minicollagen-1 solution to 70°C showed a 20% decrease of the negative ellipticity observed at 207 nm (**Figure 4**, inset), whereas mammalian collagen has been reported to undergo significant denaturation at higher temperatures (Tiffany and Krimm, 1972). The thermal stability of recombinant minicollagen-1 is a useful tool in its purification from soluble bacterial extracts, as it remains in solution after heat treatment of the extracts at 80°C, while a majority of the bacterial contaminating proteins precipitate. The CD spectrum of recombinant minicollagen-1 was also measured in the presence of 1M urea, a chaotrope that has been shown to significantly affect the secondary structure of collagen (Lopes et al., 2014). In contrast to the thermal stability observed earlier, the recombinant minicollagen-1 CD spectrum demonstrated significant changes in the presence of urea, with the negative ellipticity at 207 nm being completely abrogated in the presence of the chaotrope (**Supplementary Figure 7**). The only signature peak remaining in the spectrum displayed a small negative ellipticity at 218 nm. In total, this indicates an increase in random conformational states, and potential urea resistant aggregation of recombinant minicollagen-1.

The presence of the CRDs at the amino and carboxy termini of the minicollagens distinguishes them from the other collagens and suggests that their structure may be modulated by the redox state of the sulfhydryl side chains. In order to measure the oxidation state of the cysteine sulfurs in the purified, recombinant minicollagen-1, a colorimetric assay was performed using Ellman's reagent, where a chromophore is produced upon reduction of the reagent's disulfide bonds in the presence of reducing free sulfhydryl groups from an analyte (Ellman, 1959). For comparison, a calibration plot was created using reduced cysteine to indicate the absorbance generated from Ellman's reagent per reducing equivalent present in the reaction (**Figure 5A**). There are 12 cysteines present per minicollagen-1

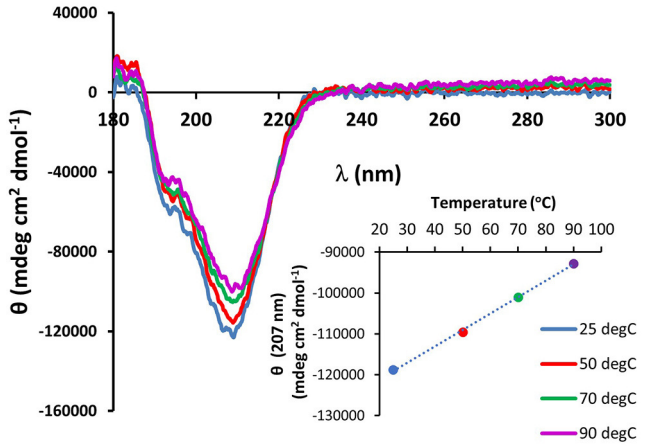

FIGURE 4 | CD spectroscopy of non-tagged recombinant minicollagen-1 (1.4 μM) with increasing temperatures. The temperatures are indicated on the figure. The ellipticity measured at 207 nm as a function of temperature is plotted (inset).

monomer, so the theoretical positions of all potential reducing equivalents (in groups of two) from the assayed 21.5 nmoles of recombinant minicollagen-1 were indicated on the calibration plot (**Figure 5A**). When the recombinant minicollagen-1 (21.5 nmoles) was reacted with Ellman's reagent, the resulting absorbance was less than the theoretical value for the presence of one reducing equivalent, indicating that all of the cysteine sulfurs in the recombinant minicollagen-1 were oxidized as disulfides. This is consistent with the idea that minicollagens store disulfide bonds intra-molecularly to be mobilized for the creation of mechanically robust materials (Engel et al., 2001). To test the role of the disulfide bonds in the structure of recombinant minicollagen-1, its CD spectrum was determined in the presence of 1 mM DTT. Similar to the results obtained with urea, the presence of DTT strongly decreased the negative elipticity observed at 207 nm, while leaving a small negative ellipticity at 218 nm (**Figure 5B**). In contrast, long collagen structure, as determined by CD spectroscopy, has been shown to be unaffected by DTT concentrations up to 5 mM (Lopes et al., 2014). Furthermore, the reduction of recombinant minicollagen-1 leads to increased migration on SDS-PAGE, suggesting that disulfide bond reduction alters the conformation of the protein (**Supplementary Figure 8**). The data indicate that disulfide bonding between sulfhydryls in the cysteine rich domains is a significant factor in stabilizing the secondary structure of recombinant minicollagen-1, consistent with the proposed role of these domains in regulating the material properties of the inner nematocyst wall.

Mobilization of minicollagen cysteine disulfide bonds is proposed to be a key mechanism in the formation and sclerotization of the nematocyst inner wall (Engel et al., 2001). To date, the natural mechanism of disulfide metathesis in the nematocyst inner wall is unknown, so an artificial stimulus to induce disulfide bond rearrangement was sought in order to create recombinant minicollagen-1 hydrogels. The photo-catalyst $Ru(II)(bpy)_3^{2+}$ can create protein hydrogels through sulfate radical chemistry and the formation of dityrosine crosslinks (Fancy and Kodadek, 1999; Elvin et al., 2005). Other studies have utilized sulfate radical chemistry to create hydrogels crosslinked with disulfide bonds that are degradable with reducing agents (Gaulding et al., 2012). Therefore, $Ru(II)(bpy)_3^{2+}$ mediated photo-crosslinking was tested for its ability to initiate disulfide metathesis and inter-chain crosslinking of recombinant minicollagen-1 to create hydrogels. By photo crosslinking (as described in Materials and Methods), the recombinant minicollagen-1 solution demonstrated clear gelation and could be cast into different shapes (cylindrical shape for mechanical testing and dome shape for evaluating effect of reducing reagents) as well as immersed in aqueous salt solutions without dissolving (**Figure 6**). To test the stability of the hydrogels in the presence of a reducing environment, small 20 μl recombinant minicollagen-1 hydrogels were created with a small amount of rhodamine labeled recombinant minicollagen-1 added to more easily visualize the resulting hydrogels once the photo-initiator was removed. After chelation of the $Ru(II)(bpy)_3^{2+}$, a water stable pink hydrogel was observed (**Figure 6B**, lower panel). However, when a reducing agent (β-mercaptoethanol) was added to the chelation mix (CRB), the recombinant minicollagen-1 hydrogels dissolved (**Figure 6B**). The dissolution of photo-crosslinked recombinant minicollagen-1 hydrogels was also observed when β-mercaptoethanol was added alone or when a different reducing agent (DTT) was added. Thus, $Ru(II)(bpy)_3^{2+}$ mediated photo-crosslinking can create hydrogels of recombinant minicollagen-1, at least in part, through the metathesis of disulfide bonds present in the terminal cysteine rich domains. In order to measure mechanical properties, cylindrical hydrogels were cast from 17 wt% aqueous solution of minicollagen-1 as described (Materials and Methods). The equilibrium swelling degree of 17 wt% minicollagen-1 hydrogel was calculated as 5.24 ± 0.85 in deionized water. The compressive elastic modulus was measured using a CellScale Microtester G2 (**Figure 7**). The minicollagen-1 hydrogels were found to have nearly linear stress response up to the maximum measured strain of 15% and to unload with minimal hysteresis (**Figure 7**). The compressive elastic modulus was found to be 9.3 ± 0.4 KPa. Previously, it was shown that the marine sandworm protein, Nvjp-1, could be made into hydrogels through photo-crosslinking with $Ru(II)(bpy)_3^{2+}$ or crosslinking with horseradish peroxidase (Chou et al., 2017; Gupta et al., 2018). Nvjp-1 hydrogel creation with these reagents occurs through the formation of dityrosine crosslinks (Fancy and Kodadek, 1999; Partlow et al., 2014). The compressive elastic modulus of photo-crosslinked minicollagen-1 hydrogels compared favorably with that of horseradish peroxidase catalyzed Nvjp-1 hydrogels (**Supplementary Figure 9**). These data show that minicollagen-1 crosslinking through disulfide metathesis is able to create robust hydrogels whose mechanical properties are comparable to protein hydrogels created with irreversible covalent crosslinks.

DISCUSSION

In this study, the heterologous expression and purification of recombinant minicollagen-1 in *E. coli* at milligram levels is demonstrated for the first time, and the ability to express

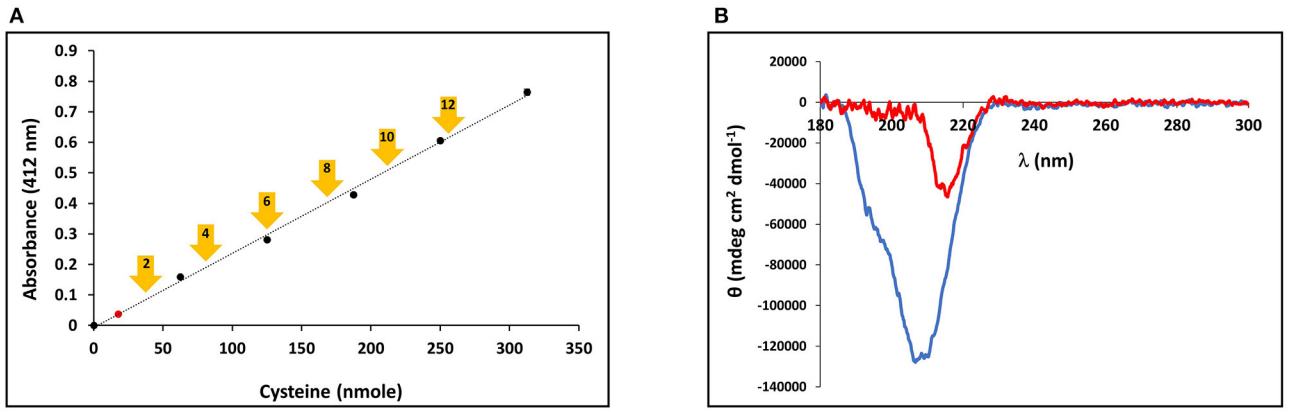

FIGURE 5 | (A) Calibration curve of Ellman's reagent reduction with the assayed amounts of reduced cysteine indicated. The measured absorbance of 21.5 nmoles minicollagen-1 assayed with Ellman's reagent is indicated as a red dot on the calibration curve. The theoretical absorbance expected for Ellman's reagent reduction by the indicated number of recombinant minicollagen-1 free sulfhydryls based on the 21.5 nmoles of the recombinant minicollagen-1 assayed (yellow arrows). **(B)** CD spectroscopy of non-tagged recombinant minicollagen-1 (1.4 μM) in the absence (blue line) and presence (red line) of 1 mM DTT.

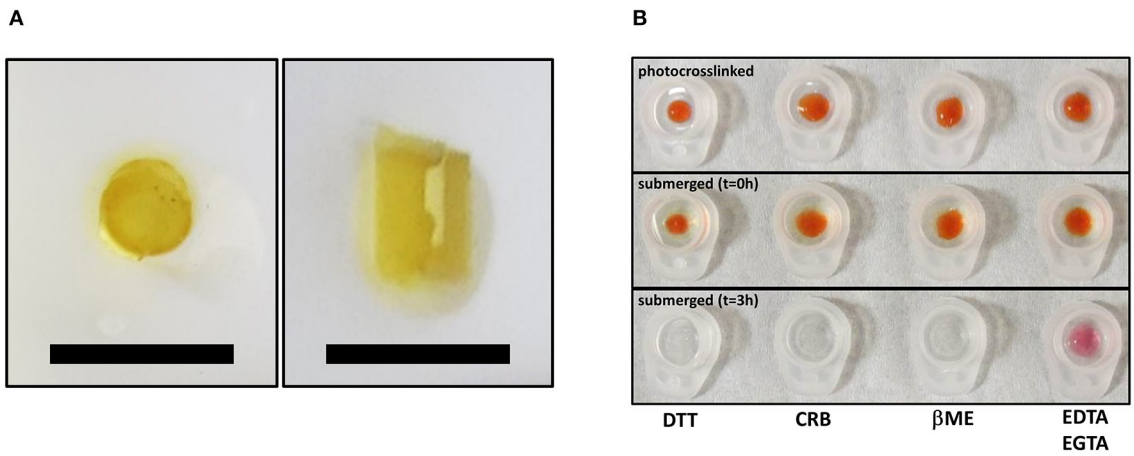

FIGURE 6 | (A) Top view (left) and side view (right) of same free-standing, photo-crosslinked non-tagged recombinant minicollagen-1 (17 wt%) hydrogels that was used for mechanical testing. The scale bars are 1 cm. **(B)** Photo-crosslinked dome shaped hydrogels of 10 wt% minicollagen (doped with rhodamine labeled recombinant minicollagen-1 before removal of $Ru(II)(bpy)_3^{2+}$ (upper) and immediately after submersion in the indicated treatment solutions ($t = 0$ h), or after 3 h in the indicated solutions. DTT (10 mM), CRB (10 mM EDTA, 1 mM EGTA, 1% β-mercaptoethanol), βME (1% β-mercaptoethanol), and 10 mM EDTA/1 mM EGTA are indicated on the figure.

and purify relatively large amount of the protein has enabled the creation of hydrogels that can be mechanically tested. However, there are difficulties that heterologous expression of recombinant minicollagen-1 presents, and yields will need to be increased if recombinant minicollagens are to be used for practical applications. The culture conditions were important in increasing the yield of minicollagen-1, where induction at low temperatures (25°C) and constant oxygenation through air sparging were found to increase expression levels. The low net yields of minicollagen-1 may be due to losses experienced during purification, but are also likely due to poor expression resulting from ribosomal stalling at the long stretches of prolines that flank the central collagen-like domain. Earlier studies showed that the bacterial translation elongation factor, EF-P, is responsible for mediating expression of transcripts coding for stretches of proline longer than two residues (Doerfel et al., 2013; Ude et al., 2013). A bicistronic construct co-expressing EF-P with the His-tagged recombinant minicollagen-1 was created and tested for His-recombinant minicollagen-1 expression. Although co-expression of EF-P with recombinant minicollagen-1 increased expression levels, it is possible that expression can be further increased. EF-P is post-translationally modified with a β-lysyllysine that is essential for function (Park et al., 2012). Thus, it is possible that the over-expressed EF-P is sub-stoichiometrically modified and therefore not operating at full functionality. The gene product YjeK is responsible for the isomerization reaction that creates the β-lysine from α-lysine, and YjeA is the ligase that attaches the β-lysine moiety to a lysine

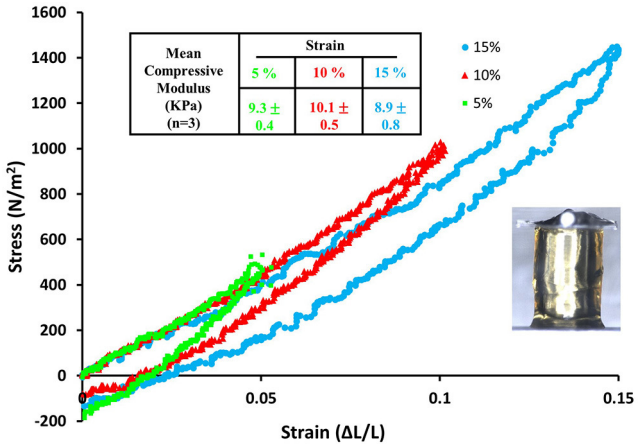

FIGURE 7 | Stress vs. strain curve for compression and then recovery of a 17 wt% recombinant minicollagen-1 photo-crosslinked hydrogel obtained by sequential 5, 10, and 15 % compression. The table on top of the graph summarizes the mean compressive modulus that was calculated from mechanical testing of three hydrogels. The inset image shows the recombinant minicollagen hydrogel under compression using the Microtester G2.

side chain on EF-P (Yanagisawa et al., 2010). Future attempts at expression optimization will create a polycistronic construct where the EF-P modifying enzymes, YjeK and YjeA, will be co-expressed with the EF-P and recombinant minicollagen-1. This approach will hopefully create a system whereby proteins and peptides with high proline content can be efficiently produced in a prokaryotic system.

A key question related to recombinant minicollagen-1 is whether it forms the trimeric quaternary structure observed for the long collagens as well as minicollagens heterologously expressed in mammalian cell culture platforms (Engel et al., 2001). Proline hydroxylation is a post-translational modification that has been implicated in the stabilization of the extended collagen triple helix, and previous studies indicate that the minicollagens also contain hydroxyproline (Lenhoff et al., 1957; Engel et al., 2001). The heterologously expressed recombinant minicollagen-1 is expected to contain no proline hydroxylation, as is known for the bacterial collagens (Mohs et al., 2007). This combined with the short collagen-like region contained in recombinant minicollagen-1 suggests that formation of the triple helical quaternary structure would be unfavorable. This is supported by the CD spectra of the recombinant minicollagen-1, which does not contain the positive ellipticity at 222 nm observed in the long collagens (**Figure 2**). Recent studies have suggested that this absorbance is a better indicator of proper collagen structure than the negative ellipticity at ∼200 nm (Lopes et al., 2014). Comparing the TEM micrographs from the recombinant minicollagen-1 to those obtained previously for minicollagen-1 expressed and purified from a mammalian culture system is informative. Expression of minicollagen-1 in a mammalian cell-line yielded short, aligned rod like structures that had dimensions consistent with those expected from a trihelical collagen-like central structure (Engel et al., 2001). Additionally, amino acid analysis indicated that ∼20% of the proline residues were hydroxylated. TEM micrographs of recombinant minicollagen-1 show bundles of oriented fibrils with no small rod-like structures evident (**Figure 3**). In fact, the structures formed by recombinant minicollagen-1 are more similar to those observed with cnidoin, a silk-like protein found with the minicollagens in the inner wall of the nematocyst (Balasubramanian et al., 2012; Beckmann et al., 2015). Like the minicollagens, cnidoin contains CRDs at the amino and carboxy termini of the protein and mammalian cell line expressed forms of cnidoin have shown a propensity to self-assemble into oriented fibrillar bundles (Beckmann et al., 2015). In addition, cnidoin has been shown to have elastomeric properties and adopts an extended disordered structure found in other elastomeric proteins (Beckmann et al., 2015). In the future, it will be interesting to see if the self-assembly into fibrillar bundles observed with cnidoin and recombinant minicollagen-1 are mediated by the terminal CRDs. Together, the data suggest that recombinant minicollgen-1 is not forming ordered secondary structures in solution, and does not form the trihelical quaternary structure observed with the long collagens or minicollagens expressed from metazoan sources. This is likely due, at least in part, to the inability of the *E. coli* expression system to proline hydroxylate recombinant minicollagen-1. Systems have been developed in bacteria to hydroxylate heterologously expressed collagen on proline (Ramshaw et al., 2019), so future studies will look at the role of proline hydroxylation in the self-assembly and stability recombinant minicollagen-1.

Regardless of whether recombinant minicollagen-1 adopts a trihelical structure, the protein demonstrates interesting properties that may make it useful in material applications, even in an unmodified form. The combination of CRDs, polyproline stretches and the short collagen-like central region make the minicollagen family a potentially unique material additive. Previous studies have shown that polyproline sequences can be distinguished from collagen-like sequences by environmental conditions, such as increased temperature and the existence of chaotropes (Tiffany and Krimm, 1972; Gutierrez-Cruz et al., 2001; Whittington et al., 2005; Lopes et al., 2014). The negative ellipticity demonstrated by the CD spectrum of minicollagen-1 is very heat stable (**Figure 4**), which is a property shared by polyproline peptides, but not collagen (Tiffany and Krimm, 1972; Gutierrez-Cruz et al., 2001). Alternatively, the negative ellipticity observed in recombinant minicollagen-1 CD spectra was very sensitive to the presence of urea, which is a property shared by collagen (Lopes et al., 2014). However, recombinant minicollagen-1 appears to be significantly more sensitive to urea than what has been reported for long collagen (**Supplementary Figure 7**). In contrast to what was observed with recombinant minicollagen-1, urea has been shown to increase the polyproline II helical structure of polyproline sequences (Gutierrez-Cruz et al., 2001; Whittington et al., 2005). Interestingly, the presence of DTT had a strong effect on the recombinant minicollagen-1, abrogating the negative ellipticity observed at 207 nm as was observed with urea treatment (**Figure 5B**). This is consistent with SDS-PAGE analysis where recombinant minicollagen-1 is observed to migrate faster when run under reducing conditions compared to the migration of

the non-reduced protein (**Supplementary Figure 8**). The latter observations likely reflect the reduced ability of recombinant minicollagen-1 to bind SDS as compared to the more globular protein molecular weight standards, and indicate a change in protein conformation between oxidized and reduced states. The sensitivity of recombinant minicollagen-1 to reducing agents is distinct from what is observed with polyproline and collagen sequences, which demonstrate little to no change in secondary structure in the presence of reducing agents (Lopes et al., 2014). Therefore, recombinant minicollagen-1 appears to adopt a disordered conformation but has unique properties compared to other proline rich sequences, and can be distinguished by its sensitivity to reducing agents. This sensitivity may present a useful handle for the tuning of properties in recombinant minicollagen-1 based materials.

The above observations point to a dominant role of the terminal CRDs in the stabilization of recombinant minicollagen-1 secondary structure. The CRDs are present in numerous proteins involved in nematocyst biosynthesis and function (Ozbek et al., 2009; Balasubramanian et al., 2012). Recently, it was shown that the CRDs facilitate multimerization of proteins through direct interaction with each other, and that certain CRD sequences enable a higher interaction valency than others (Tursch et al., 2016). The dynamic nature of the CRD disulfide bonds has been demonstrated in the creation of re-codable surfaces where surface chemistry of a substrate can be written and re-written using the reversible nature of the CRD disulfide bonds (Gegenhuber et al., 2017). In the current study, the ability to utilize photocrosslinking in the creation of recombinant minicollagen-1 hydrogels through the mobilization of the CRD stored disulfides is a demonstration of how these domains may be used to create structured materials. Mechanical testing of the minicollagen-1 hydrogels yielded a compressive elastic modulus in the KPa range, comparable to the mechanical properties measured in other protein-based hydrogels created with irreversible covalent crosslinking (**Supplementary Figure 9**) (Partlow et al., 2014). This is important since the reversible nature of disulfide crosslinking allows for controlled degradation as well as the potential for dynamic reconfiguration. It is also significant that the recombinant minicollagen-1 demonstrates the ability to self-assemble into fibrils and fibril bundles with periodic spacing (**Figure 3**). Therefore, the recombinant minicollagen-1 presented in this study may be looked at as a naïve material precursor, with the potential for scalable expression and the ability to form hydrogels whose properties can be programmed with posttranslational modifications.

DATA AVAILABILITY STATEMENT

The datasets generated for this study are available on request to the corresponding author.

AUTHOR CONTRIBUTIONS

SF, PD, MC, AP, and SY performed processing, and characterization of materials. MC expressed and purified recombinant proteins. CH and JS performed TEM measurements. MG, PD, LD, MS, and RN conceived ideas and designed the experiments. All authors contributed to data analysis, discussions, and manuscript writing.

FUNDING

We are funded by a research grant from AFOSR, grant number RXCOR096.

ACKNOWLEDGMENTS

The authors thank Dr. Peter A. Mirau for assistance in performing NMR analysis. The authors also thank Mr. Benjamin Floyd and Capt. Byron Muhlenberg for assistance performing experiments. The authors acknowledge support of this work by the Air Force Office of Scientific Research and the Office of the Secretary of Defense Synthetic Biology for Military Environments program. PD is adjunct faculty at Wright State University, Dayton, Ohio.

SUPPLEMENTARY MATERIAL

The Supplementary Material for this article can be found online at: https://www.frontiersin.org/articles/10.3389/fchem.2019.00950/full#supplementary-material

REFERENCES

Adamczyk, P., Meier, S., Gross, T., Hobmayer, B., Grzesiek, S., Bachinger, H. P., et al. (2008). Minicollagen-15, a novel minicollagen isolated from *Hydra*, forms tubule structures in nematocysts. *J. Mol. Biol.* 376, 1008–1020. doi: 10.1016/j.jmb.2007.10.090

Antoine, E. E., Vlachos, P. P., and Rylander, M. N. (2014). Review of collagen I hydrogels for bioengineered tissue microenvironments: characterization of mechanics, structure, and transport. *Tissue Eng. Part B Rev.* 20, 683–696. doi: 10.1089/ten.teb.2014.0086

Antoine, E. E., Vlachos, P. P., and Rylander, M. N. (2015). Tunable collagen I hydrogels for engineered physiological tissue micro-environments. *PLoS ONE* 10:e0122500. doi: 10.1371/journal.pone.0122500

Balasubramanian, P. G., Beckmann, A., Warnken, U., Schnolzer, M., Schuler, A., Bornberg-Bauer, E., et al. (2012). Proteome of *Hydra* nematocyst. *J. Biol. Chem.* 287, 9672–9681. doi: 10.1074/jbc.M111.328203

Beckmann, A., Xiao, S., Muller, J. P., Mercadante, D., Nuchter, T., Kroger, N., et al. (2015). A fast recoiling silk-like elastomer facilitates nanosecond nematocyst discharge. *BMC Biol.* 13:3. doi: 10.1186/s12915-014-0113-1

Cao, Y., Yao, Y., Li, Y., Yang, X., Cao, Z., and Yang, G. (2019). Tunable keratin hydrogel based on disulfide shuffling strategy for drug delivery and tissue engineering. *J. Colloid Interface Sci.* 544, 121–129. doi: 10.1016/j.jcis.2019.02.049

Chou, C. C., Martin-Martinez, F. J., Qin, Z., Dennis, P. B., Gupta, M. K., Naik, R. R., et al. (2017). Ion effect and metal-coordinated cross-linking for multiscale design of Nereis jaw inspired mechanomutable materials. *ACS Nano* 11, 1858–1868. doi: 10.1021/acsnano.6b07878

Crookes, W. J., Ding, L. L., Huang, Q. L., Kimbell, J. R., Horwitz, J., and McFall-Ngai, M. J. (2004). Reflectins: the unusual proteins of squid reflective tissues. *Science* 303, 235–238. doi: 10.1126/science.1091288

Degtyar, E., Harrington, M. J., Politi, Y., and Fratzl, P. (2014). The mechanical role of metal ions in biogenic protein-based materials. *Angew. Chem. Int. Ed.* 53, 12026–12044. doi: 10.1002/anie.201404272

Doerfel, L. K., Wohlgemuth, I., Kothe, C., Peske, F., Urlaub, H., and Rodnina, M. V. (2013). EF-P is essential for rapid synthesis of proteins containing consecutive proline residues. *Science* 339, 85–88. doi: 10.1126/science.1229017

Ellman, G. L. (1959). Tissue sulfhydryl groups. *Arch. Biochem. Biophys.* 82, 70–77. doi: 10.1016/0003-9861(59)90090-6

Elvin, C. M., Carr, A. G., Huson, M. G., Maxwell, J. M., Pearson, R. D., Vuocolo, T., et al. (2005). Synthesis and properties of crosslinked recombinant pro-resilin. *Nature* 437, 999–1002. doi: 10.1038/nature04085

Engel, U., Ozbek, S., Streitwolf-Engel, R., Petri, B., Lottspeich, F., and Holstein, T. W. (2002). Nowa, a novel protein with minicollagen Cys-rich domains, is involved in nematocyst formation in *Hydra*. *J Cell Sci.* 115(Pt 20), 3923–3934. doi: 10.1242/jcs.00084

Engel, U., Pertz, O., Fauser, C., Engel, J., David, C. N., and Holstein, T. W. (2001). A switch in disulfide linkage during minicollagen assembly in *Hydra* nematocysts. *EMBO J.* 20, 3063–3073. doi: 10.1093/emboj/20.12.3063

Fancy, D. A., and Kodadek, T. (1999). Chemistry for the analysis of protein-protein interactions: rapid and efficient cross-linking triggered by long wavelength light. *Proc. Natl. Acad. Sci. U.S.A.* 96, 6020–6024. doi: 10.1073/pnas.96.11.6020

Gaulding, J. C., Smith, M. H., Hyatt, J. S., Fernandez-Nieves, A., and Lyon, L. A. (2012). Reversible inter- and intra-microgel cross-linking using disulfides. *Macromolecules* 45, 39–45. doi: 10.1021/ma202282p

Gegenhuber, T., Abt, D., Welle, A., Özbek, S., Goldmann, A. S., and Barner-Kowollik, C. (2017). Spatially resolved photochemical coding of reversibly anchored cysteine-rich domains. *J. Mater. Chem. B* 5, 4993–5000. doi: 10.1039/C7TB00962C

Gupta, M. K., Becknell, K. A., Crosby, M. G., Bedford, N. M., Wright, J., Dennis, P. B., et al. (2018). Programmable mechanical properties from a worm jaw-derived biopolymer through hierarchical ion exposure. *ACS Appl. Mater. Interfaces* 10, 31928–31937. doi: 10.1021/acsami.8b10107

Gutierrez-Cruz, G., Van Heerden, A. H., and Wang, K. (2001). Modular motif, structural folds and affinity profiles of the PEVK segment of human fetal skeletal muscle titin. *J. Biol. Chem.* 276, 7442–7449. doi: 10.1074/jbc.M008851200

Hattori, S., Sakai, K., Watanabe, K., and Fujii, T. (1996). The induction of metachromasia and circular dichroism of coomassie brilliant blue R-250 with collagen and histone H1 is due to the low content of hydrophobic amino acid residues in these proteins. *J. Biochem.* 119, 400–406. doi: 10.1093/oxfordjournals.jbchem.a021255

Holstein, T. W., Benoit, M., Herder, G. V., David, C. N., Wanner, G., and Gaub, H. E. (1994). Fibrous mini-collagens in hydra nematocysts. *Science* 265, 402–404. doi: 10.1126/science.265.5170.402

Kurz, E. M., Holstein, T. W., Petri, B. M., Engel, J., and David, C. N. (1991). Mini-collagens in hydra nematocytes. *J. Cell Biol.* 115, 1159–1169. doi: 10.1083/jcb.115.4.1159

Lenhoff, H. M., Kline, E. S., and Hurley, R. (1957). A hydroxyproline-rich intracellular, collagen-like protein of *Hydra* nematocysts. *Biochim. Biophys. Acta* 26, 204–205. doi: 10.1016/0006-3002(57)90074-4

Li, X., Sun, Q., Li, Q., Kawazoe, N., and Chen, G. (2018). Functional hydrogels with tunable structures and properties for tissue engineering applications. *Front. Chem.* 6:499. doi: 10.3389/fchem.2018.00499

Lopes, J. L., Miles, A. J., Whitmore, L., and Wallace, B. A. (2014). Distinct circular dichroism spectroscopic signatures of polyproline II and unordered secondary structures: applications in secondary structure analyses. *Protein Sci.* 23, 1765–1772. doi: 10.1002/pro.2558

Meier, S., Jensen, P. R., Adamczyk, P., Bachinger, H. P., Holstein, T. W., Engel, J., et al. (2007). Sequence-structure and structure-function analysis in cysteine-rich domains forming the ultrastable nematocyst wall. *J. Mol. Biol.* 368, 718–728. doi: 10.1016/j.jmb.2007.02.026

Mohs, A., Silva, T., Yoshida, T., Amin, R., Lukomski, S., Inouye, M., et al. (2007). Mechanism of stabilization of a bacterial collagen triple helix in the absence of hydroxyproline. *J. Biol. Chem.* 282, 29757–29765. doi: 10.1074/jbc.M703991200

Nuchter, T., Benoit, M., Engel, U., Ozbek, S., and Holstein, T. W. (2006). Nanosecond-scale kinetics of nematocyst discharge. *Curr. Biol.* 16, R316–R318. doi: 10.1016/j.cub.2006.03.089

Ozbek, S., Balasubramanian, P. G., and Holstein, T. W. (2009). Cnidocyst structure and the biomechanics of discharge. *Toxicon* 54, 1038–1045. doi: 10.1016/j.toxicon.2009.03.006

Park, J. H., Johansson, H. E., Aoki, H., Huang, B. X., Kim, H. Y., Ganoza, M. C., et al. (2012). Post-translational modification by beta-lysylation is required for activity of *Escherichia coli* elongation factor P (EF-P). *J. Biol. Chem.* 287, 2579–2590. doi: 10.1074/jbc.M111.309633

Partlow, B. P., Hanna, C. W., Rnjak-Kovacina, J., Moreau, J. E., Applegate, M. B., Burke, K. A., et al. (2014). Highly tunable elastomeric silk biomaterials. *Adv. Funct. Mater.* 24, 4615–4624. doi: 10.1002/adfm.201400526

Petrone, L., Kumar, A., Sutanto, C. N., Patil, N. J., Kannan, S., Palaniappan, A., et al. (2015). Mussel adhesion is dictated by time-regulated secretion and molecular conformation of mussel adhesive proteins. *Nat. Commun.* 6:8737. doi: 10.1038/ncomms9737

Ramshaw, J. A. M., Werkmeister, J. A., and Glattauer, V. (2019). Recent progress with recombinant collagens produced in *Escherichia coli*. *Curr. Opin. Biomed. Eng.* 10, 149–155. doi: 10.1016/j.cobme.2019.06.001

Starborg, T., Kalson, N. S., Lu, Y., Mironov, A., Cootes, T. F., Holmes, D. F., et al. (2013). Using transmission electron microscopy and 3View to determine collagen fibril size and three-dimensional organization. *Nat. Protoc.* 8, 1433–1448. doi: 10.1038/nprot.2013.086

Tan, S., Kern, R. C., and Selleck, W. (2005). The pST44 polycistronic expression system for producing protein complexes in *Escherichia coli*. *Protein Expr. Purif.* 40, 385–395. doi: 10.1016/j.pep.2004.12.002

Tiffany, M. L., and Krimm, S. (1972). Effect of temperature on the circular dichroism spectra of polypeptides in the extended state. *Biopolymers* 2, 2309–2316. doi: 10.1002/bip.1972.360111109

Tursch, A., Mercadante, D., Tennigkeit, J., Grater, F., and Ozbek, S. (2016). Minicollagen cysteine-rich domains encode distinct modes of polymerization to form stable nematocyst capsules. *Sci. Rep.* 6:25709. doi: 10.1038/srep25709

Ude, S., Lassak, J., Starosta, A. L., Kraxenberger, T., Wilson, D. N., and Jung, K. (2013). Translation elongation factor EF-P alleviates ribosome stalling at polyproline stretches. *Science* 339, 82–85. doi: 10.1126/science.1228985

Weber, J. (1989). Nematocysts (stinging capsules of Cnidaria) as Donnan-potential-dominated osmotic systems. *Eur. J. Biochem.* 184, 465–476. doi: 10.1111/j.1432-1033.1989.tb15039.x

Weber, J. (1990). Poly(gamma-glutamic acid)s are the major constituents of nematocysts in *Hydra* (Hydrozoa, Cnidaria). *J. Biol. Chem.* 265, 9664–9669.

Whittington, S. J., Chellgren, B. W., Hermann, V. M., and Creamer, T. P. (2005). Urea promotes polyproline II helix formation: implications for protein denatured states. *Biochemistry* 44, 6269–6275. doi: 10.1021/bi050124u

Yanagisawa, T., Sumida, T., Ishii, R., Takemoto, C., and Yokoyama, S. (2010). A paralog of lysyl-tRNA synthetase aminoacylates a conserved lysine residue in translation elongation factor P. *Nat. Struct. Mol. Biol.* 17, 1136–1143. doi: 10.1038/nsmb.1889

Zhang, Y. S., and Khademhosseini, A. (2017). Advances in engineering hydrogels. *Science* 356:eaaf3627. doi: 10.1126/science.aaf3627

Conflict of Interest: SF, JS, AP, and CH are employed by the company UES, Inc.

The remaining authors declare that the research was conducted in the absence of any commercial or financial relationships that could be construed as a potential conflict of interest.

frontiers in Chemistry

ORIGINAL RESEARCH
published: 28 January 2020
doi: 10.3389/fchem.2020.00007

Hydrogels With Tunable Mechanical Properties Based on Photocleavable Proteins

Dongfang Xiang[1,2], *Xin Wu*[1,2], *Wei Cao*[1], *Bin Xue*[1], *Meng Qin*[1]*, *Yi Cao*[1,2,3,4]* and *Wei Wang*[1,4]*

[1] Key Laboratory of Intelligent Optical Sensing and Integration, National Laboratory of Solid State Microstructure, and Department of Physics, Collaborative Innovation Center of Advanced Microstructures, Nanjing University, Nanjing, China, [2] Shenzhen Research Institute of Nanjing University, Shenzhen, China, [3] Chemistry and Biomedicine Innovation Center, Nanjing University, Nanjing, China, [4] Institute of Brain Science, Nanjing University, Nanjing, China

Hydrogels with photo-responsive mechanical properties have found broad biomedical applications, including delivering bioactive molecules, cell culture, biosensing, and tissue engineering. Here, using a photocleavable protein, PhoCl, as the crosslinker we engineer two types of poly(ethylene glycol) hydrogels whose mechanical stability can be weakened or strengthened, respectively, upon visible light illumination. In the photo weakening hydrogels, photocleavage leads to rupture of the protein crosslinkers, and decrease of the mechanical properties of the hydrogels. In contrast, in the photo strengthening hydrogels, by properly choosing the crosslinking positions, photocleavage does not rupture the crosslinking sites but exposes additional cryptical reactive cysteine residues. When reacting with extra maleimide groups in the hydrogel network, the mechanical properties of the hydrogels can be enhanced upon light illumination. Our study indicates that photocleavable proteins could provide more designing possibilities than the small-molecule counterparts. A proof-of-principle demonstration of spatially controlling the mechanical properties of hydrogels was also provided.

Keywords: photocleavable protein, tunable mechanical properties, hydrogel, spatially control, artificial extracellular matrices, on-demand, drug delivery

OPEN ACCESS

Edited by:
Nikhil Kumar Singha, Indian Institute of Technology Kharagpur, India

Reviewed by:
Artur J. M. Valente, University of Coimbra, Portugal
Guillermo Javier Copello, National Council for Scientific and Technical Research (CONICET), Argentina

***Correspondence:**
Meng Qin
qinmeng@nju.edu.cn
Yi Cao
caoyi@nju.edu.cn
Wei Wang
wangwei@nju.edu.cn

Specialty section:
This article was submitted to Polymer Chemistry, a section of the journal Frontiers in Chemistry

Received: *09 October 2019*
Accepted: *07 January 2020*
Published: *28 January 2020*

Citation:
Xiang D, Wu X, Cao W, Xue B, Qin M, Cao Y and Wang W (2020) Hydrogels With Tunable Mechanical Properties Based on Photocleavable Proteins. Front. Chem. 8:7. doi: 10.3389/fchem.2020.00007

INTRODUCTION

Photo-switchable proteins have been widely used in many fields, including super resolution imaging, optogenetics, fluorescent sensors, and recently as switchable crosslinkers for the engineering of photo-responsive hydrogels (Christie, 2007; Rogan and Roth, 2011; Shcherbakova et al., 2012, 2015; Nienhaus and Nienhaus, 2014; Guntas et al., 2015; Koetting et al., 2015; Niopek et al., 2016; Coquelle et al., 2018). Comparing to other environment-responsive hydrogels, photo-responsive hydrogels have drawn considerable interest (Murphy et al., 2007; Yuan et al., 2008; Gillette et al., 2010; Patterson and Hubbell, 2010; Davis et al., 2011; Yoshikawa et al., 2011; Burdick and Murphy, 2012; Stowers et al., 2015; Abdeen et al., 2016; Han and Lin, 2016), because their mechanical properties can be remotely and non-invasively controlled upon light illumination (Kloxin et al., 2009; Guvendiren and Burdick, 2012; Rosales et al., 2015; Kim et al., 2019; Nowak and Ravoo, 2019; Wu et al., 2019). Generally, most photo-responsive hydrogels are based on the switch between oligomeric and monomeric states of proteins upon light illumination. For example, the reversible change between tetramers and monomers of Dronpa145N can lead to photo-controlled

gel-sol transition or reversible change of the stiffness of the hydrogels (Lyu et al., 2017; Xin et al., 2017). Similarly, the switch between dimeric and monomeric states of cyanobacterial phytochrome 1 can lead to the reversible softening and strengthening of the hydrogels, which allowed dynamic control of the migration of immune cells and mechanotransduction of stem cells (Hörner et al., 2019). The change between dimeric and monomeric states of UVR8-1 led to the design of hydrogels for photo-controlled protein delivery and cell separation (Zhang et al., 2015). Green light induced tetrameric to monomeric transition of the C-terminal adenosylcobalamin binding domain (CarHC) can cause the dissolution of the hydrogels for the stem cell/protein release (Wang et al., 2017). Recently, it was shown that the photo-induced conformational change of LOV2 domains can be used to dynamically control the mechanical properties of the corresponding proteins (Liu et al., 2018). This method is unique in that it does not involve oligomeric photo-switchable proteins but utilize the change of crosslinker length. It is desirable to explore new operation mode of photo-controllable hydrogels based on photo-responsive proteins.

Here, we report two new types of photo-controllable hydrogels based on photo cleavable fluorescent protein PhoCl. PhoCl protein was engineered by Campbell group in 2013 (Zhang et al., 2017). Upon the illumination of violet light (∼400 nm), the chromophore undergoes a β-elimination reaction, leading to the cleavage of the polypeptide backbone. The two fragments of the protein then spontaneously dissociate and become unstructured. We envisioned that this reaction can lead to two effects: (i) photo-induced cleavage of the PhoCl and (ii) exposure of reactive sidechains inside the barrel structure of the protein. Based on these two effects, we design two types of hydrogels whose mechanical stability can be lowered or elevated upon photo illumination, respectively. We anticipate that these hydrogels can be used as artificial extracellular matrices for cell culture and as cargos for on-demand drug delivery.

MATERIALS AND METHODS

Gene Construction

PhoCl and its sequences have been reported. The gene encoding Pho-Weak and Pho-Strong proteins (**Supplementary Figure 1**) were purchased from Genscript and cloned into the pQE80L vector between *BamH*I and *Kpn*I restriction enzyme sites. To produce the pQE80L::Pho-Weak-$(GB1)_2$ and pQE80l::Pho-Strong-$(GB1)_2$, two GB1 (MDTYKLILNGKTLKGETTTEA VDAATAEKVFKQYANDNGVDGEWTYDDATKTFTVTERS) fragments cut by *BamH*I and *Kpn*I restriction enzymes were inserted between *Bgl*II and *Kpn*I sites of pQE80L::Pho-Weak and pQE80l::Pho-Strong, respectively. All genes bear a N-terminal 6×His tag sequence from the pQE80L vector to facilitate affinity purification of expressed proteins.

Protein Expression and Purification

All proteins were expressed in *Escherichia coli* strain BL21. The bacterial cells were grown at 37°C in LB medium supplemented with 100 $\mu g \cdot mL^{-1}$ ampicillin to an OD600 of 0.5 followed by adding 240 $\mu g \cdot mL^{-1}$ isopropyl β-D-1-thiogalactopyranoside to induce protein expression overnight at 25°C. The *E. coli* cells were harvested by centrifugation and the 6×His-tagged proteins were purified using Ni^{2+}-NTA protein resin (GE healthcare, Shanghai, China). The purified proteins were dialyzed against phosphate-buffered saline (PBS) buffer (10 mM, pH7.4, containing 137 mM NaCl and 2.7 mM KCl) and stored at 4°C before use.

Characterization of PhoCl Mutants

All the photoconversion for ultraviolet-visual (UV-Vis) spectroscopy measurements and fluorescence spectra measurements were performed with a light emitting diode (LED) lamp (M405L3c, THORLABS, USA). Absorbance spectra were acquired with V-550 UV/VIS Spectrophotometer (JASCO). Fluorescence spectra were acquired with FP-6500 Spectrofluorometer (JASCO). Circular dichroism spectra were acquired with J-815 CD Spectrometer (JASCO) at room temperature. MALDI-TOF Mass spectra of PhoCl mutants before and after N-methylmaleimide labeling were recorded using an autoflex TOF/TOF mass spectrometer (Bruker Daltonics).

Preparation of PhoCl-PEG Hydrogels

To prepare Pho-Weak-PEG hydrogels, the Pho-Weak and 4-armed-PEG-Mal (Mw: 20 k, Laysan Bio, Inc) were first dissolved in PBS buffer and then were quickly mixed at a molar ratio of 2:1. To prepare Pho-Strong-PEG hydrogels, the Pho-Strong and 4-armed-PEG-Mal solutions were mixed at a molar ratio of 1:2. After preparing the gels at room temperature, they were incubated at 37°C for at least 2 h in dark conditions to ensure the hydrogels were stable.

Characterization of PhoCl-PEG Hydrogels

The photoconversion for rheology measurements was performed with the same LED lamp (M405L3c, THORLABS, USA) as the spectral experiments. Light intensity was 468.6 $mW \cdot cm^{-2}$ in all experiments as measured by an optical power meter (PM100USB, THORLABS, Gemany) with thermal power sensor (S405C, THORLABS, Gemany). The rheological properties of PhoCl-PEG hydrogels measurements were carried out using a HAAKE RheoStress 6000 (Thermo Scientific) at 25°C.

RESULTS AND DISCUSSION

Design of Photo-Controllable Hydrogels

In wild-type PhoCl, there are two buried (Cys28 and Cys98) but no solvent exposed cysteine residues. Photocleavage takes place at His231 (**Supplementary Figure 1**), which is part of the chromophore after maturation. In order to incorporate the PhoCl proteins into the hydrogel network, we designed two PhoCl mutants named as Pho-Weak and Pho-Strong proteins, respectively. Each of these two mutants contains two additional solvent exposed cysteine residues that are ready to react with maleimide containing polyethylene glycol (PEG) to formed hydrogels (named as PhoCl-PEG hydrogels hereafter). In the Pho-Weak mutant, one of the cysteine residues is at the 54th position, while the other is attached to the C-terminal end (**Figure 1A** and **Supplementary Figure 1**). Photocleavage of

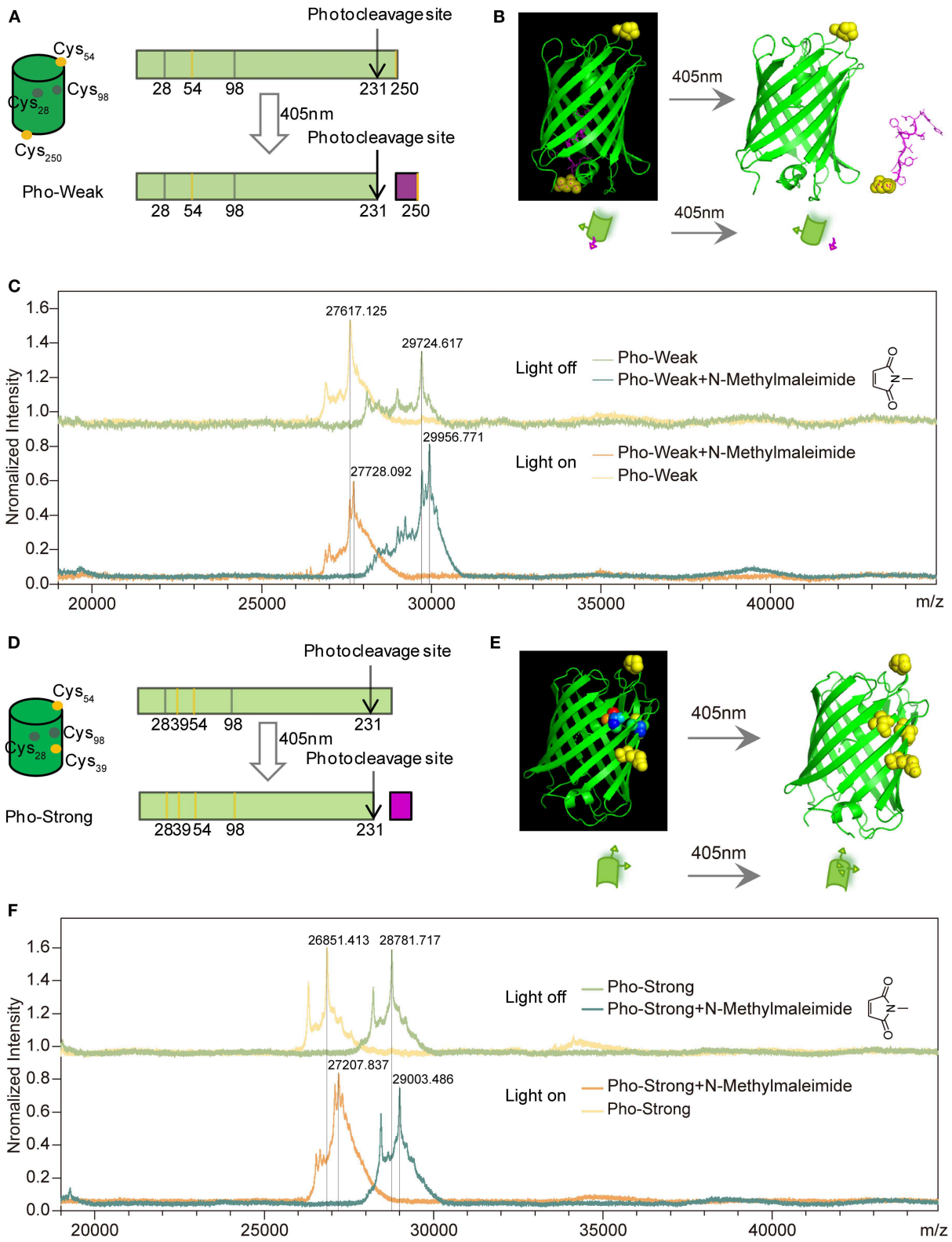

FIGURE 1 | Design of PhoCl mutants. **(A)** Schematic of the design of Pho-Weak. Two solvent exposed cysteines at 54 and 250 positions (colored in yellow) were introduced to wild type PhoCl for crosslinking with maleimide groups in PEG to form hydrogels. The photocleavage reaction leads to the rupture of the linkage between the two crosslinking sites. **(B)** Schematic illustration of the dissociation process. **(C)** MALDI-TOF before and after Pho-Weak photocleavage excited at

(Continued)

FIGURE 1 | 405 nm. Two N-Methylmaleimide (Mw:111.1) reacted with Pho-Weak in the dark and the rupture of the linkage between the two crosslinking sites. **(D)** Schematic of the design of Pho-Strong. Photocleavage does not break the linkage between the two crosslinking sites (Cys39 and Cys 54) but expose two cryptic cysteine residues (Cys28 and Cys98, colored in gray). **(E)** Schematic illustration of the light-induced exposure of additional cysteine residues. **(F)** MALDI-TOF of Pho-Strong. Two N-Methylmaleimide crosslinked with Pho-Strong in the dark and more crosslinking sites were formed due to the light-induced exposure of additional cysteine residues.

Pho-Weak proteins causes the rupture of the sequence between the two cysteine residues (**Figure 1B**). To confirm this design, we used MALDI-TOF mass spectroscopy to characterize the reactivity of the cysteine residues and the photolysis products. A small maleimide containing molecule, N-methylmaleimide, was used for labeling and the mass gain after reaction is 111.1 Da (Δ). The MALDI-TOF experiments confirmed that the solvent exposed cysteines of Pho-Weak can successfully react with N-methylmaleimide leading to a mass gain of ∼2 × Δ (**Figure 1C**). After photocleavage, the increase of the mass of the larger fragment was ∼1 × Δ, suggesting that the cleavage site was in between the two labeled cysteine residues. In the Pho-Strong mutant, the two solvent exposed cysteine residues are introduced at the 39 and 54th positions (**Figure 1D** and **Supplementary Figure 1**). Even after photocleavage, the two cysteine residues are still attached to the same fragment (**Figure 1E**). Similarly, this design was confirmed by the MALDI-TOF experiments (**Figure 1F**). Before photolysis, the mass gain after labeling was ∼2×Δ; after photolysis and further reacting with extra N-methylmaleimide, the mass gain was ∼3.2 × Δ, indicating that some of the originally buried cysteine residues were exposed and reacted with maleimide. Therefore, the crosslinking density increased after photocleavage of Pho-Strong mutants.

The hydrogels whose mechanical properties can be enhanced and decreased upon light illumination were prepared based on Pho-Weak and Pho-Strong proteins, respectively. The solvent exposed thiol groups of the two proteins can react with maleimide functionalized 4-armed polyethylene glycol (4-armed-PEG-Mal) to form hydrogel networks (**Figure 2A**). In the photo-weakening hydrogel, the ratio of maleimide and solvent exposed thiol groups is 1:1 and there were no additional maleimide groups available to react with the freshly exposed Cys28 and Cys98 (**Figure 2B**). Photocleavage reaction leads to the decrease of the mechanical stability or even gel-sol transition of the corresponding hydrogels. In the photo-strengthening hydrogel, the ratio of maleimide and the total thiol groups (including both the solvent exposed and the buried ones) is 1:1. Photocleavage of Pho-Strong does not cause the decrease of crosslinking density, as the two photocleavage site is outside the crosslinking sequence (**Figure 2A**). Moreover, because there are additional maleimide groups available from the hydrogel network, new crosslinking sites are readily formed with the exposed cysteine residues (Cys28 and Cys98) after the dissociation of the cleaved fragment (**Figure 2C**). This results in the elevation of the mechanical stability of the hydrogels after photocleavage. In order to quantify the amount of thiol reacted with maleimide in the hydrogel network, we used a model system by replacing 4-armed PEG-Mal with linear PEG-Mal (only a single maleimide group at the end of each PEG polymer) and analyzed the amount of reacted proteins based on the SDS-PAGE (**Supplementary Figure 2**). The yields for the Pho-Weak and Pho-Strong were 54 and 65%, respectively. Note that, some cysteine residues may have already formed disulfide bonds before reacting with maleimide groups in the hydrogels, which can also serve as the crosslinks.

Characterization of the Photocleavage of PhoCl Mutants

To make sure that the photocleavage properties of the proteins were not affected by the introduction of cysteine mutations, we first characterized their photocleavage properties in solution. The solution of Pho-Weak protein showed characteristic green fluorescence of PhoCl (**Figure 3A**) (Zhang et al., 2017). After irradiated at 405 nm light for 30 min, the color of Pho-Weak solution changed to brown, consistent with the color change of wild type PhoCl (Zhang et al., 2017). Similarly, UV-vis Spectroscopy of Pho-Weak was also changed and showed a broad absorbance from ∼400 to 500 nm after photocleavage (**Figure 3B**). The fluorescence of Pho-Weak was greatly dimmed after photocleavage (**Figure 3C**). Using fluorescence change as the indicator, we can estimate the photocleavage kinetics. Pho-Weak was completely cleaved in ∼20 min (**Figure 3D**). The structural change of Pho-Weak was confirmed by the CD spectra. The major negative peak at ∼215 nm corresponding to the β sheet structure was greatly reduced after cleavage (**Figure 3E**). To further confirm that Pho-Weak was cleaved by light illumination, we used SDS-PAGE to characterize the size of photolyzed samples. Because the short fragment is too small to be resolved in SDS-PAGE, we flanked two GB1 proteins as the tag to the C-terminus of Pho-Weak. Clearly, after photocleavage, two additional peaks corresponding to the two fragments appeared (**Figure 3F**). This indicated that the peptide linkage was completely ruptured. We also performed the characterization of Pho-Strong protein. It showed the same properties as the Pho-Weak protein (**Figures 4A–F**). The photocleavage kinetics of Pho-Strong was a bit slower than Pho-Weak proteins ($t_{1/2}$ of ∼120 s for Pho-Weak and ∼270 s for Pho-Strong proteins, respectively). Note that, the photocleavage rates of both Pho-Weak and Pho-Strong proteins were faster than that of wild type PhoCl ($t_{1/2}$ of ∼500 s) (Zhang et al., 2017). The photocleavage reaction involves a violet light -induced β-elimination on the conjugated chromophore and the subsequent cleavage of the polypeptide chain. Although the cysteine mutants were distant from the chromophore, they can still affect the photocleavage kinetics. In some of the mutants we tried, the cysteine mutants lost the photocleavage properties because the cysteine mutation sites were at the same loop of the photocleavage site.

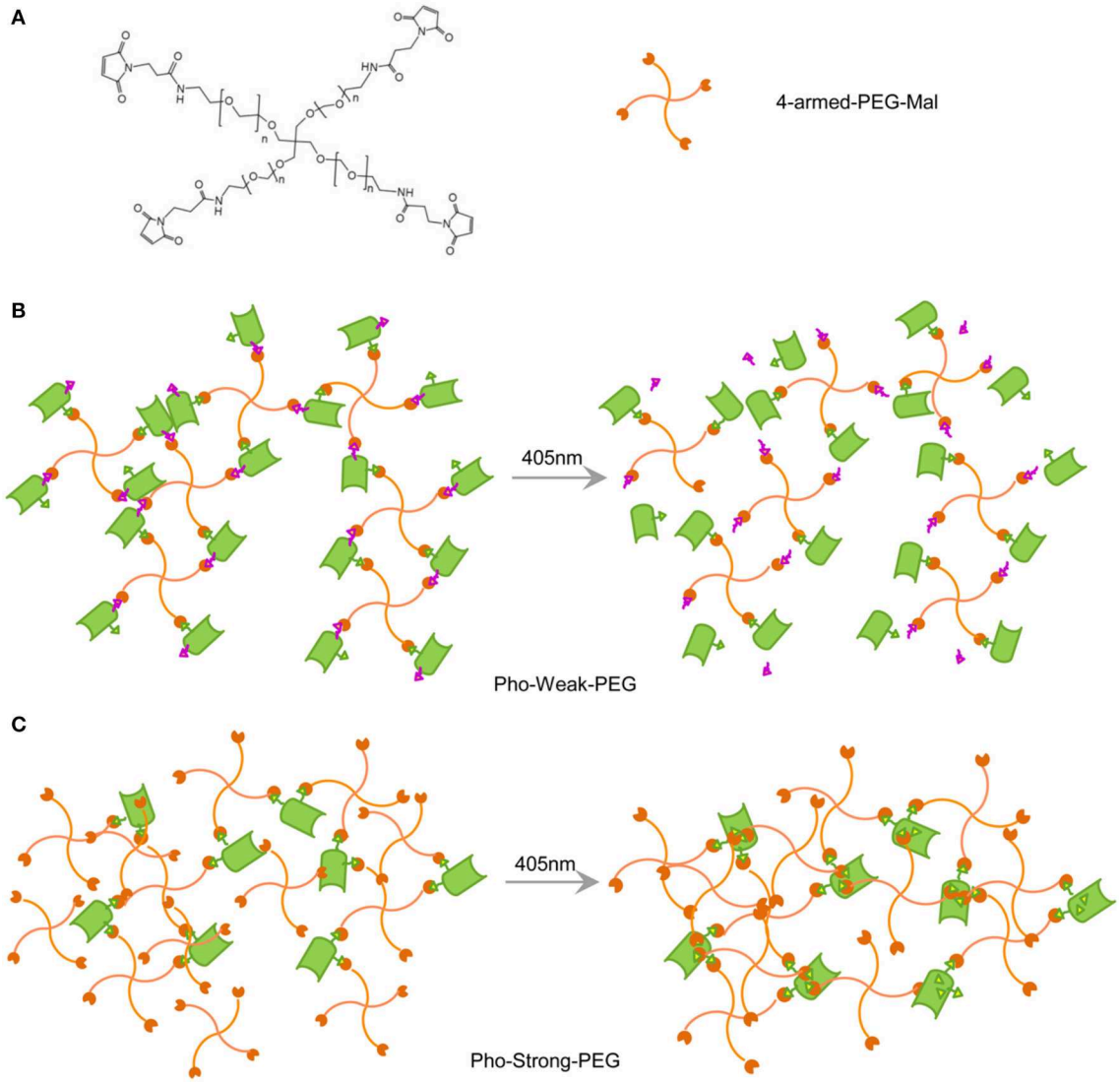

FIGURE 2 | Design of PhoCl-PEG hydrogels. **(A)** Chemical structure of 4-armed-PEG-Mal. The maleimide-terminated end of each arm can react with thiol groups of cysteines when they are solvent exposed. **(B)** Schematic illustration of the Pho-Strong-PEG hydrogel in dark (left) and the photo-switching process of the hydrogel (right). **(C)** Schematic illustration of the Pho-Weak-PEG hydrogel in dark (left) and the photo-switching process of the hydrogel (right).

Mechanical Properties of PhoCl-PEG Hydrogel

To form the Pho-Weak-PEG hydrogels, Pho-Weak and 4-arm-PEG-Mal were mixed at a molar ratio of 2:1 (solvent exposed thiol:Mal = 1:1) at dark to form Pho-Weak-PEG hydrogel. Thanks to the quick reaction between thiol and maleimide, the hydrogels were formed in <5 min. Rheological measurement showed that the storage modulus G′ of the hydrogels was constantly higher than the loss modulus G″ over a broad frequency range, confirming that a gel network was formed (**Figure 5A**). With the increase of the protein concentrations, both G′ and G″ increased accordingly. When the hydrogel was irradiated by 405 nm light (468.6 mW·cm^{-2}) for 30 min, both G′ and G″ were greatly reduced, confirming the photo-weakening property of the hydrogels. We also monitored the change of the rheological properties of the Pho-Weak-PEG hydrogels at different photo illumination time. A continuous decrease of G′ was observed, indicating that the crosslinking density of the hydrogels were decreased. When 30 mg·mL^{-1} of Pho-Weak was used, the G′ was dropped even lower than G″ after ∼1,000 s, indicating that the hydrogel was completely converted to liquid (**Figures 5B,C**). Note that due to the high concentrations of proteins in the hydrogel, the photocleavage efficiency for Pho-Weak proteins was much lower than that in solution. The efficiency was also inversely correlated with the thickness of the hydrogels.

To form the Pho-Strong-PEG hydrogels, Pho-Strong and 4-armed-PEG-Mal were mixed at a molar ratio of 1:1 (total

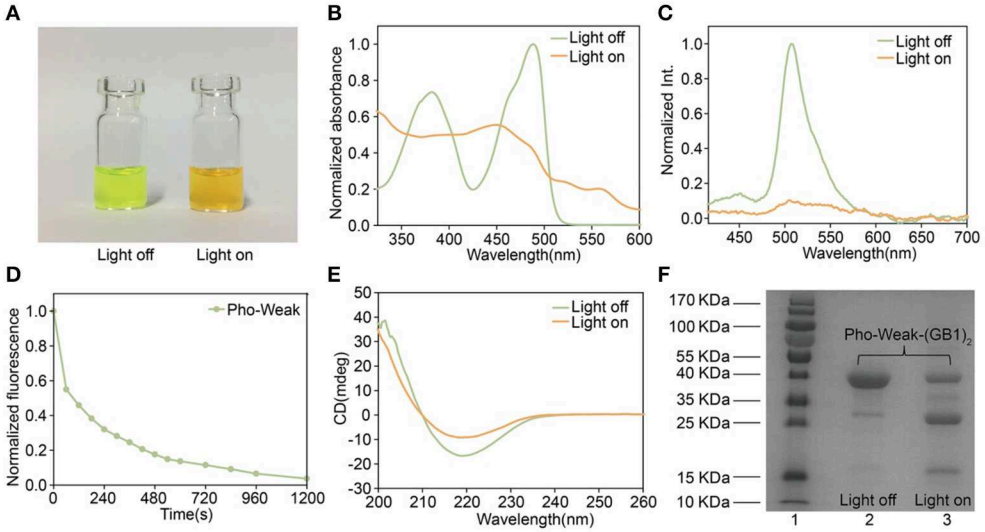

FIGURE 3 | Characterization of Pho-Weak. **(A)** Photographs of Pho-Weak solutions before and after light illumination. **(B)** UV–vis absorbance changes after photocleavage. **(C)** Fluorescence spectra before and after photocleavage excited at 405 nm. **(D)** Kinetics of dissociation, as determined by the decrease of green fluorescence after illumination. **(E)** Circular dichroism spectra before and after photocleavage. **(F)** SDS-PAGE analysis of Pho-Weak-$(GB1)_2$ before and after photocleavage. The band at ∼ 13 kDa corresponds to the fragment containing $(GB1)_2$.

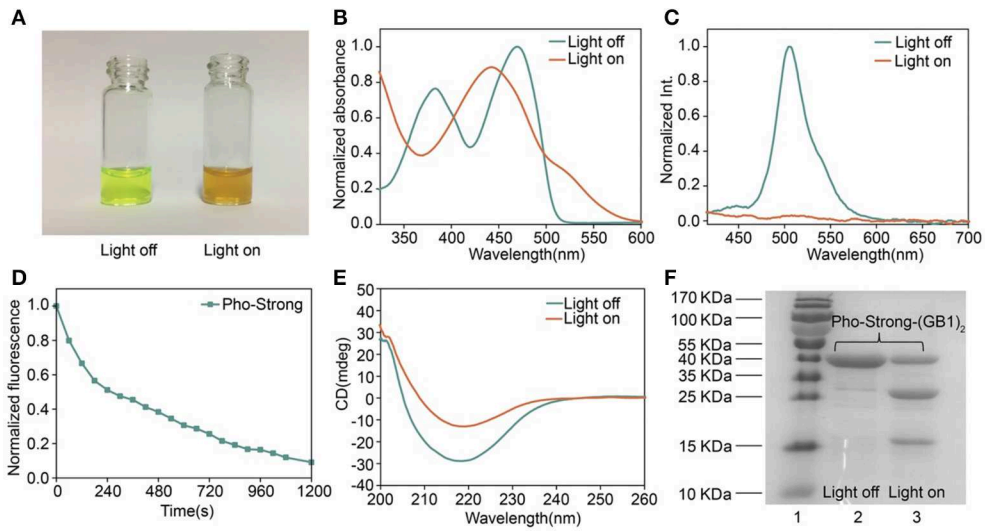

FIGURE 4 | Characterization of Pho-Strong. **(A)** Photographs of Pho-Strong solutions before and after light illumination. **(B)** UV–vis absorbance changes after photocleavage. **(C)** Fluorescence spectra before and after photocleavage excited at 405 nm. **(D)** Kinetics of dissociation, as determined by the decrease of green fluorescence after illumination. **(E)** Circular dichroism spectra before and after photocleavage. **(F)** SDS-PAGE analysis of Pho-Strong-$(GB1)_2$ before and after photocleavage. The band at ∼ 13 kDa corresponds to the fragment containing $(GB1)_2$.

thiol: Mal = 1:1) at dark to form Pho-Strong-PEG hydrogels, so that parts of PEG arms of the 4-armed-PEG-Mal were still free without participating in the hydrogel network (**Figure 2C**). When the hydrogels were illuminated at 405 nm light (468.6 mW·cm^{-2}) for 40 min, the mechanical properties of the hydrogels became higher (**Figure 5D**). The constant increase of the mechanical properties of the hydrogels upon photo illumination were observed for the Pho-Strong-PEG hydrogels, further confirming the successful design of the photo-strengthening hydrogels (**Figure 5E**). Moreover, in the photo-strengthening process, there were no protein aggregation or dehydration effects observed (**Figure 5F**), suggesting that the increase of the mechanical stability was mainly due to the formation of thiol-maleimide adducts with newly exposed cysteine residues.

It is worth mentioning that both Pho-Weak-PEG and Pho-Strong-PEG hydrogels used in these experiments were not under swelling equilibrium. The swelling of the hydrogels in PBS

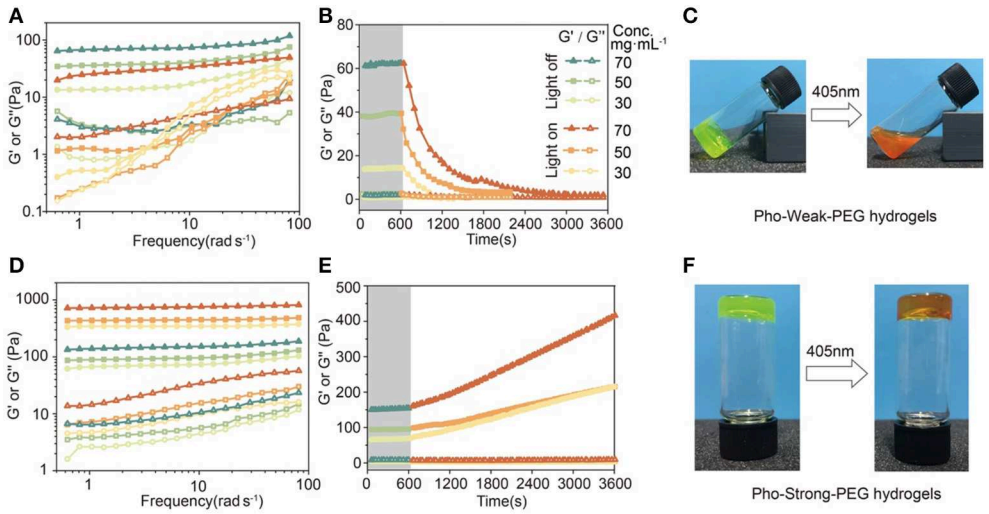

FIGURE 5 | Rheological properties and photo-conversion of PhoCl-PEG hydrogels. **(A)** Frequency sweep of hydrogels with different Pho-Weak concentrations before and after photocleavage. **(B)** Real-time monitoring the photo-weakening of hydrogel by rheology (Frequency: 1 Hz). **(C)** Optical photographs of Pho-Weak-PEG hydrogels: pristine (left, gel) and after photo illumination (right, viscous liquid). **(D)** Frequency sweep of hydrogel with different Pho-Strong concentrations before and after photocleavage. **(E)** Real-time monitoring the photo-weakening of hydrogel by rheology (Frequency: 1 Hz). **(F)** Optical photographs of Pho-Strong-PEG hydrogels: pristine (left) and after photo illumination (right). The legend next to **(B)** applies to **(A, B, D, E)**.

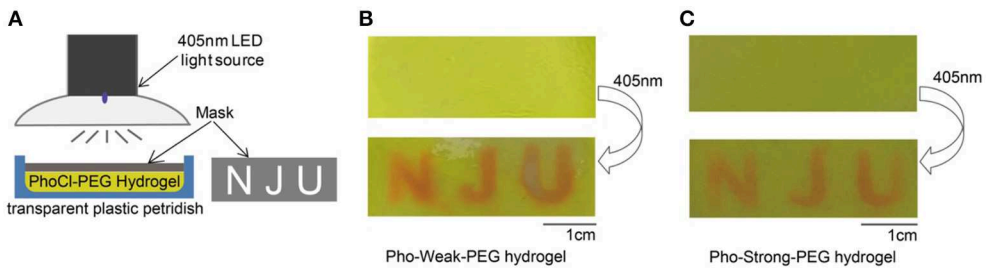

FIGURE 6 | Spatially Control the Mechanical Properties of PhoCl-PEG hydrogels. **(A)** Schematic diagram of the experiment. **(B)** The letters of "NJU" were printed on a Pho-Weak-PEG hydrogel by photo illumination at 405 nm for 40 min through a mask. **(C)** The letters of "NJU" were printed on a Pho-Strong-PEG hydrogel by photo illumination at 405 nm for 40 min through the same mask.

buffers can also the mechanical properties. The swelling ratios of the Pho-Weak-PEG and Pho-Strong-PEG hydrogels before photolysis were 154 and 196%, respectively, after immersing in PBS buffer for 24 h. Nonetheless, the photo-weakening and photo-strengthening trends of the hydrogels were not affected by the swelling of the hydrogels.

Spatially Control the Mechanical Properties of PhoCl-PEG Hydrogels

We next explore the use of light to control the mechanical properties of PhoCl-PEG hydrogels in 2D. Both Pho-Weak-PEG and Pho-Strong-PEG hydrogels were prepared in plastic petridishes of ∼ 1 mm thick. Then the hydrogels were covered by an alumina foil mask with different patterns (**Figure 6A**). After illumination under 405 nm light for 40 min, a clear pattern at the light exposed area can be formed (**Figures 6B,C**). Note that, because the Pho-Weak-PEG hydrogel was partially converted to liquid, the liquidized part was mobile and slowly diffused to the surroundings (**Figure 6B**). We envisioned that this type of hydrogels can be used for protein/cell delivery in the future. In contrast, the edge of the patterns on the Pho-Strong-PEG hydrogel was much sharper (**Figure 6C**). It is worth mentioning that as the photocleavage causes the detachment of the C-terminal fragment, peptide or protein release function can be also implement in the Pho-Strong-PEG hydrogels without the dissolution of the hydrogels. This may be even advantageous for long-term on-demand release of functional proteins directly linked to the C-terminal of Pho-Strong protein upon light irradiation. The light convertible mechanical properties also make the hydrogels ideal candidates for the study of the effect of mechanical cues on cell migration, spreading, and differentiation *in vitro*.

CONCLUSION

In summary, here we demonstrated the use of a photocleavable protein, PhoCl, as crosslinkers, and multiple-armed PEG as backbones to prepare photo-responsive hydrogels. We

engineered two exposed cysteine residues to PhoCl to specifically react with the maleimide group at each end of the PEG arms to form the hydrogels. By choosing proper crosslinking positions, we were able to rationally weakening or strengthening the mechanical properties of the hydrogels upon light illumination. We envision that the release of functional protein/peptide fragments or the expose of bioactive cell binding ligands can be realized simultaneous along with the change of mechanical properties upon light illumination. Therefore, it can be used as an indispensable tool to study the effect of mechanical and chemical cues on stem cell differentiation, cell migration, and so on. Moreover, as the crosslinking density of the hydrogels is greatly changed, it can also be used as a platform for cell capture or cell release. Exploring the biomedical applications of the PhoCl-PEG hydrogels will be our next endeavor.

DATA AVAILABILITY STATEMENT

The raw data supporting the conclusions of this article will be made available by the authors, without undue reservation, to any qualified researcher.

AUTHOR CONTRIBUTIONS

YC, MQ, and WW conceived the idea and supervised the project. YC designed the whole research, and revised the manuscript. DX constructed the plasmids, expressed and purified the proteins, characterized proteins and the hydrogels, and wrote the manuscript. XW and WC were involved in plasmid construction and protein expression. BX helped to prepare and characterize the hydrogels.

FUNDING

This research work was financially supported by the National Natural Science Foundation of China (11674153) and the Basic Research Project of Science and Technology Plan of Shenzhen (JCYJ20170818110643669).

SUPPLEMENTARY MATERIAL

The Supplementary Material for this article can be found online at: https://www.frontiersin.org/articles/10.3389/fchem.2020.00007/full#supplementary-material

REFERENCES

Abdeen, A. A., Lee, J., Bharadwaj, N. A., Ewoldt, R. H., and Kilian, K. A. (2016). Temporal modulation of stem cell activity using magnetoactive hydrogels. *Adv. Healthc. Mater.* 5, 2536–2544. doi: 10.1002/adhm.201600349

Burdick, J. A., and Murphy, W. L. (2012). Moving from static to dynamic complexity in hydrogel design. *Nat. Commun.* 3:1269. doi: 10.1038/ncomms2271

Christie, J. M. (2007). Phototropin blue-light receptors. *Annu. Rev. Plant Biol.* 58, 21–45. doi: 10.1146/annurev.arplant.58.032806.103951

Coquelle, N., Sliwa, M., Woodhouse, J., Schirò, G., Adam, V., Aquila, A., et al. (2018). Chromophore twisting in the excited state of a photoswitchable fluorescent protein captured by time-resolved serial femtosecond *crystallography. Nat. chem.* 10, 31–37. doi: 10.1038/nchem.2853

Davis, K. A., Burke, K. A., Mather, P. T., and Henderson, J. H. (2011). Dynamic cell behavior on shape memory polymer substrates. *Biomaterials* 32, 2285–2293. doi: 10.1016/j.biomaterials.2010.12.006

Gillette, B. M., Jensen, J. A., Wang, M., Tchao, J., and Sia, S. K. (2010). Dynamic hydrogels: switching of 3D microenvironments using two-component naturally derived extracellular matrices. *Adv. Mater.* 22, 686–691. doi: 10.1002/adma.200902265

Guntas, G., Hallett, R. A., Zimmerman, S. P., Williams, T., Yumerefendi, H., Bear, J. E., et al. (2015). Engineering an improved light-induced dimer (iLID) for controlling the localization and activity of signaling proteins. *Proc. Natl. Acad. Sci. U.S.A.* 112, 112–117. doi: 10.1073/pnas.1417910112

Guvendiren, M., and Burdick, J. A. (2012). Stiffening hydrogels to probe short- and long-term cellular responses to dynamic mechanics. *Nat. Commun.* 3:792. doi: 10.1038/ncomms1792

Han, S., and Lin, C. C. (2016). Tuning stiffness of cell-laden hydrogel: Via host-guest interactions. *J. Mater. Chem. B* 4, 4969–4974. doi: 10.3389/conf.FBIOE.2016.01.02362

Hörner, M., Raute, K., Hummel, B., Madl, J., Creusen, G., Thomas, O. S., et al. (2019). Phytochrome-based extracellular matrix with reversibly tunable mechanical properties. *Adv. Mater.* 31:e1806727. doi: 10.1002/adma.201806727

Kim, I., Bang, W. Y., Park, W. H., Han, E. H., and Lee, E. (2019). Photo-crosslinkable elastomeric protein-derived supramolecular peptide hydrogel with controlled therapeutic CO-release. *Nanoscale* 11, 17327–17333. doi: 10.1039/C9NR06115K

Kloxin, A. M., Kasko, A. M., Salinas, C. N., and Anseth, K. S. (2009). Photodegradable hydrogels for dynamic tuning of physical and chemical properties. *Science* 324, 59–63. doi: 10.1126/science.1169494

Koetting, M. C., Peters, J. T., Steichen, S. D., and Peppas, N. A. (2015). Stimulus-responsive hydrogels: theory, modern advances, and applications. *Mater. Sci. Eng. R Rep.* 93, 1–49. doi: 10.1016/j.mser.2015.04.001

Liu, L., Shadish, J. A., Arakawa, C. K., Shi, K., Davis, J., and DeForest, C. A. (2018). Cyclic stiffness modulation of cell-aden protein–polymer hydrogels in response to user-specified stimuli including light. *Adv. Biosys.* 2:1800240. doi: 10.1002/adbi.201870111

Lyu, S., Fang, J., Duan, T., Fu, L., Liu, J., and Li, H. (2017). Optically controlled reversible protein hydrogels based on photoswitchable fluorescent protein dronpa. *Chem. Commun. (Camb)* 53, 13375–13378. doi: 10.1039/C7CC06991J

Murphy, W. L., Dillmore, W. S., Modica, J., and Mrksich, M (2007). Dynamic hydrogels: translating a protein conformational change into macroscopic motion. *Angew. Chem. In. Ed. Engl.* 46, 3066–3069. doi: 10.1002/anie.200604808

Nienhaus, K., and Nienhaus, G. U. (2014). Fluorescent proteins for live-cell imaging with super-resolution. *Chem. Soc. Rev.* 43, 1088–1106. doi: 10.1039/C3CS60171D

Niopek, D., Wehler, P., Roensch, J., Eils, R., and Di Ventura, B. (2016). Optogenetic control of nuclear protein export. *Nat. Commun.* 7:10624. doi: 10.1038/ncomms10624

Nowak, B., and Ravoo, B. J. (2019). Magneto- and photo-responsive hydrogels from the co-assembly of peptides, cyclodextrins, and superparamagnetic nanoparticles. *Faraday Discuss* 219, 220–228. doi: 10.1039/C9FD00012G

Patterson, J., and Hubbell, J. A. (2010). Enhanced proteolytic degradation of molecularly engineered PEG hydrogels in response to MMP-1 and MMP-2. *Biomaterials* 31,7836–7845. doi: 10.1016/j.biomaterials.2010.06.061

Rogan, S. C., and Roth, B. L. (2011). Remote control of neuronal signaling. *Pharmacol. Rev.* 63,291–315. doi: 10.1124/pr.110.003020

Rosales, A. M., Mabry, K. M., Nehls, E. M., and Anseth, K. S. (2015). Photoresponsive elastic properties of azobenzene-containing poly(ethylene-glycol)-based hydrogels. *Biomacromolecules* 16, 798–806. doi: 10.1021/bm501710e

Shcherbakova, D. M., Shemetov, A. A., Kaberniuk, A. A., and Verkhusha, V. V. (2015). Natural photoreceptors as a source of fluorescent proteins,

biosensors, and optogenetic tools. *Annu. Rev. Biochem.* 84, 519–550. doi: 10.1146/annurev-biochem-060614-034411

Shcherbakova, D. M., Subach, O. M., and Verkhusha, V. V. (2012). Red fluorescent proteins: advanced imaging applications and future design. *Angew. Chem. Int. Ed. Engl.* 51, 10724–10738. doi: 10.1002/anie.201200408

Stowers, R. S., Allen, S. C., and Suggs, L. J. (2015). Dynamic phototuning of 3D hydrogel stiffness. *Proc Natl Acad Sci U.S.A* 112, 1953–1958. doi: 10.1073/pnas.1421897112

Wang, R., Yang, Z., Luo, J., Hsing, I. M., and Sun, F. (2017). B12-dependent photoresponsive protein hydrogels for controlled stem cell/protein release. *Proc. Natl. Acad. Sci. U.S.A.* 114, 5912–5917. doi: 10.1073/pnas.1621350114

Wu, H., Qin, Z., Yu, X., Li, J., Lv, H., and Yang, X. (2019). On-demand removable hydrogels based on photolabile cross-linkings as wound dressing materials. *J. Mater. Chem. B* 7, 5669–5676. doi: 10.1039/C9TB01544B

Xin, W., Wenmao, H., Wen-Hao, W., Bin, X., Dongfang, X., Li, Y., et al. (2017). Reversible hydrogels with tunable mechanical properties for optically controlling cell migration. *Nano Res.* 11, 5556–5565. doi: 10.1007/s12274-017-1890-y

Yoshikawa, H. Y., Rossetti, F. F., Kaufmann, S., Kaindl, T., Madsen, J., Engel, U., et al. (2011). Quantitative evaluation of mechanosensing of cells on dynamically tunable hydrogels. *J. Am. Chem. Soc.* 133, 1367–1374. doi: 10.1021/ja1060615

Yuan, W., Yang, J., Kopecková, P., and Kopecek, J. (2008). Smart hydrogels containing adenylate kinase: translating substrate recognition into macroscopic motion. *J. Am. Chem. Soc.* 130, 15760–15761. doi: 10.1021/ja805634x

Zhang, W., Lohman, A. W., Zhuravlova, Y., Lu, X., Wiens, M. D., Hoi, H., et al. (2017). Optogenetic control with a photocleavable protein. *PhoCl.* 14, 391–394. doi: 10.1038/nmeth.4222

Zhang, X., Dong, C., Huang, W., Wang, H., Wang, L., Ding, D., et al. (2015). Rational design of a photo-responsive UVR8-derived protein and a self-assembling peptide-protein conjugate for responsive hydrogel formation. *Nanoscale* 7, 16666–16670. doi: 10.1039/C5NR05213K

Conflict of Interest: A patent based on this research was filed.

The authors declare that the research was conducted in the absence of any commercial or financial relationships that could be construed as a potential conflict of interest.

frontiers in Chemistry

ORIGINAL RESEARCH
published: 30 January 2020
doi: 10.3389/fchem.2020.00036

Dual-Enzyme Crosslinking and Post-polymerization for Printing of Polysaccharide-Polymer Hydrogel

Saiji Shen, Jiayin Shen, Hongdou Shen, Chu Wu, Ping Chen and Qigang Wang**

School of Chemical Science and Engineering, School of Life Science and Technology, Tongji University, Shanghai, China

Polymer hydrogels are ideal bioprinting scaffolds for cell-loading and tissue engineering due to their extracellular-matrix-like structure. However, polymer hydrogels that are easily printed tend to have poor strength and fragile properties. The gradually polymerized reinforcement after hydrogel printing is a good method to solve the contradiction between conveniently printed and high mechanical strength requirement. Here, a new succinct approach has been developed to fabricate the printable composite hydrogels with tunable strength. We employed the HRP@GOx dual enzyme system to initiate the immediate crosslinking of chondroitin sulfate grafted with tyrosine and the gradual polymerization of monomers to form the composite hydrogels. The detailed two-step gelation mechanism was confirmed by the Fluorescence spectroscopy, Electron paramagnetic resonance spectroscopy and Gel permeation chromatography, respectively. The final composite hydrogel combines the merits of enzymatic crosslinking hydrogels and polymerized hydrogels to achieve adjustable mechanical strength and facile printing performance. The dual-enzyme regulated polymer composite hydrogels are the promising bioscaffolds as organoid, implanted materials, and other biomedical applications.

Keywords: enzymatic crosslinking, enzymatic polymerization, composite hydrogel, 3D printing, adjustable-strength

OPEN ACCESS

Edited by:
Yi Cao,
Nanjing University, China

Reviewed by:
Huaimin Wang,
Westlake Institute for Advanced Study (WIAS), China
Chuncai Kong,
Xi'an Jiaotong University (XJTU), China

****Correspondence:***
Ping Chen
chenping@tongji.edu.cn
Qigang Wang
wangqg66@tongji.edu.cn

Specialty section:
This article was submitted to Polymer Chemistry, a section of the journal Frontiers in Chemistry

Received: *19 November 2019*
Accepted: *13 January 2020*
Published: *30 January 2020*

Citation:
Shen S, Shen J, Shen H, Wu C, Chen P and Wang Q (2020) Dual-Enzyme Crosslinking and Post-polymerization for Printing of Polysaccharide-Polymer Hydrogel. Front. Chem. 8:36. doi: 10.3389/fchem.2020.00036

INTRODUCTION

Hydrogels with three-dimensional networks have received wide attention due to their successful applications in tissue engineering (Yue et al., 2015; Mohamad et al., 2018; Qu et al., 2018, 2019; Edri et al., 2019; Feng et al., 2019), biocatalysis (Diaz et al., 2010), biosensor (Wang et al., 2019), cell culture (Lou et al., 2017; Luo et al., 2019), drug delivery (Gao et al., 2018; Xu et al., 2019), biomedicines (Liow et al., 2017), wound healing (Ahmed et al., 2017), and 3D printing (Censi et al., 2011; Pataky et al., 2012; Malda et al., 2013; Li et al., 2015; Loebel et al., 2017; Lin et al., 2019). In general, hydrogels formed by natural polysaccharides are suitable for 3D printing and encapsulating biomolecules. However, they generally have poor elasticity and weak mechanical properties. The covalently bonded crosslinked network (polymeric hydrogel) is elastically deformable, and still maintains strong mechanical properties (Sun et al., 2012; Zhang X. N. et al., 2018). However, they generally lack a suitable porous structure to diffuse biomolecules, and it is difficult to obtain a good viscidity window for extruded 3D printing, which are important factors in tissue-repair and 3D

printing. An effective way to ensure these two advantages is to use a polysaccharide hydrogel in combination with a polymeric material.

Free radical polymerization (Hume et al., 2011) is the most common technique used to prepare polymer hydrogels. Utilization of enzyme to catalyzes the polymerization of monomers is a suitable method for constructing a biomimetic material, due to enzymatic polymerization has the advantages of high efficiency, high specificity, controllable activity, mild reaction conditions and no toxic residues compared with traditional polymerization. As early as 1950, researchers used xanthine oxidase for catalytic reactions (Kalckar et al., 1950). Our group and other researchers have explored several oxidoreductases to catalyze electron transfer reactions and produce free radicals that can initiate the formation of polymer hydrogels (Wei et al., 2016; Zhang et al., 2017; Zhang Q. et al., 2018). For the typical HRP/laccase initiation system, reductive acetylacetone is catalytically oxidized to form carbon radicals and initiate polymerization by hydrogen peroxide or oxygen, respectively (Tsujimoto et al., 2001; Kohri et al., 2012). Enzyme-catalyzed tyrosine-modified polysaccharides and proteins are a very effective strategy for the preparation of injectable and printable hydrogels, which are a free radical-induced cross-linking process. We note that the HRP/GOx/Glucose system can also initiate *in situ* free radical polymerization of small molecular monomers beyond the radical-crosslinking of tyrosine. This may provide an inspiring approach for designing the printable composite hydrogel with tunable mechanical strength.

Despite the success in the design of composite hydrogels, the use of hard hydrogels for 3D printing to generate complex structures remains a huge challenge. Therefore, we report a concise dual enzyme HRP/GOx-mediated redox initiation to achieve crosslinking of modified polysaccharides and further co-polymerized with monomers to achieve high toughness composite hydrogel. The crosslinkable polysaccharide hydrogel with lower mechanical strength can be printed in a 3D structure due to the printable viscidity window and fast crosslinking. Under the action of time, the dual-enzyme and tyrosine of the polysaccharide system further initiate polymerization of the various monomers. The co-polymerization with the double bond grafted polysaccharide gradually increases the toughness of the hydrogel to obtain a composite hydrogel which has good mechanical properties.

There are two processes in designing of composite hydrogels (**Figure 1A**): (i) crosslinkable hydrogel (Gel I) and (ii) polymeric/crosslinked hydrogel (Gel II). The entire hydrogel precursor solution consists of horseradish peroxidase (HRP), glucose oxidase (GOx), glucose, grafted tyrosine and double bond chondroitin sulfate (GMA-CS-Ph-OH), acrylamide monomers and deionized water. First, GOx catalyzes the oxidation of glucose to gluconic acid and H_2O_2, then HRP and H_2O_2 oxidize tyrosine-modified chondroitin sulfate to immediately form Gel I. Then, tyrosine form α-carbon radical under the oxidation of the HRP@GOx system to gradually initiate polymerization of the monomer and crosslink with the polysaccharide grafting double bond to form Gel II. The α-carbon radicals from tyrosine molecules were detected by electron paramagnetic resonance (EPR) measurements (**Figure 6B**).

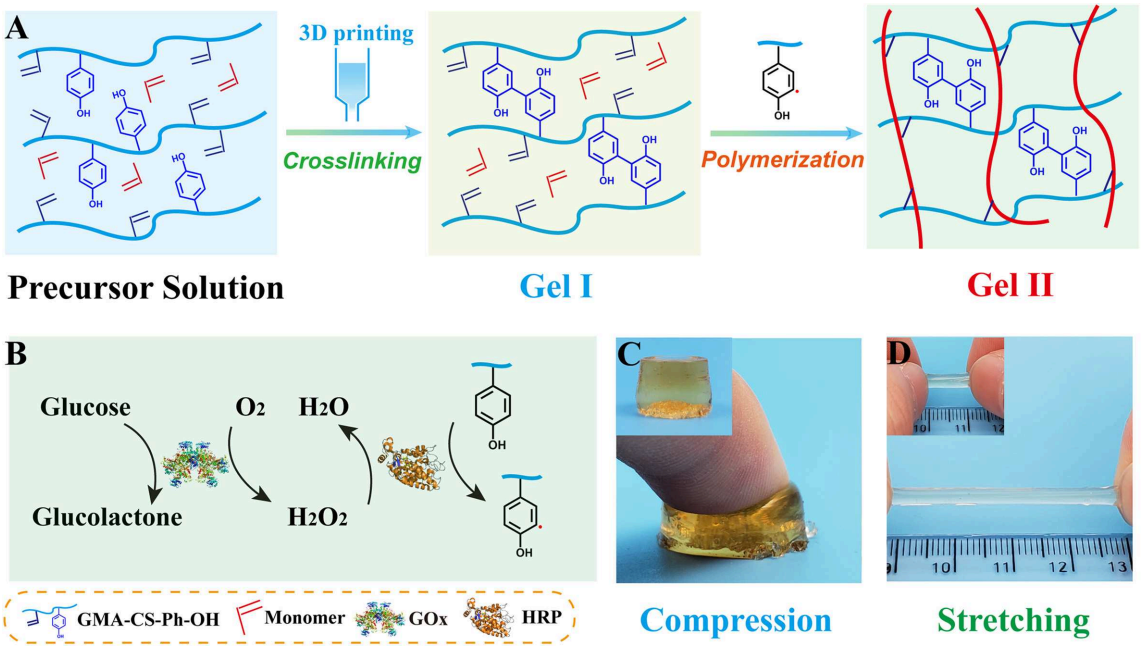

FIGURE 1 | (A) Schematic of the preparation of Gel I and Gel II; **(B)** Enzymatic reaction illustration of HRP@GOx system; **(C)** Optical image of Gel II under compression; **(D)** Optical image of Gel II under stretching [Gel II in **(C,D)** have different diameter, which cause different colors to be reflected under the same shooting conditions].

MATERIALS AND METHODS

Materials

Acrylamide (AAm), tyramine hydrochloride were purchased from Aladdin Industrial Corporation. N, N-Dimethyl Acrylamide (DMAA), N-isopropyl acrylamide (NIPAM) were purchased from Tokyo Chemical Industry Co., Ltd. Poly (ethylene glycol) methacrylate (PEGMA) was purchased from Sigma-Aldrich (Shanghai) Trading Co., Ltd. Glycidyl methacrylate (GMA), N-hydroxysuccinimide (NHS), 1-(3-Dimethylaminopropyl)-3-ethylcarbodiimide hydrochloride (EDC-HCl), and deuteroxide (D_2O) were purchased from Energy Chemical. Hydrochloric acid (HCl), D-(+)-Glucose were purchased from Sinopharm Chemical Reagent Co., Ltd. Chondroitin sulfate (CS, Molecular weight: 5×10^4 KD), Horseradish peroxidase (HRP, ≥300 U/mg), Glucose oxidase (GOx, 239 U/mg) and dialysis bag were purchased from Shanghai Baoman Biotechnology Co., Ltd. Deionized water was used to prepare the solution throughout the experiments unless otherwise stated.

Methods

Synthesis of GMA-CS

2.00 g of chondroitin sulfate was added to 50 ml of deionized water, stirred until the chondroitin sulfate was completely dissolved in room temperature, and pH was adjusted to 3.5 with HCl. Then, 521.2 mg of GMA was added, and the system was stirred at 50°C for 24 h. After completion, it was dialyzed in deionized water for 3 days with a dialysis bag which has a molecular weight of 3,500 to remove impurities, and the dialyzed liquid was placed in a freeze dryer to remove water to obtain GMA-CS.

Synthesis of GMA-CS-Ph-OH

2.00 g of GMA-CS was added to 50 ml of deionized water, stirred until the GMA-CS was completely dissolved in room temperature. Then, 695.4 mg of tyramine hydrochloride, 1151.6 mg of EDC-HCl and 691.4 mg NHS were added, and the reaction was stirred at room temperature for 12 h. After completion, it was dialyzed in deionized water for 3 days with a dialysis bag which has a molecular weight of 3,500 to remove impurities, and the dialyzed liquid was placed in a freeze dryer to remove water to obtain tyrosine modified GMA-CS (GMA-CS-Ph-OH).

Preparation of Functionalized Chondroitin Sulfate Crosslinking Hydrogel (Gel I) and Composite Hydrogel (Gel II)

GMA-CS-Ph-OH, monomers, HRP (20 mg/ml), and GOx (20 mg/ml) were completely dissolved in deionized water at room temperature to prepare a precursor solution. Subsequently, 100 mM Glucose was quickly added to the precursor solution and stirred uniformly. After a period of standing, the GMA-CS-Ph-OH in the precursor solution immediately formed a crosslinking hydrogel (Gel I) under the oxidation of the HRP@GOx system. After forming the crosslinking hydrogel, the

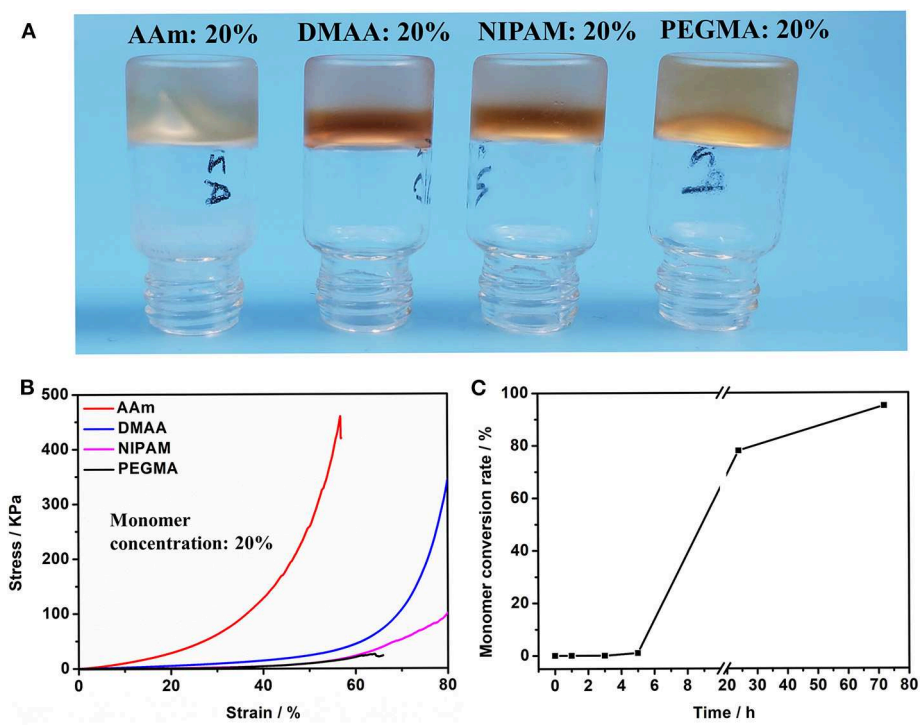

FIGURE 2 | (A) Optical image of Gel II composed of different monomers (including AAm, DMAA, NIPAM, and PEGMA); **(B)** Compressive tests of Gel II composed of different monomers (including AAm, DMAA, NIPAM, and PEGMA). **(C)** The conversion of AAm in Gel II is calculated using the ^{1}H-NMR spectra.

HRP@GOx system in Gel I will continue to oxidize tyrosine, causing tyrosine to generate α-carbon free radicals, gradually initiating polymerization of the monomer to form composite hydrogel (Gel II).

Characterization

The mechanical properties of the hydrogel were characterized via utilizing an electronic universal testing machine. ^{1}H-NMR was used to characterize conversion rates of GMA-CS-Ph-OH and monomers. The network structure inside the hydrogel was characterized by using Scanning Electron Microscopy (SEM). The frequency sweep tests of the hydrogel were characterized via using a rheometer (Rheometer). The tyrosine/di-tyrosine structure of precursor solution/Gel I were characterized by utilizing F-7000 FL Spectrophotometer. The detection of carbon free radicals were performed via using the Bruker Electron Paramagnetic Resonance (EPR). The degree of polymerization of the Gel I and Gel II were tested by using Gel Permeation Chromatography (GPC). The crosslinking hydrogel (Gel I) was printed via GeSim bioscaffold 3.2 3D printer.

RESULTS AND DISCUSSION

The preparation of the composite hydrogel is straightforward and requires no additional initiator. First, GMA-CS-Ph-OH was oxidized under the catalysis of dual enzyme catalytic system HRP@GOx to form α-carbon radicals (**Figure 1B**). Subsequently, a GMA-CS-Ph-OH hydrogel with three-dimensional network structure (Gel I, **Figure 1A**) was immediately formed via crosslinking reaction. Due to the strong steric-hindrance effect of crosslinked GMA-CS-Ph-OH, GMA-CS-Ph-OH with α-carbon radicals presented in the system won't occur crosslinking reaction after Gel I formation. Finally, the acrylamide monomers were polymerized under the initiation of α-carbon radicals, and gradually formed composite hydrogel

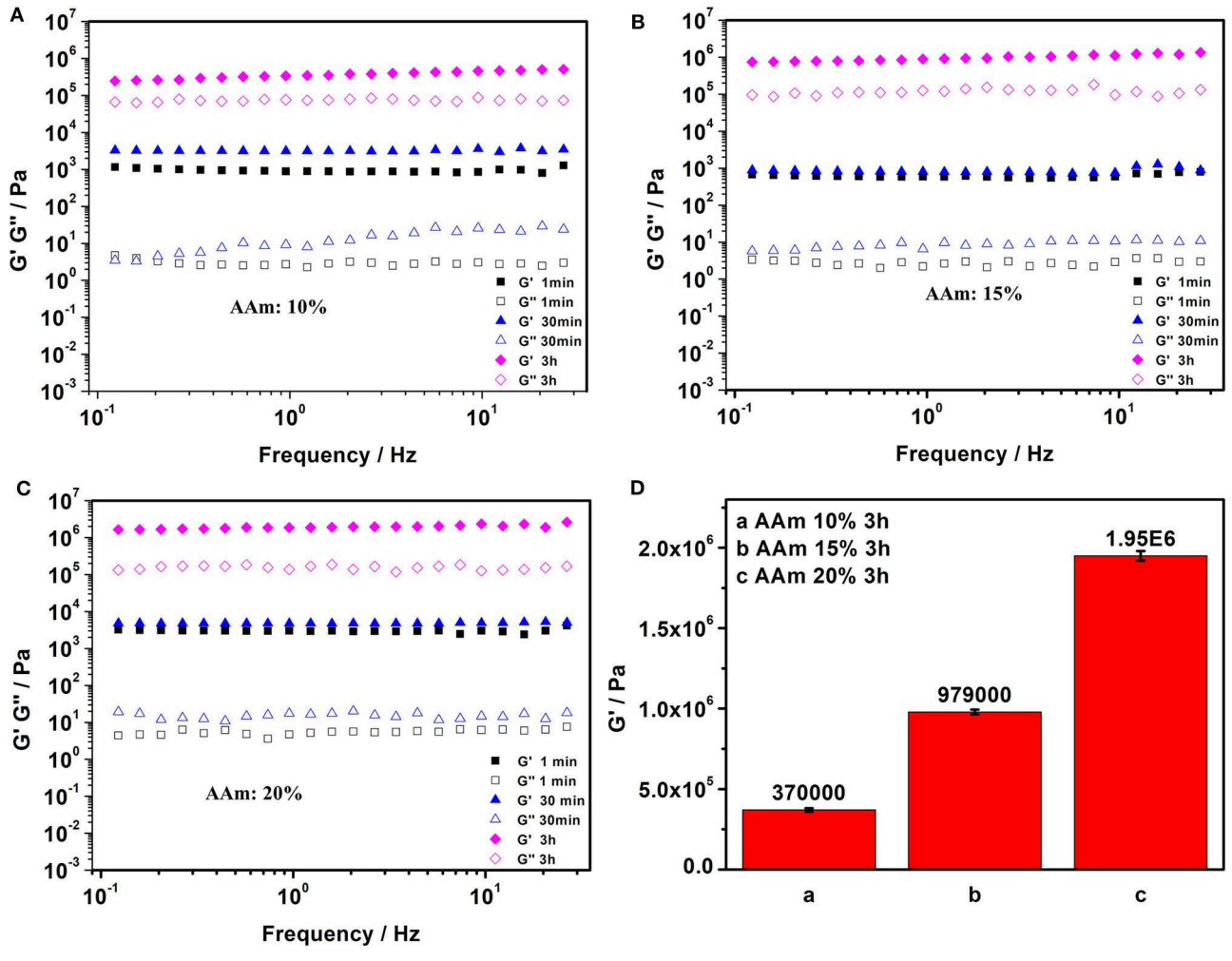

FIGURE 3 | Frequency sweep tests of Gel II contains **(A)** 10 wt% AAm, **(B)** 15 wt% AAm, and **(C)** 20 wt% AAm when the reaction time were 1 min, 30 min, and 3h; **(D)** The value of G' in Frequency sweep tests of Gel II contains 10 wt% AAm, 15 wt% AAm, 20 wt% AAm, respectively, when the reaction time was 3 h. Each bar represents the mean ($n = 22$) ± SD.

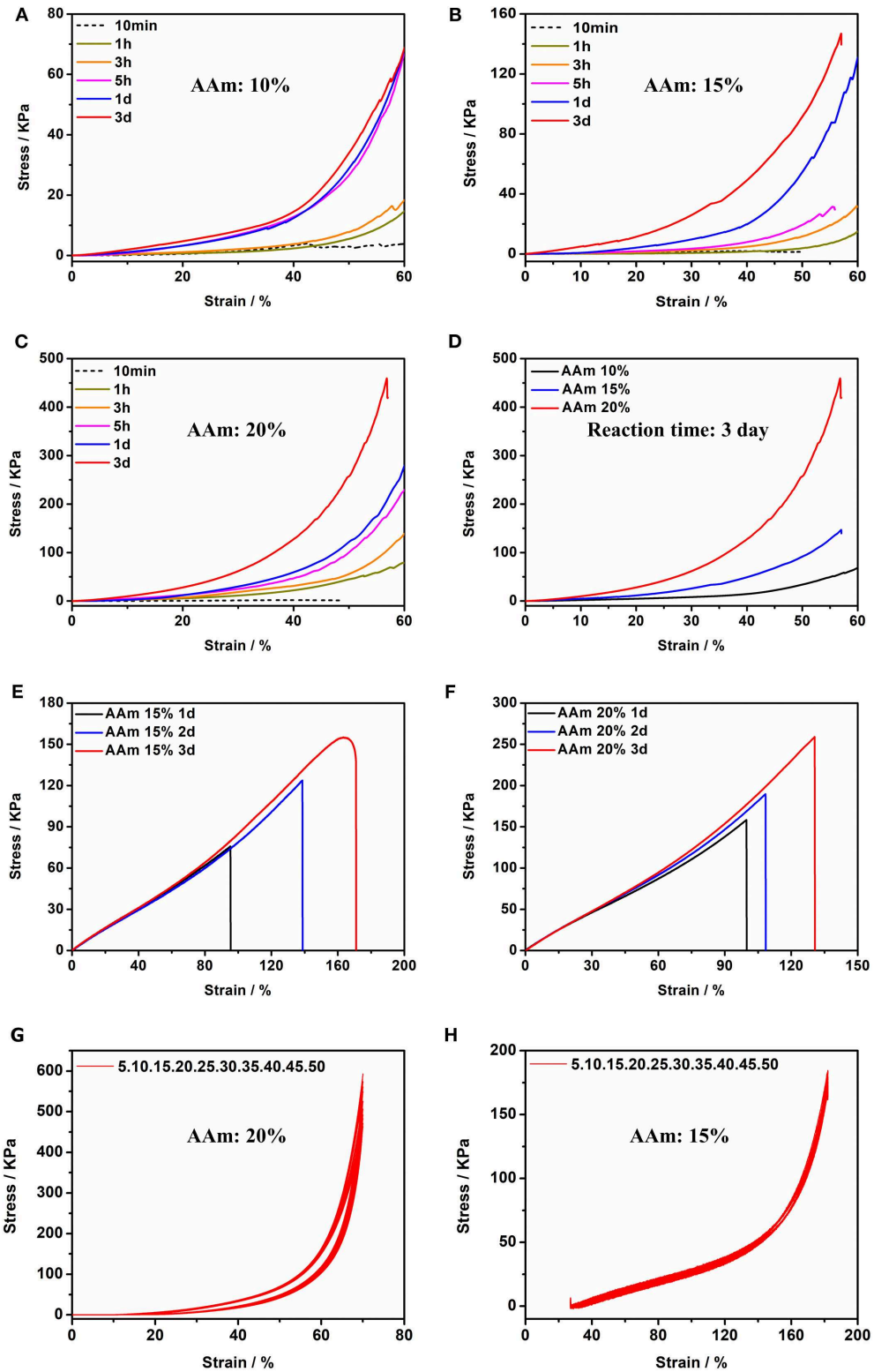

FIGURE 4 | Compression tests of Gel II contains **(A)** 10 wt% AAm, **(B)** 15 wt% AAm and **(C)** 20 wt% AAm when the reaction time were 10 min, 1, 3, 5 h, 1 d, and 3 d **(D)** Compression tests of Gel II contains 10, 15, and 20 wt% AAm, respectively, when the reaction time was 3 d; Tensile test of Gel II contains **(E)** 15 wt% and **(F)** 20 wt% AAm when the reaction time was 1, 2, and 3 d; **(G)** Cyclic compression test of Gel II contains 20 wt% AAm; **(H)** Cyclic tensile test of Gel II contains 15 wt% AAm.

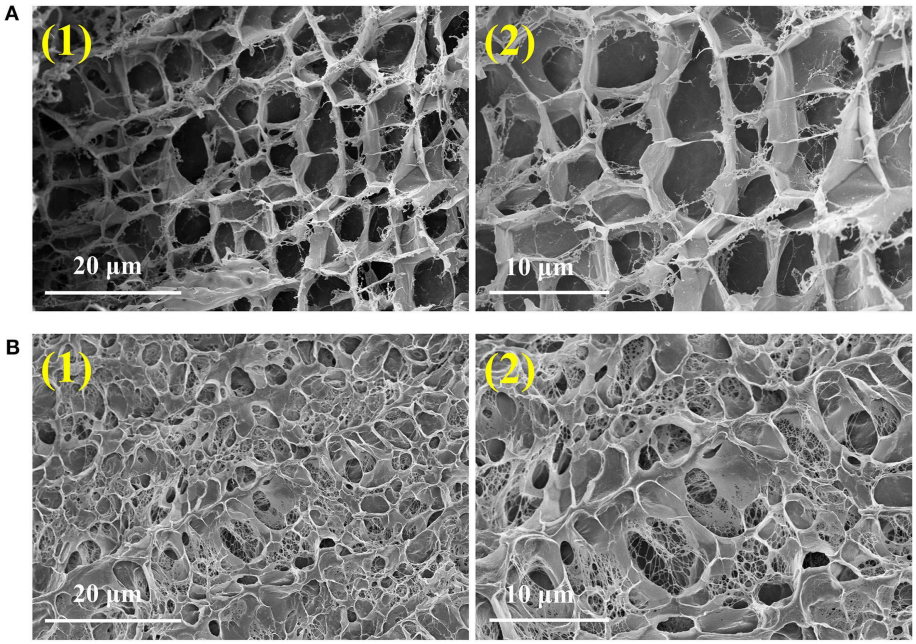

FIGURE 5 | SEM images of Gel I **(A)** and Gel II **(B)**.

(Gel II) with a semi-interpenetrating network structure with Gel I (**Figure 1A**). Therefore, the composite hydrogel can be formed by simply mixing the reaction solution and maintaining it at room temperature.

Subsequently, we investigated the polymerization reaction of a number of acrylamide monomers catalyzed by HRP@GOx. As shown in **Figure 2A**, AAm, DMAA, NIPAM, and PEGMA can be all polymerized under the catalysis of HRP@GOx, and form Gel II with a semi-interpenetrating network structure with Gel I. Its mechanical properties are determined by the intrinsic properties of the monomer, such as the molecular structure (**Figure 2B**). The reason for this phenomenon is that GMA-CS-Ph-OH generates α-carbon radicals under the catalysis of HRP@GOx, and then non-selective α-carbon radical can initiate *in situ* polymerization of acrylamide monomers without the need for additional initiators.

The acrylamide (AAm) was experiment as a template molecule. The gelation process was monitored via ^{1}H-NMR (25°C). After 5 h, the intensity of the characteristic peak of the double group of AAm began to decrease significantly. After 3 days, the double group of AAm were saturated quantitatively (**Figure 2C**), which corresponded to the formation of Gel II, whereas the gelator conversion test showed that 94.9 ± 1.2% (mean ± SD) of AAm participated in the polymerization reaction. In order to evaluate the effect of quantity of AAm in the crosslinking process, a series of composite hydrogels containing different amounts of AAm (10, 15, 20 wt%) were prepared for comparison of mechanical properties. Gel II containing different concentrations of AAm all reached optimal mechanical properties within 3 days of reaction. **Figures 3A–D** revealed the results of frequency-dependent sweep measurements at a constant strain of 0.03%. The values for both storage modulus (G′) and loss modulus (G″) increased gradually with an increase in the amount of AAm. When the amount of AAm was 20 wt%, the G' of Gel II reached 1.95×10^{6} Pa. the G' of Gel II was 0.37×10^{6} Pa when the amount of AAm is 10 wt%. Whether the amount of AAm is 10 or 20 wt%, the values of storage modulus (G′) always much higher than loss modulus (G″), which confirmed inherent high elastic properties of Gel II. In the compression test, the fracture stress and the elastic modulus also increased as the amount of AAm increased (**Figures 4A–D**). When the amount of AAm is 15 wt%, the tensile properties were optimal (**Figures 4E,F**) (Gel II can be stretched 2.7 and 2.3 times, respectively, with 15 and 20 wt% AAm, and cannot be stretched with 10 wt% AAm). According to the above discussion, Gel II with different mechanical properties can be obtained by change the amount of AAm. The compression cycle and the tensile cycle test were, respectively, performed on Gel II contains 20 and 15 wt% AAm. Even after 50 cycles, the compression and tensile curves were almost coincident, indicating that Gel II formed under the catalysis of HRP@GOx without additional initiators has excellent stability (**Figures 4G,H**).

Scanning Electron Microscopy (SEM, **Figure 5**) confirmed that Gel II had a similar porous network structure as Gel I, but with smaller pore size and closer network structure. The SEM image of Gel I (**Figure 5A**) exhibited entangled irregular fibers structure, which was the matrix of Gel II (**Figure 5B**) had a different morphology with fibers that were tightly crosslinked to each other and intertwined with Gel I. It is proved that the density of nanofibers in Gel II is higher than that of the Gel I network, which proves that the crosslinking process of GMA-CS-Ph-OH promotes the formation of Gel II.

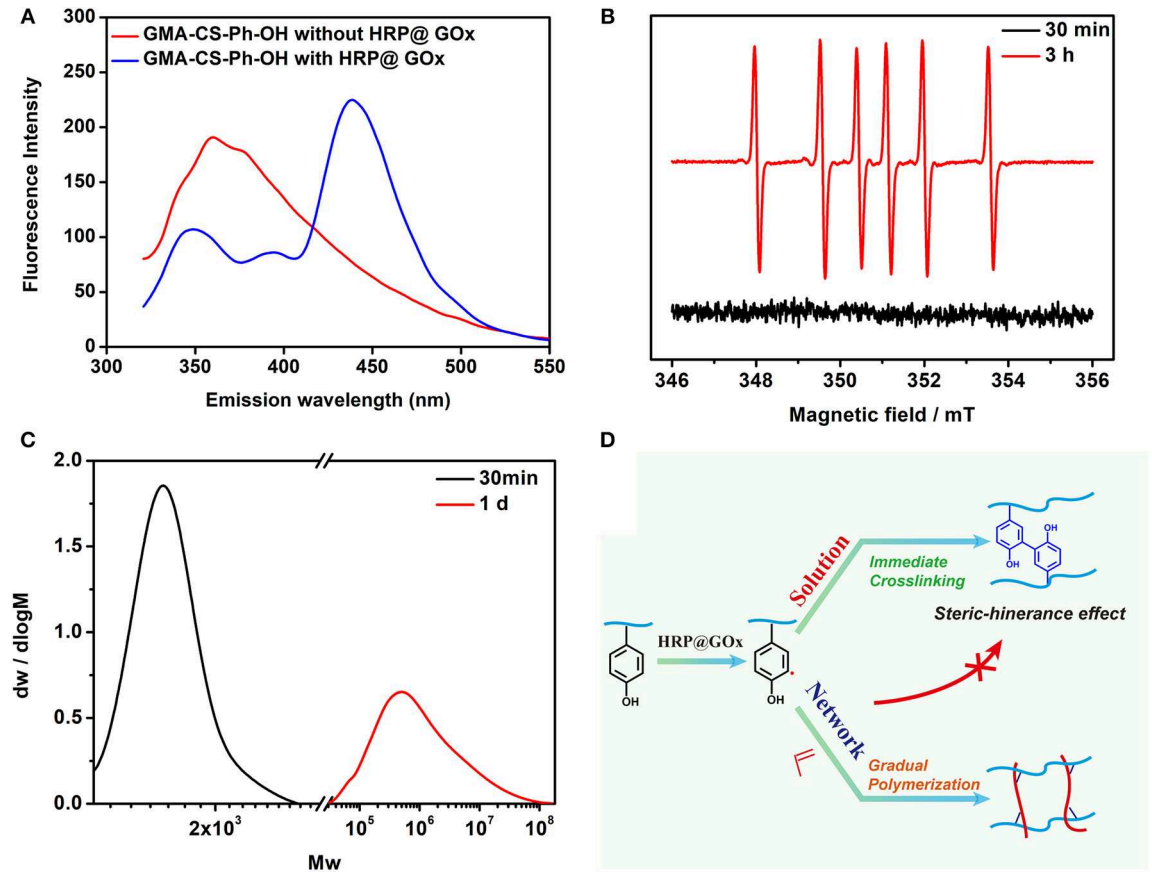

FIGURE 6 | (A) Fluorescence Spectroscopy spectrum of GMA-CS-Ph-OH with and without HRP@GOx; **(B)** EPR spectrum of the DMPO radical adduct formed in HRP@GOx, GMA-CS-Ph-OH, and AAm reaction system at 30 min (black line) and 3 h (red line); **(C)** The GPC spectrum of Gel I (black line) and Gel II (red line); **(D)** Mechanism illustration of catalytic oxidation of tyrosine via HRP@GOx system.

Fluorescence Spectroscopy, Electron paramagnetic resonance (EPR) spectroscopy, and Gel Permeation Chromatography (GPC) were performed to verify the gelation mechanism. When the excitation wavelength is 300 nm, Tyrosine has a characteristic fluorescence emission peak at 360 nm, while di-tyrosine has a characteristic fluorescence emission peak at 425 nm. Therefore, fluorescence spectroscopy was used to characterize the reaction process. As shown in **Figure 6A**, GMA-CS-Ph-OH exhibited a characteristic fluorescence emission peak of tyrosine at ca. 360 nm. When the HRP@GOx catalytic system was presented, not only the characteristic fluorescence emission peak of di-tyrosine occurs at 438 nm, but also the characteristic fluorescence emission peak belonging to tyrosine appears at 348 nm. This may be attributed to the steric-hindrance effect of the GMA-CS-Ph-OH crosslinking reaction, which results in the presence of a portion of unbound GMA-CS-Ph-OH in the system. The characteristic fluorescence emission peaks of tyrosine and di-tyrosine were both shifted, which may be attributed to the influence of the molecular structure of the enzyme. EPR was utilized to detect radicals in the system at different reaction times. Dimethyl pyridine N-oxide (DMPO) was employed to trap the unstable and short-lifetime free radicals to form a long-lived nitroxide for EPR characterization. As shown in **Figure 6B** (black line), no carbon radicals were detected at the reaction for 30 min, which was belonged to the fact that the GMA-CS-Ph-OH molecules were oxidized to immediately form a dimer via the combination of α-carbon radicals. When the reaction is carried out for 3 h, the EPR spectrum of the reacted system demonstrated a sextet signal (red line) with a g value of 2.005, AN = 1.67 mT, AH = 2.38 mT, which were coincident with the values of a DMPO trapped carbon centered radical (Buettner, 1987), it is attributed to the completion of the crosslinking reaction of GMA-CS-Ph-OH, and remaining carbon radicals in the reaction system will initiate the polymerization of AAm. The EPR results confirmed our hypothesis that there is a process of gradual polymerization of AAm after GMA-CS-Ph-OH immediate crosslinking. The molecular weight distribution of the Gel I and Gel II formed after crosslinking and polymerization were measured by GPC (**Figure 6C**). The number-average molecular weight (Mn) of Gel I and Gel II were 1.67×10^3 and 1.63×10^6, which proves the polymerization of AAm in polysaccharide network. Based on the above results, the gelation mechanism is proposed: as shown in **Figure 6D**, tyrosine of GMA-CS-Ph-OH generates α-carbon

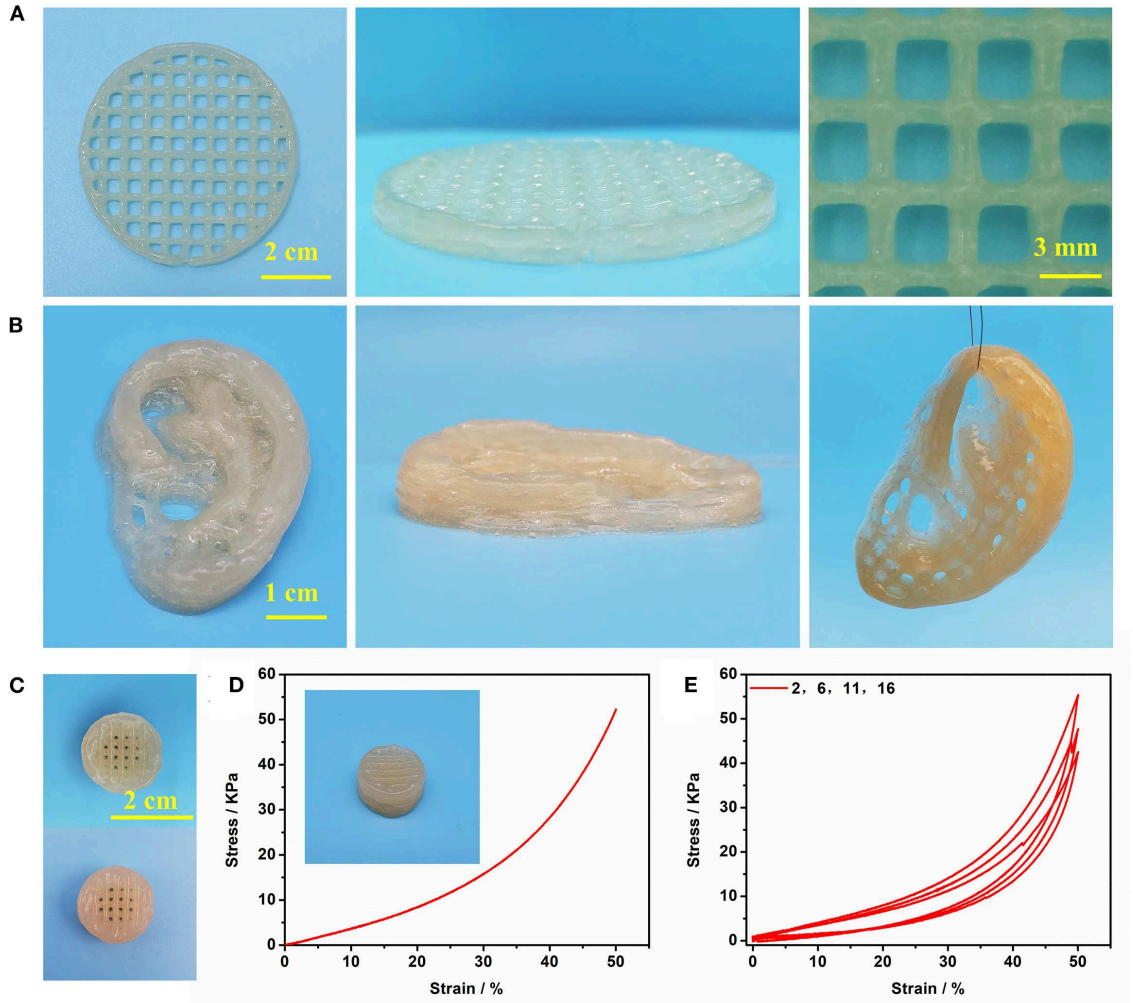

FIGURE 7 | (A) The printed shape "button" with several layers; **(B)** The printed shape "ears" with several layers; **(C)** The printed 3D shape "button" (up) and enhanced 3D shape "button" (bottom); **(D)** Compressive test of enhanced 3D shape "button"; **(E)** cyclic compression test of enhanced 3D shape "button".

radicals under catalytic oxidation of the HRP@GOx system. In solution environment, α-carbon radicals tend to react with each other to initiate crosslinking reaction of the GMA-CS-Ph-OH. When GMA-CS-Ph-OH was crosslinked and then obtained a highly viscous network structure, α-carbon radicals were difficult to react with each other due to steric-hindrance effect, resulting in α-carbon radicals tending to induce polymerization of acrylamide monomers.

Gel II can retain its shape even under compression and tensile relative to the weaker Gel I. As shown in **Figure 4C**, Gel II can resist over 57% compression and has an 86.73 KPa Young's modulus, whereas Gel I only has a 3.29 KPa Young's modulus. Furthermore, the cylindrical composite hydrogel has well compression performance (**Figure 1C**) and could be stretched to about 4 times its initial length without collapse (**Figure 1D**). Because of these properties (such as *in situ* formation and enhanced mechanical properties of Gel II), the precursor solution was used for 3D printing. First, we imported the designed 3D model into the printer, selected the appropriate printing pressure and speed, and then quickly injected the configured precursor solution into the print cylinder for printing. The shapes of "button" (**Figure 7A**) and "ears" (**Figure 7B**) with several layers were 3D printed. The printed 3D model was statically cured (**Figure 7C**) and then subjected to compression test (**Figure 7D**) and cyclic compression test (**Figure 7E**), and the 3D model exhibited greater compression performance even after cyclic compression 16 times. This result demonstrates that the composite hydrogels could be used as novel printable scaffold materials with enhanced mechanical properties.

CONCLUSION

In summary, we have developed a new strategy for the mild preparation of polymer composite hydrogels for 3D printing via using the dual enzyme HRP@GOx systems. The preparation process of polysaccharide-polymer composite

hydrogel comprises two steps: (1) GMA-CS-Ph-OH is immediately crosslinked to form a polysaccharide hydrogel with weak mechanical strength but printable; (2) The gradual polymerization form composite hydrogel of adjustable strength after immediate crosslinking. The monomer conversion of the composite hydrogel was detected to be 95% via ^{1}H-NMR. Composite hydrogels have adjustable strength from 3.29 to 86.73 KPa along with various type and concentration of monomers. The mechanism analyses confirmed the immediate cross-linking at diluted solution and gradually polymerized reinforcement within viscous polysaccharide network. Therefore, our polymer composite hydrogels have denser pore and nanoscale network relative to only polysaccharide hydrogels. With excellent biocompatible and mechanically adjustable abilities, the composite hydrogel is particularly interesting for 3D printing to fabricate precision structures for tissue repairing and tissue engineering.

DATA AVAILABILITY STATEMENT

The datasets generated for this study are available on request to the corresponding author.

AUTHOR CONTRIBUTIONS

SS and QW conceived the study. SS, JS, HS, CW, PC, and QW had input in the experimental design. SS and QW analyzed the data. SS drafted the manuscript with support from QW and PC. All authors read, commented on, and approved the paper.

ACKNOWLEDGMENTS

We acknowledge the support of the National Key Research and Development Program (No. 2016YFA0100800) and the National Natural Science Foundation of China (No. 51873156).

REFERENCES

Ahmed, A. S., Mandal, U. K., Taher, M., Susanti, D., and Jaffri, J. M. (2017). PVA-PEG physically cross-linked hydrogel film as a wound dressing: experimental design and optimization. *Pharm. Dev. Technol.* 23, 751–760. doi: 10.1080/10837450.2017.1295067

Buettner, G. (1987). Spin trapping: ESR parameters of spin adducts. *Free Radic. Bio Med.* 3, 259–303. doi: 10.1016/S0891-5849(87)80033-3

Censi, R., Schuurman, W., Malda, J., di Dato, G., Burgisser, P. E., Dhert, W. J. A., et al. (2011). A printable photopolymerizable thermosensitive p(HPMAm-lactate)-PEG hydrogel for tissue engineering. *Adv. Funct. Mater.* 21, 1833–1842. doi: 10.1002/adfm.201002428

Diaz, D. D., Kuhbeck, D., and Koopmans, R. J. (2010). Stimuli-responsive gels as reaction vessels and reusable catalysts. *Chem. Soc. Rev.* 40, 427–448. doi: 10.1039/C005401C

Edri, R., Gal, I., Noor, N., Harel, T., Fleischer, S., Adadi, N., et al. (2019). Personalized hydrogels for engineering diverse fully autologous tissue implants. *Adv. Mater.* 31:1803895. doi: 10.1002/adma.201803895

Feng, Q., Li, Q. T., Wen, H. J., Chen, J. X., Liang, M. H., Huang, H. H., et al. (2019). Injection and self-assembly of bioinspired stem cell-laden gelatin/hyaluronic acid hybrid microgels promote cartilage repair *in vivo*. *Adv. Funct. Mater.* 1906690. doi: 10.1002/adfm.201906690

Gao, G., Jiang, Y. W., Jia, H. R., and Wu, F. G. (2018). Near-infrared light-controllable on-demand antibiotics release using thermo-sensitive hydrogel-based drug reservoir for combating bacterial infection. *Biomaterials* 188, 83–95. doi: 10.1016/j.biomaterials.2018.09.045

Hume, P. S., Bowman, C. N., and Anseth, K. S. (2011). Functionalized PEG hydrogels through reactive dip-coating for the formation of immunoactive barriers. *Biomaterials* 32, 6204–6212. doi: 10.1016/j.biomaterials.2011.04.049

Kalckar, H. M., Kjeldgaard, N. O., and Klenow, H. (1950). Xanthopterin oxidase. *Biochimica et Biophys. Acta* 5, 575–585. doi: 10.1016/0006-3002(50)90203-4

Kohri, M., Kobayashi, A., Fukushima, H., Kojima, T., Taniguchi, T., Saito, K., et al. (2012). Enzymatic miniemulsion polymerization of styrene with a polymerizable surfactant. *Polym. Chem.* 3, 900–906. doi: 10.1039/c2py00542e

Li, C., Faulkner-Jones, A., Dun, A. R., Jin, J., Chen, P., Xing, Y. Z., et al. (2015). Rapid formation of a supramolecular polypeptide-DNA hydrogel for *in situ* three-dimensional multilayer bioprinting. *Angew. Chem. Int. Ed.* 54, 3957–3961. doi: 10.1002/anie.201411383

Lin, Z. F., Wu, M. M., He, H. M., Liang, Q. F., Hu, C. S., Zeng, Z. W., et al. (2019). 3D printing of mechanically stable calcium-free alginate-based scaffolds with tunable surface charge to enable cell adhesion and facile biofunctionalization. *Adv. Funct. Mater.* 29:1808439. doi: 10.1002/adfm.201808439

Liow, S. S., Dou, Q. Q., Kai, D., Li, Z. B., Sugiarto, S., Yu, C. Y. Y., et al. (2017). Long-term real-time *in vivo* drug release monitoring with AIE thermogelling polymer. *Small* 13:1603404. doi: 10.1002/smll.201603404

Loebel, C., Rodell, C. B., Chen, M. H., and Burdick, J. A. (2017). Shear-thinning and self-healing hydrogels as injectable therapeutics and for 3D-printing. *Nat. Protoc.* 12, 1521–1541. doi: 10.1038/nprot.2017.053

Lou, J. Z., Stowers, R., Nam, S. M., Xia, Y., and Chaudhuri, O. (2017). Stress relaxing hyaluronic acid-collagen hydrogels promote cell spreading, fiber remodeling, and focal adhesion formation in 3D cell culture. *Biomaterials* 154, 213–222. doi: 10.1016/j.biomaterials.2017.11.004

Luo, H. B., Xu, C. S., Liu, Z. W., Yang, L., Hong, Y. D., Liu, G. S., et al. (2019). Neural differentiation of bone marrow mesenchymal stem cells with human brain-derived neurotrophic factor gene-modified in functionalized self-assembling peptide hydrogel *in vitro*. *J. Cell. Biochem.* 120, 2828–2835. doi: 10.1002/jcb.26408

Malda, J., Visser, J., Melchels, F. P., Jungst, T., Hennink, W. E., Dhert, W. J. A., et al. (2013). 25th anniversary article: engineering hydrogels for biofabrication. *Adv. Mater.* 25, 5011–5028. doi: 10.1002/adma.201302042

Mohamad, N., Loh, E. Y. X., Fauzi, M. B., Ng, M. H., and Amin, M. C. I. (2018). *In vivo* evaluation of bacterial cellulose/acrylic acid wound dressing hydrogel containing keratinocytes and fibroblasts for burn wounds. *Drug Deliv. and Transl. Res.* 9, 444–452. doi: 10.1007/s13346-017-0475-3

Pataky, K., Braschler, T., Negro, A., Renaud, P., Lutolf, M. P., and Brugger, J. (2012). Microdrop printing of hydrogel bioinks into 3D tissue-like geometries. *Adv. Mater.* 24, 391–396. doi: 10.1002/adma.201102800

Qu, J., Zhao, X., Liang, Y. P., Xu, Y. M., Ma, P. X., and Guo, B. L. (2019). Degradable conductive injectable hydrogels as novel antibacterial, anti-oxidant wound dressings for wound healing. *Chem. Eng. J.* 362, 548–560. doi: 10.1016/j.cej.2019.01.028

Qu, J., Zhao, X., Liang, Y. P., Zhang, T. L., Ma, P. X., and Guo, B. L. (2018). Antibacterial adhesive injectable hydrogels with rapid self-healing, extensibility and compressibility as wound dressing for joints skin wound healing. *Biomaterials* 183, 185–199. doi: 10.1016/j.biomaterials.2018.08.044

Sun, J. Y., Zhao, X. H., Illeperuma, W. R. K., Chaudhuri, O., Oh, K. H., Mooney, D. J., et al. (2012). Highly stretchable and tough hydrogels. *Nature* 489, 133–136. doi: 10.1038/nature11409

Tsujimoto, T., Uyama, H., and Kobayashi, S. (2001). Polymerization of vinyl monomers using oxidase catalysts. *Macromol. Biosci.* 1, 228–232. doi: 10.1002/1616-5195(20010801)1:6<228::AID-MABI228>3.0.CO;2-S

Wang, L. F., Gao, G. R., Zhou, Y., Xu, T., Chen, J., Wang, R., et al. (2019). Tough, adhesive, self-healable, and transparent ionically conductive zwitterionic nanocomposite hydrogels as skin strain sensors. *ACS Appl. Matet. Inter.* 11, 3506–3515. doi: 10.1021/acsami.8b20755

Wei, Q. C., Xu, M. C., Liao, C. A., Wu, Q., Liu, M. Y., Zhang, Y., et al. (2016). Printable hybrid hydrogel by dual enzymatic polymerization with superactivity. *Chem. Sci.* 7, 2748–2752. doi: 10.1039/C5SC02234G

Xu, J. B., Feng, Q., Lin, S., Yuan, W. H., Li, R., Li, J. M., et al. (2019). Injectable stem cell-laden supramolecular hydrogels enhance *in situ* osteochondral regeneration via the sustained co-delivery of hydrophilic and hydrophobic chondrogenic molecules. *Biomaterials* 210, 51–61. doi: 10.1016/j.biomaterials.2019.04.031

Yue, K., Trujillo-de Santiago, G., Alvarez, M. M., Tamayol, A., Annabi, N., and Khademhosseini, A. (2015). Synthesis, properties, and biomedical applications of gelatin methacryloyl (GelMA) hydrogels. *Biomaterials* 73, 254–271. doi: 10.1016/j.biomaterials.2015.08.045

Zhang, Q., Lv, Y. N., Liu, M. Y., Wang, X., Mi, Y. L., and Wang, Q. G. (2018). Nanoinitiator for enzymatic anaerobic polymerization and graft enhancement of gelatin-PAAM hydrogel. *J. Mater. Chem. B* 6, 1402–1409. doi: 10.1039/C7TB03244G

Zhang, S., Wei, Q. C., Shang, Y. H., Zhang, Q., and Wang, Q. G. (2017). D-Serine enzymatic metabolism induced formation of a powder-remoldable PAAM–CS hydrogel. *Chem. Commun.* 53, 12270–12273. doi: 10.1039/C7CC06733J

Zhang, X. N., Wang, Y. J., Sun, S. T., Hou, L., Wu, P. Y., Wu, Z. L., et al. (2018). A tough and stiff hydrogel with tunable water content and mechanical properties based on the synergistic effect of hydrogen bonding and hydrophobic interaction. *Macromolecules* 51, 8136–8146. doi: 10.1021/acs.macromol.8b01496

Conflict of Interest: The authors declare that the research was conducted in the absence of any commercial or financial relationships that could be construed as a potential conflict of interest.

frontiers in Chemistry

ORIGINAL RESEARCH
published: 04 February 2020
doi: 10.3389/fchem.2020.00050

Chitosan/Xanthan Gum Based Hydrogels as Potential Carrier for an Antiviral Drug: Fabrication, Characterization, and Safety Evaluation

Nadia Shamshad Malik[1], Mahmood Ahmad[2], Muhamad Usman Minhas[3], Ruqia Tulain[3], Kashif Barkat[4], Ikrima Khalid[5] and Qandeel Khalid[6]*

[1] Department of Pharmacy, Capital University of Science & Technology, Islamabad, Pakistan, [2] Faculty of Pharmacy, University of Central Punjab, Lahore, Pakistan, [3] Faculty of Pharmacy, University of Sargodha, Sargodha, Pakistan, [4] Faculty of Pharmacy, University of Lahore, Lahore, Pakistan, [5] Faculty of Pharmaceutical Sciences, Government College University, Faisalabad, Pakistan, [6] Department of Pharmacy, The University of Faisalabad, Faisalabad, Pakistan

This study investigated the use of pure polymer chitosan (CS), xanthan gum (XG), monomer 2-acrylamido-2-methylpropane sulfonic acid (AMPS) and initiator potassium persulfate (KPS) as drug carrier system crosslinked through N′ N′-methylene bis-acrylamide (MBA) for controlled drug delivery of acyclovir (ACV). ACV is highly effective and selective antiviral drugs used for prophylaxis and treatment against herpes simplex viruses (HSV) infections. Present oral marketed formulations are associated with number of side effects and shortcomings which hampered its clinical effectiveness. Hydrogels (FCX1-FCX9) composed of CS, XG, AMPS, MBA, and KPS were prepared by free radical polymerization technique and characterized through FTIR, PXRD, thermal analysis and SEM. Swelling dynamics and drug release behavior was also investigated. FTIR studies confirmed that ACV was successfully encapsulated into hydrogel polymeric network. SEM revealed porous structure whereas thermal analysis showed enhanced thermal stability of polymeric network. PXRD indicated amorphous dispersion of ACV during preparation process. Swelling dynamics and ACV release behavior from developed hydrogels was dependent on pH of the medium and concentration of pure reactants used. Korsmeyer-Peppas model was best fit to regression coefficient. The present work demonstrated a potential for developing a pH sensitive hydrogel for an antiviral drug ACV by using pure polymers CS, XG, and monomer AMPS.

Keywords: chitosan, xanthan gum, acyclovir, AMPS, hydrogel, pH- sensitive

OPEN ACCESS

Edited by:
Yi Cao,
Nanjing University, China

Reviewed by:
Tasuku Nakajima,
Hokkaido University, Japan
Qiang Chen,
Henan Polytechnic University, China

***Correspondence:**
Mahmood Ahmad
dr.mahmoodphd@gmail.com

Specialty section:
This article was submitted to Polymer Chemistry, a section of the journal Frontiers in Chemistry

Received: *06 November 2019*
Accepted: *16 January 2020*
Published: *04 February 2020*

Citation:
Malik NS, Ahmad M, Minhas MU, Tulain R, Barkat K, Khalid I and Khalid Q (2020) Chitosan/Xanthan Gum Based Hydrogels as Potential Carrier for an Antiviral Drug: Fabrication, Characterization, and Safety Evaluation. Front. Chem. 8:50. doi: 10.3389/fchem.2020.00050

INTRODUCTION

Acyclovir (ACV), an antiviral drug, is a purine nucleoside analog, used against viruses of the herpes group (Nair et al., 2014). Currently it is available in the market as topical ointment, as capsules in the strength of 200 mg and as tablets in strength of 200 mg, 400 mg and 800 mg (Kubbinga et al., 2015). The mean plasma half-life of the drug is 3 h (Naik and Raval, 2016). In conventional drug delivery system, administration of ACV is required five times a day which results in undesirable

side effects associated with high dose (Gandhi et al., 2014). Furthermore, the present marketed formulations are related to variety of disadvantages after oral administration (Naik et al., 2014). The adsorption of ACV from gastrointestinal tract is carrier mediated, so elevation of dose of ACV has caused saturation of carrier system, dose related side effects and reduced bioavailability (Malik et al., 2017a,b). All above short comings associated with marketed products have placed the need of different approaches like polymeric drug delivery system.

Polymeric drug delivery systems such as hydrogels have presented one of the most compelling areas of research and remarkable scope for researchers in drug delivery system. Among several approaches in the design and development of polymeric drug delivery systems, a pH responsive hydrogel for controlled release of ACV is desirable. As ACV undergoes absorption from small intestine, a pH responsive hydrogel could contribute to improve absorption and enhance bioavailability of the ACV by demonstrating pH dependent swelling dynamics and drug release behavior (Luengo et al., 2002; Zhang et al., 2014).

Hydrogels have been classified as three-dimensional insoluble hydrophilic polymeric networks (Hoffman, 2012). They can absorb huge quantity of aqueous solution, thus causing them to swell. The swelling behavior of hydrogel is due to presence of hydrophilic groups whereas mechanical strength is due to physical or chemical network cross-linking. Hydrogels have a tendency to become rubbery soft and exhibit excellent resemblance with living tissues when they are in swollen state (Caló and Khutoryanskiy, 2015). However, conventional hydrogels are usually associated with inherent critical limitations in morphology and properties e.g., morphological inhomogeneity, weak mechanical strength, limited swelling at equilibrium and poor response to stimuli (Hamidi et al., 2008). Hence, an elegant strategy to overcome these inherent drawbacks and to impart desired features and characteristics on to hydrogels is to fabricate hydrogels by utilizing novel characteristics and combined properties of two different biodegradable and biocompatible polymers which possess essential abilities for chemical modification (Annabi et al., 2014).

In particular, hydrogels prepared in this way are considered as promising candidates for controlled release of encapsulated products in drug delivery systems. Moreover, these hydrogels possess an added advantage of tuneable physical properties, good mechanical strength, desirable swelling dynamics, enzymatic resistance, non-toxicity, and preservation of polymers biocompatible characteristics (Li and Mooney, 2016).

Chitosan (CS) has been the subject of increasing interest since the last few years as a polymeric carrier for drug delivery systems due to its biocompatibility, biodegradability and non-toxic nature (Van Vlierberghe et al., 2011). It is a copolymer of glucosamine and N-acetylglucosamine connected by (1–4) linkage (Bhattarai et al., 2010). It is regarded as one of the most widely used biomaterials and only unique polymer with cationic character which enables its binding to negatively charged materials such as anionic polymers, nucleic acids and enzymes (Bernkop-Schnürch and Dünnhaupt, 2012). It can be used efficiently to synthesize hydrogels with favorable physicochemical properties by utilizing its –NH2 and –OH functional groups for graft polymerization reaction (Berger et al., 2004; Elgadir et al., 2015).

Xanthan gum (XG) is an anionic, extracellular polysaccharide secreted by the microorganism Xanthomonas campestris. An anionic character is due to presence of both glucuronic acid and pyruvic acid groups in the side chain (Petri, 2015). It has attained considerable attention as one of the most successful hydrocolloids due to its high functionality, predominantly in critical environments such as acid, high salt and high shear stress (Kang et al., 2019). Besides, it offers a potential utility as drug carrier due to its ability to conjugate with other polymers, proteins, peptides and non-peptides where these conjugates exhibit stability toward degrading enzymes, inertness, biocompability, and efficient solubility. XG affinity for water enhances the solubility of drugs or carriers which are hydrophobic in nature (Benny et al., 2014; Kumar et al., 2018). Moreover, relatively small amount of xanthan gum can be used to retard *in vitro* drug release and provide zero-order release kinetics (Shalviri et al., 2010).

2-Acrylamido-2-methylpropanesulfonic acid (AMPS) is a hydrophilic monomer with both ionic and non-ionic moieties (Kabiri et al., 2011). This amide monomer demonstrates strong resistance to salts and better stability against hydrolysis due to the presence of sulfonic functional group in its structure (Mahmood et al., 2016). When AMPS is cross-linked with natural polymers, this ionizable sulfonate groups in AMPS imparts characteristic pH-sensitive behavior to the developed polymeric network (Sohail et al., 2015).

This work aimed at establishing a novel approach for the synthesis of pH dependent hydrogel for ACV through non-covalent grafting of AMPS on to polymeric network of XG and CS. Crosslinking and ionic interactions between the amino groups of chitosan and carboxyl groups of xanthan gum was carried out to develop hydrogels. Graft copolymerization of monomer AMPS was done on to CS-XG backbone utilizing sulfonate group of AMPS. CS, a cationic polymer, is chosen as polymeric carrier due to its biocompatibility, biodegradability and non-toxic nature. XG, an anionic hydrophilic polymer enhances the solubility of drugs or carriers which are hydrophobic in nature. Moreover, monomer AMPS impart pH-sensitive swelling characteristics to the developed hydrogel. This enables the hydrogel to release ACV through specific targeting to the absorption site in small intestine and enhances bioavailability of drug.

Therefore, a new approach of conjugating a cationic polymer CS with anionic polymer XG has been reported in our study to obtain hydrogel with desired properties. By optimizing the formulation parameters and composition, xanthan–chitosan hydrogel with different crosslinking densities were prepared with desired mechanical strength, pH-sensitive swelling behavior and drug release properties of hydrogel network.

MATERIALS AND METHODS

Materials

ACV was obtained from Brooks Pharmaceuticals (Pvt) Ltd. Karachi, Pakistan. The pure polymers xanthan gum (XG) and chitosan medium molecular weight, Mw 190–310 kDa, degree of deacetylation 75–85%, viscosity 200-800cP] were purchased from Sigma-Aldrich (UK). Monomer 2-acrylamido-2-methylpropane sulfonic acid (AMPS) and cross linker N′ N′-methylene bis-acrylamide (MBA) were procured from Sigma-Aldrich (USA). Fluka (Denmark) supplied the analytical grade initiator potassium persulfate (KPS).

Synthesis of Hydrogel Formulations

Hydrogels (FCX1-FCX9) with different content of chitosan (CS), xanthan gum (XG), 2-acrylamido-2-methylpropane sulfonic acid (AMPS), N′ N′-methylene bis-acrylamide (MBA) and potassium persulfate (KPS) were prepared by using free radical polymerization technique. First of all, a pre weighted amount of pure polymer, CS has been dissolved in 1% aqueous solution of acetic acid at 25°C. The dissolved oxygen has been removed from reaction mixture by purging nitrogen gas from it for 20 min. XG was dissolved in 25 mL of distilled water at 40°C. The two prepared polymer solutions were blended and stirred for 2 h at 250 rpm. This reaction mixture was later placed in a thermostatic water bath and temperature was increased up to 50°C. An initiator i.e. KPS was added with constant stirring to above reaction mixture to generate free radicals. On the other hand, monomer AMPS and crosslinking agent MBA were dissolved separately in distilled water at 25°C. After dissolving and homogenizing the mixture of AMPS and MBA, it was added to above prepared reaction mixture of polymers and initiator. Distilled water was used for adjustment of final volume. The final solution was stirred at 5,000 rpm for 6 h while maintaining the temperature of 65°C and inert atmosphere until clear, homogeneous solution was produced. The resulting solution mixture was transferred to dried glass test tubes and positioned in water bath for 12 h. After removal, prepared hydrogels were cut into uniform size i.e., 8 mm and then washing was carried out using ethanol water mixture (70:30) to eliminate species which are unreacted. A stable value of pH of washing solution indicated complete removal of unreacted components. The discs were further dried in lyophilizer −55°C till drying equilibrium. **Table 1** indicated hydrogels (FCX1-FCX9) developed using different concentration of reactants.

TABLE 1 | Hydrogels (FCX1-FCX9) using different concentration of reactants.

Sample code	Polymer		Monomer	Initiator	Crosslinking agent
	g/100 g CS	g/100 g XG	g/100 g AMPS	g/100 g KPS	g/100 g MBA
FCX1	8	2	25	0.5	0.6
FCX2	8	2	35	2	0.6
FCX3	4	1	35	0.5	0.6
FCX4	8	2	35	0.5	1.2
FCX5	12	2	35	0.5	0.6
FCX6	8	3	35	1.5	0.6
FCX7	8	2	35	0.5	0.6
FCX8	8	2	15	0.5	0.6
FCX9	8	2	35	0.5	1.8

Drug Loading

Drug loading was carried out by immersing dried hydrogels in ACV 1% solution at 25°C. The drug solution of specific concentration was prepared using 0.2 M phosphate buffer solution, maintained at pH 7.4. Developed hydrogels were kept in ACV solution for drug loading until they attain constant weight. After removal from ACV solution, hydrogels were further subjected to freeze drying on lyophilizer.

Fourier Transform Infrared Spectroscopy (FTIR)

For recording FTIR spectra of the reactants and ACV loaded hydrogels, crushing of samples were done using KBr at a pressure of 600 kg/cm^2 to obtain desired pallets. A range between 4,000 and 600 cm^{-1} was selected for spectral scans by employing Bruker FTIR (Tensor 27 series, Bruker Corporation, Germany) instrument, using attenuated total reflectance (ATR) technology accompanying software OPUS data collection.

Scanning Electron Microscopy (SEM)

Structural morphology of hydrogels was investigated using SEM images. Powdered samples were sputtered with gold and placed on aluminum stub. JEOL analytical scanning electron microscope (JSM-6490A, Tokyo Japan) was used to conduct scanning.

Thermal Analysis

Thermal analysis of polymers, monomer and the hydrogel sample were done on thermal analysis system (TA instrument Q2000 Series, West Sussex, UK). For conducting thermal analysis, samples were heated at the heating rate of 10°C /min with a flow rate of 20 mL/min up to 500°C in a nitrogen atmosphere.

Powder X-Ray Diffraction (PXRD) Analysis

Powder X-ray diffraction (PXRD) was used to investigate nature of the synthesized hydrogels. Samples were investigated using X-ray diffractometer (x-Pert, PAN analytical, The Netherlands). The angle of diffraction was varied from 10 to 50°.

Swelling Studies

For investigating swelling dynamics of developed hydrogel formulation, simulated gastric fluid (SGF) and simulated intestinal fluid (SIF) were used as swelling media. Initially, the developed hydrogels were soaked in simulated media maintained at 37°C. After specified time period, hydrogels have been removed and blotted off cautiously to get rid of any liquid droplets adhered on the surface. Hydrogels in swollen state were weighed on an electronic measuring balance. They were then

subject to drying until achievement of constant weight in a lyophilizer. The swelling index was calculated as mentioned in Equation (1).

$$Swellingindex\ (Q) = \frac{Ms}{Md} \quad (1)$$

Where Ms indicates mass of swollen hydrogels at predetermined time interval and Md represents the weight of dried hydrogels.

Determination of Drug Entrapment Efficiency (DEE)

Estimation of drug entrapment efficiency was carried out by crushing ACV loaded hydrogels of known weights carefully in mortar and pestle. They were then soaked in 100 mL of phosphate buffer solution having pH 7.4 for 24 h. After that, sonication was carried out for 20 min to carry extraction of ACV. Further removal of polymeric debris was done by centrifugation at 300 rpm. Fresh solvent has been used to extract polymeric debris for any adhered drug. Analysis of clear supernatant solution was done for ACV by UV-Visible Spectrophotometer at λ max value of 256 nm. Estimation of drug entrapment efficiency of the developed hydrogels has been done by using following formula as mentioned in Equation (2).

$$\%\ Entrapment\ efficiency = \frac{\%\ Actual\ loading}{\%\ Theoratical\ loading} \times 100 \quad (2)$$

In vitro Drug Release Studies and Drug Release Kinetics

In-vitro release study of ACV from different formulations of hydrogels was designed in simulated gastrointestinal (GIT)

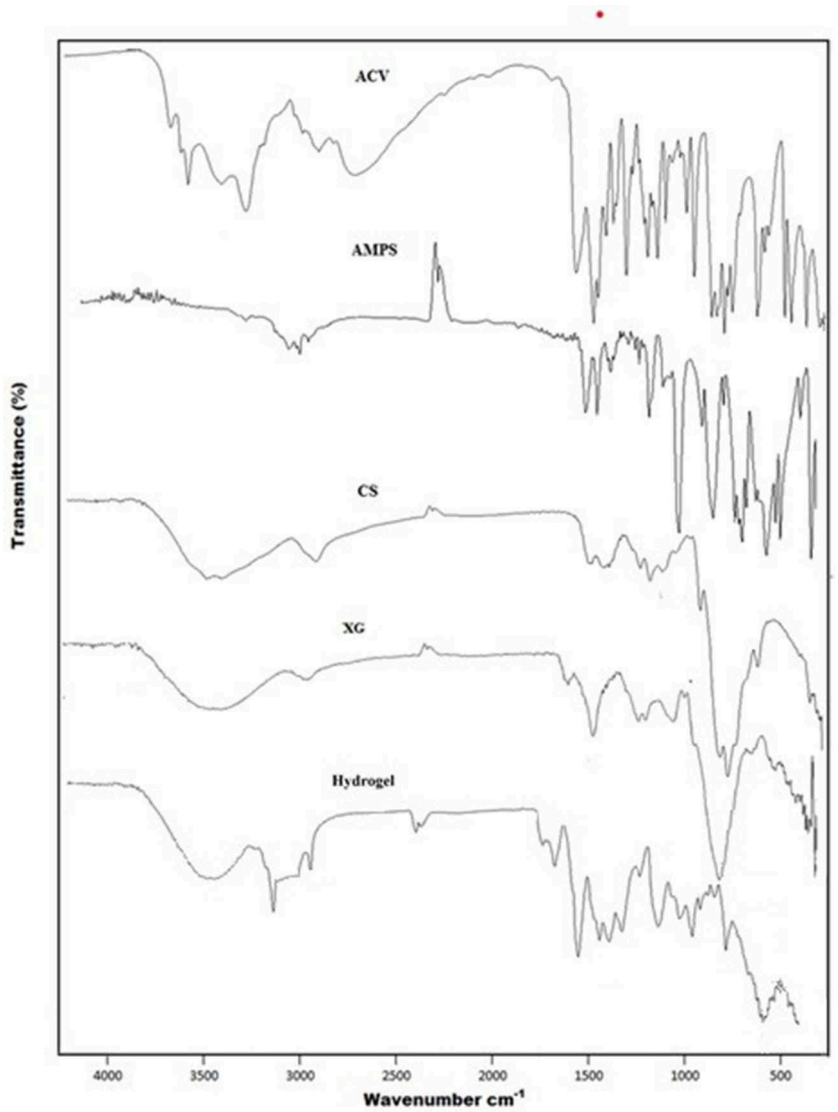

FIGURE 1 | FTIR Spectra of ACV, AMPS, CS, XG and Hydrogel.

conditions to investigate drug release behavior in different parts of GIT. For this purpose, simulated gastric fluid (SGF, 0.1MHCl, pH 1.2), followed by the simulated intestinal fluid (SIF, 0.2 M potassium dihydrogen phosphate, pH 7.4) have been used. The experiment has been conducted using a USP dissolution apparatus II (Curio; DL-0609) coupled with six baskets. The speed of stirring was kept at 50 rpm. Sample was weighed and added in 900 mL of media, which was kept at 37°C. The ACV concentration was determined spectrophotometrically using UV–Visible Spectrophotometer at the λ max value of 256 nm. Release data for various developed hydrogels was evaluated by computing various kinetic models.

Oral Acute Toxicity Study of Hydrogel

On the basis of maximum drug entrapment efficiency and *in-vitro* cumulative drug release, one hydrogel formulation was chosen for safety evaluation via acute oral toxicity study. Toxicity study was performed according to the Organization for Economic Co-operation and Development (OECD) guidelines. Ten healthy adult albino rats of wistar strain (procured from Animal Facility Center of Faculty of Pharmacy and Alternative Medicine, The Islamia University of Bahawalpur, Pakistan) with weight ranged approximately 2.5 g ± 10 were used to conduct study. They were divided in to two groups, with each group having five animals. Acute oral toxicity was conducted using

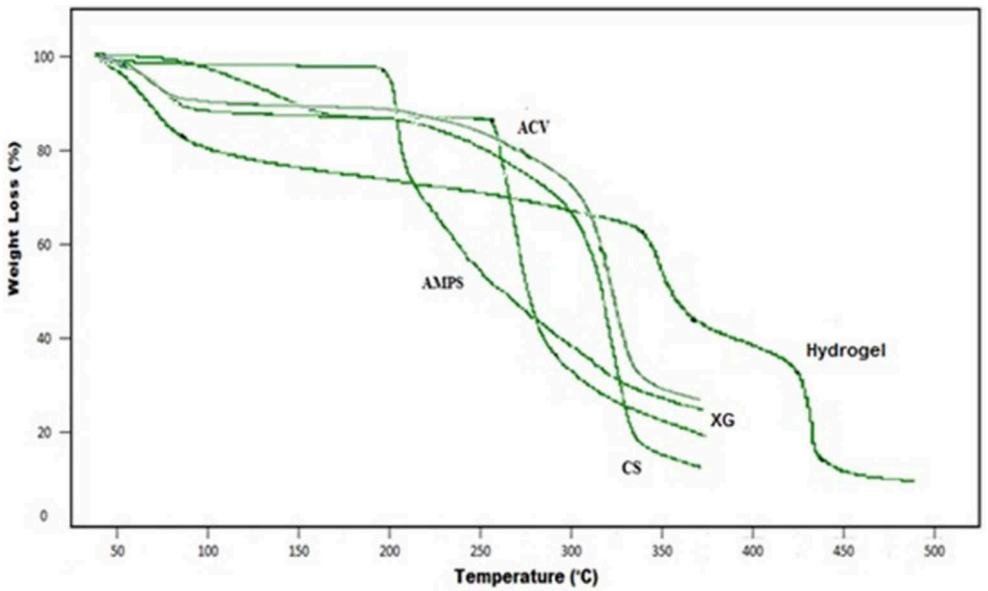

FIGURE 2 | TGA curve of ACV, AMPS, CS, XG, and Hydrogel.

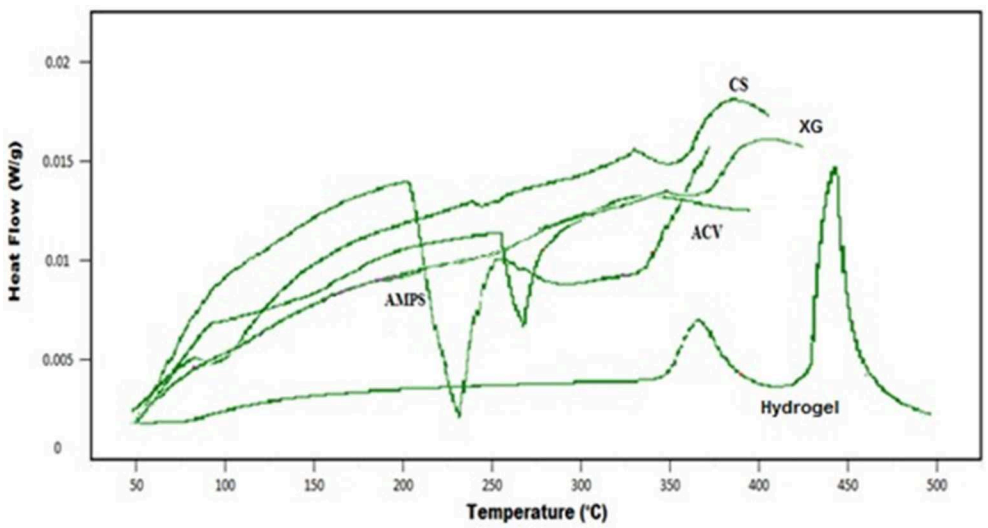

FIGURE 3 | DSC curve of ACV, AMPS, CS, XG, and Hydrogel.

maximum tolerance dose method (MTD). Animals transient room (room temperature: 25 ± 2°C, relative humidity: 65 ± 5%, 12 h light/dark cycle) was used for housing animals. All rats were provided with water *ad libitum* and balanced diet. Group A was used as control and has been administered ACV in suspension form by adding ACV powder to normal saline. Group B was used as treatment group and has been given hydrogel powder dispersion (in deionized water) through oral gavage. Both control and treatment groups were given a total dose of 5 g/kg bodyweight of their respective formulation. Rats were monitored for general conditions (the activity, energy, hair, feces, behavior pattern and other clinical signs), change in body weight, morbidity and mortality. After 14 days, rats were sacrificed by cervical dislocation. Blood sample was collected and preserved in ethylene diamine tetra acetic acid (EDTA) tubes for hematology and biochemical blood analysis. Vital organs (heart, liver spleen, kidney, stomach, and lung) were removed and weighed. All organs were preserved in 10% buffered formaldehyde, embedded in paraffin, and then segmented. The paraffin segments were stained with haematoxylin-eosin for histopathologic-examination.

The experimental protocol used in this study was reviewed and approved by Pharmacy Research Ethics Committee (PREC) of The Islamia University of Bahawalpur, Pakistan (23-2016/PREC).

Statistical Analysis

Results are indicated as Mean ± Standard error of mean (SEM). IBM SPSS Statistics 20 program was used for statistical analysis of acute oral toxicity study results. The difference between two groups was determined by one-way analysis of variance (ANOVA) with Tukey test. A value of $p < 0.05$ was regarded statistically significant.

RESULTS AND DISCUSSION

FTIR Spectroscopy

FTIR spectra of ACV, XG, CS, AMPS and developed hydrogel are shown in **Figure 1**. CS showed absorption band at 3,358 cm^{-1} represented overlapping of –OH and symmetric N–H stretching vibrations. The bands observed at 1,644, 1,605, and 1,375 cm^{-1} are due to carbonyl stretching vibration (amide-I), N–H stretching vibration (amide-II) and the C–N stretching vibration (amide-III) of pure chitosan, respectively. Another characteristic band at 1,028 cm^{-1} indicated presence of C–O stretching vibration. The pure polymer, XG showed hydrogen bonded OH groups via absorption band at 3,277 cm-^{1}. The COO^{-} groups was represented at 1,605 cm^{-1}, whereas bands at 1,417 and 1,021 cm^{-1} represent C–H bending and O–H bending vibrations, respectively. AMPS revealed peaks at 2,987 cm^{-1} representing the C–H stretching frequency of CH_2, while peaks around 1,666 and 1,613 cm^{-1} were due to C=O stretching and N–H_2 bending, respectively. Symmetric and asymmetric –SO_2 stretching bands were observed at 1,077 and 1,234 cm^{-1} respectively. In case of ACV, peaks at 3,438 and 3,178 cm^{-1} represented N–H and O–H stretching vibrations. Moreover, peaks at 2,688 and 1,707 cm^{-1} indicated presence of aliphatic C–H stretching vibrations and C=O stretching vibrations, respectively. Another prominent peak at 1,630 cm^{-1} was attributed due to N – H bending.

The FTIR spectrum of synthesized hydrogel exhibited some new peaks, with slight shifting, overlapping and disappearance of some of the characteristic peaks of pure components in polymeric network, which is an indication of formation of new hydrogel structure. Accordingly, 3,358, 1,644, 1,604, 1,375, and 1,028 cm^{-1} bands of CS, 3,277, 1,605, 1,417, and 1,021 cm^{-1} bands of XG, 2,987, 1,666, 1,613, 1,077, and 1,234 cm^{-1} bands of AMPS and 3,438, 3,178, 2,687, 1,707, and 1,630 cm^{-1} bands of ACV are shifted to 3,299 cm^{-1}, 2,920, 1,647, 1,541, 1,173, and 1,019 cm^{-1} regions in developed polymeric network.

The stretching vibration of OH and NH_2 at 3,358 and 3,277 cm^{-1} shifts to 3,299 cm^{-1} and becomes broad, indicating formation of polyelectrolyte complexes between chitosan and xanthan gum. A band observed at 2,920 cm^{-1} indicated shifting of sulfonic acid band from 2,987 cm^{-1}, to new position, representing CH stretching frequency of CH_2 in sulfonic acid. The asymmetric and symmetric bands of SO2 were shifted to new position of 1,173 and 1,019 cm^{-1} from 1,234 and 1,077 cm^{-1}, respectively, representing sulfonic acid participation in hydrogel formulation. In addition, absorption band noted at 1,647 cm^{-1} was due to carbonyl functional group, representing shifting of carbonyl stretching of CS, XG, AMPS, and ACV to new position of 1,647 cm^{-1}. The absorption bands at 1,644 and 1,605 cm^{-1} due to stretching of amide group of chitosan have been shifted to new position of 1,541 cm^{-1}, thus indicating chitosan have participated in cross linking during hydrogel formation.

All of these shifting and overlapping has suggested non-covalent grafting of monomer onto polymeric network through intermolecular rearrangement, electrostatic interaction between components such as hydrogen bonding and alteration in positions of functional groups of CS, XG, AMPS, and ACV in the developed hydrogel structure (Ray et al., 2008; Yang et al., 2013). Hence formation of new grafted polymeric network and successful entrapment of model drug ACV into developed hydrogel structure is evident (Liu et al., 2010).

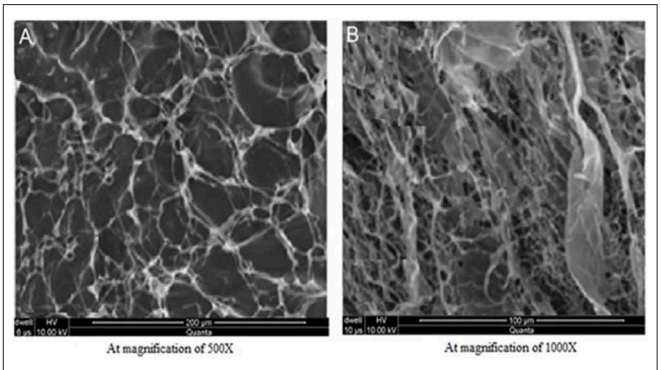

FIGURE 4 | SEM images of ACV loaded hydrogel **(A)** At 200 μm **(B)** At 100 μm.

Thermal Analysis

Figure 2 shows the TGA thermogram of developed hydrogel and individual reactants representing loss of weight at different temperature ranges. The TGA thermogram of the pure polymer chitosan (CS) represents weight loss at two stages i.e., initially due to loss of bound water at about temperature 91°C and later 35%, representing decomposition of its major structure at temperature range of 317°C. At temperature range of 355°C, chitosan also shows a residue mass of about 17%. Moreover, during decomposition of chitosan glycosidic bonds are broken leading toward production of a series of lower fatty acids and further degradation. TGA curve of XG shows 10 and 74% mass loss at about 93 and 360°C, respectively. AMPS demonstrated two-step decomposition in temperature range of 206 and 262°C with 2 and 49% weight loss, respectively. In TGA thermogram of ACV initial moisture loss was indicated at 99°C. Loss of site chain from guanosine rings was indicated at 269°C. Residual guanosine mass which was further degraded at higher temperatures of 306°C. In developed hydrogel, the initial weight loss started at 89°C which sustained up to 341°C, representing 13 and 28% weight loss, respectively. Later decomposition phase began at 370°C and continued up to 427°C, representing 40.94 and 49% weight loss, respectively, owing to melting point temperature. The decomposition at 440°C representing 62% weight loss and final decomposition of cross-linked polymeric network. However, the mass of left-over hydrogel at this temperature is still about 38%. The thermal profile of hydrogels with elevated residual weight indicates that developed polymeric matrix represented enhanced stability against thermal degradation than reactants over the entire studied range of temperature. Moreover, due to enhanced strength and interaction between the polymer and monomer, degradation for developed hydrogel starts at elevated temperature with slower weight loss rate as compared to the individual reactants (Azmeera et al., 2012). This enhanced thermal stability with shifting of endothermic peaks to elevated temperature and formation of rigid network represents higher stability (Ma et al., 2011).

TABLE 2 | Drug entrapment efficiency (%DEE) and percentage drug release at pH 1.2 and pH 7.4.

Formulation code	Drug entrapment efficiency (%DEE)	Percentage release of ACV (for 24 h period)	
		pH 1.2	pH 7.4
FCX1	79.34	30.25	85.43
FCX2	80.65	29.01	88.22
FCX3	84.99	36.45	91.02
FCX4	78.43	29.94	83.57
FCX5	83.12	35.52	90.08
FCX6	87.64	42.65	96.49
FCX7	86.12	39.25	93.49
FCX8	76.83	27.46	82.64
FCX9	80.99	32.04	88.15

Figure 3 shows the DSC thermogram of developed hydrogel and individual reactants. Model drug acyclovir showed a small band at 91°C and a sharp endothermic band at 270°C, representing an initial moisture loss followed by its melting point temperature. XG thermogram demonstrated two endothermic peaks at about 90 and 225°C, respectively. The DSC curve of AMPS represents a sharp endothermic peak at 230°C and a small peak at 342°C. CS decomposition occurs in the temperature range of 229–341°C with endothermic peaks representing degradation of its amino and N-acetyl residue. Shifting toward higher glass transition temperature of hydrogel formulation than parent components indicates higher compatibility between the individual components and formation of rigid network structure (Tummala et al., 2015), due to higher intermolecular hydrogen bonding (Gandhi et al., 2014). Thus, indicating higher thermal stability of developed polymeric network (Dey et al., 2013).

Scanning Electron Microscopy (SEM)

SEM micrographs confirmed porous structure of developed hydrogel as shown in **Figure 4**. Porous structure might also be due to presence of ionic and hydrophilic group in developed polymeric network i.e., AMPS and XG (Khalid et al., 2018). Therefore, incorporating the hydrophilic component in the hydrogel structure have increased the system hydrophilicity and subsequently porosity of hydrogels (Malik et al., 2017b). This porous architecture and connectivity of pores in developed hydrogel is highly beneficial and plays a crucial role in its swelling and deswelling kinetics. Moreover, solvent or buffer molecules

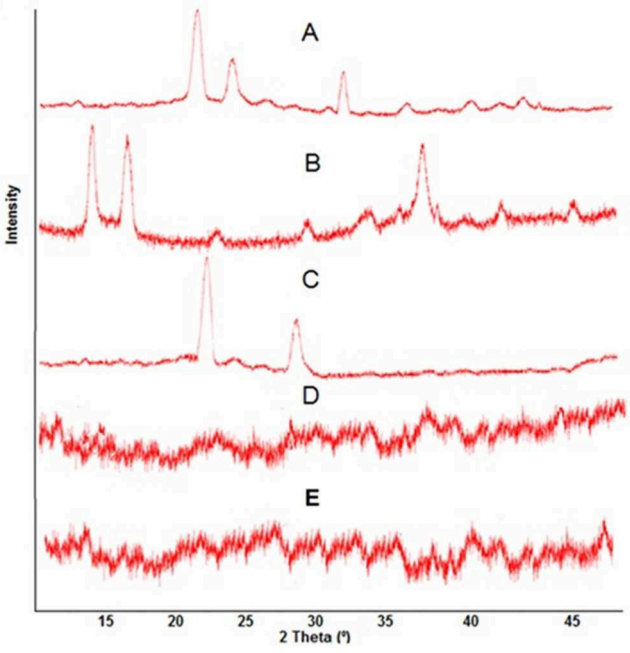

FIGURE 5 | PXRD pattern of **(A)** ACV, **(B)** CS, **(C)** XG, **(D)** ACV unloaded Hydrogel, and **(E)** ACV loaded Hydrogel.

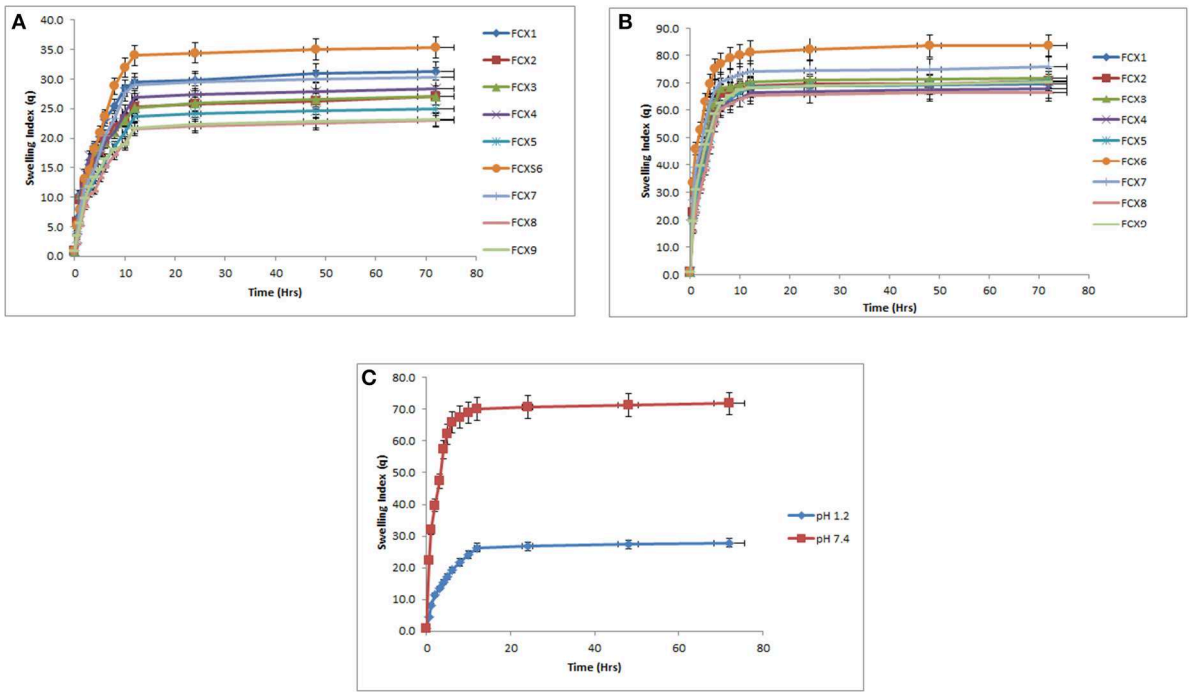

FIGURE 6 | Mean swelling index of hydrogels (FCX1 to FCX9) at pH 1.2 and pH 7.4. **(A)** Swelling index of hydrogels formulations FCX at pH 1.2. **(B)** Swelling index of hydrogels formulations at pH 7.4. **(C)** Mean swelling index of hydrogels (FCX1–FCX9) at pH 1.2 and pH 7.4.

could enter or leave the hydrogel through interconnected pores by convection, thereby facilitating the entrapment and ultimately release of incorporated ACV from them (Mukhopadhyay et al., 2014). It is obvious from **Table 2** that the most optimized hydrogel formulation FCX6 have exhibited entrapment efficiency of 90.64% and have released 87.57% of drug at pH 7.4, indicating high swelling rate and porous structure of developed polymeric network. Furthermore, freeze drying method might have contributed toward enhanced porosity of hydrogel as drying procedure had remarkable influence on preserving the porous structure of hydrogel (Kabiri and Zohuriaan-Mehr, 2004).

Powder X-Ray Diffraction (PXRD) Analysis

The PXRD spectra recorded for (a) ACV (b) CS (c) XG (d) placebo hydrogel and (e) ACV-loaded hydrogels have been shown in **Figure 5**. The sharp and intense peaks at 2 $\theta = 18.50^{\circ}$, 21.50° and 30.50° are characteristic of ACV and indicated highly crystalline nature of drug. Owing to the hydrogen bonding between hydroxyl group of chitosan, PXRD analysis of polymer revealed a crystalline structure representing a strong diffraction peak at around 13.06° and at 17.56°, respectively. XG was characterized by the presence of two prominent peaks visible at 2 $\theta = 21.5^{\circ}$ and 28.5°. However, in PXRD analysis of drug unloaded hydrogel, the sharp, and characteristic peaks of pure component were substituted by dense peaks, representing decrease in crystallinity. This decrease in crystallinity of developed hydrogel might be due to conjugation of monomer AMPS with pure polymer chitosan utilizing cross linker MBA and KPS, thus representing increase in fraction of amorphous phase. Moreover,

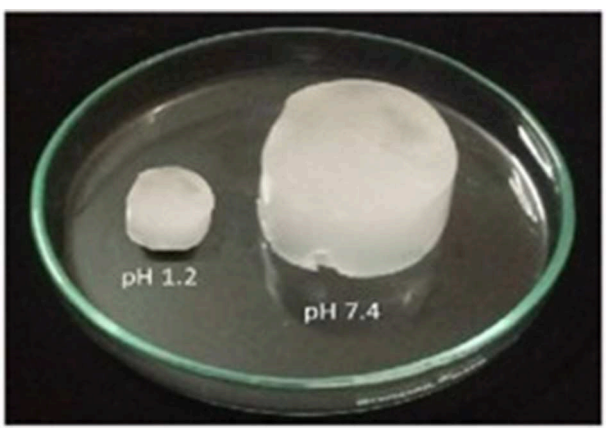

FIGURE 7 | Swollen hydrogel at pH 1.2 and pH 7.4.

the PXRD analysis of ACV loaded hydrogel disc also indicated lack of characteristic or prominent peaks of drug into polymeric matrix. The analogy in diffractogram of both ACV unloaded and ACV loaded hydrogel discs representing dispersion of drug in amorphous form into polymeric network (Stulzer et al., 2009).

Swelling Dynamics

Effect of pH on Swelling Behavior

It can be assumed that swelling behavior of developed hydrogels depends upon the presence of functional groups that could

be ionized or protonated, hydrophilic-hydrophobic interactions and relaxation of polymeric chain. It was found that developed hydrogels showed high swelling dynamics at pH 7.4 but swelling degree was less at pH 1.2. This behavior might be due to protonation of functional group of CS and AMPS at pH 1.2 and deprotonation at pH 7.4.

An AMPS is a hydrophilic monomer and has both ionic and non-ionic moieties. When AMPS is grafted on CS-XG backbone, the ionizable sulfonate groups in AMPS impart pH dependent behavior to the developed polymeric network. The pKa value of monomer AMPS is 2. Sulfonate groups of monomer AMPS undergo ionization or deprotonation at pH value of 7.4, which is higher than the pKa value of AMPS. Presence of ionized sulphonate groups increases charge density on polymeric network, thus creating strong electrostatic repulsion among its ionized –SO3– groups and producing greater expansion of the polymeric network (El-Hag Ali, 2012). This leads toward reduction or loss of intermolecular hydrogen bonding and consequently increasing the swelling dynamics of synthesized hydrogel structure (Bao et al., 2011).

At pH 1.2, which is lower than the pKa value of monomer, the sulfonate anions are protonated and associated, therefore provide strength to the hydrogen-bonding and producing strong physical interaction among hydrogel. All these factors have led toward additional strength, physical crosslinking and decrement in swelling dynamics of developed hydrogel. Thus, a significant decrease in swelling ratio has been observed with decrease in pH (Atta, 2002; Khalid et al., 2018).

CS is a weak polyelectrolyte with a pKa around 6.5. The primary NH_2 group of the polymer CS undergoes protonation at pH 1.2 and deprotonation at pH 7.4, respectively. At

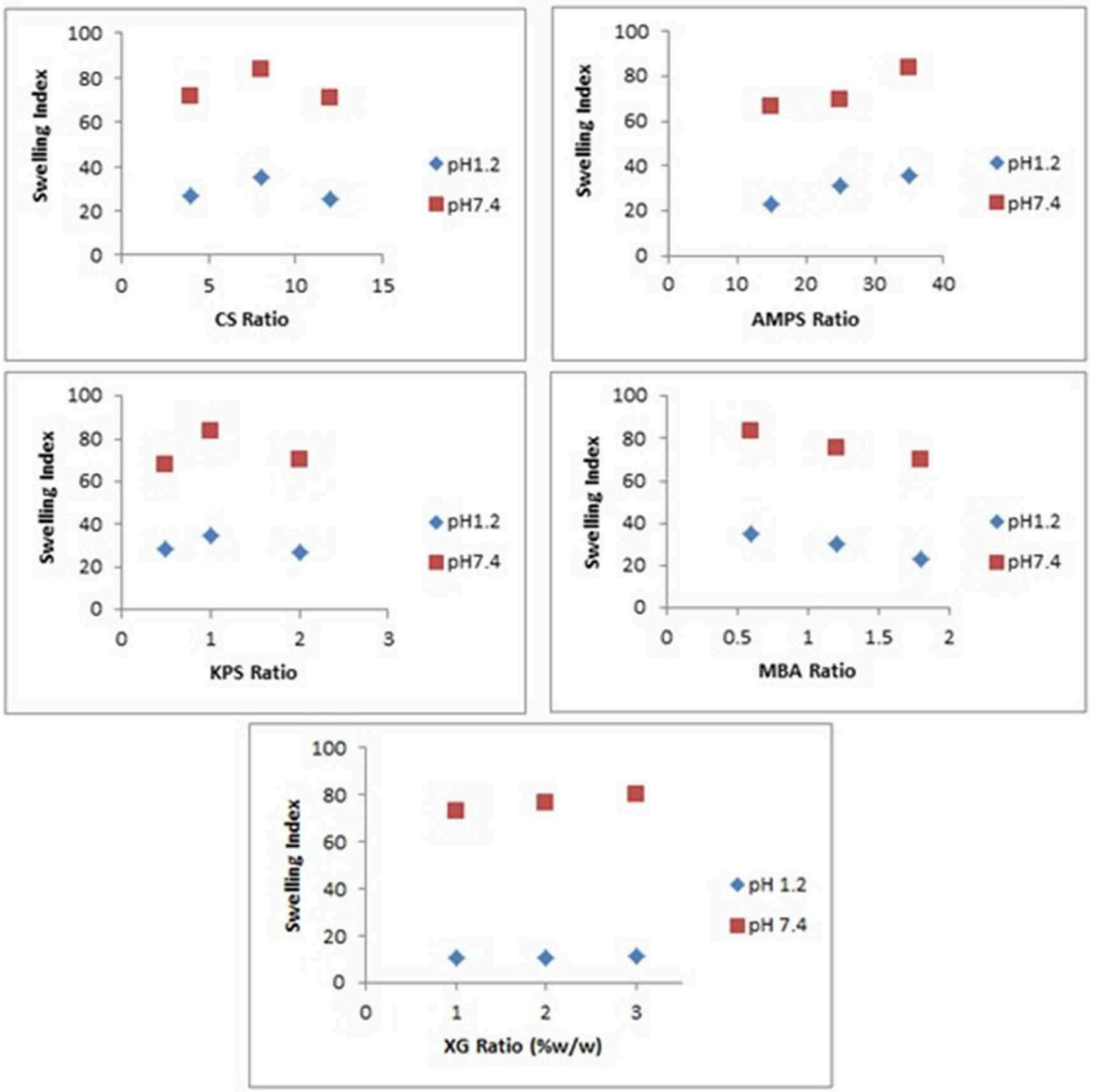

FIGURE 8 | Effect of different concentration of CS, XG, AMPS, KPS, and MBA on swelling index of hydrogels.

pH 1.2, the primary amino groups of the polymer are protonated by hydrogen ions to form NH_3^+ groups. However, due to crosslinking of chitosan within polymeric network, number of free NH2 groups in polymeric network has been decreased significantly. Also, at very acidic conditions (pH 1.2), a screening effect of the counter ions, i.e., Cl–, shields the charge of ammonium cations, thus prevents an efficient repulsion between them. Moreover, available NH_3^+ groups allow chitosan to form networks through ionic links with the sulfonate groups of the AMPS, thus swelling capacity decreases.

At pH 7.4, the sulfonate groups of AMPS are ionized, while the chitosan NH_3^+ groups change back to NH_2 groups. Under these conditions, chitosan does not form ionic links, leading to decrease cross-linking density and increase in swelling capacity of hydrogel formulation as shown in **Figures 6** and **7** (Martinez-Ruvalcaba et al., 2009).

Effect of Different Components of Hydrogels on Swelling

The effect of different concentration of reactants i.e., CS, XG, AMPS, KPS, and MBA on swelling behavior of synthesized hydrogels have been evaluated at pH 1.2 and 7.4 at temperature 37°C as shown in **Figure 8**.

Swelling of hydrogel increased on increasing concentration of CS from 4 to 8 g but decreased on further increase of CS concentration from 8 to 12 g. CS possess polyelectrolyte nature due to the presence of hydroxyl –OH and amine –NH2 polar functional groups, thus inducing an increase in translational entropy of counter ions and elevated osmotic pressure and swelling dynamics. Hence, the presence of this pure polymer in the hydrogel network increases swelling ratio of the developed hydrogel. Upon further increase of polymer concentration from 8 to 12 g, reaction mixture got highly viscous and steric effect of CS outweighs ionic effect of ionic groups of the polymer, resulting in restricted movement of water molecules, leading to a lower swelling ratio. Thus, it can be assumed from results that optimum level concentration of CS that can enhance swelling behavior is 8 g. Beyond this concentration, swelling ratio decreases (Mandal and Ray, 2014).

The effect of XG concentration on the swelling behavior of the hydrogels has been shown in **Figure 8**. Swelling of hydrogel increased on increasing concentration of XG from 1 to 3 g. Hydrogels having XG 3 g exhibited highest swelling ratio in

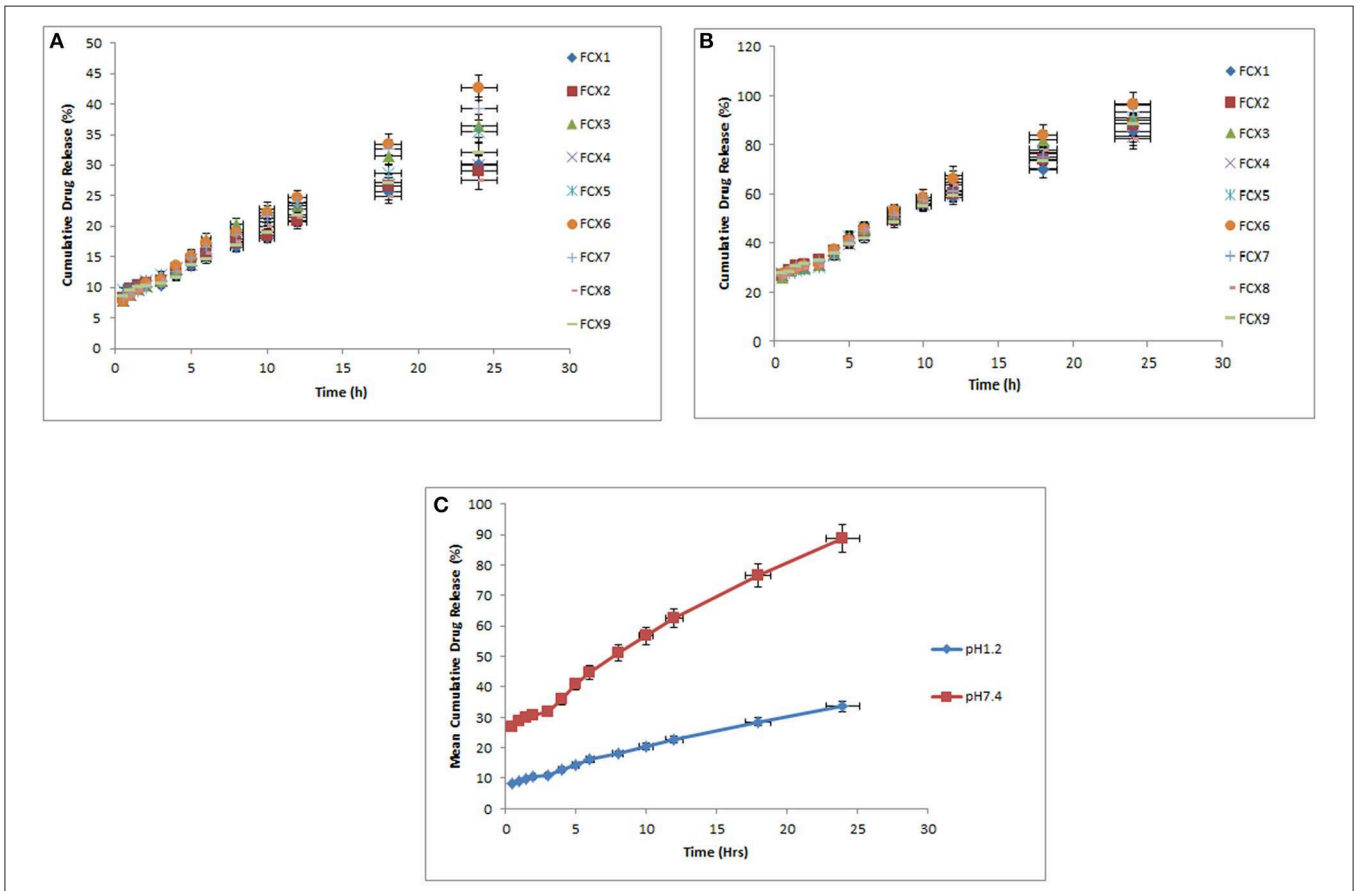

FIGURE 9 | Mean cumulative drug releases of hydrogels (FCX1 to FCX9) at pH 1.2 and pH 7.4. **(A)** Cumulative drug release of hydrogels (FCX1–FCX9) at pH 1.2. **(B)** Cumulative drug release of hydrogels (FCX1–FCX9) at pH 7.4. **(C)** Mean cumulative drug release of hydrogels (FCX1–FCX9) at pH 1.2 and pH 7.4.

comparison to formulations with lesser concentration of XG i.e., 1 and 2 g, respectively. This might be attributed to hydrophilic nature of XG and due to the presence of o-acetyl and pyruvyl residues in XG, which can be completely deprotonated at pH > 6. This deprotonation at pH > 6 led to increased charge density, greater electrostatic repulsion, greater expansion of network and increased swelling of hydrogel.

The effect of monomer concentration on the swelling capacity of the hydrogel has been investigated by varying the AMPS concentration from 15 to 35 g, respectively. It has been observed that as AMPS concentration increases from 15 to 35 g, swelling index of hydrogel increases sharply. AMPS being a hydrophilic monomer have both ionic and non-ionic groups. As the number of ionizable sulfonate groups in AMPS increases, the concentration gradient of the counter ions across the polymeric network increases. Thus, causing an increase in osmotic pressure executed by counter ions of AMPS and increase in swelling index of developed polymeric network (Qudah et al., 2013). Moreover, enhanced water absorbency has been noted on increasing monomer concentration because it increases the diffusion of AMPS across pure polymer chitosan backbone (Gad, 2008). Hence, it can be said that increasing concentration from 15 to 35 g is optimal for achieving higher swelling ratio in our developed polymeric network.

The effect of initiator concentration on the swelling behavior of the hydrogels has been shown in **Figure 8**. On increasing KPS concentration from 0.5 to 1.5 g, swelling index increases. However, with a further increase in the amount of KPS up to 2 g there is considerable decrease in swelling behavior of hydrogels. In fact initially number of active radicals increased upon increasing KPS amount up to optimal value. These active radicals have tendency to improve the growth of polymer chain and form a 3-dimensional network by process of chain transfer reaction. Thus, increasing concentration of initiator from 0.5 to 1.5 g has produced more free radicals that have enhanced the non-covalent grafting efficiency, leading to enhanced swelling behavior. However, on increasing KPS concentration from 1.5 to 2 g, this high concentration of initiator has produced large number of free radicals. These free radicals have increased the collision probability among them, thus leading to the termination of the chain reaction. The generated short graft chains could not have a tendency to form a 3D polymeric network easily, thus decreasing swelling index (Cheng et al., 2015). Thus, it has been observed that optimum KPS concentration in this study was 1.5 g.

The influence of crosslinker MBA content on the swelling index of hydrogel has also been noted by varying the crosslinker concentration from 0.6 to 1.8 g. Higher value of swelling index was achieved with lower MBA content of 0.6 g, compared to 1.2 and 1.8 g respectively. A possible explanation of reduced swelling index on increasing MBA concentration is related to crosslinking density. Higher crosslinker concentration decreases the free space among the polymeric networks, therefore producing compact and rigid framework that cannot be relaxed to sustain huge quantity of water molecules or buffer solution in which hydrogels are immersed (Kim et al., 2011). Therefore, it can be concluded that increasing crosslinker concentration from 0.6 to 1.2 g and later from 1.2 to 1.8 g has resulted an increase in crosslink density.

An increase in the crosslinking density restricts the degree of swelling due to decreased chain mobility and reduces the pH sensitivity by improving the stability of the network.

TABLE 3 | Determination of regression coefficient R^2 and release exponent "*n*" from developed hydrogels.

Sample code		Zero order kinetics	First order kinetics	Higuchi model	Korsmeyer Peppas model		Weibull model
		R^2	R^2	R^2	R^2	n	R^2
FCX1	1.2	0.991	0.457	0.974	0.996	0.604	0.932
	7.4	0.99	0.313	0.969	0.995	0.472	0.941
FCX2	1.2	0.98	0.422	0.979	0.994	0.528	0.926
	7.4	0.993	0.32	0.971	0.997	0.493	0.944
FCX3	1.2	0.98	0.493	0.979	0.991	0.462	0.889
	7.4	0.977	0.344	0.97	0.997	0.544	0.912
FCX 4	1.2	0.964	0.45	0.988	0.994	0.447	0.881
	7.4	0.98	0.326	0.966	0.998	0.443	0.926
FCX5	1.2	0.992	0.467	0.966	0.994	0.605	0.928
	7.4	0.98	0.341	0.967	0.993	0.581	0.909
FCX6	1.2	0.998	0.534	0.957	0.99	0.726	0.932
	7.4	0.99	0.355	0.964	0.999	0.575	0.932
FCX7	1.2	0.997	0.527	0.957	0.995	0.657	0.931
	7.4	0.993	0.334	0.964	0.995	0.526	0.943
FCX8	1.2	0.95	0.422	0.989	0.993	0.367	0.862
	7.4	0.962	0.325	0.972	0.992	0.43	0.894
FCX9	1.2	0.993	0.467	0.961	0.995	0.619	0.943
	7.4	0.996	0.322	0.961	0.991	0.519	0.956

Drug Entrapment Efficiency (%DEE) and Drug Release Behavior

Table 2 shows the drug entrapment efficiency (%DEE) and drug release behavior of developed hydrogels at both pH 1.2 and 7.4, respectively. Hydrogel FCX6 exhibited maximum DEE of 90.64% whereas FCX8 exhibited minimum DEE of 76.83%. It has been observed that drug entrapment efficiency in the hydrogels increases with the increase of loading time, until the amount of drug loaded reached equilibrium. %DEE increases when loading time has been increased from 2 to 3 h. However, after 3 h, capacity of hydrogel to load the drug became constant and attained equilibrium. Thus, no further increase in drug entrapment efficiency has been observed after 3 h. Therefore, for loading of ACV into the developed polymeric network, 3 h was established as the standard loading time in our study.

A decrease in amount of drug loaded in hydrogels has been observed with increasing concentration of cross-linking agent MBA. The possible reason might be due to higher cross-linking density which ultimately decreases the elasticity of polymeric structure, therefore restricting the movement of ACV from drug solution into developed hydrogel structure, leading to decrease in drug entrapment efficiency (Wang et al., 2009).

% DEE has also been increased with increasing concentration of CS used in reaction mixture from 4 to 8% and XG from 1 to 3 % respectively. Possible reasons might be enhance availability of polymer leading to improved ability of hydrogel to capture more drug molecule, thus improving drug entrapment efficiency. On increase in CS ratio from 8 to 12 %, a decrease in drug entrapment efficiency has been indicated. CS might have caused an increase in the viscosity of internal phase which showed hindrance to mass transfer and promoting decrease in % DEE. Thus, the optimal concentration of CS and XG for enhanced entrapment efficiency was 8 and 3% respectively.

In vitro drug release behavior was observed for a period of 24 h in SGF and SIF media. All formulations have shown very less drug release at pH 1.2 but it increased significantly as pH of dissolution medium increased to pH 7.4 as shown in **Figure 9**. Drug release rate has been found to be dependent on %DEE. Hydrogel formulations with lower %DEE have shown lower release of ACV as compared to those having enhanced %DEE. The possible reason might be that by residing or engaging free space of the hydrogel in swollen state, the drug in the polymeric network behaves as a plasticizer, thereby increasing the flexibility of the polymeric network and producing more spacious path for diffusion of media across it and ultimately release of ACV (Agnihotri and Aminabhavi, 2006).

The kinetics of ACV release from various hydrogel formulations was done using Linear regression analysis as shown in **Table 3**. It has been observed that Korsmeyer-Peppas model was found to best fit to our results, thus indicating that drug release from ACV loaded hydrogel formulation followed controlled-release pattern.

In addition, zero order and Higuchi were found to be closer to Korsmeyer-Peppas model. The release mechanism of ACV from developed hydrogels may be Fickian diffusion when the value of n is 0.43 or less, anomalous (non-Fickian) transport when the value of n lies between 0.43 and 0.85, and case II transport when $n = 0.85$. The value above 0.85 indicates super case II transport that relates to polymer relaxation during swelling (Siepmann and Peppas, 2012).

The value of n has been calculated and given in **Table 3** along with correlation coefficients. The values of n were confined between 0.43 and 0.85 for all developed hydrogels except FCX8 at both pH 1.2 and 7.4, respectively. Thus, indicating that ACV released from developed polymeric network followed non-Fickian transport. However, for FCX8 the values of n ranged between 0.367 and 0.430, indicating deviation of ACV release from non-Fickian mechanism to Fickian diffusion.

TABLE 4 | Clinical observation of control and hydrogel treated rats for acute oral toxicity study.

Observation	Group A Mean ± SEM	Group B Mean ± SEM
Body weight (g)		
Pre–treatment	205 ± 0.86	207 ± 1.06
Day 1	210 ± 1.52	212 ± 1.30
Day 7	215 ± 1.93	218 ± 2.06
Day 14	225 ± 2.13	226 ± 1.80
Water Intake (mL/animal/day)		
Pre–treatment	30 ± 1.40	28 ± 1.61
Day 1	28 ± 1.35	30 ± 1.35
Day 7	39 ± 1.36	40 ± 1.25
Day 14	41 ± 1.11	39 ± 1.24
Food Intake (g/animal/day)		
Pre–treatment	13 ± 1.65	16 ± 0.96
Day 1	15 ± 1.24	14 ± 0.80
Day 7	17 ± 1.35	16 ± 0.50
Day 14	19 ± 1.53	19 ± 0.38
Signs of illness	–	–
Dermal toxicity	–	–
Dermal irritation		
Ocular toxicity	–	–
Eye Irritation		
Lacrimation	–	–
Salivation	–	–
Convulsions	–	–
Hyperactivity	–	–
Touch response	+	+
Corneal reflex	+	+
Righting reflex	+	+
Gripping strength	+	+
Alertness	+	+
Mortality	–	–

Results are expressed as Mean ± SEM of 5 rats in each group. Group A-Control, Group B -FCX6 hydrogel. Both at a dose of 5g/kg bodyweight. -Sign indicates lack or absence of specified observation. + Sign indicates presence of specified observations. All values have p>0.05, indicating statistically insignificant results.

Acute Oral Toxicity Study

Owing to maximum drug entrapment efficiency and *in-vitro* cumulative drug release, FCX6 hydrogel formulation was chosen for acute oral toxicity study. Group A was used as control and group B was used as treatment group. At the given dose of 5 g /kg body weight, no toxic effects were observed in treatment group B and no mortality was found during 14-days of acute oral toxicity study similar to control group A (Ahmad et al., 2014).

Table 4 demonstrates the impact of oral administration of hydrogel on body weight, food and water utilization, behavior pattern and toxicity associated symptoms in both control group A and treatment group B. Treated group animals displayed normal behavior pattern similar to the control group. Animals were sensitive to sound, light and other stimulations. They had no salivation or vomiting, no lacrimation of eyes or running nose, no dryness of mouth or oedema. Animal feces were in regular form, free of mucus, pus or blood (Mukhopadhyay et al., 2014). The eating behavior of treatment group B was normal and they also gained weight similar to the control group A (Yuan et al., 2014).

Table 5 indicates hematology parameters of control group A and treatment group B. It is obvious from **Table 5** that all hematology parameters of treatment group B are in the standard reference range, similar to the control group A, indicating that the developed hydrogels are likely to be non-toxic (Patel et al., 2008; Gong et al., 2009). Histopathological investigation of different vital organs i.e., heart, liver, stomach, lungs, spleen and kidney of control groups A and treatment group B are indicated in **Figure 10**. Lack of variation in histopathological investigation of vital organs of treatment group B from control group A indicates that administration of the hydrogels had no formulation related toxic effect on group B. The pericardium, myocardium, and endocardium of treatment group B were in normal shape and cardiac muscles were devoid of any

TABLE 5 | Biochemical parameters of control and hydrogel treated rats for acute oral toxicity study.

Biochemical blood analysis			
Hematology parameters	**Unit**	**Group A Mean ± SEM**	**Group B Mean ± SEM**
Hemoglobin	g/dL	14.44 ± 2.52	14.23 ± 2.97
Haematocrit	%	43.43 ± 0.12	43.56 ± 0.23
Red blood cells	$10^6/\mu L$	8.61 ± 0.05	8.59 ± 0.04
Platelets	$10^3/\mu L$	990 ± 2.95	987 ± 2.86
White blood cells	$10^3/\mu L$	4.2 ± 0.14	4.5 ± 0.37
Monocytes	%	2.19 ± 0.02	2.09 ± 0.06
Neutrophils	%	27.0 ± 0.12	26.5 ± 0.08
Lymphocytes	%	75.0 ± 0.15	75.6 ± 0.06
MCV	fL(μm^3)	54.5 ± 0.23	54.6 ± 0.21
MCH	pg	17.8 ± 0.03	17.9 ± 0.01
MCHC	g/dL	33.4 ± 0.21	33.1 ± 0.31
Serum biochemistry parameters			
Triglyceride	mg/dL	72.73 ± 0.16	72.56 ± 0.09
Cholesterol	mg/dL	59.60 ± 0.07	59.67 ± 0.06
Glucose	mg/dL	110.51 ± 0.02	110.61 ± 0.05
Creatinine	mg/dL	0.66 ± 0.01	0.68 ± 0.008
Urea	mg/dL	15.63 ± 0.14	15.68 ± 0.13
Alkaline Phosphatase (ALP)	U/L	119.59 ± 0.09	121.65 ± 0.09
Aspartate Transaminase (AST)	U/L	107.49 ± 0.14	108.74 ± 0.07
Alanine Aminotransferase (ALT)	U/L	30.74 ± 0.08	29.64 ± 0.12
Creatinine Kinase (CK)	U/L	618.66 ± 0.16	621.55 ± 0.16

Results are expressed as Mean ± SEM of 5 rats in each group. Group A-Control, Group B-FCX6 hydrogel. Both at a dose of 5g/kg bodyweight. All values have $p>0.05$, indicating statistically insignificant results.

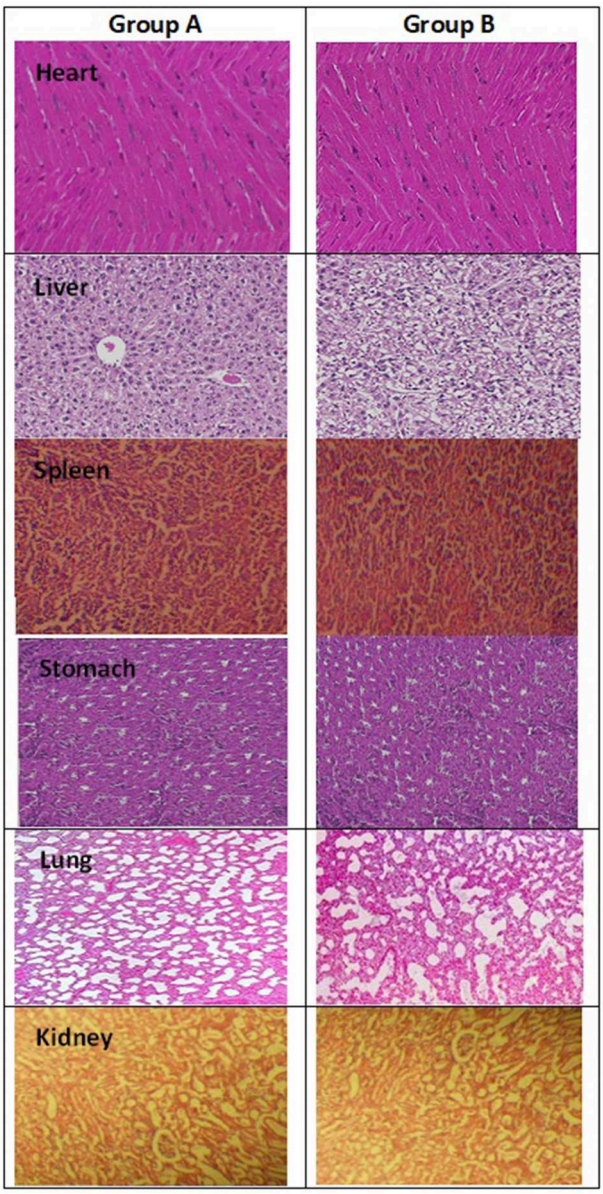

FIGURE 10 | Histopathological observations of tissues from organs of group A and group B including Heart, Liver, Spleen, Stomach, Lung, Kidney used in acute oral toxicity study.

hypertrophy (Gong et al., 2012). The mucosal lining of the stomach was normal with no signs of ulcer. The lungs showed no signs of thickening of blood vessels walls around the bronchus, no alveolar or bronchial damage, representing normal physiology. Size and shape of the kidney were normal. Liver lobules of treatment group B were present with clear dividing lines, similar to control group A. Spleen sinus was absolutely normal in both groups, without any evidence of toxicity (Chen et al., 2006; Pokharkar et al., 2009). Conclusively, no gross difference in histopathological observation was found between the control and treatment groups similar to hematological and biochemical biomarkers, attributed to normal functioning of vital organs. Hence, a dose level up to 5 g/kg body weight of developed hydrogel was well tolerated for the 14th-day study period, indicating developed hydrogels are non-toxic (Malonne et al., 2005).

CONCLUSION

Cross-linked polymeric network of CS and XG with AMPS were prepared by free radical polymerization method. FTIR confirmed successful formation of hydrogel polymeric network. SEM images indicated formation of porous structure. Swelling dynamics was found to be very low when the developed hydrogels were placed into simulated gastric fluid but increased significantly when placed in simulated intestinal fluid. The entrapment efficiency of ACV was found to be dependent upon loading time, drug to polymer ratio and concentration of cross linker used whereas the drug release behavior was influenced by drug to polymer ratio and entrapment efficiency of polymeric network. Considering the biocompatibility, pH dependent swelling and drug release behavior, ACV loaded hydrogel formulation could be considered as a promising platform that can be extended to other antiviral drugs with the aim of improving present drug delivery systems for future need.

DATA AVAILABILITY STATEMENT

The raw data supporting the conclusions of this article will be made available by the authors, without undue reservation, to any qualified researcher.

ETHICS STATEMENT

The animal study was reviewed and approved by Pharmacy Research Ethics Committee (PREC) of The Islamia University of Bahawalpur, Pakistan (23-2016/PREC).

AUTHOR CONTRIBUTIONS

MA: supervised the study. NM: carried out all the overall experiment and drafted the manuscript. MM: participated in the design of the study. RT and KB: contributed toward data analysis. IK and QK: revised the manuscript. All authors have read and approved the final manuscript.

ACKNOWLEDGMENTS

The authors are thankful to Higher Education Commission of Pakistan and Faculty of Pharmacy and Alternative Medicine, The Islamia University, Bahawalpur, Pakistan for providing the funding and support to conduct this research work.

REFERENCES

Agnihotri, S. A., and Aminabhavi, T. M. (2006). Novel interpenetrating network chitosan-poly (ethylene oxide-g-acrylamide) hydrogel microspheres for the controlled release of capecitabine. *Int. J. Pharm.* 324, 103–115. doi: 10.1016/j.ijpharm.2006.05.061

Ahmad, N., Amin, M. C. I. M., Mahali, S. M., Ismail, I., and Chuang, V. T. G. (2014). Biocompatible and mucoadhesive bacterial cellulose-g-poly (acrylic acid) hydrogels for oral protein delivery. *Mol. Pharmaceutics* 11, 4130–4142. doi: 10.1021/mp5003015

Annabi, N., Tamayol, A., Uquillas, J. A., Akbari, M., Bertassoni, L. E., Cha, C., et al. (2014). 25th anniversary article: rational design and applications of hydrogels in regenerative medicine. *Adv. Mater.* 26, 85–124. doi: 10.1002/adma.201303233

Atta, A. M. (2002). Swelling behaviors of polyelectrolyte hydrogels containing sulfonate groups. *Polym. Adv. Technol.* 13, 567–576. doi: 10.1002/pat.226

Azmeera, V., Adhikary, P., and Krishnamoorthi, S. (2012). Synthesis and characterization of graft copolymer of dextran and 2-acrylamido-2-methylpropane sulphonic acid. *Int. J. Carbohydr. Chem.* 2012:209085. doi: 10.1155/2012/209085

Bao, Y., Ma, J., and Li, N. (2011). Synthesis and swelling behaviors of sodium carboxymethyl cellulose-g-poly (AA-co-AM-co-AMPS)/MMT superabsorbent hydrogel. *Carbohydr Polym.* 84, 76–82. doi: 10.1016/j.carbpol.2010.10.061

Benny, I. S., Gunasekar, V., and Ponnusami, V. (2014). Review on application of xanthan gum in drug delivery. *Int. J. Pharm.Tech. Res.* 6, 1322–1326.

Berger, J., Reist, M., Mayer, J. M., Felt, O., Peppas, N. A., and Gurny, R. (2004). Structure and interactions in covalently and ionically crosslinked chitosan hydrogels for biomedical applications. *Eur. J. Pharm. Biopharm.* 57, 19–34. doi: 10.1016/S0939-6411(03)00161-9

Bernkop-Schnürch, A., and Dünnhaupt, S. (2012). Chitosan-based drug delivery systems. *Eur. J. Pharm. Biopharm.* 81, 463–469. doi: 10.1016/j.ejpb.2012.04.007

Bhattarai, N., Gunn, J., and Zhang, M. (2010). Chitosan-based hydrogels for controlled, localized drug delivery. *Adv. Drug Deliv. Rev.* 62, 83–99. doi: 10.1016/j.addr.2009.07.019

Caló, E., and Khutoryanskiy, V. V. (2015). Biomedical applications of hydrogels: a review of patents and commercial products. *Eur. Polym. J.* 65, 252–267. doi: 10.1016/j.eurpolymj.2014.11.024

Chen, Z., Meng, H., Xing, G., Chen, C., Zhao, Y., Jia, G., et al. (2006). Acute toxicological effects of copper nanoparticlzes *in vivo*. *Toxicol. Lett.* 163, 109–120. doi: 10.1016/j.toxlet.2005.10.003

Cheng, W. M., Hu, X. M., Wang, D. M., and Liu, G. H. (2015). Preparation and characteristics of corn straw-Co-AMPS-Co-AA superabsorbent hydrogel. *Polymers* 7, 2431–2445. doi: 10.3390/polym7111522

Dey, P., Maiti, S., and Sa, B. (2013). Gastrointestinal delivery of glipizide from carboxymethyl locust bean gum–Al3+-alginate hydrogel network: *in vitro* and *in vivo* performance. *J. Appl. Polym. Sci.* 128, 2063–2072. doi: 10.1002/app.38272

Elgadir, M. A., Uddin, M. S., Ferdosh, S., Adam, A., Chowdhury, A. J. K., and Sarker, M. Z. I. (2015). Impact of chitosan composites and chitosan nanoparticle composites on various drug delivery systems: a review. *J. Food Drug Anal.* 23, 619–629. doi: 10.1016/j.jfda.2014.10.008

El-Hag Ali, A. (2012). Removal of heavy metals from model wastewater by using carboxymehyl cellulose/2-acrylamido-2-methyl propane sulfonic acid hydrogels. *J. Appl. Polym. Sci.* 123, 763–769. doi: 10.1002/app.34470

Gad, Y. H. (2008). Preparation and characterization of poly (2-acrylamido-2-methylpropane-sulfonic acid)/Chitosan hydrogel using gamma irradiation and its application in wastewater treatment. *Radiat. Phys. Chem.* 77, 1101–1107. doi: 10.1016/j.radphyschem.2008.05.002

Gandhi, A., Jana, S., and Sen, K. K. (2014). *In-vitro* release of acyclovir loaded Eudragit RLPO® nanoparticles for sustained drug delivery. *Int. J. Biol. Macromol.* 67, 478–482. doi: 10.1016/j.ijbiomac.2014.04.019

Gong, C., Wang, C., Wang, Y., Wu, Q., Zhang, D., Luo, F., et al. (2012). Efficient inhibition of colorectal peritoneal carcinomatosis by drug loaded micelles in thermosensitive hydrogel composites. *Nanoscale* 4, 3095–3104. doi: 10.1039/c2nr30278k

Gong, C. Y., Wu, Q. J., Dong, P. W., Shi, S., Fu, S. Z., Guo, G., et al. (2009). Biodegradable *in situ* gel-forming controlled drug delivery system based on thermosensitive PCL–PEG–PCL hydrogel: Part 1—synthesis, characterization, and acute toxicity evaluation. *J. Pharm. Sci.* 98, 4684–4694. doi: 10.1002/jps.21780

Hamidi, M., Azadi, A., and Rafiei, P. (2008). Hydrogel nanoparticles in drug delivery. *Adv. Drug Deliv. Rev.* 60, 1638–1649. doi: 10.1016/j.addr.2008.08.002

Hoffman, A. S. (2012). Hydrogels for biomedical applications. *Adv. Drug Deliv. Rev.* 64, 18–23. doi: 10.1016/j.addr.2012.09.010

Kabiri, K., Omidian, H., Zohuriaan-Mehr, M. J., and Doroudiani, S. (2011). Superabsorbent hydrogel composites and nanocomposites: a review. *Polym. Compos.* 32, 277–289. doi: 10.1002/pc.21046

Kabiri, K., and Zohuriaan-Mehr, M. J. (2004). Porous superabsorbent hydrogel composites: synthesis, morphology and swelling rate. *Macromol Mater. Eng.* 289, 653–661. doi: 10.1002/mame.200400010

Kang, M., Oderinde, O., Liu, S., Huang, Q., Ma, W., Yao, F., et al. (2019). Characterization of Xanthan gum-based hydrogel with Fe3+ ions coordination and its reversible sol-gel conversion. *Carbohydr. Polym.* 203, 139–147. doi: 10.1016/j.carbpol.2018.09.044

Khalid, I., Ahmad, M., Minhas, M. U., and Barkat, K. (2018). Synthesis and evaluation of chondroitin sulfate based hydrogels of loxoprofen with adjustable properties as controlled release carriers. *Carbohydr. Polym.* 181, 1169–1179. doi: 10.1016/j.carbpol.2017.10.092

Kim, Y. H., Babu, V. R., Thangadurai, D. T., Rao, K. S. V., Cha, H. R., Kim, C. D., et al. (2011). Synthesis, characterization, and antibacterial applications of novel copolymeric silver nanocomposite hydrogels. *Bull. Korean Chem. Soc.* 32, 553–558. doi: 10.5012/bkcs.2011.32.2.553

Kubbinga, M., Nguyen, M. A., Staubach, P., Teerenstra, S., and Langguth, P. (2015). The influence of chitosan on the oral bioavailability of acyclovir—a comparative bioavailability study in humans. *Pharm. Res.* 32, 2241–2249. doi: 10.1007/s11095-014-1613-y

Kumar, A., Rao, K. M., and Han, S. S. (2018). Application of xanthan gum as polysaccharide in tissue engineering: a review. *Carbohydr. Polym.* 180, 128–144. doi: 10.1016/j.carbpol.2017.10.009

Li, J., and Mooney, D. J. (2016). Designing hydrogels for controlled drug delivery. *Nat. Rev. Mater.* 1:16071. doi: 10.1038/natrevmats.2016.71

Liu, Y., Zheng, Y., and Wang, A. (2010). Enhanced adsorption of Methylene Blue from aqueous solution by chitosan-g-poly (acrylic acid)/vermiculite hydrogel composites. *J. Environ. Sci.* 22, 486–493. doi: 10.1016/S1001-0742(09)60134-0

Luengo, J., Aránguiz, T., Sepúlveda, J., Hernández, L., and Von Plessing, C. (2002). Preliminary pharmacokinetic study of different preparations of acyclovir with β-cyclodextrin. *J. Pharm. Sci.* 91, 2593–2598. doi: 10.1002/jps.10245

Ma, X., Wei, R., Cheng, J., Cai, J., and Zhou, J. (2011). Synthesis and characterization of pectin/poly (sodium acrylate) hydrogels. *Carbohydr. Polym.* 86, 313–319. doi: 10.1016/j.carbpol.2011.04.089

Mahmood, A., Ahmad, M., Sarfraz, R. M., and Minhas, M. U. (2016). β-CD based hydrogel microparticulate system to improve the solubility of acyclovir: optimization through *in-vitro*, *in-vivo* and toxicological evaluation. *J. Drug Deliv. Sci. Technol.* 36, 75–88. doi: 10.1016/j.jddst.2016.09.005

Malik, N. S., Ahmad, M., and Minhas, M. U. (2017a). Cross-linked β-cyclodextrin and carboxymethyl cellulose hydrogels for controlled drug delivery of acyclovir. *PLoS ONE* 12:e0172727. doi: 10.1371/journal.pone.0172727

Malik, N. S., Ahmad, M., Minhas, M. U., Murtaza, G., and Khalid, Q. (2017b). Polysaccharide hydrogels for controlled release of acyclovir: development, characterization and in vitro evaluation studies. *Polym. Bull.* 74, 4311–4328. doi: 10.1007/s00289-017-1952-z

Malonne, H., Eeckman, F., Fontaine, D., Otto, A., De Vos, L., Moës, A., et al. (2005). Preparation of poly (N-isopropylacrylamide) copolymers and preliminary assessment of their acute and subacute toxicity in mice. *Eur. J. Pharm. Biopharm.* 61, 188–194. doi: 10.1016/j.ejpb.2005.05.007

Mandal, B., and Ray, S. K. (2014). Swelling, diffusion, network parameters and adsorption properties of IPN hydrogel of chitosan and acrylic copolymer. *Mater. Sci. Eng. C.* 44, 132–143. doi: 10.1016/j.msec.2014.08.021

Martinez-Ruvalcaba, A., Sánchez-Díaz, J. C., Becerra, F., Cruz-Barba, L. E., and González-Álvarez, A. (2009). Swelling characterization and drug delivery kinetics of polyacrylamide-co-itaconic acid/chitosan hydrogels. *Express Polym. Lett.* 3, 25–32. doi: 10.3144/expresspolymlett.2009.5

Mukhopadhyay, P., Sarkar, K., Bhattacharya, S., Bhattacharyya, A., Mishra, R., and Kundu, P. P. (2014). pH sensitive N-succinyl chitosan grafted polyacrylamide hydrogel for oral insulin delivery. *Carbohydr. Polym.*112, 627–637. doi: 10.1016/j.carbpol.2014.06.045

Naik, D. R., Patel, A. J., and Raval, J. P. (2014). Release Kinetics of Cellulosic Nano particulate formulation for oral administration of an antiviral drug: effect of process and formulation variables. *J. Pharm. Sci. Emerg. Drugs* 2:1. doi: 10.4172/2380-9477.1000105

Naik, D. R., and Raval, J. P. (2016). Amorphous polymeric binary blend pH-responsive nanoparticles for dissolution enhancement of antiviral drug. *J. Saudi. Chem. Soc.* 20, S168–S177. doi: 10.1016/j.jscs.2012.09.020

Nair, A. B., Attimarad, M., Al-Dhubiab, B. E., Wadhwa, J., Harsha, S., and Ahmed, M. (2014). Enhanced oral bioavailability of acyclovir by inclusion complex using hydroxypropyl-β-cyclodextrin. *Drug Deliv.* 21, 540–547. doi: 10.3109/10717544.2013.853213

Patel, C., Dadhaniya, P., Hingorani, L., and Soni, M. G. (2008). Safety assessment of pomegranate fruit extract: acute and subchronic toxicity studies. *Food Chem. Toxicol.* 46, 2728–2735. doi: 10.1016/j.fct.2008.04.035

Petri, D. F. (2015). Xanthan gum: a versatile biopolymer for biomedical and technological applications. *J. Appl. Polym. Sci.* 132. doi: 10.1002/app.42035

Pokharkar, V., Dhar, S., Bhumkar, D., Mali, V., Bodhankar, S., and Prasad, B. L. V. (2009). Acute and subacute toxicity studies of chitosan reduced gold nanoparticles: a novel carrier for therapeutic agents. *J. Biomed. Nanotechnol.* 5, 233–239. doi: 10.1166/jbn.2009.1027

Qudah, Y. H., Raafat, A. I., and Ali, A. (2013). Removal of some heavy metals from their aqueous solutions using 2-Acrylamido-2-Methyl-1-propane sulfonic acid/polyvinyl alcohol copolymer hydrogels prepared by gamma irradiation. *Arab. J. Nuclear Sci. Appl.* 46, 80–91.

Ray, D., Mohapatra, D. K., Mohapatra, R. K., Mohanta, G. P., and Sahoo, P. K. (2008). Synthesis and colon-specific drug delivery of a poly (acrylic acid-co-acrylamide)/MBA nanosized hydrogel. *J. Biomater. Sci. Polym. Ed.* 19, 1487–1502. doi: 10.1163/156856208786140382

Shalviri, A., Liu, Q., Abdekhodaie, M. J., and Wu, X. Y. (2010). Novel modified starch–xanthan gum hydrogels for controlled drug delivery: synthesis and characterization. *Carbohydr. Polym.* 79, 898–907. doi: 10.1016/j.carbpol.2009.10.016

Siepmann, J., and Peppas, N. A. A. (2012). Modeling of drug release from delivery systems based on hydroxypropyl methylcellulose (HPMC). *Adv. Drug Deliv. Rev.* 64, 163–174. doi: 10.1016/j.addr.2012.09.028

Sohail, M., Ahmad, M., Minhas, M. U., Ali, L., Khalid, I., and Rashid, H. (2015). Controlled delivery of valsartan by cross-linked polymeric matrices: synthesis, *in vitro* and *in vivo* evaluation. *Int. J. Pharm.* 487, 110–119. doi: 10.1016/j.ijpharm.2015.04.013

Stulzer, H. K., Tagliari, M. P., Parize, A. L., Silva, M. A. S., and Laranjeira, M. C. M. (2009). Evaluation of cross-linked chitosan microparticles containing acyclovir obtained by spray-drying. *Mater. Sci. Eng. C* 29, 387–392. doi: 10.1016/j.msec.2008.07.030

Tummala, S., Kumar, M. S., and Prakash, A. (2015). Formulation and characterization of 5-Fluorouracil enteric coated nanoparticles for sustained and localized release in treating colorectal cancer. *Saudi Pharm. J.* 23, 308–314. doi: 10.1016/j.jsps.2014.11.010

Van Vlierberghe, S., Dubruel, P., and Schacht, E. (2011). Biopolymer-based hydrogels as scaffolds for tissue engineering applications:

a review. *Biomacromolecules* 12, 1387–1408. doi: 10.1021/bm200083n

Wang, Q., Zhang, J., and Wang, A. (2009). Preparation and characterization of a novel pH-sensitive chitosan-g-poly (acrylic acid)/attapulgite/sodium alginate composite hydrogel bead for controlled release of diclofenac sodium. *Carbohydr. Polym.* 78, 731–737. doi: 10.1016/j.carbpol.2009.06.010

Yang, H., Wang, W., Zhang, J., and Wang, A. (2013). Preparation, characterization, and drug-release behaviors of a pH-sensitive composite hydrogel bead based on guar gum, attapulgite, and sodium alginate. *Int. J. Polym. Mater. Polym. Biomater.* 62, 369–376. doi: 10.1080/00914037.2012.706839

Yuan, G., Dai, S., Yin, Z., Lu, H., Jia, R., Xu, J., et al. (2014). Toxicological assessment of combined lead and cadmium: acute and sub-chronic toxicity study in rats. *Food Chem. Toxicol.* 65, 260–268. doi: 10.1016/j.fct.2013.12.041

Zhang, Y., Gao, Y., Wen, X., and Ma, H. (2014). Current prodrug strategies for improving oral absorption of nucleoside analogues. *Asian J. Pharm. Sci.* 2, 65–74. doi: 10.1016/j.ajps.2013.12.006

Conflict of Interest: The authors declare that the research was conducted in the absence of any commercial or financial relationships that could be construed as a potential conflict of interest.

frontiers in Chemistry

REVIEW
published: 12 February 2020
doi: 10.3389/fchem.2020.00053

Advancements and Frontiers in the High Performance of Natural Hydrogels for Cartilage Tissue Engineering

Wuren Bao[1†], Menglu Li[2†], Yanyu Yang[2,3†], Yi Wan[4], Xing Wang[2,5], Na Bi[4*] and Chunlin Li[4*]*

[1] School of Nursing, Inner Mongolia University for Nationalities, Tongliao, China, [2] Beijing National Laboratory for Molecular Sciences, State Key Laboratory of Polymer Physics & Chemistry, Institute of Chemistry, Chinese Academy of Sciences, Beijing, China, [3] College of Science and Engineering, Zhengzhou University, Zhengzhou, China, [4] Orthopaedic Department, The 8th Medical Center of Chinese PLA General Hospital, Beijing, China, [5] University of Chinese Academy of Sciences, Beijing, China

OPEN ACCESS

Edited by:
Yi Cao,
Nanjing University, China

Reviewed by:
Jun Fu,
Sun Yat-sen University, China
Xiaoying Lin,
University of Maryland, College Park, United States

***Correspondence:**
Xing Wang
wangxing@iccas.ac.cn
Na Bi
ykxbn@163.com
Chunlin Li
lee3163003@163.com

[†] These authors have contributed equally to this work

Specialty section:
This article was submitted to Polymer Chemistry, a section of the journal Frontiers in Chemistry

Received: *09 November 2019*
Accepted: *17 January 2020*
Published: *12 February 2020*

Citation:
Bao W, Li M, Yang Y, Wan Y, Wang X, Bi N and Li C (2020) Advancements and Frontiers in the High Performance of Natural Hydrogels for Cartilage Tissue Engineering. Front. Chem. 8:53. doi: 10.3389/fchem.2020.00053

Cartilage injury originating from trauma or osteoarthritis is a common joint disease that can bring about an increasing social and economic burden in modern society. On account of its avascular, neural, and lymphatic characteristics, the poor migration ability of chondrocytes, and a low number of progenitor cells, the self-healing ability of cartilage defects has been significantly limited. Natural hydrogels, occurring abundantly with characteristics such as high water absorption, biodegradation, adjustable porosity, and biocompatibility like that of the natural extracellular matrix (ECM), have been developed into one of the most suitable scaffold biomaterials for the regeneration of cartilage in material science and tissue engineering. Notably, natural hydrogels derived from sources such as animal or human cadaver tissues possess the bionic mechanical behaviors of physiological cartilage that are required for usage as articular cartilage substitutes, by which the enhanced chondrogenic phenotype ability may be achieved by facilely embedding living cells, controlling degradation profiles, and releasing stimulatory growth factors. Hence, we summarize an overview of strategies and developments of the various kinds and functions of natural hydrogels for cartilage tissue engineering in this review. The main concepts and recent essential research found that great challenges like vascularity, clinically relevant size, and mechanical performances were still difficult to overcome because the current limitations of technologies need to be severely addressed in practical settings, particularly in unpredictable preclinical trials and during future forays into cartilage regeneration using natural hydrogel scaffolds with high mechanical properties. Therefore, the grand aim of this current review is to underpin the importance of preparation, modification, and application for the high performance of natural hydrogels for cartilage tissue engineering, which has been achieved by presenting a promising avenue in various fields and postulating real-world respective potentials.

Keywords: natural hydrogel, mechanical property, hydrogel scaffolds, cartilage tissue engineering, regenerative medicine

INTRODUCTION

Natural polymeric materials are widely used in engineering and regenerating tissues for human health (e.g., skin, cartilage, bone, tracheal splints, and wound-healing vascular grafts) because of their unique advantages, namely biocompatiblity, biodegradation, favorable porsity, and achievable mechanics (Seal et al., 2001; Shin et al., 2003; Shelke et al., 2014; Sahana and Rekha, 2018; Zhang et al., 2019). Inspired by biological macromolecules within the extracellular matrix, natural polymers or biopolymers are generally obtained from various renewable resources, such as animals, plants, algae, and microorganisms found throughout the world (**Figure 1**), which can elude chronic inflammation toxicity or immunological reactions after suitable synthetic modification methodologies are applied. Thus, it is deemed that natural polymers are essential for designing bioactive compounds, for drug delivery systems for disease treatment, and for the construction of smart therapeutic systems for bioengineered functional tissues. In this case, the emergence of natural hydrogels (e.g., amino acids, proteins, polysaccharides, and glycosaminoglycans) has brought about significant clinical application values byimplant fabrication methods (Mano et al., 2007).

Regeneration of cartilage defects has historically been an enormous challenge to both orthopedic surgeons and patients,—it is reported that 60% of knee arthroscopy patients have cartilage injuries, wherein 15% of people (over 60 years old) have serious clinical features of cartilage injury (Hjelle et al., 2002; Cancedda et al., 2003; Ren et al., 2015; Walker and Madihally, 2015). Unlike most other tissues, cartilage is essentially avascular and low in cell content. Therefore, the lack of vascularization, innervation, lymphoid networks, and proper progenitor cells can greatly limit the ability of damaged cartilage to heal itself (Huey et al., 2012; Liao et al., 2014; Yuan et al., 2014; Vilela et al., 2015). Current strategies on cartilage tissue regeneration have exhibited great effects in clinical practice, including traditional microfracture (bone marrow stimulation) (Dorotka et al., 2005; Mithoefer et al., 2009), autologous chondrocyte implantation (Ruano-Ravina and Jato Diaz, 2006; Niemeyer et al., 2008; Selmi et al., 2008; Harris et al., 2010; Peterson et al., 2010), autologous osteochondral transplantation, and allogeneic osteochondral transplantation (Glenn et al., 2006; Benazzo et al., 2008; Haene et al., 2012), etc. However, there are still obvious limitations and deficiencies that include tedious *ex vivo* cell manipulation, potential tumorigenesis, therapeutic translation risk and regulatory approval. So, it is of great clinical significance

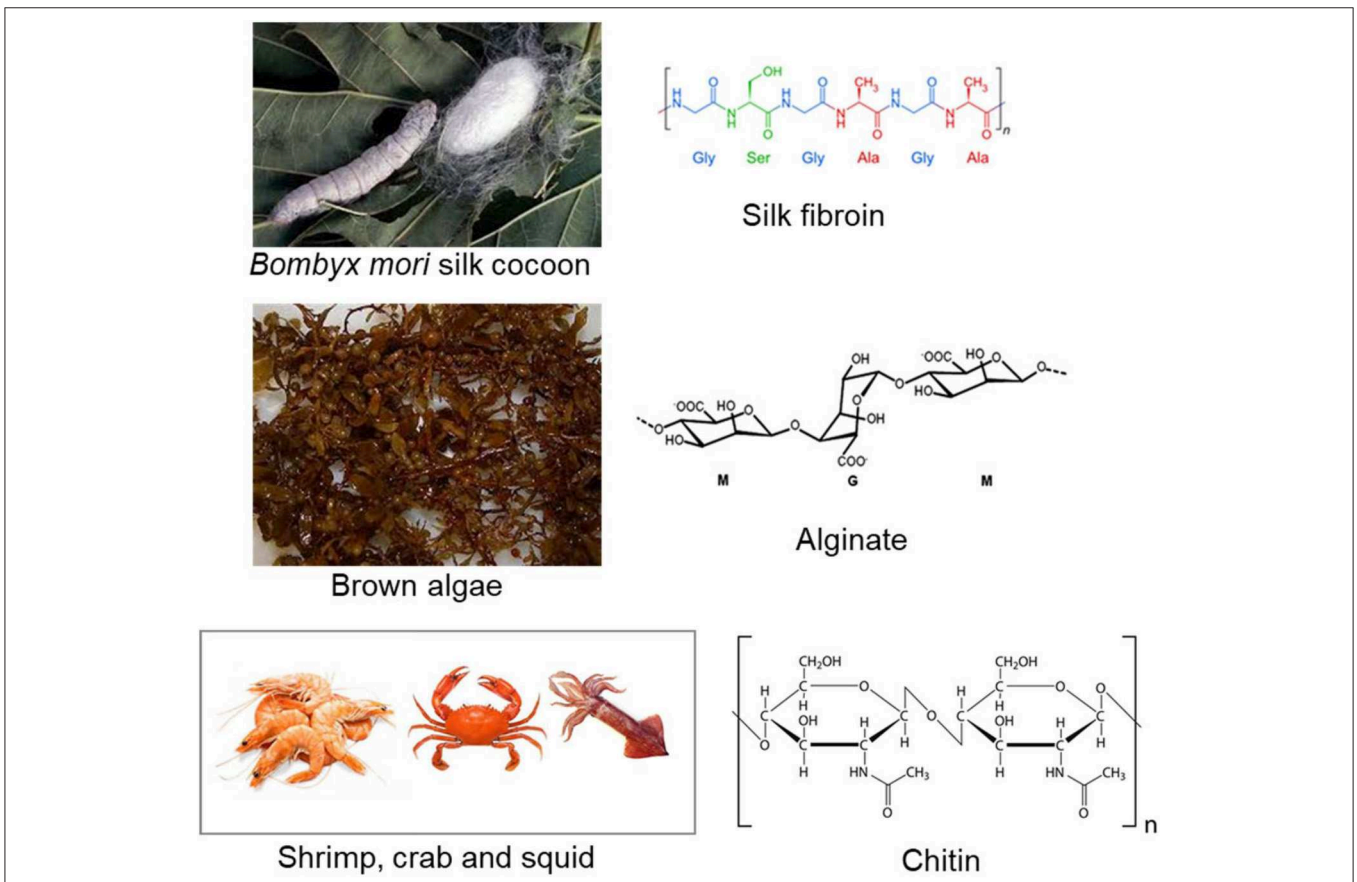

FIGURE 1 | Some natural biopolymers, derived from renewable resources, and their respective chemical structures: silk fibroin, alginate, and chitin. Reproduced from Mano et al. (2007) with permission from Copyright 2007 Royal Society.

to develop and achieve a method of complete and permanent repair of damaged cartilage.

Fortunately, tissue engineering, consisting of scaffolds, cells, and favorable growth factors, has evolved into a most promising therapeutic strategy for cartilage tissue reconstruction (Khan and Malik, 2012; Kim et al., 2012; Grottkau and Lin, 2013; Sahni et al., 2015; Wang et al., 2016). To achieve the perfectible regeneration of damaged cartilage, it is essential to offer the biodegradable scaffolds, simulate local characteristics of specific tissues, transport the tissue cells and growth factors, and provide supports to newly formed tissues (Malda et al., 2013). Ideally, cartilage tissue-engineered scaffolds should be porous, nontoxic, biocompatible, and biodegradable, and they should enhance cell differentiation and tissue generation, which need to possess high performance, matched rate between the degradation and new-tissue formation, diffused nutrients and metabolites behaviors, adhesion to the surrounding native tissue fusion, and fulfillment of the damaged sites (Hollister, 2005; Balakrishnan and Banerjee, 2011). For the construction of an ideal tissue engineering program, it is important to provide the functional biomaterials that basically mimic the natural ECM of cartilage components. Traditional approaches generally include direct implantation into tissue defects, precise incorporation of bioactive growth factor into the targeted tissues, cell-free scaffold biomaterials, and mimicking natural ECM with cell-laden architectural scaffolds, among which three-dimensional (3D) porous hydrogel scaffolds are most frequently used to promote cell organization into the extracellular matrix during reconstructive periods (Hubbell, 1995; Griffith and Naughton, 2002; Khademhosseini and Langer, 2006; Place et al., 2009; Berthiaume et al., 2011; O'brien, 2011).

Hydrogels, composed of natural or synthetic hydrophilic polymer strands connected with each other at crosslinking points, possess a unique 3D crosslinked polymeric network encompassing a wide range of chemical compositions and bulk physical properties. The hydrophilic nature of constituting polymeric chains allows the hydrogels to absorb amounts of water (more than 1,000-fold compared to their dry weight) to be applied in a variety of technological biomaterials for drug delivery and tissue regeneration, among which the *in situ* hydrogels possess the advantage of simple drug formulation and the ability to deliver both hydrophilic and hydrophobic drugs. Based on the cross-linking properties, hydrogels are classified into "chemical" and "physical" network gels. Chemically crosslinked hydrogels are generally held together by molecular bonds of synthetic polymers and possess stable, homogeneous, and adjustable structures. While physically crosslinked hydrogels are generally aggregated by secondary interactions such as molecular entangling, hydrogen bonds, ionic bonds, or hydrophobic interactions force them to form a reversible structure and self-healing properties, mainly including biodegradable natural polymers, which has several advantages over chemically cross-linked hydrogels, including solvent casting, easy fabrication, less toxic, reshaping, postprocess bulk modification, biodegradation, and so on (Eslahi et al., 2016; Li et al., 2019).

As a typical biological scaffold, hydrogels possess unique architectures of highly hydrated 3D and versatile capacities of high water content, suitable pore size and porosity, substance exchange capacity, good biodegradability performance, and extraordinary mechanical properties (Peppas et al., 2006), and can provide a suitable microenvironment and efficient biocompatibility and high strength for holding considerable promise in cartilage differentiation and cartilage-specific ECM regeneration, thus resulting in their wide usages for tissue engineering and cell therapy in various bio-applications. It is mentioned that the network pore of hydrogels played important roles in the physicochemical and mechanical signals and nutritive delivery for the cell growth. For example, pore size and high porosity were beneficial to the cell infiltration and ECM formation, while the interconnected and open pores could promote cell growth, proliferation, and migration, as well as the tissue vascularization process (Furth et al., 2007; Ma, 2008; Xiao et al., 2015). The micro-porosity was another important factor to facilitate the cell adhesion and spreading to improve the biomechanics between the hydrogel scaffolds and tissues (Karageorgiou and Kaplan, 2005; Loh and Choong, 2013). In addition, the composition, structure, biocompatibility, safety, stability, and mechanical properties of hydrogel scaffolds can also be considered to meet the needs of the cell morphology, proliferation, and differentiation in cartilage tissue regeneration for clinical scenarios (Wang et al., 2008, 2018; Spiller et al., 2011; Amini and Nair, 2012; Ji et al., 2012). As typical representatives, natural hydrogels with high performance are ideal biomaterial scaffolds for cartilage repair by their preferable reconstructions of cell growth, proliferation, and differentiation and new tissue formation.

This review will classify the preparation materials of hydrogels and summarize their typical kinds and wide applications of several typical natural hydrogels (alginate, chitosan, gelatin, collagen, hyaluronan, and natural hybrids) with good biocompatibility, improved stability, and high performance for facilitating cell delivery in the cartilage tissue engineering and regeneration medicine fields. We also summarize the different advantages, disadvantages, modification methods, and the future prospects of natural hydrogels for cartilage tissue engineering. Finally, we provide some suggestions and prospects on developing natural hydrogels via their tailored physicochemical and mechanical properties for effective cartilage tissue engineering. Understanding medical needs and concurrently lessening the difficulty of hydrogel construction should therefore be the goal for future research in this field.

CLASSIFICATION OF HYDROGELS

Hydrogels can be briefly classified into synthetic and natural polymers for cartilage tissue regeneration in biomedical applications.

Synthetic Polymers

Synthetic polymers have excellent characteristics in terms of molecular weight, degradation, and mechanical properties, with the advantage of having tailored property profiles for specific applications, exhibiting wide usage due to their controllability, reproducibility, and good mechanical properties. Representative synthetic polymers for tissue regeneration include polylactide

(PLA), poly-lactide-co-glycolide (PLGA), polyglycolide (PGA), poly-(D,L-lactic acid) (PDLLA), polycaprolactone (PCL), poly-ethylene-glycol (PEG), poly(vinyl alcohol) (PVA), poly (N-isopropylacrylamide) (PNIPAM), and polyacrylamide (PAM). These polymers can be self-reinforced to enhance their mechanical strength. However, many of these polymers present an immune response or toxicity, particularly when combined with certain polymers and are not capable of being incorporated with host tissues. They exhibit lower biological activity because of their potential for a local pH increase by acidic degradation products, inflammatory response, poor degradation, and inflammation associated with high molecular weight polymers (Katti et al., 2002; Gunja and Athanasiou, 2006; Pina and Ferreira, 2012; Pereira et al., 2014).

Natural Polymers

Natural polymers have explicit biomedical applications in tissue regeneration due to their biocompatibility, biodegradability, and macromolecular similarity to the original ECMs, which can provide a magnificent bioactivity and natural adhesive surface for cells required for bioactivity. Natural polymers used for hydrogel preparation include protein-based materials (such as gelatin, collagen, fibrin, and silk fibroin) and polysaccharide-based materials (such as hyaluronic acid, chondroitin sulfate, alginate, chitosan, and so on). In addition, natural hydrogels cannot cause immune and toxic reactions, and the degradation products are non-toxic and non-immunogenic, leading to the excretion of final metabolites outside the body safely; but, their poor stability, rapid degradation, and relatively low mechanical strength greatly limits their applications (Malafaya et al., 2007; Mano et al., 2007; Nair and Laurencin, 2007).

Although hybridization of synthetic and natural materials is an efficient and easygoing approach to integration, the advantages of constructing the hydrogels for the cartilage tissue regeneration, the undegradable components, and the unpredictable metabolites have still brought about significant limitation in actual biomedicine. Therefore, hybridization of other natural polymers or advanced biomodification of natural hydrogels to acquire better mechanics are the most promising strategies for constructing ideal biomaterial scaffolds to satisfy the requirements of cartilage repair by the designable and preferable reconstructions of cell morphology, growth, proliferation, differentiation, and new tissue formation.

NATURAL HYDROGELS FOR CARTILAGE TISSUE ENGINEERING

Alginate

Alginate (ALG), as a natural polysaccharide extracted from brown algae, consists of 1,4-chain D-mannitol acid and L-gulu acid residues and has been widely applied to encapsulate the cells due to its good biocompatibility, high hydration viscoelasticity, and physically crosslinked ability (Pelletier et al., 2001; Hashimoto et al., 2004; Cho et al., 2005, 2009; Tritz et al., 2010; Zeng et al., 2014). Compared to other natural polymers, alginate is favorable for cell function and cell-immobilized microspheres or 3D porous hydrogel scaffolds (El Khoury et al., 2014; Zehnder et al., 2015). Alginate hydrogel can support the growth and proliferation of enveloped chondrocytes and maintain their chondrocyte morphology. For example, Swieszkowski et al. found that about 80% of human chondrocytes were retained in the 3D-deposited hydrogel filaments at 14 days after culture *in vitro*. Meanwhile, the embedded chondrocytes remained round in the whole culture processes (Kosik-Koziol et al., 2017). In addition, alginate hydrogels are also used to transport mesenchymal stem cells (MSCs) for cartilage regeneration. Wang et al. prepared a multiphasic graft by linkage of a cartilaginous alginate hydrogel and a sintered poly(lactic-co-glycolic acid) microsphere scaffold using a fibrotic cartilaginous ECM. Within this condition, these culturing chondrocytes could achieve the favorable gradient transition and integration from the cartilage layers to the subchondral bone layers, exhibiting the excellent tissue repair efficacy using a defected rabbit knee model (Fonseca et al., 2014).

However, there are still some limitations in tissue engineering applications. Firstly, the physically crosslinked alginate hydrogel possesses poor stability and gradually loses its mechanical strength within a short period of time, even in the physiological environments, which always require the subsequent crosslinking processes to strengthen mechanical property (Vallee et al., 2009). Secondly, on account of low cell adhesion and cell interaction ability of alginate in mammals, cell adhesion peptide is often introduced to better support cell function (Alsberg et al., 2001). In order to overcome these defects, other bioactive substances are usually added into alginate hydrogels. Sodium citrate was added into ALG as the dispersant of hydroxyapatite (HAP). Eames et al. found that the ALG/HAP complex could trigger the chondrocytes to secrete a calcified matrix, which was testified by the favorable survival and proliferation of chondrocytes in the ALG/HAP structure and high expression level of calcified cartilage markers (You et al., 2019). Embedding bone marrow-derived mesenchymal stem cells (bMSCs) in RGD (arginine/glycine/aspartic acid)-functionalized, γ-ray alginate hydrogels could enhance the osteochondral regeneration and promote the development of a more mechanically functional repair tissue (Critchley et al., 2019). However, the poor mechanical properties of ALG-based hydrogels limited their biomedical potential in osteochondral tissue regeneration. Lu et al. aimed to prepare a high-performance biohydrogel through introducing the bacterial cellulose (BC) into a double-network hydrogel system (**Figure 2**). The compressive modulus was matched with the natural articular cartilage, while their swelling degrees obviously declined. Then, a bilayer hydrogel scaffold was fabricated via chemical and physical crosslinking methods for achieving osteochondral regeneration on the basis of the bionics principle. After the addition of another two hydroxyapatite particles with varied sizes, the results of osteochondral defect model of rabbits verified the good osteochondral repair effects of these bilayer structural scaffolds (Zhu X. B. et al., 2018).

In addition to improving the mechanical properties and cell adhesion of alginate hydrogels, alginate hydrogels were prepared as carriers for encapsulating a variety of low molecular weight drugs. Partially oxidized alginate hydrogel could realize the drug control and local administration (Bouhadir et al., 2001;

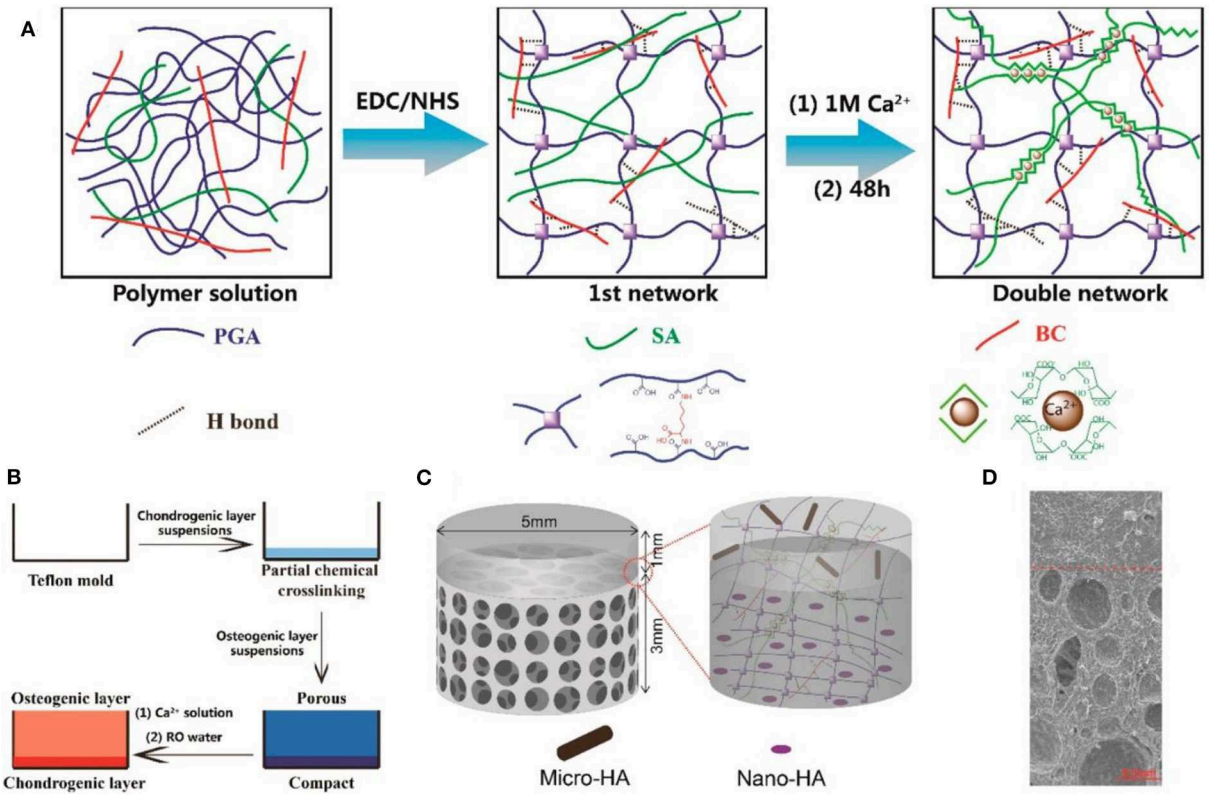

FIGURE 2 | Schematic illustration of **(A)** preparation process of BC-DN hydrogels, bilayered hydrogel scaffolds, and the structure of bilayer hydrogel. **(B)** Schematic depiction of the preparation of bilayer hydrogel scaffolds. **(C)** Schematic illustration of the structure of the bilayer hydrogel. **(D)** SEM image of bilayer hydrogel scaffolds. Reproduced from Zhu X. B. et al. (2018) with permission from Copyright 2018 American Chemical Society.

Colinet et al., 2009). Using the alginate-polymethacrylate hybrid hydrogels as the framework, the scaffold materials were prepared by crosslinking into a single porous structure on the basis of the electrostatic and covalent interactions, which overcame the mechanical property limitations of the pure alginate materials. Meanwhile, the alginate portion provided an appropriate microenvironment mimicking extracellular matrix, while the methacrylate portion could also improve the mechanical properties of resulting mixed hydrogels (Stagnaro et al., 2018).

Chitosan

Chitosan is a kind of mucopolysaccharide widely existed in nature, which is important component of connective tissue with complexation, bacteriostasis, adsorption, and antioxidant effects (Molinaro et al., 2002; Jayakumar et al., 2005). Recent reports demonstrated that chitosan can be gelated in an acidic pH or a non-solvent condition (Ribeiro et al., 2017; Xu et al., 2017; Chen Y. R. et al., 2019), and further be prepared for chitosan-based hydrogel scaffolds. Chitosan has good biocompatibility and biodegradability; therefore, it is a kind of tissue-engineering material with wide application prospects and can be considered as a potential material for cartilage repair in regenerative medicine fields. A previous study demonstrated that since chitosan is extracted from shrimp shells, participants selected for this study were allergic to at least one type of shellfish or shrimp in order to test to see if they were allergic to chitosan. The results showed no adverse reactions among participants, providing the first evidence of biosafety of chitosan in allergic patients (Waibel et al., 2011). Although a simple mixture of chitosan with other natural polymers could generate a series of functional hydrogels via the electrostatic interactions (Ma et al., 2009), the physically crosslinked networks presented the terrible dissolution behaviors and weak mechanics that greatly limited their wide applications for artificial cartilage regeneration (Yang Y. Y. et al., 2018).

To overcome the flaw of water insolubility, N-succinyl chitosan-dialdehyde starch mixture hydrogel was prepared with good solubility to repair cartilage defects (Kamoun, 2016). In addition, the sensitization and mechanism of chitosan may also need improvement in its clinical transformation. Yu et al. found that when the thermo-responsive chitosan-based hydrogels are introduced into the 3D-printed PCL scaffolds to form the composite scaffolds, the composite scaffold has good cell- and drug-carrying capacity and good mechanical strength (Dong et al., 2017). Compared with pure chitosan hydrogels, the compressive modulus of the hybrid scaffold increased significantly after the introduction of PCL scaffolds (**Figure 3A**). These hybrid scaffolds are beneficial to cell survival. After culturing in growth medium for 72 h, BMMSCs survived in both PCL and hybrid scaffolds with a lot of dead cells, but their distribution patterns were different. Importantly, it was

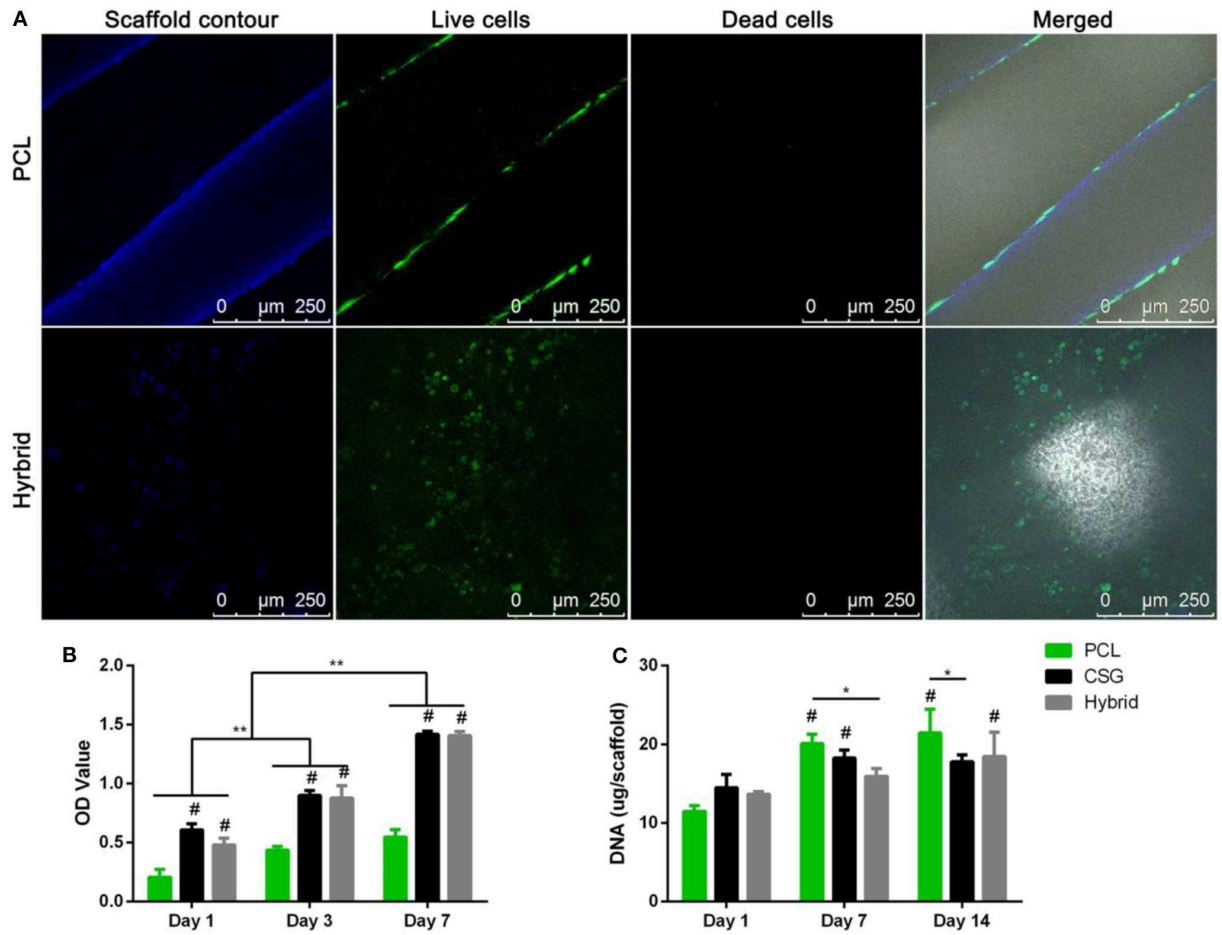

FIGURE 3 | (A) Representative images of BMMSCs attachment, viability, and distribution in composite scaffolds. Blue fluorescence represents the contours of scaffolds; merged images include bright field views to show the scaffold pores. CLSM images of Live/Dead staining demonstrated cell viability of after 72 h of culture in growth medium. (Red represents the dead cells; green represents the live cells; Scale bar = 250 μm). CCK-8 assay showed that the number of cells in the three groups increased over time **(B)**. DNA content in the various scaffolds during osteogenic culture indicating slow proliferation while MSCs differentiating into osteoblasts. Results are expressed as mean ± SD ($n = 3$, $^{*,\#}P < 0.05$, $^{**,\#\#}P < 0.01$; $^{\#}$compared to PCL group in **(B)**, and compared to day 1 in **(C)**). Reproduced from Dong et al. (2017) with permission from Copyright 2017 Springer Nature.

found that those encapsulated cells in hybrid scaffolds could not only distribute evenly in the pores but also spread on the surfaces of PCL scaffolds. A CCK assay provided consistent results indicating that these cell-scaffold composites *in vitro* culture exhibited the active proliferation for as long as 7 days (**Figure 3B**). Compared to the PCL scaffold, the cell number was greater in hydrogel and hydrogel-filled scaffolds at every time point, which indicated the excellent biocompatibility of hybrid hydrogel scaffolds compared to the highly hydrated environment of the single hydrophobic PCL scaffold. Therefore, these hybrid hydrogel scaffolds that have the satisfactory mechanical strength exhibited the favorable biomimetic micro-environments to facilitate the cell retention, growth, and distribution (**Figure 3C**).

Lee et al. prepared a smart biofunctional hydrogel for cartilage regeneration by photopolymerization of chitosan (MeGC) solution with Col II solution. TGF-β1 was conjugated into MeGC via SMCC moiety. The hydrogel system had no effect on the viability of loaded synovial mesenchymal stem cells. Compared with the pure chitosan hydrogels, the aggregation and deposition of mesenchymal stem cells were enhanced (Kim et al., 2015). Allogeneic chondrocytes were transplanted with chitosan-demineralized bone matrix composite hydrogel scaffold for cartilage injury therapy in rabbits. At 24 weeks after surgery, the cartilage defect was successfully filled and no obvious inflammatory reaction was observed (Man et al., 2016).

Gelatin

Gelatin is composed of a series of arginine-glycine-aspartic acid sequences that can benefit to improve the cell adhesion and matrix metalloproteinases capacities. Thermal reversible changes occurred in gelatin solution at 30–40°C, and crosslinked hydrogels can be physically formed by the self-gelation effects or chemically generated by the chemical reactions (Sakai et al., 2009; Liu et al., 2016; Zhu et al., 2019). Up to now, the gelatin-based composites have been utilized as suitable scaffolds for tissue

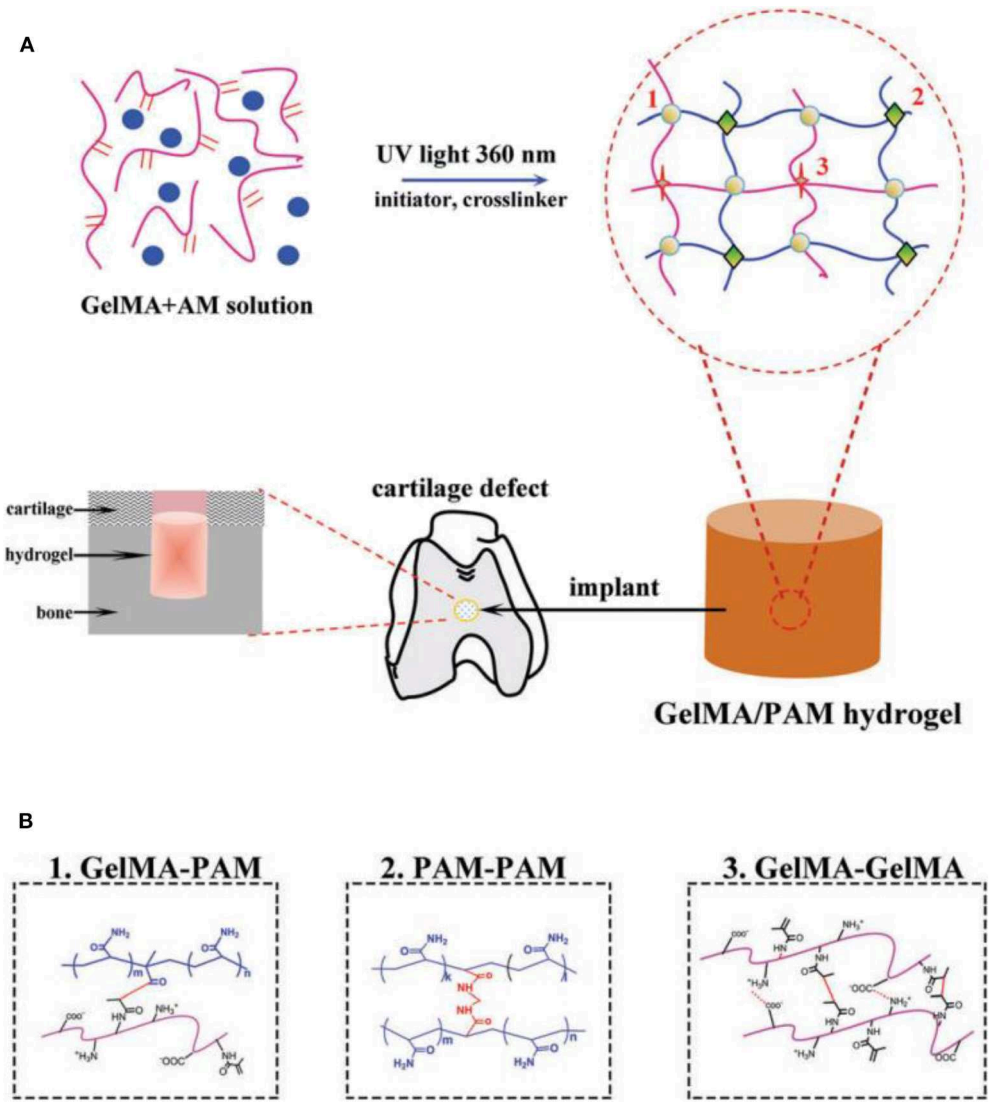

FIGURE 4 | (A) Schematic illustration for fabricating natural-synthetic GelMA-PAM biohybrid hydrogel via the photo-initiating polymerization. **(B)** Molecular crosslinking structures: covalent crosslinking between GelMA-PAM, covalent crosslinking between PAM-PAM, and covalent/physical crosslinking between GelMA-GelMA. Reproduced from Han et al. (2017) with permission from Copyright 2017 Royal Society of Chemistry.

engineering and molecule carriers in biomaterial fields. Gelatin-based hydrogels have good biodegradability, biocompatibility, and cell/tissue affinity, but poor mechanical strength and low thermal stability greatly limited their applications in biomedical cartilage repair. Fortunately, a star product of gelatin methacrylamide (GelMA) was prepared by modifying gelatin with methacrylate anhydride that exhibited the significant roles in the cartilage tissue engineering applications. Under the action of a photo-initiator, acrylamide (AM) was copolymerized with gel under ultraviolet radiation to prepare gel-based natural synthetic polymer biohybrid hydrogel. These hybrid hydrogels had better mechanical properties, degradation rate, cell adhesion, and biocompatibility (**Figure 4**; Han et al., 2017). A new cell-laden cartilage structure was prepared by a tabletop stereolithography-based 3D bioprinter, which was composed of methacrylate, polyethylene glycol diacrylate biocompatible photo-initiator, and transformed growth factor-1 embedded nanospheres. The cell vitality and proliferation rate can be tailored by regulating the component content for the promising cartilage regeneration (Zhu W. et al., 2018). Furthermore, the chemical modification of gelatin combined with 3D printing technology to prepare biological scaffolds provided a new idea for the treatment of osteoarthritis. Some researchers also had designed biological scaffolds for the transport of extracellular matrix extraneous bodies like ECM/GelMA/exosome scaffolds (Chen P. F. et al., 2019).

Although GelMA hydrogels exhibited obvious advantages in tissue engineering, they were still lacking in high mechanical

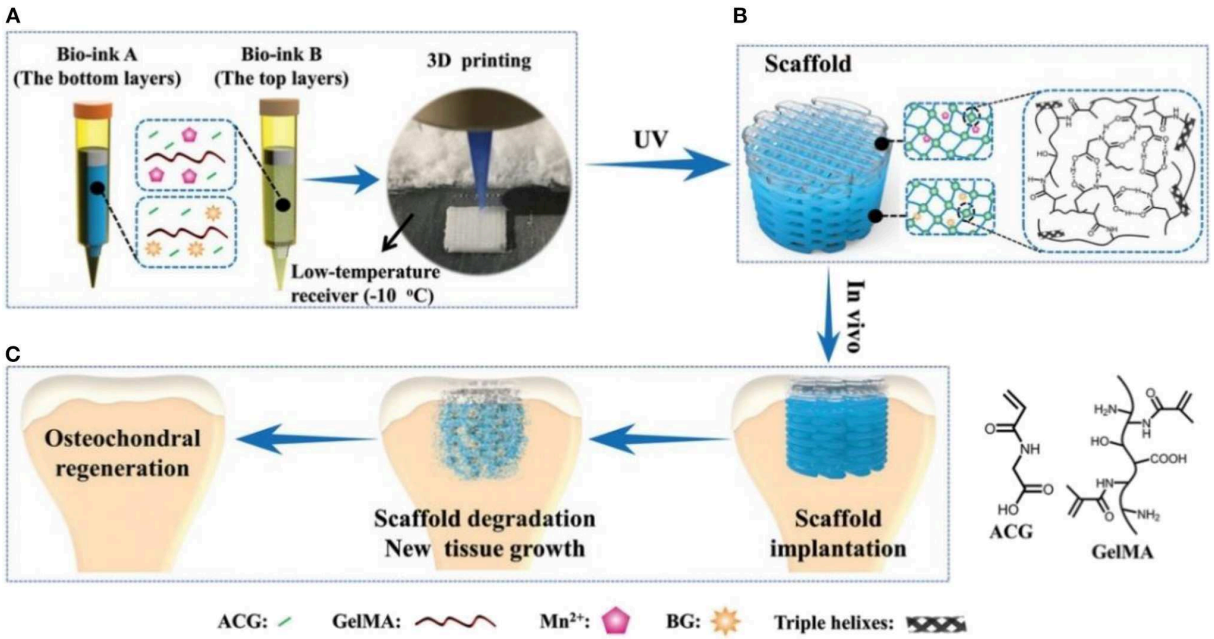

FIGURE 5 | Schematic illustration of the biohybrid gradient scaffolds for osteochondral repair by 3D printing technology. **(A)** The compositions of bio-ink A and bio-ink B and 3D-printing method of hybrid gradient scaffolds assisted with a low-temperature receiver. **(B)** Formation of hydrogel scaffold after UV light-initiated polymerization with hydrogen bonding interactions. **(C)** Osteochondral repair treated with the biohybrid gradient PACG-GelMA scaffold, with Mn^{2+} and BG being loaded on the top and bottom layers, respectively. Reproduced from Gao et al. (2019) with permission from Copyright 2019 Wiley.

properties for achieving the efficient cartilage regeneration only by the pure GelMA hydrogels. Therefore, Liu et al. constructed a biodegradable hydrogel via the photo-initiated polymerization of poly(N-acryloyl 2-glycine) (PACG) and GelMA (PACG-GelMA) (**Figure 5**), which possessed high mechanical strengths, with a tensile strength of 1.1 MPa, outstanding compressive strength of 12.4 MPa, large Young's modulus of 0.32 MPa, and high-compression modulus of 0.837 MPa. By tailoring the ACG/GelMA ratios, the temporary PACG network was stabilized by chemical crosslinking effects, thus exhibiting the adjusting biodegradability. Furthermore, they fabricated a biocompatible composite scaffold with PACG-GelMA hydrogel-bioactive glass and PACG-GelMA hydrogel-Mn^{2+} layers for osteochondral repair using 3D printing techniques. *In vitro* and *in vivo* biological results demonstrate that these biocompatible hybrid gradient hydrogel scaffolds could facilitate cell adhesion, spreading, osteogenic-oriented differentiation, gene expression, cartilage regeneration, and subchondral bone formation in a rat model (Gao et al., 2019).

Chemically modified gelatin-based hydrogel is biodegradable, and its properties are adjustable and easily micro-processed. However, further improvement is needed in forming cartilage and simulating the function of cartilage tissue (Yang et al., 2017). First, the activation of chondrocytes in the gel should be enhanced to obtain more connective tissue ECM. Second, their mechanics should be further optimized and improved. Third, it is necessary to facilely adjust the rheological properties of modified gelatin hydrogel prepolymer solutions. To achieve these goals, adding other functional components as needed will be an efficient method to enhance the properties of gelation-based hydrogels. Lu et al. developed a novel mussel-inspired strategy to improve the mechanics of GelMA hydrogels by incorporating dopamine methacrylate (ODMA) oligomers into the GelMA chains. Intercalation of ODMA made the GelMA hydrogels resilient and stable at body temperature by reducing the entangled GelMA chain density and introducing other sacrificial physical crosslinking interactions. *In vitro* and *in vivo* experiments verified that this modified ODMA-GelMA hydrogel, as a typical growth factor-free scaffold, not only provided a favorable microenvironment to promote the mesenchymal stem cell attachment and spreading, but also enhanced the cartilage regeneration after encapsulation of chondroitin sulfate or TGF-β3, which would be served as an ideal candidate hydrogel scaffold for cartilage or other tissues repair in biomedical applications (Gan et al., 2019).

Collagen

Collagen, as an important component of extracellular matrix, is a natural biological material, widely found in skin, bone, cartilage, blood vessels, teeth, and tendons, which had been widely used in biological and medical fields. Collagen hydrogels could be prepared by the UV irradiation photopolymerization, dehydrogenation heat treatment or other crosslinking reactions with aldehydes, carbimines, genipin, isocyanates, transglutaminase, etc. (Zhao et al., 2013). Collagen type I hydrogels could support mesenchymal stem cell adhesion, growth, spreading, and cartilage differentiation for the construction of engineered osteochondral structures *in vitro*

(Wang et al., 2019). Giuffrida et al. had assessed a new kind of 3D scaffold that consisted of type I collagen and human adipose-derived mesenchymal stem cells, which exhibited the favorable chondrogenic potentials. Regardless of the presence of chondrogenic inducing factors, the scaffold had a higher potential for cartilage regeneration (Calabrese et al., 2017). *In vivo* and *in vitro* experiments showed that type II collagen hydrogels containing chondrocytes supported the proliferation and chondrogenesis of mesenchymal stem cells (Pulkkinen et al., 2010; Ren et al., 2016). It was found that bovine mesenchymal stem cells were cultured in monolayer, alginate, and type II collagen hydrogel. Cell differentiation of type II collagen hydrogel was the most obvious, and the cell differentiation was time-dependent. These type II collagen hydrogels had the potential to maintain the cartilage formation in mesenchymal stem cells (Bosnakovski et al., 2006). Besides, the hybrid hydrogel prepared by type I and type II collagen could regulate the performance of the hybrid hydrogels by adjusting the content of two types of collagen. The results showed that the higher the compression modulus of hybrid hydrogel was, the more extracellular matrix the chondrocytes secreted (Yuan et al., 2016).

It is common to combine collagen with other natural biological macromolecules to prepare hybrid hydrogels by the typical chemical modification of collagen. It was shown that the preparation of hyaluronic acid and collagen hybrid scaffold material with prednisone as anti-inflammatory drug was an ideal choice for cartilage regeneration in osteoarthritis and for the sustained release system of prednisone (Mohammadi et al., 2018). Type II collagen and hyaluronic acid could prepare the injectable hydrogels *in situ*, followed by the encapsulation of cartilage cells. Chondrocytes remained alive during culture and maintained the phenotypic characteristics of chondrocytes. In addition, the expression of the chondrocyte specific genes increased with time (Kontturi et al., 2014). Biological scaffolds were prepared by mixing type I collagen with sodium alginate as 3D bioprinting ink. The mechanical strength of the scaffold was improved, and it could significantly promote the cell adhesion/growth, improve the cell proliferation, and enhance the specific gene expression of cartilage (Yang X. C. et al., 2018). After encapsulation with allogeneic chondrocytes, three-phase synthetic collagens, chondroitin sulfate, and hyaluronic acid hydrogels (CCH) were transplanted into cartilage defects, demonstrating that hybrid collagen hydrogels exhibited higher cartilage specific markers of cell growth, proliferation, GAG secretion, and gene/protein expression, which was closer to natural cartilage matrix than collagen hydrogel (**Figure 6**; Jiang et al., 2018).

Although collagen has been applied for the application of cartilage repair, its low stiffness and rapid degradation was not beneficial for chondrogenesis. Li et al. developed

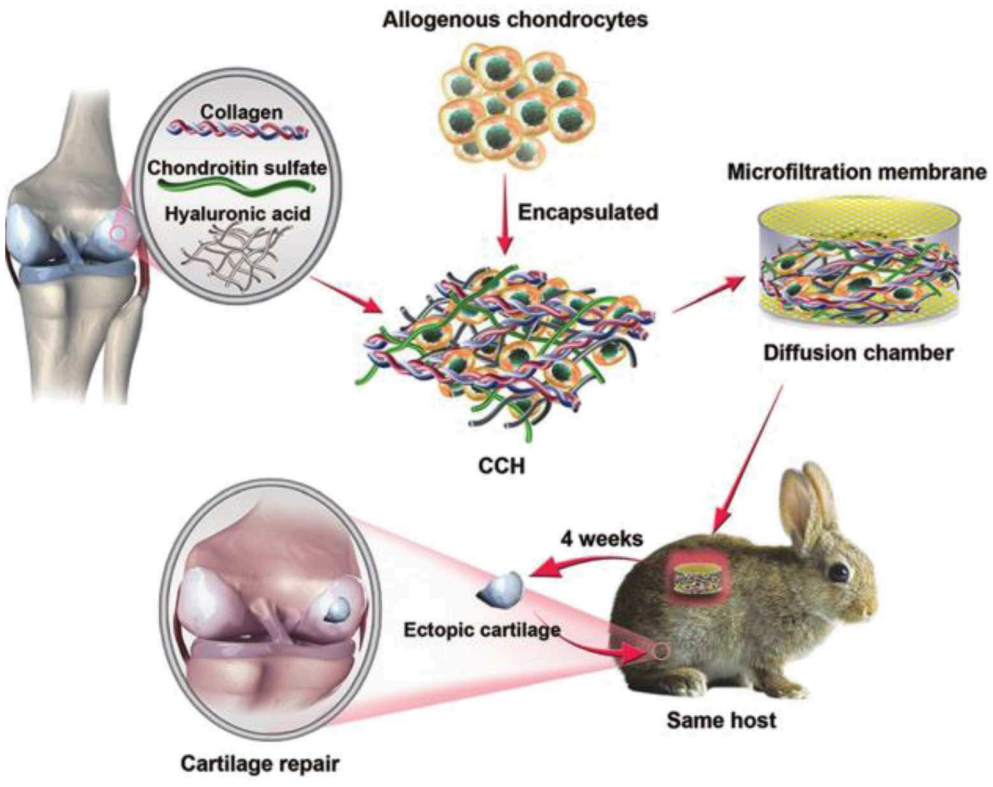

FIGURE 6 | Schematic illustration of the overall design of three-phase hybrid hydrogels. Allogeneic chondrocytes are encapsulated with a CCH hybrid hydrogel, forming the ectopic cartilage with a diffusion chamber system for cartilage repair. Reproduced from Jiang et al. (2018) with permission from Copyright 2018 Royal Society of Chemistry.

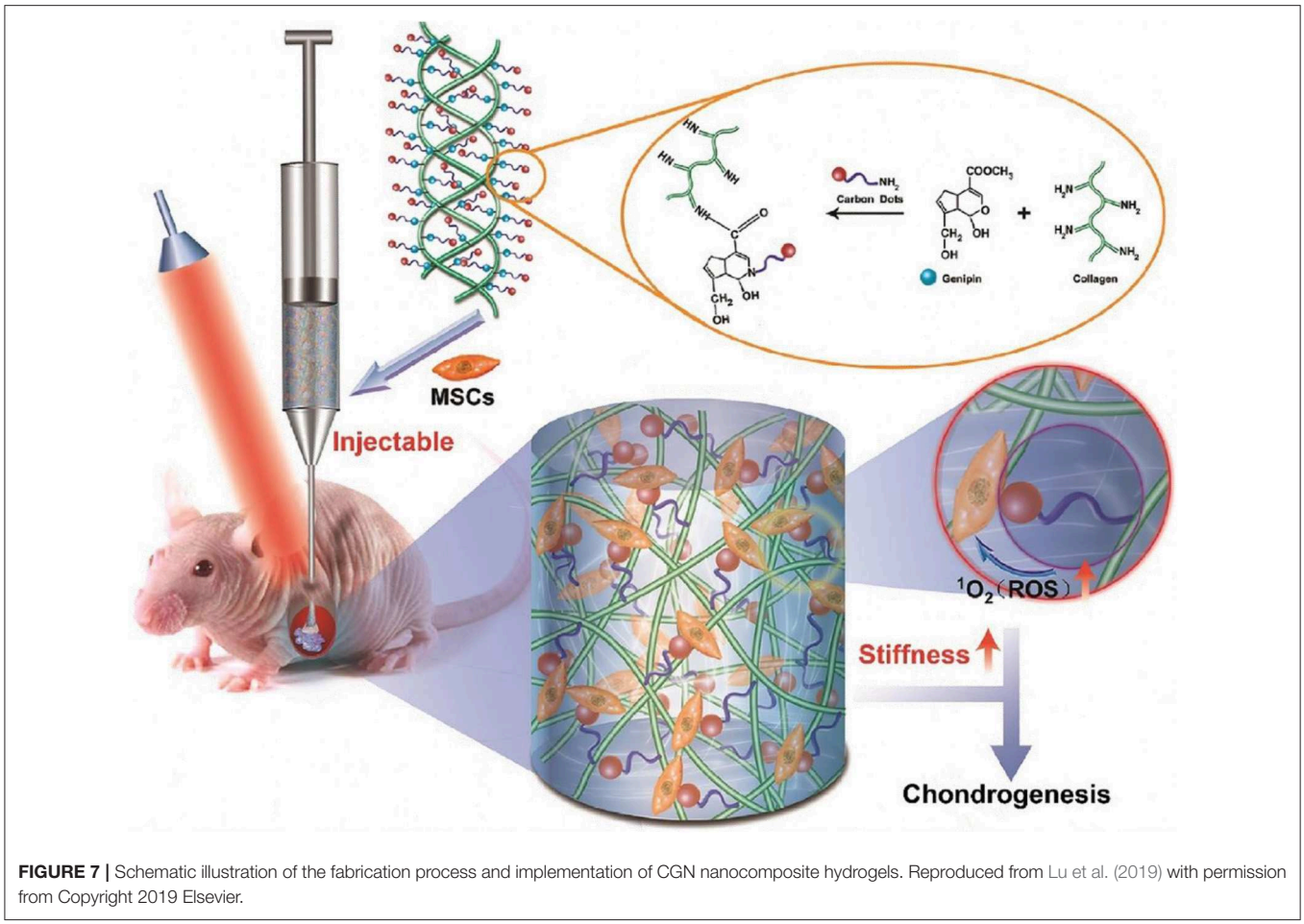

FIGURE 7 | Schematic illustration of the fabrication process and implementation of CGN nanocomposite hydrogels. Reproduced from Lu et al. (2019) with permission from Copyright 2019 Elsevier.

a kind of injectable collagen hydrogel of collagen-genipin-CD nanoparticles (CGN) through crosslinking the carbon dot nanoparticles (CD NPs) onto collagen with biocompatible crosslinker of genipin. On account of the effective linkage of genipin and CD NPs, these hydrogels showed high stiffness and produced a number of reactive oxygen species (ROS) by the photodynamic therapy (PDT). The organic combination of PDT and CGN hydrogel could obviously increase the BMSCs proliferation, upregulate the cartilage-specific gene expression, enhance the GAG secretion, and accelerate the cartilage regeneration within 8 weeks (**Figure 7**), which was attributed to the chondrogenic differentiation from the synergistic stiffness enhancement and ROS generation effect. So, this organic combination on the hydrogel injection and PDT treatment will represent a novel kind of strategy for the cartilage repair applications (Lu et al., 2019). In addition, enhancement of linkage interface between collagen hydrogels and bone-like substrates was also important for the regenerative medicine, because it is inevitable to use the heterogeneous scaffolds to achieve their multifunctionally gradient properties when the tissue cannot be completely repaired by a homogeneous graft. Therefore, improvement of the contact interface among the various layers is critical to construct the advanced hydrogel scaffolds with optimal performances. Borros et al. developed a pentafluorophenyl methacrylate (PFM) coating method through the immobilization of collagen-based hydrogels onto the desired substrate, because of high reactivity of PFM-coated substrate toward amines; in this case, the hybrid hydrogels were subsequently fibrillated and finally formed (Mas-Vinyals et al., 2019).

Hyaluronan

Hyaluronate (HA) is a typically linear polysaccharide formed by 250–25,000 repeated disaccharide units consisting of N-acetylglucosamine and D-glucuronic acid, which is a crucial component of ECM and plays an important role in cell signal transduction and wound healing (Tool, 2001; Toole, 2004). Therefore, HA-based hydrogel is recognized as one of the most promising natural materials for cartilage tissue engineering. Owing to the unique effect of hyaluronic acid on the formation of chondrocytes, the application of HA-based hydrogel containing chondrocytes has been widely studied in cartilage tissue regeneration (Barbucci et al., 2002; Chung et al., 2006; Kang et al., 2009). Hyaluronic acid was chemically modified to form derivatives with better biocompatibility and controllable biodegradation. A biocompatible *in situ* crosslinked HA hydrogel can be obtained by the biological orthogonal reaction. The hydrogel is formed by a copper-free click-reaction between the azide and dibenzyl cyclooctane, which was proven to be

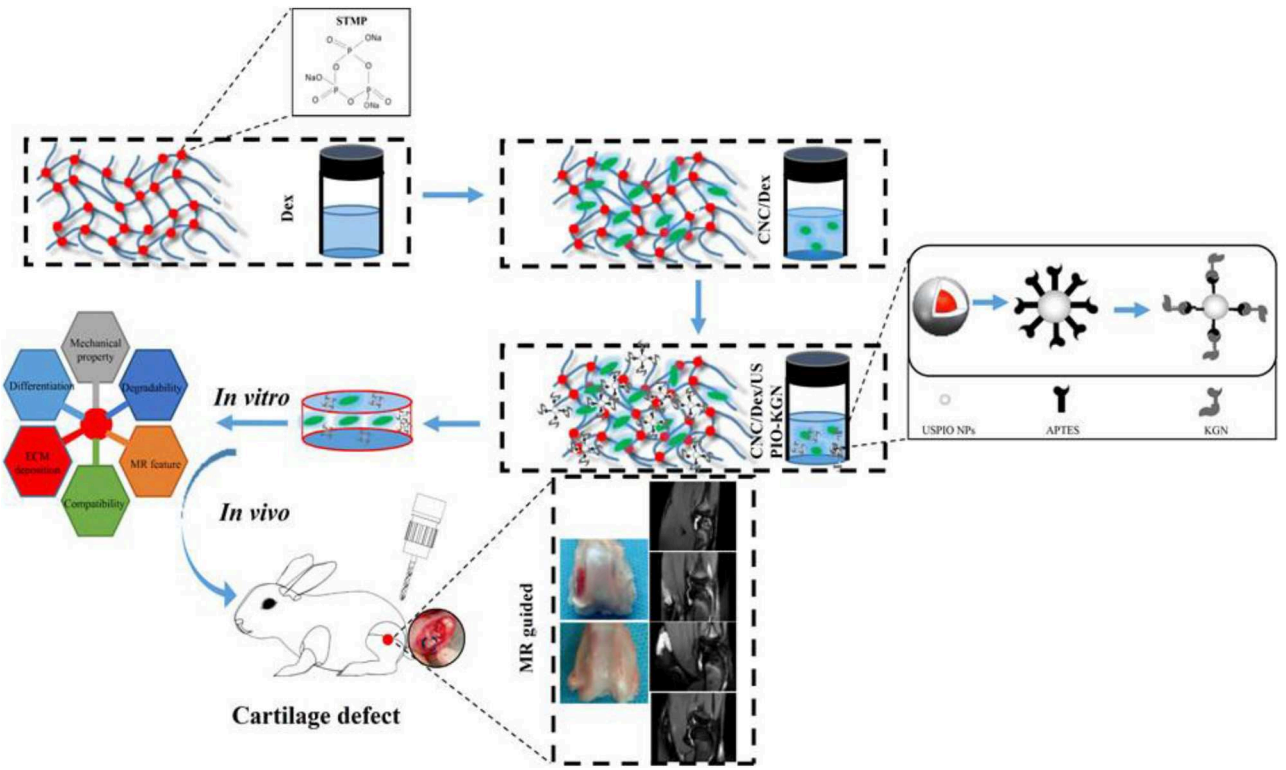

FIGURE 8 | Schematic illustration of preparation and utilization of USPIO-labeled Dex/CNC/USPIO-KGN hydrogels for artificial cartilage repair. Reproduced from Yang et al. (2019) with permission from Copyright 2019 American Chemical Society.

an injectable scaffold *in vitro* and *in vivo* (Han et al., 2018). An *in situ* photo-crosslinked hyaluronic acid was developed as a scaffold material for articular cartilage repair. The physical and mechanical properties of these crosslinking hyaluronate hydrogels are similar to the other natural hydrogels. The chondrocytes were embedded in hydrogels and cultured *in vitro*. The cells remained round and accumulated a large amount of cartilage matrix. The hydrogel was inserted into the cartilage defect, and a large amount of cartilage matrix accumulated within 2 weeks after the surgery (Nettles et al., 2004). In the other method, HA was modified by the methacrylate anhydride and photopolymerized into a network with extensive physical properties. The volume expansion rate of the network was distributed between 8 and 42%, the compression modulus was 2–100 kPa, and the degradation time increased from <1 d to nearly 38 days (Burdick et al., 2005). Later, some studies showed that using visible green light instead of ultraviolet light to activate the crosslinked system would not damage the properties of materials. The compression modulus of hydrogel network can be adjusted to 3–146 kPa (Fenn and Oldinski, 2016). Therefore, the hyaluronic acid hydrogels prepared by chemical modification have adjustable biodegradability and mechanical properties and better optical crosslinking ability.

In terms of the biological safety of implantation materials, the extracellular matrix degradability has gained increasing attention in tissue engineering. Cheng et al. prepared a completely bio degradable hydrogel by combining synthetic and natural polysaccharide polymers with their respective features. By mixing polyphosphate copolymer poly(butynyl phospholane)-random-poly(ethylethylene phosphate) (PBYP-r-PEEP) with thiolated hyaluronic acid (HA-SH) via the thiolyne "click" reaction, the fabricated HA/PPE hydrogel, supporting the human mesenchymal stem cells (hMSCs) adhesion and growth, could promote the cell-cell interactions with the enzymatic biodegradability and expand the range of biodegradable biomaterials for tissue engineering (Hao et al., 2019). In addition, Guo et al. prepared a kind of USPIO-KGN for cartilage repair by means of a stable non-protein compound of kartogenin (KGN) that promoted the BMSCs differentiation into chondrocytes via the grafting onto surface of ultrasmall superparamagnetic iron-oxide (USPIO) to finally integrate into the cellulose nanocrystal/dextran hydrogels (**Figure 8**). It was found that KGN was sustainably released for a long time, thus recruiting endogenous host cells and inducing the BMSCs differentiation into the chondrocytes for achieving the effective cartilage regeneration, with verification of both *in vitro* and *in vivo* experiments (Yang et al., 2019).

Natural Hybrid Hydrogels

Combination of various natural hydrogels is an ideal strategy for fabrication of smart and excellent hybrid scaffolds with high performance for cartilage tissue engineering and biomaterial

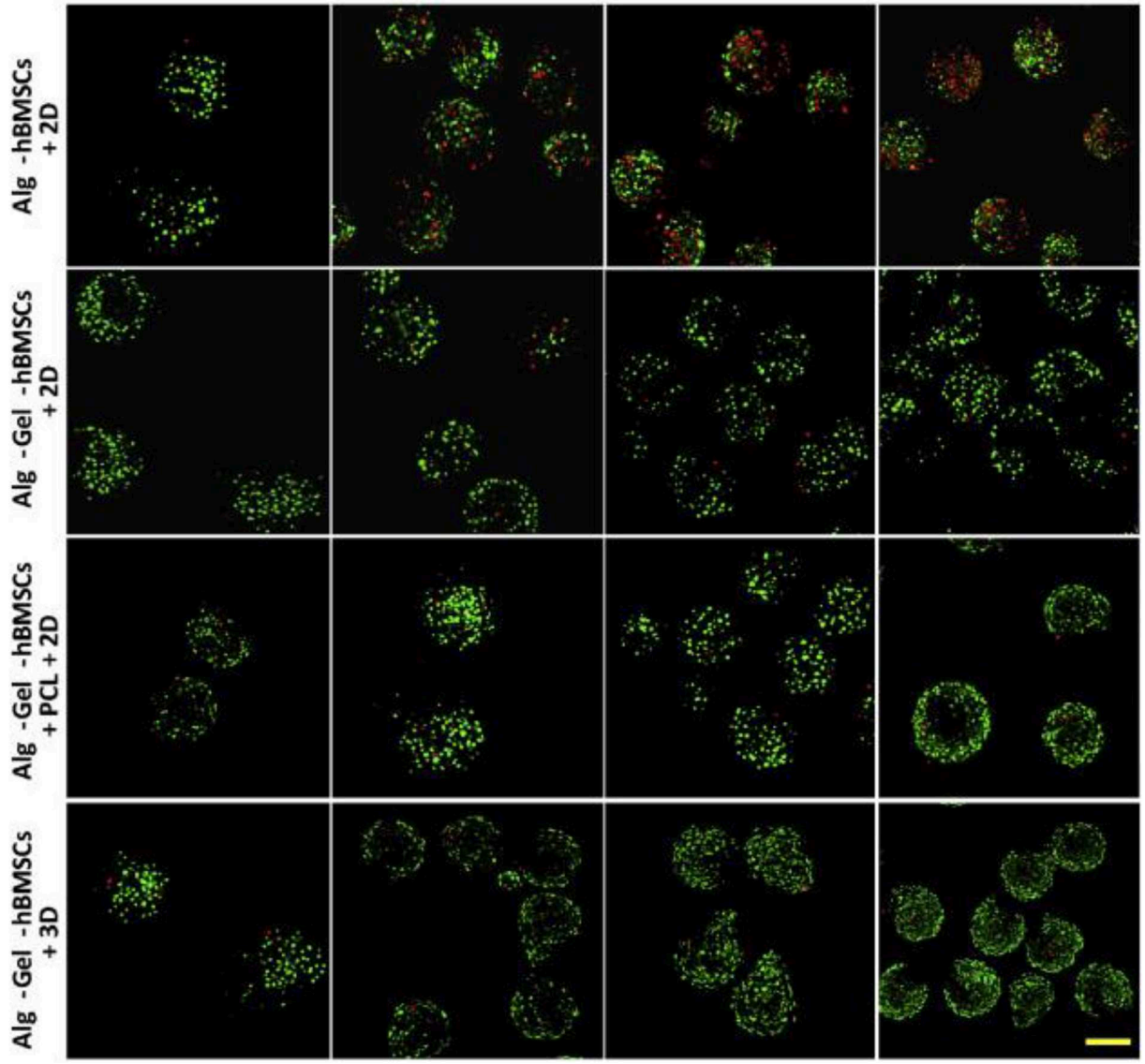

FIGURE 9 | Live/Dead staining of ALG-hBMSCs, ALG-Gel-hBMSCs, and ALG-Gel-hBMSCs/3D-printed PCL scaffold with 2D well plate culture and ALG-Gel-hBMSCs with 3D bioreactor culture on day 0, 3, 7, and 14, respectively. Scale bar = 200 μm. Reproduced from Xu et al. (2019) with permission from Copyright 2019 Elsevier.

fields. Lee et al. demonstrated a covalent method for conjugation of ALG to HA, to form the hyaluronate-alginate hybrid hydrogel (HAH) with the crosslinker of ethylenediamine in the Ca^{2+} solutions, which exhibited great potential as a scaffold for cartilage regeneration. Also, they used various types of linkers to obtain another series of HAH hydrogels by physical crosslinking methods. The mechanical property of HAH hydrogel was feasibly tailored by manipulating the linker between ALG and HA. Meanwhile, various linkers within the HAHs cultured in HAH hydrogel could also affect the chondrogenic differentiation of ATDC5 cells and be employed to fabricate the multifunctional scaffolds for cartilage regeneration (Park and Lee, 2014). Eglin et al. reported an optimization of human bone marrow stromal cell (hBMSC)-loaded alginate-gelatin microspheres within the 3D-printed PCL scaffolds for construction of mechanically stabilized and biologically supportive tissue engineering of cartilage (**Figure 9**; Xu et al., 2019). Tunable mechanical properties of composite hydrogels are important for biomedical applications. Tang et al. synthesized the strontium alginate/chondroitin sulfate (ALG/CS-Sr) composite hydrogels and analyzed the effect of strontium chloride concentration on the dynamically mechanical property. Cell viability assay revealed the good cytocompatibility of this hydrogel with the adequate characterization of flow

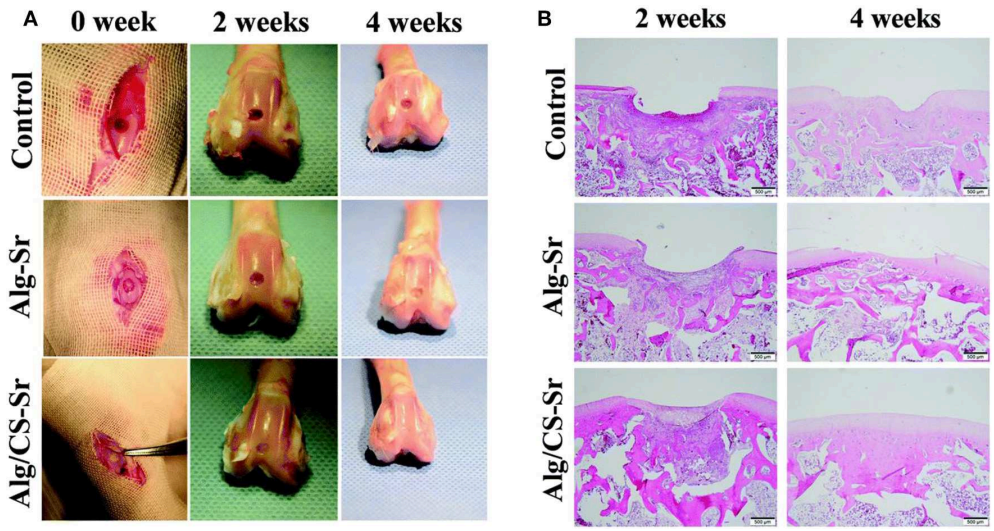

FIGURE 10 | ALG hydrogel aiding cartilage defect repair in a rabbit model: **(A)** photographs of knee joints in the control group and the ALG hydrogel group at the 0, 2, and 4 weeks after post-operation. **(B)** H&E staining of cartilage defect. Reproduced from Ma et al. (2019) with permission from Copyright 2019 Royal Society of Chemistry.

cytometry, qPCR, and western blotting analysis, which verified this kind of composite ALG/CS-Sr hydrogel could exert a positive effect on the apoptosis inhibition with the anti-inflammatory effects in articular cartilage regeneration fields (**Figure 10**; Ma et al., 2019).

MECHANICS OF NATURAL HYDROGELS FOR CARTILAGE TISSUE ENGINEERING

Conventional hydrogels normally possess breakable characters that will decrease their stability and thus cannot be utilized for specific tissue applications such as bone, cartilage, and tendon. To overcome this issue, two effective strategies have been developed for cartilage tissue engineering. One is the hybridization of hydrogels with other polymers, nanoparticles, or nanofibers. For example, regenerated silk fibroin and chitin nanofiber have been used to improve the mechanical strength of GelMA hydrogels by β-sheet folding and self-assembly, respectively. The hydrogel elastic modulus increases by 1,000-fold, and strain-to-failure enhances by around 200% after chitin nanofiber assembly (Hassanzadeh et al., 2016). The hydrogels also demonstrate good cell viability, promotive cell differentiation, and stable vasculature formation. Collagen-based hydrogels with a 10-fold increase in stiffness have been realized after mixing very low amount of chemically functionalized nanoparticles as crosslinker epicenters to make collagen chains crosslinked on the surface of nanoparticles (Jaiswal et al., 2016). On account of the interactions between nanoparticles and polymer chains, the mechanical properties of hybrid hydrogels can be enhanced. The other strategy is to prepare interpenetrating polymer network (IPN) hydrogels with high mechanics and fracture strength, which has gained a lot of attention for cartilage tissue engineering (Dragan, 2014). Double networks (DN) are introduced in hydrogels to enhance mechanical property for cartilage tissue engineering (Gong et al., 2003; Yasuda et al., 2009; Fukui et al., 2014). The feature of DN hydrogels is the formulation of, first, a densely crosslinked hydrogel, and second, a loose network. The first network serves as sacrificial bonds to disperse the stress, while the second polymer chains work as hidden length that can extend to sustain large deformation (Haque et al., 2012). Similarly, ionic crosslinked chitosan with low molecular weight is used to work as the second crosslinking component to enhance the mechanical strength of the UV-initiated PAM hydrogel (Ma et al., 2009; Li et al., 2018).

However, due to the big gap of mechanical property between the ordinary hydrogel materials and human tissues, scientists have been seeking to improve mechanical strength of the hydrogels in recent years. Generally, there are several different ways that have been proven to enhance the mechanical strength of the hydrogels, including increasing the crosslink density, reducing the gel swelling degree, introducing the fibrous reinforcing agent and the preparation of interpenetrating networks (Anseth et al., 1996; Haraguchi and Takehisa, 2002; Sakai et al., 2008; Hunt et al., 2014; Ahadian et al., 2015; Hao et al., 2017). Especially, double network (DN) hydrogel provides an excellent idea to gain high strength for cartilage tissue engineering (Chen et al., 2015; Higa et al., 2016; Yan et al., 2017). DN hydrogel possesses two different types of network structures: the highly crosslinked polyelectrolyte networks and the lowly crosslinked or non-crosslinked neutral network structures. The former provides a rigid bracket for DN hydrogels, while the latter fills in rigid network and absorbs external stress (Sun et al., 2012; Yang et al., 2016; Golafshan et al., 2017). Until now, however, the study of the DN hydrogels in the field of biological materials, especially in the field of for cartilage tissue engineering

applications are still at the initial stages with sums of challenges (Gu et al., 2018).

SUMMARY AND PERSPECTIVES

This paper reviews the advancements of several mechanically natural hydrogel biomaterials designed and applied in cartilage tissue engineering in recent years. It has been found that the high performance of natural hydrogels has better biocompatibility and biodegradability and is more conducive to cell survival. One of the keys to cartilage tissue regeneration is to promote cartilage integration as well as subchondral bone regeneration, because these two tissues have various topological structures and moduli that requires the hydrogel scaffolds to simulate different structures and functions simultaneously. In addition, the cartilage repair effect is associated with the deposition and remodeling of ECM of the cartilage cells. If the degradation rate of repaired material is not well-matched, the ECM cannot deposit in the defect area that is harming the cartilage regeneration. Based on this feature, natural hydrogel has a controllable degradation rate, good biocompatibility, and outstanding mechanical property, so it is an ideal cartilage tissue engineering material. Meanwhile, high mechanism of hydrogel scaffolds loaded with regenerative drugs or cell that promote cartilage regeneration have been widely used in recent years. We only selected and highlighted some typical examples to raise the reader's interest and awareness about the high performance of natural hydrogels for cartilage tissue engineering.

With the development of tissue engineering and the regenerative medicine, it has been found that tissue regeneration and reconstruction require a multifunctional scaffold to load and deliver tissue-specific cells; in this case, hydrogel scaffolds are recognized as ideal biomaterials for tissue engineering like cartilage, bone, skin, heart valves, nerves, tendons, etc., because the composition, structure, morphology, function, and mechanics are closely similar to the natural tissue extracellular matrix. The natural hydrogels and 3D architecture scaffolds combined with various bioactive molecules, genes, and cells, as well as the tunable mechanical properties, have the capacity to guide and promote the *in vivo* implantation and development of multifunctional engineered tissues. Thus, these natural hydrogel scaffolds with customized morphologies and suitable mechanical behaviors are a series of exciting prospects in cartilage tissue engineering by tailorable retention and delivery abilities of cells and growth factors within the injury site, thus realizing the cell adhesion, growth, spreading, and differentiation, as well as the extensive applications, hereafter referred to as biohydrogels with high mechanical properties in tissue augmentation, repair, reconstruction, and regeneration.

Yet, it should be noted that it remains a major challenge to fully restore cartilage to its original composition, architecture, mechanics, and biofunction. For example, simultaneous achievement of integrating cartilage and subchondral bone regeneration has been a critical challenge in tissue engineering, because the difference in structure and modulus represents two distinct types of tissues that should be carefully considered to overcome the difficulties in simulating the structures and functions of the hybrid or bi-phase hydrogel scaffolds. In this, the part of cartilage repair exhibited a highly elastic modulus to bear pressure and resist friction and to facilitate the extracellular matrix, enhance the chondrogenesis expression of MSCs or chondrocytes, inhibit the hypertrophic differentiation, and contribute to the chondrocyte mineralization. Another part of subchondral bone repair could effectively contribute to the formation of a blood vessel network within the hydrogels to facilitate nutrient transport, stimulate osteoblast proliferations, and provide great support for regenerative cartilage. More importantly, integration of the surrounding cartilage and the implants should possess strong interfacial adhesion that can be significantly considered and enhanced for regenerated cartilage. Additionally, smart incorporations of intelligent or self-guided features like self-assembly and/or functional flexibility for dynamic biological demands also played essential roles in the fabrication and development of a new kind of high-performance natural hydrogel to obtain the full cartilage regeneration in biomedical applications.

It should be further noted that although there have been some limited clinically approved tissue-engineered products for the clinical trials status quo in recent years, a rapid progress toward more advanced and targeted therapies is still of note in promoting microfabrication techniques and developing the cellular scaffold-based approaches. It is concluded that an ideal natural hydrogel for achieving the cartilage tissue engineering should synchronously possess the following characterizations: (1) biological activity and biomimetic function; (2) mechanical reinforcement; (3) integration of cartilage with bone tissue, and (4) transport of drugs and growth factors. Therefore, the intelligent and hybrid hydrogel scaffolds with complex architectures should be well-fabricated for realizing the customized clinic treatments, and the corresponding research on the mechanical and biological behaviors of hydrogel scaffolds should also be emphasized to ensure powerful tissue interactions, resorption, and hierarchical architecture for enabling the tissue engineering implants. With this understanding, future work should forcefully focus on identifying the secondary, tertiary, and higher order architectures of hybrid nature-derived hydrogels, quantifying their composition, morphology and function, characterizing their binding pockets and interactions with cell surface receptors, and finally, turning them into a clinical tissue engineering biomaterial for effective cartilage tissue engineering. In this sense, we will establish such methodology or criteria on the design and development of final biological tissue engineering products for regenerative medicine, which makes natural hydrogel scaffolds more advantageous on adjustable structure, better strength, adequate immune response, adhesive interfacial binding force, and good biodegradability for enabling real applications in human patients.

This exciting goal will hopefully be achieved by the scientific community with the lessons learned from the literature in this review. Therefore, we are strongly convinced that with the help of continuous developments of natural hydrogels and exquisite adjustment of their physicochemical and mechanical properties for effective cartilage tissue engineering, more advanced multi-responsive histological engineering products with optimized architectures and

functions will be eventually created to obtain greater manipulation and higher availability for various biomedical applications. While newly responsive hydrogel compositions, structures and mechanical properties will hopefully be continually developed, and the ability to obtain smart biomaterials with topological complexity is excitingly expanding in the next generation of outstanding tissue engineering products.

AUTHOR CONTRIBUTIONS

XW, NB, and CL conceived and designed the content of the paper. WB, ML, and YY collected the researched literatures, arranged the outline of collected documents, and wrote the articles. YW made important suggestions and helped revise the paper. All authors reviewed and commented on the entire manuscript.

FUNDING

This research was funded by the Science Research Program of Inner Mongolia University for Nationalities (NMDYB17132), National Natural Science Foundation of China (NSFC, 51973226 and 51803188), the China Postdoctoral Science Foundation (2019T120636 and 2018M642783), and the Henan Postdoctoral Science Foundation (001801001).

REFERENCES

Ahadian, S., Sadeghian, R. B., Salehi, S., Ostrovidov, S., Bae, H., Ramalingam, M., et al. (2015). Bioconjugated hydrogels for tissue engineering and regenerative medicine. *Bioconjugate Chem.* 26, 1984–2001. doi: 10.1021/acs.bioconjchem.5b00360

Alsberg, E., Anderson, K. W., Albeiruti, A., Franceschi, R. T., and Mooney, D. J. (2001). Cell-interactive alginate hydrogels for bone tissue engineering. *J. Dent. Res.* 80, 2025–2029. doi: 10.1177/00220345010800111501

Amini, A. A., and Nair, L. S. (2012). Injectable hydrogels for bone and cartilage repair. *Biomed. Mater.* 7:24105. doi: 10.1088/1748-6041/7/2/024105

Anseth, K. S., Bowman, C. N., and BrannonPeppas, L. (1996). Mechanical properties of hydrogels and their experimental determination. *Biomaterials* 17, 1647–1657. doi: 10.1016/0142-9612(96)87644-7

Balakrishnan, B., and Banerjee, R. (2011). Biopolymer-based hydrogels for cartilage tissue engineering. *Chem. Rev.* 111, 4453–4474. doi: 10.1021/cr100123h

Barbucci, R., Lamponi, S., Borzacchiello, A., Ambrosio, L., Fini, M., Torricelli, P., et al. (2002). Hyaluronic acid hydrogel in the treatment of osteoarthritis. *Biomaterials* 23, 4503–4513. doi: 10.1016/S0142-9612(02)00194-1

Benazzo, F., Cadossi, M., Cavani, F., Fini, M., Giavaresi, G., Setti, S., et al. (2008). Cartilage repair with osteochondral autografts in sheep: effect of biophysical stimulation with pulsed electromagnetic fields. *J. Orthop. Res.* 26, 631–642. doi: 10.1002/jor.20530

Berthiaume, F., Maguire, T. J., and Yarmush, M. L. (2011). Tissue engineering and regenerative medicine: history, progress, and challenges. *Annu. Rev. Chem. Biomol. Eng.* 2, 403–430. doi: 10.1146/annurev-chembioeng-061010-114257

Bosnakovski, D., Mizuno, M., Kim, G., Takagi, S., Okumura, M., and Fujinaga, T. (2006). Chondrogenic differentiation of bovine bone marrow mesenchymal stem cells (MSCs) in different hydrogels: influence of collagen type II extracellular matrix on MSC chondrogenesis. *Biotechnol. Bioeng.* 93, 1152–1163. doi: 10.1002/bit.20828

Bouhadir, K. H., Alsberg, E., and Mooney, D. J. (2001). Hydrogels for combination delivery of antineoplastic agents. *Biomaterials* 22, 2625–2633. doi: 10.1016/S0142-9612(01)00003-5

Burdick, J. A., Chung, C., Jia, X. Q., Randolph, M. A., and Langer, R. (2005). Controlled degradation and mechanical behavior of photopolymerized hyaluronic acid networks. *Biomacromolecules* 6, 386–391. doi: 10.1021/bm049508a

Calabrese, G., Forte, S., Gulino, R., Cefali, F., Figallo, E., Salvatorelli, L., et al. (2017). Combination of collagen-based scaffold and bioactive factors induces adipose-derived mesenchymal stem cells chondrogenic differentiation *in vitro*. *Front Physiol.* 8:50. doi: 10.3389/fphys.2017.00050

Cancedda, R., Dozin, B., Giannoni, P., and Quarto, R. (2003). Tissue engineering and cell therapy of cartilage and bone. *Matrix Biol.* 22, 81–91. doi: 10.1016/S0945-053X(03)00012-X

Chen, P. F., Zheng, L., Wang, Y. Y., Tao, M., Xie, Z., Xia, C., et al. (2019). Desktop-stereolithography 3D printing of a radially oriented extracellular matrix/mesenchymal stem cell exosome bioink for osteochondral defect regeneration. *Theranostics* 9, 2439–2459. doi: 10.7150/thno.31017

Chen, Q., Chen, H., Zhu, L., and Zheng, J. (2015). Fundamentals of double network hydrogels. *J. Mater. Chem. B* 3, 3654–3676. doi: 10.1039/C5TB00123D

Chen, Y. R., Zhou, Z. X., Zhang, J. Y., Yuan, F. Z., Xu, B. B., Guan, J., et al. (2019). Low-molecular-weight heparin-functionalized chitosan-chondroitin sulfate hydrogels for controlled release of TGF-β3 and *in vitro* neocartilage formation. *Front. Chem.* 7:745. doi: 10.3389/fchem.2019.00745

Cho, S. H., Lim, S. M., Han, D. K., Yuk, S. H., Il Im, G., and Lee, J. H. (2009). Time-dependent alginate/polyvinyl alcohol hydrogels as injectable cell carrier. *J. Biomater. Sci. Polym. E.* 20, 863–876. doi: 10.1163/156856209X444312

Cho, S. H., Oh, S. H., and Lee, J. H. (2005). Fabrication and characterization of porous alginate/polyvinyl alcohol hybrid scaffolds for 3D cell culture. *J. Biomater. Sci. Polym. E.* 16, 933–947. doi: 10.1163/1568562054414658

Chung, C., Mesa, J., Randolph, M. A., Yaremchuk, M., and Burdick, J. A. (2006). Influence of gel properties on neocartilage formation by auricular chondrocytes photoencapsulated in hyaluronic acid networks. *J. Biomed. Mater. Res. A* 77, 518–525. doi: 10.1002/jbm.a.30660

Colinet, I., Dulong, V., Mocanu, G., Picton, L., and Le Cerf, D. (2009). New amphiphilic and pH-sensitive hydrogel for controlled release of a model poorly water-soluble drug. *Eur. J. Pharm. Biopharm.* 73, 345–350. doi: 10.1016/j.ejpb.2009.07.008

Critchley, S., Cunniffe, G., O'Reilly, A., Diaz-Payno, P., Schipani, R., McAlinden, A., et al. (2019). Regeneration of osteochondral defects using developmentally inspired cartilaginous templates. *Tissue Eng. Part A* 25, 159–171. doi: 10.1089/ten.tea.2018.0046

Dong, L., Wang, S. J., Zhao, X. R., Zhu, Y. F., and Yu, J. K. (2017). 3D-printed poly (ε-caprolactone) scaffold integrated with cell-laden chitosan hydrogels for bone tissue engineering. *Sci. Rep.* 7:13412. doi: 10.1038/s41598-017-13838-7

Dorotka, R., Windberger, U., Macfelda, K., Bindreiter, U., Toma, C., and Nehrer, S. (2005). Repair of articular cartilage defects treated by microfracture and a three-dimensional collagen matrix. *Biomaterials* 26, 3617–3629. doi: 10.1016/j.biomaterials.2004.09.034

Dragan, E. S. (2014). Design and applications of interpenetrating polymer network hydrogels. A review. *Chem. Eng. J.* 243, 572–590. doi: 10.1016/j.cej.2014.01.065

El Khoury, D., Goff, H. D., Berengut, S., Kubant, R., and Anderson, G. H. (2014). Effect of sodium alginate addition to chocolate milk on glycemia, insulin, appetite and food intake in healthy adult men. *Eur. J. Clin. Nutr.* 68, 613–618. doi: 10.1038/ejcn.2014.53

Eslahi, N., Abdorahim, M., and Simchi, A. (2016). Smart polymeric hydrogels for cartilage tissue engineering: a review on the chemistry and biological functions. *Biomacromolecules* 17, 3441–3463. doi: 10.1021/acs.biomac.6b01235

Fenn, S. L., and Oldinski, R. A. (2016). Visible light crosslinking of methacrylated hyaluronan hydrogels for injectable tissue repair. *J. Biomed. Mater. Res. B* 104, 1229–1236. doi: 10.1002/jbm.b.33476

Fonseca, K. B., Gomes, D. B., Lee, K., Santos, S. G., Sousa, A., Silva, E. A., et al. (2014). Injectable MMP-sensitive alginate hydrogels as hMSC delivery systems. *Biomacromolecules* 15, 380–390. doi: 10.1021/bm4016495

Fukui, T., Kitamura, N., Kurokawa, T., Yokota, M., Kondo, E., Gong, J. P., et al. (2014). Intra-articular administration of hyaluronic acid increases the volume of the hyaline cartilage regenerated in a large osteochondral defect by implantation of a double-network gel. *J. Mater. Sci.* 25, 1173–1182. doi: 10.1007/s10856-013-5139-3

Furth, M. E., Atala, A., and Van Dyke, M. E. (2007). Smart biomaterials design for tissue engineering and regenerative medicine. *Biomaterials* 28, 5068–5073. doi: 10.1016/j.biomaterials.2007.07.042

Gan, D. L., Xu, T., Xing, W. S., Wang, M. H., Fang, J., Wang, K. F., et al. (2019). Mussel-inspired dopamine oligomer intercalated tough and resilient gelatin methacryloyl (GelMA) hydrogels for cartilage regeneration. *J. Mater. Chem. B* 7, 1716–1725. doi: 10.1039/C8TB01664J

Gao, F., Xu, Z. Y., Liang, Q. F., Li, H. F., Peng, L. Q., Wu, M. M., et al. (2019). Osteochondral regeneration with 3D-printed biodegradable high-strength supramolecular polymer reinforced-gelatin hydrogel scaffolds. *Adv. Sci.* 6:1900867. doi: 10.1002/advs.201900867

Glenn, R. E., McCarty, E. C., Potter, H. G., Juliao, S. F., Gordon, J. D., and Spindler, K. P. (2006). Comparison of fresh osteochondral autografts and allografts: a canine model. *Am. J. Sports Med.* 34, 1084–1093. doi: 10.1177/0363546505284846

Golafshan, N., Gharibi, H., Kharaziha, M., and Fathi, M. (2017). A facile one-step strategy for development of a double network fibrous scaffold for nerve tissue engineering. *Biofabrication* 9:025008. doi: 10.1088/1758-5090/aa68ed

Gong, J. P., Katsuyama, Y., Kurokawa, T., and Osada, Y. (2003). Double-network hydrogels with extremely high mechanical strength. *Adv. Mater.* 15, 1155–1158. doi: 10.1002/adma.200304907

Griffith, L. G., and Naughton, G. T. (2002). Tissue engineering-current challenges and expanding opportunities. *Science* 295, 1009–1014. doi: 10.1126/science.1069210

Grottkau, B. E., and Lin, Y. F. (2013). Osteogenesis of adipose-derived stem cells. *Bone Res.* 1:133. doi: 10.4248/BR201302003

Gu, Z., Huang, K., Luo, L., Zhang, L., Kuang, T., Chen, Z., et al. (2018). Double network hydrogel for tissue engineering. *Wiley Interdiscip. Rev. Nanomed. Nanobiotechnol.* 10:e1520. doi: 10.1002/wnan.1520

Gunja, N. J., and Athanasiou, K. A. (2006). Biodegradable materials in arthroscopy. *Sports Med. Arthrosc.* 14, 112–119. doi: 10.1097/00132585-200609000-00002

Haene, R., Qamirani, E., Story, R. A., Pinsker, E., and Daniels, T. R. (2012). Intermediate outcomes of fresh talar osteochondral allografts for treatment of large osteochondral lesions of the talus. *J. Bone Joint Surg.* 94, 1105–1110. doi: 10.2106/JBJS.J.02010

Han, L., Xu, J. L., Lu, X., Gan, D. L., Wang, Z. X., Wang, K. F., et al. (2017). Biohybrid methacrylated gelatin/polyacrylamide hydrogels for cartilage repair. *J. Mater. Chem. B* 5, 731–741. doi: 10.1039/C6TB02348G

Han, S. S., Yoon, H. Y., Yhee, J. Y., Cho, M. O., Shim, H. E., Jeong, J. E., et al. (2018). *In situ* cross-linkable hyaluronic acid hydrogels using copper free click chemistry for cartilage tissue engineering. *Polym. Chem.* 9, 20–27. doi: 10.1039/C7PY01654A

Hao, Y., He, J. L., Ma, X., Feng, L., Zhu, M., Zhai, Y. X., et al. (2019). A fully degradable and photocrosslinked polysaccharide-polyphosphate hydrogel for tissue engineering. *Carbohydr. Polym.* 225:115257. doi: 10.1016/j.carbpol.2019.115257

Hao, Z., Song, Z., Huang, J., Huang, K., Panetta, A., Gu, Z., et al. (2017). The scaffold microenvironment for stem cell based bone tissue engineering. *Biomater. Sci.* 5, 1382–1392. doi: 10.1039/C7BM00146K

Haque, M. A., Kurokawa, T., and Gong, J. P. (2012). Super tough double network hydrogels and their application as biomaterials. *Polymer* 53, 1805–1822. doi: 10.1016/j.polymer.2012.03.013

Haraguchi, K., and Takehisa, T. (2002). Nanocomposite hydrogels: a unique organic-inorganic network structure with extraordinary mechanical, optical, and swelling/de-swelling properties. *Adv. Mater.* 14, 1120–1124. doi: 10.1002/1521-4095(20020816)14:16<1120::AID-ADMA1120>3.0.CO;2-9

Harris, J. D., Siston, R. A., Pan, X. L., and Flanigan, D. C. (2010). Autologous chondrocyte implantation: a systematic review. *J. Bone Joint Surg.* 92, 2220–2233. doi: 10.2106/JBJS.J.00049

Hashimoto, T., Suzuki, Y., Tanihara, M., Kakimaru, Y., and Suzuki, K. (2004). Development of alginate wound dressings linked with hybrid peptides derived from laminin and elastin. *Biomaterials* 25, 1407–1414. doi: 10.1016/j.biomaterials.2003.07.004

Hassanzadeh, P., Kazemzadeh-Narbat, M., Rosenzweig, R., Zhang, X., Khademhosseini, A., Annabi, N., et al. (2016). Ultrastrong and flexible hybrid hydrogels based on solution self-assembly of chitin nanofibers in gelatin methacryloyl (gelma). *J. Mater. Chem. B* 4, 2539–2543. doi: 10.1039/C6TB00021E

Higa, K., Kitamura, N., Kurokawa, T., Goto, K., Wada, S., Nonoyama, T., et al. (2016). Fundamental biomaterial properties of tough glycosaminoglycan-containing double network hydrogels newly developed using the molecular stent method. *Acta Biomater.* 43, 38–49. doi: 10.1016/j.actbio.2016.07.023

Hjelle, K., Solheim, E., Strand, T., Muri, R., and Brittberg, M. (2002). Articular cartilage defects in 1,000 knee arthroscopies. *Arthroscopy* 18, 730–734. doi: 10.1053/jars.2002.32839

Hollister, S. J. (2005). Porous scaffold design for tissue engineering. *Nat. Mater.* 4, 518–524. doi: 10.1038/nmat1421

Hubbell, J. A. (1995). Biomaterials in tissue engineering. *Nat. Biotechnol.* 13, 565–576. doi: 10.1038/nbt0695-565

Huey, D. J., Hu, J. C., and Athanasiou, K. A. (2012). Unlike bone, cartilage regeneration remains elusive. *Science* 338, 917–921. doi: 10.1126/science.1222454

Hunt, J. A., Chen, R., van Veen, T., and Bryan, N. (2014). Hydrogels for tissue engineering and regenerative medicine. *J. Mater. Chem. B* 2, 5319–5338. doi: 10.1039/C4TB00775A

Jaiswal, M. K., Xavier, J. R., Carrow, J. K., Desai, P., Alge, D., and Gaharwar, A. K. (2016). Mechanically stiff nanocomposite hydrogels at ultralow nanoparticle content. *ACS Nano* 10, 246–256. doi: 10.1021/acsnano.5b03918

Jayakumar, R., Prabaharan, M., Reis, R. L., and Mano, J. F. (2005). Graft copolymerized chitosan-present status and applications. *Carbohydr. Polym.* 62, 142–158. doi: 10.1016/j.carbpol.2005.07.017

Ji, W., Yang, F., Seyednejad, H., Chen, Z., Hennink,W. E., Anderson, J. M., et al. (2012). Biocompatibility and degradation characteristics of PLGA-based electrospun nanofibrous scaffolds with nanoapatite incorporation. *Biomaterials* 33, 6604–6614. doi: 10.1016/j.biomaterials.2012.06.018

Jiang, X., Liu, J., Liu, Q., Lu, Z., Zheng, L., Zhao, J., et al. (2018). Correction: therapy for cartilage defects: functional ectopic cartilage constructed by cartilage-simulating collagen, chondroitin sulfate and hyaluronic acid (CCH) hybrid hydrogel with allogeneic chondrocytes. *Biomater. Sci.* 6:2270. doi: 10.1039/C8BM00354H

Kamoun, E. A. (2016). N-succinyl chitosan-dialdehyde starch hybrid hydrogels for biomedical applications. *J. Adv. Res.* 7, 69–77. doi: 10.1016/j.jare.2015.02.002

Kang, J. Y., Chung, C. W., Sung, J. H., Park, B. S., Choi, J. Y., Lee, S. J., et al. (2009). Novel porous matrix of hyaluronic acid for the three-dimensional culture of chondrocytes. *Int. J. Pharm.* 369, 114–120. doi: 10.1016/j.ijpharm.2008.11.008

Karageorgiou, V., and Kaplan, D. (2005). Porosity of 3D biomaterial scaffolds and osteogenesis. *Biomaterials* 26, 5474–5491. doi: 10.1016/j.biomaterials.2005.02.002

Katti, D. S., Lakshmi, S., Langer, R., and Laurencin, C. T. (2002). Toxicity, biodegradation and elimination of polyanhydrides. *Adv. Drug Deliv. Rev.* 54, 933–961. doi: 10.1016/S0169-409X(02)00052-2

Khademhosseini, A., and Langer, R. (2006). Drug delivery and tissue engineering. *Chem. Eng. Prog.* 102:38.

Khan, W. S., and Malik, A. (2012). Hot topic: stem cell therapy and tissue engineering applications for cartilage regeneration. *Curr. Stem Cell Res. T* 7, 241–242. doi: 10.2174/157488812800793063

Kim, J., Lin, B., Kim, S., Choi, B., Evseenko, D., and Lee, M. (2015). Indigenous and integrated innovation driving the boom in China's high-speed rail technologies. *J. Biol. Eng.* 9:1. doi: 10.1186/1754-1611-9-1

Kim, T. G., Shin, H., and Lim, D. W. (2012). Biomimetic scaffolds for tissue engineering. *Adv. Funct. Mater.* 22, 2446–2468. doi: 10.1002/adfm.201103083

Kontturi, L. S., Jarvinen, E., Muhonen, V., Collin, E. C., Pandit, A. S., Kiviranta, I., et al. (2014). An injectable, *in situ* forming type II collagen/hyaluronic acid hydrogel vehicle for chondrocyte delivery in cartilage tissue engineering. *Drug Deliv. Transl. Res.* 4, 149–158. doi: 10.1007/s13346-013-0188-1

Kosik-Koziol, A., Costantini, M., Bolek, T., Szoke, K., Barbetta, A., Brinchmann, J., et al. (2017). PLA short sub-micron fiber reinforcement of 3D bioprinted alginate constructs for cartilage regeneration. *Biofabrication* 9:044105. doi: 10.1088/1758-5090/aa90d7

Li, L., Yu, F., Zheng, L. M., Wang, R. L., Yan, W. Q., Wang, Z. X., et al. (2019). Natural hydrogels for cartilage regeneration: Modification, preparation and application. *J. Orthop. Transl.* 17, 26–41. doi: 10.1016/j.jot.2018.09.003

Li, X., Sun, Q., Li, Q., Kawazoe, N., and Chen, C. (2018). Functional hydrogels with tunable structures and properties for tissue engineering applications. *Front. Chem.* 6:499. doi: 10.3389/fchem.2018.00499

Liao, J., Shi, K., Ding, Q., Qu, Y., Luo, F., and Qian, Z. (2014). Recent developments in scaffold-guided cartilage tissue regeneration. *J. Biomed. Nanotechnol.* 10, 3085–3104. doi: 10.1166/jbn.2014.1934

Liu, Y., Xu, L., Liu, J. S., Liu, X. Y., Chen, C. H., Li, G. Y., et al. (2016). Graphene oxides cross-linked with hyperbranched polyethylenimines: preparation, characterization and their potential as recyclable and highly efficient adsorption materials for lead(II) ions. *Chem. Eng. J.* 285, 698–708. doi: 10.1016/j.cej.2015.10.047

Loh, Q. L., and Choong, C. (2013). Three-dimensional scaffolds for tissue engineering applications: role of porosity and pore size. *Tissue Eng. Part B Rev.* 19, 485–502. doi: 10.1089/ten.teb.2012.0437

Lu, Z. H., Liu, S. J., Le, Y. G., Qin, Z. N., He, M. W., Xu, F. B., et al. (2019). An injectable collagen-genipin-carbon dot hydrogel combined with photodynamic therapy to enhance chondrogenesis. *Biomaterials* 218:119190. doi: 10.1016/j.biomaterials.2019.05.001

Ma, F., Qu, R. J., Sun, C. M., Wang, C. H., Ji, C. N., Zhang, Y., et al. (2009). Adsorption behaviors of Hg(II) on chitosan functionalized by amino-terminated hyperbranched polyamidoamine polymers. *J. Hazard. Mater.* 172, 792–801. doi: 10.1016/j.jhazmat.2009.07.066

Ma, F. B., Ge, Y. M., Liu, N., Pang, X. C., Shen, X. Y., and Tang, B. (2019). *In situ* fabrication of a composite hydrogel with tunable mechanical properties for cartilage tissue engineering. *J. Mater. Chem. B* 7, 2463–2473. doi: 10.1039/C8TB01331D

Ma, P. X. (2008). Biomimetic materials for tissue engineering. *Adv. Drug Deliv. Rev.* 60, 184–198. doi: 10.1016/j.addr.2007.08.041

Malafaya, P. B., Silva, G. A., and Reis, R. L. (2007). Natural-origin polymers as carriers and scaffolds for biomolecules and cell delivery in tissue engineering applications. *Adv. Drug Deliv. Rev.* 59, 207–233. doi: 10.1016/j.addr.2007.03.012

Malda, J., Visser, J., Melchels, F. P., Jungst, T., Hennink, W. E., Dhert, W. J. A., et al. (2013). 25th anniversary article: engineering hydrogels for biofabrication. *Adv. Mater.* 25, 5011–5028. doi: 10.1002/adma.201302042

Man, Z. T., Hu, X. Q., Liu, Z. L., Huang, H. J., Meng, Q. Y., Zhang, X., et al. (2016). Transplantation of allogenic chondrocytes with chitosan hydrogel-demineralized bone matrix hybrid scaffold to repair rabbit cartilage injury. *Biomaterials* 108, 157–167. doi: 10.1016/j.biomaterials.2016.09.002

Mano, J., Silva, G., Azevedo, H., Malafaya, P., Sousa, R., Silva, S., et al. (2007). Natural origin biodegradable systems in tissue engineering and regenerative medicine: present status and some moving trends. *J. R. Soc. Interface* 4, 999–1030. doi: 10.1098/rsif.2007.0220

Mas-Vinyals, A., Gilabert-Porres, J., Figueras-Esteve, L., and Borros, S. (2019). Improving linking interface between collagen-based hydrogels and bone-like substrates. *Colloids Surfaces B* 181, 864–871. doi: 10.1016/j.colsurfb.2019.06.046

Mithoefer, K., McAdams, T., Williams, R. J., Kreuz, P. C., and Mandelbaum, B. R. (2009). Clinical efficacy of the microfracture technique for articular cartilage repair in the knee: an evidence-based systematic analysis. *Am. J. Sports Med.* 37, 2053–2063. doi: 10.1177/0363546508328414

Mohammadi, F., Samani, S. M., Tanideh, N., and Ahmadi, F. (2018). Hybrid scaffolds of hyaluronic acid and collagen loaded with prednisolone: an interesting system for osteoarthritis. *Adv. Pharm. Bull.* 8, 11–19. doi: 10.15171/apb.2018.002

Molinaro, G., Leroux, J. C., Damas, J., and Adam, A. (2002). Biocompatibility of thermosensitive chitosan-based hydrogels: an *in vivo* experimental approach to injectable biomaterials. *Biomaterials* 23, 2717–2722. doi: 10.1016/S0142-9612(02)00004-2

Nair, L. S., and Laurencin, C. T. (2007). Biodegradable polymers as biomaterials. *Prog. Polym. Sci.* 32, 762–798. doi: 10.1016/j.progpolymsci.2007.05.017

Nettles, D. L., Vail, T. P., Morgan, M. T., Grinstaff, M. W., and Setton, L. A. (2004). Photocrosslinkable hyaluronan as a scaffold for articular cartilage repair. *Ann. Biomed. Eng.* 32, 391–397. doi: 10.1023/B:ABME.0000017552.65260.94

Niemeyer, P., Pestka, J. M., Kreuz, P. C., Erggelet, C., Schmal, H., Suedkamp, N. P., et al. (2008). Characteristic complications after autologous chondrocyte implantation for cartilage defects of the knee joint. *Am. J. Sports Med.* 36, 2091–2099. doi: 10.1177/0363546508322131

O'brien, F. J. (2011). Biomaterials & scaffolds for tissue engineering. *Mater. Today* 14, 88–95. doi: 10.1016/S1369-7021(11)70058-X

Park, H., and Lee, K. Y. (2014). Cartilage regeneration using biodegradable oxidized alginate/hyaluronate hydrogels. *J. Biomed. Mater. Res.* 102, 4519–4525. doi: 10.1002/jbm.a.35126

Pelletier, S., Hubert, P., Payan, E., Marchal, P., Choplin, L., and Dellacherie, E. (2001). Amphiphilic derivatives of sodium alginate and hyaluronate for cartilage repair: rheological properties. *J. Biomed. Mater. Res.* 54,102–108. doi: 10.1002/1097-4636(200101)54:1<102::AID-JBM12>3.0.CO;2-1

Peppas, N. A., Hilt, J. Z., Khademhosseini, A., and Langer, R. (2006). Hydrogels in biology and medicine: from molecular principles to bionanotechnology. *Adv. Mater.* 18, 1345–1360. doi: 10.1002/adma.200501612

Pereira, D., Canadas, R., Silva-Correia, J., Marques, A., Reis, R., and Oliveira, J. (2014). Gellan gum-based hydrogel bilayered scaffolds for osteochondral tissue engineering. *Key Eng. Mater.* 587, 255–260. doi: 10.4028/www.scientific.net/KEM.587.255

Peterson, L., Vasiliadis, H. S., Brittberg, M., and Lindahl, A. (2010). Autologous chondrocyte implantation: a long-term follow-up. *Am. J. Sports Med.* 38, 1117–1124. doi: 10.1177/0363546509357915

Pina, S., and Ferreira, J. (2012). Bioresorbable plates and screws for clinical applications: a review. *J. Healthc. Eng.* 3, 243–260. doi: 10.1260/2040-2295.3.2.243

Place, E. S., Evans, N. D., and Stevens, M. M. (2009). Complexity in biomaterials for tissue engineering. *Nat. Mater.* 8, 457–470. doi: 10.1038/nmat2441

Pulkkinen, H. J., Tiitu, V., Valonen, P., Jurvelin, J. S., Lammi, M. J., and Kiviranta, I. (2010). Engineering of cartilage in recombinant human type II collagen gel in nude mouse model *in vivo*. *Osteoarthr. Cartilage* 18, 1077–1087. doi: 10.1016/j.joca.2010.05.004

Ren, K., He, C., Xiao, C., Li, G., and Chen, X. (2015). Injectable glycopolypeptide hydrogels as biomimetic scaffolds for cartilage tissue engineering. *Biomaterials* 51, 238–249. doi: 10.1016/j.biomaterials.2015.02.026

Ren, X., Wang, F. Y., Chen, C., Gong, X. Y., Yin, L., and Yang, L. (2016). Engineering zonal cartilage through bioprinting collagen type II hydrogel constructs with biomimetic chondrocyte density gradient. *BMC Musculoskel. Dis.* 17:301. doi: 10.1186/s12891-016-1130-8

Ribeiro, J. C. V., Vieira, R. S., Melo, I. M., Araújo, V. M. A., and Lima, V. (2017). Versatility of chitosan-based biomaterials and their use as scaffolds for tissue regeneration. *Sci. World J.* 2017, 1. doi: 10.1155/2017/8639898

Ruano-Ravina, A., and Jato Diaz, M. (2006). Autologous chondrocyte implantation: a systematic review. *Osteoarthr. Cartilage* 14, 47–51. doi: 10.1016/j.joca.2005.07.017

Sahana, T. G., and Rekha, P. D. (2018). Biopolymers: applications in wound healing and skin tissue engineering. *Mol. Biol. Rep.* 45, 2857–2867. doi: 10.1007/s11033-018-4296-3

Sahni, V., Tibrewal, S., Bissell, L., and Khan, W. S. (2015). The role of tissue engineering in achilles tendon repair: a review. *Curr. Stem Cell Res. T.* 10, 31–36. doi: 10.2174/1574888X09666140710103154

Sakai, S., Hirose, K., Taguchi, K., Ogushi, Y., and Kawakami, K. (2009). An injectable, *in situ* enzymatically gellable, gelatin derivative for drug delivery and tissue engineering. *Biomaterials* 30, 3371–3377. doi: 10.1016/j.biomaterials.2009.03.030

Sakai, T., Matsunaga, T., Yamamoto, Y., Ito, C., Yoshida, R., Suzuki, S., et al. (2008). Design and fabrication of a high-strength hydrogel with ideally homogeneous network structure from tetrahedron-like macromonomers. *Macromolecules* 41, 5379–5384. doi: 10.1021/ma800476x

Seal, B., Otero, T., and Panitch, A. (2001). Polymeric biomaterials for tissue and organ regeneration. *Mater. Sci. Eng. R Rep.* 34, 147–230. doi: 10.1016/S0927-796X(01)00035-3

Selmi, T. A. S., Verdonk, P., Chambat, P., Dubrana, F., Potel, J. F., Barnouin, L., et al. (2008). Autologous chondrocyte implantation in a novel alginate-agarose hydrogel: outcome at two years. *J. Bone Joint Surg.* 90, 597. doi: 10.1302/0301-620X.90B5.20360

Shelke, N. B., James, R., Laurencin, C. T., and Kumbar, S. G. (2014). Polysaccharide biomaterials for drug delivery and regenerative engineering. *Polym. Adv. Technol.* 25, 448–460. doi: 10.1002/pat.3266

Shin, H., Jo, S., and Mikos, A. (2003). Biomimetic materials for tissue engineering. *Biomaterials* 24, 4353–4364. doi: 10.1016/S0142-9612(03)00339-9

Spiller, K. L., Maher, S. A., and Lowman, A. M. (2011). Hydrogels for the repair of articular cartilage defects. *Tissue Eng. Part B Rev.* 17, 281–299. doi: 10.1089/ten.teb.2011.0077

Stagnaro, P., Schizzi, I., Utzeri, R., Marsano, E., and Castellano, M. (2018). Alginate-polymethacrylate hybrid hydrogels for potential osteochondral tissue regeneration. *Carbohydr. Polym.* 185, 56–62. doi: 10.1016/j.carbpol.2018.01.012

Sun, J. Y., Zhao, X., Illeperuma, W. R. K., Chaudhuri, O., Oh, K. H., Mooney, D. J., et al. (2012). Highly stretchable and tough hydrogels. *Nature* 489, 133–136. doi: 10.1038/nature11409

Tool, B. P. (2001). Hyaluronan in morphogenesis. *Semin.Cell Dev. Biol.* 12, 79–87. doi: 10.1006/scdb.2000.0244

Toole, B. P. (2004). Hyaluronan: from extracellular glue to pericellular cue. *Nat. Rev. Cancer* 4, 528–539. doi: 10.1038/nrc1391

Tritz, J., Rahouadj, R., de Isla, N., Charif, N., Pinzano, A., Mainard, D., et al. (2010). Designing a three-dimensional alginate hydrogel by spraying method for cartilage tissue engineering. *Soft Matter* 6:5165. doi: 10.1039/c000790k

Vallee, F., Muller, C., Durand, A., Schimchowitsch, S., Dellacherie, E., Kelche, C., et al. (2009). Synthesis and rheological properties of hydrogels based on amphiphilic alginate-amide derivatives. *Carbohydr. Res.* 344, 223–228. doi: 10.1016/j.carres.2008.10.029

Vilela, C. A., Correia, C., Oliveira, J. M., Sousa, R. A., Espregueira-Mendes, J., and Reis, R. L. (2015). Cartilage repair using hydrogels: a critical review of *in vivo* experimental designs. *ACS Biomater. Sci. Eng.* 1, 726–739. doi: 10.1021/acsbiomaterials.5b00245

Waibel, K. H., Haney, B., Moore, M., Whisman, B., and Gomez, R. (2011). Safety of chitosan bandages in shellfish allergic patients. *Mil. Med.* 176, 1153–1156. doi: 10.7205/MILMED-D-11-00150

Walker, K. J., and Madihally, S. V. (2015). Anisotropic temperature sensitive chitosan-based injectable hydrogels mimicking cartilage matrix. *J. Biomed. Mater. Res. B* 103, 1149–1160. doi: 10.1002/jbm.b.33293

Wang, S. J., Jiang, D., Zhang, Z. Z., Chen, Y. R., Yang, Z. D., Zhang, J. Y., et al. (2019). Biomimetic nanosilica-collagen scaffolds for *in situ* bone regeneration: toward a cell-free, one-step surgery. *Adv. Mater.* 31:1904341. doi: 10.1002/adma.201904341

Wang, X., Gao, P. Y., Yang, Y. Y., Guo, H. X., and Wu, D. C. (2018). Dynamic and programmable morphology and size evolution via a living hierarchical self-assembly strategy. *Nat. Commun.* 9:2772. doi: 10.1038/s41467-018-05142-3

Wang, Y., Rudym, D. D.,Walsh, A., Abrahamsen, L., Kim, H. J., Kim, H. S., et al. (2008). *In vivo* degradation of three-dimensional silk fibroin scaffolds. *Biomaterials* 29, 3415–3428. doi: 10.1016/j.biomaterials.2008.05.002

Wang, Y. J., Shang, S. H., and Li, C. Z. (2016). Aligned biomimetic scaffolds as a new tendency in tissue engineering. *Curr. Stem Cell Res. Ther.* 11, 3–18. doi: 10.2174/1574888X10666150220155921

Xiao, X., Wang, W., Liu, D., Zhang, H., Gao, P., Geng, L., et al. (2015). The promotion of angiogenesis induced by three-dimensional porous beta-tricalcium phosphate scaffold with different interconnection sizes via activation of PI3K/Akt pathways. *Sci. Rep.* 5:9409. doi: 10.1038/srep09409

Xu, Y., Han, J., and Lin, H. (2017). Fabrication and characterization of a self-crosslinking chitosan hydrogel under mild conditions without the use of strong bases. *Carbohydr. Polym.* 156, 372–379. doi: 10.1016/j.carbpol.2016.09.046

Xu, Y. C., Peng, J., Richards, G., Lu, S. B., and Eglin, D. (2019). Optimization of electrospray fabrication of stem cell-embedded alginate-gelatin microspheres and their assembly in 3D-printed poly(ε-caprolactone) scaffold for cartilage tissue engineering. *J. Orthop. Transl.* 18, 128–141. doi: 10.1016/j.jot.2019.05.003

Yan, X., Chen, Q., Zhu, L., Chen, H., Wei, D., Chen, F., et al. (2017). High strength and self-healable gelatin/polyacrylamide double network hydrogels. *J. Mater. Chem. B* 5, 7683–7691. doi: 10.1039/C7TB01780D

Yang, B., Yao, F., Hao, T., Fang, W., Ye, L., Zhang, Y., et al. (2016). Development of electrically conductive double-network hydrogels via one-step facile strategy for cardiac tissue engineering. *Adv. Health. Mater.* 5, 474–488. doi: 10.1002/adhm.201500520

Yang, J. Z., Zhang, Y. S., Yue, K., and Khademhosseini, A. (2017). Cell-laden hydrogels for osteochondral and cartilage tissue engineering. *Acta Biomaterial.* 57, 1–25. doi: 10.1016/j.actbio.2017.01.036

Yang, W., Zhu, P., Huang, H. L., Zheng, Y. Y., Liu, J., Feng, L. B., et al. (2019). Functionalization of novel theranostic hydrogels with kartogenin-grafted USPIO nanoparticles to enhance cartilage regeneration. *ACS Appl. Mater. Interfaces* 11, 34744–34754. doi: 10.1021/acsami.9b12288

Yang, X. C., Lu, Z. H., Wu, H. Y., Li, W., Zheng, L., and Zhao, J. M. (2018). Collagen-alginate as bioink for three-dimensional (3D) cell printing based cartilage tissue engineering. *Mater. Sci. Eng. C* 83, 195–201. doi: 10.1016/j.msec.2017.09.002

Yang, Y. Y., Wang, X., Yang, F., Wang, L. N., and Wu, D. C. (2018). Highly elastic and ultratough hybrid ionic-covalent hydrogels with tunable structures and mechanics. *Adv. Mater.* 30:1707071: doi: 10.1002/adma.201707071

Yasuda, K., Kitamura, N., Gong, J. P., Arakaki, K., Kwon, H. J., Onodera, S., et al. (2009). A novel double-network hydrogel induces spontaneous articular cartilage regeneration *in vivo* in a large osteochondral defect. *Macromol. Biosci.* 9, 307–316. doi: 10.1002/mabi.200800223

You, F., Chen, X. B., Cooper, D. M. L., Chang, T. J., and Eames, B. F. (2019). Homogeneous hydroxyapatite/alginate composite hydrogel promotes calcified cartilage matrix deposition with potential for three-dimensional bioprinting. *Biofabrication* 11:015015. doi: 10.1088/1758-5090/aaf44a

Yuan, L., Li, B., Yang, J., Ni, Y., Teng, Y., Guo, L., et al. (2016). Effects of composition and mechanical property of injectable collagen I/II composite hydrogels on chondrocyte behaviors. *Tissue Eng. Part A* 22, 899–906. doi: 10.1089/ten.tea.2015.0513

Yuan, T., Zhang, L., Li, K. F., Fan, H. S., Fan, Y. J., Liang, J., et al. (2014). Collagen hydrogel as an immunomodulatory scaffold in cartilage tissue engineering. *J. Biomed. Mater. Res. B* 102, 337–344. doi: 10.1002/jbm.b.33011

Zehnder, T., Sarker, B., Boccaccini, A. R., and Detsch, R. (2015). Evaluation of an alginate-gelatine crosslinked hydrogel for bioplotting. *Biofabrication* 7:025001. doi: 10.1088/1758-5090/7/2/025001

Zeng, L., Yao, Y. C., Wang, D. A., and Chen, X. F. (2014). Effect of microcavitary alginate hydrogel with different pore sizes on chondrocyte culture for cartilage tissue engineering. *Mater. Sci. Eng. C* 34, 168–175. doi: 10.1016/j.msec.2013.09.003

Zhang, J. F., Luo, Z. P., Wang, W. J., Yang, Y. Y., Li, D. W., and Ma, Y. Z. (2019). One-pot synthesis of bio-functionally water-soluble POSS derivatives via efficient click chemistry methodology. *React. Funct. Polym.* 140, 103–110. doi: 10.1016/j.reactfunctpolym.2019.04.013

Zhao, W., Jin, X., Cong, Y., Liu, Y. Y., and Fu, J. (2013). Degradable natural polymer hydrogels for articular cartilage tissue engineering. *J. Chem. Technol. Biotechnol.* 88:327. doi: 10.1002/jctb.3970

Zhu, C. X., Xia, Y. X., Zai, Y. Y., Dai, Y. Q., Liu, X. Y., Bian, J., et al. (2019). Adsorption and desorption behaviors of HPEI and thermoresponsive HPEI based gels on anionic and cationic dyes. *Chem. Eng. J.* 369, 863–873. doi: 10.1016/j.cej.2019.03.169

Zhu, W., Cui, H. T., Boualam, B., Masood, F., Flynn, E., Rao, R. D., et al. (2018). 3D bioprinting mesenchymal stem cell-laden construct with core-shell nanospheres for cartilage tissue engineering. *Nanotechnology* 29:185101. doi: 10.1088/1361-6528/aaafa1

Zhu, X. B., Chen, T. J., Feng, B., Weng, J., Duan, K., Wang, J. X., et al. (2018). Biomimetic bacterial cellulose-enhanced double-network hydrogel with excellent mechanical properties applied for the osteochondral defect repair. *ACS Biomater. Sci. Eng.* 4:3534. doi: 10.1021/acsbiomaterials.8b00682

Conflict of Interest: The authors declare that the research was conducted in the absence of any commercial or financial relationships that could be construed as a potential conflict of interest.

frontiers in Chemistry

ORIGINAL RESEARCH
published: 18 February 2020
doi: 10.3389/fchem.2020.00028

A PEGDA/DNA Hybrid Hydrogel for Cell-Free Protein Synthesis

Jinhui Cui[1†], Dan Wu[1,2†], Qian Sun[3], Xiuzhu Yang[4], Dandan Wang[1], Miao Zhuang[4], Yiheng Zhang[5,6], Mingzhe Gan[1,2] and Dan Luo[7,8*]*

[1] CAS Key Laboratory of Nano-Bio Interface, Suzhou Institute of Nano-Tech and Nano-Bionics, Chinese Academy of Sciences, Suzhou, China, [2] School of Nano-Tech and Nano-Bionics, University of Science and Technology of China, Hefei, China, [3] School of Pharmacy, Xi'an Jiaotong University, Xi'an, China, [4] PLD Technology Co., Ltd., Suzhou, China, [5] Central Laboratory, School of Medicine, Renji Hospital, Shanghai Jiao Tong University, Shanghai, China, [6] State Key Laboratory of Oncogenes and Related Genes, Shanghai Cancer Institute, School of Medicine, Renji Hospital, Shanghai Jiao Tong University, Shanghai, China, [7] Department of Biological and Environmental Engineering, Cornell University, Ithaca, NY, United States, [8] Kavli Institute at Cornell for Nanoscale Science, Cornell University, Ithaca, NY, United States

Cell-free protein synthesis (CFPS) has the advantage of rapid expression of proteins and has been widely implemented in synthetic biology and protein engineering. However, the critical problem limiting CFPS industrial application is its relatively high cost, which partly attributes to the overexpense of single-use DNA templates. Hydrogels provide a possible solution because they can preserve and reutilize the DNA templates in CFPS and have great potential in elevating the protein production yield of the CFPS. Here, we presented a low-cost hybrid hydrogel simply prepared with polyethylene glycol diacrylate (PEGDA) and DNA, which is capable of high-efficient and repeated protein synthesis in CFPS. Parameters governing protein production specific to hybrid hydrogels were optimized. Structures and physical properties of the hybrid hydrogel were characterized. Transcription and expression kinetics of solution phase system and gel phased systems were investigated. The results showed that PEGDA/DNA hydrogel can enhance the protein expression of the CFPS system and enable a repeated protein production for tens of times. This PEGDA/DNA hybrid hydrogel can serve as a recyclable gene carrier for either batch or continuous protein expression, and paves a path toward more powerful, scalable protein production and cell-free synthetic biology.

Keywords: hybrid hydrogel, cell-free protein synthesis, chemical cross-linking, DNA hydrogel, PEGDA

OPEN ACCESS

Edited by:
Yi Cao,
Nanjing University, China

Reviewed by:
Wenguang Liu,
Tianjin University, China
Chaenyung Cha,
Ulsan National Institute of Science and Technology, South Korea

***Correspondence:**
Mingzhe Gan
mzgan2010@sinano.ac.cn
Dan Luo
dl79@cornell.edu

† These authors have contributed equally to this work

Specialty section:
This article was submitted to Polymer Chemistry, a section of the journal Frontiers in Chemistry

Received: *09 November 2019*
Accepted: *09 January 2020*
Published: *18 February 2020*

Citation:
Cui J, Wu D, Sun Q, Yang X, Wang D, Zhuang M, Zhang Y, Gan M and Luo D (2020) A PEGDA/DNA Hybrid Hydrogel for Cell-Free Protein Synthesis. Front. Chem. 8:28. doi: 10.3389/fchem.2020.00028

INTRODUCTION

Cell-free protein synthesis (CFPS) is an *in vitro* life simulation system that synthesizes proteins using cell extracted machinery, exogenous substrates, and DNA or RNA templates without the constraint of cells. CFPS is a versatile technology and has been widely applied in the field of biological research. CFPS systems can use linear DNA template amplified by PCR for protein expression and realize rapid and parallel expression of multiple target genes. The open nature of the CFPS system allows unique environmental control and freedom of design, thus enabling simple and efficient protein production, as well as synthesis of proteins that are difficult to express in living cells, such as transmembrane proteins and toxic proteins (Lim et al., 2016; Henrich et al., 2017; Thoring et al., 2017). It is likely that in the near future, the toolkit of CFPS systems can be further expanded and optimized to facilitate the expression of any desired proteins. In addition, cell-free reactions are scalable, ranging from microliter to liter scale (Zawada et al., 2011). Scaling

up the cell-free protein production system to the liter scale is the basis for large-scale production of pharmaceutical relevant proteins (Stech et al., 2013).

Although CFPS technology has progressed rapidly over the past decade, there are still some challenges to overcome. The problem of high cost and low production yield limited its application in industry. In order to improve the life time of the template and the yield of protein for CFPS, many efforts have been taken from the perspective of inhibiting the activity of the nuclease, preparing an extract from genetically modified strains, improving energy regeneration and byproducts recycling, etc. (Caschera and Noireaux, 2014; Fujiwara and Doi, 2016; Schoborg et al., 2016). These efforts, indeed, improved the protein production of CFPS to a certain degree. But vast DNA consumption in large-scale reactions is still one of the bottlenecks in limiting the development of CFPS industrialization. Hydrogels-incorporated gene templates provided a possible solution to this problem.

Hydrogels are three-dimensional polymeric networks made of highly hydrophilic monomers (Hoare and Kohane, 2008; Pan et al., 2013; Wei et al., 2016; Glass et al., 2018). In the past few decades, numerous hydrogels have been developed based on natural and synthetic molecules such as cellulose, chitosan, polypeptide and poly(acrylic acid), poly(ethylene glycol), and poly(ethylene glycol) diacrylate (PEGDA).

DNA is a natural polymer material that possesses many unique and fascinating properties, including intrinsic genetic functions, broad biocompatibility, precise molecular recognition capability, tunable multifunctionality, and convenient programmability. DNA can be used as the only component of a hydrogel or a cross-linker connecting the main building blocks to form hybrid hydrogels through chemical reactions or physical entanglement. The application of DNA hydrogels has drawn much attention in recent years. For instance, target stimuli-responsive DNA hydrogels were engineered based on DNA aptamers that cross-linked with linear polyacrylamide chains to sense changes of pH, temperature, or the concentration of metabolite and release their load as a result of such a change (Yang et al., 2008). DNA hydrogels were developed as a platform for controlled release delivery of antigens due to their highly efficient cross-linking maintenance in a physiological environment, which allows *in situ* encapsulation and preservation of payloads (Nishikawa et al., 2014).

We previously invented a DNA hydrogel that was termed as P-gel for CFPS. P-gel exhibited great potential in elevating protein production efficiency, yield, and reusability (Park et al., 2009a,b; Kahn et al., 2016). To further reduce the DNA consumption in protein producing hydrogel, in this study, we successfully constructed a PEGDA/DNA hybrid hydrogel for CFPS. The cost of PEGDA/DNA hybrid hydrogel was reduced more than 30 times compared to that of P-gel. The optimized PEGDA/DNA hybrid hydrogel enhanced protein production 22.7-fold over the solution phased reactions. The characterization, transcription, and expression kinetic studies provided an insight into the mechanism of the protein production enhancement. Moreover, it was proved that the PEGDA/DNA hybrid hydrogel can be reused 10 times in CFPS, which showed great potential in large-scale CFPS application.

MATERIALS AND METHODS

Materials

All chemicals, unless otherwise stated, were purchased from Sigma-Aldrich and were used as received. Bacteria *Escherichia coli* BL21 (DE3) strain was preserved in our laboratory. Plasmid pID-sfGFP was reconstructed from a gift plasmid pIJ8660 from Professor Lixin Zhang (East China University of Science and Technology) with a fragment deletion from restriction sites *Nhe*I to *Age*I. Plasmid pUTI-beacon was constructed by replacing the sfGFP gene of pID-sfGFP with the gene coding a urinary trypsin inhibitor protein Bikunin. All primers including 5′ acrydite modified primers and molecular beacon oligos were synthesized by Synbio Technologies. High-fidelity Pfu DNA polymerase for PCR amplification was purchased from Beyotime Biotechnology.

Preparation of PEGDA/DNA Hybrid Hydrogel

The DNA part for the construction of PEGDA/DNA hybrid hydrogel was prepared by PCR with 5′ acrydite modified primers F1/R1 (**Table 1**). Plasmid pID-sfGFP was used as the template for PCR amplification. The reactions contained 1 × high-fidelity PCR master mix with 1 × Pfu buffer (Beyotime). Thermocycling for PCR was 30 s at 98°C for the initial denaturation followed by 10 cycles of 10 s at 95°C, 30 s at 65°C, and 30 s at 72°C and a final extension of 5 min at 72°C. The amplified DNA product was purified with Cycle Pure kit (Omega, Bio-tek) and stored at −20°C before use. The DNA template in the hybrid hydrogel for real-time measurement of mRNA transcription was prepared in the same way as 5′ acrydite modified primers F2/R2 (**Table 1**) and plasmid pUTI-beacon as the PCR template.

To prepare the PEGDA/DNA hybrid hydrogel, PEGDA (M_n = 575) was mixed with acrydite modified linear DNA PCR product at predetermined percentage and concentration, respectively. After fully mixing, a certain amount of ammonium persulfate (APS) and tetramethylethylenediamine (TEMED) were added at equimolar concentrations to start the reaction and were polymerized at room temperature for 3 h unless specified to form the PEGDA/DNA hybrid hydrogel. After the reaction, the hydrogel was soaked and washed with 1 × PBS buffer and

TABLE 1 | Primer and molecular beacon sequences.

Primer	Sequence
F1	5′-Acrydite-TGGAGCGGATCGGGGATTGT-3′
R1	5′-Acrydite-CCGGTCGACTCTAGCTAGAG-3′
F2	5′-Acrydite-ACGTAACTCTAACGTTGACCGGCTGCAGCCC-3′
R2	5′-Acrydite-AGAGTTACGTTGAGAGAGTTAAGCTTGAATTCGG ATCCTTACAGC-3′
Beacon target	5′-AACTCTCTCAACGTAACTCTCTCAACGT-3′
Beacon probe	5′-FAM/mCmCmGmCmAmAmAmAmCmGmUmUmGmAmGm AmGmAmGmAmUmAmAmGmCmGmG-BHQ1-3′

absolute ethanol three times, respectively, to remove the partially reacted monomers and excessive initiators in the hydrogel.

Scanning Electron Microscopy

For scanning electron microscopy (SEM), the hydrogel was freeze-dried for 24 h and brittle-fractured with liquid nitrogen to obtain its cross section. After Au-sputter coating, the microstructure of the freeze-dried hydrogel was observed with field emission scanning electron microscope (FE-SEM S4800, Hitachi).

Swelling Tests of PEGDA/DNA Hybrid Hydrogel

Swelling tests were conducted by using a gravimetric method. Lyophilized hydrogels with confirmed weights were immersed in the CFPS reaction buffer solution (described below). At selected time intervals, the hydrated gels were taken out and wiped with a filter paper to remove excess water from the gel surface and were then weighed. The swelling ratio (SR) was calculated according to the following equation:

$$\mathrm{SR} = W_t / W_d$$

where W_d and W_t denote the weight of the dried hydrogel and the weight of the swollen hydrogel, respectively.

Rheological Characterization of Hydrogel

For rheological measurements, the hydrogel was prepared at 100-μl scale with and without the component of DNA (100 ng/μl). The pre-gel mixture was added to a round shape mold matched with the parallel plate of the rheometer as prepared. After gelation, the gel was taken out from the mold and rheological characterization was conducted with a rheometer (Kinexus pro+). An 8-mm parallel-plate geometry and a gap of 2 mm are used for all experiments, which are done at 25°C. A solvent trap is used to prevent water evaporation during the measurements. Frequency sweep measurements are carried out over the frequency range 0.1–10 Hz, and a deformation amplitude $\gamma 0 = 0.01$ is selected to ensure that the oscillatory deformation is within the linear regime.

Cell-Free Protein Production With DNA Hydrogels

The crude extract was prepared as described in Caschera and Noireaux (2014) with slight modifications. *E. coli* BL21 Rosetta2 DE3 strain was used as the lysate source. Besides, isopropyl-thiogalactopyranoside (IPTG, 1 mM) was added to the culture media to induce the production of T7 RNA polymerase when culture OD600 reached 0.6. The cell-free reaction buffer was composed of 50 mM HEPES (pH 8), 1.5 mM ATP and GTP, 0.9 mM CTP and UTP, 0.2 mg/ml tRNA, 0.26 mM coenzyme A, 0.33 mM NAD, 0.75 mM cAMP, 0.068 mM folinic acid, 1 mM spermidine, 30 mM 3-PGA, 1 mM DTT, 2% PEG8000, and 3 mM of each of the 20 amino acids. The Mg-glutamate and K-glutamate concentrations were 4 and 80 nM, respectively.

The cross-linked PEGDA/DNA hybrid hydrogel containing a certain amount of PEGDA and linear DNA was used for cell-free protein production in a solution containing 6.67 μl of cell-free lysate, 10.73 μl of the reaction buffer, and nuclease-free water. Two microliters of the hydrogel was used for CFPS. The reaction volume was 20 μl unless stated otherwise. The reactions were incubated at 30°C in a thermomixer (Eppendorf Thermomixer C) with 1,000 rpm for 15 h. End-point fluorescence was measured with a plate reader (BioTek synergy/H1) and was used to determine the concentration of GFP products according to a GFP standard curve (**Figure S3**). For the reuse of hybrid hydrogel, after each cycle of reaction, the reaction tube was centrifuged at 1,500 rpm for 3 min, and the supernatant was pipetted out and stored for quantification. The remainder of the hydrogel was washed three times with 1 × PBS and added to a fresh lysate solution for CFPS reactions.

Real-Time Measurement of mRNA Transcription

The real-time transcription of mRNA in CFPS reaction was measured with a molecular beacon. The beacon probe bonds to a two-time repeat target sequence (**Table 1**) tagged after the UTI gene once the mRNA was transcribed. One hundred micromolar beacon probe was annealed with a procedure of incubation under a gradient temperature from 95°C to 25°C and stored at 4°C before use. The beacon probe was added to the CFPS reaction at a final concentration of 1 μM, and the reactions were conducted in 96-well plates at 30°C and monitored in real time for 6 h by a plate reader (BioTek synergy/H1).

RESULTS AND DISCUSSION

Principle of PEGDA/DNA Hybrid Hydrogel

The principle for the design of the PEGDA/DNA hybrid hydrogel was to prepare a hydrogel that not only can efficiently express the protein of interests in a cell-free system but also can be easily recovered from the reaction solution in a batch reaction mode or can serve as a long-term template in a continuous reaction mode. A schematic illustration of the preparation process and the structure model of the PEGDA/DNA hybrid hydrogel is shown in **Figure 1**. First, to prepare the hybrid hydrogel DNA component, which contained the gene template for protein expression, a pair of 5′-acrydite modified oligonucleotide primers was used to PCR amplify linear DNA from a plasmid (**Figure S1**). The amplified DNA contains acrydite groups on its both ends and includes all the necessary transcription elements for protein expression *in vivo,* such as a promoter, a ribosome binding site, the gene of interest (*sfgfp* for latter optimization), and a translation terminator. Then, the acrydite modified DNA was mixed with PEGDA. The acrydite group on DNA and the acrylate group on PEGDA were cross-linked and polymerized under the free radical induced addition reaction, when the radical initiator ammonium persulfate (APS) and catalyst tetramethylethylenediamine (TEMED) were added. The resultant hydrogel can be regarded as a PEGDA/DNA hybrid network structure where linear DNA immobilized on the gel matrix. The hydrogel was then submerged in a CFPS system containing cell extract, energy, substrates, salts, and other

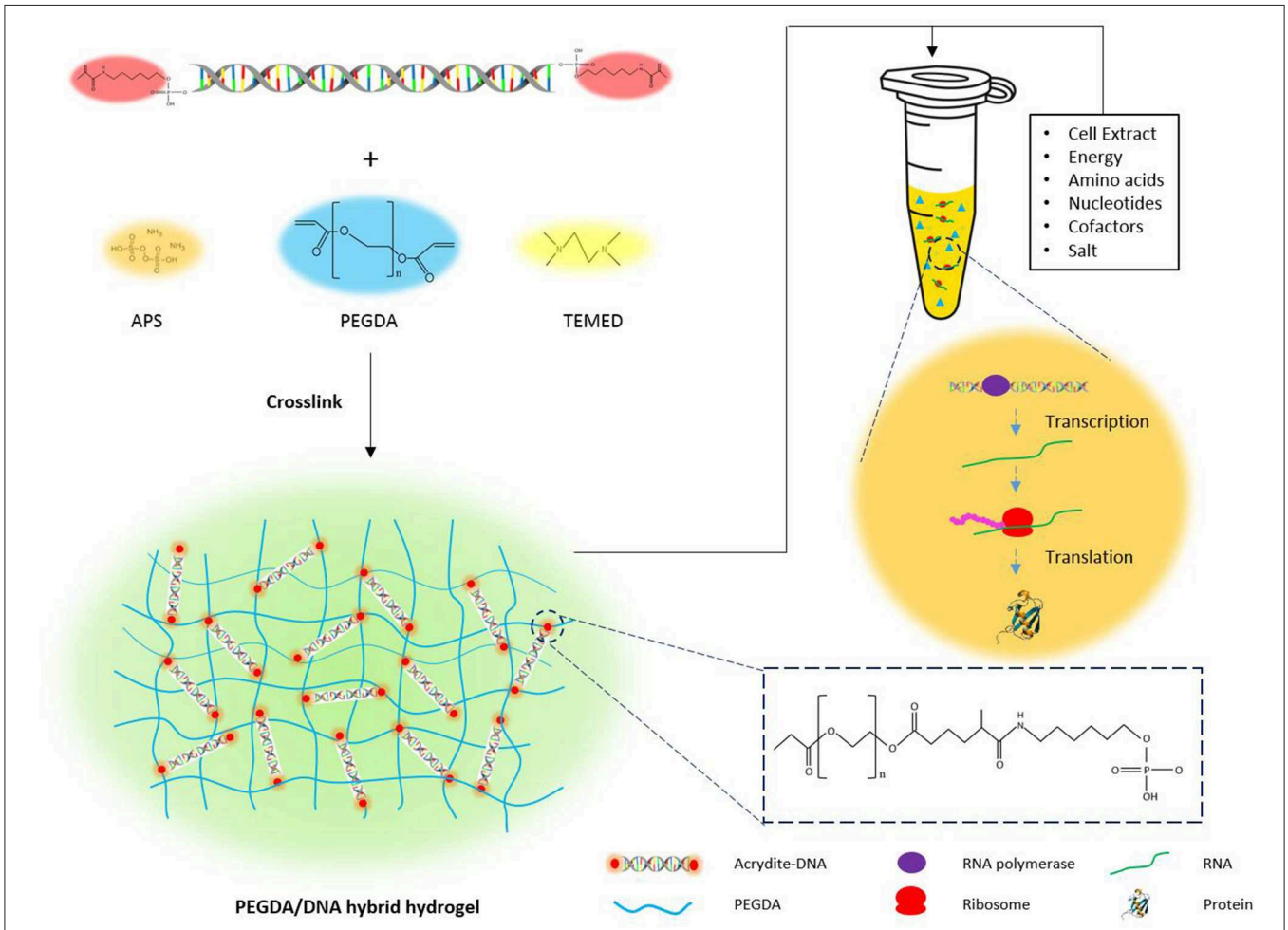

FIGURE 1 | The schematic illustration of the preparation of PEGDA/DNA hydrogel and its use for cell-free protein production.

cofactors needed for protein synthesis to facilitate protein expression in a cell-free manner.

Optimization of PEGDA/DNA Hybrid Hydrogel for CFPS

As a free radical induced reaction product, the hybrid gel mechanical property and functionality were correlated with the reaction parameters. Different reaction parameters resulted diverse mechanical properties and performances of hybrid hydrogels in CFPS. We investigated and optimized the parameters governing protein production that were specific to PEGDA/DNA hybrid hydrogels. These parameters included the concentration of PEGDA, the concentration of APS, reaction gelation time and the amount of DNA in the gel scaffolding.

We first optimized the PEGDA concentration of the hybrid hydrogel with fixed DNA amount at 100 ng for 2 μL hybrid hydrogel in each CFPS reaction. The protein expression results demonstrated that, with the PEGDA concentration ranging from 0.5 to 15%, PEGDA/DNA hybrid hydrogels exhibited overall higher efficiency and better yield under most of PEGDA concentrations compared to the solution phased reactions with linear DNA template (**Figure 2A**). However, the protein yield increased dramatically when the PEGDA concentration increased from 0.5 to 2% and decreased significantly when the PEGDA concentration decreased from 2 to 5%. Two percentage of PEGDA in hybrid hydrogel exhibited most efficient protein production and the protein yield was 270 μg/mL and represented 9.5-fold enhancement over the solution phased reaction. The increase of protein expression at lower PEGDA concentration can be explained by the improved gene stability, high local concentration and fast turnover rate of enzymes in gel format CFPS reactions (Park et al., 2009b; Yang et al., 2013; Guo et al., 2019). While the decrease of protein expression with higher PEGDA concentration could be possibly due to the small pore size of the gel caused by high density of PEGDA. Too small pore size hindered enzymes interacted with the gene inside the gel, thus stopped the gene transcription.

To investigate the effect of APS concentration to the performance of the hybrid hydrogel in CFPS, we fixed the

PEGDA and DNA concentration of the gel (2% and 100 ng in 2 μL gel) and varied the APS concentration used in the preparation of hybrid hydrogel from 0 to 2%. As shown in **Figure 2B**, the expression of sfGFP was highest at 0.1% and decreased dramatically when the APS concentration more than 0.2%. APS functioned as an initiator to generate free radicals which leads to the crosslinking reaction in the gelling system. The higher the concentration of APS, the shorter time required for the gelation and the higher density of cross-linking. At lower APS concentration, the performance of the gel was improved because of the same reason of improved gene stability, high local concentration and fast enzyme turnover rate as at low PEGDA concentration. The decrease of protein expression with higher APS concentration was possibly due to the damage of DNA during gel formation as higher APS concentration provided more free radical which was a common factor causing damage to DNA molecules, resulting that the template could not be transcribed and translated, and the fluorescent protein could not be further expressed.

We noticed that gelation time could affect the gel formation and eventually affect hydrogel functionality in CFPS. Thus, we further optimized the gelation time effect to the protein production of CFPS with hybrid hydrogels formed under different gelling times. At fixed PEGDA, APS and DNA concentration (2%, 0.1%, and 100 ng in 2 μL gel), indeed, the protein production yield increased with prolonged gelation time at the first hour and became stable when the gelation time was more than 2 h (**Figure 2C**).

The above results demonstrated that the PEGDA/DNA hybrid hydrogel could efficiently enhance the protein production in CFPS. To further optimize the protein production yield with PEGDA/DNA hybrid hydrogel, we explored the gene amount effect by varying the DNA amount in the hydrogel while keeping the concentration of PEGDA, APS and gelation time constant (2%, 0.1%, and 3 h). Compared to the solution phased CFPS reaction, the hydrogel system constantly enhanced protein expression in all tested DNA amounts and the protein expression reached plateau with 300 ng of DNA in 2 μL gel (equal to a concentration of 15 ng/μL of solution phased CFPS reaction) (**Figure 2D**). In particular, 300 ng DNA produced 691 ng/μL sfGFP protein representing 22.7-fold enhancement over the solution phased reaction. The protein production yield was slightly decreased when the DNA amount more than 500 ng. This could be attribute to the crowding effect which too crowd molecule environment hindered the diffusion and shuttling of enzymes in gel format of CFPS reaction (Guo et al., 2019).

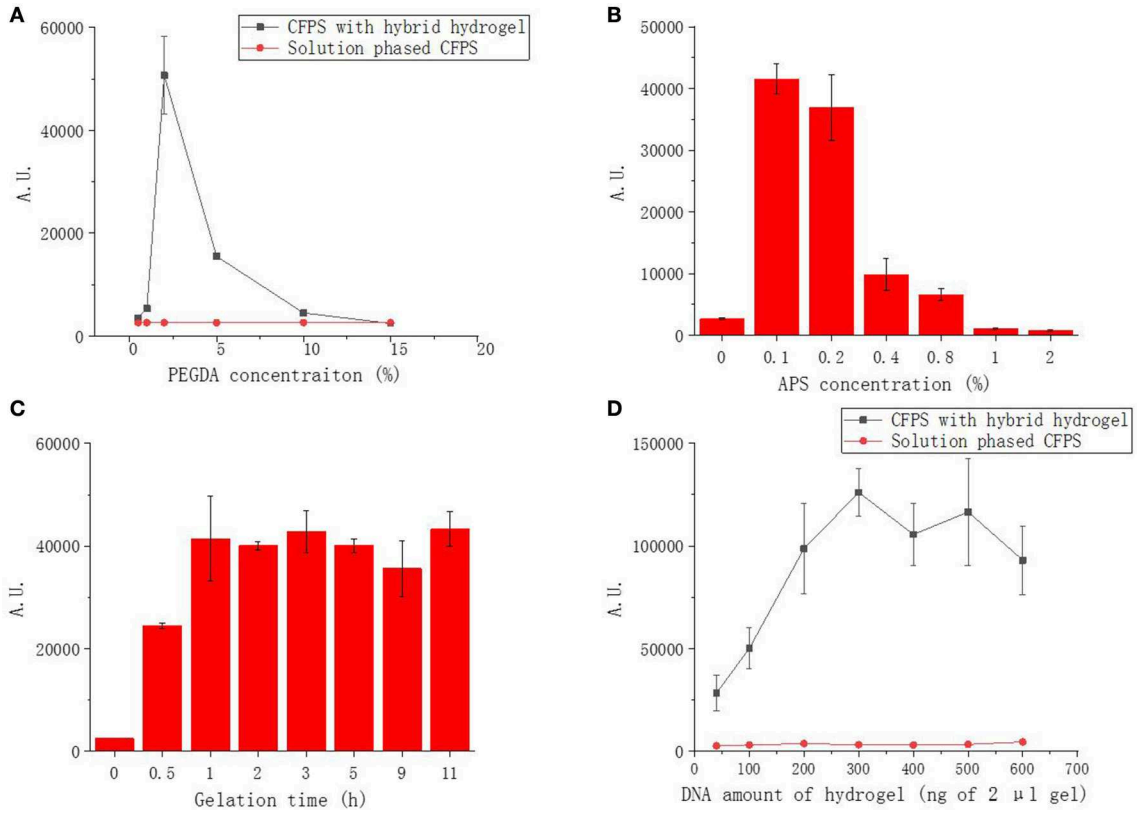

FIGURE 2 | Functional sfGFP expression from PEGDA/DNA hybrid hydrogel phased CFPS with different parameters. **(A)** Effect of PEGDA concentration on fluorescent protein expression. **(B)** Effect of APS concentration on fluorescent protein expression. **(C)** Effect of gelation time on fluorescent protein expression. **(D)** Effect of DNA amount in gel on fluorescent protein expression.

Characterization of Functional PEGDA/DNA Hybrid Hydrogel

From the above results, we have seen that PEGDA/DNA hybrid hydrogel can produce protein with higher efficiency and yield compared with solution phased CFPS. To understand the mechanism of the improvements, we decided to further study the characteristics of functional hybrid hydrogels with the PEGDA concentrations of 2% and 5% as they showed significant protein production improvements in CFPS reactions.

Scanning microscopy images were used to reflect the three-dimensional network structure of hydrogels with/without DNA and different PEGDA concentrations. **Figure 3** showed that with the incorporation of DNA to their gel networks, both 2 and 5% hydrogel become more porous than the gel with PEGDA only. In addition, hybrid hydrogels with 2% of PEGDA were more uniform than that with 5%, which indicated lower PEGDA concentration led to a more homogeneous network. Besides that, the pore size of 2% hydrogel was bigger than that of 5%. These results could partially explain the reason that the hybrid hydrogel with 2% of PEGDA showed a better performance in protein production than 5%. Hydrogel with 5% of PEGDA had a denser gel structure which might hinder the diffusion and shuttling of enzymes, substrates and reaction intermediates inside of the gel when doing CFPS and thus lowered the protein production efficiency. The photographs of patterned PEGDA/DNA hybrid hydrogel with 2% of PEGDA were shown in **Figure 4A**. The gel was stained with DNA-specific dye GelRed and the fluorescent image indicated the incorporation of DNA within the hydrogel.

The swelling of a cross-linked polymer by solvent is often used to assess cross-linking density (Oh et al., 1998). Swelling tests demonstrated that 5% hydrogel had a greater cross-linking density. With the extension of immersion time in CFPS reaction buffer, the swelling rate of two hybrid hydrogel increased sharply and 2% hydrogel swelled approximate 800%, while 5% hydrogels swelled approximate 600%. The biggest SR of 5% hydrogel was smaller than that of 2% (**Figure 4B**). The lower PEGDA content, the smaller the cross-linking density, and the greater swelling rate of the hydrogel. The addition of DNA to the gel networks did not change the swelling properties of the hydrogels.

Cross-linking density determines the mechanical property of the hydrogel (Hong et al., 2015). Low cross-linking density often results a soft gel with more elasticity, while high cross-linking density leads to a tough gel with less elasticity. By changing the concentration of PEGDA, we obtained a series of hybrid hydrogels with different stiffness (data not shown). However, hydrogels for CFPS should neither too soft which could be smashed by the shearing force during CFPS reaction nor too tough and dense which have already been proved by above results of lower protein production efficiency. In order to better understand the physical characteristics of the hybrid hydrogels, we further investigated the rheological properties of the hydrogels as they can reflect molecular motions in polymer sensitively (Li et al., 2017). The storage moduli G' and loss moduli G" of 2 and 5% hydrogels as a function of angular frequency are detected by frequency sweep measurements on a rheometer. The results showed that in either 2 or 5% hydrogels with or without DNA, the storage moduli G' of all hydrogels were obviously dependent on frequency and slightly increased with the augment of frequency (**Figures 4C,D**). The storage modulus in the low frequency region responding to frequency reflected an entanglement gel network or other physical networks (Rubinstein and Colby, 2003). On the other hand, the loss modulus G" of the hydrogels were also dependent on frequency. Loss modulus represents the energy dissipation capacity during deformation and the dependence of G" on frequency indicated that our hydrogels were viscoelastic rather than elastic. Moreover,

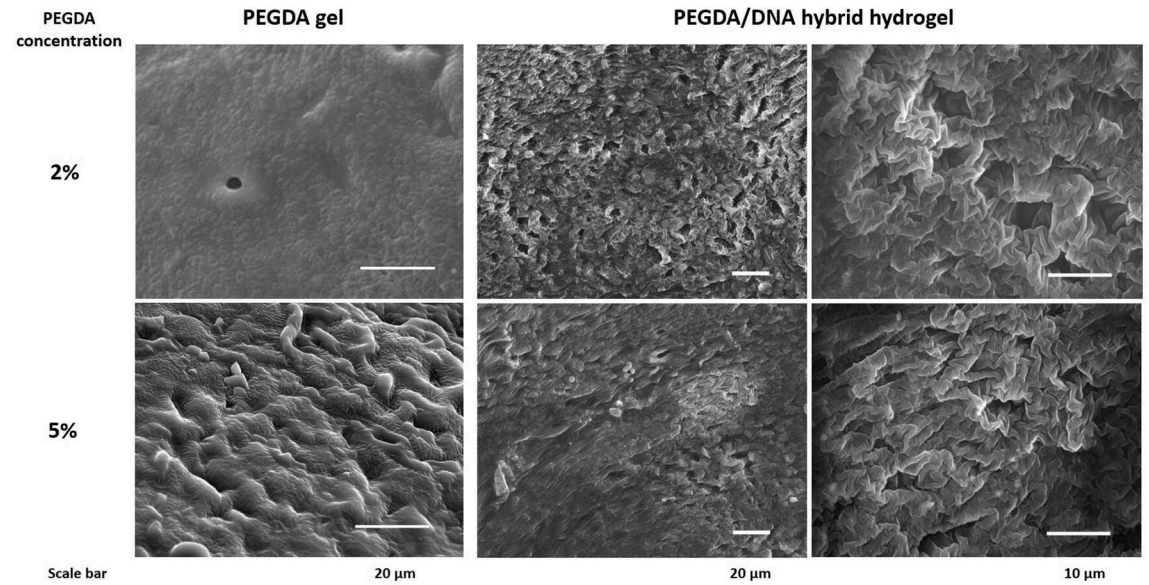

FIGURE 3 | Scanning microscopy images of hydrogel with/without DNA and different concentration of PEGDA.

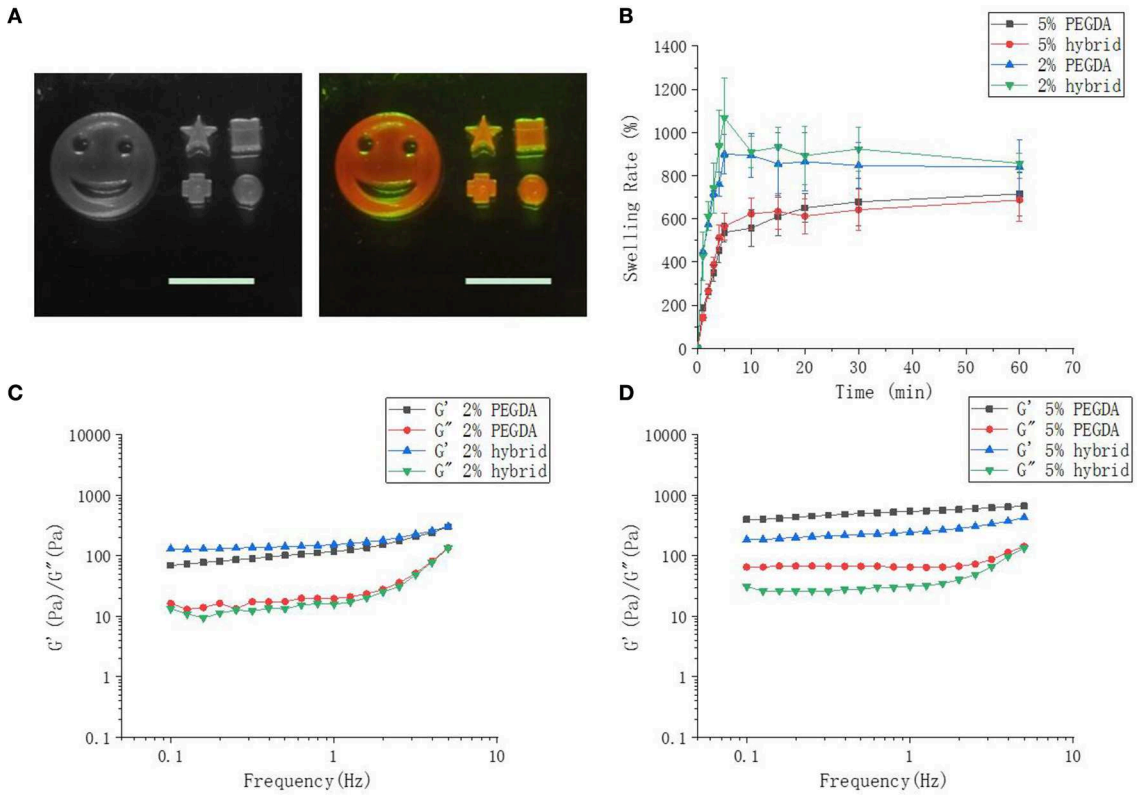

FIGURE 4 | Hybrid hydrogel, swelling and rheology characterizations. **(A)** Images of different patterned hybrid hydrogel with 2% of PEGDA. The scale bar is 1 cm. The right image shows fluorescent gel stained with GelRed. **(B)** Swelling rate of 2 and 5% of hybrid hydrogel in CFPS reaction buffer. **(C,D)** Rheological characterization of 2% and 5% hydrogels.

the dependence degree of G' was close to 0 and G' was higher than G" indicated that chemical cross-linking still dominated though physical entanglement constituted part of the gel network. The addition of DNA to 2% hydrogel did not change the rheological properties of the hydrogel too much compared to that to 5%.

Transcription and Expression Kinetics of Hybrid Hydrogel Phased CFPS

The characterization study of functional hybrid hydrogels showed evidences of their intrinsic properties were conducive to facilitate protein expression. We next employed molecular beacon and fluorescent protein sfGFP to study the kinetics of hydrogel phased cell-free gene transcription and protein expression. The mRNA of a non-fluorescent protein Bikunin was transcribe from the hybrid hydrogel with a 4-time repeat molecular beacon target to monitor the transcription kinetics. Bikunin is a serine protease inhibitor found in the blood serum and urine of humans and other animals. It is also known as urinary trypsin inhibitor (UTI) which is a pharmaceutical protein for the treatment of acute pancreatitis and other diseases (Pugia and Lott, 2005). The main source of pharmaceutical Bikunin is human urine and the recombinant protein is hard to be expressed in living cells with traditional protein expression method. The mRNA yield of UTI were measured in real-time by plate reader with the addition of a molecular beacon probe, which was a hairpin-shaped oligonucleotide probe (Guo et al., 2019). The fluorophore and quencher modified beacon probe was linearized by hybridizing to the mRNA sequence of UTI and then led a fluorescent signal. Protein expression kinetics was conducted by measuring the fluorescent signal of sfGFP instead of molecular beacon in a similar approach.

The transcription kinetic curves showed, at the same amount of gene template, the transcription of mRNA from hybrid hydrogels were always higher than that from solution phased linear DNA (**Figure 5A**). This indicated that the up-regulation of protein expression with PEGDA/DNA hybrid hydrogel was due to the enhancement of mRNA transcription and spatial localization of gene template can accelerate the transcription speed and increase the mRNA yield. Hydrogel with 2% PEGDA had an even higher mRNA transcription level than hydrogel with 5%. This was probably due to the high cross-linking density of 5% hydrogel caused steric hindrance for RNA polymerase and other transcription factors. Similar results were observed for sfGFP expression kinetics (**Figure 5B**). But to our surprise, solution phased reaction showed stronger expression at the initial stage of the experiment which indicated that the translation efficiency of solution phased reaction was higher than that of hydrogel phased reactions. This was reasonable because that translation

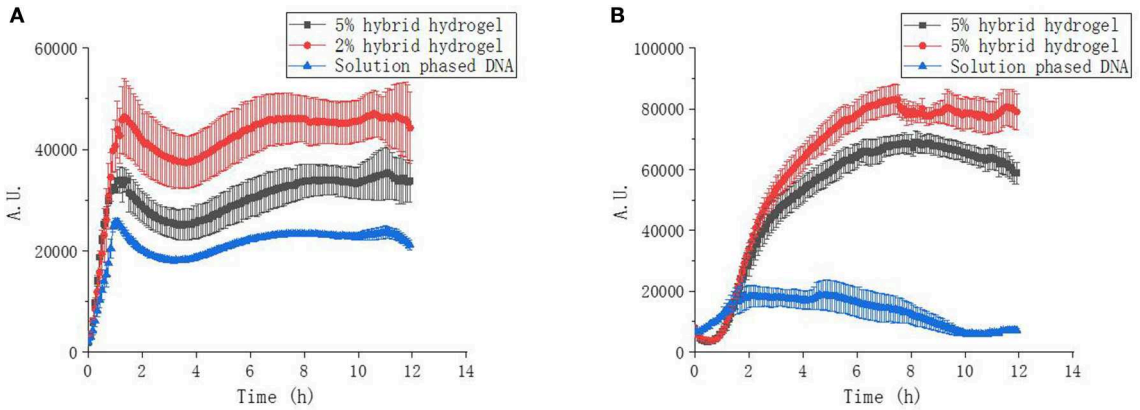

FIGURE 5 | Transcription and expression kinetics of CFPS reactions. **(A)** UTI transcription kinetics of hybrid hydrogels and solution phased CFPS reactions. **(B)** sfGFP expression kinetics of hybrid hydrogels and solution phased CFPS reactions.

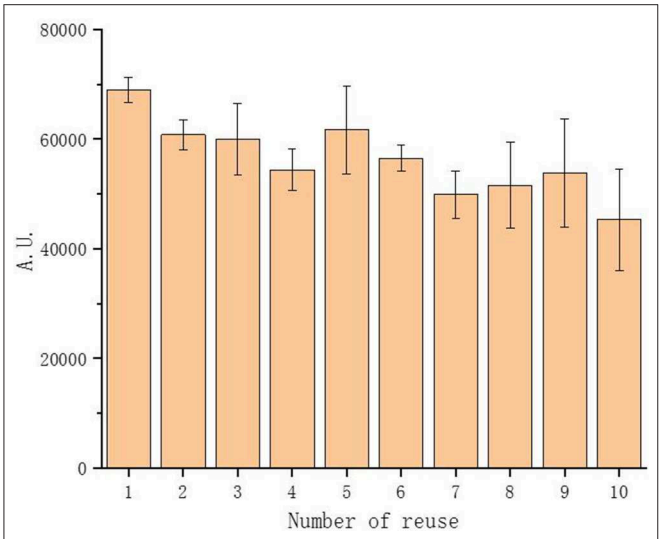

FIGURE 6 | Reuse of PEGDA/DNA hybrid hydrogel.

machinery and substrates were homogenously distributed over the entire reaction environment. To accomplish the translation process, either the mRNA needed to diffuse out of the hydrogel or the translation machinery and substrates required to shuttle and diffused into the hydrogel in the gel phased reaction. More importantly, proteins expressed in hydrogel phased CFPS were totally soluble and functional (**Figure S2**).

Reuse of PEGDA/DNA Hybrid Hydrogel for CFPS

Traditional CFPS utilize solution phased DNA as protein expression template. One of the problems using solution phased DNA for CFPS is that the template DNA are more likely to be lost due to degradation and adhesion on the reaction vessel wall, resulting in low protein production yield and large amounts of gene demand for numerous batches of reactions. On the other hand, hydrogels with the mount of gene templates inside the gel matrix appeared to be protected against degradation due to the characteristic structures and can be easily recovered by a simple centrifugation from lysates after expression for reuse. To confirm that, we tested our PEGDA/DNA hybrid hydrogel as a recyclable gene carrier for repeated protein production with CFPS. As expected, the hybrid hydrogel can successfully be reused up to 10 times without significant loss on protein production yields (**Figure 6**).

CONCLUSION

In conclusion, we presented a strategy for constructing a hybrid hydrogel integrating cross-linking chemicals, PEGDA in our case, and DNA *via* free radical induced polymerization. The PEGDA/DNA hybrid hydrogel can enhance protein expression of CFPS system and serve as recyclable gene carrier for repeated protein production. We believed that, with further exploitation, this PEGDA/DNA hybrid hydrogel can be developed as a platform and applied to large scale cell-free protein production in either batch or continuous mode. The development of PEGDA/DNA hybrid hydrogel paved a path toward more powerful, scalable protein production and cell-free synthetic biology.

DATA AVAILABILITY STATEMENT

The datasets generated for this study are available on request to the corresponding author.

AUTHOR CONTRIBUTIONS

JC and DWu designed and conducted the experiments, performed data analysis, and prepared the manuscript. QS, XY, DWa, MZ, and YZ assisted in designing and performing experiments. MG and DL supervised the study. All authors contributed to the writing of the manuscript.

ACKNOWLEDGMENTS

We acknowledge supports from the National Natural Science Foundation of China (21778071 and 31400087) and the Suzhou Institute of Nano-Tech and Nano-Bionics (Y5AAS11001). MG acknowledges support from the Youth Innovation Promotion Association CAS (2015257). DL acknowledges support from the Kavli Institute at Cornell for Nanoscale Science. We thank Prof. Lixin Zhang for providing plasmids.

SUPPLEMENTARY MATERIAL

The Supplementary Material for this article can be found online at: https://www.frontiersin.org/articles/10.3389/fchem.2020.00028/full#supplementary-material

REFERENCES

Caschera, F., and Noireaux, V. J. B. (2014). Synthesis of 2.3 mg/ml of protein with an all *Escherichia coli* cell-free transcription–translation system. *Biochimie* 99, 162–168. doi: 10.1016/j.biochi.2013.11.025

Fujiwara, K., and Doi, N. (2016). Biochemical preparation of cell extract for cell-free protein synthesis without physical disruption. *PLoS ONE* 11:e0154614. doi: 10.1371/journal.pone.0154614

Glass, S., Trinklein, B., Abel, B., and Schulze, A. (2018). TiO2 as photosensitizer and photoinitiator for synthesis of photoactive TiO_2-PEGDA hydrogel without organic photoinitiator. *Front. Chem.* 6:340. doi: 10.3389/fchem.2018.00340

Guo, X. C., Bai, L. H., Li, F., Huck, W. T. S., and Yang, D. Y. (2019). Branched DNA architectures produced by PCR-based assembly as gene compartments for cell-free gene-expression reactions. *ChemBioChem.* 20, 2597–2603. doi: 10.1002/cbic.201900094

Henrich, E., Sormann, J., Eberhardt, P., Peetz, O., Mezhyrova, J., Morgner, N., et al. (2017). From gene to function: cell-free electrophysiological and optical analysis of ion pumps in nanodiscs. *Biophys. J.* 113, 1331–1341. doi: 10.1016/j.bpj.2017.03.026

Hoare, T. R., and Kohane, D. S. (2008). Hydrogels in drug delivery: progress and challenges. *Polymer* 49, 1993–2007. doi: 10.1016/j.polymer.2008.01.027

Hong, S. M., Sycks, D., Chan, H. F., Lin, S. T., Lopez, G. P., Guilak, F., et al. (2015). 3D printing of highly stretchable and tough hydrogels into complex, cellularized structures. *Adv. Mater.* 27, 4035–4040. doi: 10.1002/adma.201501099

Kahn, J. S., Ruiz, R. C. H., Sureka, S., Peng, S. M., Derrien, T. L., An, D., et al. (2016). DNA microgels as a platform for cell-free protein expression and display. *Biomacromolecules* 17, 2019–2026. doi: 10.1021/acs.biomac.6b00183

Li, J. B., Liu, H. C., Wang, C., and Huang, G. S. (2017). A facile method to fabricate hybrid hydrogels with mechanical toughness using a novel multifunctional cross-linker. *RSC Adv.* 7, 35311–35319. doi: 10.1039/C7RA05645A

Lim, H. J., Park, Y. J., Jang, Y. J., Choi, J. E., Oh, J. Y., Park, J. H., et al. (2016). Cell-free synthesis of functional phospholipase A1 from *Serratia* sp. *Biotechnol. Biofuels* 9:159. doi: 10.1186/s13068-016-0563-5

Nishikawa, M., Ogawa, K., Umeki, Y., Mohri, K., Kawasaki, Y., Watanabe, H., et al. (2014). Injectable, self-gelling, biodegradable, and immunomodulatory DNA hydrogel for antigen delivery. *Control. Release* 180, 25–32. doi: 10.1016/j.jconrel.2014.02.001

Oh, K. S., Oh, J. S., Choi, H. S., and Bae, Y. C. (1998). Effect of cross-linking density on swelling behavior of NIPA gel particles. *Macromolecules* 31, 7328–7335. doi: 10.1021/ma971554y

Pan, S. F., Luo, S., Li, S., Lai, Y. S., Geng, Y. Y., He, B., et al. (2013). Ultrasound accelerated gelation of novel L-lysine based hydrogelators. *Chem. Commun.* 49, 8045–8047. doi: 10.1039/c3cc44767g

Park, N., Kahn, J. S., Rice, E. J., Hartman, M. R., Funabashi, H., Xu, J. F., et al. (2009a). High-yield cell-free protein production from P-gel. *Nat. Protoc.* 4, 1759–1770. doi: 10.1038/nprot.2009.174

Park, N., Um, S. H., Funabashi, H., Xu, J. F., and Luo, D. (2009b). A cell-free protein-producing gel. *Nat. Mater.* 8, 432–437. doi: 10.1038/nmat2419

Pugia, M. J., and Lott, J. A. (2005). Pathophysiology and diagnostic value of urinary trypsin inhibitors. *Clin. Chem. Lab. Med.* 43, 1–16. doi: 10.1515/CCLM.2005.001

Rubinstein, M., and Colby, R. H. (2003). *Polymer Physics.* Vol. 23. New York, NY: Oxford University Press.

Schoborg, J. A., Clark, L. G., Choudhury, A., Hodgman, C. E., and Jewett, M. C. (2016). Yeast knockout library allows for efficient testing of genomic mutations for cell-free protein synthesis. *Synth. Syst. Biotechnol.* 1, 2–6. doi: 10.1016/j.synbio.2016.02.004

Stech, M., Broedel, A. K., Quast, R. B., Sachse, R., and Kubick, S. (2013). Cell-free systems: functional modules for synthetic and chemical biology. *Adv. Biochem. Eng. Biotechnol.* 137, 67–102. doi: 10.1007/10_2013_185

Thoring, L., Dondapati, S. K., Stech, M., Wuestenhagen, D. A., and Kubick, S. (2017). High-yield production of "difficult-to-express" proteins in a continuous exchange cell-free system based on CHO cell lysates. *Sci. Rep.* 7:11710. doi: 10.1038/s41598-017-12188-8

Wei, Z., Zhao, J. Y., Chen, Y. M., Zhang, P. B., and Zhang, Q. Q. (2016). Self-healing polysaccharide-based hydrogels as injectable carriers for neural stem cells. *Sci. Rep.* 6:12. doi: 10.1038/srep37841

Yang, D., Peng, S., Hartman, M. R., Gupton-Campolongo, T., Rice, E. J., Chang, A. K., et al. (2013). Enhanced transcription and translation in clay hydrogel and implications for early life evolution. *Sci. Rep.* 3:3165. doi: 10.1038/srep03165

Yang, H., Liu, H., Kang, H., and Tan, W. (2008). Engineering target-responsive hydrogels based on aptamer - target interactions. *Am. Chem. Soc.* 130:6320. doi: 10.1021/ja801339w

Zawada, J. F., Yin, G., Steiner, A. R., Yang, J., Naresh, A., Roy, S. M., et al. (2011). Microscale to manufacturing scale-up of cell-free cytokine production-a new approach for shortening protein production development timelines. *Biotechnol. Bioeng.* 108, 1570–1578. doi: 10.1002/bit.23103

Conflict of Interest: XY and MZ are employed by PLD Technology Co., Ltd.

The remaining authors declare that the research was conducted in the absence of any commercial or financial relationships that could be construed as a potential conflict of interest.

frontiers in Chemistry

ORIGINAL RESEARCH
published: 25 February 2020
doi: 10.3389/fchem.2020.00115

Study on Large Deformation Behavior of Polyacrylamide Hydrogel Using Dissipative Particle Dynamics

*Jincheng Lei, Shuai Xu, Ziqian Li and Zishun Liu**

International Center for Applied Mechanics, State Key Laboratory for Strength and Vibration of Mechanical Structures, Xi'an Jiaotong University, Xi'an, China

Meso-scale models for hydrogels are crucial to bridge the conformation change of polymer chains in micro-scale to the bulk deformation of hydrogel in macro-scale. In this study, we construct coarse-grain bead-spring models for polyacrylamide (PAAm) hydrogel and investigate the large deformation and fracture behavior by using Dissipative Particle Dynamics (DPD) to simulate the crosslinking process. The crosslinking simulations show that sufficiently large diffusion length of polymer beads is necessary for the formation of effective polymer. The constructed models show the reproducible realistic structure of PAAm hydrogel network, predict the reasonable crosslinking limit of water content and prove to be sufficiently large for statistical averaging. Incompressible uniaxial tension tests are performed in three different loading rates. From the nominal stress-stretch curves, it demonstrated that both the hyperelasticity and the viscoelasticity in our PAAm hydrogel models are reflected. The scattered large deformation behaviors of three PAAm hydrogel models with the same water content indicate that the mesoscale conformation of polymer network dominates the mechanical behavior in large stretch. This is because the effective chains with different initial length ratio stretch to straight at different time. We further propose a stretch criterion to measure the fracture stretch of PAAm hydrogel using the fracture stretch of C-C bonds. Using the stretch criterion, specific upper and lower limits of the fracture stretch are given for each PAAm hydrogel model. These ranges of fracture stretch agree quite well with experimental results. The study shows that our coarse-grain PAAm hydrogel models can be applied to numerous single network hydrogel systems.

Keywords: polyacrylamide hydrogel, dissipative particle dynamics, large deformation behavior, effective network, fracture criterion

OPEN ACCESS

Edited by:
Kerstin G. Blank, Max Planck Institute of Colloids and Interfaces, Germany

Reviewed by:
Akash Arora, Massachusetts Institute of Technology, United States
Armand Soldera, Université de Sherbrooke, Canada

****Correspondence:***
Zishun Liu
zishunliu@mail.xjtu.edu.cn

Specialty section:
This article was submitted to Polymer Chemistry, a section of the journal Frontiers in Chemistry

Received: *04 December 2019*
Accepted: *07 February 2020*
Published: *25 February 2020*

Citation:
Lei J, Xu S, Li Z and Liu Z (2020) Study on Large Deformation Behavior of Polyacrylamide Hydrogel Using Dissipative Particle Dynamics. Front. Chem. 8:115. doi: 10.3389/fchem.2020.00115

INTRODUCTION

A hydrogel is a network of polymer chains swollen in water. Synthetic hydrogels have developed rapidly since the landmark research by Wichterle and Lím (1960). Due to the large water content, hydrogels can be bio-compatible, highly compliant and exhibit low friction, making them widely used for personal care and medical applications, such as superabsorbent diapers (Masuda, 1994), contact lenses (Caló and Khutoryanskiy, 2015), drug delivery (Li and Mooney, 2016; Liu et al., 2017), tissue engineering (Lee and Mooney, 2001; Haque et al., 2012; Lienemann et al., 2012; Xu et al., 2018), and wound dressing (Li et al., 2017). However, the large water content also makes

hydrogels have very low resistance to deformation and fracture (Zheng et al., 2018; Xu and Liu, 2019) and hard to be used as load-bearing structures. Since Gong's (Gong et al., 2003) work, diverse efforts have been made to design tough hydrogels by building dissipations into the networks (Zhao, 2014). Examples include double-network hydrogels (Gong et al., 2003; Henderson et al., 2010), poly(vinyl alcohol) hydrogels with crystalline domains (Peppas and Merrill, 1976; Stauffer and Peppast, 1992), hydrogels with hybrid physical and chemical crosslinkers (Kong et al., 2003; Shull, 2012; Sun et al., 2012), and hydrogels with transformable domains (Brown et al., 2009). It is well-known that the hyper-elastic nature of hydrogel originates from its crosslinking polymer network (Liu Z. et al., 2015). Yet the crosslinking polymer network in hydrogels still stays in the realm of hypothesis since the dynamic experimental observations and determinations are inconvenient at such a micro level. In order to reveal the true nature of the crosslinking polymer network during the deformation and fracture of hydrogels, we have to bring ourselves down to the mesoscale or even molecular scale, where molecular dynamics (MD) simulations and Monte-Carlo simulations could be an effective approach.

Researchers have proposed all-atom models (Tönsing and Oldiges, 2001; Oldiges and Tönsing, 2002; Wu et al., 2009; Mathesan et al., 2016; Xu et al., 2016; Hou et al., 2019) to investigate the structural and physical properties of hydrogels, such as the hydrogen-bond configuration and thermal conductivity. These models usually contain only several short polymer chains whose lengths are in the same scale of the persistent length of polymer chains. This makes them hard to depict the compliant polymer network in hydrogels. Besides, most researches focus on the equilibrium properties of hydrogels without bearing loads. An et al. (2019) investigated the mechanical properties of hydrogels via MD simulations, but the strain is small. Jang et al. (2007) obtained the stress-strain curve under large strain, but the stress level is several orders of magnitude larger (as well as An et al.'s work) than real situations. Although many general force fields, including consistent valence force field (CVFF) (Dauber-Osguthorpe et al., 1988), optimized potentials for liquid simulations (OPLS) force field (Kaminski et al., 1994), GROMACS force field (Berendsen et al., 1995), DREIDING force field (Mayo et al., 1990), etc., have been proposed and can be applied to the polymer-solvent system, the sophisticated atomic models with too many structural details hinders the extension of length scale and time scale. Since the large deformation behavior of hydrogels originates from the conformation change of the polymer network in mesoscale, a coarse-grain model of hydrogels balancing the structural features and computational time is in great need.

Dissipative particle dynamics (DPD) (Hoogerbrugge and Koelman, 1992; Koelman and Hoogerbrugge, 1993) is a mesoscale particle method that bridges the gap between macroscopic and microscopic simulations. Combining with coarse-grain methods, it is very suitable for simulating gaseous or fluid systems. DPD has been successfully applied to diverse areas of interests, especially to simulate the equilibrium and dynamical properties of polymers in solution as well as polymer gels (Spenley, 2000; Maiti and McGrother, 2004; Symeonidis et al., 2005; Zhao, 2014). When applying DPD, or other coarse grained MD simulations to study polymers or polymer gels, a physical crosslinking process is crucial to construct real polymer network. However, many previous works (Wu et al., 2009; Nawaz and Carbone, 2014; Mathesan et al., 2016; Jin et al., 2018; Hou et al., 2019; Xing et al., 2019) construct polymer models based on hypothetical cross-linked network structures which inevitably loses some structural components, such as branch chains, polymer loops, unreacted monomers, short segments et al. For instance, Xing et al. (2019) constructed 3D cross-linked networks for DNA hydrogels, while the chain length between cross-linking points was set to be constant. Jin et al. (2018) built randomly cross-linked polymer networks with the real cross-linking densities, while all the polymer chains are forced to crosslink.

In this study, the polyacrylamide hydrogel is taken to be the representative material. We build the bead-spring models of PAAm hydrogel by using DPD to simulate the crosslinking process from the mixture of monomers, cross-linkers and water. Details on the model construction are discussed in section Materials and Methods. The large deformation and fracture behavior of our PAAm hydrogel models are discussed in section Results.

MATERIALS AND METHODS

In this section, a series of bead-spring models for PAAm hydrogel are constructed and tested using DPD simulations. In addition, a full-atom model for PAAm chain is also constructed and tested using classical MD simulations to provide the fracture criterion of the polymer chains in DPD simulations. All these simulations are performed in large-scale atomic/molecular massive parallel simulator (LAMMPS) (Plimpton, 1995).

Governing Equation of DPD Simulations

DPD method shares the common features of coarse-grained MD as the larger length scale and time scale by predigesting the exquisite atomic interactive force in classical MD. A softer interactive force between particles is adopted in DPD simulations and divided into three parts as (Groot and Warren, 1997)

$$\begin{aligned}
\vec{F}_i &= \sum_{j\neq i} \vec{F}_{ij}^{C} + \vec{F}_{ij}^{D} + \vec{F}_{ij}^{R} \\
F_{ij}^{C} &= a_{ij}\omega\left(r_{ij}\right), \; F_{ij}^{D} = -\gamma\omega^2\left(r_{ij}\right)\left(\hat{r}_{ij}\cdot\vec{v}_{ij}\right), \\
F_{ij}^{R} &= \sigma\omega\left(r_{ij}\right)\alpha\left(\Delta t\right)^{-\frac{1}{2}} \\
\omega\left(r_{ij}\right) &= \begin{cases} 1-\frac{r_{ij}}{R_c}, & r_{ij}\leq R_c \\ 0, & r_{ij} > R_c \end{cases}
\end{aligned}$$

where r_{ij} is distance between two beads. The F_{ij}^{C} is the conservative force. It acts as the repulsive force between two particles within the cutoff R_c, which is linearly related to the particle distance with the repulsive coefficient a_{ij}. The F_{ij}^{D} is the dissipative force which always points to the opposite direction of the relative velocity $\vec{v}_{ij}$ along the center line of two particles. It

represents the effect of viscosity, depending on a coefficient γ and the distance between particles. The F_{ij}^R is the random force. It also depends on a coefficient $\sigma = \sqrt{2kT\gamma}$ and the distance between two particles as well as a random variable α with the standard normal distribution. Since the dissipative force and random force act as the energy sink and source, the balance between two forces as a thermostat can be ensured by $\sigma = 3$, following the Groot's (Groot and Warren, 1997; Groot and Rabone, 2001) work.

Besides, it is convenient to normalize the mass of particles, the energy and the length of interactive cutoff as non-dimensional $m = kT = R_c = 1$, where k is the Boltzmann constant and T the temperature. Thus, the Newton's second law governing the particles motion is expressed by $\frac{d^2\vec{r}_i}{dt^2} = \vec{F}_i$. Meanwhile, the unit temperature $T = 1$ in normalized DPD refers to absolute temperature 300 K. The time unit in DPD simulations is also normalized as $\tau = \sqrt{mR_c^2/kT} = 1$.

An additional bonding force acting as the bonds between polymer beads is described as

$$\vec{F}_i^B = \sum_j C(r_{ij} - r_0)\hat{r}_{ij}$$

where C is the bond coefficient. A soft bond coefficient 4.0 (Rao et al., 2014; Wei et al., 2017) is used in the crosslinking simulations, while $C = 116,000$ is adopted in tension simulations to match the real ratio of C-C bond strength to the heat fluctuation. r_0 is the equilibrium bond length between two polymer beads. We take the mean distance between two beads $r_0 = R_c = 1$.

Coarse-Graining

Three types of molecules are coarse-grained in our study, i.e., acrylamide(AAm), methylenebisacrylamide (MBAA) and water as shown in **Figure 1**. Since the mass of all particles in DPD simulations are considered to be the same, one AAm bead refers to two AAm monomers, one MBAA bead refers to one MBAA molecules, and one water bead refers to eight water molecules, to make sure their relative molecular weights are close. The validity of a coarse-grained model is determined by the interactive parameters in force field. According to Groot and Warren (1997) and Liu M. B. et al. (2015), the repulsive coefficient a for the same type of beads can be approximated by

$$a_{ii} = \frac{75kT}{\rho}$$

where ρ is the number of beads in the volume of R_c^3. Previous researchers chose $\rho = 3$ to get a better match on the compressibility of the model fluid (Liu M. B. et al., 2015). However, this high number density of beads leads to pure repulsion, because the mean distance between beads is much smaller than the repulsion cutoff R_c in conservative force F^C. It makes the model solution under very high hydrostatic pressure when the number density is higher than $\sqrt{2}$ for the closest packing beads. Here we choose $\rho = \sqrt{2}$ to simulate the crosslinking process only affected by the viscosity and heat fluctuations, where the repulsion force between closest packing beads just vanishes. For different types of beads, Groot (Groot and Warren, 1997; Groot and Rabone, 2001) suggest the repulsive coefficient a_{ij} is linearly related to the Flory-Huggins parameters χ_{ij} with $a_{ij} = a_{ii} + 3.27kT\chi_{ij}$, where the χ_{ij} characterizes the mixture energy needed to form an equilibrium interaction between two clusters. We assume the monomer beads and crosslinker beads are the same type of beads denoted as polymer beads, and we take the repulsive coefficient $\chi_{ij} = 0.57$ between polymer beads with water beads (Wei et al., 2017).

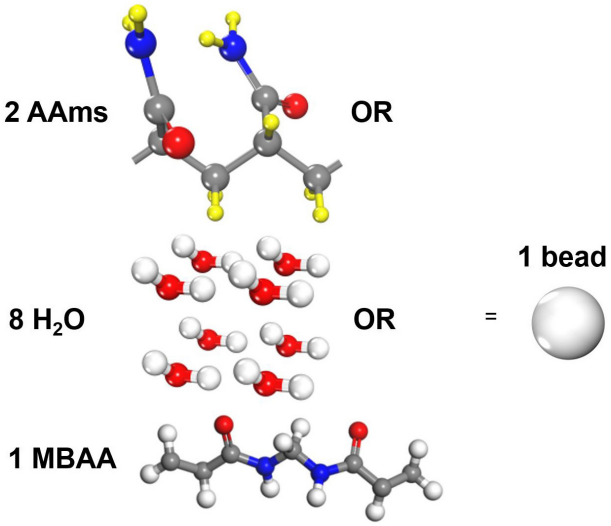

FIGURE 1 | Coarse-grain scale of the polyacrylamide hydrogel model (One AAm bead refers to two connected AAm monomers. One water bead refers to eight water molecules. One MBAA bead refers to one MBAA molecule).

The real time scale of a DPD time unit can be estimated by comparing the diffusivity of water beads with the real diffusivity of water as follows (Groot and Rabone, 2001)

$$\tau = \frac{N_m D_{simu} R_{cr}^2}{D_{water}},$$

where the N_m is the coarse-grained scale representing the water molecule number that a water bead is, D_{water} the real diffusivity of water $2.43 \times 10^{-9}\ m^2/s$, R_{cr} the real length of the DPD cutoff which can be obtained by the real volume of one water beads as 6.98 Å. The simulated diffusivity of water D_{simu} can be obtained from three independent simulations and calculated by $D_{simu} = \frac{\langle r^2 \rangle}{6t} = 0.212 \pm 0.002$ as shown in **Figure 2**, where $\langle r^2 \rangle$ is the mean square displacement of all water beads. Therefore, the real time for DPD unit time is about 340.0 ps.

Modeling and Testing

As mentioned in introduction, most current models of polymer network are constructed based on the theoretical hypothesis, such as full crosslinking, crosslinking with certain orientation or certain degree of polymerization etc. However, the real polymer networks in PAAm hydrogels are mostly imperfect. In order

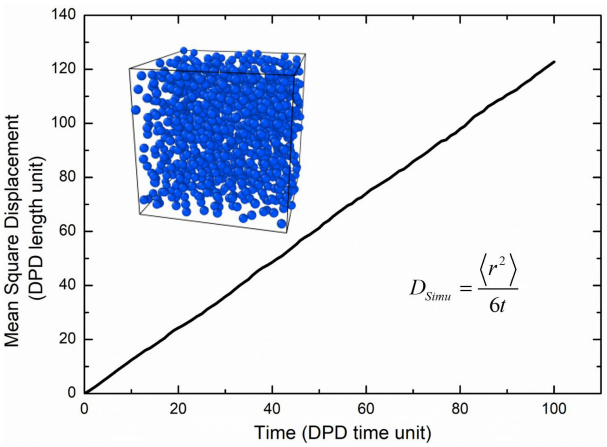

FIGURE 2 | Self-diffusion of water beads.

to reveal the real conformation of the polymer network, we simulate the crosslinking process of the precursor solution. The crosslinking process of PAAm hydrogel in experiments often lasts hours because it is a growth of polymer chains guided by initiator (Sun and Marshall, 1981), such as tetramethylethylenediamine (TEMED) (Bai et al., 2017; Tang et al., 2017; Zhang et al., 2018; Lei et al., 2019). Although the time scale of DPD simulation is increased by coarse-grain method, it still cannot affords the full simulation of real crosslinking process to capture both the growth of polymer chains and the diffusion of monomers and crosslinkers in precursor solution. However, when the amount of initiator is close to the magnitude of precursor, the growth of polymer chains starts from everywhere in precursor solution, so that it can be simply regarded as the simultaneously bonding process as long as reactant molecules are close enough. Moreover, if we consider unreacted molecules to be identical in the precursor solution, it would not make much difference on the crosslinking polymer network when the diffusion length of unreacted molecules is much larger than their mean distance within our simulation time.

Based on the assumptions above, we conduct the following crosslinking simulations. Random mixture models with water content 80% are built and crosslinked under different temperatures. Temperature in DPD simulations determines the diffusion length of beads. Low temperature with insufficient diffusion length leads to localized polymerization in which it's hard to form an effective polymer network throughout hydrogel. In order to find the proper temperature for crosslinking in DPD simulations, we choose six temperatures, i.e., $T = 1, 3, 5, 7, 9, 11$, to investigate the effect of diffusion length on the crosslinking process. Meanwhile, the effect of different water contents on the crosslinking process is investigated by simulating the crosslinking process of random mixture models with different water content 99, 98, 97, 96, and 95%. These high water contents are chosen to find the lowest crosslinking threshold of precursor content.

All random mixture models are composed of 125,000 beads with the certain precursor mass ratio AAm:MBAA = 1:0.002. For example, models with water content 80% have 100,000 water beads, 24,954 AAm beads and 46 MBAA beads. The simulation box size is $(44.54R_c)^3$. NVT ensemble is adopted as the thermostat. Time step is set as 0.01 DPD time. The mixture models are relaxed for 10,000 time steps first. Then the crosslinking process is performed by creating bonds between polymer beads every 10 time steps within 500,000 time steps, when the distance between two polymer beads is smaller than one DPD cutoff R_c. The crosslinked models are then cooled down to $T = 1$ within 100,000 time steps and relaxed for another 100,000 time steps. For each water content and temperature, three independent models are generated for statistical averaging. **Figure 3A** is one of the models and **Figure 3B** show its polymer network without water beads, where blue beads are AAm beads, red beads are MBAA beads and green beads are water beads. All the following figures about the model structure are shown without water beads for better view.

Polymer chains in all models are classified into different chain types for structural analysis. Incompressible uniaxial tension tests are simulated in NVT ensemble with $T = 1$ in three loading rates 0.005, 0.001, and 0.0002 per DPD time unit. It should be noted that the loading rates here are true strain rate for the convenience of the implementation of incompressible uniaxial tension in LAMMPS. Thus, the true strain rates in other two directions are set to be half of the loading rate. Time step for tension tests is set as 0.001 DPD time.

Fracture Criterion of Polyacrylamide Chain

The large deformation of PAAm hydrogel is dominated by the polymer network conformation change in mesoscale, while the fracture of polymer chains is determined by the bond break in atomic scale. In order to obtain the fracture criterion of polymer chains in PAAm hydrogel, we build a full-atom model for PAAm chains with two connected AAm monomers as shown in the inset in **Figure 4**. This model corresponds to one AAm bead in our DPD simulations. Consistent valence force field (CVFF) (Dauber-Osguthorpe et al., 1988) is adopted to characterize the electrostatic forces, van der Waals interactions, bonds, bond angles, dihedrals and impropers between atoms. Detailed force field parameters can be found in **Supplementary Material**. Tension is imposed along chain direction in NVT ensemble with the loading rate 0.01/ps and temperature $T = 300K$. The time step is set as 0.1 fs. The energy-strain curve in **Figure 4** shows the fracture of AAm chains occurs when the engineering strain is 0.225. This strain is chosen to be the fracture criterion we use to analyze the fracture properties of PAAm hydrogel models in DPD simulations.

RESULTS

Model Validation

In order to find a proper temperature for crosslinking simulations, six temperatures, i.e., $T = 1, 3, 5, 7, 9, 11$, is used to control the diffusion length of precursor beads in the crosslinking simulations. **Figures 5A–C** show part of the PAAm hydrogel models after crosslinking under temperatures $T = 1, 5, 9$, respectively. To analyze the generated complex

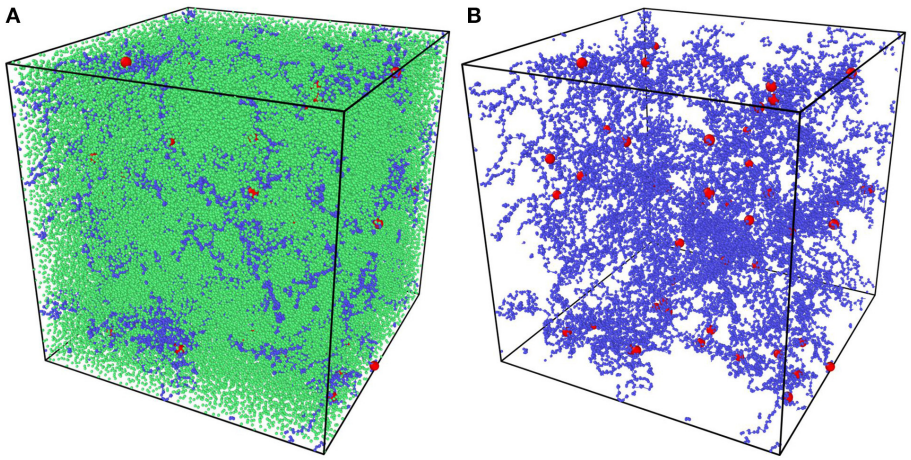

FIGURE 3 | (A) The coarse-grain PAAm hydrogel model. **(B)** The coarse-grain PAAm hydrogel model without water beads (Blue beads are AAm beads. Red beads are MBAA beads. Green beads are water beads).

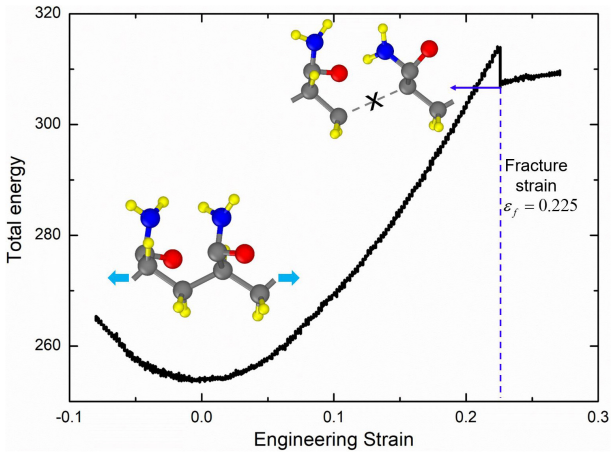

FIGURE 4 | The energy-strain curve of the PAAm chains (The PAAm chain model is composed of two AAm monomers. The fracture strain is 0.225).

structure of PAAm hydrogel models, polymer chains in all models are classified into five types, i.e., effective network chains, branch chains, isolated chains, crosslinking loops and isolated loops, as the schematic diagram shown in **Figure 5D**. Effective network chains form the crosslinking network throughout the hydrogel model. Branch chains attach to the effective network. It may be a chain with one free end or a loop. Isolated chains, crosslinking loops and isolated loops have no covalent bonds with effective network. The number and length of each type of chains are counted and averaged between the same groups of models. The crosslinking rate can be obtained by $N_{bond}/\left(N_{AAm}+2N_{MBAA}\right)$, where N_{bond} is the total bond number, N_{AAm} the number of AAm beads, N_{MBAA} the MBAA beads, and $N_{AAm}+2N_{MBAA}$ the maximum bonds between these monomers and crosslinkers. The final crosslinking rate for all models is above 99.97%. This indicates the crosslinking process in every model is sufficient. Chain numbers and number fractions for different type of chains are counted for all models. The chain lengths for different type of chains are counted as the bond number in current chain. The chain length fraction is calculated by the current chain length over total chain length.

The diffusion length of polymer beads is the key to the formation of polymer network. **Figure 6A** shows the diffusion length per DPD time unit in different temperatures. When $T = 1$, the diffusion length per DPD time unit is $1.13R_c$. This is even lower than the mean distance between polymer beads $1.52R_c$ marked as red dashed line in **Figure 6A**. It makes the precursor solution fail to form polymer network as shown in **Figure 5A**. Polymer beads crosslinking with neighbors form large amount of isolated loops with short length, corresponding to the largest chain number as shown in **Figure 6B** and the highest length fraction of isolated loops. With the increase of temperature from 3 to 11, the diffusion length per DPD time unit is much larger than the mean distance of polymer beads as shown in **Figure 6A**. Polymer network forms in crosslinking process. Both the number fraction and the length fraction of effective network chains shown in **Figures 6B**, **7A** rise up with the temperature increasing. The length fraction of effective network chains reach to the top when $T = 9$. Meanwhile, the total chain number and the length fraction of effective chains and isolated loops tends to converge when temperature increases. This convinces us that our crosslinking simulations are sufficient in high temperatures and our PAAm hydrogel models are reliable. We also note that in **Figure 7A** the length fraction of isolated loops converges to about 7% with the temperature increasing. It indicates that the larger diffusion length, which may results from higher temperature, longer gelation time or more sufficient stirring in experiments, cannot eliminate the formation of isolated loops. The success of forming polymer network proves

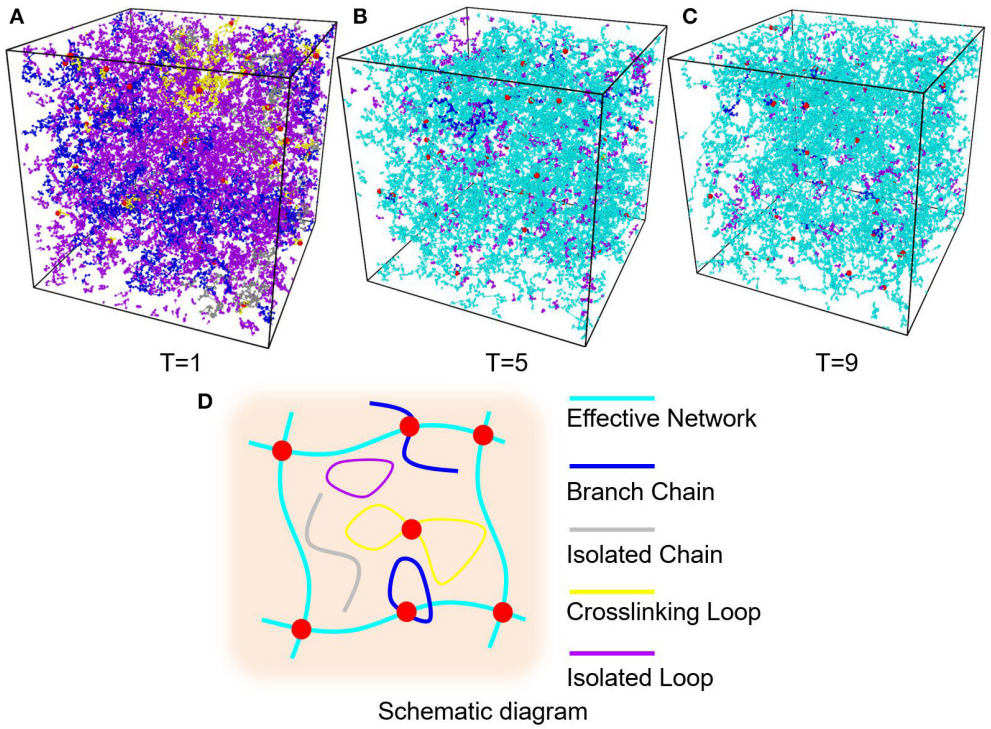

FIGURE 5 | (A) PAAm hydrogel models crosslinking when $T = 1$. **(B)** PAAm hydrogel models crosslinking when $T = 5$. **(C)** PAAm hydrogel models crosslinking when $T = 9$. **(D)** Schematic diagram of the different types of chains in PAAm hydrogel (Cyan chains are effective network chains. Blue chains are branch chains. Gray chains are isolated chains. Yellow chains are crosslinking loops. Magenta chains are isolated loops).

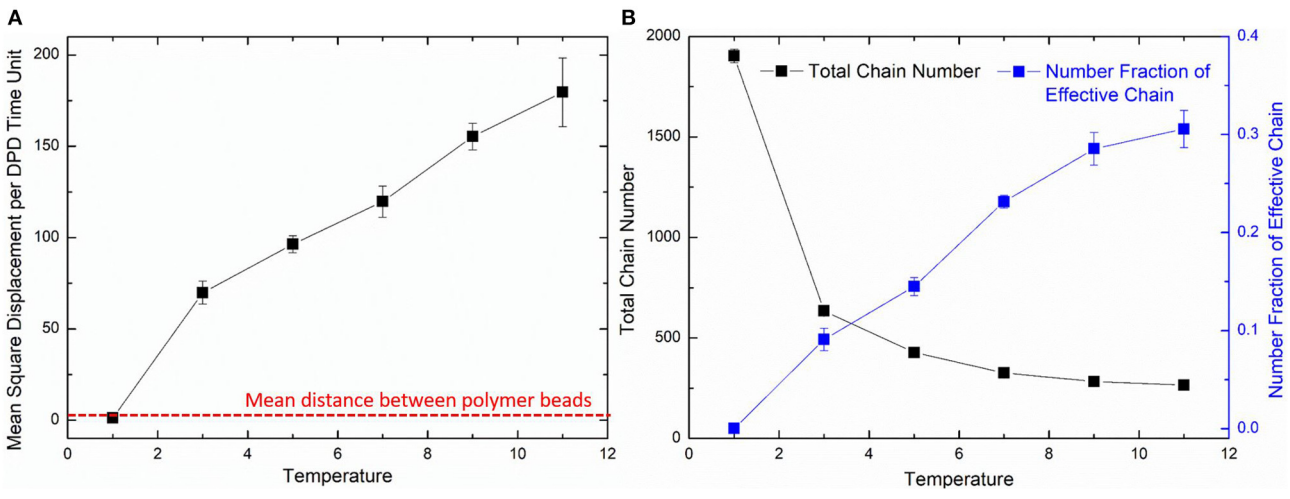

FIGURE 6 | (A) The diffusion length of polymer beads in different temperatures. **(B)** The total chain number and the number fraction of effective chains in PAAm hydrogel models crosslinking under different temperatures.

that our crosslinking simulation is a practical way to construct PAAm hydrogel model.

Further validation of our crosslinking method are conducted by predicting the crosslinking limit of the polymer content. Random mixture models with five water content 99, 98, 97, 96, and 95% are crosslinking with the temperature $T = 9$. **Figure 7B** shows the effective chain ratio of models with different water contents. It can be seen that models with water content 99% fail to form polymer network. Meanwhile, one of the three models with water content 97% also fails to form polymer network as well as one of the three models with water content 98%. These simulations give the crosslinking limit of water content 97%, which is very close to the swelling limit of many PAAm hydrogels in experiments (Zhang et al., 2018). The prediction

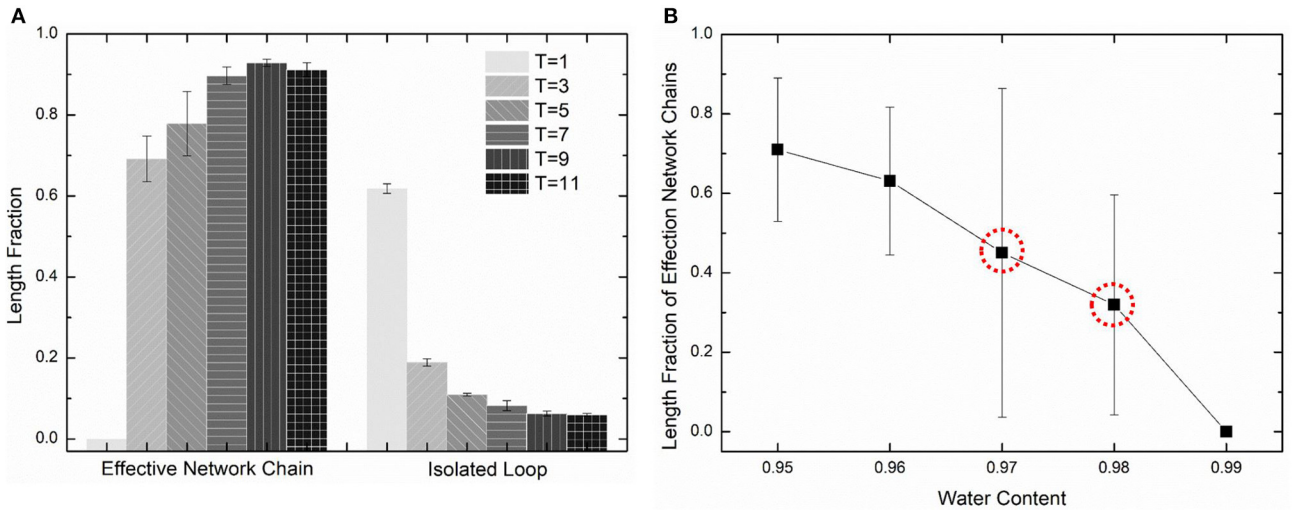

FIGURE 7 | (A) The length fraction of effective network chains and isolated loops in PAAm hydrogel models crosslinking under different temperature. **(B)** The length fraction of effective network chains in PAAm hydrogel models crosslinking under different water contents.

of crosslinking limit also proves the validity of our crosslinking simulations and PAAm hydrogel models.

We choose three PAAm hydrogel models with water content 80% crosslinking at $T = 9$ for further discussion. **Figure 8A** shows the number fraction and the length fraction of all types of chains in these models. Error bars for both the number fraction and length fraction indicate that our crosslinking process is reproducible. We denote all chains except effective network chains as ineffective chains. Only $7.1 \pm 0.9\%$ of polymer beads form ineffective chains, including branch chains $0.9 \pm 0.4\%$ and isolated loops $6.2 \pm 0.6\%$. Because the mean contour length of ineffective chains $8.8 \pm 0.7r_0$ is much lower than the effective network chains $288.7 \pm 10.5r_0$, the length fraction of effective chains is $92.9 \pm 0.9\%$ though the number fraction is $28.5 \pm 1.7\%$. Such high mean contour length leads to compliant effective network with the chain conformation more winding than other full-atom models (Tönsing and Oldiges, 2001; Oldiges and Tönsing, 2002; Wu et al., 2009; Mathesan et al., 2016; Xu et al., 2016; An et al., 2019; Hou et al., 2019) and coarse-grain models (Nawaz and Carbone, 2014; Wei et al., 2017; Xing et al., 2019) of PAAm hydrogels. This mean contour length is very close to that estimated by $N_{AAm} : 2N_{MBAA} = 271$ from precursor ratio. The mean end-to-end distance of effective network chains is $47.0 \pm 3.6r_0$. The distributions of the initial length ratio which is the end-to-end distance over the contour length of each effective network chain in three models are shown in **Figure 8B**. It can be seen that the initial length ratio of effective chains shows nearly a Maxwell distribution. In order to validate the statistical properties of our models, we also present the distribution of two orientation angles (θ, φ in **Figure 9A**) and the ratio of the end-to-end distance to the contour length of all effective network chains in **Figure 9B**. The distribution of the chain orientation angle θ is almost uniform and the distribution of the chain orientation angle φ is almost sine-shaped. It proves that our model is sufficiently large to bridge the molecular and continuum properties of PAAm hydrogel.

Water beads are uniformly distributed around polymer chains. Water molecules in hydrogels are trapped by hydrophilic functional groups in polymer network via hydrogen bonds. The coverage of these hydrogen bonds is only within several water molecules away, meaning that the so-called bound water in hydrogels should be distributed uniformly surrounding polymer network and other chains. The hydrophilia of the polymer beads is embodied in our simulation as the relatively small Flory-Huggins parameter χ. It can be seen that our PAAm hydrogel models give reasonable crosslinking threshold and show sufficiently realistic and large polymer network in PAAm hydrogel. It convinces us to use these models to investigate the structural and mechanical properties of PAAm hydrogel.

Large Deformation Behavior

In this section, Uniaxial tension tests with constant volume with $\lambda_1 = \lambda, \lambda_2 = \lambda_3 = \lambda^{-\frac{1}{2}}$, where λ_i is the stretch in i-th direction, are performed in DPD simulations to investigate the large deformation behavior of PAAm hydrogels with water content 80%. The nominal stress of the incompressible uniaxial tension test is obtained from

$$P_{11} = \frac{2\sigma_1 - \sigma_2 - \sigma_3}{2\lambda}$$

where σ_i is the Virial stress in each direction.

Three loading rates, i.e., 0.005, 0.001, and 0.0002 per DPD time unit, are imposed on PAAm hydrogel models. **Figure 10A** shows the nominal stress-stretch curves of three PAAm hydrogel models under three loading rates. It shows that our PAAm hydrogel models capture both the viscoelastic and the hyperelastic behaviors. All three models shows the loading rate-dependent behavior. This is because the viscosity of all beads is embedded in DPD force field F^D. Higher

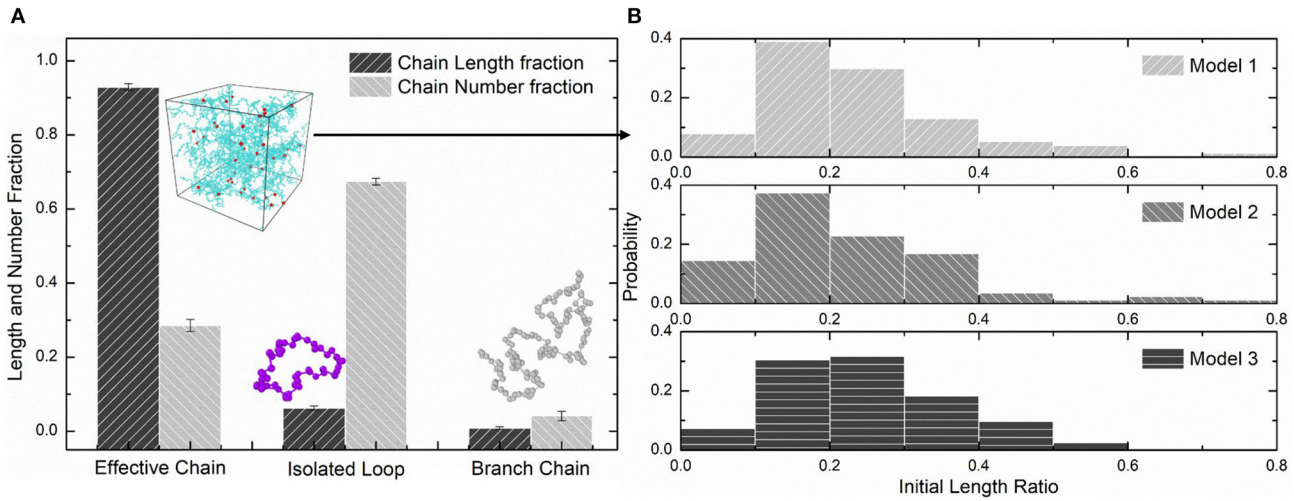

FIGURE 8 | (A) The length fraction and number fraction of different types of chains in PAAm hydrogel models crosslinking under $T = 9$. **(B)** The distribution of the initial length ratio of the effective network chains in three PAAm hydrogel models crosslinking under $T = 9$.

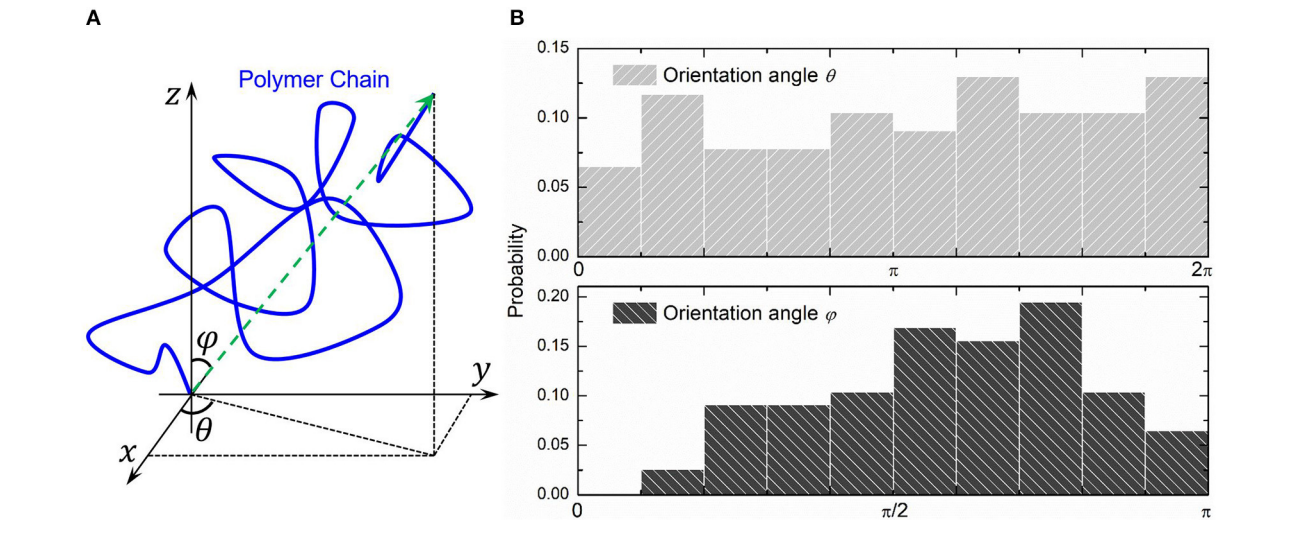

FIGURE 9 | (A) The orientation angles (θ, φ) of a polymer chain. **(B)** The probability distribution of two orientation angles of all effective network chains.

loading rate causes more intensive rebound of bonded beads, leading to the higher dissipative force. Compared to previous experimental results (Lei et al., 2019; Yang et al., 2019), the loading rate-dependent behavior is much more significant since the loading rates we adopt in our DPD simulations are far larger than realistic ones used in experiments. Considering the loading rate-dependent behavior and the computational resources, we choose loading rate 0.001 per DPD time unit for further discussion. The hyperelasticity is shown in the initial part of the stress-stretch curve during uniaxial tension. The hardening stage can also be found where the stretch is large, which is cause by the stretch limit of polymer chains. We also present the bond stretch in effective chains during the uniaxial tension tests as the solid lines shown in **Figure 10B**. It shows that significant bond stretch occurs in the hardening stage where effective chains are stretched to almost straight. The trend of the nominal stress-stretch curves agrees well with experimental results (Bai et al., 2017; Zhang et al., 2018; Yang et al., 2019). The scattered stretch limit where hardening stage occurs in PAAm hydrogels with the same water content are also found.

Although the number fraction and length fraction of each type of chains in three PAAm hydrogel models only have a <2% standard deviation, their mechanical behaviors in **Figure 10A** show much differences, especially when the stretch is large. This is not what the current theory of hydrogels can predict. Therefore, we compare our simulation results with current constitutive theory of polymers to reveal the underlying

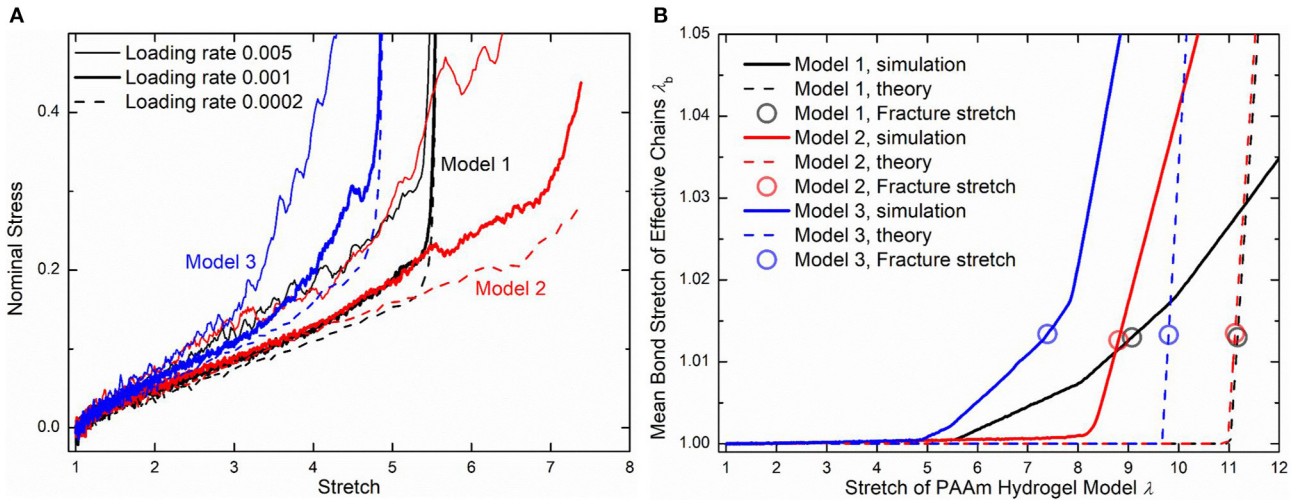

FIGURE 10 | (A) The nominal stress-stretch curves of three PAAm hydrogel models under uniaxial tension tests with three loading rates 0.005, 0.001, and 0.0002. **(B)** Mean bond stretch vs. the stretch of PAAm hydrogel model curves (Solid lines are the mean bond stretch of PAAm hydrogel models vs. model stretch curves. Dashed lines are the theoretical mean bond stretch vs. model stretch curves. Dots are the fracture point. Model 1, 2, and 3 are three independent PAAm hydrogel models with the water content 80%. Data for Mode 1, 2, and 3 are colored as black, red, and blue).

mechanism of the large deformation behavior of PAAm hydrogel. In current constitutive theory (Huang et al., 2020), two key parts, i.e., the free energy of a single chain and the statistical sum of the free energy of all chain, are crucial to bridge the mesoscale chain conformation change to the bulk mechanical response of hydrogels. Considering the polymer chains in our DPD simulations are close to the so-call freely joint chains, the Langevin chain model is adopted to characterize the free energy of a single chain

$$W_{chain} = kTN\left(\lambda_c l_0 \beta + \ln\frac{\beta}{\sinh\beta}\right),\ \beta = \mathcal{L}^{-1}\left(\lambda_c l_0\right)$$

where kT is the thermodynamics energy unit, N the number of Kuhn segments in current chain, λ_c the stretch of chain with respect to the mean initial length ratio of current chain $l_0 = \frac{L_0}{N_b b_0}$, L_0 the mean end-to-end distance of current chain, $N_b r_0$ the mean contour length with the mean bond number N_b and the bond length r_0. Since the inverse Langevin function $\mathcal{L}^{-1}$ is singular when $\lambda_c l_0 = 1$, the Langevin model often need additional modification (Mao et al., 2017). Li and Bouklas (2020) proposed the stretching force of a polymer chain caused by the conformation entropy change can also stretch bonds in polymer chains. Thus, the modified chain stretch λ_c turns out to be λ_c/λ_b, where λ_b is the mean stretch of bonds in effective chains. Combining with the bond force F^B in section Governing Equation of DPD Simulations, this modification circumvents the singularity of the inverse Langevin function by giving the relationship of chain stretch λ_c to the mean bond stretch λ_b as follows

$$\lambda_c = \frac{\lambda_b}{l_0}\mathcal{L}\left(\frac{N_b^2}{N}\frac{C}{kT}\lambda_b\left(\lambda_b - 1\right)\right)$$

In order to statistically sum up the free energy of all effective chains, the mean stretch of all effective chains $\langle\lambda_c\rangle = \sqrt{I_1/3}$ and mean number of Kuhn segments $\langle N\rangle$ are used to formulate the total free energy of hydrogel model as follows

$$W = nkT\langle N\rangle\left(\sqrt{\frac{I_1}{3}}\frac{l_0}{\lambda_b}\beta + \ln\frac{\beta}{\sinh\beta}\right),\ \beta = \mathcal{L}^{-1}\left(\sqrt{\frac{I_1}{3}}\frac{l_0}{\lambda_b}\right)$$

where n is the effective chain density. I_1 is the first invariant of the deformation gradient of bulk hydrogel model with $I_1 = \lambda_1^2+\lambda_2^2+\lambda_3^2 = \lambda^2 + 2\lambda^{-1}$, which connect the chain conformation change in mesoscale to the bulk deformation in continuum. Thus, the $\lambda_b - \lambda$ relationship between mean bond stretch and the stretch of PAAm hydrogel models can be obtained theoretically by solving following equation

$$\sqrt{\frac{I_1}{3}} = \frac{\lambda_b}{l_0}\mathcal{L}\left(\frac{N_b^2}{N}\frac{C}{kT}\lambda_b\left(\lambda_b - 1\right)\right)$$

Figure 10B compare the theoretically $\lambda_b - \lambda$ relationship with that measured in simulations. It is very clear that there are large discrepancies between theoretical predictions and simulation results. Parameter study for the $\lambda_b - \lambda$ relation is performed to find the reason for the large discrepancies. **Figures 11A,B** shows the $\lambda_b - \lambda$ relationship with the different bond strength parameter $\frac{C}{kT}$ and different mean initial length ratio l_0, respectively. Combining **Figures 10B**, **11A**, we can find that the simulation results show a much softer mean bond stretching process during uniaxial tension of PAAm hydrogel models than theoretical predictions, although such a large bond strength parameter $\frac{C}{kT} = 116{,}000$ is used in both simulations and theory. From lines in **Figures 12A–C**, we can find that the softer mean bond stretch of the whole model is moderated by the unsynchronized

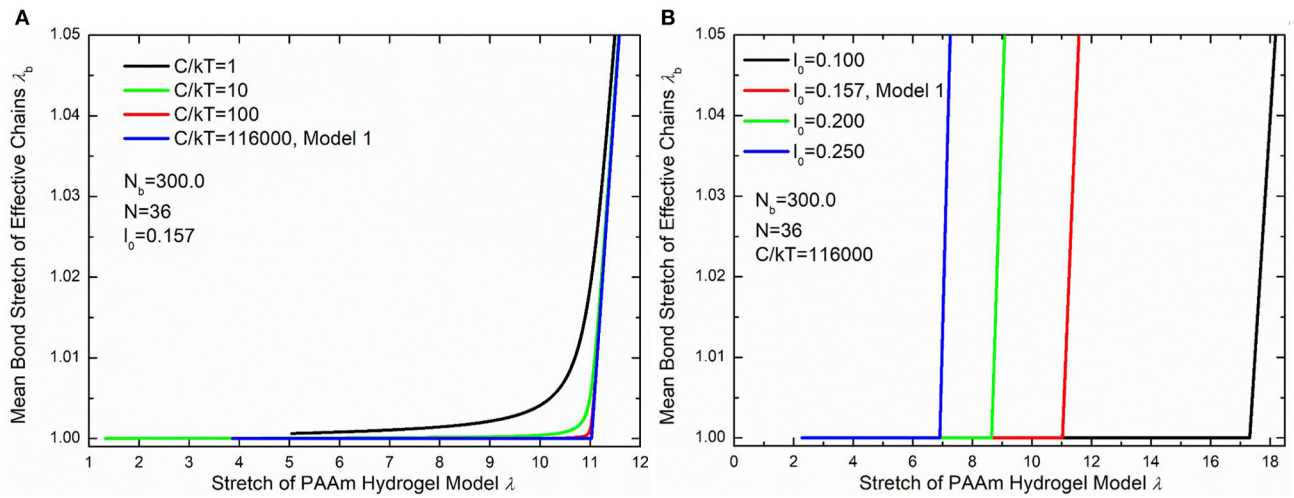

FIGURE 11 | Parameter study of the $\lambda_b - \lambda$ relationship. **(A)** The $\lambda_b - \lambda$ relationship with different bond strengths. **(B)** The $\lambda_b - \lambda$ relationship with different initial length ratios.

stretch of different effective chains. Also, the flat stress-stretch curves for hydrogel actually result from the superposition of the unsynchronized stiff bond stretching behavior of large amount of chains. In **Figure 11B**, we can find that the critical stretch where significant bond stretch occurs depends on the initial length ratio. The discrepancy of critical stretch between theory and simulation is because of the use of mean initial length ratio. As shown in **Figure 8B**, the initial length ratio of effective chains distributes in a very wide range. Chains with high initial length ratio first stretch to almost straight, so that using the lower mean initial length ratio overestimates the critical stretch in **Figure 11B**.

The nominal stress-stretch curves and the $\lambda_b - \lambda$ relation indicates that current continuum constitutive theory for hydrogel is only valid in small stretch, while the mechanical response under large deformation near fracture needs detailed structural models. The statistical averaging structural properties, such as water content and mean chain length, smears out the wide distribution of the possible conformation of effective chains, while specific structural features are what dominate the large deformation behavior of hydrogel.

Fracture Criterion

The randomness of the polymer network in hydrogel makes it hard to give an accurate fracture criterion. The widely used fracture toughness works poor as the fracture criterion of hydrogels since it often counts the deformation energy far away from the crack. As shown in the PAAm hydrogel models, the stretch limit is the key property that determines the fracture of a polymer chain. A stretch criterion is more general which can be applied in different polymer network systems and more practical for different loading conditions. In this section, we propose a stretch criterion of the fracture of hydrogels.

The critical energy to the fracture of a polymer chains is equal to the fracture energy of one C-C bond

$$W_{cr} = \frac{C}{2} r_0^2 \left(\lambda_b^{cr} - 1\right)^2$$

where λ_b^{cr} is the critical stretch when a C-C bond breaks. This critical free energy corresponds to the critical mean stretch of all bonds $\bar{\lambda}_b^{cr}$ in this chain with

$$W_{cr} = \frac{N_b C}{2} r_0^2 \left(\bar{\lambda}_b^{cr} - 1\right)^2$$

Thus, the fracture criterion for a single chain can be expressed as

$$\bar{\lambda}_b^{cr} = 1 + \frac{\lambda_b^{cr} - 1}{\sqrt{N_b}}$$

Using the $\bar{\lambda}_b^{cr}$ =1.225 when $N_b = 2$ obtained in **Figure 4**, the critical stretch of a C-C bond λ_b^{cr} is 1.318. The critical mean stretch of a C-C bond λ_b^{cr} is then related to the first invariant of the bulk deformation gradient by substituting the critical mean stretch $\bar{\lambda}_b^{cr}$ into the $\lambda_b - \lambda$ relation. As the dots shown in **Figure 10B**, for three models with the N_b = 600.0, 558.6, 573.6, the theoretical fracture stretch are 11.2, 11.1 and 9.8, and the fracture stretch measured from simulations are 9.1, 8.8, and 7.4, respectively. There are much discrepancies between the theoretical results and simulation results, mainly because the equal-chain-length assumption in current constitutive theory overestimates the mean chain stretch by $\langle \lambda_c \rangle = \sqrt{I_1/3}$. Furthermore, the fracture stretch measured from simulations using the mean bond stretch of all effective chains should be the upper limit of the real fracture stretch. Considering the unsynchronized stretch of different effective chains, 50% of effective chains may have been broken when the mean bond stretch of all effective chains reaches fracture stretch. This amount of chain scission is enough for the macroscopic fracture of hydrogel. On the other hand, we can get the lower limit of the fracture stretch by analyzing the fracture stretch of every effective chains. Blue dots in **Figures 12A–C** are the fracture stretch where the first effective chain (as shown in **Figure 12D**) is about to break, while red dots are fracture stretch obtained from mean bond stretch of all effective chains. It gives limited ranges of the

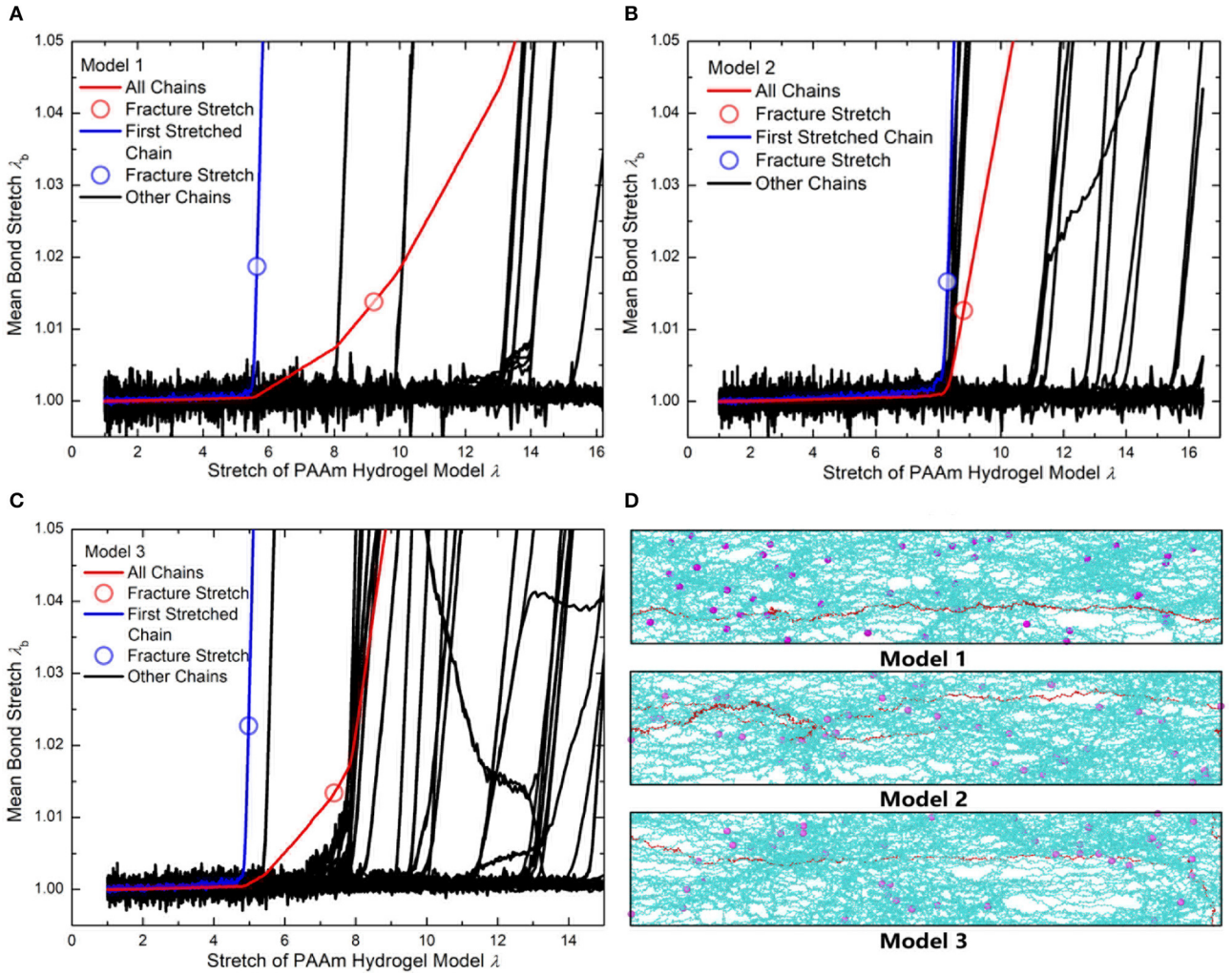

FIGURE 12 | (A) The mean bond stretch of every effective chains and the total mean bond stretch vs. stretch of Model 1. **(B)** The mean bond stretch of every effective chains and the total mean bond stretch vs. stretch of Model 2. **(C)** The mean bond stretch of every effective chains and the total mean bond stretch vs. stretch of Model 1 (Blue line is the first polymer chain stretched to fracture in each model. Red line is the total mean bond stretch vs. model stretch in each model. Black lines are the mean bond stretch of the rest effective chains in each model). **(D)** The configuration of three models when model stretch is 3.7 (Cyan lines are effective chains. Purple particles are MBAA beads. Red line is the first effective chain stretched to fracture in each model).

fracture stretch of our three PAAm hydrogel models as 5.6–9.1, 8.3–8.8, and 5.0–7.4, respectively. These ranges almost cover the fracture stretch of PAAm hydrogels with the water content 78% in previous experiments (Zhang et al., 2018) as 5.5, 8.6 and 6.1.

Our coarse-grain PAAm hydrogel models are the representative models for numerous hydrogels since only the repulsive coefficient a is adjustable for different hydrogel system. Hydrogels share the same large deformation mechanism with the conformation change of the complex polymer network, so that the detailed mesoscale model is such a powerful tool to bridge the molecular movement to bulk deformation.

CONCLUSIONS

In this study, we propose a method to construct the mesoscale PAAm hydrogel models and investigate the large deformation and fracture mechanism of PAAm hydrogel using DPD simulations. The coarse-grain PAAm hydrogel models are constructed by simulating the crosslinking process in experiments. Different temperatures are tested for achieving sufficient diffusion length of polymer beads for sufficient crosslinking. It shows that the formation of polymer network in crosslinking process only occurs when the diffusion length of polymer beads is much larger than the mean distance of polymer beads. However, the increasing of diffusion length, which may caused by the increasing of temperature, gelation time or stirring in experiments, cannot eliminate the formation of isolated loops. Our PAAm hydrogel models have realistic structure of polymer network, including the compliant effective network, branch chains, isolated chains, crosslinking loops and isolated loops. The degree of polymerization of the effective network chains is almost the same to the theoretical estimation. Our crosslinking

simulations also show the upper limit of the water content for forming polymer network is about 97% which is close to the swelling limit of PAAm hydrogel in experiments. The scale of our PAAm hydrogel models are proved to be sufficiently large by the uniformly distributed orientation of effective chains. Incompressible uniaxial tension tests are performed in three different loading rates using our PAAm hydrogel models with the water content 80%. The nominal stress-stretch curves reflect both the hyperelasticity and the viscoelasticity of our PAAm hydrogel models. However, the scattered large deformation behaviors of PAAm hydrogel models with the same water content indicate that the mesoscale conformation of polymer network have great impact on the mechanical behavior in large stretch, because the effective chains with a wide range of initial length ratio stretch to straight at different time during deformation. Furthermore, we propose a stretch criterion of the fracture of PAAm hydrogel using the fracture stretch of C-C bonds. By analyzing our PAAm hydrogel models, specific upper and lower limit of the fracture stretch are given for each PAAm hydrogel models. These ranges agree quite well with experimental results. Our coarse-grain PAAm hydrogel models can be applied to numerous single network hydrogel systems.

DATA AVAILABILITY STATEMENT

All datasets generated for this study are included in the article/**Supplementary Material**.

AUTHOR CONTRIBUTIONS

JL, SX, and ZLi: investigation. ZLiu: resources, supervision, and funding acquisition. JL and SX: writing—original draft preparation. ZLi and ZLiu: writing—review and editing.

FUNDING

This work was supported by the National Natural Science Foundation of China through grant numbers 11820101001, 11811530287, and 11572236.

SUPPLEMENTARY MATERIAL

The Supplementary Material for this article can be found online at: https://www.frontiersin.org/articles/10.3389/fchem.2020.00115/full#supplementary-material

REFERENCES

An, M., Demir, B., Wan, X., Meng, H., Yang, N., and Walsh, T. R. (2019). Predictions of thermo-mechanical properties of cross-linked polyacrylamide hydrogels using molecular simulations. *Adv. Theory Simulations* 2:1800153. doi: 10.1002/adts.201800153

Bai, R., Yang, Q., Tang, J., Morelle, X. P., Vlassak, J. J., and Suo, Z. (2017). Fatigue fracture of tough hydrogels. *Extreme Mech. Lett.* 15, 91–96. doi: 10.1016/j.eml.2017.07.002

Berendsen, H. J., van der Spoel, D., and van Drunen, R. (1995). GROMACS: a message-passing parallel molecular dynamics implementation. *Comput. Phys. Commun.* 91, 43–56. doi: 10.1016/0010-4655(95)00042-E

Brown, A. E., Litvinov, R. I., Discher, D. E., Purohit, P. K., and Weisel, J. W. (2009). Multiscale mechanics of fibrin polymer: gel stretching with protein unfolding and loss of water. *Science* 325, 741–744. doi: 10.1126/science.1172484

Caló, E., and Khutoryanskiy, V. V. (2015). Biomedical applications of hydrogels: a review of patents and commercial products. *Euro. J. Polym.* 65, 252–267. doi: 10.1016/j.eurpolymj.2014.11.024

Dauber-Osguthorpe, P., Roberts, V. A., Osguthorpe, D. J., Wolff, J., Genest, M., and Hagler, A. T. (1988). Structure and energetics of ligand binding to proteins: *Escherichia coli* dihydrofolate reductase-trimethoprim, a drug-receptor system. *Proteins Struct. Funct. Bioinformatics* 4, 31–47. doi: 10.1002/prot.340040106

Gong, J. P., Katsuyama Y., Kurokawa T., and Osada Y. (2003). Double-network hydrogels with extremely high mechanical strength. *Adv Mater.* 15, 1155–1158. doi: 10.1002/adma.200304907

Groot, R. D., and Rabone, K. (2001). Mesoscopic simulation of cell membrane damage, morphology change and rupture by nonionic surfactants. *Biophys. J.* 81, 725–736. doi: 10.1016/S0006-3495(01)75737-2

Groot, R. D., and Warren, P. B. (1997). Dissipative particle dynamics: bridging the gap between atomistic and mesoscopic simulation. *J. Chem. Phys.* 107, 4423–4435. doi: 10.1063/1.474784

Haque, M. A., Kurokawa, T., and Gong, J. P. (2012). Super tough double network hydrogels and their application as biomaterials. *Polymer* 53, 1805–1822. doi: 10.1016/j.polymer.2012.03.013

Henderson, K. J., Zhou, T. C., Otim, K. J., and Shull, K. R. (2010). Ionically cross-linked triblock copolymer hydrogels with high strength. *Macromolecules* 43, 6193–6201. doi: 10.1021/ma100963m

Hoogerbrugge, P., and Koelman, J. (1992). Simulating microscopic hydrodynamic phenomena with dissipative particle dynamics. *Europhys. Lett.* 19:155. doi: 10.1209/0295-5075/19/3/001

Hou, D., Xu, J., Zhang, Y., and Sun, G. (2019). Insights into the molecular structure and reinforcement mechanism of the hydrogel-cement nanocomposite: an experimental and molecular dynamics study. *Compos. B Eng.* 177:107421. doi: 10.1016/j.compositesb.2019.107421

Huang, R., Zheng, S. J., and Liu, Z. S. (2020). Recent advances of the constitutive models of smart materials- hydrogels and shape memory polymers, *Int. J. Appl. Mech.* 12:2050014. doi: 10.1142/S1758825120500143

Jang, S. S., Goddard, W. A., and Kalani, M. Y. S. (2007). Mechanical and transport properties of the poly (ethylene oxide)–poly (acrylic acid) double network hydrogel from molecular dynamic simulations. *J. Phys. Chem. B* 111, 1729–1737. doi: 10.1021/jp0656330

Jin, K., Barreiro, D. L., Martin-Martinez, F. J., Qin, Z., Hamm, M., Paul, C. W., et al. (2018). Improving the performance of pressure sensitive adhesives by tuning the crosslinking density and locations. *Polymer* 154, 164–171. doi: 10.1016/j.polymer.2018.08.065

Kaminski, G., Duffy, E. M., Matsui, T., and Jorgensen, W. L. (1994). Free energies of hydration and pure liquid properties of hydrocarbons from the OPLS all-atom model. *J. Phys. Chem.* 98, 13077–13082. doi: 10.1021/j100100a043

Koelman, J., and Hoogerbrugge, P. (1993). Dynamic simulations of hard-sphere suspensions under steady shear. *Europhys. Lett.* 21:363. doi: 10.1209/0295-5075/21/3/018

Kong, H. J., Wong, E., and Mooney, D. J. (2003). Independent control of rigidity and toughness of polymeric hydrogels. *Macromolecules* 36, 4582–4588. doi: 10.1021/ma034137w

Lee, K. Y., and Mooney, D. J. (2001). Hydrogels for tissue engineering. *Chem. Rev.* 101, 1869–1880. doi: 10.1021/cr000108x

Lei, J., Zhou, Z., and Liu, Z. (2019). Side chains and the insufficient lubrication of water in polyacrylamide hydrogel—a new insight. *Polymers* 11:1845. doi: 10.3390/polym11111845

Li, B., and Bouklas, N. (2020). A variational phase-field model for brittle fracture in polydisperse elastomer networks. *Int. J. Solids Struct.* 182, 193–204. doi: 10.1016/j.ijsolstr.2019.08.012

Li, J., Celiz, A. D., Yang, J., Yang, Q., Wamala, I., Whyte, W., et al. (2017). Tough adhesives for diverse wet surfaces. *Science* 357, 378–381. doi: 10.1126/science.aah6362

Li, J., and Mooney, D. J. (2016). Designing hydrogels for controlled drug delivery. *Nat. Rev. Mater.* 1:16071. doi: 10.1038/natrevmats.2016.71

Lienemann, P. S., Lutolf, M. P., and Ehrbar, M. (2012). Biomimetic hydrogels for controlled biomolecule delivery to augment bone regeneration. *Adv. Drug Deliv. Rev.* 64, 1078–1089. doi: 10.1016/j.addr.2012.03.010

Liu, J., Pang, Y., Zhang, S., Cleveland, C., Yin, X., Booth, L., et al. (2017). Triggerable tough hydrogels for gastric resident dosage forms. *Nat. Commun.* 8:124. doi: 10.1038/s41467-017-00144-z

Liu, M. B., Liu, G. R., Zhou, L. W., and Chang, J. Z. (2015). Dissipative particle dynamics (DPD): an overview and recent developments. *Arch. Comput. Methods Eng.* 22, 529–556. doi: 10.1007/s11831-014-9124-x

Liu, Z., Toh, W., and Ng, T. Y. (2015). Advances in mechanics of soft materials: a review of large deformation behavior of hydrogels. *Int. J. Appl. Mech.* 07:1530001. doi: 10.1142/S1758825115300011

Maiti, A., and McGrother, S. (2004). Bead–bead interaction parameters in dissipative particle dynamics: relation to bead-size, solubility parameter, surface tension. *J. Chem. Phys.* 120, 1594–1601. doi: 10.1063/1.1630294

Mao, Y., Talamini, B., and Anand, L. (2017). Rupture of polymers by chain scission. *Extreme Mech. Lett.* 13, 17–24. doi: 10.1016/j.eml.2017.01.003

Masuda, F. (1994). Trends in the development of superabsorbent polymers for diapers, in superabsorbent polymers. *Am. Chem. Soc.* 573, 88–98. doi: 10.1021/bk-1994-0573.ch007

Mathesan, S., Rath, A., and Ghosh, P. (2016). Molecular mechanisms in deformation of cross-linked hydrogel nanocomposite. *Mater. Sci. Eng. C* 59, 157–167. doi: 10.1016/j.msec.2015.09.087

Mayo, S. L., Olafson, B. D., and Goddard, W. A. (1990). DREIDING: a generic force field for molecular simulations. *J. Phys. Chem.* 94, 8897–8909. doi: 10.1021/j100389a010

Nawaz, S., and Carbone, P. (2014). Coarse-graining poly(ethylene oxide)–poly(propylene oxide)–poly(ethylene oxide) (PEO–PPO–PEO) block copolymers using the MARTINI force field. *J. Phys. Chem. B* 118, 1648–1659. doi: 10.1021/jp4092249

Oldiges, C., and Tönsing, T. (2002). Molecular dynamic simulation of structural, mobility effects between dilute aqueous CH 3 CN solution and crosslinked PAA Part 1. *Struct. Phys. Chem. Chem. Phys.* 4, 1628–1636. doi: 10.1039/b110238a

Peppas, N. A., and Merrill, E. W. (1976). Poly(vinyl alcohol) hydrogels: reinforcement of radiation-crosslinked networks by crystallization. *J. Polym. Sci. Polym. Chem. Ed.* 14, 441–457. doi: 10.1002/pol.1976.170140215

Plimpton, S. (1995). Fast parallel algorithms for short-range molecular dynamics. *J. Comput. Phys.* 117, 1–19. doi: 10.1006/jcph.1995.1039

Rao, Z., Huo, Y., and Liu, X. (2014). Dissipative particle dynamics and experimental study of alkane-based nanoencapsulated phase change material for thermal energy storage. *RSC Adv.* 4, 20797–20803. doi: 10.1039/C4RA02699C

Shull, K. R. (2012). Materials science: a hard concept in soft matter. *Nature* 489, 36–38. doi: 10.1038/489036a

Spenley, N. (2000). Scaling laws for polymers in dissipative particle dynamics. *Europhys. Lett.* 49:534. doi: 10.1209/epl/i2000-00183-2

Stauffer, S. R., and Peppast, N. A. (1992). Poly (vinyl alcohol) hydrogels prepared by freezing-thawing cyclic processing. *Polymer* 33, 3932–3936. doi: 10.1016/0032-3861(92)90385-A

Sun, J.-Y., Zhao, X., Illeperuma, W. R., Chaudhuri, O., Oh, K. H., Mooney, D. J., et al. (2012). Highly stretchable and tough hydrogels. *Nature* 489:133. doi: 10.1038/nature11409

Sun, M., and Marshall, E. (1981). Gels. *Sci. Am.* 244, 124–138. doi: 10.1038/scientificamerican0181-124

Symeonidis, V., Karniadakis, G. E., and Caswell, B. (2005). Dissipative particle dynamics simulations of polymer chains: scaling laws and shearing response compared to DNA experiments. *Phys. Rev. Lett.* 95:076001. doi: 10.1103/PhysRevLett.95.076001

Tang, J., Li, J., Vlassak, J. J., and Suo, Z. (2017). Fatigue fracture of hydrogels. *Extreme Mech. Lett.* 10, 24–31. doi: 10.1016/j.eml.2016.09.010

Tönsing, T., and Oldiges, C. (2001). Molecular dynamic simulation study on structure of water in crosslinked poly (N-isopropylacrylamide) hydrogels. *Phys. Chem. Chem. Phys.* 3, 5542–5549. doi: 10.1039/b109281m

Wei, Q., Wang, Y., Zhang, Y., and Chen, X. (2017). Aggregation behavior of nano-silica in polyvinyl alcohol/polyacrylamide hydrogels based on dissipative particle dynamics. *Polymers* 9:611. doi: 10.3390/polym9110611

Wichterle, O., and Lím, D. (1960). Hydrophilic gels for biological use. *Nature* 185, 117–118. doi: 10.1038/185117a0

Wu, Y., Joseph, S., and Aluru, N. R. (2009). Effect of cross-linking on the diffusion of water, ions, and small molecules in hydrogels. *J. Phys. Chem. B* 113, 3512–3520. doi: 10.1021/jp808145x

Xing, Z., Ness, C., Frenkel, D., and Eiser, E. (2019). Structural and linear elastic properties of DNA hydrogels by coarse-grained simulation. *Macromolecules* 52, 504–512. doi: 10.1021/acs.macromol.8b01948

Xu, L., Zhao, X., Xu, C., and Kotov, N. A. (2018). Water-rich biomimetic composites with abiotic self-organizing nanofiber network. *Adv. Mater.* 30:1703343. doi: 10.1002/adma.201703343

Xu, S., and Liu, Z. (2019). A nonequilibrium thermodynamics approach to the transient properties of hydrogels. *J. Mech. Phys. Solids* 127, 94–110. doi: 10.1016/j.jmps.2019.03.008

Xu, S., Wang, Y., Hu, J., and Liu, Z. (2016). Atomic understanding of the swelling and phase transition of polyacrylamide hydrogel. *Int. J. Appl. Mech.* 8:1640002. doi: 10.1142/S1758825116400020

Yang, C., Yin, T., and Suo, Z. (2019). Polyacrylamide hydrogels. I. network imperfection. *J. Mech. Phys. Solids* 131, 43–55. doi: 10.1016/j.jmps.2019.06.018

Zhang, E., Bai, R., Morelle, X. P., and Suo, Z. (2018). Fatigue fracture of nearly elastic hydrogels. *Soft Matter* 14, 3563–3571. doi: 10.1039/C8SM00460A

Zhao, X. (2014). Multi-scale multi-mechanism design of tough hydrogels: building dissipation into stretchy networks. *Soft Matter* 10, 672–687. doi: 10.1039/C3SM52272E

Zheng, S., Li, Z., and Liu, Z. (2018). The fast homogeneous diffusion of hydrogel under different stimuli. *Int. J. Mech. Sci.* 137, 263–270. doi: 10.1016/j.ijmecsci.2018.01.029

Conflict of Interest: The authors declare that the research was conducted in the absence of any commercial or financial relationships that could be construed as a potential conflict of interest.

frontiers in Chemistry

ORIGINAL RESEARCH
published: 25 February 2020
doi: 10.3389/fchem.2020.00106

High-Strength Albumin Hydrogels With Hybrid Cross-Linking

Shaoping Lu[1†], Lin Zhu[1†], Qilin Wang[1], Zhao Liu[1], Chen Tang[1], Huan Sun[1], Jia Yang[1], Gang Qin[1], Gengzhi Sun[2] and Qiang Chen[1]*

[1] School of Materials Science and Engineering, Henan Polytechnic University, Jiaozuo, China, [2] Key Laboratory of Flexible Electronics (KLOFE), Institute of Advanced Materials (IAM), Jiangsu National Synergetic Innovation Center for Advanced Materials (SICAM), Nanjing Tech University (NanjingTech), Nanjing, China

Natural protein-based hydrogels possess excellent biocompatibility; however, most of them are weak or brittle. In the present work, high strength hybrid dual-crosslinking BSA gels (BSA DC gels), which have both chemical cross-linking and physical cross-linking, were fabricated by a facile photoreaction-heating process. BSA DC gels showed high transparency (light transmittance of ∼90%) and high strength. At optimal conditions, BSA DC gel exhibited high compressive strength ($\sigma_{c,f}$) of 37.81 ± 2.61 MPa and tensile strength ($\sigma_{t,f}$) of 0.62 ± 0.078 MPa, showing it to be much stronger than physically cross-linked BSA gel (BSA PC gel) and chemically cross-linked BSA gel (BSA CC gel). More importantly, BSA DC gel displayed non-swelling properties while maintaining high strength in DI water, pH = 3.0, and pH = 10.0. Moreover, BSA DC gel also demonstrated large hysteresis, rapid self-recovery, and excellent fatigue resistance properties. It is believed that our BSA DC gel can potentially be applied in biomedical fields.

Keywords: protein hydrogels, high strength, non-swelling, self-recovery, fatigue resistance

OPEN ACCESS

Edited by:
Kerstin G. Blank, Max Planck Institute of Colloids and Interfaces, Germany

Reviewed by:
Nonappa, Aalto University, Finland
Patricia Diaz-Rodriguez, University of La Laguna, Spain
Bernhard V. K. J. Schmidt, University of Glasgow, United Kingdom

****Correspondence:***
Qiang Chen
chenqiang@hpu.edu.cn

† These authors have contributed equally to this work

Specialty section:
This article was submitted to Polymer Chemistry, a section of the journal Frontiers in Chemistry

Received: *06 December 2019*
Accepted: *04 February 2020*
Published: *25 February 2020*

Citation:
Lu S, Zhu L, Wang Q, Liu Z, Tang C, Sun H, Yang J, Qin G, Sun G and Chen Q (2020) High-Strength Albumin Hydrogels With Hybrid Cross-Linking. Front. Chem. 8:106. doi: 10.3389/fchem.2020.00106

INTRODUCTION

Because of excellent biocompatibility, natural protein hydrogels have attracted a great deal of attention and have been used in a wide range of biological and biomedical fields (Koetting et al., 2016; Partlow et al., 2016; Silva et al., 2017; Jo et al., 2018; Gacanin et al., 2019). However, the poor mechanical properties of natural protein hydrogels is one of the main drawbacks impeding their application in some cases (Silva et al., 2017; Tang et al., 2018). Recently, great efforts have been made to enhance the mechanical properties of natural protein hydrogels, and some strategies have been developed, including nanocomposite (Yuk et al., 2016; Qin et al., 2017; Wang et al., 2017, 2018), physical cross-linking (Toivonen et al., 2015; Feng et al., 2018; Yan et al., 2019; Zhang et al., 2019), solvent induction (Li et al., 2016; Zhang et al., 2016; Hashemnejad et al., 2017; Zhu et al., 2018), double network (Bhattacharjee et al., 2015; Luo et al., 2016; Rangel-Argote et al., 2018; Tavsanli and Okay, 2019), hybrid cross-linking (Moura et al., 2011; Epstein-Barash et al., 2012; Xu et al., 2016; Nojima and Iyoda, 2018; Yang et al., 2018), and so on.

Among them, hybrid cross-linking, consisting of chemical and physical cross-linkings, is a simple and effective method of preparing high-performance natural protein hydrogels, especially for silk fibroin (SF) hydrogels. For example, Numata et al. (2017) reported the creation of hybrid SF hydrogels via an enzymatic oxidation reaction to form chemical cross-links between dityrosine residues and phase separation of silk solution to produce physical cross-links, which demonstrated high a compressive strength of ∼14 MPa. Okay and coworkers found that SF cryogels showed remarkable properties (compressive modulus of 48 MPa and strength of 970 kPa) if chemical

cross-linkers (ethylene glycol diglycidyl ether) were added into the cryogelation system (Yetiskin et al., 2017). Nevertheless, these high strength hybrid natural protein hydrogels are mainly fibril protein hydrogels, and little attention focuses on natural globulin protein hydrogels.

Bovine serum albumin (BSA) is one of the typical natural globulin proteins with a large number of functional groups, which provide many possibilities for chemical cross-linking of BSA to form covalent BSA gels. It is well-known that tyrosine groups can form dityrosine bonds via enzymatic reaction, and these play an important role in the mechanical properties of natural materials (Endrizzi et al., 2006; Partlow et al., 2014; Tavsanli and Okay, 2019). Considering that BSA has 21 tyrosines, it is an ideal template for the design and synthesis of natural globulin protein hydrogels via dityrosine bonds. However, dityrosine bond cross-linked BSA gels may exhibit brittle properties, similar to other gels (Sun and Huang, 2016; Fernandez-Castano Romera et al., 2017; Lü et al., 2017; Kabb et al., 2018; Picchioni and Muljana, 2018).

Herein, high-strength hybrid dual-crosslinking BSA gels (BSA DC gels) were fabricated by covalent cross-linking of BSA via dityrosine bonds followed by heat-induced denaturation of protein to form physical cross-linkings between BSA molecules. BSA is selected in the present work because it has plenty of tyrosine groups, low cost, high water solubility, and good biocompatibility. BSA DC gels showed high transparency and high strength. Under optimal conditions, BSA DC gel exhibited high compressive strength ($\sigma_{c,f}$) of 37.81 ± 2.61 MPa and tensile strength ($\sigma_{t,f}$) of 0.62 ± 0.078 MPa, showing it to be much stronger than physically cross-linked BSA gel (BSA PC gel, $\sigma_{c,f}$ of 3.10 ± 0.06 MPa and $\sigma_{t,f}$ of 0.06 MPa) and chemically cross-linked BSA gel (BSA CC gel, $\sigma_{c,f}$ of 2.49 ± 0.29 MPa and $\sigma_{t,f}$ of 0.25 MPa). More importantly, BSA DC gel displayed non-swelling properties while maintaining high performance in DI water, pH = 3.0, and pH = 10.0. Owing to the presence of physical interactions, BSA DC gel also demonstrated large hysteresis, rapid self-recovery and excellent fatigue resistance properties.

RESULTS AND DISCUSSION

Network Structure and Morphology

As shown in **Figure 1A**, BSA DC gel was prepared by a mild, simple, and "one-pot" method. First, BSA was chemically cross-linked by dityrosine bonds via ammonium persulfate (APS) and tris[2,2′-bipyridine] ruthenium dichloride [Ru(II)]-induced photoreaction under white light (i.e., BSA CC gel). Then, the gel was heated to induce denaturation of BSA, which formed a physically cross-linked network. BSA PC gel was fabricated via directly heating the BSA solution without the photoreaction. The appearance of the three BSA gels is shown in **Figure 1B**. BSA CC gel and BSA DC gel were red-brown (**Figure 1B**), indicating the formation of dityrosine bonds after photoreaction. The gelation mechanism of tyrosine-rich protein via APS/Ru(II) under white light is well-known and is illustrated in **Figure 1A** (Partlow et al., 2016; Silva et al., 2017). Interestingly, different from BSA PC gel, which had an opaque milk-white color, BSA CC gel and BSA DC gel showed high transparency, and the logo of our university could be clearly seen through them (**Figure 1B**). The light transmittance of BSA DC gel at visible light range reached up to 90%, while ultraviolet (UV) light could not transmit through the gel and was totally absorbed (**Figure 1C**). The results indicate that our BSA DC gel might potentially be applied as a UV shielding material. Moreover, a peak at ∼460 nm on the UV adsorption spectrum of BSA DC gel was detected (**Figure S1**), indicating the formation of dityrosine bonds (Ma et al., 2016; Lee et al., 2019). The formation of dityrosine bonds was also characterized by FTIR (**Figure 1D**). Compared to BSA PC gel, new peaks at 617 and 698 cm^{-1} were distinctly detected for BSA CC gel and BSA DC gel, which were the evidence for dityrosine bonds. Compared to BSA CC gel, the characteristic peak of –OH groups in BSA DC gel was shifted from 3,300 to 3,298 cm^{-1}, and the amide I in BSA DC gel was shifted from 1,662 to 1,658 cm^{-1}(Militello et al., 2004), indicating that there are physical interactions after heat-induced denaturation. The morphologies of freeze-dried BSA PC gel, BSA CC gel, and BSA DC gel are illustrated in **Figure 2**. BSA PC gel exhibited a particle-aggregation network structure, which was consistent with our previous report (Tang et al., 2018, **Figures 2a,b**). BSA CC gel displayed a heterogeneous porous network structure (1–5 μm, **Figures 2c,d**). Compared to BSA CC gel, BSA DC gel demonstrated a much denser porous network structure, and the pore size was 50–200 nm. The denser network structure of BSA DC gel might be attributable to the higher cross-linking density compared to BSA CC gel.

Mechanical Properties

Owing to the hybrid cross-linking network structure, BSA DC gel possessed high strength. Three cylindrical samples (8.5 × 10 mm) of BSA DC gel could withstand 5 kg weight without breakage (**Figure 3**a_1). As shown in **Figure 3**a_2, BSA DC gel sustained its weight without bending; however, BSA PC gel and BSA CC gel were bent because of their weight. Compressive and tensile tests were conducted to evaluate the mechanical properties of BSA DC gels. From **Figure 3b**, it can be clearly seen that BSA DC gel exhibited much better compressive properties. Consistently, BSA DC gel showed compressive strength (σ_c) of 37.81 ± 2.61 MPa, which was 12 and 15 times larger than BSA PC gel (3.10 ± 0.06 MPa) and BSA CC gel (2.49 ± 0.29 MPa) (**Figure 3c**), respectively. Similarly, the compressive modulus of BSA DC gel was 1515 ± 43 kPa, which was much stiffer than those of BSA PC gel (254 ± 8 kPa) and BSA CC gel (284 ± 48 kPa), respectively. Meanwhile, BSA DC gel displayed high tensile properties (**Figure 3d**): the tensile strength (σ_f) was 0.62 ± 0.078 MPa. In contrast, the σ_f values of BSA PC gel and BSA CC gel were 0.06 ± 0.008 and 0.25 ± 0.04 MPa, respectively. BSA DC gel also showed a higher tensile modulus (2939 ± 289 kPa), which was the reason that BSA DC gel could sustain its weight without bending. Statistical analysis was also performed (**Figures 3d,e**). BSA DC gels exhibited significant differences compared to BSA CC gel and BSA PC gel ($p < 0.01$), indicating that hybrid cross-linking is an effective strategy for improving the mechanical properties of BSA gels.

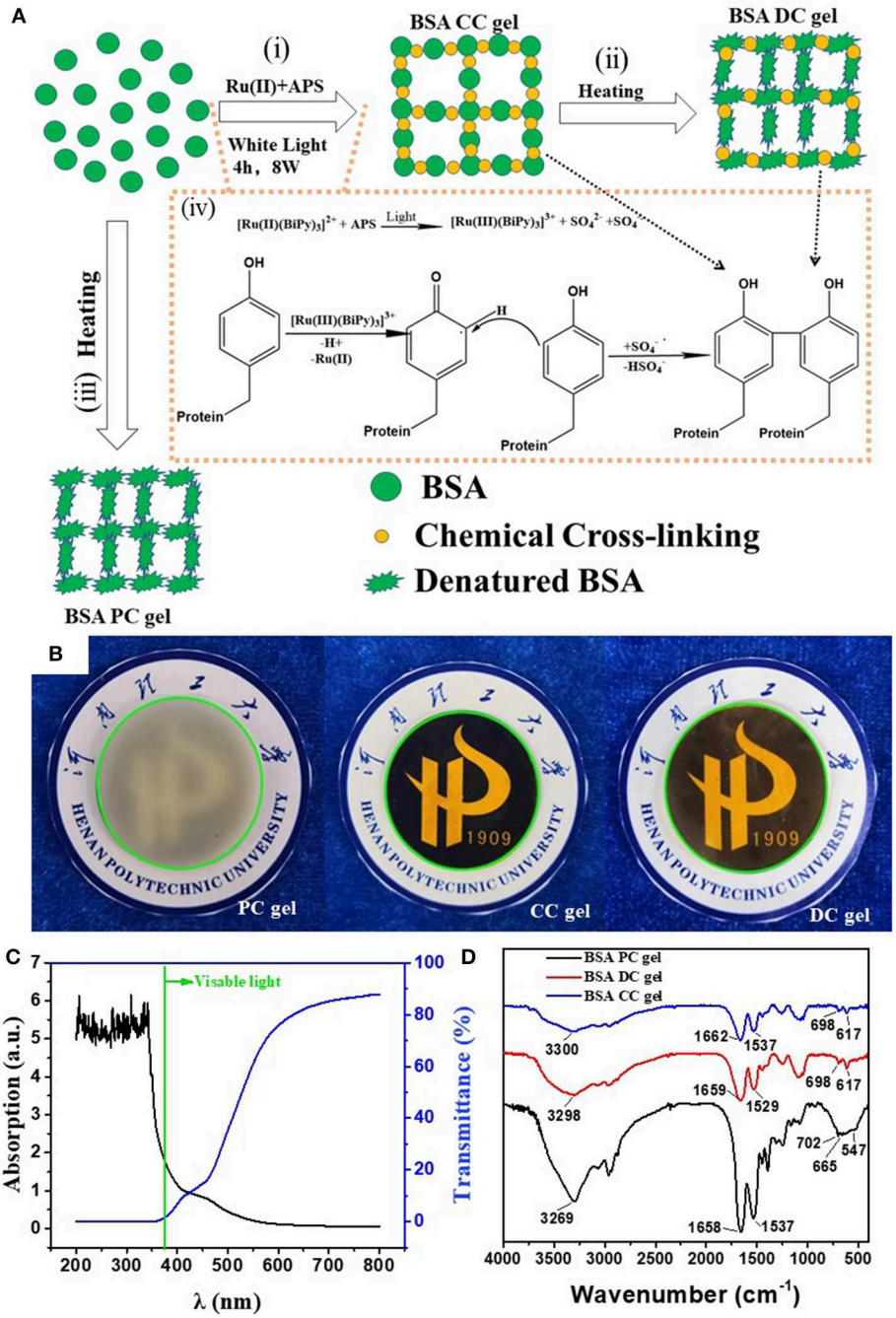

FIGURE 1 | (A) Illustration of the preparation and network structure of BSA DC gel; **(B)** appearance of three BSA gels; **(C)** transmittance and adsorption of BSA DC gel; **(D)** FTIR of BSA DC gel, BSA PC gel, and BSA CC gel.

The effects of various parameters, such as BSA concentration (C_{BSA}), Ru(II) concentration [$C_{Ru(II)}$], exposure time, heating temperature, and heating time, on the compressive properties of BSA DC gels were also investigated, and the results are summarized in **Table S1**. The compressive properties increased along with the increase in C_{BSA}, i.e., σ_c and E_c increased from 0.54 ± 0.03 to 34.73 ± 2.92 MPa and from 292 ± 17 to 1,320 ± 25 kPa, respectively. At C_{BSA} =100 mg/mL, BSA DC gel was too week to test. Compared to the gel at C_{BSA} = 300 mg/mL, the σ_c value of the gel at C_{BSA} = 400 mg/mL was significantly increased from 3.22 ± 0.61 to 26.00 ± 2.10 MPa. The highest value reached was 34.73 ± 2.92 MPa at C_{BSA} = 500 mg/mL. The presence of Ru(II) was also important for achieving high-strength BSA DC gels. Without Ru(II), σ_c was only 3.10 ± 0.06 MPa. However,

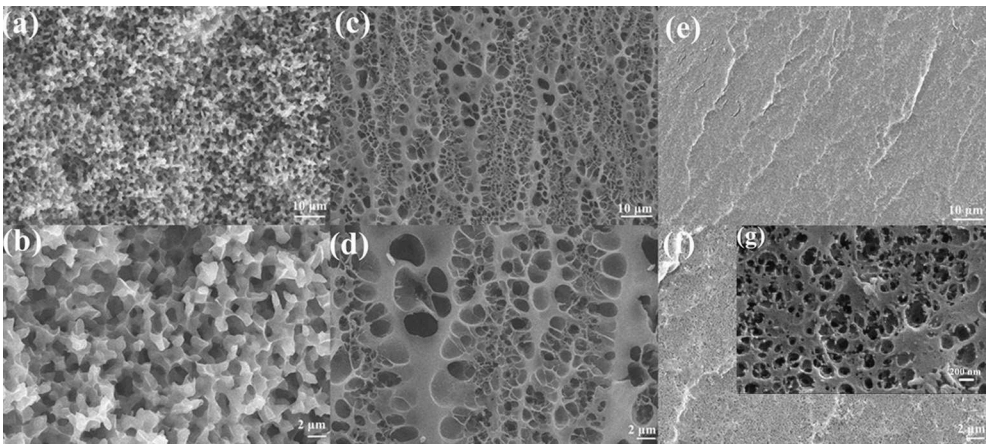

FIGURE 2 | SEM images of **(a,b)** BSA PC gel, **(c,d)** BSA CC gel, and **(e,f,g)** BSA DC gel. Scale bars of **(a,c,e)** are 10 μm, while scale bar of **(b,d,f)** is 2 μm. Scale bar of **(g)** is 200 nm.

after adding a very small amount of Ru(II) ($C_{Ru(II)} = 200\,\mu M$), σ_c reached up to 23.45 ± 1.37 MPa. The compressive properties of BSA DC gel were the best at $C_{Ru(II)} = 600\,\mu M$ (σ_c of 34.73 ± 2.92 MPa and E_c of 1320 ± 25 kPa). Unfortunately, the compressive properties deteriorated if $C_{Ru(II)} > 600\,\mu M$, probably because of excessive cross-linking of dityrosine. From **Table S1**, it can be found that the exposure time under white light has little effect on the compressive properties of BSA DC gel. Nevertheless, the exposure time distinctly influenced the mechanical properties of BSA CC gel, and it was difficult for it to gain enough strength to be removed from the mold if the exposure time was <4 h. Therefore, all of the BSA DC gels were prepared under exposure for 4 h. Moreover, the denaturation temperature and time also affected the compressive properties. BSA DC gel achieved the best compressive strength at a heating temperature of 80°C and a heating time of 10 min. Unless otherwise stated, we mainly focus on the BSA DC gel prepared at optimal conditions, i.e., C_{BSA} of 500 mg/mL, $C_{Ru(II)}$ of 600 μM, exposure time of 4 h, heating temperature of 80°C, and heating time of 10 min, which achieved σ_c of 37.81 ± 2.61 MPa and E_c of 1515 ± 43 kPa.

Rheology

Rheological tests were also conducted to evaluate the viscoelastic properties of BSA gels. As shown in **Figure 4A**, under low shear strain ($\gamma \leq 1\%$), all the three BSA gels exhibited a plateau without a change in storage modulus (G'), however, G' deceased along with shear strain as $\gamma > 1\%$. In contrast, the loss modulus (G'') was perpetually increased with an increase in shear strain. Clearly, at $\gamma \leq 1\%$, G' of BSA DC gel was 4,457 Pa, which was greater than those of BSA PC gel (2167 Pa) and BSA CC gel (627 Pa). We estimated the effective network chain density (N_1) of the gels by $G_e = N_1RT$, where G_e, R, and T are the equilibrium shear modulus, gas constant, and absolute temperature, respectively. Taking the room temperature (~25°C) as the reference temperature, the estimated N_1 values were 172, 85, and 24 mol/m^3 for BSA DC gel, BSA PC gel, and BSA CC gel, respectively. Distinctly, the results indicate that BSA DC gel demonstrates much higher cross-linking density compared to the other two gels, which was consistent with the morphological results in **Figure 2**. Moreover, compared to BSA CC gel, N_1 for BSA DC gel increased 7.2 times, inferring that the physical cross-linkings induced by heat denaturation of BSA were dominant in BSA DC gel. In **Figure 4B**, all the three gels can be seen to show ω-dependent behaviors, and G' and G'' increased as ω increased, indicating that they displayed viscoelasticity. In addition, G' was always larger than G'' for the three BSA gels, implying that they exhibit elastic properties under small deformation ($\gamma = 0.1\%$).

Non-swelling Properties

The stability of hydrogel in aqueous solution is a key parameter for their potential applications. Therefore, the swelling of the three BSA gels in various solvents was investigated (**Figure 5**). Photographs of the three BSA gels at the as-prepared and swollen state are presented in **Figure 5a**. Except for BSA CC, which was gel slightly swollen in pH = 3, all of the three BSA gels demonstrated negligible size change in DI water, pH = 3 and pH = 10, indicating non-swelling properties in these solutions. However, in 8 M urea and 4 M guanidine hydrochloride (GdnHCl) solution, all three BSA gels had an obvious size increase, indicating that the gels swelled significantly in the two solutions. It is well-known that urea and GdnHCl are classical denaturants for proteins. The swelling of the BSA gels indicates that there is unfolding of BSA in these gels. The gels differed, however, in that BSA DC gel was non-swollen in sodium dodecyl sulfate (SDS) solution, while BSA PC gel and BSA CC gel swelled distinctly in SDS solution. To quantitatively evaluate the swelling properties of BSA gels, the weights of swollen and as-prepared gels were measured. The swelling kinetics of the three BSA gels are illustrated in **Figures 5b–d**. Consistently, the three BSA gels were almost unswelling in DI water, pH = 3, and pH = 10. All three BSA gels swelled substantially in 8 M urea and 4 M GdnHCl solution. Specifically, BSA DC gel had the largest swelling ratio in 8 M urea and 4 M GdnHCl solution after swelling for 7 days, i.e., 3.65 g/g and 2.35 g/g, respectively; however, it

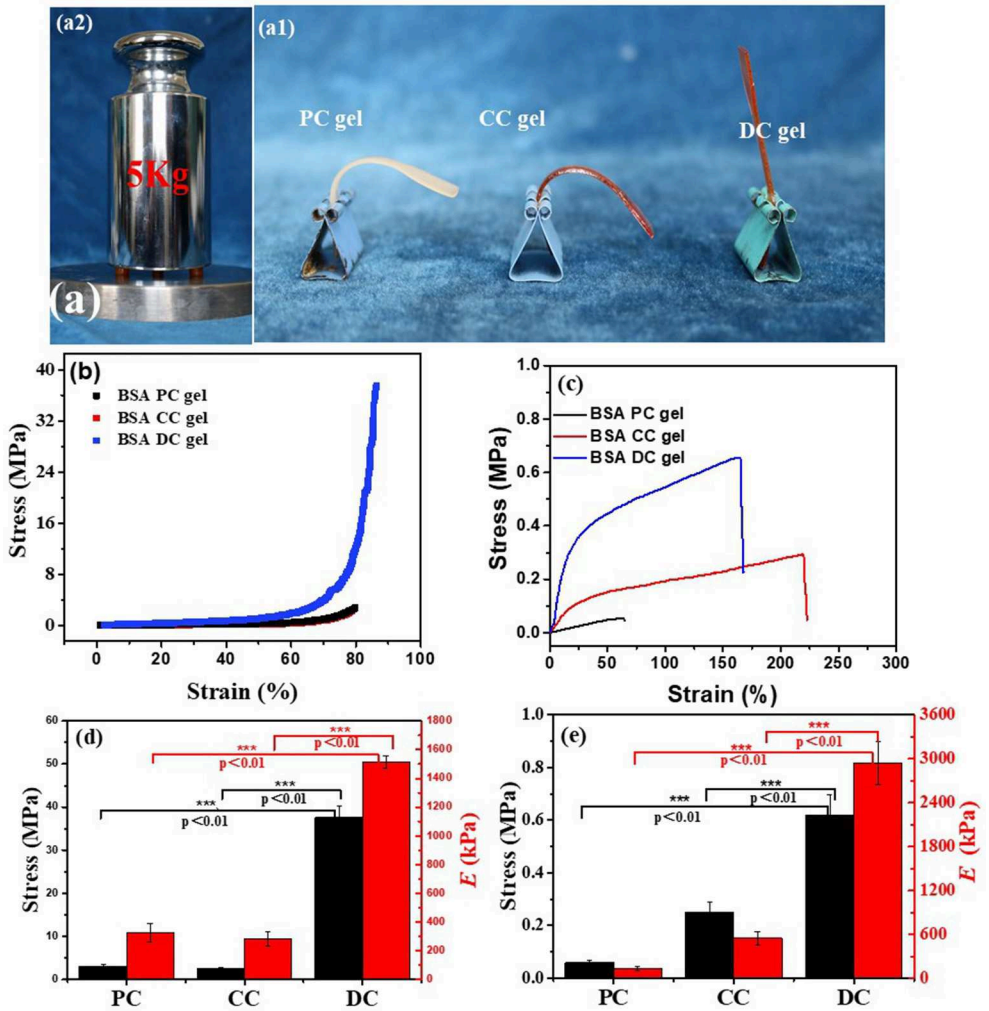

FIGURE 3 | (a) BSA DC gel could bear a 5 kg weight without breakage (a_1), and BSA DC gel could also sustain its own weight without bending, while BSA PC gel and BSA CC gel were bent (a_2); **(b)** compressive and **(c)** uniaxial tensile stress–stain curves of the three BSA gels; **(d)** compressive modulus and compressive strength and **(e)** tensile modulus and tensile strength of the three BSA gels.

was an exception in being unswollen in SDS solution. The non-swelling mechanism of BSA DC gels is still unclear. Probably, it is a feature of the BSA biomacromolecule. As shown in **Figures 5a–d**, regardless of physical or chemical cross-linkings, BSA PC gels and BSA CC gels are not swollen in DI water, pH = 3.0, and pH = 10.0. However, in denaturant solution, both of them are swollen significantly. The results indicate that BSA is further unfolded in the denaturant solution, while it maintained its conformation in DI water and at various pH values. Therefore, BSA DC gels are also non-swollen in water with various pHs. However, the synergistic effect of physical and chemical cross-linkings may also play an important role in suppressing the unfolding of BSA in SDS solution. Therefore, BSA PC gel and BSA CC gel swell markedly in SDS solution, while BSA DC gel is unswelling. The compressive properties of BSA DC gel after swelling are illustrated in **Figure 5e**. After swelling, the σ_c values of BSA DC gel in DI water, pH = 3.0, pH = 10.0, and 20 mM SDS solution were 35.85 ± 5.66, 23.60 ± 3.21, 30.27 ± 5.17, and 17.34 ± 2.23 MPa (**Figure 5e**, **Figure S2** and **Table S2**), respectively. However, the σ_c values were only 0.028 ± 0.004 and 0.025 ± 0.002 MPa after swelling in 8 M urea and 4 M GdnHCl, respectively. The results indicate that our BSA DC gels are unswollen in water and maintain good compressive properties after swelling in water.

Hysteresis, Self-Recovery, and Fatigue Resistance

Cyclic loading-unloading compressive tests were performed to evaluate the energy dissipation capacity of BSA DC gels. As shown in **Figure 6A**, BSA CC gel showed negligible hysteresis, while both BSA PC gel and BSA DC gel exhibited large hysteresis loops at a compressive strain of 50%. Moreover, the hysteresis loop of BSA DC gel was much larger than that of BSA PC gel.

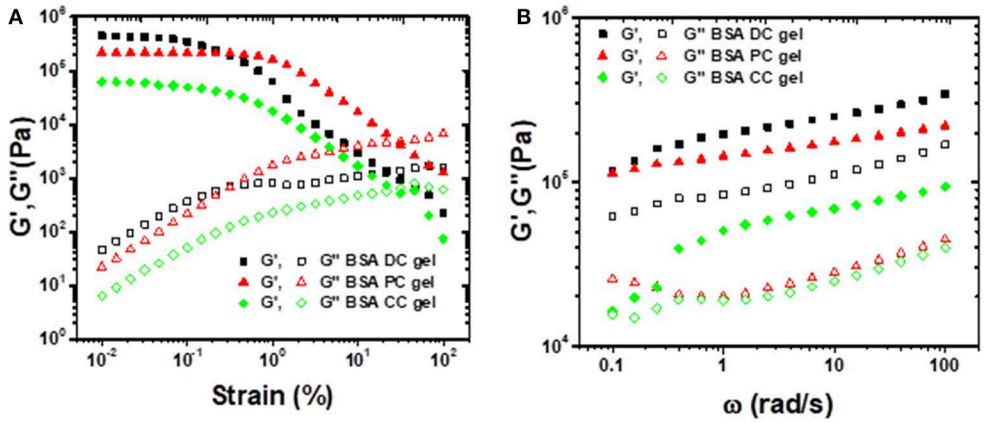

FIGURE 4 | (A) Strain sweep experiments performed from 0.01 to 100% strain under a frequency of 10 rad/s; **(B)** frequency sweep experiments performed from 0.1 to 100 rad/s under a shear strain of 0.1%.

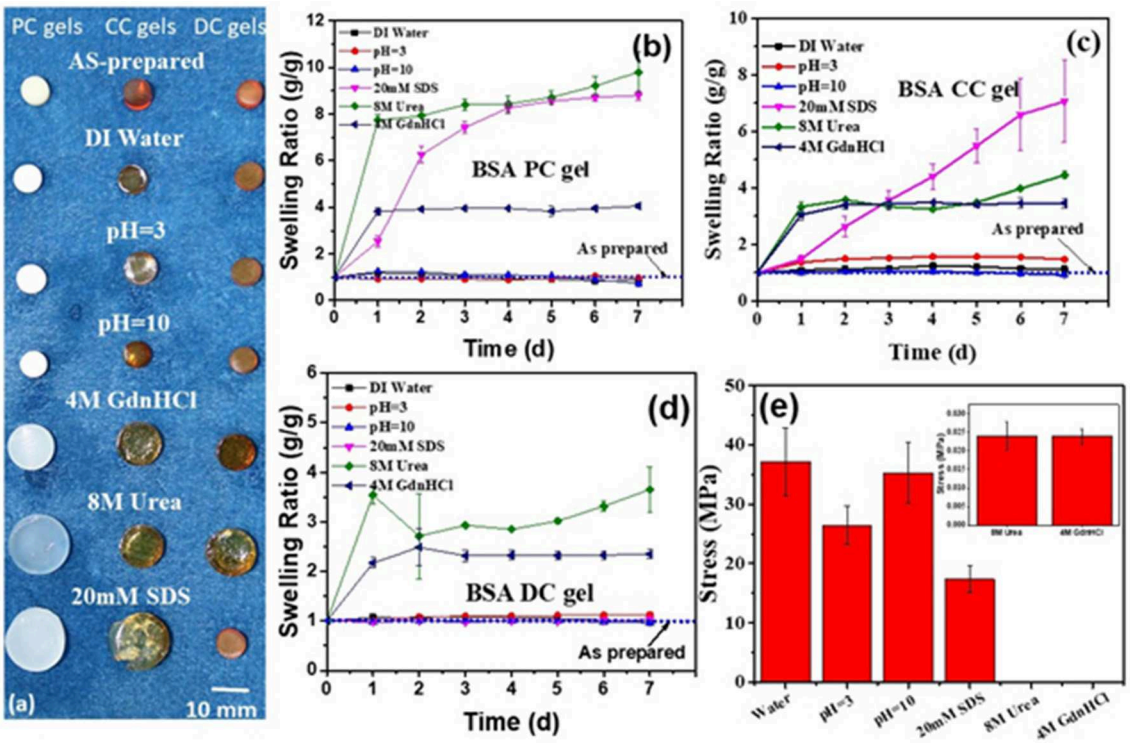

FIGURE 5 | (a) Photographs of three BSA gels after swelling in different solutions (inset reveals magnified plot in 8 M urea and 4 M GdnHCl solution; the scale is 10 mm); the swelling ratio in different solutions of BSA PC gel **(b)**, BSA CC gel **(c)**, and BSA DC gel **(d,e)** compressive strength of BSA DC gels after swelling in various solutions.

Specifically, the dissipated energies of BSA DC gel, BSA PC gel, and BSA CC gel were 120.04, 34.46, and 4.23 kJ/cm^3 (**Figure 6B**), respectively. The results indicate that BSA DC gel exhibits much larger energy dissipation ability, which is the reason why BSA DC gel demonstrates higher compressive strength than the other two BSA gels. The hysteresis loops also increased with increasing compressive strain, and U_{hys} increased from 2.36 to 624.75 kJ/m^3 as compressive strain increased from 10 to 80% (**Figures S3A,B**). Besides, successive loading-unloading without an interval between two consecutive loading cycles for BSA DC gel was also performed (**Figures S3C,D**). The hysteresis loops also increased with the increase in compressive strains, and distinct overlap was detected between two consecutive loading cycles, indicating that BSA DC gel partially recovers

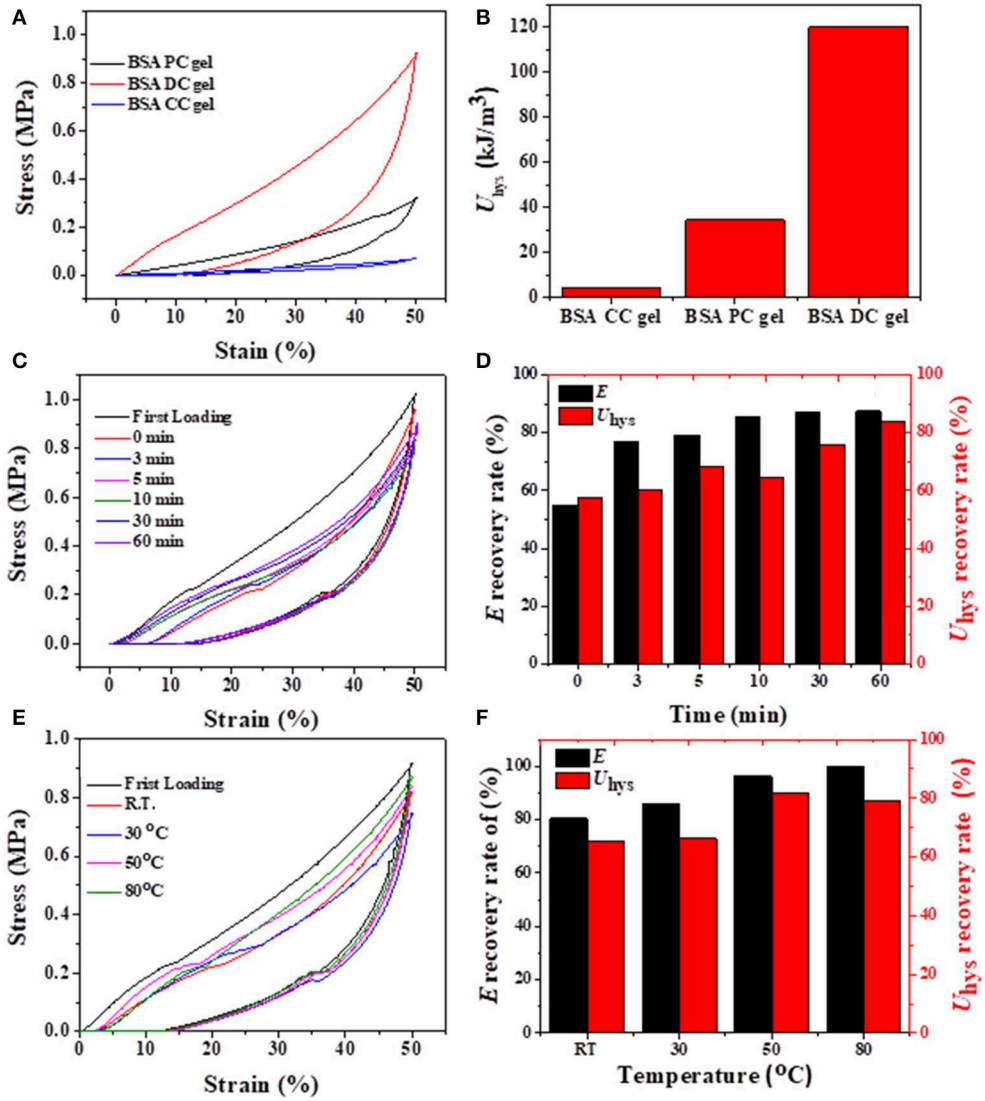

FIGURE 6 | (A) Loading-unloading curves of three BSA gels and **(B)** corresponding dissipated energies; **(C,D)** recovery of BSA DC gel at RT for various times; **(E,F)** recovery of BSA DC gel at various temperatures with 5 min recovery time between two consecutive loading cycles.

during the unloading. Therefore, the recovery behavior of BSA DC gel at room temperature (RT) for various recovery times was investigated (**Figures 6C,D**), and it was found that the hysteresis loops became larger when the recovery time was longer. Two recovery rates, i.e., stiffness recovery (based on E) and toughness recovery (based on U_{hys}), were defined as in our previous reports (Chen et al., 2017). Without recovery time, the stiffness and toughness of BSA DC gel were recovered to 55 and 58%, respectively. Impressively, with recovery for only 3 min, the recovery rates for stiffness and toughness reached up to 77 and 60%, respectively. At a recovery time of 60 min, stiffness recovery and toughness recovery were 87 and 84%, respectively. The effect of recovery temperature on the recovery of BSA DC gels was also investigated (**Figures 6E,F**). The hysteresis loops also increased with the increase in recovery temperature, and stiffness recovery and toughness recovery reached up to 100 and 87% at 80°C, respectively. The results indicate that our BSA DC gels demonstrated excellent and rapid self-recovery properties.

Considering that our BSA DC gels displayed excellent self-recovery properties at RT, they might also show fatigue resistance. As shown in **Figure 7A**, 10 successive loading-unloading cycles for the same BSA DC gel demonstrated that the hysteresis loops became the same after several loading cycles. Specifically, E and U_{hys} were approximately 908 kPa and 74 kJ/m^3 after several loading cycles (**Figure 7B**), respectively. Moreover, the BSA DC gel maintained integrity without breakage after the 10th loading cycle (data not shown). The results indicate that our BSA DC gels also have excellent fatigue resistance.

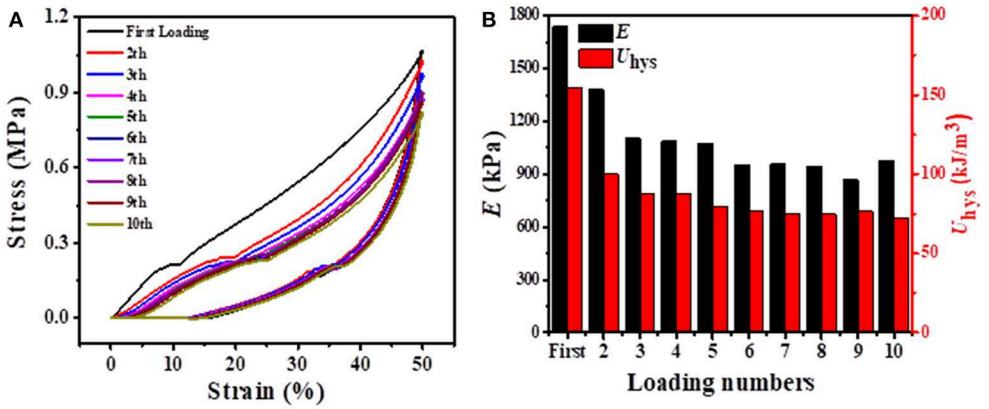

FIGURE 7 | (A) 10 successive loading-unloading cycles for the same BSA DC gel with 3 min recovery time between two consecutive loading cycles at a compressive strain of 50%; **(B)** corresponding elastic modulus and dissipated energy with loading cycling.

CONCLUSION

In summary, BSA DC gels, featuring hybrid chemical and physical cross-linkings, were prepared by a facile photoreaction-heating process. Owing to the hybrid cross-linkings, BSA DC gels demonstrated high strength, large hysteresis, rapid self-recovery, and excellent fatigue resistance at room temperature. The compressive strength of BSA DC gels was 37.81 ± 2.61 MPa, which was comparable to articular cartilage. More interestingly, BSA DC gel displayed high transparency and non-swelling properties while maintaining its high performances in DI water, pH = 3.0, and pH = 10.0. With a combination of simple preparation, high strength, and non-swelling properties, it is believed that BSA DC gels can potentially be applied in biomedical fields.

EXPERIMENTAL SECTION

Materials

Ammonium persulfate (APS, ≥98%) was purchased from Aladdin (Shanghai), and Bovine serum albumin (BSA, 98%) and tris(2,2′-bipyridine) ruthenium(II) dichloride [Ru(II)] were purchased from Sigma-Aldrich Inc. All materials were used without further purification.

Preparation of BSA DC Gels

BSA DC gels were prepared by a photoreaction-heating process as reported. Briefly, BSA (500 mg/mL), APS (300 mM), and Ru(II) (600 μM) were first dissolved into DI water. The precursor solution obtained was then injected into a cylindrical mold (D = 8.5 mm) and was exposed to white light (at a power of 8 W) for 4 h. The gel was then heated in a water bath (60–90°C) for 0–30 min. After cooling to room temperature, BSA DC gels were stored at 4°C for testing. BSA CC gels were synthesized via photoreaction without heating, while BSA PC gels were fabricated via heating pure BSA solution [without APS or Ru(II)] at 80°C for 10 min.

Characterizations

Mechanical Tests

Compressive and tensile tests were carried out with a WSM-10 kN machine (Changchun Zhineng Instrument Company). For compressive tests, the cylindrical gel samples (diameter = 8.5 mm, height = 10 mm) were conducted at 5 mm/min. The compressive stress (σ_c) was defined as F/A_0, where F is the force applied to the sample and A_0 is the initial cross-sectional area of the sample. The compressive strain was estimated as h/h_0, where h is the height of deformed gel and h_0 is the original height. The uniaxial tests of BSA DC gels (thickness = 1 mm and length = 60 mm) were pulled up at a constant rate of 100 mm/min. The tensile stress and strain were measured as F'/A_0' and l/l_0, where F′ is the force applied to the sample, A_0' is the initial cross-sectional area of the sample, l is the length of the stretched specimen, and l_0 is the original length. The compressive and tensile moduli were calculated from the slope of the linear region of the stress-strain curves. At least three independent experiments were conducted. The errors were calculated via Excel. The arithmetic mean value of the data was calculated first, and then the standard deviation (S.D.) was calculated. Statistical analysis was done by one-way analysis of variance (ANOVA) and LSD's multiple comparison post-test with a 99.9% confidence interval among the applied treatments ($p < 0.01$). Cyclic loading tests of gels were also performed by the abovementioned machine at 5 mm/min with maximum strain from 10 to 80%. Successive loading-unloading tests were done on the same gel specimen. For self-recovery tests, the samples were recovered at different temperatures (RT to 80°C) for various times (0–60 min). The dissipated energies were calculated via the area between loading-unloading curves. The recovery rates were defined as the rate of dissipated energy ($U_{hys,t}$) or elastic modulus (Et) to the first loading cycle ($U_{hys,0}$ or E_0). Stiffness recovery was defined as the ratio of the elastic modulus at various times or temperatures to that of the first loading cycle, while toughness recovery was evaluated as the ratio of dissipated energies at various times or temperatures to those of the first loading cycle at a maximum compressive strain of 50%.

Swelling Tests

As-prepared hydrogels (diameter = 8.5 mm, height = 10 mm) were firstly weighed and then immersed in different solutions at 25°C. After a predetermined time, the swollen hydrogels were taken out and weighed again. The swelling ratio (SR) was obtained from the following equation: $SR = m_t/m_0$, where m_0 and m_t are the weight of as-prepared gel and swollen gel, respectively.

Other Tests

Scanning electron microscope (SEM) tests were performed using a MERLIN Compact instrument (Zeiss, Germany) at a voltage of 15 KV. All the gel samples were frozen and fractured in liquid nitrogen, and they were then dried in a lyophilizer. Before the tests, the samples were coated with a thin layer of gold. Fourier transform infrared spectra (FT-IR) of the BSA hydrogel powders were obtained with a Bruker Tensor 27. The BSA gel sheet was cut into a disk for rheological tests (thickness = 1 mm, diameter = 25 mm). Rheological tests were carried out on a rheometer (Anton Paar, MCR302) via the plate-plate mode. Amplitude sweep tests were carried out at ω of 10 rad/s and 25°C. Frequency sweep tests were performed at a strain of 0.1%, ω of 0.1–100 rad/s, and at 25°C. The ultraviolet spectrum of BSA DC gel was recorded on a double-beam UV-visible spectrophotometer (General Analytical Instruments Co. Ltd, TU-1901, Beijing).

DATA AVAILABILITY STATEMENT

The raw data supporting the conclusions of this article will be made available by the authors, without undue reservation, to any qualified researcher.

AUTHOR CONTRIBUTIONS

The manuscript was prepared by QC and GS, and the gels were synthesized by SL, LZ, and QW. The tests were cooperated and finished by SL, ZL, CT, and HS. The data were analyzed by JY, GQ, and GS.

ACKNOWLEDGMENTS

QC was grateful for financial support, in part, from the National Natural Science Foundation of China (21504022), Henan Province (17HASTIT006, NSFRF1605, and 2016GGJS-039), and Henan Polytechnic University (72105/001 and 672517/005).

SUPPLEMENTARY MATERIAL

The Supplementary Material for this article can be found online at: https://www.frontiersin.org/articles/10.3389/fchem.2020.00106/full#supplementary-material

REFERENCES

Bhattacharjee, P., Kundu, B., Naskar, D., Maiti, T. K., Bhattacharya, D., and Kundu, S. C. (2015). Nanofibrous nonmulberry silk/PVA scaffold for osteoinduction and osseointegration. *Biopolymers* 103, 271–284. doi: 10.1002/bip.22594

Chen, H., Liu, Y., Ren, B., Zhang, Y., Ma, J., Xu, L., et al. (2017). Super bulk and interfacial toughness of physically crosslinked double-network hydrogels. *Adv. Funct. Mater.* 27:1703086. doi: 10.1002/adfm.201703086

Endrizzi, B. J., Huang, G., Kiser, P. F., and Stewart, R. J. (2006). Specific covalent immobilization of proteins through dityrosine cross-links. *Langmuir* 22, 11305–11310. doi: 10.1021/la0618216

Epstein-Barash, H., Stefanescu, C. F., and Kohane, D. S. (2012). An in situ cross-linking hybrid hydrogel for controlled release of proteins. *Acta Biomater.* 8, 1703–1709. doi: 10.1016/j.actbio.2012.01.028

Feng, Q., Wei, K., Zhang, K., Yang, B., Tian, F., Wang, G., et al. (2018). One-pot solvent exchange preparation of non-swellable, thermoplastic, stretchable and adhesive supramolecular hydrogels based on dual synergistic physical crosslinking. *NPG Asia Mater.* 10:e455. doi: 10.1038/am.2017.208

Fernandez-Castano Romera, M., Lafleur, R. P. M., Guibert, C., Voets, I. K., Storm, C., and Sijbesma, R. P. (2017). Strain stiffening hydrogels through self-assembly and covalent fixation of semi-flexible fibers. *Angew Chem. Int. Ed. Engl.* 56, 8771–8775. doi: 10.1002/anie.201704046

Gacanin, J., Hedrich, J., Sieste, S., Glasser, G., Lieberwirth, I., Schilling, C., et al. (2019). Autonomous ultrafast self-healing hydrogels by ph-responsive functional nanofiber gelators as cell matrices. *Adv. Mater.* 31:e1805044. doi: 10.1002/adma.201805044

Hashemnejad, S. M., Huda, M. M., Rai, N., and Kundu, S. (2017). Molecular insights into gelation of di-fmoc-l-lysine in organic solvent–water mixtures. *ACS Omega* 2, 1864–1874. doi: 10.1021/acsomega.7b00108

Jo, M., Min, K., Roy, B., Kim, S., Lee, S., Park, J. Y., et al. (2018). Protein-based electronic skin akin to biological tissues. *ACS Nano* 12, 5637–5645. doi: 10.1021/acsnano.8b01435

Kabb, C. P., O'Bryan, C. S., Deng, C. C., Angelini, T. E., and Sumerlin, B. S. (2018). Photoreversible covalent hydrogels for soft-matter additive manufacturing. *ACS Appl. Mater. Interfaces* 10, 16793–16801. doi: 10.1021/acsami.8b02441

Koetting, M. C., Guido, J. F., Gupta, M., Zhang, A., and Peppas, N. A. (2016). pH-responsive and enzymatically-responsive hydrogel microparticles for the oral delivery of therapeutic proteins: Effects of protein size, crosslinking density, and hydrogel degradation on protein delivery. *J. Control Release* 221, 18–25. doi: 10.1016/j.jconrel.2015.11.023

Lee, J., Ju, M., Cho, O. H., Kim, Y., and Nam, K. T. (2019). Tyrosine-rich peptides as a platform for assembly and material synthesis. *Adv. Sci.* 6:1801255. doi: 10.1002/advs.201801255

Li, Z., Zheng, Z., Yang, Y., Fang, G., Yao, J., Shao, Z., et al. (2016). Robust protein hydrogels from silkworm silk. *ACS Sustain. Chem. Eng.* 4, 1500–1506. doi: 10.1021/acssuschemeng.5b,01463

Lü, S., Bai, X., Liu, H., Ning, P., Wang, Z., Gao, C., et al. (2017). An injectable and self-healing hydrogel with covalent cross-linking *in vivo* for cranial bone repair. *J. Mater. Chem. B* 5, 3739–3748. doi: 10.1039/C7TB00776K

Luo, K., Yang, Y., and Shao, Z. (2016). Physically crosslinked biocompatible silk-fibroin-based hydrogels with high mechanical performance. *Adv. Funct. Mater.* 26, 872–880. doi: 10.1002/adfm.201503450

Ma, X., Sun, X., Hargrove, D., Chen, J., Song, D., Dong, Q., et al. (2016). A biocompatible and biodegradable protein hydrogel with green and red autofluorescence: preparation, characterization and *in vivo* biodegradation tracking and modeling. *Sci. Rep.* 6:19370. doi: 10.1038/srep19370

Militello, V., Casarino, C., Emanuele, A., Giostra, A., Pullara, F., and Leone, M. (2004). Aggregation kinetics of bovine serum albumin studied by FTIR spectroscopy and light scattering. *Biophys. Chem.* 107, 175–187. doi: 10.1016/j.bpc.2003.09.004

Moura, M. J., Faneca, H., Lima, M. P., Gil, M. H., and Figueiredo, M. M. (2011). *In situ* forming chitosan hydrogels prepared via ionic/covalent co-cross-linking. *Biomacromolecules* 12, 3275–3284. doi: 10.1021/bm200731x

Nojima, T., and Iyoda, T. (2018). Egg white-based strong hydrogel via ordered protein condensation. *NPG Asia Mater.* 10:e460. doi: 10.1038/am.2017.219

Numata, K., Ifuku, N., Masunaga, H., Hikima, T., and Sakai, T. (2017). Silk resin with hydrated dual chemical-physical cross-links achieves high strength and toughness. *Biomacromolecules* 18, 1937–1946. doi: 10.1021/acs.biomac.7b00376

Partlow, B. P., Applegate, M. B., Omenetto, F. G., and Kaplan, D. L. (2016). Dityrosine cross-linking in designing biomaterials. *ACS Biomater. Sci. Eng.* 2, 2108–2121. doi: 10.1021/acsbiomaterials.6b00454

Partlow, B. P., Hanna, C. W., Rnjak-Kovacina, J., Moreau, J. E., Applegate, M. B., Burke, K. A., et al. (2014). Highly tunable elastomeric silk biomaterials. *Adv. Funct. Mater.* 24, 4615–4624. doi: 10.1002/adfm.201400526

Picchioni, F., and Muljana, H. (2018). Hydrogels based on dynamic covalent and non covalent bonds: a chemistry perspective. *Gels* 4:21. doi: 10.3390/gels4010021

Qin, H., Zhang, T., Li, H. N., Cong, H. P., Antonietti, M., and Yu, S. H. (2017). Dynamic au-thiolate interaction induced rapid self-healing nanocomposite hydrogels with remarkable mechanical behaviors. *Chemistry* 3, 691–705. doi: 10.1016/j.chempr.2017.07.017

Rangel-Argote, M., Claudio-Rizo, J. A., Mata-Mata, J. L., and Mendoza-Novelo, B. (2018). Characteristics of collagen-rich extracellular matrix hydrogels and their functionalization with poly(ethylene glycol) derivatives for enhanced biomedical applications: a review. *ACS Appl. Bio Mater.* 1, 1215–1228. doi: 10.1021/acsabm.8b00282

Silva, M. A., Lenton, S., Hughes, M., Brockwell, D. J., and Dougan, L. (2017). Assessing the potential of folded globular polyproteins as hydrogel building blocks. *Biomacromolecules* 18, 636–646. doi: 10.1021/acs.biomac.6b01877

Sun, Y., and Huang, Y. (2016). Disulfide-crosslinked albumin hydrogels. *J. Mater. Chem. B* 4, 2768–2775. doi: 10.1039/C6TB00247A

Tang, Z., Chen, Q., Chen, F., Zhu, L., Lu, S., Ren, B., et al. (2018). General principle for fabricating natural globular protein-based double-network hydrogels with integrated highly mechanical properties and surface adhesion on solid surfaces. *Chem. Mater.* 31, 179–189. doi: 10.1021/acs.chemmater.8b03860

Tavsanli, B., and Okay, O. (2019). Mechanically robust and stretchable silk/hyaluronic acid hydrogels. *Carbohydr. Polym.* 208, 413–420. doi: 10.1016/j.carbpol.2018.12.088

Toivonen, M. S., Kurki-Suonio, S., Schacher, F. H., Hietala, S., Rojas, O. J., and Ikkala, O. (2015). Water-resistant, transparent hybrid nanopaper by physical cross-linking with chitosan. *Biomacromolecules* 16, 1062–1071. doi: 10.1021/acs.biomac.5b00145

Wang, L., Jiang, X., Zhang, M., Yang, M., and Liu, Y. N. (2017). *In situ* assembly of au nanoclusters within protein hydrogel networks. *Chem. Asian J.* 12, 2374–2378. doi: 10.1002/asia.201700915

Wang, L., Liang, K., Jiang, X., Yang, M., and Liu, Y. N. (2018). Dynamic protein-metal ion networks: a unique approach to injectable and self-healable metal sulfide/protein hybrid hydrogels with high photothermal efficiency. *Chemistry* 24, 6557–6563. doi: 10.1002/chem.201705841

Xu, D., Huang, J., Zhao, D., Ding, B., Zhang, L., and Cai, J. (2016). High-flexibility, high-toughness double-cross-linked chitin hydrogels by sequential chemical and physical cross-linkings. *Adv. Mater.* 28, 5844–5849. doi: 10.1002/adma.201600448

Yan, Y., Cheng, B., Chen, K., Cui, W., Qi, J., Li, X., et al. (2019). Enhanced osteogenesis of bone marrow-derived mesenchymal stem cells by a functionalized silk fibroin hydrogel for bone defect repair. *Adv. Healthc. Mater.* 8:e1801043. doi: 10.1002/adhm.201801043

Yang, Y., Wang, X., Yang, F., Wang, L., and Wu, D. (2018). Highly elastic and ultratough hybrid ionic–covalent hydrogels with tunable structures and mechanics. *Adv. Mater.* 30:1707071. doi: 10.1002/adma.201707071

Yetiskin, B., Akinci, C., and Okay, O. (2017). Cryogelation within cryogels: silk fibroin scaffolds with single-, double- and triple-network structures. *Polymer* 128, 47–56. doi: 10.1016/j.polymer.2017.09.023

Yuk, H., Zhang, T., Lin, S., Parada, G. A., and Zhao, X. (2016). Tough bonding of hydrogels to diverse non-porous surfaces. *Nat. Mater.* 15, 190–196. doi: 10.1038/nmat4463

Zhang, X., Liu, W., Yang, D., and Qiu, X. (2019). Biomimetic supertough and strong biodegradable polymeric materials with improved thermal properties and excellent UV-Blocking performance. *Adv. Funct. Mater.* 29:1806912. doi: 10.1002/adfm.201806912

Zhang, Y., Li, S., Ma, M., Yang, M., Wang, Y., Hao, A., et al. (2016). Tuning of gel morphology with supramolecular chirality amplification using a solvent strategy based on an Fmoc-amino acid building block. *New J. Chem.* 40, 5568–5576. doi: 10.1039/C6NJ00092D

Zhu, Z., Ling, S., Yeo, J., Zhao, S., Tozzi, L., Buehler, M. J., et al. (2018). High-strength, durable all-silk fibroin hydrogels with versatile processability toward multifunctional applications. *Adv. Func. Mater.* 28:1704757. doi: 10.1002/adfm.201704757

Conflict of Interest: The authors declare that the research was conducted in the absence of any commercial or financial relationships that could be construed as a potential conflict of interest.

frontiers in Chemistry

ORIGINAL RESEARCH
published: 26 February 2020
doi: 10.3389/fchem.2020.00120

Dynamic Responsive Formation of Nanostructured Fibers in a Hydrogel Network: A Molecular Dynamics Study

Jan Zidek[1]*, *Andrey Milchev*[2] *and Josef Jancar*[1,3]

[1] Advanced Polymers and Composites, Central European Institute of Technology (CEITEC), Brno University of Technology, Brno, Czechia, [2] Institute of Physical Chemistry, Bulgarian Academy of Sciences, Sofia, Bulgaria, [3] SCITEG, Brno, Czechia

In an effort to study natural fiber formation, such as, e.g., spider silk, we present a model, which is capable of forming biomimetic fibrillar nanostructure from a hydrogel micellar network. The latter consists of interacting atomic groups which form cores of micelles, and of flexible chains forming the shells of the micelles. Micelles are connected in a compact network by linearly stretched chains. The structural elements of the network can be transformed during deformation from micellar into fibrillary type and their evolution is found to depend significantly on strain rate. Our model suggests a set of conditions suitable for the formation of nanostructured fibrillar network. It demonstrates that a fibrillar structure is only formed upon sufficiently fast stretching while, in contrast, the micellar gel structure is preserved, if the material is pulled slowly. We illustrate this key aspect by a minimalistic model of only four chains as part of the whole network, which provides a detailed view on the mechanism of fibril formation. We conclude that such a simplified structure has similar functionality and is probably responsible for the formation of nano-structured molecular fibrils in natural materials.

Keywords: hydrogel, molecular dynamics, relaxation, deformation, nanostructured, network, self-assembly

OPEN ACCESS

Edited by:
Yi Cao,
Nanjing University, China

Reviewed by:
Xinpeng Xu,
Guangdong Technion-Israel Institute of Technology (GTIIT), China
Hong-ming Ding,
Soochow University, China

***Correspondence:**
Jan Zidek
jan.zidek@ceitec.vutbr.cz

Specialty section:
This article was submitted to Polymer Chemistry, a section of the journal Frontiers in Chemistry

Received: *08 November 2019*
Accepted: *10 February 2020*
Published: *26 February 2020*

Citation:
Zidek J, Milchev A and Jancar J (2020) Dynamic Responsive Formation of Nanostructured Fibers in a Hydrogel Network: A Molecular Dynamics Study. Front. Chem. 8:120. doi: 10.3389/fchem.2020.00120

1. INTRODUCTION

The arrangement of molecules in natural materials is assumed to be optimal for their efficient functioning, motivating thus the efforts to mimic the natural arrangement also in man-made materials. Natural materials comprise a sequence of atomic groups, assembled in hierarchical structure on the nanometer and supermolecular level. Tensile deformation plays a key role in the formation of biological materials, such as spider silk, where the final structure consists of nano-crystalline inclusions incorporated in the rubbery network. In fact, the drawing of fibers is frequently used in laboratory and in industry (Mondal et al., 2008; Peng C. A. et al., 2017), and has been recently improved by means of electrospinning (Svachova et al., 2016; Srivastava, 2017). The electrospinning provides stretching of material at significantly higher stretching rates than simple mechanical deformation. Wang and Hashimoto (2018) observed a correlation between stretching rate and orientation of molecules during the electrospinning. They performed electrospinning of poly-vinylalcohol from water solution and recorded the process by high speed camera. Observed were domains of fibrillar material and bulges from disordered material whereby a higher speed of spinning lead to a decrease of the amorphous bulge size. The nanostructural arrangement has thus clear relation to the strain rate. Generally, however, the formation of nanostructured fibrils is still

poorly understood while modeling studies suggest, that the formation of fibrils is based on plastic deformation of polymers.

In what follows we demonstrate that the rate of stretching governs the ultimate structure and superior properties of such natural materials. We develop a model, which mimics the functionality of spider silk in a simplified form, illustrating the formation of nanostructured fibrillar domains (Zidek et al., 2016). The resulting fibrillar structure formed by tensile deformation persists even after the deforming force is removed. The formation mechanism itself can be controlled by the stretching rate. The system is a micellar hydrogel network with an initial atomistic configuration, which behaves differently upon quick or slow deformation as the analysis of the structural evolution during the stretching process shows. Owing to the adopted simplified model, the mechanism of fiber formation can be readily monitored, suggesting the possibility of generating and testing similar materials of desired structure in a laboratory.

Our basic assumption is that the stretching rate controls fiber formation as has been observed and described recently (Zidek et al., 2016). In order to address the question as to why fibrils are formed only under specific circumstances, we consider the simplest structure, where structural aspects of the transformation become clearly visible in contrast to more complex natural materials. A relevant property of such system is that of block copolymer material with constant block length, end-capped by some interacting groups as, e.g., copolymer poly-lactide/glycolide/PEG, end-capped by itaconic acid (Michlovska et al., 2016). Our model reveals how an orientationally ordered structure can be created from this type of materials. The principles of the model are based on the notion of bundling (Benetatos and Jho, 2016) albeit there is currently no general theory of bundling in polymers. Bundles are assemblies of aligned semiflexible macromolecules, which are separated from other bundles by an amorphous matrix, or by empty space and do not aggregate into a single infinite bundle containing all molecules. In a network with covalent and physical crosslinks the semistiff polymer chains are usually attracted by Van der Waals and electrostatic forces. An essential factor is the existence of high energy barriers in the system, preventing condensation of all molecules into a single fibril. For instance, the bundling of DNA proceeds by transformation from thoroidal to rod-like shape whereby stable bundles are created (as in our model) whenever loops of chains can be transformed into bundles of straight chains overcoming a certain energy barrier.

An important precursor of the nanostructured self assembly is the domain structure. Nilebäck et al. (2018) investigated the self assembly of two neat materials, which are present in the natural silk. The first material represents a 4-fold repetition of alternated polyalanine and glycine-rich regions (4Rep), and the second one itself is globular C-terminal (CT). Both neat components form a disordered material as does a physical mixture thereof. The self-assembly to the fibrillar structure has been observed only in the case when 4Rep is connected to CT. Our fibers are also composed from domains of soft micellar structure and interconnected segments of stretched chain.

An appropriate system, which can lead to bundles of molecules, is the solvated macromolecular network. An advantageous prerequisite situation thereby is a network that is swollen by the solvent. Several macromolecules can then stick together forming a fibril while the network does not collapse into a single fibril. That is probably the case of the spider silk. The original structure of spider silk fibroin is a micellar network (Jin and Kaplan, 2003; Walker et al., 2015) (**Figure 1A**). It is a liquid-like protein gel which remains liquid in the spider body, where deformation is slow, due to the micellar structure of the hydrogel. During quick extrusion, this gel is then transformed into a liquid crystal structure (**Figure 1B**), stretched chains (**Figure 1C**) and subsequently into β-sheets (**Figure 1D**). The initiating factor of the transformation is deformation of material *outside* the spider body.

The fibrils observed in spider silk (Wang et al., 2006; Perry et al., 2010) have well-defined molecular structure. Among the possible factors, which are believed to play a key role in self-assembly from the primary atomistic sequence, are exactly located interacting sites and side groups. Moreover, the transformation of a natural material is sensitive to a number of external conditions, such as *pH* (**Figures 1A–D**) and/or temperature. Originally, a micellar structure from silk spidroin is formed, followed by phase separation due to ion exchange acidification and water removal. During the second phase, a liquid crystalline phase is formed. Next, the pulling of fibers forms the final structure (Liu and Zhang, 2014). It has been found, that the stretching can induce hydrophobicity of the material (Lele et al., 2001) owing to cooperative hydrogen bonding of polymer chains. The detailed description morphology is provided by wide angle X-ray diffraction (Grubb and Jelinski, 1997). The liquid crystal transformation into final fiber is achieved by re-orientation during the stretching as an affine deformation of a network with inclusions.

Our model describes only mechanical transformation of the structure and does not include the chemical changes in the real spider silk fibers during formation. However, the induced hydrophobicity is observed as well. The energy of solvation is found to switch from negative to positive values. As a result, the stretching of the network leads to expulsion of water from the network.

The final structure of fibers is given by a specific sequence of amino acids that take part in the formation of β-sheets and sequences rich in poly-glycine [**Figure 1D**-sequence (1)], which form flexible chains. The sequences of β-sheets of nanocrystals must be aligned [**Figure 1D**-sequence (2)]. Also the end-to-end distance of a soft chain, rich in poly-glycine, connecting two β-sheets must be controlled. To some extent, the final structure of fiber material is encoded in the primary sequence of the amino acids. Also in our model the ability to form fibrillar structure is encoded in the alternating sequence of interacting acrylic acid (*AA*) and polyethylene glycol (PEG) molecules. The fibers of polyethylene contain domains of crystalline phase (Lee and Rutledge, 2011; Yamamoto, 2013), which alternate with large amorphous domains. The atomistic structure of spider silk and our model are micellar in the phase of geometry optimization.

The technique of thread drawing is an important aspect too, which determines the ultimate structure of the material. Andersson et al. (2017) considered laboratory drawing of silk

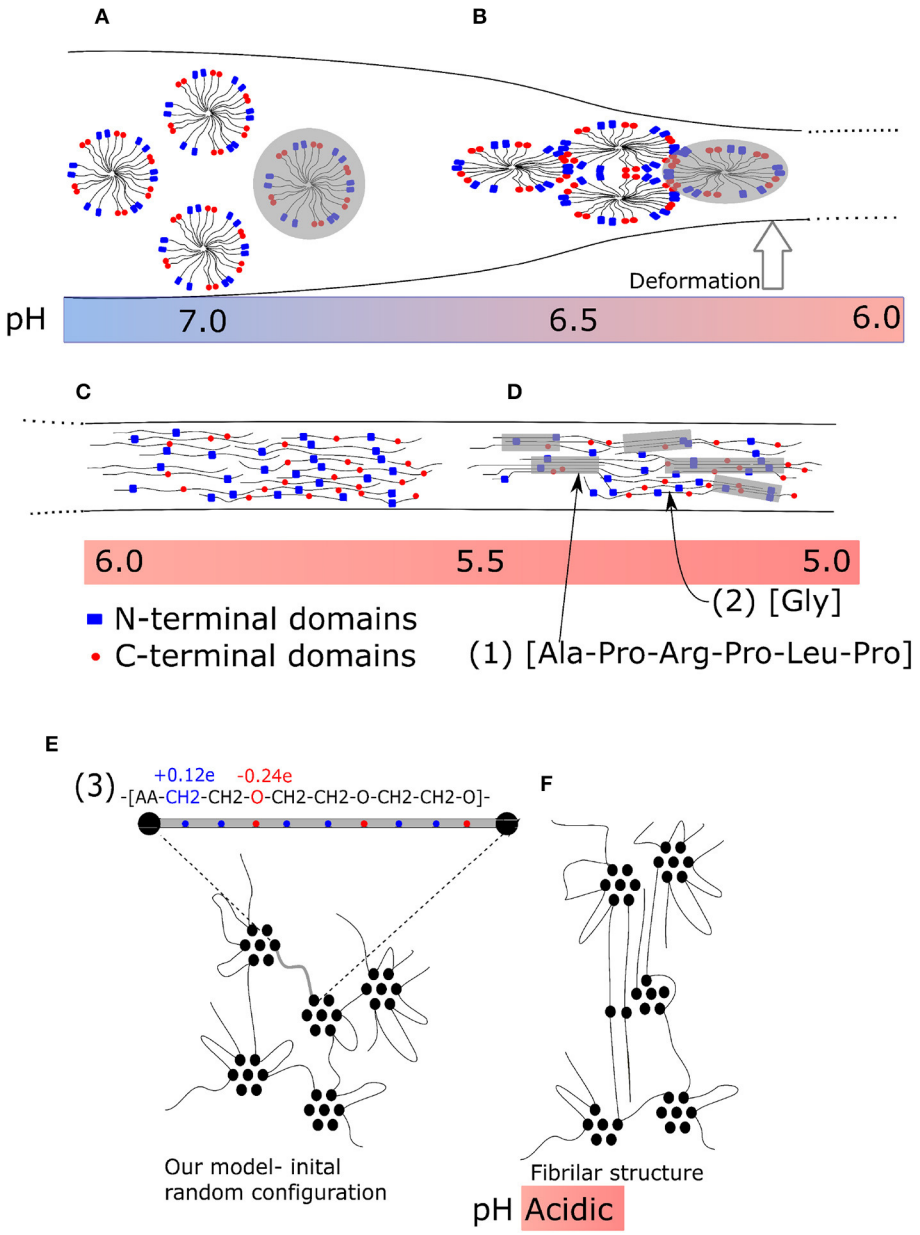

FIGURE 1 | Fiber formation mechanism of spider silk during tensile deformation. **(A)** Micellar network: not deformed; **(B)** Liquid crystalline phase: moderate deformation; **(C)** Nanocrystalline fibrillar structure: strong deformation. **(A–C)** Enlarged parts of structures. (1) Typical secondary structure (amino acid sequence) of nanocrystalline chain, (2) typical flexible connecting chain rich in glycine, and (3) a repeating unit of our model. **(D)** Final structure of spider silk with β-sheets. **(E)** Micellar structure before deformation; **(F)** model nano-fibrillar structure after deformation.

spidroin and compared the laboratory-made and naturally spun fibers originating from exactly the same structure of natural silk fibroin so as to investigate the effect of fiber elongation. The laboratory spun fiber did not have exactly the same structure as the natural fiber. The principal property of spider silk, formation of β-sheets, was observed to a less extent in man-made fiber than in natural fiber. In contrast, fiber produced in laboratory contained rather helical ordering.

Another example of biological material formed by stretching is the fibronectin. This material contains cryptic sites (Zhong et al., 1998), which include disulfide bridges in particular position (Zhong et al., 1998; Peleg et al., 2012). The position of disulfide bridges is regulated by the *integrin* protein in molecular structure. The role of cryptic sites is to *align* the molecular structure, when it is stretched. In the fibronectin, the configuration of primary structure is an important factor too. We also found that the formation of intermolecular bridges has effect in our model. At

present, we can only decrease the ability of fiber formation by the addition of random covalent bonds. When the concentration of covalent bonds exceeds a threshold, the fibrillar structure completely disappears (Zidek et al., 2016).

Molecular modeling is a powerful method for studying fiber formation by self-assembly of molecular structures, and several investigations have been carried out recently. The deformation and failure of self-assembled hydrogels were investigated by Hammond and Kamm (2008). They applied a coarse-grained model using molecular dynamics for the deformation of collagen bundles, which serve as building blocks of the oriented filament structure of collagen. Structural self-assembly from their precursor structure is frequently modeled in proteins. In particular, the secondary structure of spider silk was modeled recently (Gray et al., 2016). The irreversible formation of oriented blocks was observed also in swollen polymers (Miyazaki et al., 2006; Peng N. et al., 2017). As well, the strain-induced crystallization is typical for some biomaterials like the above mentioned spider silk (Peng C. A. et al., 2017), collagen fibrils (Buehler, 2006) or poly-lactides (Stoclet, 2016). In this work we demonstrate that the formation of fibrillar structure can be achieved from materials with very simple micellar structure (**Figure 1E**). The primary structure of our model appears favorable for the formation of bundles (**Figure 1F**). An essential factor thereby is the periodical sequence of constant blocks of poly(ethylene glycol) alternating with interacting groups of acrylic acid [**Figure 1E**-sequence (3)]. In principle, this is a common material, which does not have any special structure and needs no pre-ordering before stretching.

2. MODELS AND METHODS

2.1. Network Model

Fiber formation was investigated by utilizing two models: a network model and a four-chains model. Both models complement and comply with one another while each model provides different kind of information.

Our *network model* describes a rather general micellar structure, which serves as a prerequisite for the formation of fibrils. The network has been uniaxially stretched and the resulting structure was monitored during the stretching. Therefore, this model provides information about the response of a general network structure to tensile deformation. The system is a representative cubic box of a hydrogel network with 5 nm side size. The model is composed of 8 macromolecular chains with each chain comprising 200 molecular groups. The macromolecular phase is solvated by 2,447 molecules of water. The motion of atomic groups of chains and of the solvent and the deformation of the material were modeled by molecular dynamics simulation.

The structure of material is presented in **Figure 2**. **Figure 2a** shows the primary structure, which is based on a repeating unit of acrylic acid (*AA*), methylene group (CH_2), and oxygen (*O*). **Figures 2b–d** show some structural elements, which have formed during the initial MD simulation. A single chain with given primary structure spontaneously forms loops and stretched chains (**Figure 2b**). The structure consists of cores of micelles, mostly made of *AA*-groups, and of flexible shells of micelles comprised of PEG chains. The micelles are organized into a micellar network (**Figure 2d**), as shown schematically in **Figure 1D** too.

The potential energy of the network was calculated from contribution of bonding energy, non-bonding Van der Waals interactions and electrostatic forces. The Hamiltonian of the simulation was calculated:

$$\mathcal{H} = \sum_{nb} U_b + \sum_{na} U_a + \sum_{np} U_{el} + \sum_{np} U_{LJ} \qquad (1)$$

where nb is number of bonds, na is a number of bending angles and np is a number of non-bonding pairs. The energy of bonds

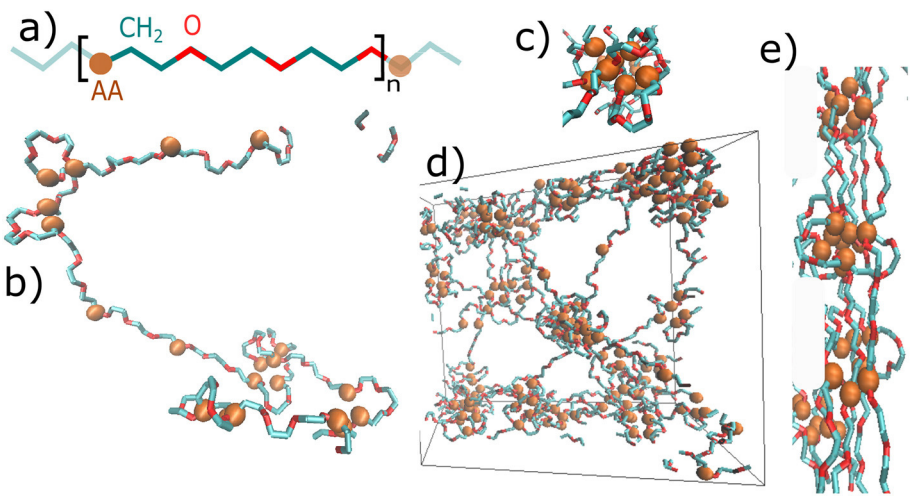

FIGURE 2 | Snapshots of the hydrogel molecular structure: **(a)** primary structure—repeating unit of the chain: blue—methylene group of polyethylene glycol, red—oxygen of polyethylene glycol, *AA*—physically interacting group; **(b)** Secondary structure of a single chain: loops and stretched chains; **(c)** a single micelle; **(d)** dry phase of network: entire box (box side = 5*nm*); **(e)** fibril formed by deformation.

TABLE 1 | List of stretching rates (r) applied in this work.

$r[ns^{-1}]$	Word description
0.01	Slow
0.02	0.2 × quick
0.05	Moderate, 0.5 × quick
0.1	Quick
0.2	2 × quick
0.5	5 × quick
1	Quickest, 10 × quick

and angles was calculated from harmonic potential, non-bonding interactions were taken as Lennard Jones potential function and the electrostatic potential was calculated from Coulomb electrostatic interaction potential. The details are presented in **Supplementary Material**.

The model was deformed at constant volume. The uniaxial stretching in z-direction was completed by compression in xy-directions. The model box has been stretched using seven different stretching rates. The rates are chosen in a logarithmic scale from 0.01 to 1 ns^{-1}. In what follows we use the term "slow" for the deformation speed of 0.01 ns^{-1}, and "quick" for 0.1 ns^{-1}. The slow and quick deformations are found to induce significantly different network evolution. Therefore, we have examined the intermediate rates between slow and quick so as to get a better notion of the transition between both. Below, the rates are mostly referred to as a ratio to the quick deformation rate (**Table 1**).

These stretching rates are high in comparison to those used in real experiments. Molecular dynamics simulation deals with times in the range of hundreds of ns or μs. Stretching rates in classic deformation take approximately (10^{-12} s^{-1}). The estimated stretching speed of electrospun material in the article of Wang and Hashimoto (2018), measured from image analysis of the high speed camera, was (10^{-7} s^{-1}). Nevertheless, a clear qualitative correlation between stretching rate and the process of orientation was observed in our simulation too. The results for one stretching rate of network model were calculated from 4 independent simulations with different initial atomistic configuration.

The deformation of the system is reflected by the change in energy density, which can be transformed itself into a stress-strain relationship. The stress strain relationships are presented elsewhere (cf. Zidek et al., 2016, 2017b). We assume that the structure gets organized during the stretching and bundles form. The bundles are objects of three or more mutually aligned chains. An example of bundles is displayed in **Figure 2e**. Bundles were analyzed according to their orientation in space or depending on the degree of twisting (see the **Supplementary Material**). An object is identified as a bundle, when it satisfies several conditions:

- The bundle must be composed of 3 or more aligned short flexible chains.
- The end-to-end distance of all chains in the bundle between two physical clusters must be sufficiently long, >0.65 nm.
- The bundle must connect two physical clusters.

The next aspect of deformation is the damage of the physical network and its recovery with time. The damage affects the micellar structure of the network, displayed by the cores of micelles, which form *physical clusters* (PCLs) in the network. The strength of a physical network is proportional to the volume fraction of PCLs. Therefore, the damage can be estimated as a decrease of the volume fraction of PCLs. A structural recovery means that the structure after deformation has been restored to the original one (**Figure 2d**).

The volume fraction of physical clusters is calculated in this work by triangulation of space between the interacting groups, namely, by 3D-Delaunay triangulation (DT). DT is itself a mathematical algorithm, which creates a triangular 3-dimensional mesh from the interacting AA-groups in the cores of micelles. The distribution of connecting lines is related to the fraction of clusters. Detailed information about the modeling method and the parameters of the models are provided in **Supplementary Material**.

2.2. The Four Chains Model

A disadvantage of the network model is that one cannot specifically control the mutual position of particular chains, the combination of angles between stretched chains as well as their end-to-end distances, even though the network model shows the evolution of the entire network structure.

The auxiliary "4-chains model" is a minimalistic one, composed of only four flexible chains which span interacting groups. The four chains model is a structural element which is present also in the network model (**Figure 3A**). This simplified model controls the mutual orientation of chains and their end-to-end distances (**Figure 3B**). The composition of chains can be varied and one can analyze its influence on the formation of fibrils, which is not possible within the network model.

The bundles and fibrils were identified in the network model and in the four chains model (**Figures 3C,D**). We characterized the resulting fibril shape by means of the 2nd Legendre polynomial (P_2), which describes the orientation of different segments (each segment standing for two consecutive bonds) of the chains. The orientation of a segment is determined with respect to the fiber vector. The latter is sum of the end-to-end vectors of all four chains. P_2 describes the correlation of the fiber orientation with the individual segments of the chains, whereby $P_2 = -0.5$, when the segments are oriented perpendicular the to fiber, $P_2 = 0$, for randomly oriented segments, and $P_2 = 1$, when all segments are parallel to the fiber:

$$P_2 = 0.5(3\langle\cos^2\theta\rangle - 1), \tag{2}$$

where θ is the angle of a segment with the fibril vector.

2.3. Relaxation of Network

The relaxation was analyzed immediately after the system was deformed. In fact, the relaxation contains several effects which occur during different time scales. That is why we performed three relaxation simulations lasting 1, 100, and 100,000 ps (100 ns) with the same initial configuration and initial random seed.

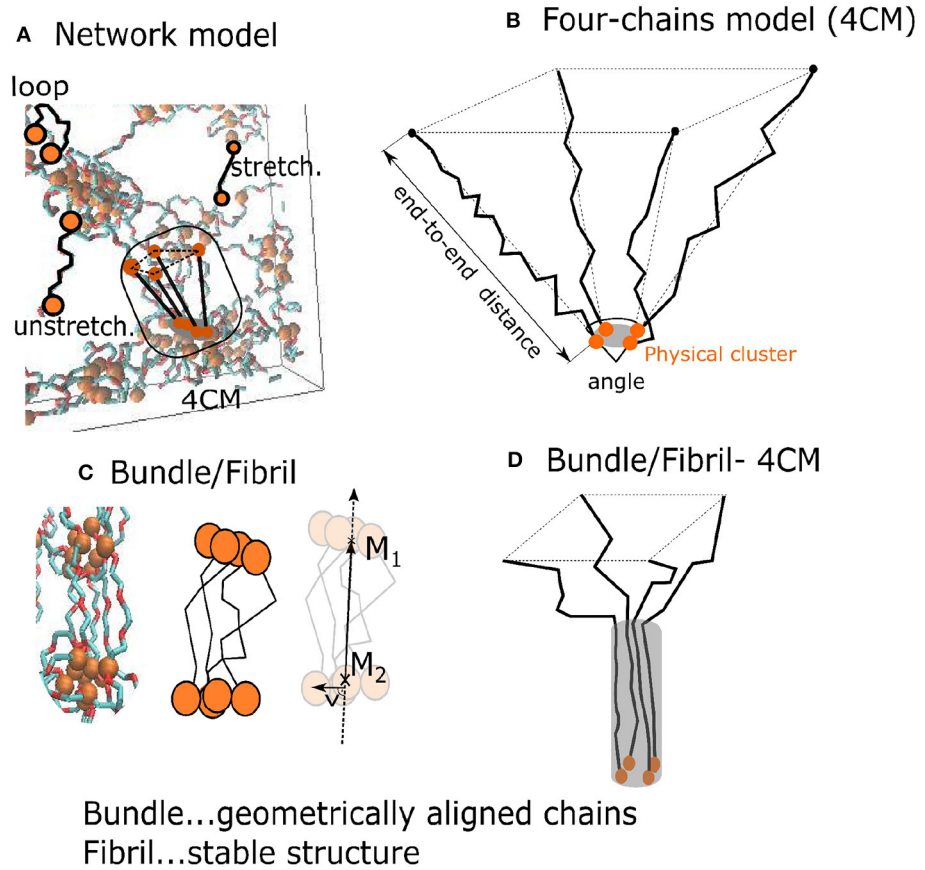

FIGURE 3 | Two models of the hydrogel: **(A)** A network model with a subset of four 4 PEG chains around a physical crosslink; **(B)** "4-chains model"—four randomly generated freely rotating chains with known length and mutual angle. The orange disks are interacting *AA*-groups; **(C)** a fibril with a fiber vector $M_1\bar{M}_2$; **(D)** black lines denote chain segments aligned over some distance from the one end.

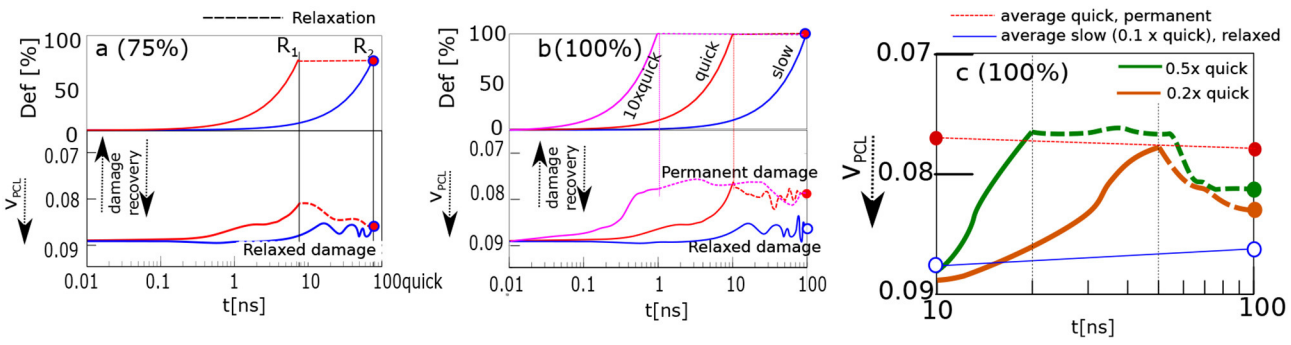

FIGURE 4 | Damage recovery, when the sample is stretched and held in stretched state. Panels correspond to stretching ratios: **(a)** 75%; **(b)** 100%, "slow," "quick," 10 × "quick"; **(c)** 100%0.2× "quick," 0.5× "quick." Upper parts of **(a,b)** display stretching ratio, lower parts—damage, i.e., the inverse volume fraction of physical crosslinks, V_{PCL}. Reference points with the same stretching ratio and simulation time, R_1—blue, magenta curves, R_2—all curves.

Each relaxation is characterized by specific correlation function, taken as the average of dot products of vectors in time 0 and t:

$$f(t) = \langle x(0) \cdot x(t) \rangle \tag{3}$$

where x is a specific property at zero time and at time t. Observables are the inertia (velocity vector), bond/angle relaxation (bond vector), conformation relaxation (bond vector), relaxation of physical clusters (probability of presence in physical cluster) and relaxation of bundles and fibrils (bundle

vector). Details are presented in **Supplementary Material**. The correlation functions were fitted to exponential decay.

3. RESULTS

In our recent study (Zidek et al., 2017b) we described the deformation and macroscopic changes in a model structure of a hydrogel. We found that the stable fibrils appear, when the deformation is quick and sufficiently strong. The model revealed sensitivity to strain rate during deformation, i.e., to "slow" and "quick" (quick = 10× slow) deformation, starting with identical initial atomistic configurations, and external conditions, such as temperature. The qualitative difference in deformation behavior in both cases was related to damage in the primary micellar network whereby slow deformation leads to hydrogel network recovery while quick deformation was found to form permanent fibrillar structure that remained stable with time even against reverse deformation. Apparently, the structural recovery depends on the ability of the system to recreate spontaneously its original micellar structure.

3.1. Damage Recovery Within the General Network Model

The recovery of the physical network was calculated by analyzing the time evolution of the volume fraction of physical clusters (cores of micelles, **Figure 2c**). The response of the material is recorded in **Figure 4**. The upper panel shows deformation in % as a function of time. The lower panel displays a reciprocal function of volume fraction of physical clusters. It describes the degree of physical network damage.

The model structure was slowly stretched in the computer experiment. The stretching rate was 100% deformation in 100 ns. The network was stretched up to 75%, and 100% of its original size. The course of slow deformation is shown as a blue curve. The network was stretched until the reference point R_2. Alternatively, the same structure was stretched quickly by 10 times higher rate than the slow one: cf. red curve, **Figure 4**. The deformation was stopped at time R_1. The simulation box was then held in a stretched state until the time R_2. Thus, both samples were stretched effectively to the *same* stretching ratio within the same total time interval yet with a different deformation history.

The results from **Figure 4a** about the network stretched up to 75%, can be interpreted in terms of dynamic structural recovery. In that case the damage is a function of the stretching degree and rate.

Dynamic recovery is *not* observed in **Figure 4b**, when the network is stretched to 100% deformation. In that case, the quickly deformed network stays damaged. We analyzed different reasons, as to why the damage did not vanish. For example, we extended the time of relaxation to 1000 *ns*. Alternatively, the network was compressed by reverse deformation to its original undeformed shape. None of those lead to a recovery.

We found permanent fibers (**Figure 2e**) in the network, which proved persistent. At temperature 300 *K*, the fibrils could not be removed in any way.

The "quick" and "slow" deformations are limiting cases. While the network relaxes during the "slow" deformation, during a "quick" deformation this is not the case so permanent transformations occur after the deformation. We analyzed the evolution of network after 2×, 5×, and 10× increase of the "quick" deformation rate. The fastest deformation (10× "quick") is presented in **Figure 4b**. This fastest deformation leads to permanent changes similar to "quick" deformation.

Next we explore intermediate stretching rates between "slow" and "quick" in more detail. The first finding is, that there is ∼50 ns period after the moderate deformation. During this period the damage persists before the onset of relaxation.

Another observation is that the network undergoes only partial relaxation (see **Figure 4c**), whereby the damage persists longer than the displayed interval of 100 ns as a longer simulation indicates. Probably, the lack of complete recovery is due to partial formation of fibrils.

It has been suggested in the literature, that the changes can be caused by solvent effect. It has been known that a similar effect of the small monomer and solvent molecules can play important role in the structure transition of the deformed networks (Warner and Terentjev, 1996). The water molecules are expelled which facilitates the alignment and bundling of fibers as the hydrogel is stretched. We investigated the solvation effect during the deformation of our network (Zidek et al., 2017a). It was found that the reconstruction of solvent may influence the deformation response only in the case of strong electrostatic interaction between polymer chains and water molecules as in the case of polyelectrolyte network. In the present network we use moderate electrostatic interaction between chains and water. In that case, one observes a reconstruction of the solvent. We found that solvent had only minor influence on mechanical response of polymers.

For the detailed structural analysis of the fiber formation mechanism we consider a structural component in the atomistic configuration, namely a short flexible chain, SFC (**Figure 5**). Such chains are parts of the macromolecular chain along with the end atomic groups of SFC, i.e., the *AA* (acrylic acid) groups. The positions of these interacting groups are fixed within the existing clusters. Three consecutive polyethylene glycol monomers (each monomer made of three atomic groups) separated by *AA*-groups define a SFC. In the present model, all SFCs consist of 11 segments.

Two *AA*-groups at both ends of a chain may belong to the same physical cluster so that this SFC is a loop. Alternatively, both chain-ends can be part of different clusters and the SFC is then a connecting chain. The motion of chain-ends is thus restricted inside, or between physical clusters, while the other segments of the chain can move freely in space. So in our model we deal with freely rotating chains with fixed chain ends and weak non-bonding interaction. Their motion in space is then determined by thermal displacements of the chains.

A histogram of end-to-end distances, r_e, of unrestricted SFC should display a Gaussian peak. The actual end-to-end distance distribution, however, is more complex (cf. **Figure 5**). According to this histogram, the SFCs can be put into four classes, depending on their end-to-end distances, r_e. In addition, we take

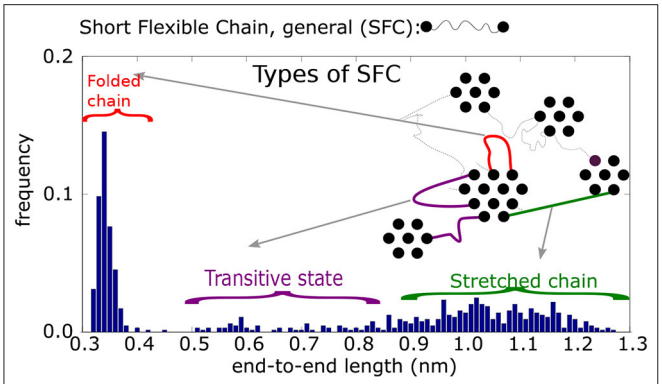

FIGURE 5 | Histogram of end-to-end distances r_e of Short Flexible Chains. A SFC is the part of a chain between two physical crosslinks: schematic picture of four types of SFC and their end-to-end distances.

into account the connectivity of physical clusters, distinguishing between cases when the chain is connected by both ends to the same cluster (i.e., a loop), or a chain (unstretched or stretched) bridges two different clusters.

1. The first class are loops of type 1 ($r_e \leq 0.42$ nm, mostly $r_e \approx 0.35$ nm). Both ends of the chain are connected to groups within the same cluster. The groups themselves are nearest neighbors.
2. The second class is a loop of type 2 ($0.42 \leq r_e \leq 0.65$ nm). Similar to the previous type, loop 2 connects the interacting groups inside a single cluster. The groups, however, are not nearest neighbors.
3. The third class is that of unstretched chains ($0.65 \leq r_e \leq 0.85$ nm), that span two neighboring physical clusters. Such chains are flexible and the segments can move perpendicular to the chain backbone. They can reach relatively large distances away from the connecting line of the chain ends.
4. The fourth class is a stretched chain ($r_e \geq 0.85$ nm), connecting two physical clusters. The chain segments reside on the connecting line between interacting groups.

As stated above, a SFC of certain class can be transformed into another class by deformation. The transformations are observed during the stretching of the sample. When the initial structure is simulated without deformation, however, the classes of SFCs remain stable.

We studied the transformation of the SFCs during the deformation. One might claim that they largely preserve the stationary state whereby all SFCs which are transformed into a different class are replaced by chains from another class that are transformed back into the particular class. For example, during the slow deformation 120 loops out of 640 were transformed into a stretched state, and another 120 stretched chains were transformed back into loops, indicating, that the total concentration of structural components did not change. These transformations are similar for slow and quick deformation.

The next specific property is that the transformations occur always between neighbor classes in a sequence of loop 1 $\leftrightarrow$ loop 2 $\leftrightarrow$ unstretched chain $\leftrightarrow$ stretched chain, whereas transformations between extremes, loop 1 $\leftrightarrow$ stretched chain are practically absent. Transitions that skip an intermediate class are seldom too. The observed transitions are reversible (see **Figure 6A**).

In the case of unstretched state, a chain has chance to form a fibril. To this end it is important to have more such neighbor chains in its vicinity. We find that a fibril is created when at least two chains start from an unstretched state (**Figure 6B**), then the respective transition turns irreversible.

We find that a favorable situation for the formation of fibrils emerges during quick deformation and this raises the question why the formation mechanism favors quick deformation and not a slow one.

The unstretched SFC remains unstable during a limited time. After that, it is transformed either to a stretched chain or a loop. Transition from a loop to a stretched state through unstretched state is induced by deformation. During a quick deformation, the chains change state nearly simultaneously as they have to comply quickly with the imposed stretching. Whenever this occurs, a fibril is formed. We find that a fibril is created when at least two chains start from an unstretched state (**Figure 6B**), then the respective transition turns irreversible.

In a slow deformation, the stretching of this chain takes 10 times longer than during the quick one. The neighboring chains may remain unchanged so that a given chain terminates its transformation before the neighboring chains begin to deform. The chain transformations are not synchronized and various combinations of neighboring chains can be observed (**Figure 6C**).

The formation of fibrils requires synchronous deformation of macromolecules. Favorable combination of SFCs, happens when both neighboring chains are in the class of unstretched chains. A fiber structure can hardly emerge from two chains which are in significantly different classes, say, one of them being a loop, or if one of the chains is stretched and the other—unstretched. The fiber formation is also unlikely for a pair of stretched chains.

3.2. The Role of Collective Alignment of Chains

Deformation changes the network topology. Ejection from the spider body in natural systems, or tensile deformation in our model, contribute to chains' alignment and ensure the necessary narrow orientation whereas the undeformed sample has random orientation of chains.

We find that for the formation of fibrils in the network model one needs a synchronous transformation of several SFCs residing initially in an unstretched state. Within the general network model the study of this behavior is complicated as there are too few neighboring chains with common orientation within the limited size of the sample and therefore they seldom deform simultaneously. The simultaneous deformation of several SCFs is readily examined within our simple model of four chains, each of which is here made of 60 segments, attached to a single physical cross-link while the opposite chain ends are fixed in certain distance from the physical cluster (**Figure 7A**).

We consider first the orientation of chains as it explains why fiber formation is not observed at small deformation of

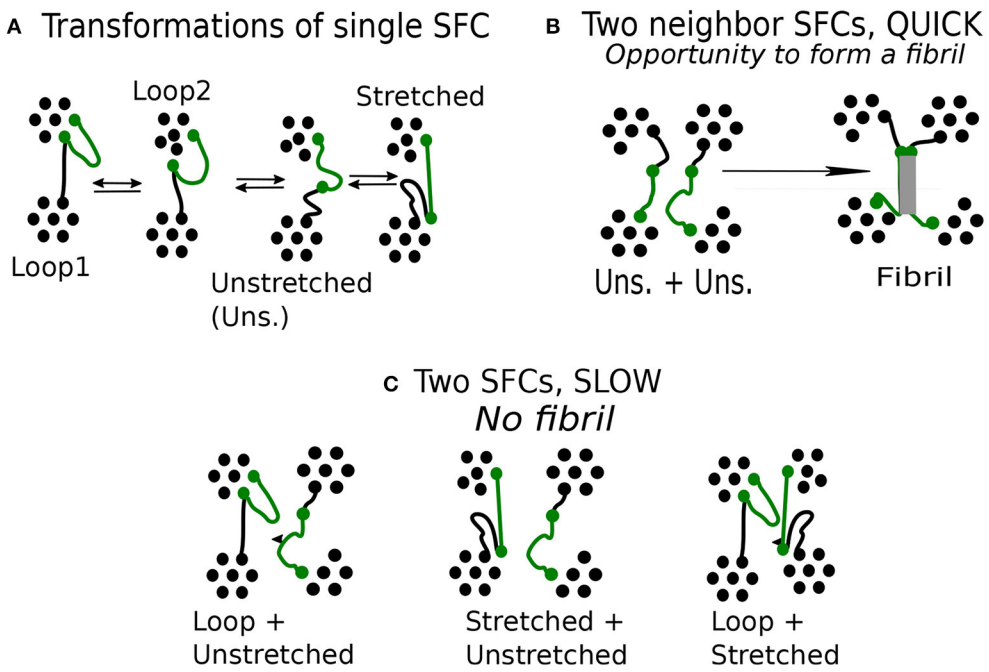

FIGURE 6 | Mechanism of fibrillar structure formation in the network model: **(A)** Reversible transitions of single flexible chain (green). **(B)** Specific configuration of two unstretched chain, observed during quick deformation. **(C)** Specific configuration of two chains, observed during slow deformation.

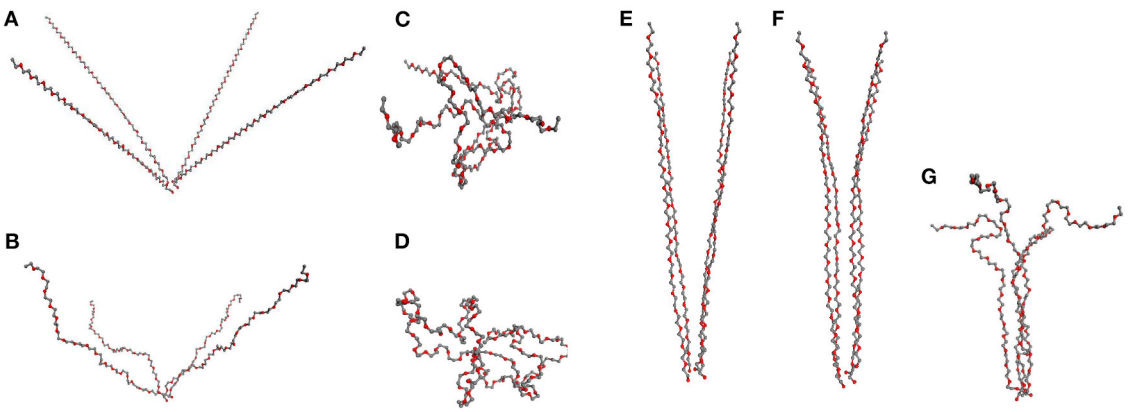

FIGURE 7 | "Four chains model": **(A–D)** 4 PEG chains initially at angle 50° with subsequent relaxation: **(A)** stretched chains, **(B)** unstretched chains; **(C)** loops of type 2, **(D)** loops type of 1. **(E–G)** PEG chains initially at angle 10°, relaxing subsequently to partially aligned stretched chains, **(F)**, in **(G)** a fibril after relaxation.

the network. In that case, the individual chains are mostly oriented at large angle (**Figure 7A**) regarding each other. The simulation starts with all the chains sufficiently stretched, then upon subsequent reduction of the end-to-end distances of the chains one observes two scenarios depending on their mutual orientation.

If the chains are not sufficiently parallel, they are transformed into loops and are not part of any organized structure (**Figures 7A–D**). The formation of fibrils in network models is observed only when the chains form a small angle ($\leq$ 30°) as in **Figure 7E**, where the chains are mutually aligned at 10°. If the chains are gradually released and the end-to-end distance decreased, one finds as a result that the chains remain aligned (**Figure 7F**), with a subsequent formation of fibers in **Figure 7G** maintaining a stable fibrillar structure.

In our computer experiment we stop the chain relaxation in the moment when further compression of the chains requires energy and the relaxation is no more spontaneous. Even after that moment during the subsequent long simulation the fiber persists and its ordering appears to increase with time. The resulting structure can be broken only by an increase of temperature.

Consider now the impact of quick and slow deformation. **Figure 7** describes the situation, when all chains are relaxed simultaneously, following a quick deformation of the network

model (cf. **Figure 6B**). The chains, making originally a mutual angle $\leq 30^\circ$ among themselves, form an unstretched fibril which remains relatively stable when compressed back to a rather small end-to-end distance of the chains.

A different situation is observed after slow deformation (see figure in **Supplementary Material**) when the relaxation of chains proceeds one by one. In our simulation we see no fibril created in that case. Instead, the stretched chains transform into loops.

We have tried to quantify the process of fibril formation (assumed to orient along the z-axis in the simulation box) by using an orientational order parameter, $P_2(\cos\theta)$, Equation (2), where θ stands for the angle between the chain segments and the fiber vector, $\vec{v}_F$. For example, with each chain comprising 60 segments, θ is calculated from the vectors ($\vec{v}_1 = A_3 - A_1$, $\vec{v}_2 = A_4 - A_2, \ldots, \vec{v}_{58} = A_{60} - A_{58}$), and $\vec{v}_F$. Results are shown in **Figure 8**. In case of alignment, P_2 stays positive, $P_2 \geq 0.3$, yet less than unity on average, indicating that the segments in fibrils are not perfectly oriented along the fiber vector. Apparently, for the chains, which make an angle 40° and larger (with no formation of fibrils), the value P_2 becomes close to zero, which reflects a random orientation of the segment. Interestingly, even the chains transformed into random loops show some increased orientation in the end phase of simulation when the end-to-end distance becomes very small (≈2 nm), presumably as a consequence of a secondary orientation of loops.

The data from our four chains model agree with our previous findings from the network model. It was found that the chains with favorable geometry and interaction tend to form fibrillar structures with each fiber consisting of 2–8 chains attached to the same physical cross-link. To this end the stretched chains have to make an angle with one another, which is 30° or less. A second condition is a high enough stretching ratio. All chains must be present simultaneously in an unstretched state at a time. Fibril formation fails, when one chain is linearly stretched, or forms a loop. In linearly stretched chains the atomic groups from two macromolecules are usually too far apart and do not interact. On the other hand, when the chains reside as loops, the segments are disordered and alignment fails too.

3.3. Bundles of Macromolecules

In the previous sections, our basic structural unit was the short flexible chain (SFC). Several SFCs could be aligned under certain conditions into a stable fibril. It seems, however, that the route from several SFCs to fibril is not direct. There occur transient objects, which we refer to as bundles. Bundles are composed of 3 or more aligned SFCs, and they appear to serve as precursors to permanent fibrils. In contrast to fibrils, however, bundles can exist temporarily. In this section, we focus on the behavior of bundles. The SFCs, which form a bundle, can be either of stretched type or unstretched. As a rule, bundles connect two clusters of AA-groups.

One can analyze several aspects of bundle properties, for example their number and weight, change of orientation in space, rotation, and twisting. The basic analysis includes the number of the bundles per simulation box as well as the number of chains in the bundle. Average values and standard deviations were calculated in four independent samples of the network. We identified 7 ± 1 bundles during 10 × "quick" deformation, 9 ± 2 bundles during "quick" deformation of the box, and 10 ± 2 in the slow deformation, so that the difference between slow and quick deformation appears statistically insignificant. The number of bundles looks small, yet, 22% of all atomic groups of the organic network participate in bundles. The bundles are mostly composed of 3 SFCs whereas bundles composed of four or five chains, occur rarely (on average, 0.625 bundles/box of four-chains, and 0.25 bundles/box of five-chains were detected).

Bundles of SFCs do rarely exist in the beginning of the simulation, and most of them appear during the deformation. The majority of bundles seems to appear in the final phase of the simulation, suggesting a predominantly dynamic nature of the process. The formation of bundles requires apparently certain time, whereby the segmental displacements of AA-groups play a role.

The behavior of bundles during simulation was observed. The average size of bundles is constant during the simulation, however, individual chains can fluctuate from one to another bundle. Regarding the geometry of bundles, we first examine the aspects, which are related to the formation of fibrils: rotation and twisting. These aspects were selected since they have different course in the slow and quick mode.

In what follows we describe the rotation of the bundle about a rotation axis pointing along the bundle. One end of the bundle is at the center of mass of the chain ends, associated with the bundle, and the same applies to the other end of the bundle. Bundle rotation is then observed when the chain end-groups move with respect to bundle axis (see **Figure 9A**), whereby such rotation sets in from the very beginning of the deformation. During rotation both ends of the bundle may rotate clockwise or counterclockwise with the same rate, otherwise the bundle is twisted. The degree of twisting is given by the change of angle between two rotation vectors (**Figure 9B**).

We find significant difference in the average twisting intensity between slow and quick deformation. The twisting is enhanced during the quick deformation, where we observe also increased formation of stable fibrils (**Figure 9B**). Thereby all the deformation rates between 0.2× and 10× faster than "quick" deformations have similar effect. The twisting intensity also increases with growing degree of deformation.

No fibrils or bundles persist after the "slow" deformation, whereas almost 100% of fibrils persist after the "quick" deformation. The consequences of moderate deformation for the relaxation behavior are generally indicated in **Figure 4c**. Even if part of the fibrils is destroyed over the whole period of relaxation, 60% of them still persist after the onset of relaxation following a delay period, as in **Figure 4c**. These 60% participate in the twisting process.

We investigated the effect of twisting also in our four-chain model, starting with unstretched chains as an initial configuration. Upon twisting, the potential energy of the four chains was found to decrease whereas when this model was simulated without twisting, the energy remained constant. It was found that the chains can twist only slightly. The most stable atomistic configuration has a twisting angle 2.5°.

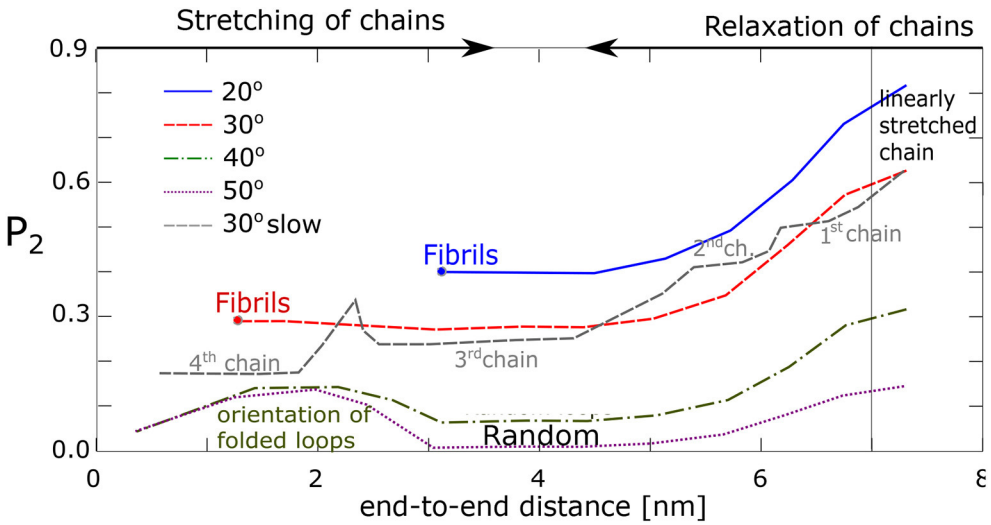

FIGURE 8 | Alignment of chain segments with the fibril axis: An orientational order parameter, P_2, as function of the chains' end-to-end distance during relaxation.

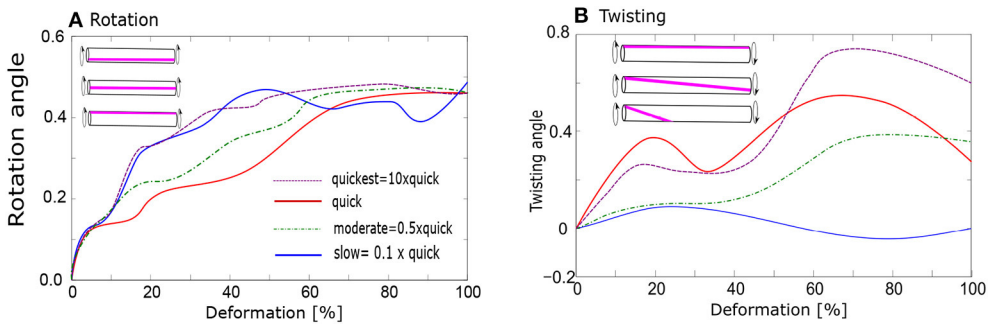

FIGURE 9 | Evolution of bundle geometry during deformation; **(A)** Rotation of bundles: average rotation angle of bundles (in radians) from the beginning of the deformation; **(B)** Twisting of bundles: average twisting angle of bundles (in radians). Various stretching rates: 10× quick, quick, moderate, and slow.

The model is simplified and therefore there are doubts about the validity of results mainly in relation to behavior of real hyrogels. From the structural aspects, our model resembles a micellar network with aggregates comprising cores, formed by hydrophobic Acrylic Acid (AA)-clusters, intermediate layer from poly-lactide-glycolide and shells, formed by hydrophilic polyethylene-glycol (PEG) chains. Model micelles are composed of two layers: core from AA, and hydrophilic PEG shell.

The proposed model provides insight into the relationship between gel structure and deformation response. The model response shows effects, which are observed in real hydrogel materials during deformation: hysteresis during forward-reverse deformation, yield stress, solvent redistribution during deformation (Zidek et al., 2017a). On the other hand, when we compare the model data to the experiment, the model values of stress appear significantly higher than the experimental ones. The limitations of mechanical response are discussed elsewhere (Zidek et al., 2016).

The model structural changes accompanying the fiber formation are minimalistic and we cannot find a corresponding experimental study of of real hydrogels on the atomistic level. However, the model deformation response matches that observed in real materials. As well the final structure is similar to the structure of materials with bundles and fibrils. That allows us to assume that the model evolution of network is similar to the evolution of real materials.

3.4. The Behavior After Deformation: Network Relaxation

One can compare the relationship between time of deformation and relaxation. While the deformation is controlled by the user and it depends on stretching rate and stretching ratio, the relaxation is a spontaneous process, which cannot be influenced by the operator.

The relaxation was analyzed by means of time-autocorrelation functions which were fitted by exponential decay. A characteristic parameter of the exponential function is the half-time of relaxation. Our network reveals several relaxation processes with significantly different relaxation times:

- Inertial motion of the atoms is calculated from the velocity autocorrelation function. This function describes the inertia of atomic groups. It was computed within 1 ps whereby the successive atomistic configuration was recorded every 1 fs.
- Relaxation of bonds and bond angles. It was calculated from the autocorrelation function of the covalent bonds over 100 ps, whereby the configurations were recorded every 0.1 ps.
- Relaxation of conformations involves rotation of bonds and change of conformations. As with the previous item, we applied the autocorrelation function of the covalent bonds within the same time range.
- Segmental hops in physical clusters. The physical clusters are cores of micelles in our model. During the segmental hops, the concentration of physical clusters in the box does not change while the interacting groups only switch from one cluster to another (performing segmental hops). The autocorrelation function identifies whether the interacting *AA* groups are still present in the initial physical clusters. The time interval of relaxation simulation is 100 ns and configurations are recorded each 0.1 ns.
- Bundles or fibrils (in the relaxation analysis they are not distinguished) change their axis orientation in space. The time autocorrelation function of bundle orientation was calculated from a 100 ns period with interval of 0.1 ns.

For comparison with the derived relaxation times, we recall that the quick deformation takes 10 ns, and the slow one lasts 100 ns, as the most relaxation processes are significantly faster than the deformation. Only the relaxation of physical clusters and bundles appears comparable to the interval of deformation.

The relaxation times were calculated for several stretching rates. The fastest stretching rate is 10 × faster than the "quick" deformation considered in the previous section. The range between fastest and slow deformation was divided into seven intervals on a logarithmic scale. A table of all relaxation times is presented in the **Supplementary Material**. Here we analyze the relaxation times in terms of relaxation after quick and slow deformation as in previous section.

A summary of the typical relaxation times after the deformation is presented in **Figure 10**. Several femtoseconds (fs) after the deformation is the interval, where the motion of atomic groups is driven by inertia. One can recognize other relaxation processes at times significantly longer than the inertial motion. The loss of inertia, driven by thermal motion, was observed also in the reference sample without deformation.

The next process pertains to the fluctuation of bonds and angles. The relaxation process is observed within the range of hundreds of fs. It describes the reorientation of covalent bonds. The relaxation is driven by thermal motion of molecules as it was observed also in the reference sample without deformation.

The conformation relaxation by rotational motion of chain segments occurs within tens of picoseconds. This motion is predominantly driven also by thermal motion, however, the degree of deformation plays a role too.

The process of segmental displacements is related to the reconstruction of micellar structure and takes place within the range of nanoseconds. Macroscopically, the micellar structure does not change, but the individual physically interacting atomic group can switch from one to another physical cluster (core of micelle). That relaxation process is unambiguously a response to deformation. We did not observe it in the reference simulation box without deformation.

During the longest interval of tens of nanoseconds one observes a reorientation of bundle axes. The reorientation implies rotation of the bundle. In the same time, we observe also a second wave of segmental hops as a means of reconstruction of the physical clusters. We can assume that in that interval, the bundles are stabilized and this affects the physical clusters.

We observed a relaxation of bundles at the intermediate stretching rate (0.5× quick) along with temporarily persistent fibers. On the other hand, at the stretching rate 0.2× "quick" the relaxation of bundle orientation cannot be analyzed, because bundles are not stable. As well the recovery of physical network starts immediately after deformation.

Bundle axis orientation and the accompanying segmental hops are specific to the fast deformation. They are not observed after the slow simulations or without deformation.

The correlation between cluster reconstruction and bundle orientation is presented in **Figure 11**. The bundle orientation autocorrelation function is compared to cluster reconstruction autocorrelation. From **Figure 11** it appears that the two processes take place simultaneously.

Thus, during the relaxation one can observe the differences between quick and slow deformation. During the slow deformation predominantly the physical network undergoes relaxation whereas after the quick deformation one observes a relaxation of the bundles and fibrils.

The relaxation times can be used to determine the Weissenberg number (W_i) as a dimensionless quantity, which indicates the typical ratio of elastic and viscous forces in our structure. W_i is calculated from the deformation rate ($\dot{\gamma}$) and the respective relaxation time τ of the particular process.

$$W_i = \frac{F(elastic)}{F(viscous)} = \dot{\gamma}\tau \tag{4}$$

The W_i was calculated for each relaxation process and each stretching rate. All numerical values are presented in the **Supplementary Material**.

Table 2 shows the values of deformation rates, relaxation times and Weissenberg numbers (W_i) for selected deformations and relaxation processes. The processes can be subdivided into 3 groups: viscous (v) ($W_i << 1$), viscoelastic (ve) ($0.5 < W_i < 2$), and elastic (e) ($W_i >> 1$).

The Weissenberg number clarifies the correlation between the relaxation times and formation of fibers. The simulations, when we observe complete recovery of the structure, contain only the viscous processes according to W_i. The other simulations, when we observe the formation of fibers, show either the viscoelastic reorientation of molecular bundles or viscoelastic reconstruction of physical clusters or micelles.

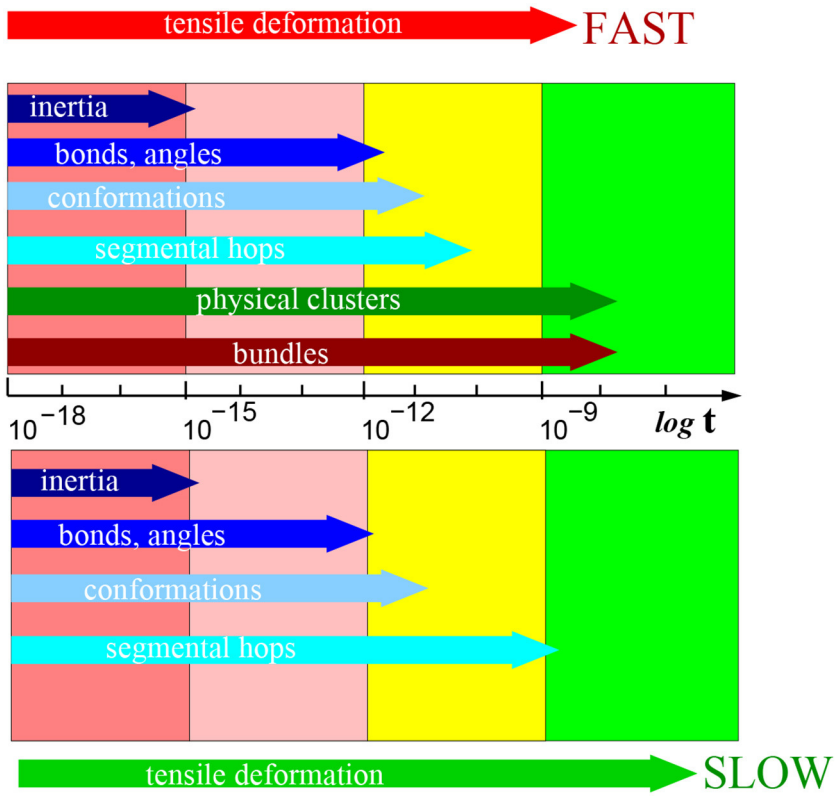

FIGURE 10 | Schematic presentation of relaxations times in [s] after slow (below) and fast (above) deformation process (on a logarithmic scale). Particular structural elements are indicated in the horizontal arrows marking the typical time interval length. A table of all relaxation times is presented in **Supplementary Material**.

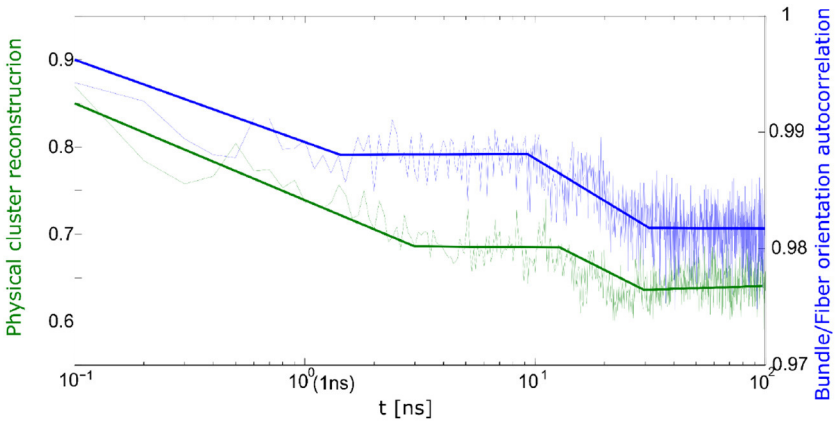

FIGURE 11 | Correlation between bundle orientation (blue) and cluster reconstruction (green) during relaxation process.

3.5. Unidirectionally Alternating Structure of the Fibrillar Phase

It has been mentioned in the Introduction that the fibrillar structure of self-assembled natural materials reveals an alternating sequence of stiff and soft blocks of proteins (quasi-crystalline blocks of β-sheets and amorphous layers rich in poly-glicine) (Nilebäck et al., 2018).

Our model demonstrates similar structural evolution to fibrillar phase upon strong and fast deformation in z-direction. An alternating sequence of layers of micelles and layers of stretched chains (solated fibrils) is also observed in the deformed sample as demonstrated in **Figure 12**. The layers enable the material to hold constant span between the aggregated layers of clusters. In our case, the stretched chains are rigid

TABLE 2 | Relaxation times (t_rel) and Weissenberg numbers (W_i) for various relaxation processes at different stretching rates; viscous (v); elastic (e); viscoelastic process (ve).

Deformation rate [ps^{-1}]	Conformations t_{rel}[ps]/ W_i	Segmental hops t_{rel}[ps]/ W_i	Bundle t_{rel}[ps]/ W_i	Fibril formation
10 × quick 10^{-3}	21.3/0.0213(v)	1,776/1.773(ve)	57,600/57.6(e)	Yes
Quick 10^{-4}	19.0/0.0019(v)	760/0.076(v)	20,300/2.03(ve)	Yes
Slow 10^{-5}	10.0/0.0001(v)	2,100/0.021(v)	–	No

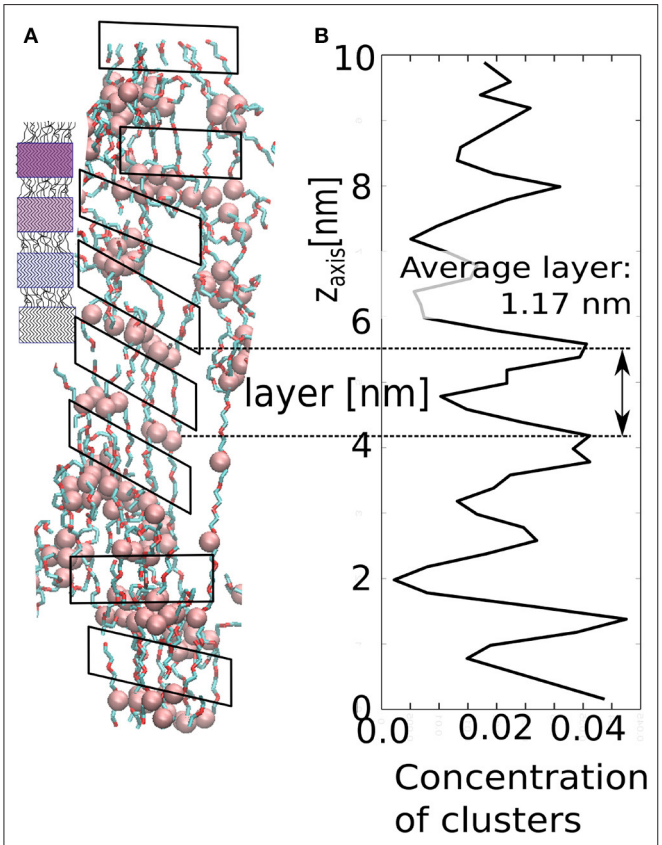

FIGURE 12 | Structure of the stretched network in our model: **(A)** small figure—schematic picture of spider silk; large figure—simulation snapshot; **(B)** local concentration of AA-clusters as along the z-axis.

segments, whereas the cluster with loop chains have viscoelastic behavior. The layer arrangement can be derived from the local concentration profile along the z-axis. Although the periodic arrangement is not perfect, one can detect an average distance between adjacent maxima. The average span is ≈1.17 nm, which is the length of stretched chains with a layer of AA-clusters.

4. CONCLUSIONS

In this work we present molecular dynamics simulations of a model, which shows the ability to form ordered fibrillar structures on molecular level. A significant result of our study is the finding that the relevant mechanism is sensitive to strain amount and rate. The fibrillar structure is formed only by both quick and large deformation.

We identified some factors, which are important for the formation of nanostructured fibrilar material. During deformation, one must achieve synchronized unfolding of macromolecules during deformation. The synchronized unfolding is activated by quick deformation. Another aspect is the ability of the chains to form bundles of aligned macromolecules. Such bundles can be stabilized by twisting and thus transformed into fibrils. Whether the macromolecules can form fibrils depends on the molecular structure. The molecular structure has been investigated here by a simplified four-chains model, which elucidates the conditions necessary for a material of certain composition to form fibrils.

The structural transformations are reflected in the relaxation process of the sample. The relaxation after fibril formation is manifested in the reorientation of fibrils and bundles. In the case of slow deformation, where fibrils are not formed, the process of reorientation is not observed.

The present model makes it possible to consider new materials, which are able to form fibrillar structure. The primary structure according to our findings can be produced in a laboratory. When one combines an appropriate primary structure and satisfies the conditions of preparation/extrusion, a nanostructured fibrilar material similar to spider silk can be achieved also in a laboratory.

DATA AVAILABILITY STATEMENT

All datasets generated for this study are available within the article and from the corresponding author on request.

AUTHOR CONTRIBUTIONS

JZ carried out the MD calculations and analyzed the data. JZ, AM, and JJ interpreted the results and developed the theoretical scheme. JZ and AM wrote the paper.

FUNDING

Funding of this work under the Project 18-17540S from the Czech Grant Agency was greatly appreciated.

SUPPLEMENTARY MATERIAL

The Supplementary Material for this article can be found online at: https://www.frontiersin.org/articles/10.3389/fchem.2020.00120/full#supplementary-material

Section 1 | Setup and parameters of molecular dynamics simulations.

Section 2 | Description of the four-chain model.

Section 3 | Description of model objects.

Section 4 | Data from relaxation of hydrogels.

REFERENCES

Andersson, M., Jia, Q., Abella, A., Lee, X.-Y., Landreh, M., Purhonen, P., et al. (2017). Biomimetic spinning of artificial spider silk from a chimeric minispidroin. *Nat. Chem. Biol.* 13, 262–264. doi: 10.1038/nchembio.2269

Benetatos, P., and Jho, Y. (2016). Bundling in semiflexible polymers. *Adv. Colloid Interface Sci.* 232, 114–126. doi: 10.1016/j.cis.2016.01.001

Buehler, M. J. (2006). Nature designs tough collagen. *Proc. Nat. Acad. Sci. U.S.A.* 133, 12285–12290. doi: 10.1073/pnas.0603216103

Gray, G., van der Vaart, A., Guo, C., Jones, J., Onofrei, D., Cherry, B., et al. (2016). Secondary structure adopted by the gly-gly-x repetitive regions of dragline spider silk. *Int. J. Mol. Sci.* 17:2023. doi: 10.3390/ijms17122023

Grubb, D. T., and Jelinski, L. W. (1997). Fiber morphology of spider silk. *Macromolecules* 30, 2860–2867. doi: 10.1021/ma961293c

Hammond, N. A., and Kamm, R. D. (2008). Elastic deformation and failure in protein filament bundles. *Biomaterials* 29, 3152–3160. doi: 10.1016/j.biomaterials.2008.04.013

Jin, H.-J., and Kaplan, D. L. (2003). Mechanism of silk processing in insects and spiders. *Nature* 424, 1057–1061. doi: 10.1038/nature01809

Lee, S., and Rutledge, G. C. (2011). Plastic deformation of semicrystalline polyethylene by molecular simulation. *Macromolecules* 44, 3096–3108. doi: 10.1021/ma1026115

Lele, A. K., Joshi, Y. M., and Mashelkar, R. (2001). Deformation induced hydrophobicity. *Chem. Eng. Sci.* 56, 5793–5800. doi: 10.1016/S0009-2509(01)00288-3

Liu, X., and Zhang, K.-Q. (2014). "Silk fiber–molecular formation mechanism, structure-property relationship and advanced applications," in *Oligomerization of Chemical and Biological Compounds*, ed C. Lesseur (London: InTechOpen).

Michlovska, L., Vojtova, L., Humpa, O., Kucerik, J., Zidek, J., and Jancar, J. (2016). Hydrolytic stability of end-linked hydrogels from plga-peg-plga macromonomers terminated by -itaconyl groups. *RSC Adv.* 6, 16808–16816. doi: 10.1039/C5RA26222D

Miyazaki, T., Hoshiko, A., Akasaka, M., Shintani, T., and Sakurai, S. (2006). Saxs studies on structural changes in a poly(vinyl alcohol) film during uniaxial stretching in water. *Macromolecules* 39, 2921–2929. doi: 10.1021/ma052595u

Mondal, A., Borah, R., Mukherjee, A., Basu, S., Jassal, M., and Agrawal, A. K. (2008). Electrospun self-assembled nanofiber yarns. *J. Appl. Polym. Sci.* 110, 603–607. doi: 10.1002/app.28673

Nilebäck, L., Arola, S., Kvick, M., Paananen, A., Linder, M. B., and Hedhammar, M. (2018). Interfacial behavior of recombinant spider silk protein parts reveals cues on the silk assembly mechanism. *Langmuir* 34, 11795–11805. doi: 10.1021/acs.langmuir.8b02381

Peleg, O., Savin, T., Kolmakov, G. V., Salib, I. G., Balazs, A. C., Kröger, M., et al. (2012). Fibers with integrated mechanochemical switches. *Biophys. J.* 103, 1909–1918. doi: 10.1016/j.bpj.2012.09.028

Peng, C. A., Russo, J., Lyda, T. A., and Marcotte, W. R. (2017). Polyelectrolyte fiber assembly of plant-derived spider silk-like proteins. *Biomacromolecules* 18, 740–746. doi: 10.1021/acs.biomac.6b01552

Peng, N., Lv, R., Jin, T., Na, B., Liu, H., and Zhou, H. (2017). Thermal and strain-induced phase separation in an ionic liquid plasticized polylactide. *Polymer* 108, 442–448. doi: 10.1016/j.polymer.2016.12.024

Perry, D. J., Bittencourt, D., Siltberg-Liberles, J., Rech, E. L., and Lewis, R. V. (2010). Piriform spider silk sequences reveal unique repetitive elements. *Biomacromolecules* 11, 3000–3006. doi: 10.1021/bm1007585

Srivastava, R. (2017). Electrospinning of patterned and 3D nanofibers. *Electrospun Nanofibers* 1:399. doi: 10.1016/B978-0-08-100907-9.00016-7

Stoclet, G. (2016). Strain-induced structural evolution of poly(l-lactide) and poly(d-lactide) blends. *Polymer* 99, 231–239. doi: 10.1016/j.polymer.2016.07.019

Svachova, V., Vojtova, L., Pavlinak, D., Vojtek, L., Sedlaková, V., Hyrsl, P., et al. (2016). Novel electrospun gelatin/oxycellulose nanofibers as a suitable platform for lung disease modeling. *Mater. Sci. Eng. C* 67, 493–501. doi: 10.1016/j.msec.2016.05.059

Walker, A. A., Holland, C., and Sutherland, T. D. (2015). More than one way to spin a crystallite. *Proc. Biol. Sci. R. Soc.* 282:20150259. doi: 10.1098/rspb.2015.0259

Wang, C., and Hashimoto, T. (2018). Self-organization in electrospun polymer solutions. *Macromolecules* 51, 4502–4515. doi: 10.1021/acs.macromol.8b00647

Wang, X., Kim, H. J., Wong, C., Vepari, C., Matsumoto, A., and Kaplan, D. L. (2006). Fibrous proteins and tissue engineering. *Mater. Today* 9, 44–53. doi: 10.1016/S1369-7021(06)71742-4

Warner, M., and Terentjev, E. (1996). Nematic elastomers–a new state of matter? *Prog. Polym. Sci.* 21, 853–891. doi: 10.1016/S0079-6700(96)00013-5

Yamamoto, T. (2013). Molecular dynamics in fiber formation of polyethylene and large deformation of the fiber. *Polymer* 54, 3086–3097. doi: 10.1016/j.polymer.2013.04.029

Zhong, C., Chrzanowska-Wodnicka, M., Brown, J., Shaub, A., Belkin, A. M., and Burridge, K. (1998). Rho-mediated contractility exposes a cryptic site in fibronectin and induces fibronectin matrix assembly. *J. Cell Biol.* 141, 539–551. doi: 10.1083/jcb.141.2.539

Zidek, J., Kulovana, E., and Jancar, J. (2017a). The effect of network solvation on the viscoelastic response of polymer hydrogels. *Polymers* 9:379. doi: 10.3390/polym9080379

Zidek, J., Milchev, A., Jancar, J., and Vilgis, T. A. (2016). Deformation-induced damage and recovery in model hydrogels–a molecular dynamics simulation. *J. Mech. Phys. Solids* 94, 372–387. doi: 10.1016/j.jmps.2016.05.013

Zidek, J., Milchev, A., Jancar, J., and Vilgis, T. A. (2017b). Dynamic mechanical response of hybrid physical covalent networks–molecular dynamics simulation. *Macromol. Symp.* 373:1600147. doi: 10.1002/masy.201600147

Conflict of Interest: JJ was employed by the company SCITEG a.s.

The remaining authors declare that the research was conducted in the absence of any commercial or financial relationships that could be construed as a potential conflict of interest.

frontiers in Chemistry

ORIGINAL RESEARCH
published: 10 March 2020
doi: 10.3389/fchem.2020.00102

Physical Organohydrogels With Extreme Strength and Temperature Tolerance

Jing Wen Zhang[1,2†], *Dian Dian Dong*[1,2†], *Xiao Yu Guan*[1,2], *En Mian Zhang*[3], *Yong Mei Chen*[1,2,3*], *Kuan Yang*[1,2], *Yun Xia Zhang*[4], *Malik Muhammad Bilal Khan*[1,2], *Yasir Arfat*[1,2] *and Yasir Aziz*[1,2]

[1] College of Bioresources Chemical and Materials Engineering, Shaanxi University of Science & Technology, Xi'an, China, [2] National Demonstration Center for Experimental Light Chemistry Engineering Education (Shaanxi University of Science & Technology), Xi'an, China, [3] State Key Laboratory for Strength and Vibration of Mechanical Structures, International Center for Applied Mechanics, School of Aerospace Engineering, Xi'an Jiaotong University, Xi'an, China, [4] Research Center for Semiconductor Materials and Devices, College of Arts and Sciences, Shaanxi University of Science & Technology, Xi'an, China

OPEN ACCESS

Edited by:
Yi Cao,
Nanjing University, China

Reviewed by:
Huiliang Wang,
Beijing Normal University, China
Bengang Li,
Nanjing Forestry University, China
Jing Chen,
Ningbo Institute of Materials Technology & Engineering (CAS), China

***Correspondence:**
Yong Mei Chen
chenyongmei@sust.edu.cn

[†] These authors have contributed equally to this work

Specialty section:
This article was submitted to Polymer Chemistry, a section of the journal Frontiers in Chemistry

Received: 06 December 2019
Accepted: 03 February 2020
Published: 10 March 2020

Citation:
Zhang JW, Dong DD, Guan XY, Zhang EM, Chen YM, Yang K, Zhang YX, Khan MMB, Arfat Y and Aziz Y (2020) Physical Organohydrogels With Extreme Strength and Temperature Tolerance. Front. Chem. 8:102. doi: 10.3389/fchem.2020.00102

Tough gel with extreme temperature tolerance is a class of soft materials having potential applications in the specific fields that require excellent integrated properties under subzero temperature. Herein, physically crosslinked Europium (Eu)-alginate/polyvinyl alcohol (PVA) organohydrogels that do not freeze at far below 0°C, while retention of high stress and stretchability is demonstrated. These organohydrogels are synthesized through displacement of water swollen in polymer networks of hydrogel to cryoprotectants (e.g., ethylene glycol, glycerol, and d-sorbitol). The organohydrogels swollen water-cryoprotectant binary systems can be recovered to their original shapes when be bent, folded and even twisted after being cooled down to a temperature as low as −20 and −45°C, due to lower vapor pressure and ice-inhibition of cryoprotectants. The physical organohydrogels exhibit the maximum stress (5.62 ± 0.41 MPa) and strain (7.63 ± 0.02), which is about 10 and 2 times of their original hydrogel, due to the synergistic effect of multiple hydrogen bonds, coordination bonds and dense polymer networks. Based on these features, such physically crosslinked organohydrogels with extreme toughness and wide temperature tolerance is a promising soft material expanding the applications of gels in more specific and harsh conditions.

Keywords: organohydrogels, high strength, anti-freezing, non-drying, temperature tolerance

INTRODUCTION

Hydrogels are the typical soft materials, by virtue of their great potentials in applications spanning from soft robotics, sensors, actuators to tissue engineering (Wegst et al., 2014; Iwaso et al., 2016; Kim et al., 2016; Banerjee et al., 2018; Dong et al., 2018; Hu et al., 2019). Nevertheless, conventional hydrogels are considered to be mechanically weak due to lack of an effective energy dissipation mechanism or intrinsic structural heterogeneity (Dhivya et al., 2015; Yuk et al., 2016), limiting utilization in some fields that require excellent mechanical properties (Gao et al., 2016; Fan et al., 2019; Lai et al., 2019). Therefore, improving mechanical properties of hydrogels became an important research hotspot. So far, versatile strategies to achieve tough hydrogels have been emerged, including double-network hydrogels (Gong et al., 2003; Gong, 2014; Liang et al., 2016; Chen et al., 2018; Jing et al., 2019), nanocomposite hydrogels (Haraguchi and Takehisa, 2002; Chen et al., 2015; GhavamiNejad et al., 2016; Liu Y. et al., 2017; Zhu et al., 2017), topological

hydrogels (Okumura and Ito, 2001; Li et al., 2018), macromolecular microsphere composite hydrogels (Huang et al., 2007; Gu et al., 2016; Zhang and Khademhosseini, 2017; Wang Z. et al., 2018), hydrophobic association hydrogels (Li et al., 2012; Mihajlovic et al., 2017; Han et al., 2018), hydrogen bonding/dipole-dipole reinforced hydrogels (Han et al., 2012; Zhang et al., 2015; Qin et al., 2018), and many others (Gong et al., 2016; Liu J. et al., 2017; Zhao et al., 2019). However, almost all of the hydrogels swollen a large amount of water in polymer networks cannot resist a cold or hot environment (Wei et al., 2014, 2015; Wang W. et al., 2018), hindering the application of tough hydrogels in harsh conditions. Subzero temperature results in freezing of hydrogels, while high temperature lead to drying (Rong et al., 2017; Zhang et al., 2018). Freezing and drying cause the hydrogels to hard, opaque and dry, which undoubtedly change the integrated mechanical properties of hydrogels, leading to unstable nature under wide temperature range (Han et al., 2017; Lou et al., 2019). So far, it is still a challenge to design a hydrogel with enhanced and tunable mechanical strength together with extreme temperature tolerance.

Recently, two approaches have been proposed to develop hydrogels with extreme temperature tolerance. One is introduction of an ionic compound (e.g., NaCl, LiCl, and $CaCl_2$) to hydrogels, i.e., the polymer networks swollen with salt water (Morelle et al., 2018), for dropping the ice point of water according to the principle of colligative properties of solution. However, water can be evaporated from polymer networks under high temperature causing unstable mechanical properties. The other strategy is the introduction of a water-cryoprotectant binary solvent system into organohydrogel (OHG) networks through synthesis or displacement (Gao et al., 2017; Rong et al., 2018). Compared with the hydrogel containing ionic compound, water-cryoprotectant binary solvent endows stable mechanical properties to gels under both low and high temperature, due to the advantages of cryoprotectants including relatively high volatile point and inhibition ice crystallization (Elliott et al., 2017). The cryoprotectants, including ethylene glycol (EG), glycerol (GC), and d-sorbitol (SB) are suitable choices for fabricating organhydrogels swollen water-cryoprotectant binary solvents, which was firstly reported by Wang's group (Shi et al., 2017).

In the present study, we found that the mechanical properties and temperature tolerance could be dramatically enhanced by fabricating tough physically crosslinked organhydrogels *via* solvent displacement approach. The tough organohydrogels were prepared through displacing cryoprotectants (i.e., EG, GC, SB) into our previously reported Eu-alginate/PVA hydrogel networks mainly crosslinked by hydrogen bonds formed among PVA polymers and coordination bonds between Na-alginate networks and Eu^{3+} ions (Wang et al., 2015; Hu et al., 2017). Multiple hydrogen bonds forming among cryoprotectants and PVA polymers enhance mechanical properties of organohydrogels. Moreover, cryoprotectants disrupt the formation of ice crystal lattices of the residual water, endowing extreme toughness and temperature tolerance to the organohydrogels. Furthermore, tunable mechanical performance of the oganohydrogels can be controlled by either selecting cryoprotectants or by varying the extent of solvent displacement. Therefore, physically crosslinked organohydrogels with enhanced and tunable mechanical properties, as well as extreme temperature tolerance could be designed and synthesized, potentially expanding scientific research and practical applications of gels.

EXPERIMENT

Materials and Methods

Polyvinyl alcohol (PVA, Mn = 205,000) and sodium alginate (Na-alginate) were purchased from Sigma-Aldrich (Shanghai, China). Alginate is a linear copolymer of α-L-guluronic acid (G unit) and β-D-mannuronic acid (M unit). Europium chloride hexahydrate ($EuCl_3{\cdot}6H_2O$) was obtained from Qufu Chemical Co. Ltd. (Qufu China). Ethylene glycol, glycerol, and d-sorbitol were supplied by Cheng Jie Chemical Engineering Co. Ltd. (Shanghai, China). All chemicals were received and used without further purification. Ultrapure water with a resistivity higher than 18.2 MΩ·cm was supplied by a Millipore Simplicity 185 system, which was deoxygenated three times by using a freeze-pump-thaw method before use.

Preparation of Eu-Alginate/PVA Hydrogel and Organohydrogels

Eu-alginate/PVA hydrogel was prepared by following the method described in our previous work (Hu et al., 2017). Briefly, Na-alginate and PVA were dissolved in ultrapure water to produce a homogeneous solution, wherein the molar ratio of Na-alginate and PVA is 1:9. The Na-alginate/PVA hydrogel was then obtained by two freeze/thaw cycles of the polymer solution. Subsequently, the Na-alginate/PVA hydrogel was soaked into the aqueous solution of $EuCl_3{\cdot}6H_2O$ (0.01 mol/L), obtaining Eu-alginate/PVA hydrogel.

Eu-alginate/PVA organohydrogels were synthesized by using solvent displacement method (Chen et al., 2018). Herein, Eu-alginate/PVA hydrogel was directly placed into a vessel containing three different cryoprotectant solutions, namely ethylene glycol (EG), glycerol (GC) solution, and d-sorbitol (SB) aqueous solution (SB: H_2O = 2:1), respectively. For the sake of brevity, we denote these Eu-alginate/PVA organohydrogels as OHG_{EGt}, OHG_{GCt}, and OHG_{SBt}. OHG refers to organohydrogels, EG, GC, and SB denote the corresponding solution, and t represents displacement time. To estimate the solvent displacement behaviors, the weight ratio (W_a/W_b, where W_b and W_a refers to the weight before and after solvent displacement, respectively) of the organohydrogels was calculated. OHG_0 means original Eu-alginate/PVA hydrogel. The synthesis procedures and structure of Eu-alginate/PVA OHG were illustrated in **Figure 1**.

Measurement of Mechanical Properties

All mechanical properties of the gels were tested on a tensile tester (CMT6503, MTS, United States). Tensile test was performed under room temperature, by setting a 500 N sensor. All the samples were cut into dumbbell-shaped with the help of a caliper in the size of tensile part 2 × 2 × 12 mm (Hengliang Liangju Co. Ltd., Shanghai, China). Both ends of the dumbbell-shaped

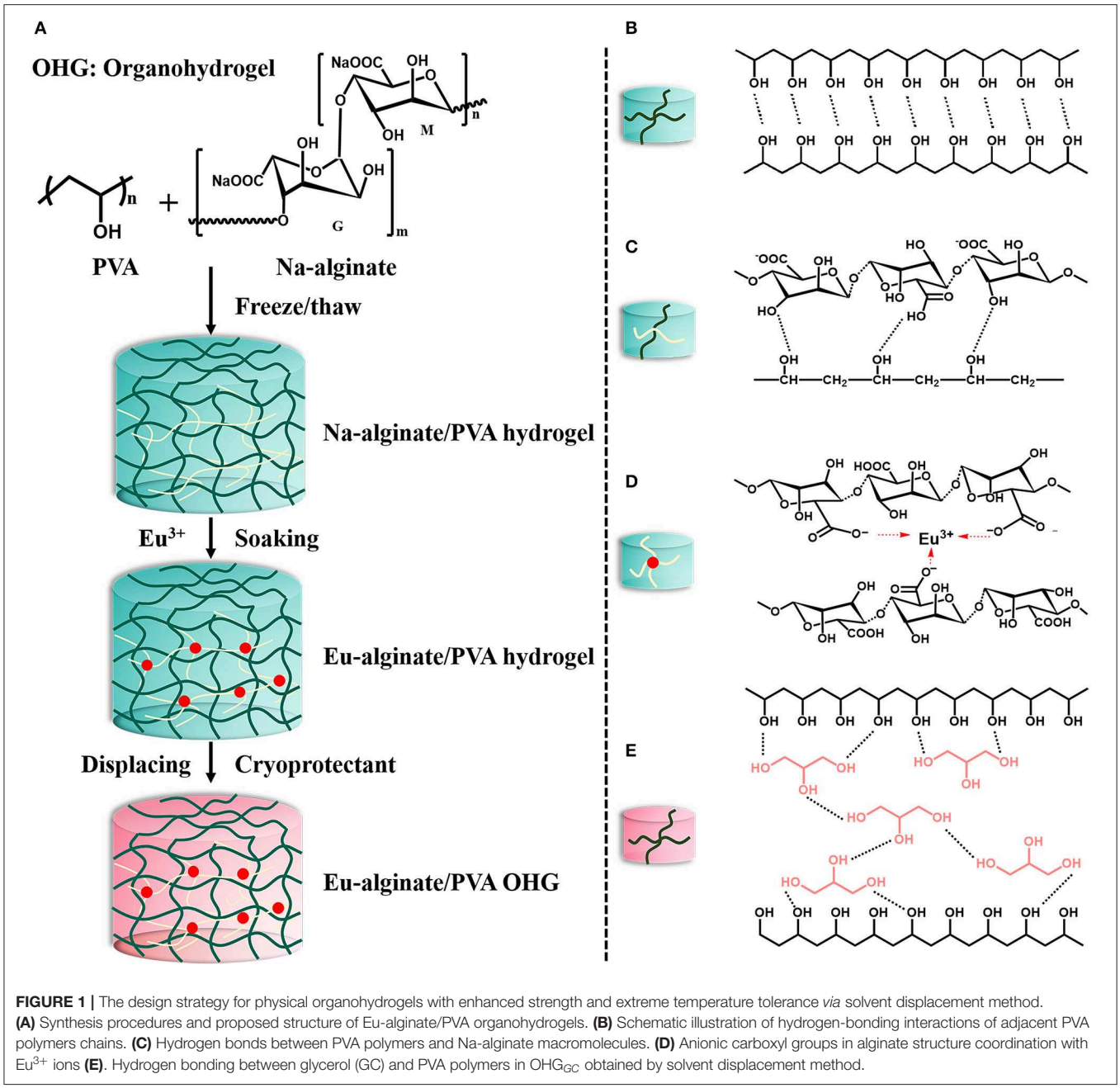

FIGURE 1 | The design strategy for physical organohydrogels with enhanced strength and extreme temperature tolerance *via* solvent displacement method. **(A)** Synthesis procedures and proposed structure of Eu-alginate/PVA organohydrogels. **(B)** Schematic illustration of hydrogen-bonding interactions of adjacent PVA polymers chains. **(C)** Hydrogen bonds between PVA polymers and Na-alginate macromolecules. **(D)** Anionic carboxyl groups in alginate structure coordination with Eu^{3+} ions **(E)**. Hydrogen bonding between glycerol (GC) and PVA polymers in OHG_{GC} obtained by solvent displacement method.

samples were connected to the clamps. The upper clamp was pulled by the load cell at a constant velocity of 100 mm min^{-1} while the lower clamp was fixed. From the stress-strain curve, the stress, Young's modulus and fracture strain of those gels can be calculated. The Young's modulus (E) could be calculated by τ = stress/strain when strain is lower than 10%, where stress represents the force causing the deformation divided by the area to which the force is applied, and strain denotes the ratio of the change in elongation compared to the original length of the sample. Since strain is a dimensionless quantity, the unit of E is same as that of stress. Fracture strain is the maximum deformation tensile length that an object or substance can withstand, which can be calculated by $\varepsilon = (L–L_0)/L_0$, where L_0 and L is the original and deformation length of the sample, respectively.

Characterization of Non-drying and Anti-freezing Properties

To gain further insight into the non-drying property of organohydrogels, the weight rate (W_t/W_0) was calculated. The initial weight of the sample was recorded as W_0. W_t denotes the weight of the corresponding sample heated with different displacement times. The organohydrogels were heated at the temperature of 50°C. Characterization of the anti-freezing

property of organohydrogel was carried out by freezing the organohydrogels at the temperature of −20°C or even −45°C for 2 h. The frozen organohydrogels were quickly folded or twisted and then left to recover freely. After 5 min, the anti-freezing property of the organohydrogels was illustrated in the digital pictures.

Structural Characterization

Characterization of the gels including morphology, composition, and crystalline structure, was carried out to further understand the solvent displacement mechanism. The morphology of the organohydrogel samples was visualized using a field-emission scanning electron microscopy (SEM, JROL JSM-7000F, Japan). Fourier transform infrared (FTIR) spectrum was collected at ambient temperature using a Nicolet 5700 FTIR spectrometer (Thermo Scientific, United States) over a wavelength ranges from 400 to 4,000 cm^{-1} after 64 scans at 2 cm^{-1} resolution. X-ray diffraction (XRD) patterns of the gels were obtained at room temperature on a Philips X'Pert pro MPD diffractometer, using Cu-Kα radiation (λ = 1.5406 Å) in the range of 2θ = 10–90° and the scanning rate was set at 0.02°/s. The hydrogel and organohydrogels were freeze-dried, before characterizing by the SEM and FTIR. The XRD results were directly obtained from the as-prepared hydrogel and organohydrogels.

RESULTS AND DISCUSSIONS

Synthesis of the Eu-Alginate/PVA Organohydrogels

The main synthetic procedures including three sequential steps to obtain the Eu-alginate/PVA organohydrogels were shown in **Figure 1A**. Firstly, homogeneous solution of PVA and Na-alginate was freezed/thawed for two cycles to obtain Na-alginate/PVA hydrogel. The procedure facilitates the formation of hydrogen bonds between the polymer chains in the Na-alginate/PVA hydrogel. The hydrogen bonds formed between hydroxyl groups (–OH) of PVA polymers (**Figure 1B**) as well as between carboxyl groups (–COOH) of Na-alginate macromolecules and the hydroxyl groups of PVA polymers in the crosslinked nodes (**Figure 1C**). Subsequently, Na-alginate/PVA hydrogel was immersed in $EuCl_3$ solution, and Eu^{3+} ions are easily accessible to anionic carboxyl groups in alginate structure center to form coordinate bonds (**Figure 1D**). Eu^{3+} ions, with low toxicity and antibacterial property, not only provide the photoluminescent property but also serve as physical crosslinkers for Na-alginate. Furthermore, coordination bonds between trivalent Eu^{3+} ions and the carboxyl ligands of Na-alginate act as physical sacrificial bonds for energy dissipation, leading to good mechanical property. A tough Eu-alginate/PVA hydrogel could be obtained, and the hydrogel exhibits a dual physically crosslinked polymer networks including hydrogen bonds forming between polymer chains, as well as coordination bonds between Eu^{3+} ions and $–COO^-$ groups, while the dual crosslinked polymer networks endow tough mechanical behavior to the hydrogel (Hu et al., 2017).

Then, the Eu-alginate/PVA hydrogel was soaked into cryoprotectant solutions for a certain time to obtain organohydrogels swollen water-cryoprotectant binary solvent of EG, GC, and SB, respectively. Owing to osmotic pressure, a large amount of water in the hydrogel networks was displaced by cryoprotectants (bottom in **Figure 1A**). Furthermore, based on the principle of dissolution in a similar material structure, cryoprotectant molecules containing hydroxyl groups could be dispersed well in polymer networks to form hydrogen bonds with PVA polymer chains, obtaining the final extreme tough and temperature tolerant organohydrogels denoted as OHG_{EG}, OHG_{GC}, and OHG_{SB}. We anticipate that the organohydrogels exhibit the superior mechanical properties in virtue of multiple hydrogen bonds between cryoprotectant molecules and PVA polymer chains (**Figure 1E**, taking OHG_{GC} as an example).

Figure 2 shows the weight rate (W_a/W_b, where W_b, W_a represents the weight before and after solvent displacement, respectively) of organohydrogels with the displacement time ranging from 0.5 to 6 h. The weight rate is dependent on displacement time of the cryoprotectants. As can be seen, with increased displacement time, the weight rate of the organohydrogels decreased and finally almost reached a displacement equilibrium state. Especially, the weight rate (W_a/W_b) of OHG_{EG}, OHG_{GC}, and OHG_{SB} all decreased quickly at initial 0.5 h, from 1 to 0.55, 0.63, and 0.58, respectively (**Figure 2A**). The water in the hydrogel system usually exists in three states, i.e., free water, intermediate water, and nonrotational bound water (Cerveny et al., 2005; Wu et al., 2019). The fast-decreased weight rate is attributed to the fact that most of the "free water" in hydrogel networks is displaced quickly due to unbound water molecules. However, the intermediate water weakly interacted with the polymer networks is displaced slowly with the cryoprotectant molecules. Moreover, it is difficult for the strongly bound water to undergo solvent displacement. As an example, with the displacement time ranging from 0 to 6 h, the fast shrank and decreased volume of the ethylene glycol based organohydrogel (OHG_{EG}) could be visualized at initial time (<0.5 h) and then it slowed down (**Figure 2B**). These results indicate a successful solvent displacement between the water and cryoprotectant molecules. With this approach, the Eu-alginate/PVA hydrogel was transformed into Eu-alginate/PVA organohydrogels with dense polymer networks swollen water-cryoprotectant binary solvent, leading to enhanced capabilities of mechanical properties, moisture holding and temperature tolerance.

Mechanical Properties of the Eu-Alginate/PVA Organohydrogels

The effects of cryoprotectants on the mechanical properties of organohydrogels were tested by tensile experiments. **Figure 3** shows the mechanical properties (tensile strength, fracture strain and Young's modulus) of the organohydrogels (OHG_{EG}, OHG_{GC}, and OHG_{SB}) displaced by three different cryoprotectants. The tensile strength (**Figure 3B**), fracture strain (**Figure 3C**), and Young's modulus (**Figure 3D**) of the organohydrogels were higher than that of original Eu-alginate/PVA hydrogel, which can be ascribed to the synergistic effect of the multiple hydrogen bonds and the dense polymer networks. For instance, the tensile

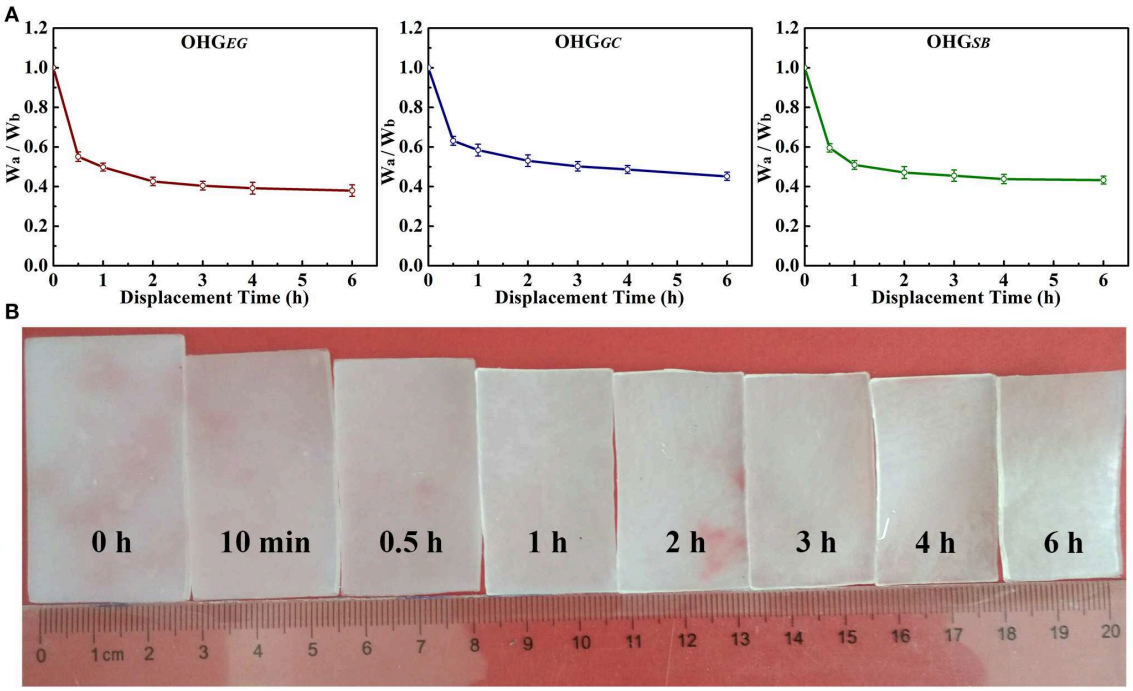

FIGURE 2 | Weight rate (W_a/W_b) of the organohydrogels **(A)**. W_a denotes the weight of the gel immersed in different cryoprotectant solution [ethylene glycol (EG), glycerol (GC), and d-sorbitol (SB) solutions] with different displacement time. W_b represents the original weight of the Eu-alginate/PVA hydrogel. **(B)** Digital pictures show change in the size of OHG_{EG} with prolonged displacement time of 0 h, 10 min, 0.5 h, 1 h, 2 h, 3 h, 4 h and 6 h.

strength of OHG_{SB} increases from 0.58 ± 0.06 MPa to as high as 5.62 ± 0.41 MPa, fracture strain raised from 4.07 ± 0.04 to as high as 7.63 ± 0.02 and Young's modulus ascended from 0.16 ± 0.01 to 1.08 ± 0.03 MPa as the displacement time gradually increased to 6 h. The tensile strength is higher than many of the previously reported organohydrogels, such as polydopamine decorating carbon nanotubes (PDA-CNT)/copolymer of acrylamide (AM) and acrylic acid (AA) (PAM-co-PAA) organohydrogel (0.07 MPa stress, 7.01 strain, Han et al., 2017), PVA/poly(3,4-ethylenedioxythiophene):polystryrene sulfonate (PEDOT:PSS) organohydrogel (2.1 MPa stress, 7.60 strain, Rong et al., 2017), and gelation organohydrogel (2.06 MPa stress, 6.88 strain, Qin et al., 2019), as shown in **Figure S1**. The dramatic enhancement in mechanical properties of the organohydrogels is directly related to crosslinking density, which dominated by the largely increased hydrogen bonds between the cryoprotectant molecules and polymer chains in the organohydrogels (Pan et al., 2018). Interestingly, the tensile strength and the Young's modulus of OHG_{EG} and OHG_{GC} increased by increasing displacement time and then its tended to balance. The tensile strength of OHG_{EG} and OHG_{GC} prepared at displacement time of 3 and 4 h reached to 3.20 ± 0.37 and 3.45 ± 0.42 MPa, respectively. The Young's modulus of the organohydrogels reached to 0.98 ± 0.34 and 0.99 ± 0.42 MPa, respectively. The excellent tensile strength and Young's modulus achieved in the shorter displacement time could be attributed to the smaller molecules of EG and GC than SB. Overall, based on solvent displacement method, the mechanical strength of the physically crosslinked organohydrogels can be dramatically enhanced. In addition, the types of cryoprotectants and displacement time play important roles in controlling mechanical performances of organohydrogels to fulfill the requirements in specific potential applications.

The Non-drying and Anti-freezing Properties of the Eu-Alginate/PVA Organohydrogels

To demonstrate the organohydrogels with a temperature tolerance (−45–50°C), we investigated the non-drying and anti-freezing properties of the organohydrogels (OHG_{EG}, OHG_{GC}, OHG_{SB}), as shown in **Figure 4**. Firstly, to demonstrate non-drying property, the organohydrogels immersed in EG, GC, and SB for different time (0–6 h) were heated at the temperature of 50°C (0–13 h). The weight rate was calculated by (W_t/W_0), where W_0 and W_t denotes for the weight of organohydrogels before heating and heating for certain time, respectively (**Figure 4B**). The weight of organohydrogels decreased by increasing heating time and then it tended to balance, due to that remaining water was evaporated from the organohydrogels. Furthermore, the organohydrogels treated with long displacement time showed high weight rate (W_t/W_0). Notably, it was found that the weight rate of the OHG_{GC} at the displacement time of 6 h exhibited the highest weight rate (over 0.9), because lower vapor pressure (compared to glycol) and fast exchange kinetics of glycerol (small molecular size compared to sorbitol) (Rajan and Matsumura, 2018). In contrast, the original hydrogel showed the lowest weight

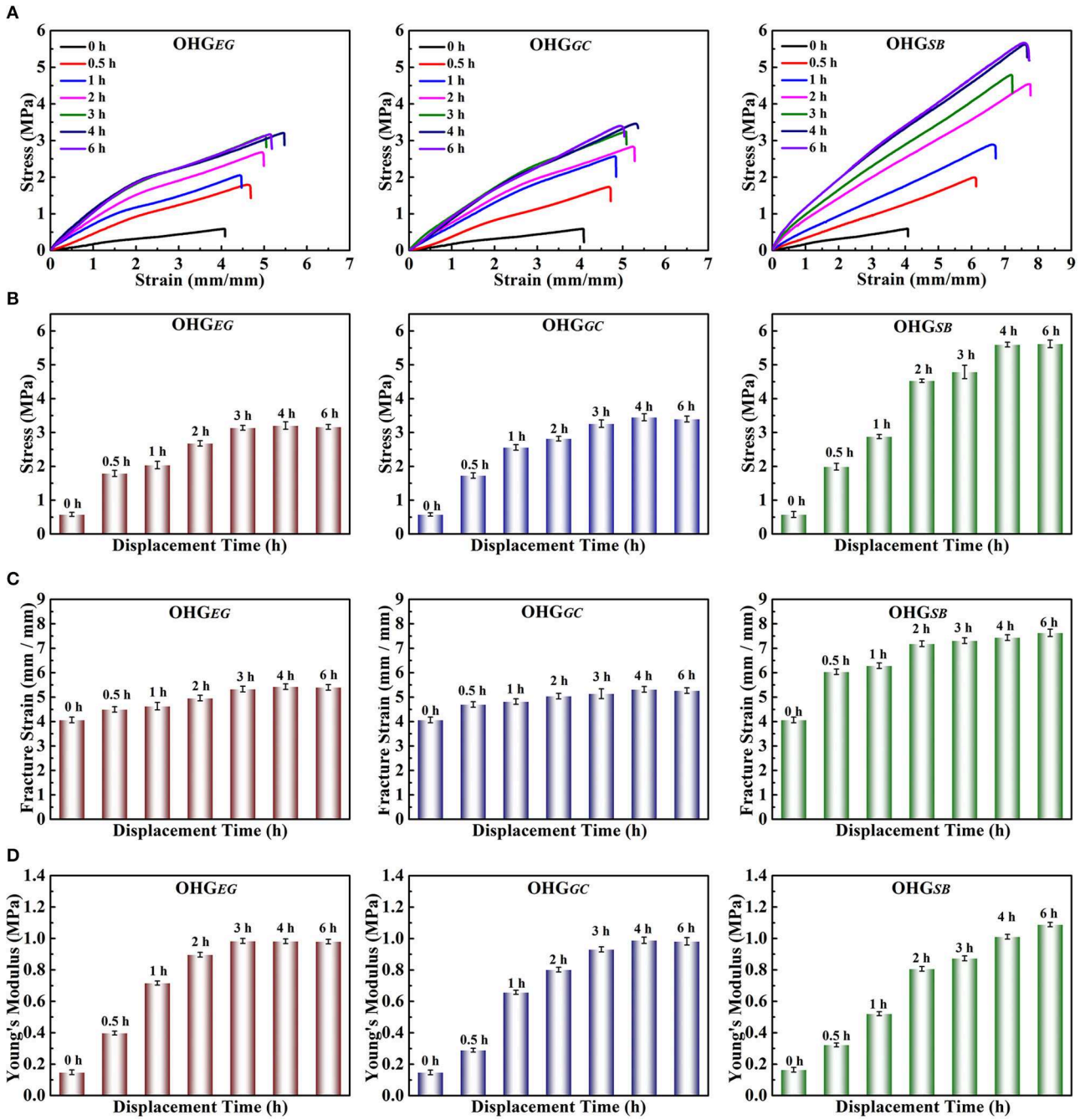

FIGURE 3 | Mechanical properties of the Eu-alginate/PVA organohydrogels (OHG_{EG}, OHG_{GC}, OHG_{SB}) treated with cryoprotectants for different times. **(A)** stress-strain curves, **(B)** stress-displacement time histogram, **(C)** Fracture strain-displacement time histogram, **(D)** Young's modulus-displacement time histogram.

rate (0.18), indicating that OHG_0 does not show non-drying ability due to volatilization of water.

In addition, the anti-freezing properties of the organohydrogels, i.e., deformation behaviors (c, bend; d, twist for 3 × 360°; e, fold) and corresponding recovery states were demonstrated in **Figure 4**. The behaviors of the organohydrogels and hydrogel under the sub-zero temperature were obviously different. The organohydrogels exhibited outstanding deformation behavior, but the original hydrogel could not recover after bending under the sub-zero temperature. The frozen hydrogel (OHG_0) displayed a non-transparent and white morphology due to formation of an aggregate of ice crystals in the polymer networks (**Figure 4C**). The organohydrogels displaced by different cryoprotectants for 4 h,

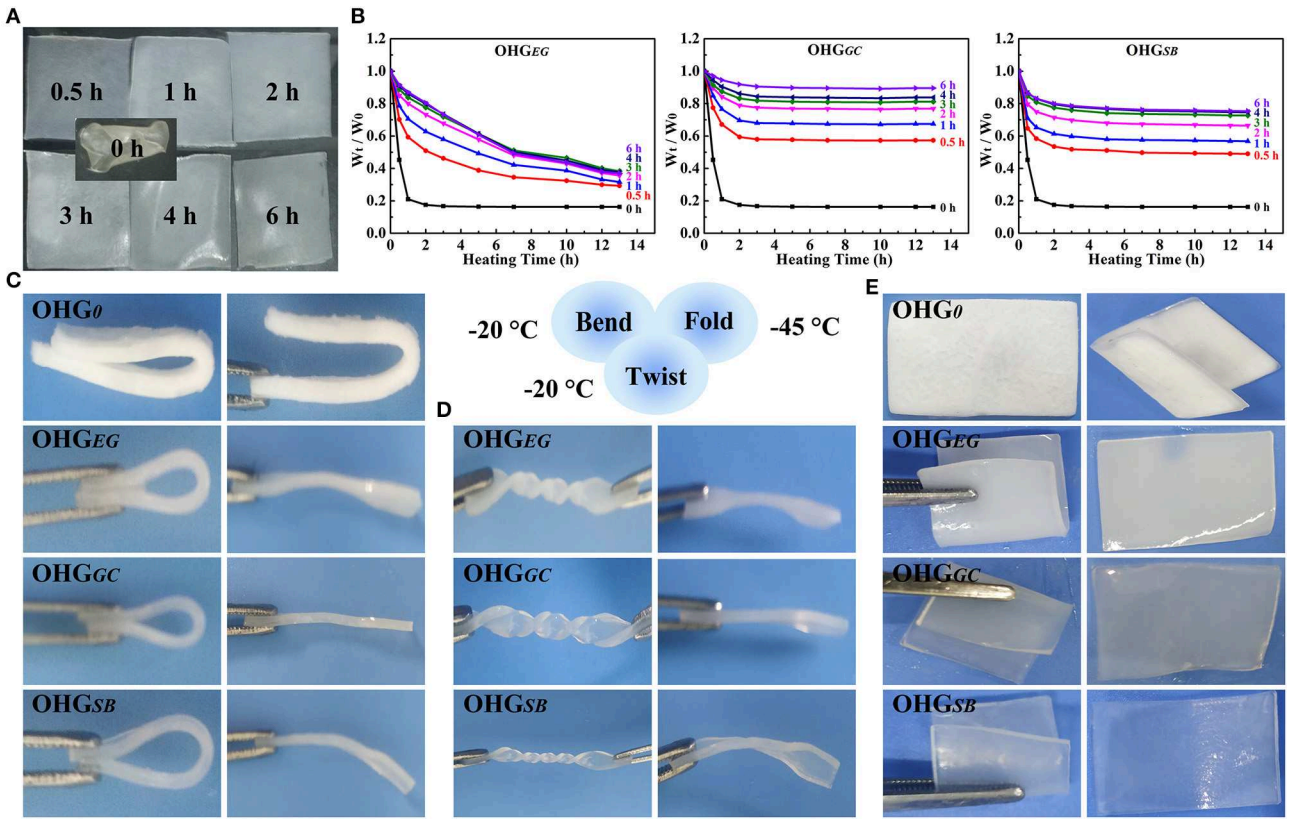

FIGURE 4 | Non-drying **(A,B)** and anti-freezing **(C–E)** properties of the organohydrogels. **(A)** Digital pictures of the organohydrogels soaked in GC solution for different times (0, 0.5, 1, 2, 3, 4, 6 h) and then heated in a vacuum oven at 50°C until constant weight was gained. **(B)** Weight retention rate of OHG_{EG}, OHG_{GC}, and OHG_{SB} with different immersion time under heating at 50°C for different heating time. W_0 is the initial weight of the organohydrogels (OHG_0), while W_t denotes the weight of the samples heated for different times at the temperature of 50°C. The mechanical deformation behaviors (**C**, bent; **D**, twisted for 3 × 360°; **E**, fold) and corresponding recovery state (after free recovery for 5 min) of the organohydrogels soaked for 4 h and then cooled at −20°C **(C,D)** and −45°C **(E)**.

for example, OHG_{EG4}, OHG_{GC4}, and OHG_{SB4}, showed good recovery behaviors after being bent and twisted for 3 × 360° at −20°C (**Figure 4D**). To further demonstrate the anti-freezing property of the organohydrogels, the organohydrogels and hydrogel were placed in a harsh condition (−45°C). In fact, the hydrogel became rigid and fragile owing to being frozen and even generated cracks on the surface during folding under the sub-zero temperature. In contrast, the organohydrogels (OHG_{EG4}, OHG_{GC4}, and OHG_{SB4}) could return to their initial states after being bent and folded (**Figure 4E**). The excellent anti-freezing ability is due to the ice-inhibiting effect of cryoprotectants disrupting the formation of ice crystal lattices of the residual water molecules. The results demonstrate that the cryoprotectant based organohydrogels exhibit excellent non-drying and anti-freezing property, indicating the potential applications under a broad temperature range.

The Microstructure of Organohydrogels and Hydrogel

To further demonstrate the effect of microstructural changes of organohydrogels and hydrogel on their performances, the SEM, XRD, and FTIR analyses were performed, respectively. As shown in the SEM images (**Figure 5A**), the original hydrogel (OHG_0) displayed a distinct porous structure with loose texture, because water molecules form a lot of ice crystals under subzero temperature, and leading to porous structure mainly occupied by water after sublimation of ice crystals from the hydrogel processed by vacuum freeze-drying (Ricciardi et al., 2004). On the other hand, organohydrogels after 0.5 h displacement, i.e., $OHG_{EG(0.5)}$, $OHG_{GC(0.5)}$, and $OHG_{SB(0.5)}$ presents dense structure after same treatment processes, because cryoprotectants prevent formation of ice crystals. The organohydrogels with dense structure correspond to volume shrinkage of organohydrogels because hydrophilic polymers do not swell well in the cryoprotectants (**Figure 2**).

Additionally, the unique microstructures could strengthen the crystallization among PVA polymer chains. It could be verified by XRD patterns where the crystal peak of PVA became more intense in the organohydrogels ($OHG_{EG(0.5)}$, $OHG_{GC(0.5)}$, and $OHG_{SB(0.5)}$), than that of hydrogels (**Figure 5B**). The Eu-alginate/PVA hydrogel and organohydrogels do not show sharp crystalline diffraction peaks of PVA, because the presence of Na-alginate and Eu^{3+} ions inhibit the crystallization of PVA (Hu et al., 2017). The Eu-alginate/PVA hydrogel has a halo

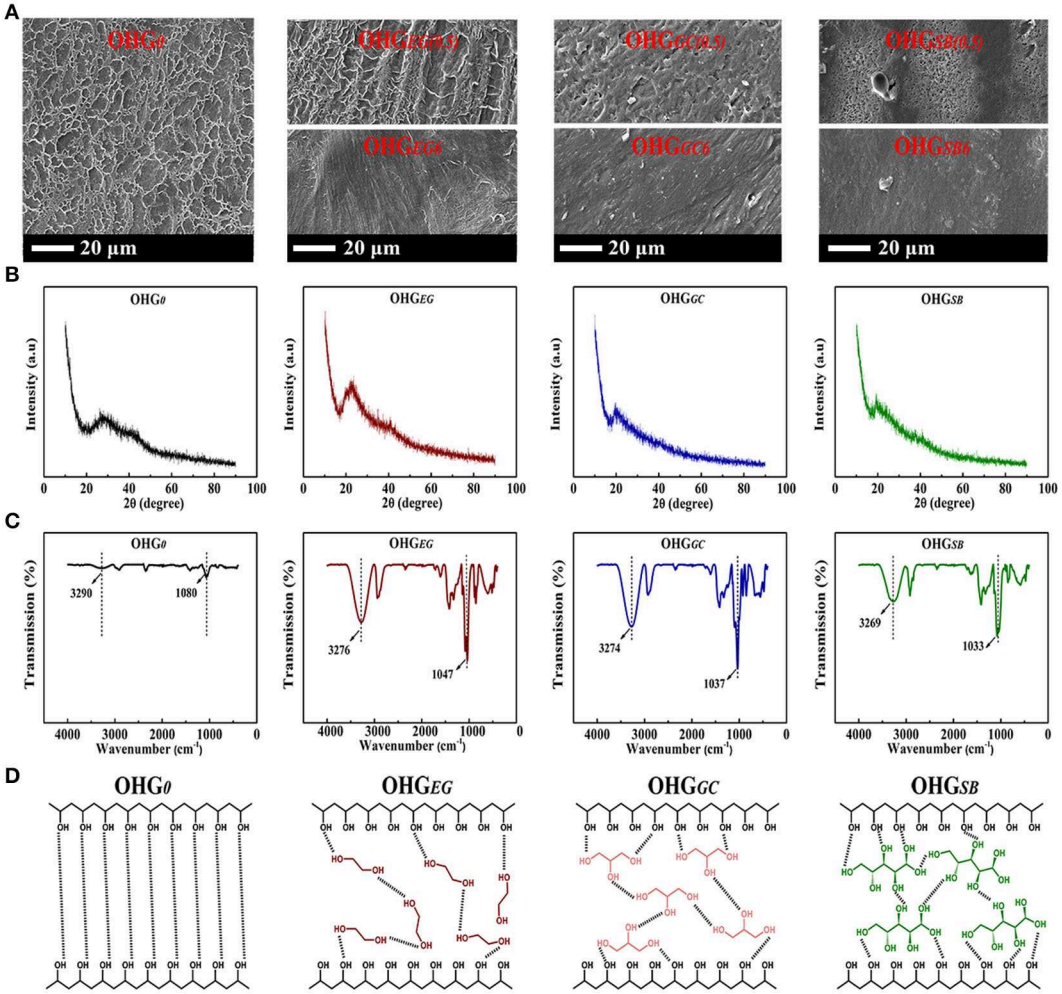

FIGURE 5 | (A) SEM images of the gels [OHG_0, $OHG_{EG(0.5)}$, $OHG_{GC(0.5)}$, $OHG_{SB(0.5)}$, OHG_{EG6}, OHG_{GC6}, OHG_{SB6}], **(B)** XRD patterns and **(C)** FTIR spectra of the gels (OHG_0, OHG_{EG6}, OHG_{GC6}, OHG_{SB6}). For example, $OHG_{EG(0.5)}$ represents Eu-alginate/PVA hydrogels soaking in ethylene glycol (EG) for 0.5 h, while OHG_{SB6} denotes the hydrogels soaking in d-sorbitol (SB) for 6 h. **(D)** Schematic illustrations of the hydrogen bonds (black dotted line) between PVA polymer chains in hydrogel (OHG_0), and EG, GC, SB molecules bridged PVA chains via forming hydrogen bonds in the corresponding organohydrogels.

centered at $2\theta \approx 28^\circ$ (**Figure 5B**) in the diffraction of pure water same as previous report (Ricciardi et al., 2004). The Eu-alginate/PVA hydrogel possesses a water content high enough to 85% while a low PVA content of about 13.5%, indicating crystalline diffraction peaks of PVA ($2\theta \approx 19.4$ and 20°) might be covered by the aforementioned diffraction of free pure water. After the hydrogel was transformed into organohydrogels, typical reflections of crystalline atactic PVA, with a maximum 2θ angles of 22.3, 20.1, 19.6° presents for OHG_{EG}, OHG_{GC}, and OHG_{SB} sample, respectively (Ricciardi et al., 2004). A slight shift of the peak around $2\theta = 20.0^\circ$ of three type organohydrogels could be assigned to the hydrogen bonds between PVA polymers and the cryoprotectants with different molecular structures (Zhao et al., 2019). The results indicate more crystalline PVA aggregates are formed in the organohydrogels due to the decreased relative amount of "free water," whereas a lot of swollen amorphous PVA polymer chains present in the hydrogel. The multiple hydrogen bonds including PVA crystalline domains act as knots of the gel network, promoting the enhancement of mechanical properties (**Figure 5D**).

As shown in the FTIR spectrums (**Figure 5C**), the FTIR spectrum of Eu-alginate/PVA hydrogel shows the characteristic stretching bands of –OH at 3,290 cm^{-1} and C–O at 1,080 cm^{-1}. While for the Eu-alginate/PVA organohydrogels (OHG_{EG}, OHG_{GC} and OHG_{SB}), the characteristic stretching band of –OH shifted to 3,276, 3,274, and 3,269 cm^{-1}, respectively, as well as the characteristic stretching band of C–O shifted to 1,047, 1,037, and 1,033 cm^{-1}, respectively. The shift of IR absorption bands to lower wave numbers suggests the formation of stronger H-bonding in the organohydrogels.

Based on the above analysis, schematics illustrating the interaction among PVA polymer chains and cryoprotectant molecules were presented in **Figure 5D**. After cryoprotectant displacement, the EG, GC, SB molecules could bridge PVA chains *via* abundant hydrogen bonds forming between cryoprotectants and PVA polymer chains. And the pivotal

roles of cryoprotectant molecules can be attributed to three parts, that are, (i) Enhancing the mechanical properties of organohydrogels. (ii) Restricting volatilization of the residual water to promote non-drying ability. (iii) Disrupting the formation of ice crystal lattices as well as reducing the freezing point of H_2O, both phenomena increase the anti-freezing capacity of organohydrogels. As a result, physically crosslinked organohydrogels with enhanced mechanical properties and extreme temperature tolerance could be designed and obtained by cryoprotectants displacement method.

CONCLUSIONS

In summary, physically crosslinked organohydrogels with toughness and extreme temperature tolerance were successfully fabricated by solvent displacement method. Each component of the Eu-alginate/PVA organohydrogels serves the respective role for endowing excellent integrated properties. The PVA is responsible for gel backbone, offering a certain mechanical strength facilitating hydrogen bonds formation, while alginate enables the enhanced mechanical performance of the gels by coordination with Eu^{3+} ions, and interlaces with PVA polymer chains via hydrogen bonds. More importantly, cryoprotectants disrupt the formation of ice crystal lattices of water molecules. This disruption is responsible for bridging of PVA chains through abundant and stable multiple hydrogen bonds, profiting effective energy dissipation, and restricting volatilization of the residual water. The organohydrogels feature enhanced and tunable mechanical capacity, as well as freezing/heating tolerance, potentially to be used in various fields, such as medical devices, flexible electronics, and stretchable devices.

DATA AVAILABILITY STATEMENT

All datasets generated for this study are included in the article/**Supplementary Material**.

AUTHOR CONTRIBUTIONS

YC put forward the ideas about this research and designed the experiments. JZ, DD, and EZ prepared the main materials, and completed the structural characterization and performance testing of materials. JZ and DD analyzed the data and wrote the manuscript. XG, YZ, KY, MK, YAr, and YAz revised and edited the manuscript.

FUNDING

This work was supported by the National Natural Science Foundation of China (11674263), Key Research and Development Program of Shaanxi (Program No. 2020KWZ-006). Xi'an Weiyang District Science and Technology Fund (201927), Key Intergovernmental Special Projects of the National Key R & D Plan of the People's Republic of China (No. 2018YFE0114200), the research project grant of the joint logistic support force (BLB18J014).

SUPPLEMENTARY MATERIAL

The Supplementary Material for this article can be found online at: https://www.frontiersin.org/articles/10.3389/fchem.2020.00102/full#supplementary-material

REFERENCES

Banerjee, H., Suhail, M., and Ren, H. (2018). Hydrogel actuators and sensors for biomedical soft robots: brief overview with impending challenges. *Biomimetics* 3:15. doi: 10.3390/biomimetics3030015

Cerveny, S., Colmenero, J., and Alegría, A. (2005). Dielectric investigation of the low-temperature water dynamics in the poly(vinyl methyl ether)/H_2O system. *Macromolecules* 38, 7056–7063. doi: 10.1021/ma050811t

Chen, F., Zhou, D., Wang, J., Li, T., Zhou, X., Gan, T., et al. (2018). Rational fabrication of anti-freezing non-drying tough organohydrogels by one-pot solvent displacement. *Angew. Chem. Int. Ed.* 130, 6568–6571. doi: 10.1002/ange.201803366

Chen, Q., Zhu, L., Chen, H., Yan, H., and Huang, L. (2015). A novel design strategy for fully physically linked double network hydrogels with tough, fatigue resistant, and self-healing properties. *Adv. Funct. Mater.* 25, 1598–1607. doi: 10.1002/adfm.201404357

Dhivya, S., Saravanan, S., Sastry, T. P., and Selvamurugan, N. (2015). Nanohydroxyapatite-reinforced chitosan composite hydrogel for bone tissue repair *in vitro* and *in vivo*. *J. Nanobiotechnol.* 13:40. doi: 10.1186/s12951-015-0099-z

Dong, D., Hao, T., Wang, C., Zhang, Y., Qin, Z., Yang, B., et al. (2018). Zwitterionic starch-based hydrogel for the expansion and "stemness" maintenance of brown adipose derived stem cells. *Biomaterials* 157, 149–160. doi: 10.1016/j.biomaterials.2017.12.011

Elliott, G. D., Wang, S., and Fuller, B. J. (2017). Cryoprotectants: a review of the actions and applications of cryoprotective solutes that modulate cell recovery from ultra-low temperatures. *Cryobiology* 76, 74–91. doi: 10.1016/j.cryobiol.2017.04.004

Fan, D., Tian, Y., and Liu, Z. (2019). Injectable hydrogels for localized cancer therapy. *Front. Chem.* 7:675. doi: 10.3389/fchem.2019.00675

Gao, H., Zhao, Z., Cai, Y., Zhou, J., Hua, W., Chen, L., et al. (2017). Adaptive and freeze-tolerant heteronetwork organohydrogels with enhanced mechanical stability over a wide temperature range. *Nat. Commun.* 8:15911. doi: 10.1038/ncomms15911

Gao, Y., Song, J., Li, S., Elowsky, C., Zhou, Y., Ducharme, S., et al. (2016). Hydrogel microphone for stealthy underwater listening. *Nat. Commun.* 24:13114. doi: 10.1038/ncomms13114

GhavamiNejad, A., SamariKhalaj, M., Aguilar, L. E., Park, C. H., and Kim, C. S. (2016). pH/NIR light-controlled multidrug release via a mussel-inspired nanocomposite hydrogel for chemo-photothermal cancer therapy. *Sci. Rep.* 6:33594. doi: 10.1038/srep33594

Gong, J. P. (2014). Materials both tough and soft. *Science* 344, 161–162. doi: 10.1126/science.1252389

Gong, J. P., Katsuyama, Y., Kurokawa, T., and Osada, Y. (2003). Double-network hydrogels with extremely high mechanical strength. *Adv. Mater.* 15, 1155–1158. doi: 10.1002/adma.200304907

Gong, Z., Zhang, G., Zeng, X., Li, J., Li, G., Huang, W., et al. (2016). High-strength, tough, fatigue resistant, and self-healing hydrogel based on dual physically cross-linked network. *ACS Appl. Mater. Interfaces* 8, 24030–24037. doi: 10.1021/acsami.6b05627

Gu, B., Sun, X., Papadimitrakopoulos, F., and Burgess, D. J. (2016). Seeing is believing, PLGA microsphere degradation revealed in PLGA microsphere/PVA hydrogel composites. *J. Control. Release* 228, 170–178. doi: 10.1016/j.jconrel.2016.03.011

Han, J., Zhao, X., Xu, W., Wang, W., Han, Y., and Feng, X. (2018). Effect of hydrophobic polypeptide length on performances of

thermo-sensitive hydrogels. *Molecules* 23:1017. doi: 10.3390/molecules23051017

Han, L., Liu, K., Wang, M., Wang, K., Fang, L., Chen, H., et al. (2017). Mussel-inspired adhesive and conductive hydrogel with long-lasting moisture and extreme temperature tolerance. *Adv. Funct. Mater.* 28:1704195. doi: 10.1002/adfm.201704195

Han, Y., Bai, T., Liu, Y., Zhai, X., and Liu, W. (2012). Zinc ion uniquely induced triple shape memory effect of dipole-dipole reinforced ultra-high strength hydrogels. *Macromol. Rapid Commun.* 33, 225–231. doi: 10.1002/marc.201100683

Haraguchi, K., and Takehisa, T. (2002). Nanocomposite hydrogels: a unique organic-inorganic network structure with extraordinary mechanical, optical, and swelling/de-swelling properties. *Adv. Mater.* 14, 1120–1124. doi: 10.1002/1521-4095(20020816)14:163.0.CO;2-9

Hu, C., Wang, M. X., Sun, L., Yang, J. H., Zrínyi, M., and Chen, Y. M. (2017). Dual-physical cross-linked tough and photoluminescent hydrogels with good biocompatibility and antibacterial activity. *Macromol. Rapid Commun.* 38:1600788. doi: 10.1002/marc.201600788

Hu, X., Gao, Z., Tan, H., Wang, H., Mao, X., and Pang, J. (2019). An injectable hyaluronic acid-based composite hydrogel by DA click chemistry with pH sensitive nanoparticle for biomedical application. *Front. Chem.* 7:477. doi: 10.3389/fchem.2019.00477

Huang, T., Xu, H., Jiao, K., Zhu, L., Brown, H., Wang, H. A., et al. (2007). A novel hydrogel with high mechanical strength: a macromolecular microsphere composite hydrogel. *Adv. Mater.* 19, 1622–1626. doi: 10.1002/adma.200602533

Iwaso, K., Takashima, Y., and Harada, A. (2016). Fast response dry-type artificial molecular muscles with [c2]daisy chains. *Nat. Chem.* 8, 625–632. doi: 10.1038/nchem.2513

Jing, Z., Xu, A., Liang, Y. Q., Zhang, Z., Yu, C., Hong, P., et al. (2019). Biodegradable poly(acrylic acid-*co*-acrylamide)/poly(vinyl alcohol) double network hydrogels with tunable mechanics and high self-healing performance. *Polymers* 11:952. doi: 10.3390/polym11060952

Kim, Y. S., Liu, M., Ishida, Y., Ebina, Y., Osada, M., Sasaki, T., et al. (2016). Thermoresponsive actuation enabled by permittivity switching in an electrostatically anisotropic hydrogel. *Nat. Mater.* 14, 1002–1007. doi: 10.1038/nmat4363

Lai, E., Yue, X., Ning, W., Huang, J., Ling, X., and Lin, H. (2019). Three-dimensional graphene-based composite hydrogel materials for flexible supercapacitor electrodes. *Front. Chem.* 7:660. doi: 10.3389/fchem.2019.00660

Li, W., An, H., Tan, Y., Lu, C., Liu, C., Li, P., et al. (2012). Hydrophobically associated hydrogels based on acrylamide and anionic surface active monomer with high mechanical strength. *Soft Matter* 8, 5078–5086. doi: 10.1039/c2sm07200a

Li, Z., Su, S., Yu, L., Zheng, Z., and Wang, X. (2018). Preparation of a photo- and thermo-responsive topological gel from anthracene-modified polyrotaxanes. *Soft Matter* 14, 2767–2771. doi: 10.1039/C8SM00376A

Liang, Z., Liu, C., Li, L., Xu, P., Luo, G., Ding, M., et al. (2016). Double-network hydrogel with tunable mechanical performance and biocompatibility for the fabrication of stem cells-encapsulated fibers and 3D assemble. *Sci. Rep.* 6:33462. doi: 10.1038/srep33462

Liu, J., Tan, C. S. Y., Yu, Z., Lan, Y., Abell, C., and Scherman, O. A. (2017). Biomimetic supramolecular polymer networks exhibiting both toughness and self-recovery. *Adv. Mater.* 29:1604951. doi: 10.1002/adma.201604951

Liu, Y., Meng, H., Qian, Z., Fan, N., Choi, W., Zhao, F., et al. (2017). A moldable nanocomposite hydrogel composed of a mussel-inspired polymer and a nanosilicate as a fit-to-shape tissue sealant. *Angew. Chem. Int. Ed.* 56, 4224–4228. doi: 10.1002/anie.201700628

Lou, D., Wang, C., He, Z., Sun, X., Luo, J., and Li, J. (2019). Robust organohydrogel with flexibility and conductivity across the freezing and boiling temperatures of water. *Chem. Commun.* 55, 8422–8425. doi: 10.1039/C9CC04239C

Mihajlovic, M., Staropoli, M., Appavou, M. S., Wyss, H. M., Pyckhout-Hintzen, W., and Sijbesma, R. P. (2017). Tough supramolecular hydrogel based on strong hydrophobic interactions in a multiblock segmented copolymer. *Macromolecules* 50, 3333–3346. doi: 10.1021/acs.macromol.7b00319

Morelle, X. P., Illeperuma, W. R., Tian, K., Bai, R., Suo, Z., and Vlassak, J. J. (2018). Highly stretchable and tough hydrogels below water freezing temperature. *Adv. Mater.* 30:1801541. doi: 10.1002/adma.201801541

Okumura, Y., and Ito, K. (2001). The polyrotaxane gel: a topological gel by figure-of-eight cross-links. *Adv. Mater.* 13, 485–487. doi: 10.1002/1521-4095(200104)13:7<485::AID-ADMA485>3.0.CO;2-T

Pan, X., Wang, Q., Ning, D., Dai, L., Liu, K., Ni, Y., et al. (2018). Ultraflexible self-healing guar gum-glycerol hydrogel with injectable, antifreeze, and strain-sensitive properties. *ACS Biomater. Sci. Eng.* 4, 3397–3404. doi: 10.1021/acsbiomaterials.8b00657

Qin, Z., Niu, R., Tang, C., Xia, J., Ji, F., Dong, D., et al. (2018). A dual-crosslinked strategy to construct physical hydrogels with high strength, toughness, good mechanical recoverability, and shape-memory ability. *Macromol. Mater. Eng.* 303:1700396. doi: 10.1002/mame.201700396

Qin, Z. H., Dong, D. Y., Yao, M. M., Yu, Q. Y., Sun, X., Guo, Q., et al. (2019). Freezing-tolerant supramolecular organohydrogel with high toughness, thermoplasticity, and healable and adhesive properties. *ACS Appl. Mater. Interfaces* 11, 21184–21193. doi: 10.1021/acsami.9b05652

Rajan, R., and Matsumura, K. (2018). Development and application of cryoprotectants. *Adv. Exp. Med. Biol.* 1081, 339–354. doi: 10.1007/978-981-13-1244-1_18

Ricciardi, R., Auriemma, F., Rosa, C. D., and Lauprêtre, F. (2004). X-ray diffraction analysis of poly(vinyl alcohol) hydrogels, obtained by freezing and thawing techniques. *Macromolecules* 37, 1921–1927. doi: 10.1021/ma035663q

Rong, Q., Lei, W., Chen, L., Yin, Y., Zhou, J., and Liu, M. (2017). Anti-freezing conductive self-healing organohydrogels with stable strain-sensitivity at subzero temperatures. *Angew. Chem. Int. Ed.* 56, 14159–14163. doi: 10.1002/anie.201708614

Rong, Q., Lei, W., Huang, J., and Liu, M. (2018). Low temperature tolerant organohydrogel electrolytes for flexible solid-state supercapacitors. *Adv. Energy Mater.* 8:1801967. doi: 10.1002/aenm.201801967

Shi, S., Peng, X., Liu, T., Chen, Y. N., He, C., and Wang, H. (2017). Facile preparation of hydrogen-bonded supramolecular polyvinyl alcohol-glycerol gels with excellent thermoplasticity and mechanical properties. *Polymer* 111, 168–176. doi: 10.1016/j.polymer.2017.01.051

Wang, M. X., Yang, C. H., Liu, Z. Q., Zhou, J., Xu, F., Suo, Z., et al. (2015). Tough photoluminescent hydrogels doped with lanthanide. *Macro. Rapid Commun.* 36, 465–471. doi: 10.1002/marc.201400630

Wang, W., Narain, R., and Zeng, H. (2018). Rational design of self-healing tough hydrogels: a mini review. *Front. Chem.* 6:497. doi: 10.3389/fchem.2018.00497

Wang, Z., Lin, M., Wang, M., Song, X., Zhang, C., Dong, Z., et al. (2018). Polymerizable microsphere-induced high mechanical strength of hydrogel composed of acrylamide. *Materials* 11:880. doi: 10.3390/ma11060880

Wegst, U. G., Bai, H., Saiz, E., Tomsia, A. P., and Ritchie, R. O. (2014). Bioinspired structural materials. *Nat. Mater.* 14, 23–36. doi: 10.1038/nmat4089

Wei, Z., Yang, J. H., Liu, Z. Q., Xu, F., Zhou, J. X., Zrínyi, M., et al. (2015). Novel biocompatible polysaccharide-based self-healing hydrogel. *Adv. Funct. Mater.* 25, 1352–1359. doi: 10.1002/adfm.201401502

Wei, Z., Yang, J. H., Zhou, J., Xu, F., Zrínyi, M., Dussault, P. H., et al. (2014). Self-healing gels based on constitutional dynamic chemistry and their potential applications. *Chem. Soc. Rev.* 43, 8114–8131. doi: 10.1039/C4CS00219A

Wu, J., Wu, Z., Lu, X., Han, S., Yang, B. R., Gui, X., et al. (2019). Ultrastretchable and stable strain sensors based on anti-freezing and self-healing ionic organohydrogels for human motion monitoring. *ACS Appl. Mater. Interfaces* 11, 9405–9414. doi: 10.1021/acsami.8b20267

Yuk, H., Zhang, T., Lin, S., Parada, G. A., and Zhao, X. (2016). Tough bonding of hydrogels to diverse non-porous surfaces. *Nat. Mater.* 15, 190–196. doi: 10.1038/nmat4463

Zhang, H., Niu, W., and Zhang, S. (2018). Extremely stretchable, stable and durable strain sensors based on double-network organogels. *ACS Appl. Mater. Interfaces* 10, 32640–32648. doi: 10.1021/acsami.8b08873

Zhang, Y., Li, Y., and Liu, W. (2015). Dipole-dipole and H-bonding interactions significantly enhance the multifaceted mechanical properties of thermoresponsive shape memory hydrogels. *Adv. Funct. Mater.* 25, 471–480. doi: 10.1002/adfm.201401989

Zhang, Y. S., and Khademhosseini, A. (2017). Advances in engineering hydrogels. *Science* 356:eaaf3627. doi: 10.1126/science.aaf3627

Zhao, X. Q., Wang, M. X., Chen, Y. M., Chen, Z. G., Suo, T., Qian, W., et al. (2019). Puncture-resistant hydrogel: placing molecular complexes along phase boundaries. *ACS Appl. Mater. Interfaces* 11, 19421–19428. doi: 10.1021/acsami.9b02328

Zhu, P., Deng, Y., and Wang, C. (2017). Graphene/cyclodextrin-based nanocomposite hydrogel with enhanced strength and thermo-responsive ability. *Carbohyd. Polym.* 174, 804–811. doi: 10.1016/j.carbpol.2017.06.081

Conflict of Interest: The authors declare that the research was conducted in the absence of any commercial or financial relationships that could be construed as a potential conflict of interest.

frontiers in Chemistry

ORIGINAL RESEARCH
published: 13 March 2020
doi: 10.3389/fchem.2020.00173

Non-cytotoxic Dityrosine Photocrosslinked Polymeric Materials With Targeted Elastic Moduli

Christopher P. Camp[1], Ingrid L. Peterson[2,3], David S. Knoff[1], Lauren G. Melcher[3], Connor J. Maxwell[1], Audrey T. Cohen[1], Anne M. Wertheimer[2,3] and Minkyu Kim[1,3,4]**

[1] Department of Biomedical Engineering, University of Arizona, Tucson, AZ, United States, [2] Applied Biosciences GIDP, University of Arizona, Tucson, AZ, United States, [3] BIO5 Institute, University of Arizona, Tucson, AZ, United States, [4] Department of Materials Science & Engineering, University of Arizona, Tucson, AZ, United States

Controlling mechanical properties of polymeric biomaterials, including the elastic modulus, is critical to direct cell behavior, such as proliferation and differentiation. Dityrosine photocrosslinking is an attractive and simple method to prepare materials that exhibit a wide range of elastic moduli by rapidly crosslinking tyrosyl-containing polymers. However, high concentrations of commonly used oxidative crosslinking reagents, such as ruthenium-based photoinitiators and persulfates, present cytotoxicity concerns. We found the elastic moduli of materials prepared by crosslinking an artificial protein with tightly controlled tyrosine molarity can be modulated up to 40 kPa by adjusting photoinitiator and persulfate concentrations. Formulations with various concentrations of the crosslinking reagents were able to target a similar material elastic modulus, but excess unreacted persulfate resulted in cytotoxic materials. Therefore, we identified a systematic method to prepare non-cytotoxic photocrosslinked polymeric materials with targeted elastic moduli for potential biomaterials applications in diverse fields, including tissue engineering and 3D bioprinting.

Keywords: photocrosslinking, tyrosine, artificial protein, hydrogel, elastic modulus, non-cytotoxic

OPEN ACCESS

Edited by:
Yi Cao,
Nanjing University, China

Reviewed by:
Xiang Gao,
Cornell University, United States
Shanshan Lv,
Beijing University of Chemical Technology, China

***Correspondence:**
Anne M. Wertheimer
awerth@email.arizona.edu
Minkyu Kim
minkyukim@email.arizona.edu

Specialty section:
This article was submitted to Polymer Chemistry, a section of the journal Frontiers in Chemistry

Received: *07 January 2020*
Accepted: *26 February 2020*
Published: *13 March 2020*

Citation:
Camp CP, Peterson IL, Knoff DS, Melcher LG, Maxwell CJ, Cohen AT, Wertheimer AM and Kim M (2020) Non-cytotoxic Dityrosine Photocrosslinked Polymeric Materials With Targeted Elastic Moduli. Front. Chem. 8:173. doi: 10.3389/fchem.2020.00173

INTRODUCTION

Polymeric biomaterials that are designed to mimic the mechanical properties of tissue matrices can direct cellular behaviors, such as proliferation and differentiation (Engler et al., 2006; Guvendiren and Burdick, 2012; Chaudhuri et al., 2016). Polymers can be chemically crosslinked to form polymer-network materials, such as hydrogels, that mimic the elastic moduli of natural tissues, ranging from 1 kPa in brain tissue to over 100 kPa in bone (Engler et al., 2006; Chaudhuri et al., 2016). Furthermore, crosslinking strategies that rapidly form hydrogels on the order of seconds to minutes are advantageous to precisely fix complex material shapes. However, rapid chemical crosslinking strategies often result in clusters of densely and sparsely crosslinked regions because polymers quickly crosslink before the reagents are well-mixed, resulting in diminished mechanical properties (Kroll and Croll, 2015; Gu et al., 2017, 2020). Therefore, a rapid crosslinking strategy with improved crosslinking homogeneity is necessary to fabricate tissue-mimicking polymeric biomaterials.

Photochemical crosslinking is a potential method to improve the consistency of crosslinking density in rapidly formed polymeric materials because solutions can be thoroughly mixed prior to activating photocrosslinking reagents. Dityrosine photocrosslinking is an attractive and simple approach that exploits light and photoinitiator-activated phenolic coupling of tyrosyl groups within synthetic or natural polymers (Aeschbach et al., 1976; Fancy and Kodadek, 1999; Partlow et al., 2016). The photoinitiator tris(2,2′-bipyridyl)ruthenium(II) ($[Ru(II)bpy_3]^{2+}$) and persulfate oxidizing agents are often used for rapid dityrosine photocrosslinking (Elvin et al., 2005, 2010; Fang and Li, 2012; Ding et al., 2013; Jeon et al., 2015; Yang et al., 2015; Kim et al., 2017; Zhang et al., 2017; Min et al., 2018; Sakai et al., 2018; Khanmohammadi et al., 2019; Lim et al., 2019). $[Ru(II)bpy_3]^{2+}$ functions by absorbing visible light and reducing a persulfate anion to reach a higher energy state, $[Ru(II)bpy_3]^{3+}$. The persulfate anion is consumed in the reaction through decomposition from $S_2O_8^{2-}$ to SO_4^{2-} and $SO_4^{\bullet-}$. $[Ru(II)bpy_3]^{3+}$ oxidizes tyrosyl phenyl groups into free radicals that spontaneously dimerize (Nickel et al., 1994). The complete process of $[Ru(II)bpy_3]^{2+}$ (Ru)-mediated crosslinking occurs on the order of seconds to minutes, and the strategy has been used to form polymeric materials, such as hydrogels, with elastic moduli ranging from 6 kPa to over 100 kPa (Elvin et al., 2010; Ding et al., 2013; Zhang et al., 2017). The range of potential elastic moduli makes the technology sufficient to form biomaterials that mimic particular tissue matrices.

Despite the benefits of Ru-mediated dityrosine photocrosslinking, there is disagreement about the possible cytotoxicity of the Ru and persulfate crosslinking reagents (Annabi et al., 2017). In preparation of dityrosine photocrosslinked polymeric materials, persulfate concentrations have ranged from at least 1 to 200 mM, and Ru concentrations from 0.1 to 3 mM (Elvin et al., 2005, 2010; Fang and Li, 2012; Ding et al., 2013; Jeon et al., 2015; Kim et al., 2017; Zhang et al., 2017; Min et al., 2018; Sakai et al., 2018; Khanmohammadi et al., 2019; Lim et al., 2019). Persulfates are strong oxidizing agents that can stress cell membranes and lead to an increased rate of apoptosis (Song et al., 2017). Ru is an intercalator that can affect DNA and cell replication (Ang and Dyson, 2006; Gill et al., 2016). Due to the potential cytotoxicity of Ru and persulfates, dityrosine photoinitiators including riboflavin or flavin mononucleotide (Kato et al., 1994; Applegate et al., 2016; Donnelly et al., 2017; Liu et al., 2018), and Rose Bengal (Spikes et al., 1999) have been used as alternatives. However, these approaches come at the cost of slower crosslinking that limit potential time-sensitive biomaterials applications, such as stereolithographic 3D bioprinting, where rapid crosslinking is beneficial (Melchels et al., 2010; Bajaj et al., 2014; Valot et al., 2019). Therefore, an evaluation of Ru photocrosslinking parameters is necessary to carefully utilize Ru crosslinking technology and guide the rapid production of non-cytotoxic dityrosine photocrosslinked polymeric materials.

We hypothesized that elastic moduli of Ru-mediated photocrosslinked materials can be targeted by controlling concentrations of Ru and persulfate where the limiting reagent dictates the elastic modulus. Moreover, we expected that hydrogels prepared from formulations where both reagents are at limiting concentrations could enhance the survivability and growth of cells compared to excessive reagent concentrations. To investigate the Ru-mediated fabrication of non-cytotoxic dityrosine polymeric materials with targeted elastic moduli, we used artificial proteins as model polymers. Advantages of artificial polypeptides include precise genetic engineering for well-controlled Tyr molarity in the system and monodispersed biosynthesis to reduce batch-to-batch variations of polymer lengths (Kim et al., 2015; Yang et al., 2017; Dzuricky et al., 2018). We utilized elastin-like polypeptides (ELP) incorporated with tyrosine residues, ELP(Tyr), as an unstructured polymer model (Roberts et al., 2015) to form dityrosine photocrosslinked hydrogels.

Artificial protein ELPs are typically composed of repeating ($GX_{aa}GVP$) pentapeptide sequences, where X_{aa} can be any amino acid except proline (Urry et al., 1985). Tyrosine and alanine residues comprise the X_{aa} positions, $[(GAGVP)_2$-GYGVP-$(GAGVP)_2]_{24}$, to construct ELP(Tyr). Tyrosine residues allow for photocrosslinking, and together with alanine residues, set the lower critical solution temperature (LCST) at 29°C to utilize the inverse transition cycling (ITC) method, a purification strategy that exploits the reversible, temperature-dependent, phase separation property of ELP (Meyer and Chilkoti, 1999; Christensen et al., 2013). The biocompatibility of ELP-based scaffolds, micelles, and hydrogels has led to its utilization in biomedical applications (Urry et al., 1991; Simnick et al., 2007), making ELP(Tyr) a suitable polymer to examine potential cytotoxic effects of Ru and persulfate concentrations when used to form dityrosine photocrosslinked materials with targeted elastic moduli (**Figure 1**).

In this study, we controlled the elastic modulus (G′) of photocrosslinked hydrogels by tuning Ru and ammonium persulfate (APS) concentrations with a constant ELP(Tyr) concentration to control the tyrosine molarity in each crosslinking formulation. Hydrogels with similar G′ that were formed by different crosslinking formulations were evaluated in cytotoxicity assays to understand changes in cytotoxicity due to differences in Ru and APS concentrations. The cytotoxicity assay tests the utility of Ru-mediated dityrosine crosslinked hydrogels in applications for which buffer exchange of the hydrogel is difficult, such as *in-situ* hydrogel applications (Bang et al., 2018) where crosslinking reagents necessarily come into direct contact with cells. This study demonstrates a systematic approach to prepare non-cytotoxic biomaterials with targeted elastic moduli given any appropriate tyrosyl-containing polymer by controlling the concentrations of Ru and APS used during photocrosslinking.

MATERIALS AND METHODS

ELP(Tyr) Synthesis

The ELP(Tyr) plasmid (**Figure S1**) was kindly provided by the Dr. Harvinder Gill laboratory (Ingrole et al., 2014). The pET-24 a(+) ELP(Tyr) plasmid was transformed into BL21(DE3) competent *Escherichia coli* (*E. coli*) cells (New England Biolabs, Ipswich, MA). One colony was amplified in 10 mL LB media

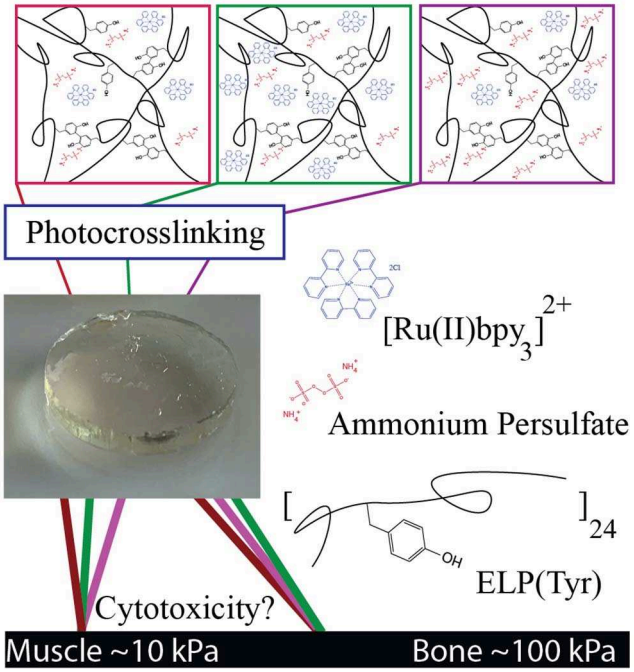

FIGURE 1 | Schematic of tyrosine-photocrosslinked hydrogels with targeted elastic moduli. Multiple formulations with various concentrations of Ru and persulfate can potentially produce hydrogels with similar elastic moduli. Each formulation may have a different degree of cytotoxicity depending on crosslinking reagent concentrations. Reagents in images are an artistic representation of higher concentrations than what is optimal for target G′ and are not representative of actual molar concentrations.

with 50 mg/L kanamycin overnight at 37°C and 220 rpm. The overnight culture was centrifuged at 3,000 × g for 15 min at 4°C. The pellet was resuspended in 2 mL LB media, and 500 μL of cell culture was added to 1 L terrific broth media with 50 mg/L kanamycin. Cultures were incubated at 37°C and 220 rpm for 24 h, centrifuged at 6,000 × g for 5 min to harvest cells, then frozen at −80°C for at least 1 h. Cell pellets were resuspended in pH 7.5 phosphate buffer and lysed using a Branson Sonifier 250 (Branson Ultrasonics, Danbury, CT). Cell debris were removed by centrifuging at 25°C, 10,800 × g for 15 min. ELP(Tyr) was purified using the inverse transition cycling method (Meyer and Chilkoti, 1999) using the described protocol (Ingrole et al., 2014). The cell lysate was heated to 40°C then centrifuged at 40°C, 8,000 × g for 15 min to pellet phase-separated ELP(Tyr). The pellet, including ELP(Tyr), was resuspended in 4°C deionized water to dissolve ELP(Tyr). The resuspended pellet solution was then centrifuged at 4°C, 20,000 × g for 15 min to remove impurities. The supernatant was transferred to a new bottle and the pellet was discarded. The process was repeated for two more cycles and purity was confirmed via SDS PAGE (**Figure S2**). The purified protein was dialyzed in 4.5 L deionized water and changed every 3+ h 7 times at 4°C. Then the soluble fraction was centrifuged and lyophilized, yielding about 350 mg ELP(Tyr) per 1 L cell culture. Lyophilized ELP(Tyr) was stored at −20°C.

Photocrosslinked ELP(Tyr) Hydrogels

The photocrosslinking solution was prepared containing 10% w/v ELP(Tyr) in pH 7.5 phosphate buffer and was mixed with various concentrations of ammonium persulfate and tris(2,2′-bipyridyl)ruthenium(II) chloride hexahydrate (Sigma-Aldrich, St. Louis, MO, USA). Molds were printed by a Formlabs FORM 2 printer with Dental SG resin (Formlabs, MA, USA). Cylindrical 14 mm diameter × 2 mm height molds were prepared for rheology. Cylindrical 20 mm diameter × 1 mm height and 8 mm diameter × 1 mm height molds were prepared for cytotoxicity assays. The crosslinking solution filled the molds and was then irradiated at a distance of 10 inches under a 24 W, 460 nm, 14 × 14 LED array for 10 min. The hydrogels were removed from the molds and stored in glass scintillation vials covered with aluminum foil.

Rheology

The viscoelastic mechanical properties of the hydrogels were analyzed by small amplitude oscillatory shear rheology on a Discovery Hybrid Rheometer 2 (TA Instruments, USA) with a sandblasted 8 mm parallel plate geometry and a sandblasted stage. Inertia, friction, and rotational mapping calibrations were performed prior to each experiment. A Peltier temperature-controlled stage maintained 4°C for all rheology testing. The cylindrical hydrogel was cut to 8 mm diameter, transferred to the stage, and aligned with the geometry before lowering the gap height until the axial force reached 0.05 N. Strain sweeps were performed from 0.01 to 1,000% shear strain at a constant 10 rad/s angular frequency. G′ was determined by averaging the data points within the linear viscoelastic region of the strain sweep (**Figure S3**). Frequency sweeps were performed from 0.01 to 100 rad/s at a constant 0.1% shear strain where it showed the chemical gel behavior, $G' > G''$. The statistical data analysis was conducted using Prism 8 software (GraphPad Software Inc., CA, USA; **Tables S1**–**S3**).

Fibroblast Culturing

For the hydrogel cytotoxicity and the MTT (3-(4,5-dimethylthiazol-2-yl)-2,5-diphenyltetrazolium bromide) assay, low passage (per ATCC guidelines) human neonatal foreskin fibroblast cells (ATCC CRL-2097) were cultured in Iscove's Modified Dulbecco's Media (IMDM) with 10% fetal bovine serum (FBS) without antibiotics at passage 12. Culturing conditions were kept at 37°C, 5% CO_2, and over 95% humidity. Assay plates (either 96 well or 12 well tissue culture treated plates) were seeded from fresh cultures that were harvested at about 75% confluence, as follows: 12-well tissue culture plates were seeded at 125,000 cells/1 mL, and 96-well tissue culture plates at 10,000 cells/100 μL per well.

Hydrogel Cytotoxicity Assay

A live dead viability/cytotoxicity kit (Invitrogen Cat# L3224) was used to assess hydrogel cytotoxicity. Prepared hydrogels remained protected from light at 4°C for up to 16 h before cytotoxicity testing. Prior to introduction to the 70–80% confluent monolayer, each hydrogel was soaked in 70% ethanol for 10 min protected from light at room temperature, soaked

in 3 mL culture media for 5–10 min twice, then gently placed into a 12 well dish. Bright field images were taken at 48 h of co-culture with human neonatal foreskin fibroblast cells (ATCC CRL-2097), then hydrogels were gently removed from the 12 well plates. Culture media was carefully discarded without disturbing the monolayer. Cells were washed three times using 1 mL of dye solution (4 μM Ethidium homodimer-1 and 0.4 μM Calcein AM dye from the kit in D-PBS). After the wash, the dye solution was removed and discarded. A final application of 500 μL dye solution was added and the plate was incubated at room temperature for 1 h, then wrapped in foil and protected from light until imaging on the Bio-Rad ZOE Fluorescent Imager.

MTT Assay

Tissue culture treated 96 well plates were seeded with 10,000 fibroblast cells/100 μL of media (IMDM + 10% FBS). After 48 h, the plate was treated with varying final concentrations of freshly prepared sterile filtered solutions as follows: ammonium persulfate (APS) (0.75 mM, 0.25 mM); $[Ru(II)bpy_3]^{2+}$ (Ru) (125, 9 μM); as well as combinations: (9 μM Ru + 0.25 mM APS, 9 μM Ru + 0.75 mM APS). Each treatment was conducted in duplicate and placed in the incubator for 24 h. After 24 h, all media was removed and replaced with 100 μL phenol red free IMDM + 10% FBS. Cells were exposed to 1.2 mM MTT solution (Invitrogen Cat# M6494) and incubated for 4 h at 37°C. Per the manufacturer's rapid protocol, after incubation, 75 μL of media was removed and 50 μL of standard cell culture dimethyl sulfoxide (DMSO) (Invitrogen Cat# D12345) was added to each well, gently mixed and incubated at 37°C for 10 min. After 10 min, the plate was placed in a standard plate reader, shaken for 20 s and read at 540 nm. The assay was repeated on 4 separate days.

RESULTS AND DISCUSSION

To investigate targeted hydrogel elastic moduli (G′), photocrosslinked ELP(Tyr) hydrogels were prepared using assorted molar concentrations of Ru ([Ru]) and APS ([APS]), then evaluated using rheology. The cytotoxicity of hydrogels from different photocrosslinking formulations with similar G′ were examined to develop a method to prepare non-cytotoxic materials using Ru-catalyzed dityrosine photocrosslinking.

Targeted Hydrogel Elastic Moduli With Multiple Material Formulations

Typical concentrations of Ru and APS used in dityrosine photocrosslinked hydrogels range from 100 to 1,000 μM Ru and 10 to 100 mM APS (Elvin et al., 2010; Fang and Li, 2012; Ding et al., 2013; Zhang et al., 2017; Min et al., 2018). The conversion of $[Ru(II)bpy_3]^{2+}$ to $[Ru(II)bpy_3]^{3+}$ consumes APS, thus we expect G′ can be controlled by modulating [APS] in the crosslinking formulation. We investigated variable [APS] from 15 to 120 mM with [Ru] held constant at 125 μM (squares in **Figure 2A**). We observed that a particular G′ can be targeted below 24 kPa by modulating [APS] up to 60 mM. There was no significant difference between G′ with 60 mM APS and 120 mM APS ($P = 0.769$, **Table S2**), indicating that either a limited molarity of tyrosine or Ru was keeping G′ from increasing between 60 and 120 mM APS. To determine whether G′ plateaued due to limited [Ru] or [tyrosine] in the crosslinking formulation, we prepared hydrogels with higher concentrations of Ru, the same concentration of ELP(Tyr), and the same range of APS concentrations.

Photocrosslinked hydrogels were prepared with a 4-fold higher [Ru] to explore a possible increase in hydrogel G′. When [Ru] was increased from 125 to 500 μM at 120 mM APS, G′ of hydrogels were enhanced from ∼24 to 38.6 ± 2.5 kPa (triangles in **Figure 2A**). Contrasting with 125 μM Ru, G′ (22.2 ± 5.2 kPa) for 500 μM Ru was enhanced by 74% when increasing APS from 60 to 120 mM. We attempted to examine the maximum G′ for 500 μM Ru by increasing [APS] beyond 120 mM, but these hydrogels fractured during crosslinking, making further hydrogel measurements not reproducible (**Figure S4**). Consequently, for ELP(Tyr) hydrogels with 500 μM Ru, [APS] can be modulated to target a particular G′ up to 40 kPa.

To investigate further control of hydrogel G′ using Ru, we tested a 4-fold decrease in [Ru] from 125 to 31 μM. G′ of prepared hydrogels with 31 μM Ru ranged from ∼8–10 kPa (circles in **Figure 2A**), and showed no significant differences in G′ for [APS] between 15 and 120 mM ($P > 0.05$ for all comparisons, **Table S2**). In summary, 31 μM Ru caused G′ to plateau at all measured APS concentrations (circles in **Figure 2A**), 125 μM Ru caused G′ to increase between 15 and 60 mM APS but plateau between 60 and 120 mM APS (squares in **Figure 2A**), while for 500 μM Ru, G′ increased continuously without plateauing (triangles in **Figure 2A**). This confirms that [Ru] must be high enough (≥500 μM) for APS to be used to modulate G′ up to 40 kPa.

Furthermore, we investigated controlling G′ by holding [APS] constant and modulating [Ru] from 31 to 500 μM to ascertain whether both Ru and APS can act as limiting reagents (**Figure 2B**). In crosslinking formulations with 15 mM APS, all hydrogels had similar G′ ranging from ∼8 to 11 kPa (circles in **Figure 2B**; $P > 0.05$ for all comparisons, **Table S3**). For constant 30 and 60 mM APS, there was an increase in G′ when [Ru] was increased from 31 to 125 μM ($P = 0.0022$; $P < 0.0001$, **Table S3**). However, G′ plateaued when [Ru] was increased from 125 to 500 μM ($P > 0.05$, **Table S3**). While 120 mM APS was held constant in crosslinking formulations, G′ continously increased from 10.3 ± 0.8 kPa at 31 μM Ru to 38.6 ± 2.5 kPa at 500 μM Ru (inverted triangles in **Figure 2B**; $P < 0.0001$, **Table S3**). Altogether, G′ was enhanced when [Ru] increased between 125 and 500 μM for constant 120 mM APS but plateaued when [APS] was 60 mM or below. Thus, controlling the concentration of Ru can be used to target G′ of ELP(Tyr) hydrogels when the APS concentration is not limiting.

When either [Ru] or [APS] is held constant, the other reagent concentration can be modulated to change hydrogel G′. While it has been shown that G′ of Ru-mediated dityrosine crosslinked materials can be altered by modulating persulfate or polymer concentrations in crosslinking formulations with high [Ru] (≥1 mM) (Jeon et al., 2015; Yang et al., 2015), with these results, it can be concluded that [Ru], [APS], and the tyrosyl-incorporated polymer concentration can all control G′ of Ru-mediated dityrosine photocrosslinked hydrogels independent of an excess concentration of other parameters.

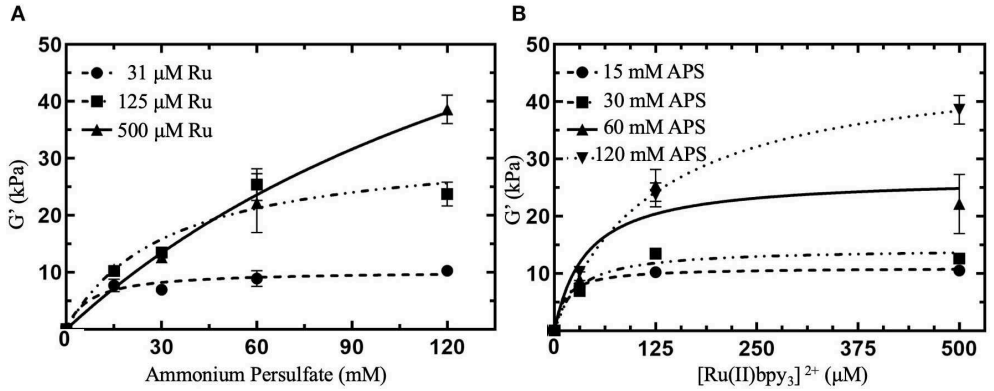

FIGURE 2 | Shear elastic modulus (G′) of photocrosslinked polymeric hydrogels with various concentrations of crosslinking reagents. G′ were collected from linear viscoelastic region from small amplitude oscillatory shear measurements (**Figure S3**) and averaged ($N = 3$ for each data point). **(A)** G′ for hydrogels with APS molar concentrations, [APS], ranging from 15 to 120 mM with constant [Ru] between 31 and 500 μM. **(B)** G′ for hydrogels with [Ru] varied from 31 to 500 μM with constant [APS] ranging from 15 to 120 mM. All hydrogels contained 10 w/v % ELP(Tyr) dissolved in pH 7.5 phosphate buffer and were subject to 10 min of blue light photoactivation for crosslinking. Error bars represent standard deviation. Curves are least square fitting to the hyperbolic model that assumes the independent variable is a reagent that reaches saturating concentrations. **(B)** Is the reformatting of data in **(A)** with the x-axis relevent to [Ru] to investigate constant [APS]. For formulations with 0 mM [Ru] or [APS], we assumed $G' = 0$ kPa since the hydrogel was not formed.

Multiple photocrosslinking formulations with different concentrations of Ru and APS can target similar G′ of polymeric materials because Ru and APS can each function as a limiting reagent with respect to G′. For example, 31 μM Ru limits G′ for APS between 15 and 120 mM, resulting in ∼8–10 kPa hydrogels (circles in **Figure 2A**), while 15 mM APS limits G′ for Ru between 31 and 500 μM, also resulting in ∼8–11 kPa hydrogels (circles in **Figure 2B**). Additionally, optimal formulations can be prepared that contain limiting concentrations of both reagents that target a specific G′, such as 8–11 kPa (**Figure S5**). Although multiple formulations can be used to prepare polymeric materials with similar G′, excess reagents can impact hydrogel cytotoxicity. Therefore, it is necessary to investigate how reagent concentrations that prepare hydrogels can adversely affect cytotoxicity to inform if they are suitable to prepare biomaterials.

Cytotoxicity Analysis of Hydrogels Prepared by Multiple Crosslinking Formulations

To examine potential cytotoxic effects of different formulations when preparing Ru-mediated crosslinked polymeric hydrogels with similar elastic moduli (G′), we prepared three formulations of various [Ru] and [APS] that each target G′ to ∼10 kPa (**Figure 2**): low [Ru] and low [APS] (31 μM Ru, 15 mM APS), high [Ru] and low [APS] (125 μM Ru, 15 mM APS), and low [Ru] and high [APS] (31 μM Ru, 120 mM APS).

The prepared hydrogels were applied to human primary fibroblasts at 70–80% confluence in clutures to understand if some formulations can negatively impact cell growth. We found that hydrogels prepared with low APS and either low or high Ru (**Figures 3A,B**) showed no cytotoxicity compared to controlled cell growth with no hydrogel added (**Figure 3D**). In contrast, the hydrogels prepared with low Ru and high APS were cytotoxic (**Figure 3C**). Therefore, the amount of APS leaching out from the hydrogel and coming into contact with the fibroblasts is likely correlated with the increase in cytotoxicity.

We anticipated that the total mass of APS in the hydrogel could be the major factor compared to the APS molar concentration in the hydrogel because the total mass of released APS will increase the APS concentration in a given cell culture volume for the fibroblast cytotoxicity assay. To understand the impact of hydrogel volume on fibroblast cytotoxicity, we compared the 20 mm diameter × 1 mm height hydrogels that caused cytotoxicity (**Figure 3C**) to 8 mm diameter × 1 mm height hydrogels with various formulations in fibroblast cytotoxicity assays. The hydrogel volume to well volume ratio was 1:3 for the larger hydrogels and 1:20 for the smaller hydrogels. The smaller hydrogels showed no fibroblast cytotoxicity irrespective of formulation after 48 h (**Table S4**), while the larger hydrogels with 31 μM Ru and 120 mM APS were cytotoxic after 48 h (**Figure 3C**), indicating that the hydrogel with the greater total mass of APS showed increased cytotoxicity.

To confirm that the mass of APS in hydrogels will impact cytotoxicity, we added the total mass of APS used in the cytotoxic 20 mm diameter hydrogels with 120 mM APS to 8 mm diameter hydrogels, bringing the concentration in the 8 mm hydrogels to 750 mM APS. We found that the hydrogels with 120 mM APS did not disrupt cell growth compared to the control with no hydrogels added (**Figures S6A,C**), but despite constant G′ and hydrogel volume, hydrogels with 750 mM APS disrupted cell growth (**Figure S6B**). Thus, the total amount of APS is the major parameter that determines cytotoxicity. Cytotoxicity assays performed by other groups have shown that biomaterials prepared with Ru-mediated crosslinking showed no cytotoxicity (Elvin et al., 2009; Syedain et al., 2009; Lv et al., 2013; Keating et al., 2019). This may be a result of lower amounts of excess APS in crosslinking formulations, testing being conducted on confluent monolayers or cells with low rates of proliferation

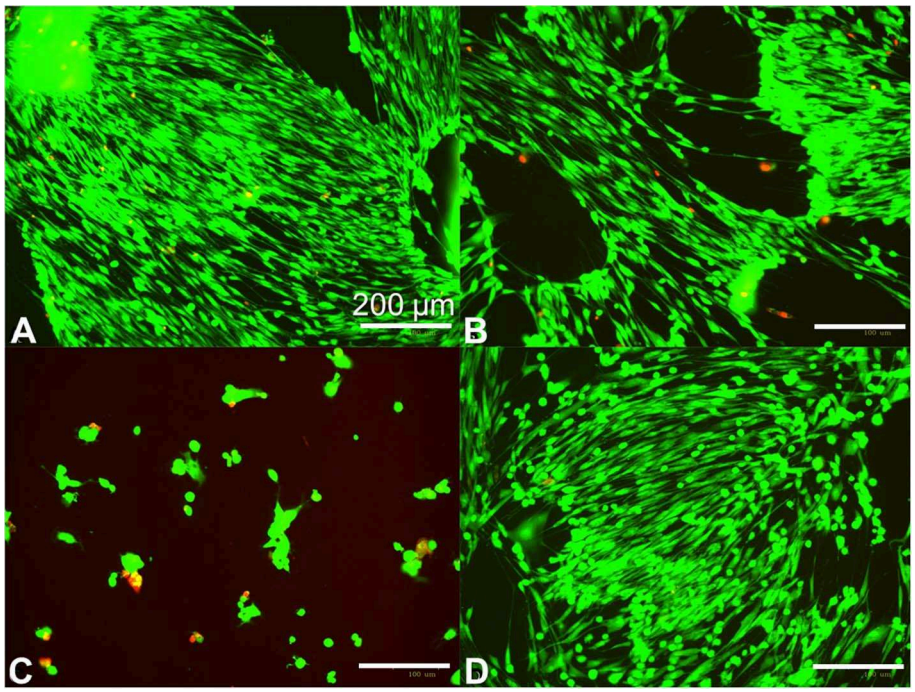

FIGURE 3 | Human fibroblast cytotoxicity/viability assay for ∼10 kPa hydrogels prepared using different photocrosslinking formulations. Fibroblasts were seeded at 125,000 cells per well and grown overnight in standard 12 well dishes, then treated at 70–80% confluence with 20 mm diameter × 1 mm height crosslinked hydrogels for 48 h. Hydrogels were prepared with 10 w/v% ELP(Tyr) and 125 μM Ru/15 mM APS **(A)**, 31 μM Ru/15 mM APS **(B)**, and 31 μM Ru/120 mM APS **(C)**. The hydrogel was omitted in the control well **(D)**. Green fluorescence indicates live cells while red indicates dead cells. Bright field images are available in **Figure S7**.

(Williams et al., 2005), or the testing of hydrogels with smaller volumes and a lower total mass of crosslinking reagents relative to cell media volume to dilute excess reagents.

The direct impact of [Ru] and [APS] on fibroblast cytotoxicity was quantified using MTT assays. We found [Ru] up to 125 μM did not affect fibroblast cytotoxicity, while [APS] even at 0.25 mM showed cytotoxicity (**Figure S8**). These data indicate that high APS concentrations should be carefully avoided in crosslinking formulations due to acute cytotoxicity. It has been suggested that the consumption of APS in the reaction reduces the toxicity of produced hydrogels compared to the formulation before photoactivation (Elvin et al., 2009). Yet, hydrogels with the higher [APS] depicted in **Figure 3C** were cytotoxic. In those hydrogels, 120 mM APS is in excess of the concentration necessary to reach ∼10 kPa because similar G′ can be obtained with 15 mM APS at the same low Ru concentration (circles in **Figure 2A**). It is expected that the excess APS was not consumed in the reaction since G′ was limited by low [Ru]. Thus, the hydrogel leaked unreacted APS into the fibroblast media and caused cytotoxicity. The hydrogel cytotoxicity was reduced for smaller hydrogels because the amount of excess APS that leaked out into the media was less than the larger hydrogel prepared with the same [APS] in the constant well volume. However, smaller hydrogels or larger well volumes to reduce [APS] in cell media may not realistically represent possible clinical applications. Therefore, hydrogels that are prepared with just enough APS to target the elastic modulus while avoiding excess [APS] can result in lower unreacted [APS] in the prepared hydrogel for reduced cytotoxicity.

A similar approach to preparing crosslinking formulations is necessary when considering [Ru]. Since Ru is implicated as a DNA intercalator, avoiding excess [Ru] in crosslinking formulations could improve biocompatibility of Ru-mediated photocrosslinked materials. We found that modulation of [Ru] was effective to control G′ such that low [Ru] could consistently target a lower G′ independent of [APS] and excess crosslinking time. Yet, the recyclability of Ru in this reaction has led to speculation that Ru cannot be effectively used to modulate G′ (Syedain et al., 2009). The cyclic conversion of $[Ru(II)bpy_3]^{2+}$ to $[Ru(II)bpy_3]^{3+}$ by APS oxidation and back to $[Ru(II)bpy_3]^{2+}$ by tyrosyl reduction would seem to allow for lower [Ru] to reach the same G′ given more time. However, the activity of Ru was temporally limited for the photocrosslinking of ELP(Tyr), shown by formulations with excess [APS] but lower G′ compared to formulations with the same [APS] but increased [Ru] (circles compared to triangles in **Figure 2A**). This finding indicates [Ru] and [APS] must be high enough to target a particular G′. Yet, excess [Ru] and [APS] can be avoided for enhanced biocompatibility by systematically evaluating possible formulations to reach a target G′ value for a given tyrosyl-containing polymer.

CONCLUSIONS

We identified a systematic method for utilizing rapid Ru-mediated dityrosine photocrosslinking technology to form non-cytotoxic polymeric materials with elastic moduli (G′) that

mimic natural tissues. G′ of hydrogels can be targeted by modulating the concentrations of $[Ru(II)bpy_3]^{2+}$ (Ru) and ammonium persulfate (APS), potentially due to a temporally limited activity of Ru and the consumption of APS during the reaction. Our results indicate that prototypes of Ru-mediated photocrosslinked polymeric biomaterials can lead to false cytotoxicity results when the ratio of hydrogel volume to cell media volume is small; therefore, cytotoxicity assays should be thorough to investigate volume limitations of biomaterials relative to the surrounding cells given a particular crosslinking formulation. Additionally, monitoring cell growth by beginning the cytotoxicity assay with cells that are not fully confluent instead of 100% confluent monolayers is a better approach for wound healing models and surgical implantation of hydrogels where cell growth around the material is necessary. Finally, Ru and APS should both be set at limiting concentrations to reach a desired G′ such that Ru concentrations are low, and a larger percentage of APS is consumed in the reaction. Taking these steps can unlock the benefits of rapidly preparing Ru-mediated photocrosslinked non-cytotoxic polymeric biomaterials with targeted elastic moduli and temporal control of Ru activation for translation to clinical applications where rapid polymer crosslinking is preferred.

DATA AVAILABILITY STATEMENT

The raw data supporting the conclusions of this article will be made available by the authors, without undue reservation, to any qualified researcher.

AUTHOR CONTRIBUTIONS

MK conceived the project. MK and AW designed the overall experiments. CC, IP, DK, LM, CM, AC, and AW designed and performed the individual experiments. CC, AW, and MK wrote the manuscript. All authors edited the manuscript.

FUNDING

This research was supported by the Accelerate for Success award from Research, Discovery & Innovation at the University of Arizona and in part by the University of Arizona Biomedical Engineering Department (CC), the University of Arizona Applied Biosciences GIDP (IP), the National Heart, Lung, and Blood Institute of the National Institutes of Health (T32HL007955; DK), and the ARCS Foundation Templin Endowment (DK). The content was solely the responsibility of the authors and does not necessarily represent the official views of the National Institutes of Health.

ACKNOWLEDGMENTS

The authors would like to thank Dr. Dongkyun Kang laboratory at the University of Arizona for providing 3D-printed molds to fabricate hydrogels.

SUPPLEMENTARY MATERIAL

The Supplementary Material for this article can be found online at: https://www.frontiersin.org/articles/10.3389/fchem.2020.00173/full#supplementary-material

REFERENCES

Aeschbach, R., Amado, R., and Neukom, H. (1976). Formation of dityrosine cross-links in proteins by oxidation of tyrosine residues. *Biochim. Biophys. Acta* 439, 292–301. doi: 10.1016/0005-2795(76)90064-7

Ang, W. H., and Dyson, P. J. (2006). Classical and non-classical ruthenium-based anticancer drugs: towards targeted chemotherapy. *Eur. J. Inorg. Chem.* 20, 4003–4018. doi: 10.1002/ejic.200600723

Annabi, N., Zhang, Y. N., Assmann, A., Sani, E. S., Cheng, G., Antonio, D. L., et al. (2017). Engineering a highly elastic human protein-based sealant for surgical applications. *Sci. Transl. Med.* 9:eaai7466. doi: 10.1126/scitranslmed.aai7466

Applegate, M. B., Partlow, B. P., Coburn, J., Marelli, B., Pirie, C., Roberto, P., et al. (2016). Photocrosslinking of silk fibroin using riboflavin for ocular prostheses. *Adv. Mater. Technol.* 28, 2417–2420. doi: 10.1002/adma.201504527

Bajaj, P., Schweller, R. M., Khademhosseini, A., West, J. L., and Bashir, R. (2014). 3D biofabrication strategies for tissue engineering and regenerative medicine. *Annu. Rev. Biomed. Eng.* 16, 247–276. doi: 10.1146/annurev-bioeng-071813-105155

Bang, S., Jung, U., Noh, I. (2018). Synthesis and biocompatibility characterizations of *in situ* chondroitin sulfate-gelatin hydrogel for tissue engineering. *Tissue Eng. Regen. Med.* 15, 25–35. doi: 10.1007/s13770-017-0089-3

Chaudhuri, O., Gu, L., Klumpers, D., Darnell, M., Bencherif, S. A., James, C., et al. (2016). Hydrogels with tunable stress relaxation regulate stem cell fate and activity. *Nat. Mater.* 15, 326–334. doi: 10.1038/nmat4489

Christensen, T., Hassouneh, W., Trabbic-Carlson, K., and Chilkoti, A. (2013). Predicting transition temperatures of elastin-like polypeptide fusion proteins. *Biomacromolecules* 14, 1514–1519. doi: 10.1021/bm400167h

Ding, Y., Li, Y., Qin, M., Cao, Y., and Wang, W. (2013). Photo-cross-linking approach to engineering small tyrosine-containing peptide hydrogels with enhanced mechanical stability. *Langmuir* 29, 13299–13306. doi: 10.1021/la4029639

Donnelly, P. E., Chen, T., Finch, A., Brial, C., Maher, S. A., and Torzilli, P. A. (2017). Photocrosslinked tyramine-substituted hyaluronate hydrogels with tunable mechanical properties improve immediate tissue-hydrogel interfacial strength in articular cartilage. *J. Biomater. Sci. Polym. Ed.* 28, 582–600. doi: 10.1080/09205063.2017.1289035

Dzuricky, M., Roberts, S., and Chilkoti, A. (2018). Convergence of artificial protein polymers and intrinsically disordered proteins. *Biochemistry* 57, 2405–2414. doi: 10.1021/acs.biochem.8b00056

Elvin, C. M., Brownlee, A. G., Huson, M. G., Tebb, T. A., Kim, M., Russell, E., et al. (2009). The development of photochemically crosslinked native fibrinogen as a rapidly formed and mechanically strong surgical tissue sealant. *Biomaterials* 30, 2059–2065. doi: 10.1016/j.biomaterials.2008.12.059

Elvin, C. M., Carr, A. G., Huson, M. G., Maxwell, J. M., Pearson, R. D., Tony, V., et al. (2005). Synthesis and properties of crosslinked recombinant pro-resilin. *Nature* 437, 999–1002. doi: 10.1038/nature04085

Elvin, C. M., Vuocolo, T., Brownlee, A. G., Sando, L., Huson, M. G., Nancy, E., et al. (2010). A highly elastic tissue sealant based on photopolymerised gelatin. *Biomaterials* 31, 8323–8331. doi: 10.1016/j.biomaterials.2010.07.032

Engler, A. J., Sen, S., Sweeney, H. L., and Discher, D. E. (2006). Matrix elasticity directs stem cell lineage specification. *Cell* 126, 677–689. doi: 10.1016/j.cell.2006.06.044

Fancy, D. A., and Kodadek, T. (1999). Chemistry for the analysis of protein-protein interactions: rapid and efficient cross-linking triggered by long wavelength light. *Proc. Natl. Acad. Sci. U.S.A.* 96, 6020–6024. doi: 10.1073/pnas.96.11.6020

Fang, J., and Li, H. (2012). A facile way to tune mechanical properties of artificial elastomeric proteins-based hydrogels. *Langmuir* 28, 8260–8265. doi: 10.1021/la301225w

Gill, M. R., Harun, S. N., Halder, S., Boghozian, R. A., Ramadan, K., Haslina, A., et al. (2016). A ruthenium polypyridyl intercalator stalls DNA replication forks, radiosensitizes human cancer cells and is enhanced by Chk1 inhibition. *Sci. Rep.* 6:31973. doi: 10.1038/srep39363

Gu, Y., Zhao, J., and Johnson, J. A. (2020). Polymer networks: from plastics and gels to porous frameworks. *Angew. Chem. Int. Ed. Engl.* 59, 2–30. doi: 10.1002/anie.201902900

Gu, Y. W., Kawamoto, K., Zhong, M. J., Chen, M., Hore, M. J. A., Alex, M. J., et al. (2017). Semibatch monomer addition as a general method to tune and enhance the mechanics of polymer networks via loop-defect control. *Proc. Natl. Acad. Sci. U.S.A.* 114, 4875–4880. doi: 10.1073/pnas.1620985114

Guvendiren, M., and Burdick, J. A. (2012). Stiffening hydrogels to probe short- and long-term cellular responses to dynamic mechanics. *Nat. Commun.* 3:792. doi: 10.1038/ncomms1792

Ingrole, R. S., Tao, W., Tripathy, J. N., and Gill, H. S. (2014). Synthesis and immunogenicity assessment of elastin-like polypeptide-M2e construct as an influenza antigen. *Nano Life* 4:1450004. doi: 10.1142/S1793984414500044

Jeon, E. Y., Hwang, B. H., Yang, Y. J., Kim, B. J., Choi, B. H., Gyu. Y. J., et al. (2015). Rapidly light-activated surgical protein glue inspired by mussel adhesion and insect structural crosslinking. *Biomaterials* 67, 11–19. doi: 10.1016/j.biomaterials.2015.07.014

Kato, Y., Uchida, K., and Kawakishi, S. (1994). Aggregation of collagen exposed to uva in the presence of riboflavin–a plausible role of tyrosine modification. *Photochem. Photobiol.* 59, 343–349. doi: 10.1111/j.1751-1097.1994.tb05045.x

Keating, M., Lim M., Hu, Q., Botvinick, E. (2019). Selective stiffening of fibrin hydrogels with micron resolution via photocrosslinking. *Acta Biomater.* 87, 88–96. doi: 10.1016/j.actbio.2019.01.034

Khanmohammadi, M., Nemati, S., Ai, J., and Khademi, F. (2019). Multipotency expression of human adipose stem cells in filament-like alginate and gelatin derivative hydrogel fabricated through visible light-initiated crosslinking. *Mater. Sci. Eng. C Mater. Biol. Appl.* 103:109808. doi: 10.1016/j.msec.2019.109808

Kim, C. S., Yang, Y. J., Bahn, S. Y., and Cha, H. J. (2017). A bioinspired dual-crosslinked tough silk protein hydrogel as a protective biocatalytic matrix for carbon sequestration. *NPG Asia Mater.* 9:e391. doi: 10.1038/am.2017.71

Kim, M., Chen, W. G., Kang, J. W., Glassman, M. J., Ribbeck, K., and Olsen, B. D. (2015). Artificially engineered protein hydrogels adapted from the nucleoporin NSP1 for selective biomolecular transport. *Adv. Mater.* 27, 4207–4212. doi: 10.1002/adma.201500752

Kroll, D. M., and Croll, S. G. (2015). Influence of crosslinking functionality, temperature and conversion on heterogeneities in polymer networks. *Polymer* 79, 82–90. doi: 10.1016/j.polymer.2015.10.020

Lim, K. S., Klotz, B. J., Lindberg, G. C. J., Melchels, F. P. W., Hooper, G. J., Jos, M., et al. (2019). Visible light cross-linking of gelatin hydrogels offers an enhanced cell microenvironment with improved light penetration depth. *Macromol. Biosci.* 19:e1900098. doi: 10.1002/mabi.201900098

Liu, H. Y., Nguyen, H. D., and Lin, C. C. (2018). Dynamic peg-peptide hydrogels via visible light and fmn-induced tyrosine dimerization. *Adv. Healthc. Mater.* 7:e1800954. doi: 10.1002/adhm.201800954

Lv, S., Bu, T., Sayser, J., Bausch, A., Li, H. (2013). Towards constructing extracellular matrix-mimetic hydrogels: an elastic hydrogel constructed from tandem modular proteins containing tenascin FnIII domains. *Acta Biomater.* 9, 6481–6491. doi: 10.1016/j.actbio.2013.01.002

Melchels, F. P. W., Feijen, J., and Grijpma, D. W. (2010). A review on stereolithography and its applications in biomedical engineering. *Biomaterials* 31, 6121–6130. doi: 10.1016/j.biomaterials.2010.04.050

Meyer, D. E., and Chilkoti, A. (1999). Purification of recombinant proteins by fusion with thermally-responsive polypeptides. *Nat. Biotechnol.* 17, 1112–1115. doi: 10.1038/15100

Min, K. I., Kim, D. H., Lee, H. J., Lin, L. W., and Kim, D. P. (2018). Direct synthesis of a covalently self-assembled peptide nanogel from a tyrosine-rich peptide monomer and its biomineralized hybrids. *Angew. Chem. Int. Ed. Engl.* 57, 5630–5634. doi: 10.1002/anie.201713261

Nickel, U., Chen, Y. H., Schneider, S., Silva, M. I., Burrows, H. D., and Formosinho, S. J. (1994). Mechanism and kinetics of the photocatalyzed oxidation of p-phenylenediamines by peroxydisulfate in the presence of tri-2,2′-bipyridylylruthenium(Ii). *J. Phys. Chem.* 98, 2883–2888. doi: 10.1021/j100062a026

Partlow, B. P., Applegate, M. B., Omenetto, F. G., and Kaplan, D. L. (2016). Dityrosine cross-linking in designing biomaterials. *ACS Biomater. Sci. Eng.* 2, 2108–2121. doi: 10.1021/acsbiomaterials.6b00454

Roberts, S., Dzuricky, M., and Chilkoti, A. (2015). Elastin-like polypeptides as models of intrinsically disordered proteins. *FEBS Lett.* 589, 2477–2486. doi: 10.1016/j.febslet.2015.08.029

Sakai, S., Kamei, H., Mori, T., Hotta, T., Ohi, H., Masaki, N., et al. (2018). Visible light-induced hydrogelation of an alginate derivative and application to stereolithographic bioprinting using a visible light projector and acid red. *Biomacromolecules* 19, 672–679. doi: 10.1021/acs.biomac.7b01827

Simnick, A. J., Lim, D. W., Chow, D., and Chilkoti, A. (2007). Biomedical and biotechnological applications of elastin-like polypeptides. *Polymer Rev.* 47, 121–154. doi: 10.1080/15583720601109594

Song, C., Wang, L. Y., Ye, G. L., Song, X. P., He, Y. T., and Qiu, X. Z. (2017). Residual ammonium persulfate in nanoparticles has cytotoxic effects on cells through epithelial-mesenchymal transition. *Sci. Rep.* 7:11769. doi: 10.1038/s41598-017-12328-0

Spikes, J. D., Shen, H. R., Kopeckova, P., and Kopecek, J. (1999). Photodynamic crosslinking of proteins. iii. kinetics of the Fmn- and rose bengal-sensitized photooxidation and intermolecular crosslinking of model tyrosine-containing *N*-(2-hydroxypropyl)methacrylamide copolymers. *Photochem. Photobiol.* 70, 130–137. doi: 10.1111/j.1751-1097.1999.tb07980.x

Syedain, Z. H., Bjork, J., Sando, L., and Tranquillo, R. T. (2009). Controlled compaction with ruthenium-catalyzed photochemical cross-linking of fibrin-based engineered connective tissue. *Biomaterials* 30, 6695–6701. doi: 10.1016/j.biomaterials.2009.08.039

Urry, D. W., Parker, T. M., Reid, M. C., and Gowda, D. C. (1991). Biocompatibility of the bioelastic materials, poly(gvgvp) and its gamma-irradiation cross-linked matrix–summary of generic biological test-results. *J. Bioact. Compat. Polym.* 63, 263–282. doi: 10.1177/088391159100600306

Urry, D. W., Trapane, T. L., and Prasad, K. U. (1985). Phase-structure transitions of the elastin polypentapeptide water-system within the framework of composition temperature studies. *Biopolymers* 24, 2345–2356. doi: 10.1002/bip.360241212

Valot, L., Martinez, J., Mehdi, A., and Subra, G. (2019). Chemical insights into bioinks for 3d printing. *Chem. Soc. Rev.* 48, 4049–4086. doi: 10.1039/C7CS00718C

Williams, C. G., Malik, A. N., Kim, T. K., Manson, P. N., and Elisseeff, J. H. (2005). Variable cytocompatibility of six cell lines with photoinitiators used for polymerizing hydrogels and cell encapsulation. *Biomaterials* 26, 1211–1218. doi: 10.1016/j.biomaterials.2004.04.024

Yang, Y. J., Holmberg, A. L., and Olsen, B. D. (2017). Artificially engineered protein polymers. *Annu. Rev. Chem. Biomol. Eng.* 8, 549–575. doi: 10.1146/annurev-chembioeng-060816-101620

Yang, Y. J., Kim, C. S., Choi, B. H., and Cha, H. J. (2015). Mechanically durable and biologically favorable protein hydrogel based on elastic silklike protein derived from sea anemone. *Biomacromolecules* 16, 3819–3826. doi: 10.1021/acs.biomac.5b01130

Zhang, D., Peng, H., Sun, B. C., and Lyu, S. S. (2017). High water content silk protein-based hydrogels with tunable elasticity fabricated via a ru(ii) mediated photochemical cross-linking method. *Fibers Polym.* 18, 1831–1840. doi: 10.1007/s12221-017-7463-6

Conflict of Interest: The authors declare that the research was conducted in the absence of any commercial or financial relationships that could be construed as a potential conflict of interest.

frontiers in Chemistry

ORIGINAL RESEARCH
published: 30 June 2020
doi: 10.3389/fchem.2020.00536

Influence of Network Topology on the Viscoelastic Properties of Dynamically Crosslinked Hydrogels

Emilia M. Grad[1,2], Isabell Tunn[1], Dion Voerman[3,4], Alberto S. de Léon[1†], Roel Hammink[3,4*] and Kerstin G. Blank[1,2*]*

[1] Mechano(bio) Chemistry, Max Planck Institute of Colloids and Interfaces, Potsdam, Germany, [2] Department of Molecular Materials, Institute for Molecules and Materials, Radboud University, Nijmegen, Netherlands, [3] Department of Tumor Immunology, Radboud Institute for Molecular Life Sciences, Radboud University Medical Center, Nijmegen, Netherlands, [4] Division of Immunotherapy, Oncode Institute, Radboud University Medical Center, Nijmegen, Netherlands

Biological materials combine stress relaxation and self-healing with non-linear stress-strain responses. These characteristic features are a direct result of hierarchical self-assembly, which often results in fiber-like architectures. Even though structural knowledge is rapidly increasing, it has remained a challenge to establish relationships between microscopic and macroscopic structure and function. Here, we focus on understanding how network topology determines the viscoelastic properties, i.e., stress relaxation, of biomimetic hydrogels. We have dynamically crosslinked two different synthetic polymers with one and the same crosslink. The first polymer, a polyisocyanopeptide (PIC), self-assembles into semi-flexible, fiber-like bundles, and thus displays stress-stiffening, similar to many biopolymer networks. The second polymer, 4-arm poly(ethylene glycol) (starPEG), serves as a reference network with well-characterized structural and viscoelastic properties. Using one and the same coiled coil crosslink allows us to decouple the effects of crosslink kinetics and network topology on the stress relaxation behavior of the resulting hydrogel networks. We show that the fiber-containing PIC network displays a relaxation time approximately two orders of magnitude slower than the starPEG network. This reveals that crosslink kinetics is not the only determinant for stress relaxation. Instead, we propose that the different network topologies determine the ability of elastically active network chains to relax stress. In the starPEG network, each elastically active chain contains exactly one crosslink. In the absence of entanglements, crosslink dissociation thus relaxes the entire chain. In contrast, each polymer is crosslinked to the fiber bundle in multiple positions in the PIC hydrogel. The dissociation of a single crosslink is thus not sufficient for chain relaxation. This suggests that tuning the number of crosslinks per elastically active chain in combination with crosslink kinetics is a powerful design principle for tuning stress relaxation in polymeric materials. The presence of a higher number of crosslinks per elastically active chain thus yields materials with a slow macroscopic relaxation time but fast dynamics at the microscopic level. Using this principle for the design of synthetic cell culture matrices will yield materials with excellent long-term stability combined with the ability to locally reorganize, thus facilitating cell motility, spreading, and growth.

Keywords: hydrogel, rheology, coiled coil, polyisocyanopeptide, polyethylene glycol, relaxation time, network topology, multivalency

OPEN ACCESS

Edited by:
Clemens Kilian Weiss, Fachhochschule Bingen, Germany

Reviewed by:
Artur J. M. Valente, University of Coimbra, Portugal
Asish Pal, Institute of Nano Science and Technology (INST), India

****Correspondence:***
Alberto S. de Léon
alberto.sanzdeleon@uca.es
Roel Hammink
roel.hammink@radboudUMC.nl
Kerstin G. Blank
kerstin.blank@mpikg.mpg.de

†Present address:
Alberto S. de Léon, Department of Materials Science, University of Cádiz, Cádiz, Spain

Specialty section:
This article was submitted to Polymer Chemistry, a section of the journal Frontiers in Chemistry

Received: *30 January 2020*
Accepted: *26 May 2020*
Published: *30 June 2020*

Citation:
Grad EM, Tunn I, Voerman D, de Léon AS, Hammink R and Blank KG (2020) Influence of Network Topology on the Viscoelastic Properties of Dynamically Crosslinked Hydrogels. Front. Chem. 8:536. doi: 10.3389/fchem.2020.00536

INTRODUCTION

Biological materials are increasingly serving as inspiration for the synthesis of smart and sustainable polymeric materials, both in engineering and biomedical application areas. Integrating the desired mechanical performance with (multi-)functionality, e.g., stimuli-responsiveness and self-healing, requires a detailed understanding of how molecular structure translates into material architecture and function. Key features of biological materials are their hierarchical structure, built up via the well-defined self-assembly of molecular building blocks (Kushner and Guan, 2011; Egan et al., 2015), as well as their viscoelastic behavior (Kollmannsberger and Fabry, 2011; Gralka and Kroy, 2015) combined with non-linear stress-strain responses (Storm et al., 2005; Kollmannsberger and Fabry, 2011; Gralka and Kroy, 2015). Focusing on materials with biomedical relevance, the cytoskeleton (actin, intermediate filaments, and microtubules) and the extracellular matrix (ECM; e.g., collagen and fibrin) of mammalian cells are well-studied examples of biological hydrogel networks that combine these properties (Storm et al., 2005; Kollmannsberger and Fabry, 2011; Gralka and Kroy, 2015). Protein building blocks of the cytoskeleton and the ECM self-assemble into semi-flexible fiber bundles. The largely entropic response of these bundles to stretching forces causes the network to become stiffer with increasing deformation (stress-stiffening) (Storm et al., 2005). At the same time, these networks contain non-covalent crosslinks (Claessens et al., 2006; Schmoller et al., 2008, 2009; Lin et al., 2010; Lieleg et al., 2011; Lansky et al., 2015). These dynamic crosslinks dissociate and re-associate and are thus responsible for stress relaxation and self-healing.

Understanding the interplay between the above-mentioned characteristics is key for determining the mechanical properties of cells and tissues as well as for the development of synthetic cell culture matrices that mimic the natural ECM. For example, it has been shown that both stress-stiffening (Das et al., 2016) and stress relaxation (McKinnon et al., 2014; Chaudhuri et al., 2015, 2016; Tang et al., 2018) are key factors affecting cell spreading and stem cell differentiation. It has remained a significant challenge, however, to systematically vary these parameters and to establish relationships between network topology and linear as well as non-linear viscoelastic properties. Considering natural biopolymer networks, the majority of studies have focused on reconstituted actin networks, crosslinked with different natural crosslinking proteins (Claessens et al., 2006; Schmoller et al., 2008, 2009; Lieleg et al., 2011) or synthetic crosslinking modules (Lorenz et al., 2018). These studies have shown that the crosslink properties (kinetics and stiffness) affect network topology, elastic modulus as well as stress relaxation and aging (Claessens et al., 2006; Schmoller et al., 2008, 2009; Lieleg et al., 2011; Strehle et al., 2011; Wei et al., 2016). Analogous studies aimed at understanding the effect of crosslink kinetics on viscoelastic material responses have been performed for a number of synthetic polymeric materials. Besides investigating the effect of the crosslink properties themselves (Yount et al., 2005; Shen et al., 2007; Appel et al., 2014; Rossow et al., 2014; Grindy et al., 2015; Tunn et al., 2018), these studies have focused on the contributions of network defects such as dangling ends and loops (Annable et al., 1993; Rossow et al., 2014; Ciarella et al., 2018), crosslink functionality (Li et al., 2016; Gu et al., 2018; Tunn et al., 2019), and polymer length (Annable et al., 1993; Tan et al., 2017). Even though a direct comparison is difficult due to the different polymers used, it can generally be concluded that the number of elastically active chains and their ability to relax after crosslink dissociation are key parameters that determine the macroscopic relaxation time of a material.

With the goal of gaining more detailed insights into how network topology affects stress relaxation of hydrogels, we have crosslinked two synthetic polymer networks possessing fundamentally different network architecture with one and the same crosslink and compared the stress relaxation behavior of the resulting networks. As the crosslink, we used a synthetic coiled coil (CC; **Figure 1**). CCs are self-assembled superhelical structures (Lupas, 1996; Woolfson, 2005) that occur naturally within many cytoskeleton and ECM proteins, where they are either part of the fibers themselves (e.g., intermediate filaments and fibrin) or are structural components of actin crosslinking proteins (e.g., myosin and α-actinin). CCs possess a so-called heptad repeat sequence, termed *abgdefg* (**Figure 1**). Hydrophobic amino acids usually occupy the *a* and *d* positions. In the folded superhelical structure, the hydrophobic side chains align on one face of the helix and constitute a hydrophobic core. The *e* and *g* positions are frequently filled with charged amino acids, which play an important role in defining helix orientation and oligomerization specificity. The solvent-exposed amino acids *b*, *c*, and *f* are more variable, while their helix propensity is an important factor contributing to overall CC stability. Synthetic CCs of controlled length and sequence have evolved into tunable protein-based building blocks for synthetic biology and materials science where they find application in protein origami structures (Fletcher et al., 2013; Ljubetič et al., 2017) and as crosslinks for polymeric materials (Petka et al., 1998; Wang et al., 1999; Yang et al., 2006; Shen et al., 2007; Dånmark et al., 2016; Tunn et al., 2018, 2019). Based on their natural abundance in biological materials and their generally established application as molecular building blocks, we consider CCs to be excellent tunable crosslinks for biomimetic material design.

One network to be crosslinked with these CC building blocks consists of water-soluble, semi-flexible polyisocyanopeptides (PICs) (Cornelissen et al., 2001; Kouwer et al., 2013). PICs are fully synthetic, helical polymers, known to self-assemble into fiber-like architectures with stress-stiffening properties. Each monomer is functionalized with a dialanyl peptide, which introduces a hydrogen bond network parallel to the helical axis. These hydrogen bonds stabilize the helical structure and also contribute to the stiffness of these polymers (van Buul et al., 2013) with persistence lengths $L_p > 10$ nm (Jaspers et al., 2016; Kouwer et al., 2018; Schoenmakers et al., 2018a). Each monomer further carries oligo(ethylene glycol) units that cause a phase transition when increasing the temperature above the lower critical solution temperature (LCST). Upon heating, the polymers become hydrophobic and start to bundle, thereby forming a physically crosslinked hydrogel network at very low concentrations (Kouwer et al., 2013; Jaspers et al., 2014; Vandaele et al., 2020). Stress-stiffening PIC networks thus have

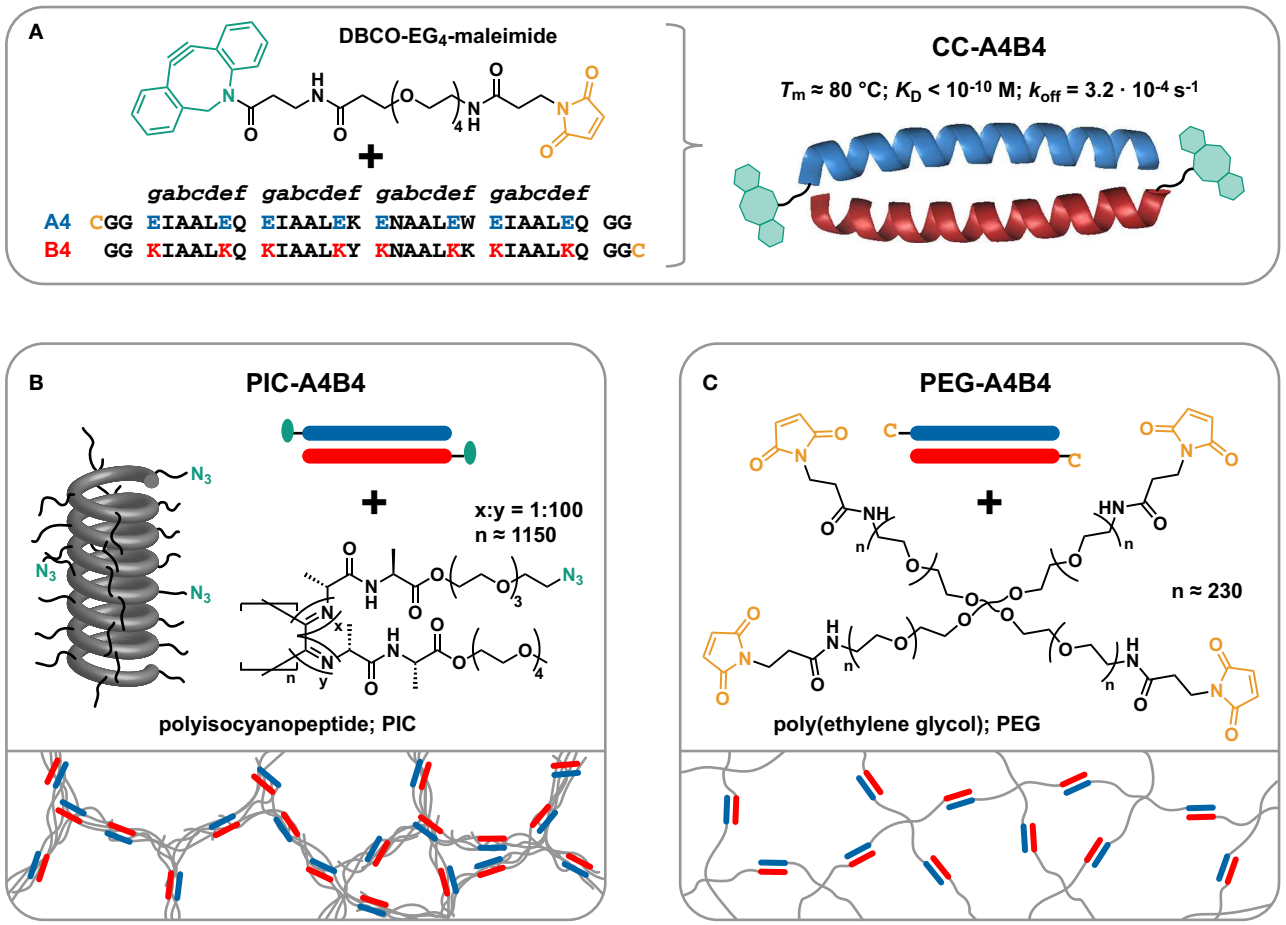

FIGURE 1 | Experimental design. **(A)** Functional groups utilized for coupling the coiled coils (CCs) to polyisocyanopeptide (PIC) and poly(ethylene glycol) (PEG) polymers. The CC-forming peptides A4 and B4 each carry a terminal cysteine (Cys; C) introduced during solid-phase peptide synthesis. The Cys is reacted with the heterobifunctional linker DBCO-EG_4-maleimide. **(B)** Synthesis of CC-crosslinked polyisocyanopeptide hydrogels (PIC-A4B4). The DBCO-functionalized CCs are reacted with the PIC polymers that carry azide groups with an average spacing of 11.5 nm. **(C)** Synthesis of CC-crosslinked poly(ethylene glycol) hydrogels (PEG-A4B4). The Cys-terminated CCs are directly reacted with maleimide-functionalized 4-arm PEG (starPEG; MW = 40 kDa).

the potential to serve as synthetic mimics of the cytoskeleton (Jaspers et al., 2017) and the ECM (Das et al., 2016), both for fundamental studies and for cell culture applications.

To fully utilize the potential of PIC hydrogels as cytoskeleton and ECM mimics, several types of crosslinks have previously been introduced into PIC networks. These include short double-stranded DNA oligonucleotides (Deshpande et al., 2016) and stimuli-responsive DNA motifs (Deshpande et al., 2017) as well as self-assembled virus capsids (Schoenmakers et al., 2018b) and covalent triazole crosslinks (Schoenmakers et al., 2018a). In the majority of these studies, the focus was placed on understanding the effect of these crosslinks on the non-linear stress-stiffening response. The CC-crosslinked PIC hydrogel (PIC-A4B4; **Figure 1**) developed here is utilized for investigating the relationship between the PIC network properties and stress relaxation. Most importantly, we compare the viscoelastic properties of these CC-crosslinked PIC networks with a well-characterized reference network, based on terminally crosslinked 4-arm poly(ethylene glycol) (PEG-A4B4; **Figure 1**; Sakai et al., 2008; Lange et al., 2011; Asai et al., 2012; Akagi et al., 2013; Grindy et al., 2015; Tunn et al., 2018). Our results show that the relaxation time assigned to CC dissociation varies between the two networks and is longer for the PIC-A4B4 network. This demonstrates that the macroscopic network relaxation time is not determined by the kinetics of the crosslinks alone. It also depends on the network topology and thus the ability of elastically active network chains to relax after crosslink dissociation. We attribute the slower relaxation of PIC-A4B4 networks to the close proximity of multiple crosslinks along the same elastically active chain, so that the dissociation of one crosslink does not necessarily relax the entire chain. Such multivalency effects thus have to be considered when designing polymeric networks with a controlled relaxation time.

MATERIALS AND METHODS

Synthesis and Characterization of Azide-Functionalized PIC Polymers

The isocyanopeptide monomers IC-AA-$(EG)_4$-OMe and IC-AA-$(EG)_3$-N_3 were synthesized according to Mandal et al. (2013). For the synthesis of azide-functionalized polymers, azide- and methoxy-terminated monomers were mixed in a 1:100 ratio (total concentration of 50 mg ml^{-1} in toluene). The $(Ni(ClO_4)_2)\bullet 6H_2O$ catalyst was dissolved in a 9:1 mixture of toluene and absolute ethanol. The pre-dissolved catalyst was added to the monomer mixture in a catalyst:monomer ratio of 1:10,000. The mixture was stirred for 2–3 days and precipitated in di-isopropyl ether (3x), resulting in an off-white solid. The polymer was analyzed with viscometry as described (Mandal et al., 2013). The average molecular weight of the polymer as determined from its viscosity is 412 kg mol^{-1}.

Synthesis of A4B4-Crosslinked PIC Hydrogels

The CC-forming peptides A4 and B4 were obtained from Pepscan (Lelystad, The Netherlands) and Proteogenix (Schiltigheim, France) in a purity >95% and with trifluoroacetic acid (TFA) counter ions. For bioconjugation, the A4 peptide carries a cysteine residue at its N-terminus while the cysteine is located at the C-terminus for B4. For both peptides, the N-terminus was amidated and the C-terminus was acetylated. Equimolar amounts of A4 and B4 (1 mM each) were dissolved in phosphate buffered saline (PBS; 10 mM Na_2HPO_4/1.8 mM KH_2PO_4 pH 7.4, 137 mM NaCl, 2.7 mM KCl) to allow CC formation. The heterobifunctional crosslinker DBCO-PEG_4-maleimide (DBCO: dibenzocyclooctyne; Jena Bioscience, Jena, Germany) was dissolved in DMSO to a concentration of 100 mM. It was added to the CC-A4B4 solution to a final concentration of 2 mM to yield a 1:1 Cys:maleimide ratio. The solution was incubated for 1 h at 4°C and 700 rpm. Functionalization of CC-A4B4 with the crosslinker was confirmed with MALDI-TOF. A desalted sample was mixed with the matrix α-cyano-4-hydroxycinnamic acid and analyzed in linear-positive mode (**Supplementary Figure 1**).

For hydrogel synthesis, the azide-functionalized PIC polymer was dissolved to a concentration of 2.5 mg ml^{-1} in PBS while incubating the sample at 4°C for 48 h. The polymer solution was mixed with the DBCO-functionalized CC-A4B4 to obtain a 1:1 ratio of azide:DBCO (0.185 mM each; 2 mg ml^{-1} PIC). During this preparation process, all components and the freshly prepared mixture were kept on ice. The mixture was immediately loaded onto the rheometer (plate pre-cooled to 7°C) and gelation was allowed to occur in the rheometer after the gap size was adjusted.

Synthesis of A4B4-Crosslinked PEG Hydrogels

The CC-forming peptides A4 and B4 were each dissolved to a concentration of 4 mM in PBS. Star-shaped 4-arm poly(ethylene glycol) (starPEG) with terminal maleimide groups (40 kDa, polydispersity index = 1.02; JenKem Technology USA, Plano, TX, USA) was dissolved to a concentration of 1 mM in PBS. The peptides A4 and B4 were mixed in a 1:1 ratio (25 μl each) to allow for CC formation. Immediately after, the starPEG solution was added to obtain a 1:1 Cys:maleimide ratio (50 μl). This yields a final concentration of 0.5 mM starPEG and a total peptide concentration of 2 mM. The reaction mixture was incubated for 15 min at 800 rpm at room temperature. After this incubation time, the sample was thoroughly mixed by pipetting up and down several times to form a homogeneous PEG-A4B4 hydrogel. In order to remove entrapped air bubbles, the hydrogel was centrifuged for 2 min at 2,000 g.

Rheology of PIC Hydrogels

All measurements were performed with a stress-controlled rheometer (MCR-302, Anton Paar, Ostfildern, Germany), using parallel-plate geometry (diameter 25 mm, stainless steel). The initial gap was adjusted to 200 μm, while controlling the normal force (0 N ± 0.1 N). Silicone oil (Sigma-Aldrich 378364, viscosity 100 cSt @ 25°C) was used to prevent sample evaporation. In general, CC-A4B4 crosslinked PIC samples (PIC-A4B4) were subjected to different temperature protocols: (1) 7°C → 55°C (rate = 1°C min^{-1}), T = 55°C constant for 90 min; (2) 7°C → 55°C (rate = 1°C min^{-1}), T = 55°C constant for 90 min, 55°C → 20°C (rate = 1°C min^{-1}), T = 20°C constant for ≥10 min; (3) 7°C → 20°C (rate = 1°C min^{-1}), T = 20°C constant for 10 h. In addition, a PIC sample without CC-A4B4 crosslinks (PIC-0) was subjected to the same protocols.

The linear viscoelastic properties (storage modulus G' and loss modulus G'') were recorded during each respective temperature protocol. The measurements were carried out at a strain amplitude γ of 1% and a frequency f of 1.6 s^{-1} (angular frequency $\omega = 10$ rad s^{-1}). The temperature protocol was followed by either an amplitude or frequency sweep. For the amplitude sweeps, f was set to 1.6 s^{-1} while γ was varied from 1 to 1,000%. For the frequency sweeps, γ was 1% and f was varied from 10 to 0.0001 s^{-1}. Each experiment was performed in triplicate. One data set is shown in the main text while the two additional data sets are presented in the **Supplementary Material**.

To investigate the non-linear viscoelastic properties of the different samples, a pre-stress protocol was performed as originally introduced and validated for dynamically crosslinked biopolymer networks by Broedersz et al. (2010). It was subsequently adapted to PIC hydrogels by Kouwer et al. (2013). Each pre-stress experiment directly followed one of the different temperature protocols (1, 2, or 3). As part of the pre-stress protocol, the samples were subjected to a constant pre-stress (σ) in the range from 0.5 to 600 Pa while a small oscillatory stress was applied in addition ($\delta\sigma$). In all cases, the amplitude of the oscillatory stress was <10% of the pre-set constant pre-stress (see **Supplementary Material** for details). At a given pre-stress, a frequency sweep was performed (0.1–10 s^{-1}) to validate that the material response is frequency independent. Subsequently, the resulting oscillatory strain ($\delta\gamma$) was determined at a frequency of 1 s^{-1}. The differential modulus K' ($\delta\sigma/\delta\gamma$) was determined from the applied oscillatory stress ($\delta\sigma$) and the measured strain ($\delta\gamma$) values. The resulting K' values were normalized to the plateau modulus G_0, which was obtained from averaging the storage modulus G' measured at the pre-stress values of 1,

1.2, and 1.5 Pa (linear viscoelastic range). K'/G_0 was plotted against the applied constant pre-stress σ. The critical stress (σ_c) was obtained from this plot and corresponds to the value of σ where K' is not constant anymore. Each experiment was performed in duplicate or triplicate. One data set is shown in the main text while the additional data sets are presented in the **Supplementary Material**.

Rheology of PEG Hydrogels

The PEG-A4B4 hydrogel was characterized using a 12 mm cone-plate geometry (gap 20 μm, stainless steel). First, an amplitude sweep was performed at 20°C. The strain amplitude γ was varied from 1 to 1,000% at a constant frequency f of 1.6 s^{-1}. Second, frequency sweeps were performed using $\gamma = 10\%$ while f ranged from 15.9 to 0.0006 s^{-1}. Frequency sweeps were carried out at different temperatures (20–55°C in steps of 5°C). A new sample was used for every frequency sweep. The experiment at 55°C was performed in triplicate. One data set is shown in the main text while the two additional data sets are presented in the **Supplementary Material**. To validate that the viscoelastic properties of the hydrogels are not affected by the measurement geometry, a control experiment was further performed with a 12 mm plate-plate geometry (gap 200 μm; see **Supplementary Material**).

Detection of Hydrophobic Bundling With Nile Red

The binding of Nile Red to hydrophobic PIC bundles was determined for PIC-0 and PIC-A4B4. Nile Red (Thermo Fisher Scientific) was dissolved in DMSO to a concentration of 1 mg ml^{-1}. For each hydrogel, two samples were prepared in PBS as described above. Nile Red was added to one sample (final concentration 10 μg ml^{-1}) while the second sample served as a reference. Subsequently, all samples were incubated over night at ∼4°C to allow complete mixing of dye and polymer. The pre-incubated samples where then subjected to a heating protocol while measuring the fluorescence intensity of Nile Red. The measurement was performed in a temperature-controlled microplate reader (Cytation5, BioTek Instruments, Inc., Winooski, VT, USA) using glass-bottom 96-well plates (SensoPlate, Greiner Bio-One, Frickenhausen, Germany). The sample was initially kept at 30°C and subsequently heated to 55°C. Following 45 min incubation at 55°C, the sample was again cooled down to 30°C. At each temperature, the fluorescence intensity was recorded. The samples were excited at 540 nm (15 nm slit width) and fluorescence emission was measured from 580 to 700 nm (15 nm slit width). Each sample was measured in triplicate and the average was taken for data analysis. The measured intensity of the reference samples was subtracted from the values measured for the Nile Red containing samples. The intensity at 655 nm (emission maximum of Nile Red) was used to compare Nile Red fluorescence at different temperatures. For this comparison, the intensity was further normalized to the initial intensity measured at 30°C.

RESULTS AND DISCUSSION

Design and Synthesis of Coiled Coil-Crosslinked PIC and PEG Networks

With the goal of investigating the influence of network topology on the relaxation time of dynamically crosslinked hydrogel networks, PIC and starPEG were crosslinked with a well-characterized CC to form the hydrogels PIC-A4B4 and PEG-A4B4 (**Figure 1**). The CC-forming peptides A4 and B4 self-assemble into a parallel 4-heptad heterodimer with high thermodynamic and kinetic stability (**Figure 1A**). The melting temperature T_m and equilibrium dissociation constant K_D have been obtained from thermal unfolding experiments performed with circular dichroism spectroscopy. These experiments yielded $T_m = 81°C$ and $K_D < 1.0 \cdot 10^{-10}$ M at 20°C (Thomas et al., 2013). T_m remains unaffected upon conjugation to PEG (Goktas et al., 2018). Using atomic force microscopy-based single-molecule force spectroscopy, the dissociation rate k_{off} was determined to be $3.2 \cdot 10^{-4}$ s^{-1} at 25°C (Goktas et al., 2018). The individual CC-forming peptides are not folded, while the CC itself is a highly rigid superhelix (Wolgemuth and Sun, 2006). The CC was functionalized with a cysteine residue at the N-terminus of A4 and at the C-terminus of B4 to allow covalent coupling to PIC and starPEG polymers (**Figure 1**).

For the synthesis of PIC hydrogels, tetra(ethylene glycol) functionalized monomers were used. These polymers possess a gelation temperature (T_{gel} = LCST) of ∼39°C in PBS (Deshpande et al., 2016), which is well below the T_m of CC-A4B4. A fraction of monomers (1:100) was equipped with a terminal azide functional group to allow peptide coupling via a heterobifunctional DBCO-EG_4-maleimide crosslinker (**Figure 1B**). The average spacing between azide functional groups can be calculated based on the known structure of polyisocyanide polymers, which is a 4_1 helix with a pitch of 0.46 nm (Cornelissen et al., 2001). The axial distance between two monomers is thus 0.115 nm. Considering that 1% of monomers carry an azide functional group, this results in an average azide spacing of ∼11.5 nm. The azide-functionalized polymer is termed PIC-0 and serves as a control for all rheology experiments.

For the synthesis of CC-crosslinked PIC-A4B4 hydrogels, an equimolar amount of the CC-forming peptides was mixed to allow CC formation. The folded CC was subsequently reacted with DBCO-EG_4-maleimide in a 1:1 thiol:maleimide ratio. The yield of this reaction was estimated to be 90% using MALDI-TOF (**Supplementary Figure 1**). Subsequently, the DBCO-functionalized CC was added to the azide-containing PIC to allow CC-mediated crosslinking via a strain-promoted azide-alkyne cycloaddition reaction (N_3:DBCO = 1:1). The yield of this reaction was previously quantified for a similar system (PIC crosslinked with DNA) and was determined to be 90% (Deshpande et al., 2016). Considering the yield of both reactions, it can be assumed that ∼80% of CC-forming peptides are coupled to the PIC polymer. This ultimately results in an average spacing of CC-forming peptides of ∼14 nm, which is similar to the L_p of closely related tri(ethylene glycol) functionalized PIC polymers (12–30 nm) (Jaspers et al., 2016; Kouwer et al., 2018; Schoenmakers et al., 2018a). It can thus be assumed that the L_p

and the distance between crosslinks is on a similar length scale. The progress of the conjugation reaction was further followed with rheology, recording the evolution of the storage modulus G' as a function of time. Performing this experiment below the LCST ensures that the crosslinking of individual polymers is monitored and that hydrophobically stabilized bundles are absent. The observed increase in G' indicates that a network is indeed formed as a result of the CC-mediated crosslinking reaction (**Supplementary Figure 2**).

Maleimide-functionalized starPEG was used for the synthesis of the terminally crosslinked starPEG reference network (PEG-A4B4). This allowed for the direct conjugation of thiol-containing CCs to the maleimide-functionalized starPEG without the need of the heterobifunctional DBCO-PEG$_4$-maleimide crosslinker (**Figure 1C**). For crosslinking the starPEG network, we also employed pre-assembled CCs to utilize the same synthetic strategy as used for the PIC-A4B4 networks. The starPEG concentration used was close to the critical overlap concentration where the resulting hydrogels possess a very small number of entanglements (Asai et al., 2012; Akagi et al., 2013). In terminally crosslinked starPEG hydrogels, the distance between crosslinks is defined by the size of each PEG chain, characterized by a polydispersity index of 1.02. This is a key difference to the PIC-A4B4 networks, where the distance between crosslinks is distributed around an average value that is determined by the density of azide functional groups and the yield of the coupling reaction.

Bundle Formation and Network Topology of Coiled Coil-Crosslinked PIC Networks

Before comparing the stress relaxation behavior of PIC-A4B4 and PEG-A4B4 hydrogels, we first investigated the contributions of CC-crosslinking and hydrophobic bundling to the overall network properties of PIC-A4B4. We mixed DBCO-functionalized CC-A4B4 and PIC, transferred the sample to the rheometer, immediately heated from 7 to 55°C and incubated the sample at 55°C while recording the storage modulus G'. Upon heating, CC-crosslinking and bundle formation are expected to occur simultaneously. The sample was subsequently re-cooled to 20°C and its properties were compared to a control sample without CC crosslinks (PIC-0). In addition, the properties of re-cooled PIC-A4B4 were compared to a sample never heated to 55°C but incubated at 20°C for an extended period of time (10 h) (**Supplementary Figure 2**).

When gradually heating the PIC-A4B4 and PIC-0 samples from 7 to 55°C, G' was higher for the PIC-A4B4 samples already at the start of the recording (**Figure 2**). This suggests that first CC crosslinks have already formed between individual polymers while the sample was maintained at 7°C. Upon heating, G' increased and hydrophobic bundles appeared in both samples, as visualized using the fluorophore Nile Red (**Supplementary Table 1**). Nile Red responds to hydrophobic environments with enhanced fluorescence emission and is thus a versatile reporter for bundle formation. The LCST transition appears to be broader for PIC-A4B4 than for PIC-0, suggesting that CC-crosslinks may interfere with the tight packing of PIC polymers in the bundles. This is confirmed when comparing the increase in Nile Red fluorescence for the PIC-A4B4 and PIC-0 samples. While Nile Red fluorescence increased almost 10-fold for PIC-0 only a 6-fold increase was observed for PIC-A4B4. When maintaining the samples at a constant temperature of 55°C, a plateau in G' was reached. The G' plateau was higher for PIC-A4B4 (440–460 Pa; **Figure 2A**) than for PIC-0 (240-250 Pa; **Figure 2B**). This provides first evidence that CC crosslinks are present in hydrophobically bundled PIC networks at 55°C and that these crosslinks contribute to the overall viscoelastic properties of these networks. When re-cooling both samples below the LCST, Nile Red fluorescence decreased to the starting value. This clearly shows that no hydrophobic bundles remain at temperatures below the LCST. At 20°C, the PIC-0 sample was a solution with very low G'. In contrast, G' increased upon cooling for the PIC-A4B4 sample (**Figure 2**).

This increase in G' is unexpected and has further not been observed for any other crosslinked PIC network (Deshpande et al., 2016, 2017; Schoenmakers et al., 2018a,b). As the L_p of individual PIC polymers decreases with lowering the temperature, a decrease in G' is expected for bundled PIC networks as long as the network structure is not altered (Kouwer et al., 2013). One possible explanation for the observed increase in G' is that the thermodynamic stability of the CC crosslinks increases while the sample is being cooled. Additional CC crosslinks thus form and stabilize the bundles. This does not explain the behavior of the PIC-A4B4 network at temperatures below the LCST, however, where the bundled network structure is no longer held together via hydrophobic interactions. We propose that the presence of CC crosslinks kinetically traps the polymers in the bundled state even though the polymers have become hydrophilic. At temperatures below the LCST, k_{off} of the CC crosslinks is low ($t_{1/2}$ = 35 min at 25°C) so that the trapped bundle structures remain for extended periods of time and reorganize only slowly. This is supported by the evolution of G' during repeated heating-cooling cycles (**Supplementary Figure 3**). Once the re-cooled sample is kept at 20°C, G' starts to decrease continuously. Moreover, G' decreases faster when a new heating cycle is started (i.e., k_{off} increases with temperature). Once the LCST is reached, hydrophobic bundles appear again and G' starts to increase. It is likely that prolonged incubation at 20°C yields the same final network structure and viscoelastic properties as a sample that was never subjected to any heating-cooling cycle (**Supplementary Figure 2**). It should be noted that internal stress may accumulate in trapped bundle structures, which may further contribute to the increase in G' upon cooling. Internal stress is also relaxed via crosslink dissociation as has been observed for actin networks polymerized in the presence of the crosslinking protein fascin (Lieleg et al., 2011).

At this moment, we can only speculate about the structure of the network equilibrated at 20°C. Considering the properties of individual polymers, the estimated distance between CCs is ∼14 nm. This is on the same length scale as the L_p determined for closely related tri(ethylene glycol) functionalized PIC polymers (12–30 nm) (Jaspers et al., 2016; Kouwer et al., 2018; Schoenmakers et al., 2018a). As a result of their increased

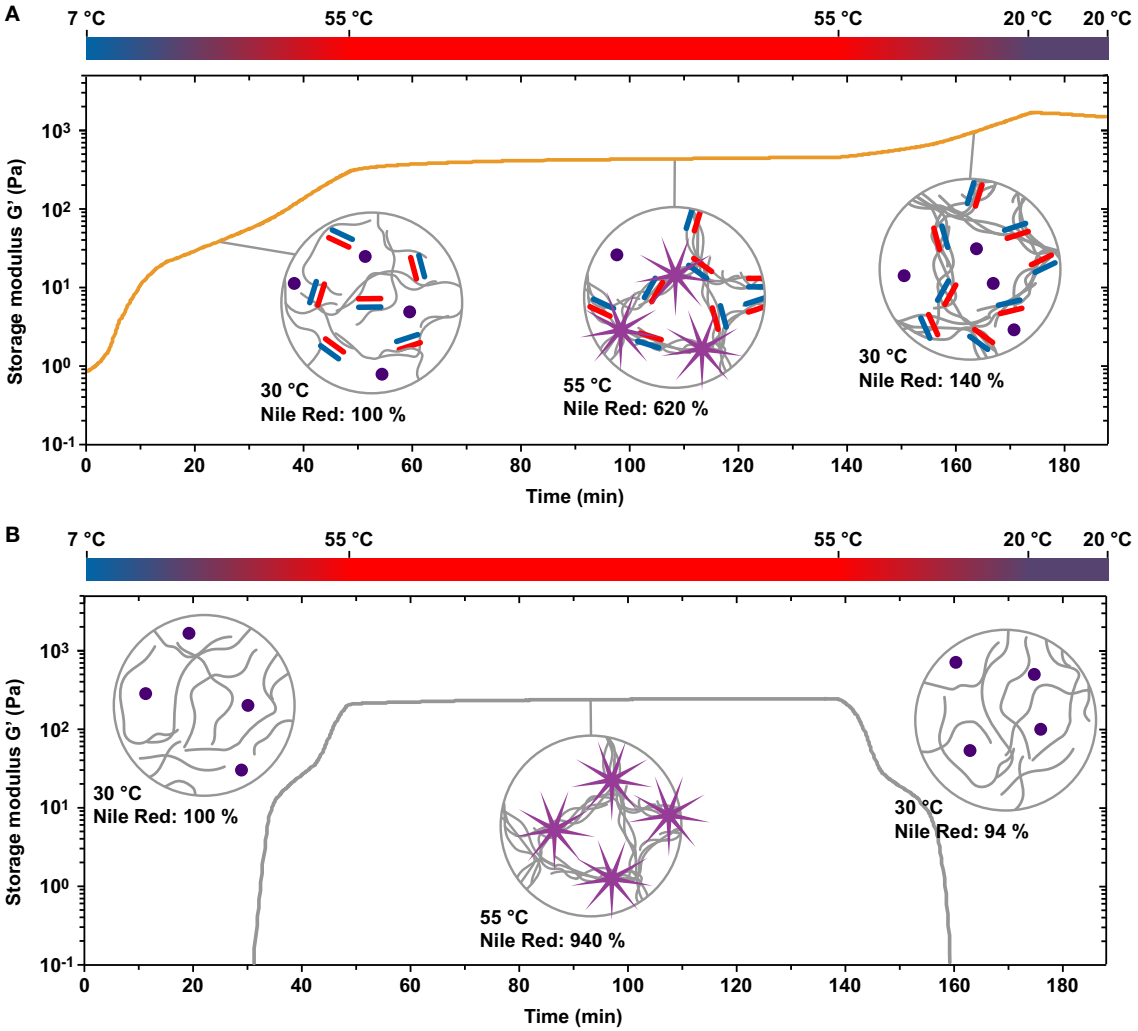

FIGURE 2 | Temperature-induced hydrophobic bundle formation and gelation of PIC-A4B4 and PIC-0 hydrogels. **(A)** Evolution of the storage modulus G' as a function of time when subjecting PIC-A4B4 to temperature protocol 2 (7°C → 55°C → 20°C). **(B)** Evolution of the storage modulus G' as a function of time when subjecting PIC-0 to temperature protocol 2. The measurements were performed with a strain amplitude of 1% and a frequency of 1.6 s^{-1}. Hydrophobic bundle formation was visualized in a temperature-controlled microplate reader using the fluorophore Nile Red, which is known to increase in intensity in hydrophobic environments. The intensity (measured at λ_{ex} = 540 nm and λ_{em} = 655 nm) was normalized to the state of the sample at a temperature of 30°C during the initial heating step.

bulkiness, we expect L_p to be larger for our tetra(ethylene glycol) functionalized polymers. The average distance between crosslinks is thus expected to be at least similar to—and possibly shorter than—the L_p of individual PIC polymers. Crosslinking may thus cause the partial alignment of PIC polymers into bundle-like structures even at temperatures below the LCST. When comparing G' of the PIC-A4B4 networks, G' is clearly lower for networks equilibrated at 20°C (62 Pa after 10 h of incubation; **Supplementary Figure 2**) than for hydrophobically bundled networks at 55°C (440–460 Pa; **Figure 2A**). CC-crosslinking alone is thus not sufficient to obtain a fully bundled network. The network structure is most likely heterogeneous and consists of a mixture of CC-crosslinked bundles and individual polymers.

Stress-Stiffening Properties of Coiled Coil-Crosslinked PIC Networks

Subjecting the PIC-A4B4 sample to different temperature protocols has shown that the resulting network topology is different when the sample is maintained at temperatures below or above the LCST. In addition, a kinetically trapped bundle structure exists after the sample has been subjected to a heating-cooling cycle. PIC hydrogels are known to display stress-stiffening, which directly results from the presence of bundled, semi-flexible fiber structures. To gain insight into the effect of different network topologies on these non-linear viscoelastic properties, we determined the stress-stiffening response with rheology. We used an established pre-stress protocol where a small amplitude oscillatory stress is applied to the sample in

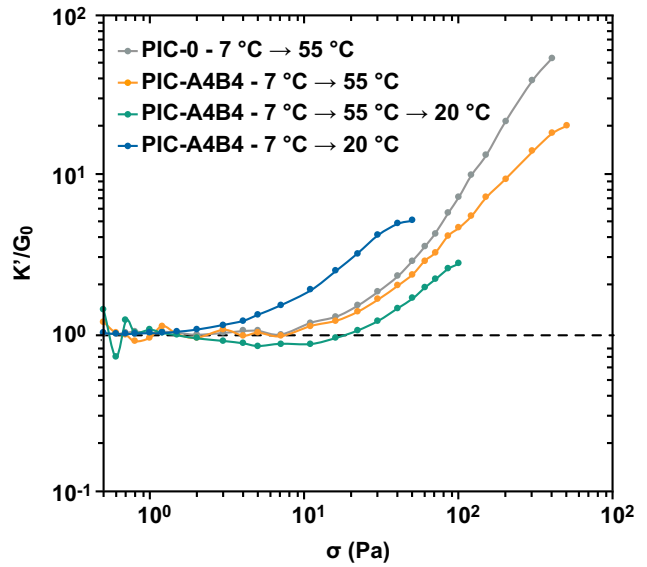

FIGURE 3 | Stress-stiffening of PIC hydrogels. The PIC-A4B4 and PIC-0 samples (pre-treated with the respective temperature protocol) were subjected to a defined pre-stress σ and the normalized differential modulus K'/G_0 was determined. The measurement was performed in triplicate. The additional data sets are shown in **Supplementary Figure 4** and **Supplementary Tables 3–6**. Lines are drawn to guide the eye.

TABLE 1 | Summary of parameters describing the properties of PIC-A4B4 and PIC-0 hydrogels.

Sample	PIC-0	PIC-A4B4	PIC-A4B4	PIC-A4B4
Preparation	Protocol 1: 7°C → 55°C 55°C constant	Protocol 1: 7°C → 55°C 55°C constant	Protocol 2: 7°C → 55°C 55°C constant 55°C → 20°C 20°C constant	Protocol 3: 7°C → 20°C 20°C constant
Crosslinks	Bundling	CC + bundling	CC	CC
G_0 (Pa)	242 ± 18	265 ± 28	711 ± 182	69 ± 4
Stiffening index m	1.42 ± 0.03	1.01 ± 0.04	0.71 ± 0.05	0.68 ± 0.08
Critical stress σ_c (Pa)	24.0 ± 1.3	17.9 ± 1.7	44.6 ± 11.6	4.1 ± 0.6
Critical strain γ_c (%)	10	6.8	6.3	5.9

The values represent the mean of 3 independent experiments ± the standard error of the mean (SEM).

the presence of a constant pre-stress. Performing a series of such measurements, the pre-stress is gradually increased. We measured the oscillatory strain response at a specific frequency (1 s^{-1}). This method is gentle to the sample and recommended for studying transient material responses in the non-linear regime (Broedersz et al., 2010; Kouwer et al., 2013). It provides the normalized differential modulus (K'/G_0; see Materials and Methods for details) as a function of the applied pre-stress (**Figure 3**). Two characteristic parameters can be extracted from this data to describe the stress-stiffening response. These are the slope or stiffening index m, which describes the intensity of the material response to the applied stress, and the critical stress σ_c. The latter provides the stress value where the non-linear response sets in and thus describes the mechanosensitivity of the material.

Before starting the pre-stress protocol, the PIC-A4B4 sample was subjected to 3 different temperature protocols to obtain the above-mentioned network topologies: protocol 1 (7°C → 55°C) yields hydrophobically bundled networks stabilized by additional CC crosslinks; protocol 2 (7°C → 55°C → 20°C) results in kinetically trapped bundles that lack hydrophobic interactions; protocol 3 (7°C → 20°C) yields the equilibrium structure solely formed via CC-crosslinking. In addition, a PIC-0 sample subjected to protocol 1 was used as a control to determine the stress-stiffening response in the absence of CC crosslinks.

The PIC-A4B4 and PIC-0 samples measured in the presence of hydrophobically stabilized bundles (55°C) show a highly similar stress-stiffening response (**Figure 3** and **Supplementary Figure 4**). The only difference is a reduced slope/stiffening index (**Table 1**), which becomes more and more apparent with increasing pre-stress. A similar reduction in slope was observed for PIC networks crosslinked with virus capsids (Schoenmakers et al., 2018b). We conclude that the difference in stiffening index for PIC-A4B4 and PIC-0 originates from the rupture of CC crosslinks, while the overall stress-stiffening response of the hydrogel is determined by the hydrophobically bundled PIC network.

The PIC-A4B4 samples subjected to protocols 2 or 3 show a stress-stiffening response in the absence of hydrophobically stabilized bundles; however, with a lower stiffening index (**Figure 3**, **Supplementary Figure 4**, **Table 1**, and **Supplementary Tables 7–9**). This confirms that these samples contain semi-flexible structures, but to a smaller extent. While the stiffening indices for the two samples are highly similar, a clear difference is observed for σ_c (4.1 Pa for the equilibrated sample and 44.6 Pa for the sample containing kinetically trapped bundles). This is a direct result of the different temperature histories of these samples. The sample containing kinetically trapped bundles displays a plateau modulus G_0 of 711 Pa at the start of the pre-stress protocol. In contrast, G_0 is only 69 Pa for the sample equilibrated at 20°C. The observed difference in σ_c can be directly related to the critical strain γ_c using Hooke's Law: $G_0 = \sigma_c/\gamma_c$. This relationship was used before to explain the stress-stiffening behavior of different PIC networks (Jaspers et al., 2014). Knowing G_0 and σ_c, we can thus calculate γ_c, which is ∼6% for both samples. This clearly shows that the non-linear response of these networks, which are stabilized by CC crosslinks only, sets in at the same applied strain and is determined by the CC-crosslinked network structure.

Material Failure of Coiled Coil-Crosslinked PIC Hydrogels

The non-linear rheology experiments described above suggest that material failure is determined by the interactions that stabilize the network. If hydrophobically stabilized bundles are present, they dominate the material response and the respective materials fail at a higher stress than samples that contain CC crosslinks only (**Figure 3**). This suggests that the CC crosslinks break before the hydrophobically stabilized bundles disintegrate,

as indicated by the different stiffening index for PIC-0 and PIC-A4B4 networks measured above the LCST. To confirm this result, we performed amplitude sweeps with the goal of determining the linear viscoelastic range (**Figure 4** and **Supplementary Figure 5**). Again, we observed that the PIC-A4B4 sample measured above the LCST possessed similar properties as the PIC-0 sample (**Figure 4A**). Also in this experiment, the PIC-A4B4 containing hydrophobically stabilized bundles (55°C) tolerated larger deformation than the PIC-A4B4 hydrogels only stabilized by CC crosslinks (20°C) (**Figure 4B**). It is interesting to note that the equilibrated PIC-A4B4 sample and the kinetically trapped sample fail in a highly similar strain range, even though their G_0 differs ∼10-fold. This may suggest that the force propagates through the network via individual polymer chains and that the spatial organization of elastically active crosslinks is similar in both hydrogels. Lacking structural information about these networks, however, it is impossible to derive any further conclusions about their failure mechanism.

Stress Relaxation in Coiled Coil-Crosslinked PIC and PEG Hydrogels

For the following analysis of stress relaxation, we thus primarily focus on measurements above the LCST (55°C), where the structure of the PIC-A4B4 network is well-defined and contains hydrophobically stabilized bundles as well as CC crosslinks. To obtain information about the importance of network topology for stress relaxation, we compare the PIC-A4B4 hydrogel to terminally crosslinked starPEG, which serves as a well-characterized reference network. The frequency sweeps were performed at 55°C (**Figure 5** and **Supplementary Figures 6, 8**). For the PIC-A4B4 and PIC-0 hydrogels, all frequency sweeps were performed at a strain amplitude of 1%, while a strain amplitude of 10% was used for the PEG-A4B4 hydrogels. Both strain amplitudes lie in the linear viscoelastic range as determined from amplitude sweeps (**Supplementary Figures 5, 8**).

When comparing the viscoelastic properties of PIC-A4B4 with PIC-0, two key differences are observed. For PIC-A4B4, G' is increased at high frequencies when compared to low frequencies. In contrast, G' is almost constant for PIC-0 over the entire frequency range tested (**Figure 5A** and **Supplementary Figure 7**). For PIC-A4B4, a local maximum in the loss modulus G'' is further observed at a frequency of ∼0.1 s^{-1}, while this maximum is absent in the PIC-0 sample. Interestingly, the position of the local maximum coincides with the mentioned increase in G' (**Figure 5A**).

A comparison with PEG-A4B4 provides more detailed insights into the origin of these features. We have shown earlier that the viscoelastic properties of CC-crosslinked starPEG networks are well-described with the Maxwell model (Tunn et al., 2018, 2019). These networks show a crossover between G' and G'' at a characteristic frequency f_{max}. This frequency correlates with the kinetic properties of the crosslinks (Grindy et al., 2015; Tunn et al., 2018). At frequencies smaller f_{max}, $G'' > G'$ and the material behaves like a viscous liquid. At frequencies larger f_{max}, $G'' < G'$ and the material behaves like an elastic solid (**Figure 5B**). f_{max} is directly related to the relaxation time τ of the material via $\tau = 1/f_{max}$. In other words, the CC crosslinks only contribute to the stability of the network at high frequencies where their kinetics is slower than the timescale of the applied oscillation. We thus assign the local maximum observed for PIC-A4B4 to the dissipative contribution of the CC crosslinks even though no crossover between G' and G'' is observed. The macroscopic relaxation behavior is still largely determined by the properties of the PIC network even though the presence of CC crosslinks increases the stiffness of the material by 60% at the highest frequency tested (**Supplementary Table 10**).

Further proof for this interpretation was obtained from frequency sweeps performed over a range of temperatures from 55 to 20°C (**Figures 5C,D**). For both PIC-A4B4 and PEG-A4B4, a shift of the G'' maximum to lower frequencies is observed. This is expected as the crosslink kinetics becomes

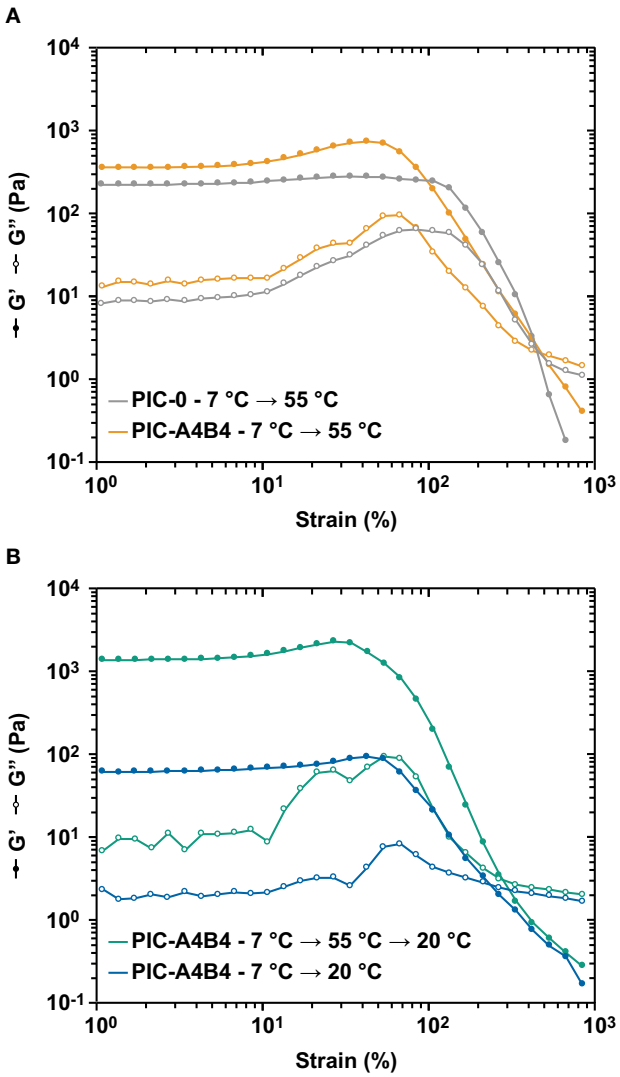

FIGURE 4 | Amplitude sweeps of PIC. **(A)** Comparison of PIC-A4B4 and PIC-0 measured above the LCST at 55°C. **(B)** Comparison of the PIC-A4B4 sample equilibrated at 20°C and the PIC-A4B4 sample with trapped bundles, measured at 20°C. Each amplitude sweep was performed at a constant frequency of 1.6 s^{-1} while the strain amplitude γ was varied from 1 to 1,000%. Each measurement was performed in triplicate. The additional data sets are shown in **Supplementary Figure 5**. Lines are drawn to guide the eye.

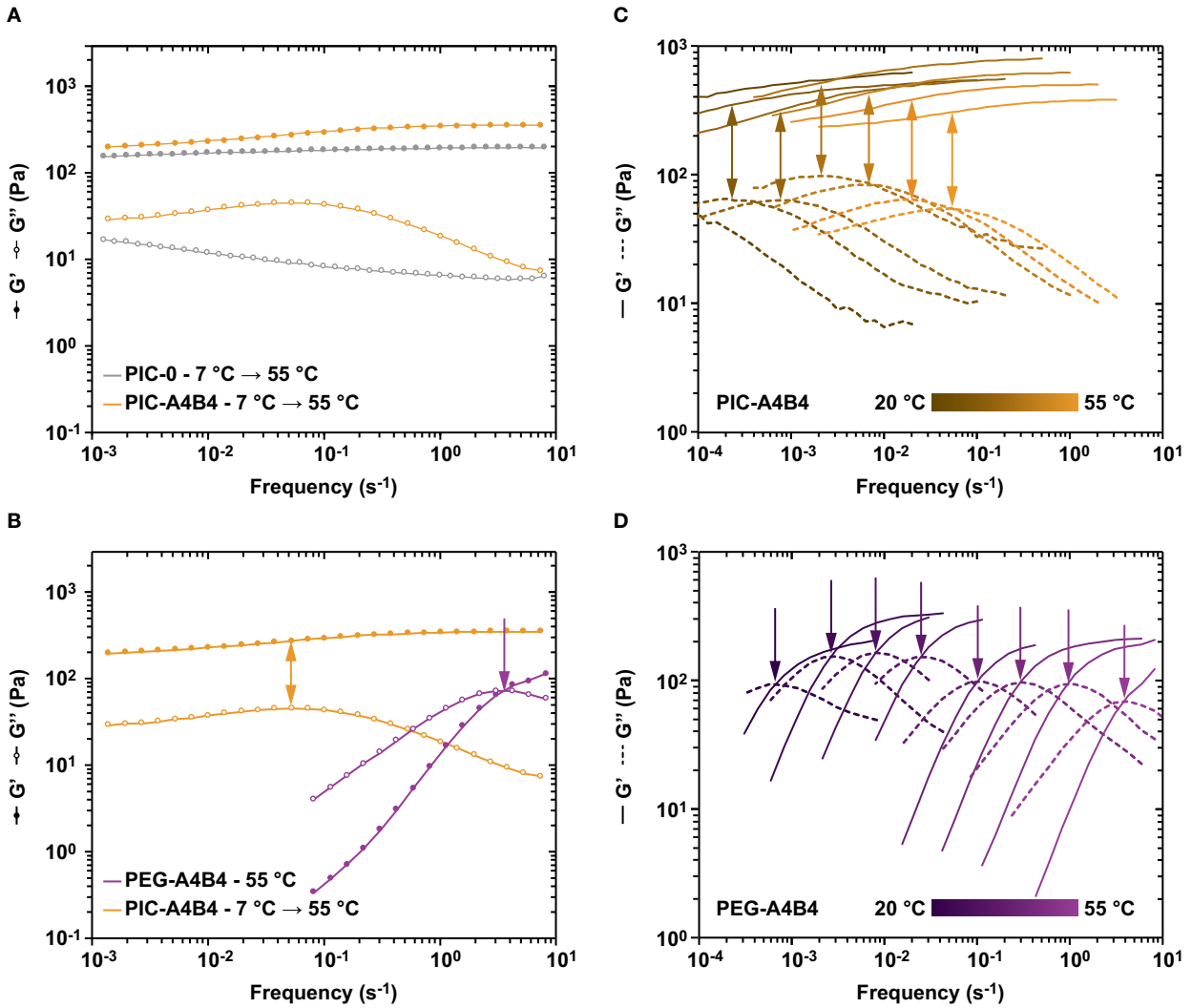

FIGURE 5 | Frequency sweeps of PIC and PEG hydrogels. **(A)** Comparison of PIC-A4B4 and PIC-0 subjected to temperature protocol 1. Lines are drawn to guide the eye. **(B)** Comparison of PIC-A4B4 (temperature protocol 1) and PEG-A4B4 (measured at 55°C). Lines are drawn to guide the eye. **(C)** Comparison of the viscoelastic properties of PIC-A4B4 at different temperatures, ranging from 20 to 55°C. **(D)** Comparison of the viscoelastic properties of PEG-A4B4 at different temperatures, ranging from 20 to 55°C. For the PIC hydrogels, each frequency sweep was performed at a strain amplitude of 1%, while it was set to 10% for the PEG hydrogels. These strain amplitudes are in the linear viscoelastic range of each respective hydrogel. The frequency was varied from 0.0001 to 10 s^{-1}. Additional data sets are shown in **Supplementary Figure 6**.

slower with decreasing temperature. It should be noted that a detailed interpretation of this data is difficult for PIC-A4B4, however, as the kinetically trapped network rearranges during the measurement. Furthermore, the LCST transition is crossed so that contributions from hydrophobic PIC bundling are hidden just as temperature-dependent changes in the L_p of individual PIC polymers and bundles. Despite the contribution of these unquantified additional factors, the shift of the G'' maximum with temperature is similar for PIC-A4B4 and PEG-A4B4 samples.

The most striking result of the PIC-A4B4 and PEG-A4B4 comparison is the clear difference in relaxation times between these networks over the entire temperature range tested. At a temperature of 55°C, the relaxation time differs by approximately two orders of magnitude, even though the crosslink used is exactly the same. This suggests that crosslink kinetics is not the only parameter that determines the relaxation time of a material. In the PEG-A4B4 network, two PEG arms are terminally connected via exactly one crosslink. In the absence of entanglements, crosslink dissociation therefore immediately relaxes an elastically active chain. In a well-crosslinked starPEG network, stress relaxation should thus indeed be mostly determined by the dissociation rate of the crosslink [$k_{off} = 3.2 \cdot 10^{-4}$ s^{-1} at 25°C (Goktas et al., 2018)]. Our results show f_{max} of $\sim 2.5 \cdot 10^{-3}$ s^{-1} at 25°C, which is one order of magnitude higher than k_{off}. This difference is explained by

the presence of network defects, such as loops and superchains, which are known to speed up network relaxation (Annable et al., 1993; Rossow et al., 2014; Ciarella et al., 2018).

The network topology of PIC-A4B4 at 55°C is very different. In hydrophobically stabilized bundles, the CCs form multiple crosslinks within the bundles. Considering a mean polymer length of 412 nm and an average CC spacing of ∼14 nm, one polymer is connected within the bundle via ∼30 crosslinks. In addition, each bundle is estimated to consist of 7–9 polymers so that the next crosslink is on average found within <4 nm along the bundle. Further considering the high L_p of the polymers, re-association of dissociated CCs is thus easily possible. It is, therefore, extremely unlikely that the dissociation of one CC crosslink allows relaxation of a polymer chain or even the entire bundle. Stress relaxation instead requires the dissociation of several crosslinks simultaneously. Multivalent binding of CC crosslinks, determined by the topology of the bundled PIC network, is thus the most likely explanation for the observed increase in the relaxation time.

Based on this knowledge, we now compare the relaxation time of PIC-A4B4 networks below the LCST where hydrophobically stabilized bundles are absent (**Supplementary Figures 6D,E**). Also, for these networks the relaxation time is significantly lower than for PEG-A4B4 (**Supplementary Figures 6C, 8B**). For the PIC-A4B4 hydrogels measured at 20°C, no local maximum in G'' is visible in the accessible frequency range and the maximum is most likely located at much lower frequencies. This suggests that the relaxation of elastically active chains is also hindered by multivalent CC interactions at 20°C, confirming our earlier interpretation that PIC-A4B4 networks also contain bundle-like structures below the LCST. In fact, no significant difference in the frequency dependence is observed for the network equilibrated at 20°C and the network containing kinetically trapped bundles, suggesting that elastically active chains relax in a similar fashion. Even though we are not able to quantitatively compare the relaxation times, our combined results provide sufficient evidence to conclude that the combination of network topology and crosslink kinetics determines the relaxation behavior of elastically active chains in dynamically crosslinked hydrogel networks.

CONCLUSIONS

Introducing CC crosslinks into PIC and starPEG networks has allowed us to directly compare stress relaxation in dynamically crosslinked hydrogels of different network topology. The CC-crosslinked and fiber-like PIC network retains its stress-stiffening properties and displays a relaxation time approximately two orders of magnitude longer than the starPEG reference network. This clearly shows that stress relaxation is determined by a combination of crosslink kinetics and network topology. In the PIC hydrogel, each polymer is connected to the network via multiple CC crosslinks. Stress relaxation of elastically active chains thus requires the simultaneous dissociation of several CCs. In contrast, each elastically active chain is connected by exactly one crosslink in the starPEG network. Controlling the number of crosslinks per chain thus appears to be a possible new design principle for tuning the viscoelastic properties of synthetic polymeric materials. Especially when combined with semi-flexible polymers, adjusting the distance between crosslinks to the persistence length may facilitate the formation of fiber bundles and introduce stress-stiffening behavior into such materials. Hierarchical assembly, stress relaxation and non-linear stress-strain responses are thus tightly connected and can only be engineered in combination. Nature has elegantly utilized this concept in the cytoskeleton and the ECM. These structures show slow macroscopic stress relaxation, but contain fine-tuned dynamic crosslinks that facilitate local network reorganization. This specific interplay between macroscopic and microscopic properties allows cell motility and spreading while maintaining the overall shape of tissues. The CC-crosslinked PIC network serves as an excellent model system to tune crosslink density, kinetics, and thermodynamics independently. This may ultimately provide a stress-stiffening network for cell culture experiments where macroscopic stress relaxation and local crosslink dynamics are decoupled.

DATA AVAILABILITY STATEMENT

The datasets generated for this study can be found in Edmond — the Open Access Data Repository of the Max Planck Society (https://dx.doi.org/10.17617/3.3z).

AUTHOR CONTRIBUTIONS

EG, AL, RH, and KB: conceptualization and validation. EG, IT, DV, and AL: investigation. KB: resources and project administration. EG, IT, and KB: data curation and visualization. EG: writing—original draft. AL, RH, and KB: writing—review and editing. RH, AL, and KB: supervision. AL and KB: funding acquisition. All authors have given approval to the final version of the manuscript.

FUNDING

This work was funded by the Netherlands Organization for Scientific Research (NWO; 711.013.010 and 024.002.009), the Max Planck Society, the International Max Planck Research School on Multiscale Bio-Systems, the Alexander von Humboldt Foundation, and the German Research Foundation (DFG; 189853844-TRR 102, project B17).

ACKNOWLEDGMENTS

We thank Swapneel Deshpande and Hans Heus for inspiring discussions in the early stages of this project.

SUPPLEMENTARY MATERIAL

The Supplementary Material for this article can be found online at: https://www.frontiersin.org/articles/10.3389/fchem.2020.00536/full#supplementary-material

REFERENCES

Akagi, Y., Gong, J. P., Chung, U.-I., and Sakai, T. (2013). Transition between phantom and affine network model observed in polymer gels with controlled network structure. *Macromolecules* 46, 1035–1040. doi: 10.1021/ma302270a

Annable, T., Buscall, R., Ettelaie, R., and Whittlestone, D. (1993). The rheology of solutions of associating polymers: comparison of experimental behavior with transient network theory. *J. Rheol.* 37, 695–726. doi: 10.1122/1.550391

Appel, E. A., Forster, R. A., Koutsioubas, A., Toprakcioglu, C., and Scherman, O. A. (2014). Activation energies control the macroscopic properties of physically cross-linked materials. *Angew. Chem. Int. Ed.* 53, 10038–10043. doi: 10.1002/anie.201403192

Asai, H., Fujii, K., Ueki, T., Sakai, T., Chung, U.-I., Watanabe, M., et al. (2012). Structural analysis of high performance ion-gel comprising tetra-PEG network. *Macromolecules* 45, 3902–3909. doi: 10.1021/ma300244u

Broedersz, C. P., Kasza, K. E., Jawerth, L. M., Münster, S., Weitz, D. A., and Mackintosh, F. C. (2010). Measurement of nonlinear rheology of cross-linked biopolymer gels. *Soft. Matter.* 6, 4120–4127. doi: 10.1039/c0sm00285b

Chaudhuri, O., Gu, L., Darnell, M., Klumpers, D., Bencherif, S. A., Weaver, J. C., et al. (2015). Substrate stress relaxation regulates cell spreading. *Nat. Commun.* 6:6365. doi: 10.1038/ncomms7365

Chaudhuri, O., Gu, L., Klumpers, D., Darnell, M., Bencherif, S. A., Weaver, J. C., et al. (2016). Hydrogels with tunable stress relaxation regulate stem cell fate and activity. *Nat. Mater.* 15, 326–334. doi: 10.1038/nmat4489

Ciarella, S., Sciortino, F., and Ellenbroek, W. G. (2018). Dynamics of vitrimers: defects as a highway to stress relaxation. *Phys. Rev. Lett.* 121:058003. doi: 10.1103/PhysRevLett.121.058003

Claessens, M. M. A. E., Bathe, M., Frey, E., and Bausch, A. R. (2006). Actin-binding proteins sensitively mediate F-actin bundle stiffness. *Nat. Mater.* 5, 748–753. doi: 10.1038/nmat1718

Cornelissen, J. J., Donners, J. J., De Gelder, R., Graswinckel, W. S., Metselaar, G. A., Rowan, A. E., et al. (2001). β-Helical polymers from isocyanopeptides. *Science* 293, 676–680. doi: 10.1126/science.1062224

Dånmark, S., Aronsson, C., and Aili, D. (2016). Tailoring supramolecular peptide–poly(ethylene glycol) hydrogels by coiled coil self-assembly and self-sorting. *Biomacromolecules* 17, 2260–2267. doi: 10.1021/acs.biomac.6b00528

Das, R. K., Gocheva, V., Hammink, R., Zouani, O. F., and Rowan, A. E. (2016). Stress-stiffening-mediated stem-cell commitment switch in soft responsive hydrogels. *Nat. Mater.* 15, 318–325. doi: 10.1038/nmat4483

Deshpande, S. R., Hammink, R., Das, R. K., Nelissen, F. H. T., Blank, K. G., Rowan, A. E., et al. (2016). DNA-responsive polyisocyanopeptide hydrogels with stress-stiffening capacity. *Adv. Funct. Mater.* 26, 9075–9082. doi: 10.1002/adfm.201602461

Deshpande, S. R., Hammink, R., Nelissen, F. H. T., Rowan, A. E., and Heus, H. A. (2017). Biomimetic stress sensitive hydrogel controlled by DNA nanoswitches. *Biomacromolecules* 18, 3310–3317. doi: 10.1021/acs.biomac.7b00964

Egan, P., Sinko, R., Leduc, P. R., and Keten, S. (2015). The role of mechanics in biological and bio-inspired systems. *Nat. Commun.* 6:7418. doi: 10.1038/ncomms8418

Fletcher, J. M., Harniman, R. L., Barnes, F. R. H., Boyle, A. L., Collins, A., Mantell, J., et al. (2013). Self-assembling cages from coiled-coil peptide modules. *Science* 340, 595–599. doi: 10.1126/science.1233936

Goktas, M., Luo, C., Sullan, R. M. A., Bergues-Pupo, A. E., Lipowsky, R., Vila Verde, A., et al. (2018). Molecular mechanics of coiled coils loaded in the shear geometry. *Chem. Sci.* 9, 4610–4621. doi: 10.1039/C8SC01037D

Gralka, M., and Kroy, K. (2015). Inelastic mechanics: a unifying principle in biomechanics. *Biochim. Biophys. Acta, Mol. Cell Res.* 1853, 3025–3037. doi: 10.1016/j.bbamcr.2015.06.017

Grindy, S. C., Learsch, R., Mozhdehi, D., Cheng, J., Barrett, D. G., Guan, Z., et al. (2015). Control of hierarchical polymer mechanics with bioinspired metal-coordination dynamics. *Nat. Mater.* 14, 1210–1216. doi: 10.1038/nmat4401

Gu, Y., Alt, E. A., Wang, H., Li, X., Willard, A. P., and Johnson, J. A. (2018). Photoswitching topology in polymer networks with metal–organic cages as crosslinks. *Nature* 560, 65–69. doi: 10.1038/s41586-018-0339-0

Jaspers, M., Dennison, M., Mabesoone, M. F. J., Mackintosh, F. C., Rowan, A. E., and Kouwer, P. H. J. (2014). Ultra-responsive soft matter from strain-stiffening hydrogels. *Nat. Commun.* 5:5808. doi: 10.1038/ncomms6808

Jaspers, M., Pape, A. C. H., Voets, I. K., Rowan, A. E., Portale, G., and Kouwer, P. H. J. (2016). Bundle formation in biomimetic hydrogels. *Biomacromolecules* 17, 2642–2649. doi: 10.1021/acs.biomac.6b00703

Jaspers, M., Vaessen, S. L., Van Schayik, P., Voerman, D., Rowan, A. E., and Kouwer, P. H. J. (2017). Nonlinear mechanics of hybrid polymer networks that mimic the complex mechanical environment of cells. *Nat. Commun.* 8:15478. doi: 10.1038/ncomms15478

Kollmannsberger, P., and Fabry, B. (2011). Linear and nonlinear rheology of living cells. *Annu. Rev. Mater. Res.* 41, 75–97. doi: 10.1146/annurev-matsci-062910-100351

Kouwer, P. H. J., De Almeida, P., Ven Den Boomen, O., Eksteen-Akeroyd, Z. H., Hammink, R., Jaspers, M., et al. (2018). Controlling the gelation temperature of biomimetic polyisocyanides. *Chin. Chem. Lett.* 29, 281–284. doi: 10.1016/j.cclet.2017.11.002

Kouwer, P. H. J., Koepf, M., Le Sage, V. A. A., Jaspers, M., Van Buul, A. M., et al. (2013). Responsive biomimetic networks from polyisocyanopeptide hydrogels. *Nature* 493, 651–655. doi: 10.1038/nature11839

Kushner, A. M., and Guan, Z. (2011). Modular design in natural and biomimetic soft materials. *Angew. Chem., Int. Ed.* 50, 9026–9057. doi: 10.1002/anie.201006496

Lange, F., Schwenke, K., Kurakazu, M., Akagi, Y., Chung, U.-I., Lang, M., et al. (2011). Connectivity and structural defects in model hydrogels: a combined proton NMR and monte carlo simulation study. *Macromolecules* 44, 9666–9674. doi: 10.1021/ma201847v

Lansky, Z., Braun, M., Lüdecke, A., Schlierf, M., Ten wolde, P. R., Janson, M. E., et al. (2015). Diffusible crosslinkers generate directed forces in microtubule networks. *Cell* 160, 1159–1168. doi: 10.1016/j.cell.2015.01.051

Li, Q., Barrett, D. G., Messersmith, P. B., and Holten-Andersen, N. (2016). Controlling Hydrogel mechanics via bio-inspired polymer–nanoparticle bond dynamics. *ACS Nano* 10, 1317–1324. doi: 10.1021/acsnano.5b06692

Lieleg, O., Kayser, J., Brambilla, G., Cipelletti, L., and Bausch, A. R. (2011). Slow dynamics and internal stress relaxation in bundled cytoskeletal networks. *Nat. Mater.* 10, 236–242. doi: 10.1038/nmat2939

Lin, Y.-C., Yao, N. Y., Broedersz, C. P., Herrmann, H., Mackintosh, F. C., and Weitz, D. A. (2010). Origins of elasticity in intermediate filament networks. *Phys. Rev. Lett.* 104:058101. doi: 10.1103/PhysRevLett.104.058101

Ljubetič, A., Lapenta, F., Gradišar, H., Drobnak, I., Aupič, J., Strmšek, Ž., et al. (2017). Design of coiled-coil protein-origami cages that self-assemble *in vitro* and *in vivo*. *Nat. Biotechnol.* 35, 1094–1101. doi: 10.1038/nbt.3994

Lorenz, J. S., Schnau, ß, J., Glaser, M., Sajfutdinow, M., Schuldt, C., Käs, J. A., et al. (2018). Synthetic transient crosslinks program the mechanics of soft, biopolymer-based materials. *Adv. Mater.* 30:1706092. doi: 10.1002/adma.201706092

Lupas, A. (1996). Coiled coils: new structures and new functions. *Trends Biochem. Sci.* 21, 375–382. doi: 10.1016/0968-0004(96)10052-9

Mandal, S., Eksteen-Akeroyd, Z. H., Jacobs, M. J., Hammink, R., Koepf, M., Lambeck, A. J. A., et al. (2013). Therapeutic nanoworms: towards novel synthetic dendritic cells for immunotherapy. *Chem. Sci.* 4, 4168–4174. doi: 10.1039/c3sc51399h

McKinnon, D. D., Domaille, D. W., Cha, J. N., and Anseth, K. S. (2014). Biophysically defined and cytocompatible covalently adaptable networks as viscoelastic 3D cell culture systems. *Adv. Mater.* 26, 865–872. doi: 10.1002/adma.201303680

Petka, W. A., Harden, J. L., Mcgrath, K. P., Wirtz, D., and Tirrell, D. A. (1998). Reversible hydrogels from self-assembling artificial proteins. *Science* 281, 389–392. doi: 10.1126/science.281.5375.389

Rossow, T., Habicht, A., and Seiffert, S. (2014). Relaxation and dynamics in transient polymer model networks. *Macromolecules* 47, 6473–6482. doi: 10.1021/ma5013144

Sakai, T., Matsunaga, T., Yamamoto, Y., Ito, C., Yoshida, R., Suzuki, S., et al. (2008). Design and fabrication of a high-strength hydrogel with ideally homogeneous network structure from tetrahedron-like macromonomers. *Macromolecules* 41, 5379–5384. doi: 10.1021/ma800476x

Schmoller, K. M., Lieleg, O., and Bausch, A. R. (2008). Internal stress in kinetically trapped actin bundle networks. *Soft. Matter.* 4, 2365–2367. doi: 10.1039/b808582j

Schmoller, K. M., Lieleg, O., and Bausch, A. R. (2009). Structural and viscoelastic properties of actin/filamin networks: cross-linked versus bundled networks. *Biophys. J.* 97, 83–89. doi: 10.1016/j.bpj.2009.04.040

Schoenmakers, D. C., Rowan, A. E., and Kouwer, P. H. J. (2018a). Crosslinking of fibrous hydrogels. *Nat. Commun.* 9:2172. doi: 10.1038/s41467-018-04508-x

Schoenmakers, D. C., Schoonen, L., Rutten, M. G. T. A., Nolte, R. J. M., Rowan, A. E., Van Hest, J. C. M., et al. (2018b). Virus-like particles as crosslinkers in fibrous biomimetic hydrogels: approaches towards capsid rupture and gel repair. *Soft. Matter.* 14, 1442–1448. doi: 10.1039/C7SM02320K

Shen, W., Kornfield, J. A., and Tirrell, D. A. (2007). Dynamic properties of artificial protein hydrogels assembled through aggregation of leucine zipper peptide domains. *Macromolecules* 40, 689–692. doi: 10.1021/ma0615194

Storm, C., Pastore, J. J., Mackintosh, F. C., Lubensky, T. C., and Janmey, P. A. (2005). Nonlinear elasticity in biological gels. *Nature* 435, 191–194. doi: 10.1038/nature03521

Strehle, D., Schnauß, J., Heussinger, C., Alvarado, J., Bathe, M., Käs, J., et al. (2011). Transiently crosslinked F-actin bundles. *Eur. Biophys. J.* 40, 93–101. doi: 10.1007/s00249-010-0621-z

Tan, C. S. Y., Agmon, G., Liu, J., Hoogland, D., Janeček, E.-R., Appel, E. A., et al. (2017). Distinguishing relaxation dynamics in transiently crosslinked polymeric networks. *Polym. Chem.* 8, 5336–5343. doi: 10.1039/C7PY00574A

Tang, S., Ma, H., Tu, H.-C., Wang, H.-R., Lin, P.-C., and Anseth, K. S. (2018). Adaptable fast relaxing boronate-based hydrogels for probing cell–matrix interactions. *Adv. Sci.* 5:1800638. doi: 10.1002/advs.201800638

Thomas, F., Boyle, A. L., Burton, A. J., and Woolfson, D. N. (2013). A set of *de novo* designed parallel heterodimeric coiled coils with quantified dissociation constants in the micromolar to sub-nanomolar regime. *J. Am. Chem. Soc.* 135, 5161–5166. doi: 10.1021/ja312310g

Tunn, I., De Léon, A. S., Blank, K. G., and Harrington, M. J. (2018). Tuning coiled coil stability with histidine-metal coordination. *Nanoscale* 10, 22725–22729. doi: 10.1039/C8NR07259K

Tunn, I., Harrington, M. J., and Blank, K. G. (2019). Bioinspired histidine–Zn2+ coordination for tuning the mechanical properties of self-healing coiled coil cross-linked hydrogels. *Biomimetics* 4:25. doi: 10.3390/biomimetics4010025

van Buul, A. M., Schwartz, E., Brocorens, P., Koepf, M., Beljonne, D., Maan, J. C., et al. (2013). Stiffness versus architecture of single helical polyisocyanopeptides. *Chem. Sci.* 4, 2357–2363. doi: 10.1039/c3sc50552a

Vandaele, J., Louis, B., Liu, K., Camacho, R., Kouwer, P. H. J., and Rocha, S. (2020). Structural characterization of fibrous synthetic hydrogels using fluorescence microscopy. *Soft. Matter.* 16, 4210–4219. doi: 10.1039/C9SM01828J

Wang, C., Stewart, R. J., and Kopeček, J. (1999). Hybrid hydrogels assembled from synthetic polymers and coiled-coil protein domains. *Nature* 397, 417–420. doi: 10.1038/17092

Wei, X., Zhu, Q., Qian, J., Lin, Y., and Shenoy, V. B. (2016). Response of biopolymer networks governed by the physical properties of cross-linking molecules. *Soft. Matter.* 12, 2537–2541. doi: 10.1039/C5SM02820E

Wolgemuth, C. W., and Sun, S. X. (2006). Elasticity of α-helical coiled coils. *Phys. Rev. Lett.* 97:248101. doi: 10.1103/PhysRevLett.97.248101

Woolfson, D. N. (2005). The design of coiled-coil structures and assemblies. *Adv. Protein Chem.* 70, 79–112. doi: 10.1016/S0065-3233(05)70004-8

Yang, J., Xu, C., Wang, C., and Kopeček, J. (2006). Refolding hydrogels self-assembled from N-(2-hydroxypropyl)methacrylamide graft copolymers by antiparallel coiled-coil formation. *Biomacromolecules* 7, 1187–1195. doi: 10.1021/bm051002k

Yount, W. C., Loveless, D. M., and Craig, S. L. (2005). Strong means slow: dynamic contributions to the bulk mechanical properties of supramolecular networks. *Angew. Chem. Int. Ed.* 44, 2746–2748. doi: 10.1002/anie.200500026

Conflict of Interest: The authors declare that the research was conducted in the absence of any commercial or financial relationships that could be construed as a potential conflict of interest.

Advantages of publishing in Frontiers

OPEN ACCESS
Articles are free to read for greatest visibility and readership

FAST PUBLICATION
Around 90 days from submission to decision

HIGH QUALITY PEER-REVIEW
Rigorous, collaborative, and constructive peer-review

TRANSPARENT PEER-REVIEW
Editors and reviewers acknowledged by name on published articles

Frontiers
Avenue du Tribunal-Fédéral 34
1005 Lausanne | Switzerland

Visit us: www.frontiersin.org
Contact us: info@frontiersin.org | +41 21 510 17 00

REPRODUCIBILITY OF RESEARCH
Support open data and methods to enhance research reproducibility

DIGITAL PUBLISHING
Articles designed for optimal readership across devices

FOLLOW US
@frontiersin

IMPACT METRICS
Advanced article metrics track visibility across digital media

EXTENSIVE PROMOTION
Marketing and promotion of impactful research

LOOP RESEARCH NETWORK
Our network increases your article's readership